

CVZ 66996

Classification changed
to Unclassified

NASA NGJ
Memo dated
10/22/74

December 4, 1967

Downgraded at 3 year intervals;
declassified after 12 years
DOD DIR 5200.10

APPROVED BY: Henry J. Lopez
Henry J. Lopez
HRE Program Manager

REVISIONS				ADDITIONS			
PAGE	DATE	PAGE	DATE	PAGE	DATE	PAGE	DATE

THIS COPY IS UNCLASSIFIED

UNCLASSIFIED

FOREWORD

This Interim Technical Data Report is submitted to the NASA Langley Research Center by the AiResearch Manufacturing Company, Los Angeles, California. The document was prepared in accordance with the guidelines established by Paragraph 6.3.3.2 of NASA Statement Of Work L-4947-B.

Interim Technical Data Reports are generated on a quarterly basis for major program tasks under the Hypersonic Research Engine Project. Upon completion of a given task effort, a Final Technical Data Report will be submitted.

The document in hand presents a detailed technical discussion of the Structures and Cooling Development for the period of 3 August through 2 November 1967.



AIRESEARCH MANUFACTURING DIVISION
Los Angeles, California

67-2833

Page i

UNCLASSIFIED

UNCLASSIFIED

ACKNOWLEDGMENTS

Acknowledgments for completion of this document are herewith extended to the following contributors:

Design and Development: O. A. Buchmann, C. M. Lee, and A. I. Stern

Heat Transfer Analyses: F. M. Walters, S. M. Cho, J. A. Shupek,
A. A. Vuigner, and C. F. Young

Manufacturing: J. M. Hassett

Stress Analyses: W. G. Flieder, E. Katinszky, A. Levitsky, C. E.
Richard. and S. Tepper



AIRESEARCH MANUFACTURING DIVISION
Los Angeles, California

67-2833
Page ii

UNCLASSIFIED

CONTENTS

<u>Paragraph</u>		<u>Page</u>
1.	SUMMARY	1-1 to 1-3
1.1	Overall Engine Design	1-1
1.2	Full-Scale Component Design	1-1
1.3	Component Test Assembly Design	1-1
1.4	Full-Scale Component Manufacture	1-2
1.5	Inlet Spike Actuator	1-2
1.6	Structural Elements and Models	1-2
1.7	Compound-Curved Model	1-3
2.	PROBLEM STATEMENT	2-1
3.	TOPICAL BACKGROUND	3-1 to 3-6
3.1	General Design Guidelines	3-1
3.2	Operational Boundaries	3-3
4.	OVERALL APPROACH	4-1 to 4-6
4.1	Thermal Design	4-2
4.2	Structural Design	4-3
4.3	Mechanical Design	4-4
4.4	Manufacturing	4-5
5.	ANALYTICAL DESIGN	5-1 to 5-159
5.1	Design Conditions and Loads	5-1
5.2	Aerodynamic Heating Correlation	5-43
5.3	Engine Dynamic Analysis	5-65
5.4	Engine Vibration Model	5-75
5.5	Cooling System	5-81
5.6	Mission Coolant Requirements	5-107
5.7	Ablatively Cooled Cowl	5-119
5.8	Inlet Spike	5-133
5.9	Inlet Spike Actuator	5-141
5.10	Outer Body-Inner Body Struts	5-148
5.11	Inner Body Test Assembly	5-148



UNCLASSIFIED

CONTENTS (Continued)

<u>Paragraph</u>		<u>Page</u>
6.	DESIGN EFFORT	6-1 to 6-10
6.1	Qualification Test Engine	6-1
6.2	Inner Body Test Assembly	6-7
6.3	Inlet Spike Actuator	6-9
7.	MANUFACTURING	7-1 to 7-33
7.1	Compound-Curved Models	7-1
7.2	Flat Panels	7-7
7.3	Outer Body Leading Edge Straight Section	7-13
7.4	Strut Test Section	7-26
8.	TESTING	8-1 to 8-77
8.1	Flat Panel Rupture	8-1
8.2	Thermal Cycle Panels	8-5
8.3	Flow Test Panels	8-26
8.4	Compound Curved Model	8-38
8.5	Inlet Spike Tip	8-45
8.6	Continuous Joint Panel (Nozzle Crossover Manifold)	8-48
8.7	Leading Edge Straight Section	8-63
8.8	Support Strut	8-70
8.9	Tube-Manifold Joint Specimens	8-75
9.	FUTURE ACTION	9-1 to 9-3
9.1	Full-Scale Component Design Revision	9-1
9.2	Engine Dynamic Analyses	9-1
9.3	Inlet Spike Actuator Design	9-1
9.4	Vibration Model Design	9-1
9.5	Outerbody Leading Edge Cooling System	9-2
9.6	Component Test Assembly Design	9-2



UNCLASSIFIED

UNCLASSIFIED

CONTENTS (Continued)

<u>Paragraph</u>	<u>Page</u>
9.7 Engine Surface Insulation	9-2
9.8 "Electroshape" Forming Evaluation	9-2
9.9 Leading Edge Testing	9-2
9.10 Strut Testing	9-2
9.11 Thermal Cycle Testing	9-3
9.12 Full-Scale Component Fabrication	9-3
9.13 Fuel Conservation	9-3



AIRESEARCH MANUFACTURING DIVISION
Los Angeles, California

67-2833
Page v

UNCLASSIFIED

UNCLASSIFIED

I. SUMMARY

I.1 OVERALL ENGINE DESIGN

The layout drawing of the qualification test engine has been completed and was formally reviewed on October 10, 1967. The design as presented was based on loads and aerodynamic parameters for Mach 8, 88,000 ft operation of the engine in the free stream. Both the external loads and the environmental conditions have been revised in the meantime to reflect operation of the engine in the shock field of the X-15A-2 and to reflect the conditions that accompany unsymmetrical inlet unstarts.

The mathematical dynamic model of the engine has been completed and preliminary simulation runs have been made.

I.2 FULL-SCALE COMPONENT DESIGN

Full-scale component design has been delayed pending final definition of the revised structural loads. However, all inner body (inner shell and nozzle) detail drawings have been released for manufacture. The impact of the load changes on this component will be reflected in detail changes, rather than basic conceptual changes, and will not affect the validity of the manufacturing and test experience to be gained with the current design. The inlet spike has been reevaluated to reflect the new structural changes because of the relatively major impact the revised loads will have on its design. Detailing of the inlet spike is currently in process, following completion of the structural analysis. The outer shell is similarly being completely reevaluated for the new structural loads because of the important effect these loads have on the engine mounting structure.

Operation of the engine in the X-15A-2 shock field has also led to re-evaluation of the thermal design for the cowl leading edge.

I.3 COMPONENT TEST ASSEMBLY DESIGN

Layout design of component test assemblies and the test adapters has been initiated during the interim period involving the definition of new loads and reevaluation of the full-scale component designs with these new loads. Layout of the test assembly and adapter for the inner body has been completed. With relatively minor changes, the test adapter will be usable for the inlet spike also. Layout design of the test assembly and adapter for the leading edge is in process.



AIRESEARCH MANUFACTURING DIVISION
Los Angeles, California

67-2833
Page 1-1

UNCLASSIFIED

UNCLASSIFIED

1.4 FULL-SCALE COMPONENT MANUFACTURE

Manufacture of full-scale components falls into two basic categories. One of these involves fabrication of the shells and the tooling required to produce these shells, and the other involves fabrication of the detail parts and assemblies other than the shells. Detail design drawings for all full-scale component shells have been released. Both shell and tooling fabrication is proceeding and is not affected by revised load conditions. Fabrication of detail components is proceeding for the innerbody and the leading edge. Because the inlet spike and outer shell are both severely affected by revised load conditions, no detail fabrication has been initiated for these two components. In the case of the leading edge tip, fabrication has been stopped because of the pending redesign. Fabrication of other leading edge components is proceeding.

1.5 INLET SPIKE ACTUATOR

Reevaluation of the inlet spike actuator design, as completed on the basis of previous loads, has shown that the structural design is adequate for the revised loads. The bearing pressures with the revised loads, however, as well as the actuation forces, have increased appreciably and have led to a review of the actuator functional design. The need for increasing the bearing areas and the feasibility of using hydraulic power to drive the actuator are both being reviewed. Previously completed detail drawings for the inlet spike actuator have not been released for fabrication because major design revisions are likely.

1.6 STRUCTURAL ELEMENTS AND MODELS

Design of all structural element and model test sections has been completed, except for a revised leading edge straight section tip. Fabrication of all test sections is in process.

1.6.1 Flat Panels

All originally-planned flat-panel burst and creep-rupture testing has been completed, and thermal cycle tests have been run on several flat panels.

1.6.2 Leading Edge Straight Section

Fabrication of the initial leading edge straight section has been completed. The unit has been installed in the flow test facility for thermal calibration and cycle tests. Design of a second leading edge configuration is in process. This second configuration will reflect the design evolved for the leading edge tip assembly for operation in the airplane shock field.

The revised loading conditions will require redefinition of the leading edge tip (stagnation area). The former design, which had been previously completed, is incompatible with the extremely high heat fluxes encountered on the stagnation line (up to 1700 Btu/sec ft²). In addition, the need for coolant conservation during the ascent and descent portions of the HRE missions imposes severe requirements on the design. Analysis has been completed and revision tip layout and detail drawings are in process.



UNCLASSIFIED

UNCLASSIFIED

Except for the leading edge tip, the more severe thermal loads encountered in the airplane shock field will not be reflected in R&D component design. Basic concepts for the regeneratively-cooled shells will remain unchanged. Use of fuel-limited operation at $M_\infty = 8$, $M_L = 6.5$, $\alpha_L = 4$ deg, $q_\infty = 1800$ psf, $q_L = 3240$ psfa, will result in internal heating conditions only slightly more severe than those encountered for $M_\infty = 8$, engine in the free stream. Similarly, with small angles of attack in the shock field, heating conditions are comparable to $M_\infty = 8$, engine in the free stream design condition. Full-scale components, in turn will be evaluated thermally to the previously-used design conditions, except for the leading edge, for which temperature gradients experienced at the stagnation area in the shock field will be simulated.

1.6.3 Strut

The initial strut body has been brazed. The fixture to be used for supersonic testing of the strut is in process of fabrication.

1.7 COMPOUND-CURVED MODEL

A total of four compound-curved model shell assemblies have been brazed. Of these, the first two were fabricated from rejected parts and were used to evaluate brazing procedures. The second two compound-curved models, which incorporate headers, have been subjected to proof and high temperature burst testing. Additional shell assemblies are being fabricated, as are separate assemblies incorporating typical ring manifolds, for evaluation of manifold-to-shell brazing.



UNCLASSIFIED

2.0 PROBLEM STATEMENT

The objective of the structures and cooling development program is to analyze, design, and fabricate the regeneratively cooled surfaces and their associated structures and to verify the performance of these surfaces and structures at conditions that simulate the operating conditions expected in the flight test engine.

The Hypersonic Research Engine requires regenerative cooling on all surfaces that contact the engine airstream. The use of ablative coating on the engine aerodynamic surfaces is barred by the Statement of Work to minimize extraneous effects on engine performance. No such restriction is imposed on the engine cowl; therefore, ablative protection is used for this component.

The characteristic design problem in regeneratively cooled structures for this type of application is associated with the large heat fluxes encountered over major portions of the engine surfaces. These heat fluxes range from values of approximately 10 Btu/sec-ft² to 1400 Btu/sec-ft² on the stagnation line of the support strut leading edge. The conservation of fuel requires that these heat fluxes be accommodated at temperature differences across the regeneratively cooled surfaces which range up to approximately 600°F in flat surfaces and 1000°F in leading-edge areas. These temperature differences, in turn, result in strains that cause plastic deformation of the hot surfaces. Design therefore is governed by low-cycle fatigue conditions. Uncertainties associated with the prediction of low-cycle fatigue performance have led to heavy emphasis, in the experimental portion of the program, on the evaluation of the low-cycle fatigue performance of the engine components.

The general performance objectives set for the cooled structures are as follows:

Design life - 10 hr of hot operation, of which 3 hr are to be taken at Mach 7 to 8 flight conditions

Cycle life - 100 cycles, at conditions which produce the highest plastic strain



3. TOPICAL BACKGROUND

The cooled structures, which are being designed, fabricated, and tested as part of this task, and the associated connecting structures constitute the basic structural elements of the engine. The cooled surfaces of these structures form the aerodynamic surfaces of the engine, as shown in Figure 3.0-1.

3.1 GENERAL DESIGN GUIDELINES

The regeneratively-cooled surfaces must be designed and fabricated to minimize engine performance losses. In addition to providing the basic contours, the cooled surfaces must be fabricated and assembled in a way that avoids discontinuities; leading edges must use the minimum radius compatible with reliable structural design.

Because of the research nature of the HRE program, temperatures and pressures will be measured throughout the engine. Consequently, the engine structure must accommodate static pressure taps and metal temperature thermocouples.

The total amount of fuel available to the engine and for cooling of the structure is severely limited by X-15A-2 storage capabilities. Consequently, in cooling the structure, fuel usage in excess of combustion requirements must be minimized. To accomplish this goal, the cooled surfaces must function at maximum metal temperatures and temperature differences compatible with sound structural design.

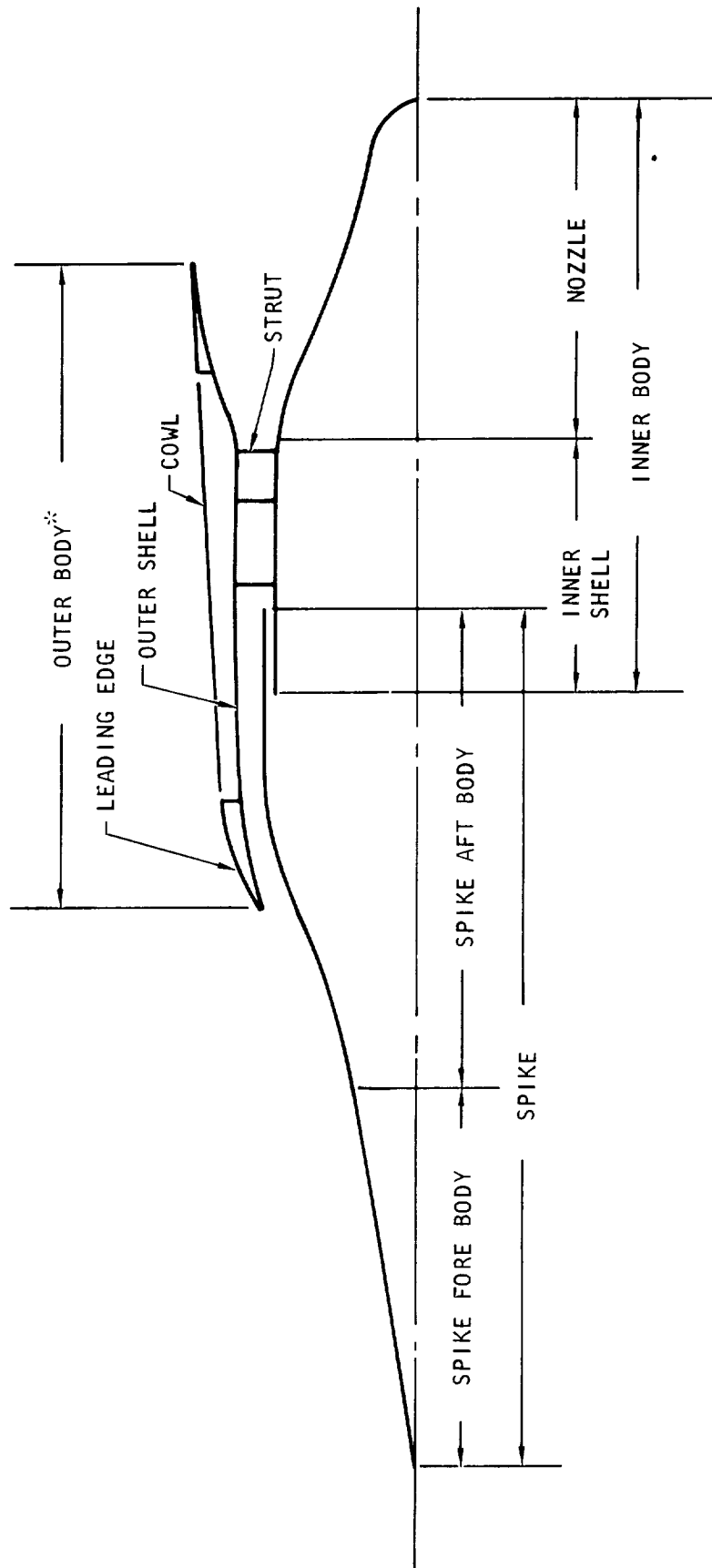
Engine internal structures and plumbing must be designed to allow space for installing fuel system components, engine controls, instrumentation transducers, and signal conditioning equipment. Because of operating limitations, electronic equipment must be installed in locations having the least severe environment.

To permit the engine to operate over the flight Mach number range from 3 to 8, the inlet spike must be translated to various positions. To conserve coolant prior to and after engine operation, the inlet spike must be translated to a position nearly in contact with the outer body leading edge. Consequently, it is necessary to have a spike actuation system capable of the desired positioning accuracy, with control provided by the control system computer.

Engine fuel pressurization is provided by a hydrogen turbopump. Therefore, the total pressure drop in the regeneratively-cooled surfaces, manifolds, and associated plumbing must be compatible with the pressure output of the turbopump.



UNCLASSIFIED



*OUTER BODY = LEADING EDGE + OUTER SHELL

A-30504

Figure 3.0-1. Cooled Structures Nomenclature



AIRESEARCH MANUFACTURING DIVISION
Los Angeles, California

67-2833
Page 3-2

UNCLASSIFIED

UNCLASSIFIED

In addition to control of temperatures and temperature differences, the integrity of the coolant structures requires that the flow routes within the engine be matched in such a way as to minimize temperature differences at axial stations for inner body and outer body surfaces. This will minimize distortion of the engine internal passages. Axial temperature discontinuities, as produced, for example, by the termination of two flow routes that differ greatly in temperature at the same station, are objectionable because of the severe thermal strains that result.

Measurement of engine internal thrust during flight is required. Consequently, external loads (drag and lift) that are transmitted directly to the thrust measuring device must be minimized. Specifically, the engine cowl has drag loads that are of the same order of magnitude as the engine thrust. Mounting of the cowl in such a way as to minimize this external drag load, and thus the uncertainties in calculation of thrust, is therefore required.

A basic engine design requirement is that malfunction of the engine will not endanger the safety of the aircraft or the life of the pilot. Therefore, provision must be made to jettison the engine. Because of probable hydrogen leakage to the engine cavities, the inner body engine cavity must either be inerted or must be capable of containing an explosive mixture of hot hydrogen and air. To accomplish this, the engine cavity will be vented to near nozzle base pressure and provisions will be made for explosion containment. During ground checkout, the engine cavity will be inerted with nitrogen.

The weight of cooled structures, inlet spike actuation system, internal supporting structures, and plumbing are most of the total engine weight. Although optimization of the structures and structural components for minimum weight is not an objective, the specified weight limitation requires careful consideration of structural weight.

The instrumentation, controls, and fuel subsystems contained in the engine cavity will require servicing prior to and after each test. Consequently, the mechanical assembly of the engine cooled structure components must provide easy access to subsystem components for replacement in the field.

3.2 OPERATIONAL BOUNDARIES

3.2.1 General Design Ground Rules

The maximum dynamic pressure specified for the current phase of the program is 2000 psfa. This compares with the specified dynamic pressure of 2500 psfa, specified for the HRE Phase I program. Consequently, the minimum altitude at Mach 8, during which cooling must be provided, is 85,000 ft, as compared to the Phase I minimum altitude of 81,000 ft. The minimum design altitude for the current program is 88,000 ft. The increased altitude results in a reduction of heat flux throughout the engine, but this reduction is offset in part by an increase in engine contraction ratio from 10 in Phase I to 4.6 in Phase IIA. In summary, the operating envelope for the engine is as follows:



AIRESEARCH MANUFACTURING DIVISION
Los Angeles, California

67-2833
Page 3-3

UNCLASSIFIED

UNCLASSIFIED

Engine Structural Design - With engine either lit or not lit, dynamic pressure (q) = 2000 psfa

Engine Cooling Design

Normal design, engine lit: $q = 1750$ psfa, $h = 88,000$ ft minimum.

Emergency design, engine lit: $q = 2000$ psfa, $h = 85,000$ ft minimum.

For the emergency design, engine lit conditions, all of the pump output pressure is available for coolant pressure drop. The dump valve opens and fuel injection valves close as the aircraft approaches these conditions from the normal operating line.

3.2.1 Engine Operating Cycles

A qualitative definition of the engine operating cycles has been formed for the purpose of providing a basis for analyzing heat transfer transients, evaluating the structural effect of transient temperature differences, establishing general control requirements and typical environmental conditions, and for defining acceptable operating cycles. The types of missions or conditions the engine must survive are as follows:

Case I - Constant M , with aircraft power on, at a constant high q

Case II - Constant M , with aircraft power off, aircraft diving

Case III - Variable M , expected to involve a change in M of 0.5 during 20-sec engine operating cycle

Case IV - Subsonic-supersonic combustion transition at $M = 6$

Case V - Inlet unstart, with shock expelled

Figure 3.2-1 is a qualitative representation of the critical cases. The common features, typical for all missions, are numbered on the figure and are as follows:

1. Launch to $M = 3+$, during which the engine structure is assumed to go from a soak at -65°F to a soak at 1140°F . No cooling is required. At the end of this period, the helium purge is performed and coolant flow started through all portions of the cooled structure.
2. Approach to test Mach number, inlet closed (leakage flow only), during which coolant flow is increased to maintain maximum structure temperature (cold surface) at 1140°F .
3. Time for retraction of inlet spike to desired position. The solid line assumes programmed cooling flow; the dashed line assumes controlled cooling flow based on temperature sensing. The approach selected will be a function of control system response and actuating system response. Controlled cooling is preferred.

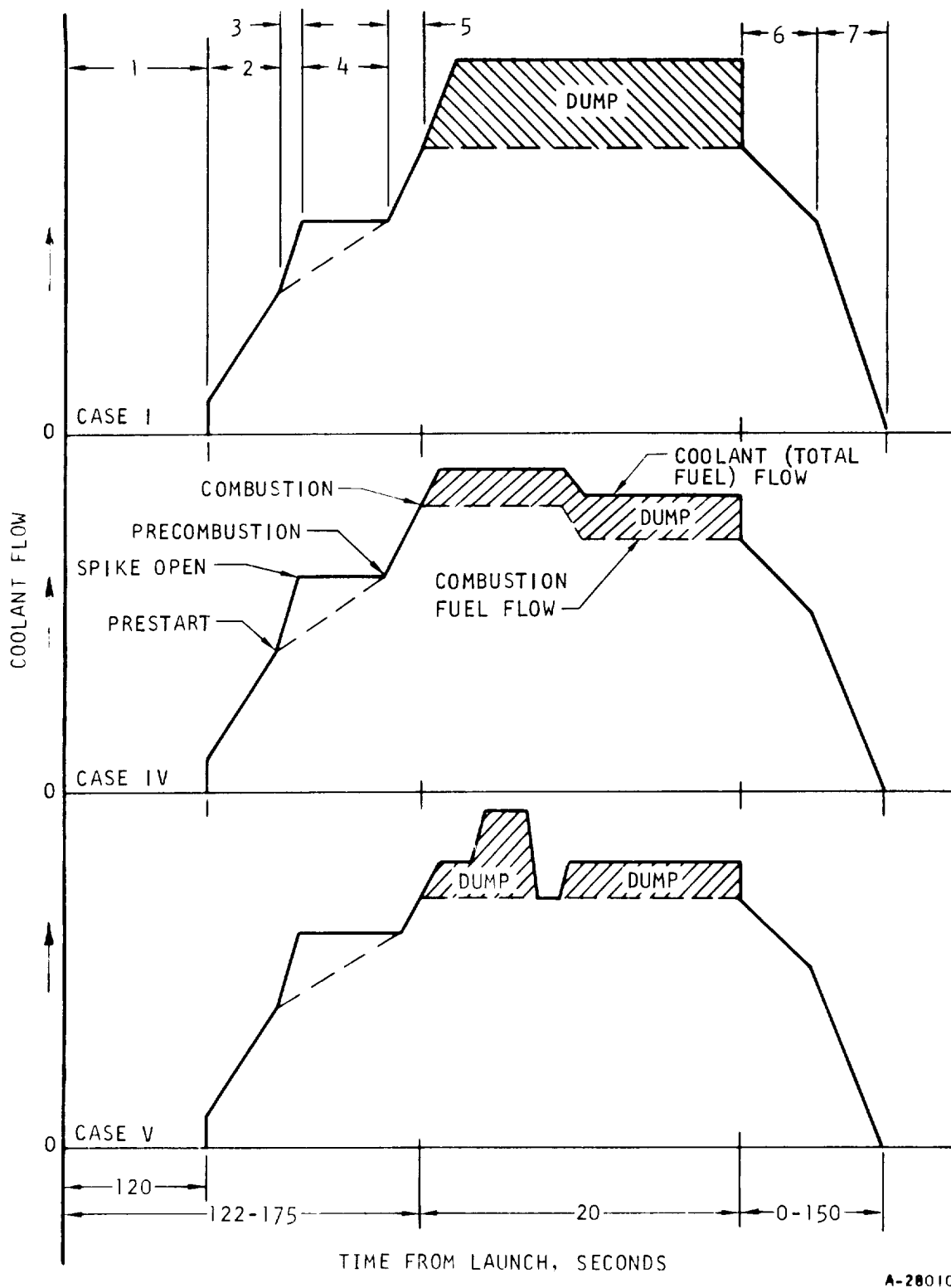


AIRESEARCH MANUFACTURING DIVISION
Los Angeles, California

67-2833
Page 3-4

UNCLASSIFIED

UNCLASSIFIED



A-28010

Figure 3.2-1. Typical Engine Operating Cycles



AIRESEARCH MANUFACTURING DIVISION
Los Angeles, California

67-2833
Page 3-5

UNCLASSIFIED

UNCLASSIFIED

4. Inlet spike in starting position, full airflow through the engine, no combustion.
5. Programmed increase in cooling flow to starting combustion equivalence ratio (ϕ). This ϕ will be less than the test ϕ . Combustion ϕ will ramp to test ϕ (not shown).
6. Combustion terminated and inlet spike being extended to closed position.
7. Inlet closed (leakage flow only), deceleration to $M = 4 +$, with coolant flow decreased to maintain maximum structure temperature at 1140°F. Helium purge.

As combustion starts, the cooling ϕ must be controlled to accommodate increasing heat fluxes. The variations among missions occurring during the combustion phase are as follows:

Case I - Shown in Figure 3.2-1. Cooling ϕ is in excess of combustion ϕ . Combustion ϕ will ramp at beginning and end of test. Ramps of 5-sec duration to and from $\phi = 1$ may be assumed at beginning and end of test.

Case II - Not shown. Represents a gradual change in conditions shown for Case I and will involve less severe transients. Not considered a design point.

Case III - Same comments as Case II, but may become a design point at lower Mach numbers because of potential for increased test time and wider Mach number range.

Case IV - Shown in Figure 3.2-1. Involves a near-step change in gas-side engine conditions during test run.

Case V - Shown in Figure 3.2-1. The general rise in pressure would be expected to cause a step-change type increase in heat flux. Spike will extend and close, then retract to operating position for second attempt at starting. At this point, either normal operation or a second unstart is possible.



UNCLASSIFIED

UNCLASSIFIED

4. OVERALL APPROACH

The diverse requirements imposed on the cooled structures require iteration of the cooled structural design with the engine aerodynamic design; the instrumentation, control, and fuel subsystems designs; and with the airplane interface design. Internal constraints on cooled structural design are imposed by the close coordination required in thermal design, structural design, mechanical design, and manufacturing. It is generally not possible to treat any one of these areas independently of the others. During Phase I of the program, the basic design concepts for the engine were defined and are basically feasible in terms of the constraints imposed on the design. These concepts and the design data generated during Phase I are being used as the starting point for design of the Phase IIA cooled structures. Component layout drawings of acceptable mechanical design and with acceptable manufacturing features form the initial step in the iteration. These layout drawings have been evaluated to establish the required thermal and structural design features. Based on these inputs, layout drawings are revised to incorporate the required features, followed by substantiation of the thermal and structural performance of the revised design.

Although the Phase I design is being used as the starting point of Phase IIA cooled structure design, each of the components is being reviewed with the objective of simplification in terms of mechanical design and manufacturing features. The interfaces between two or more components, in particular, will be re-evaluated. The interfaces include engine-to-airplane mounting, outer shell-to-inner body mounting by means of the support struts, nozzle-to-inner shell assembly, inlet spike-to-inner body assembly, inlet spike actuator-to-inlet spike and inner body mounting, leading edge-to-outer shell mounting, and cowl-to-outer shell support.

The general approach to cooled structures development places heavy emphasis on fabrication and testing of the full-scale components. A limited number of types of cooled structural elements and models are being fabricated and tested to evaluate the problems which are basic to the overall engine design, or which are sufficiently localized in nature to permit use of subscale evaluation. All significant manufacturing development and evaluation is being accomplished using the full-scale components. The nature of the required manufacturing operations for the components is such that use of subscale components would be expected to lead to only limited information on the adequacy of manufacturing techniques and processes.



UNCLASSIFIED

UNCLASSIFIED

4.1 THERMAL DESIGN

The overall thermal design approach is by analyses based on experimental data obtained from tests on similar geometric configurations and heat transfer situations. These experiment-based analyses in turn, will be verified by experiments where the geometry or fluid conditions, or both, will be like those existing for the flight engine.

The discrepancy between calculated and experimental heat flux values is large. Steps are being taken to improve the analytical techniques so that the correlation between calculated and experimental results can be improved.

The basic goals of all thermal analyses and designs are (1) limiting temperature and temperature differences to structurally-acceptable values, while keeping hydrogen cooling flow equal to or less than hydrogen flow required for combustion, and (2) at the same time maintaining hydrogen pressure drop compatible with cooling jacket pressure containment and pump outlet pressure capabilities. The limiting values for these parameters, previously used during Phase I and still being used at present, are (1) a maximum gas side metal temperature of 1700°F (2160°R), (2) a maximum primary structure temperature of 1200°F (1660°R), (3) a hydrogen pump outlet pressure of 700 psia, and (4) a fuel control valve (fuel plenum) pressure of 400 psia. An arbitrary reduction in gas side metal temperature of 100°R to a maximum of 1600°F (2060°R) is used to accommodate coolant control response and aerothermodynamic fluctuations about the mean. The 300 psi cooled structures pressure drop implied above is divided, approximately 100 psi for cooling jacket finned passages and 200 psi for all manifolding and interconnecting ducting.

The thermal design procedure involves separate calculation of aerodynamic heating and cooling jacket performance. The aerodynamic heating conditions are calculated (as during Phase I) primarily by use of the computer program H1940. Special aerodynamic heating conditions, such as shock wave-boundary layer interaction, are computed separately. Cooling jacket fin performance is calculated (as in Phase I) by use of computer program H1930. Special conditions, such as pressure and flow distributions for inlets, outlets, and bolted flange/manifolds, require separate calculations. Verification of aerodynamic and cooling jacket heat transfer and pressure drop calculations will be accomplished by actual tests. Specifically, aerodynamic heat transfer calculations will be verified by tests of engine component models, such as the combustor, and with the boilerplate engines. Calculated performance of cooled structures will be verified by full-scale component and some subscale component testing at heat flux levels and distributions comparable to those calculated for the flight engine components. The primary areas requiring verification in the cooled structures performance are flow distribution and associated temperature distribution and its effects on structural performance in terms of life and contour.



UNCLASSIFIED

4.2 STRUCTURAL DESIGN

The structural design approach utilizes a combination of analytical and experimental methods. Experimental verification of detailed parts, such as short term burst, creep rupture, and thermal fatigue tests on sandwich plate-fin elements, will be employed wherever necessary. Generally, the structural tests will be performed on composite structural elements, such as the inlet spike and the inner body assembly.

The bulk of the HRE structures consists of ring-stiffened orthotropic shell structures of variable thicknesses and contours. The ring stiffeners are also used for coolant flow manifolding and fuel injection rings for the engine combustor section. The structural loadings will produce axisymmetric and asymmetric forces and moments due to static normal pressures, acceleration, vibrational inputs, and aerodynamic flutter and buffeting effects.

Fully operational computer solutions are available to analyze axisymmetric isotropic thin shells of variable thicknesses and contours for stresses due to axisymmetric loads and temperature profiles. In addition, the isotropic shell analysis has been extended to treat orthotropic cylindrical shells with axisymmetric loads. Two MIT finite difference nodal circle solutions (SABOR III and DASHER I), which have been adapted for use on the AiResearch computer system (IBM-360/50), are available for use.

The SABOR III program is applicable for axisymmetric isotropic shells (local departures from ideal isotropy can be treated) that may be subjected to nonsymmetrical static forces. The SABOR III program may also be used to obtain the stiffness and mass matrixes for direct input into the DASHER I program to obtain dynamic response.

It would have required an extensive programming effort to modify the SABOR III and DASHER I programs to treat accurately many of the problems that will be encountered in the HRE. Rather than attempt this approach, a further survey of existing shell programs was carried out, and it was determined that an extremely applicable program had been developed under the auspices of the Analysis Group of the Theoretical Mechanics Branch, Structures Division of the Wright Patterson Air Force Base, Dayton, Ohio. This program is based upon the very recent improvements in matrix shell solutions generated by A. Kalnins (Department of Mechanics, Lehigh University). It solves the general axisymmetric orthotropic thin shell problem for symmetric and nonsymmetric loads due to static as well as dynamic inputs. The program has been successfully adapted for use on the AiResearch computer system. Although the program has been debugged, the final report describing the useability, limitations, and methods of data input has not been completed, and will not be released by the Wright Patterson Air Force Base for at least twelve months. Until a program of this magnitude has been completely checked out by trying numerous test cases, a note of caution must be exercised regarding its capabilities. Another important point is the fact that the



UNCLASSIFIED

problem inputs and the data reduction of the outputs require considerable effort on the part of the user. The existence of the program also does not eliminate or substantially reduce the work needed to generate a sound design; however, it is the objective of careful analysis to discover design inadequacies that would otherwise not be recognized.

The eventual objective of the test program is to verify the actual performance capabilities of the structures as fabricated. Although it will not be possible to predict analytically the influence of realistic fabrication restrictions and limitations on the end product, the initial analysis will identify the serious design problem areas. Results of the test program will be used to assess the extent of the changes required to achieve the structural integrity goals.

4.3 MECHANICAL DESIGN

The guidelines used in mechanical design of the cooled structures components and assembly of the components into the engine require the use of known materials and joining techniques. Standard fasteners and seals are used to the greatest extent possible. Design for brazing is aimed at minimizing the total number of braze cycles to which a given part must be subjected. In some cases, this is done by redesigning the parts to allow use of prebrazed subassemblies, substitution of machined or welded subassemblies, or substitution of bolted interfaces for brazed or welded interfaces. Also, as a general rule, all welding into or close to braze joints is being avoided, although in certain cases, such a procedure may be acceptable.

The mechanical design effort will be supported by experimental verification in selected areas. In particular, selected configurations that present analytical problems and raise questions as to manufacturing feasibility will be fabricated and tested on a subscale basis. The purpose of such tests will be to provide design data and guidance for possible design revision. Currently planned tests, which are in support of mechanical design, rather than thermal or structural design, include the following:

- Test specimen to evaluate feasibility of bolting the nozzle flange manifold to the inner shell through the removable nozzle cap.

- Fabrication of a section of the inlet spike near the spike tip to help resolve questions regarding the best manufacturing approach and hence the best design for this portion of the inlet spike.

- Fabrication of the spike-to-inner body seal to evaluate the adequacy of the design solution.

- Fabrication of a straight section of the bolted nozzle manifold to verify both the manufacturing aspects and structural integrity of the design solution.



UNCLASSIFIED

Fabrication and evaluation of the various mechanical seals used in the components to verify the adequacy of the design solution.

Fabrication of flat panels using the various instrumentation and fuel injector fittings that penetrate the regeneratively cooled surfaces to verify manufacturing feasibility and structural integrity of the design. Tests results will be used to select the final configuration used in the engine.

4.4 MANUFACTURING

The manufacturing approach being used on this program has two aspects: (1) that dealing with the approach to development of manufacturing techniques and processes, and (2) that dealing with the specific manufacturing processes planned for use.

4.4.1 Development Approach

The development of the manufacturing techniques and processes will rely primarily on full-scale components. Except where isolated problems or basic data must be obtained, the use of subscale components represents a duplication of development effort. The compound forming of the shell-face sheets in half-scale, for example, results in working with radii of curvature which are half those encountered in the full-scale part. Use of lighter gauge material to facilitate forming, on the other hand, is impractical. In addition, the size of the full-scale tooling, the machines required to use this tooling, and the unique problems associated with the forming of large thin wall shells cannot be duplicated in half-scale. As a result, a half-scale compound-curved model of the isentropic surface of the inlet spike is the only subscale component on which fabrication development work is being done. This part is being used to establish forming characteristics, evaluate electro-hydraulic forming parameters, and investigate brazing problems.

4.4.2 Fabrication Approach

The most critical area of cooled structures fabrication is in the cooled surface shell face sheets. The starting point for these shells can either be rolled and welded cone sections or flat sheets. The rolled and welded cones are bulge formed, then final sized, using electrohydraulic forming. Using flat sheets as a starting point, the shells must be deep drawn in about three stages. Final sizing of the shells occurs as for the welded cones. Of the two approaches, the one using the seam welded cone has been selected. The weld seam is not considered structurally objectionable and the approach involves fewer steps than are required for deep drawing.

To ensure adequate braze fitup, forming accuracy for the shells must be high. Specifically, it is expected that the clearance between shells must be maintained within a tolerance of approximately ± 0.001 in. Given this accuracy, the brazing of the fins between the face shape still requires special attention. To ensure sound braze joints, pressure must be exerted



UNCLASSIFIED

UNCLASSIFIED

on the shells in such a way as to provide a crushing load on the fins. The methods available for providing this braze fixturing load include the following, as a function of the component being brazed:

Graphite fixtures, with an external piece containing the assembly and an internal piece using expanding segments to exert pressure.

Steel bags placed inside the shell and pressurized to a level sufficient to deform the shell with which the bag is in contact. Containment on the external face sheet may or may not be required with this approach.

Evacuation and backfilling of the space between the two shell face sheets, using atmospheric pressure to provide the load.

Integrity of the shell joining will be experimentally evaluated and adjustments in shell forming tools and brazing procedures and fixtures made to correct problems that appear.

4.4.3 Nondestructive Testing

The critical area in fabrication of the full-scale components involves the shells themselves, as discussed in the two previous paragraphs. For structural integrity of the shells, only very limited areas of unbrazed joint areas are tolerable. These joints are detectable by proof pressure testing at sufficiently high pressure levels. Only in exceptional cases, however, will a defect that is revealed by proof pressure test be repairable. In general, a nondestructive test capable of revealing braze voids is preferable and offers better opportunity for subsequent repair. The two techniques available are radiographic inspection of the entire shell surface and the use of temperature-sensitive paint on one of the face sheets with a heating transient imposed on the other face sheet. These methods will show a braze void; that is, an unbonded joint. Weak joints are not discernable as such. In general, however, the existence of a brazed joint is reasonable assurance that adequate joint strength can be achieved. Verification of the result of radiographic or thermal inspection of the shells will be done by proof pressure testing.

The repair techniques available for unbonded joints in the shells would generally be the following:

Recycling of the complete shell to a slightly higher temperature than used during the first braze cycle. In this way, remelt and flow of the braze alloy is obtained with the objective of filling the void. Orientation of the shell in the brazing furnace can be used to assist the process.

Removal of a portion of the face sheet in the unbrazed area, addition of filler alloy and closeout using a patch, with the entire shell recycled in the brazing furnace. The applicability of this repair procedure will be a function of the location of the affected shell area in the engine gas stream.



This material contains information affecting the national defense of the United States within the meaning of the espionage laws, Title 18, U.S.C., Sections 793 and 794, the transmission or revelation of which in any manner to an unauthorized person is prohibited by law.

Downgraded at 3 year intervals;
declassified after 12 years
DOD DIR 5200.10

5.0 ANALYTICAL DESIGN

5.1 DESIGN CONDITIONS AND LOADS

5.1.1 External Flight Environment

5.1.1.1 Aerodynamic Forces and Acceleration

Table 5.1-1 provides a listing of aerodynamic external drag forces, engine net internal thrust forces, and acceleration loads for Mach numbers of 8.0, 6.5 and 5.0 at different dynamic pressures, flight angles of attack and flight yaw angles. The values given are considered to be realistic combinations of the parameters which are being used for the structural design of the HRE.

Both engine operating and engine unlit conditions are presented. The tabulated external drag values for engine operation and non-operation correspond to the wave drag on the leading edge and the total engine drag (exclusive of the external cowl drag), respectively. The net applied force to the engine thrust sensor may be computed by subtracting the tabulated external drag from the net engine internal thrust.

5.1.1.2 Flight Vibration

The HRE must withstand vibrational forces simultaneously with the aerodynamic and acceleration loads. The best information available indicates that the maximum X-15A-2 output at the engine mount points does not exceed 0.3 g. Employing this input level and further assuming an amplification factor of 10 at the engine fundamental frequency leads to a 3-g load factor (0.3×10) in all directions, which must be applied in conjunction with the acceleration and aerodynamic forces.

5.1.2 Internal Engine Environment

5.1.2.1 Normal Engine Operation

Figures 5.1-1 through 5.1-14 form the basis of the heat flux distribution curves presented in Paragraph 5.1.4. The static pressure, velocity, molecular weight and fraction of fuel burned are direct inputs to Computer Program (H1760).



UNCLASSIFIED

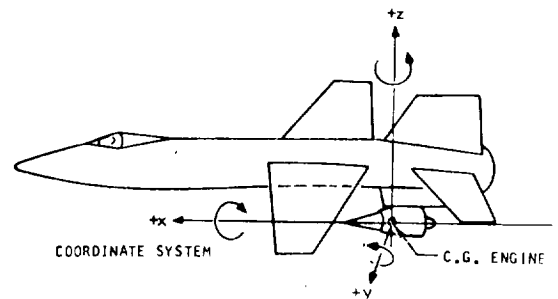
TABLE 5.1-1

FLIGHT CONDITIONS AFFECTING STRUCTURAL DESIGN OF HRE

Condition No.	M _∞	q _∞ psf	α _∞ deg	β _∞ deg	N _z g	N _x g	N _y g	M _L	q _L psf	α _L deg	β _L deg	HRE Net Internal Thrust, lb	External Drag	Normal F _z	Side F _y	Axial
n	8.0	2000	10.4	2	4.25	4.5	-1.0	6.5	3600	4.0	2.0	0	1807	1297	862	-2036
n	8.0	2000	10.4	2	4.25	-3.0	-1.0	6.5	3600	4.0	2.0	0	1807	1297	862	-2036
n	8.0	1800	11.0	2	4.25	4.5	-1.0	6.5	3240	4.0	2.0	0	1626	1167	776	-1832
n	8.0	1800	10.0	2	3.0	2.0	-1.0	6.5	3240	4.0	2.0	4340	769	969	648	+3365
n	8.0	1800	11.0	2	4.25	-3.0	-1.0	6.5	3240	4.0	2.0	0	1626	1167	776	-1832
n	8.0	1800	10.0	2	3.0	-3.0	-1.0	6.5	3240	4.0	2.0	4340	769	969	648	+3365
n	8.0	835	10.0	7	1.7	4.5	-1.0	6.5	1500	4.0	7.0	0	741	527	1280	-835
n	8.0	835	10.0	7	1.7	-1.0	-1.0	6.5	1500	4.0	7.0	0	741	527	1280	-835
n	8.0	2000	-1.0	2	-0.5	4.5	-1.0	7.5	1800	-1.0	2.0	0	904	649	431	-1018
n	8.0	2000	-1.0	2	-0.5	-3.0	-1.0	7.5	1800	-1.0	2.0	0	904	649	431	-1018
n	8.0	1800	-1.0	2	-0.5	4.5	-1.0	7.5	1620	-1.0	2.0	0	813	584	389	-916
n	8.0	1800	-1.0	2	-0.5	-3.0	-1.0	7.5	1620	-1.0	2.0	0	813	584	389	-916
n	8.0	1800	-1.0	2	-0.5	3.0	-1.0	7.5	1620	-1.0	2.0	1900	374	485	324	+1423
n	8.0	1800	-1.0	2	-0.5	-2.0	-1.0	7.5	1620	-1.0	2.0	1900	374	485	324	+1423
n	6.5	2000	9.7	2	4.25	4.5	-1.0	5.4	3200	-1.0	2.0	0	1606	1153	766	-1809
n	6.5	200	9.7	2	4.25	-3.0	-1.0	5.4	3200	-1.0	2.0	0	1606	1153	766	-1809
n	6.5	1800	10.2	2	4.25	4.5	-1.0	5.4	2880	4.0	2.0	0	1446	1037	389	-1629
n	6.5	1800	10.0	2	2.0	2.5	-1.0	5.4	2880	4.0	2.0	5280	721	861	576	+4376
n	6.5	1800	10.2	2	4.25	-3.0	-1.0	5.4	2880	4.0	2.0	0	1446	1037	389	-1629
n	6.5	1800	10.0	2	2.0	-2.0	-1.0	5.4	2880	4.0	2.0	5280	721	861	576	+4376
n	6.5	2000	-1.0	2	-0.5	4.5	-1.0	5.8	1800	-1.0	2.0	0	904	649	431	-1018
n	6.5	2000	-1.0	2	-0.5	-3.0	-1.0	5.8	1800	-1.0	2.0	0	904	649	431	-1018
n	6.5	1800	-1.0	2	-0.5	4.5	-1.0	5.8	1620	-1.0	2.0	0	813	584	389	-916
n	6.5	1800	-1.0	2	-0.5	3.0	-1.0	5.8	1620	-1.0	2.0	2740	397	485	324	+2240
n	6.5	1800	-1.0	2	-0.5	-3.0	-1.0	5.8	1620	-1.0	2.0	0	813	584	389	-916
n	6.5	1800	-1.0	2	-0.5	-2.0	-1.0	5.8	1620	-1.0	2.0	2740	397	485	324	+2240
n	5.0	2000	8.0	2	4.25	4.5	-1.0	4.2	2800	4.5	2.0	0	1405	1009	670	-1583
n	5.0	2000	8.0	2	4.25	-3.0	-1.0	4.2	2800	4.5	2.0	0	1405	1009	670	-1583
n	5.0	1800	8.8	2	4.25	4.5	-1.0	4.2	2520	4.5	2.0	0	1265	908	603	-1425
n	5.0	1800	8.8	2	2.5	3.0	-1.0	4.2	2520	4.5	2.0	5950	699	784	504	+5091
n	5.0	1800	8.8	2	4.25	-3.0	-1.0	4.2	2520	4.5	2.0	0	1265	908	603	-1425
n	5.0	1800	8.8	2	2.0	-2.0	-1.0	4.2	2520	4.5	2.0	5950	699	754	504	+5091
n	5.0	2000	-1.0	2	-0.5	4.5	-1.0	4.9	1900	-1.0	2.0	0	954	684	455	-1075
n	5.0	2000	-1.0	2	-0.5	-3.0	-1.0	4.9	1900	-1.0	2.0	0	954	684	455	-1075
n	5.0	1800	-1.0	2	-0.5	4.5	-1.0	4.9	1710	-1.0	2.0	0	858	616	409	-967
n	5.0	1800	-1.0	2	-0.5	2.0	-1.0	4.9	1710	-1.0	2.0	3310	443	511	342	+2758
n	5.0	1800	-1.0	2	-0.5	-3.0	-1.0	4.9	1710	-1.0	2.0	0	858	616	409	-967
n	5.0	1800	-1.0	2	-0.5	-2.0	-1.0	4.9	1710	-1.0	2.0	3310	443	511	342	+2758

α - angle of attack
β - angle of yaw
N - acceleration
M - Mach number
o - operating
n - nonoperating

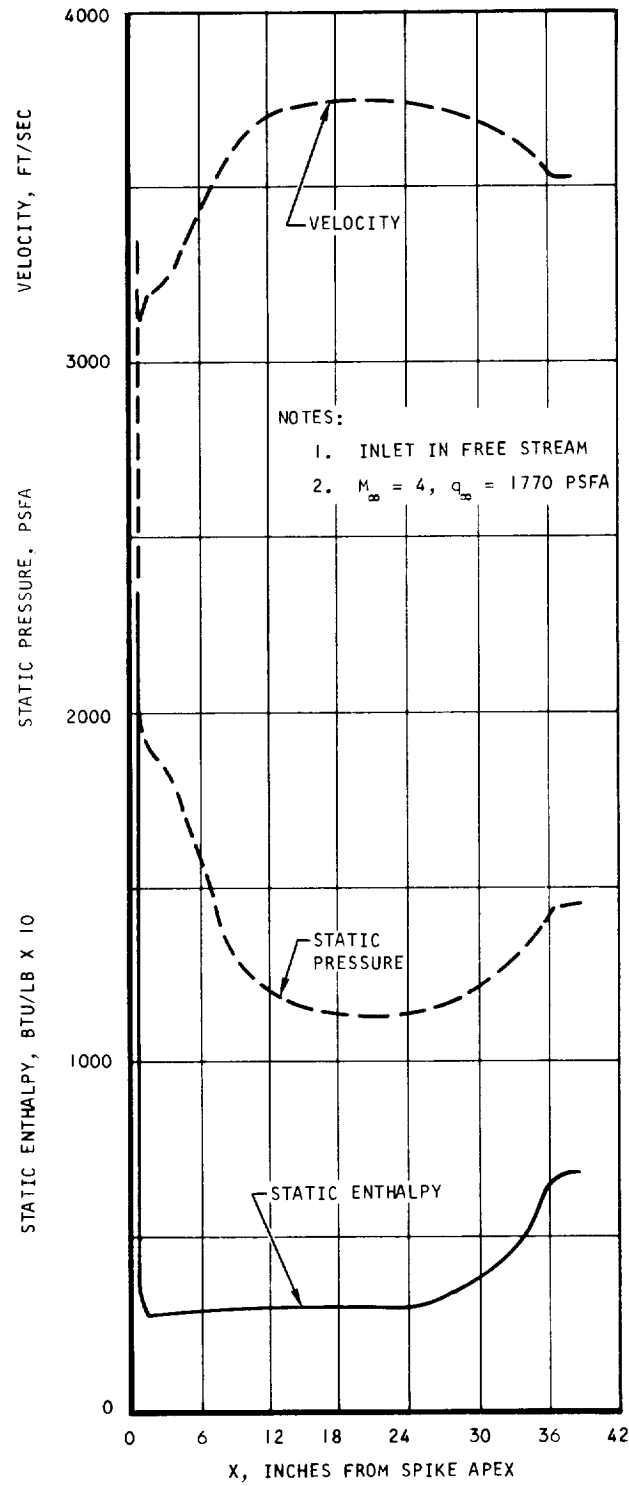
Subscripts
x - longitudinal
y - lateral
z - normal
m - free stream
L - local



AIRSEARCH MANUFACTURING DIVISION
Los Angeles, California

UNCLASSIFIED

UNCLASSIFIED



A-52183

Figure 5.1-1. Spike Fore Body Mach 4 Aerodynamic Parameters



AIRESEARCH MANUFACTURING DIVISION
Los Angeles, California

UNCLASSIFIED

UNCLASSIFIED

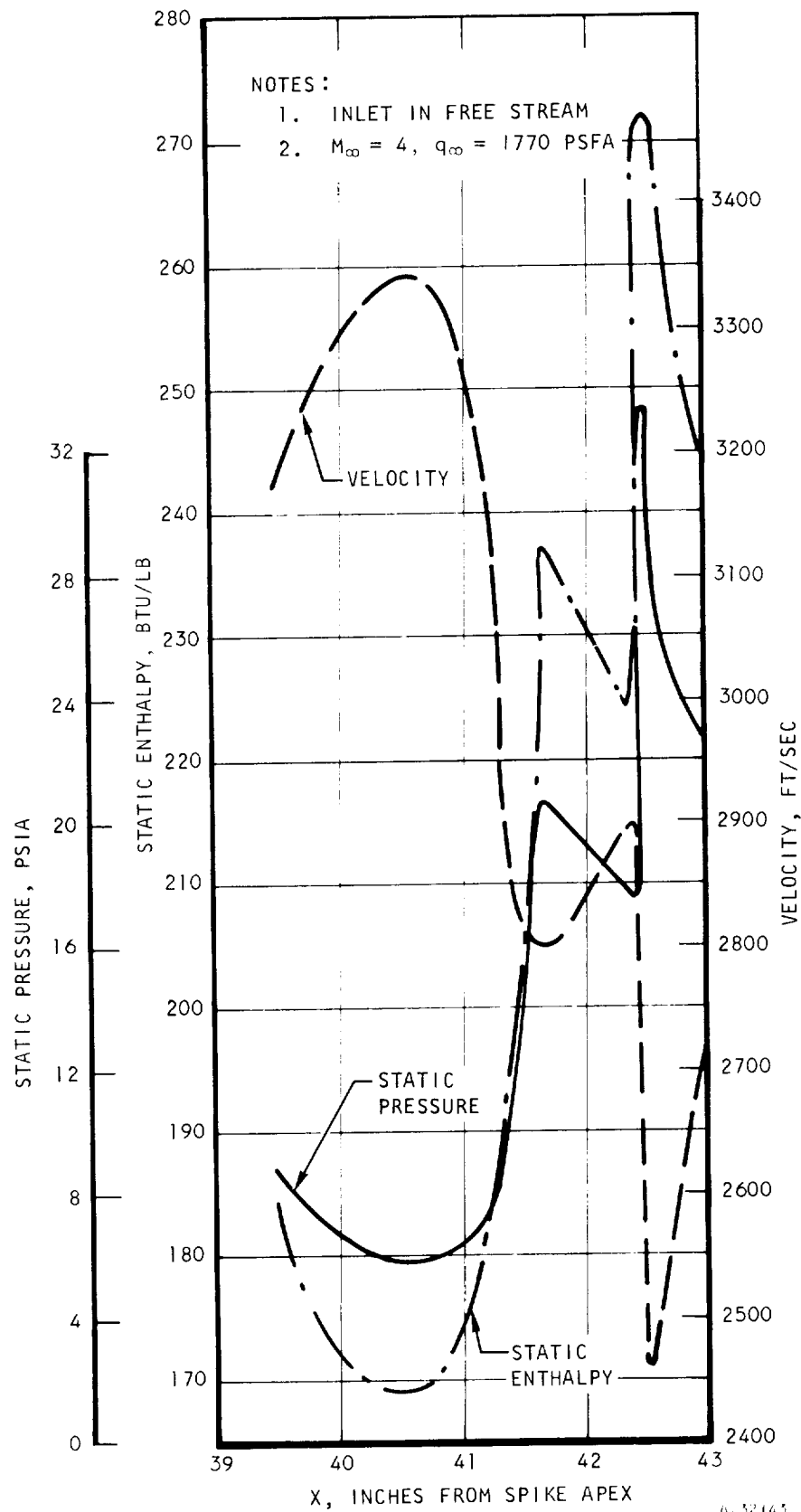
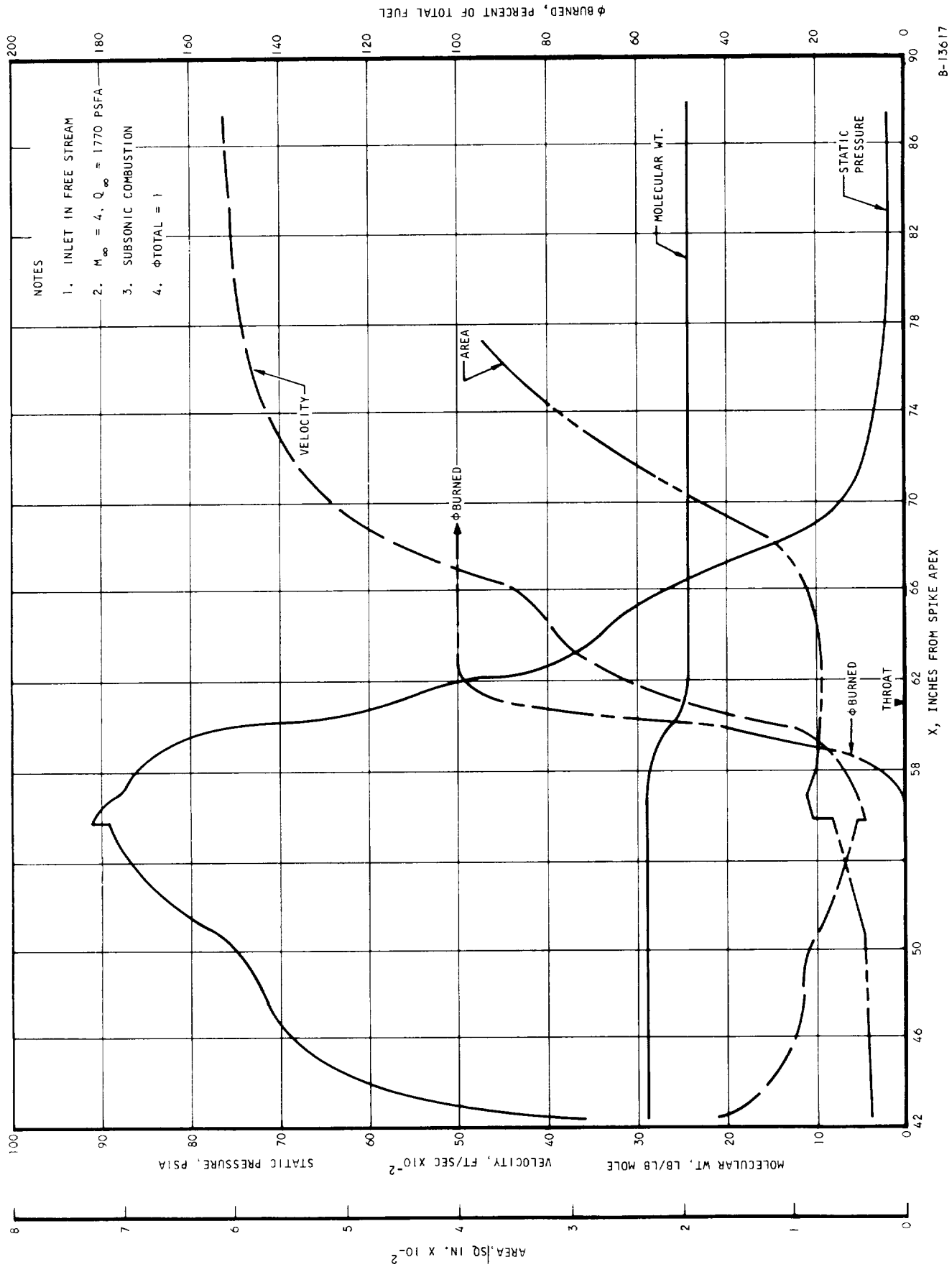


Figure 5.1-2. Spike Aft Body Mach 4 Aerodynamic Parameters



UNCLASSIFIED

UNCLASSIFIED



B-13617

Figure 5.1-3. Inner Body-Outer Shell Mach 4 Aerodynamic Parameters

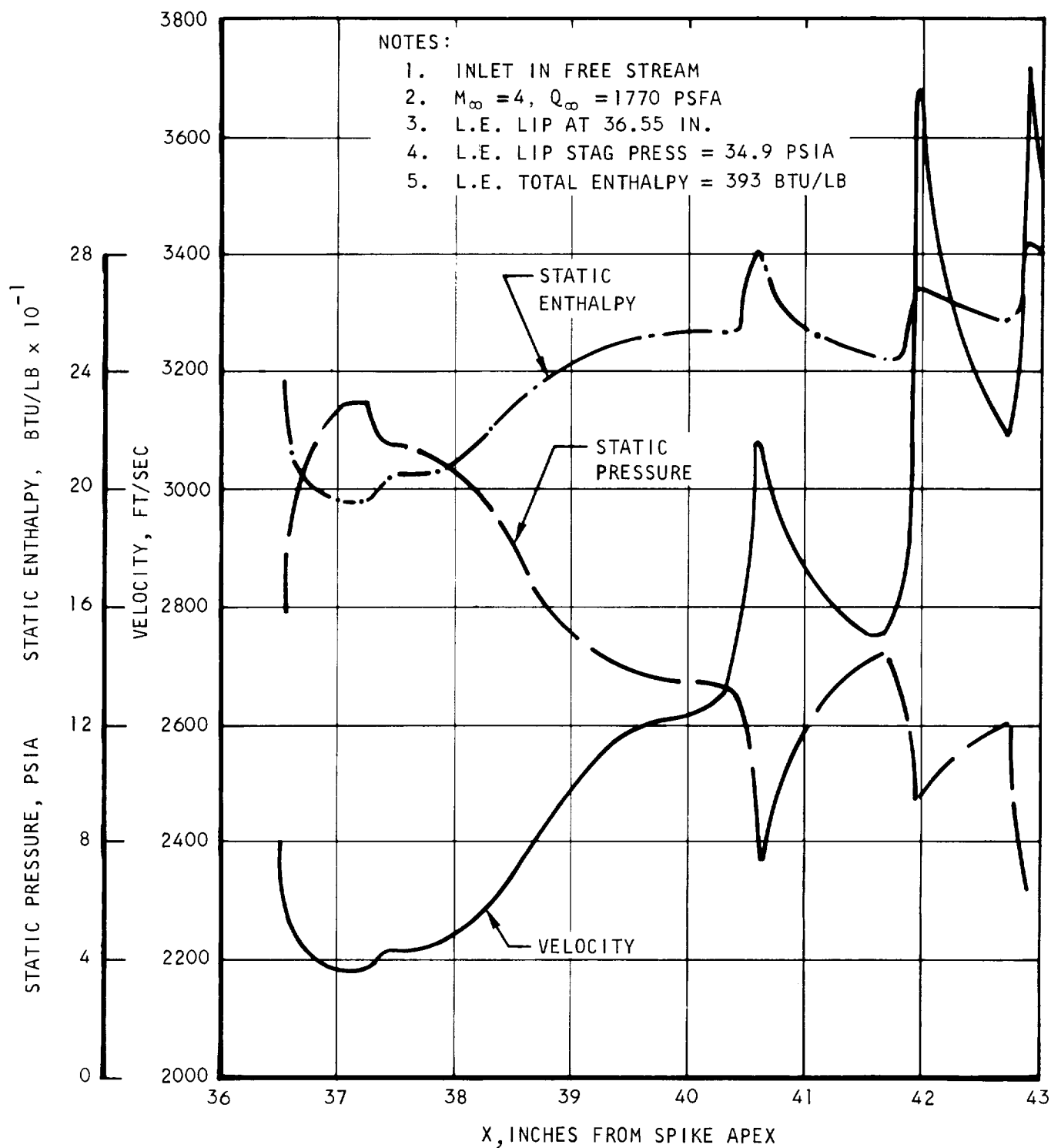


AIRESEARCH MANUFACTURING DIVISION
Los Angeles, California

UNCLASSIFIED

67-2833
Page 5-5

UNCLASSIFIED



A-32140

Figure 5.1-4. Outer Shell Mach 4 Aerodynamic Parameters

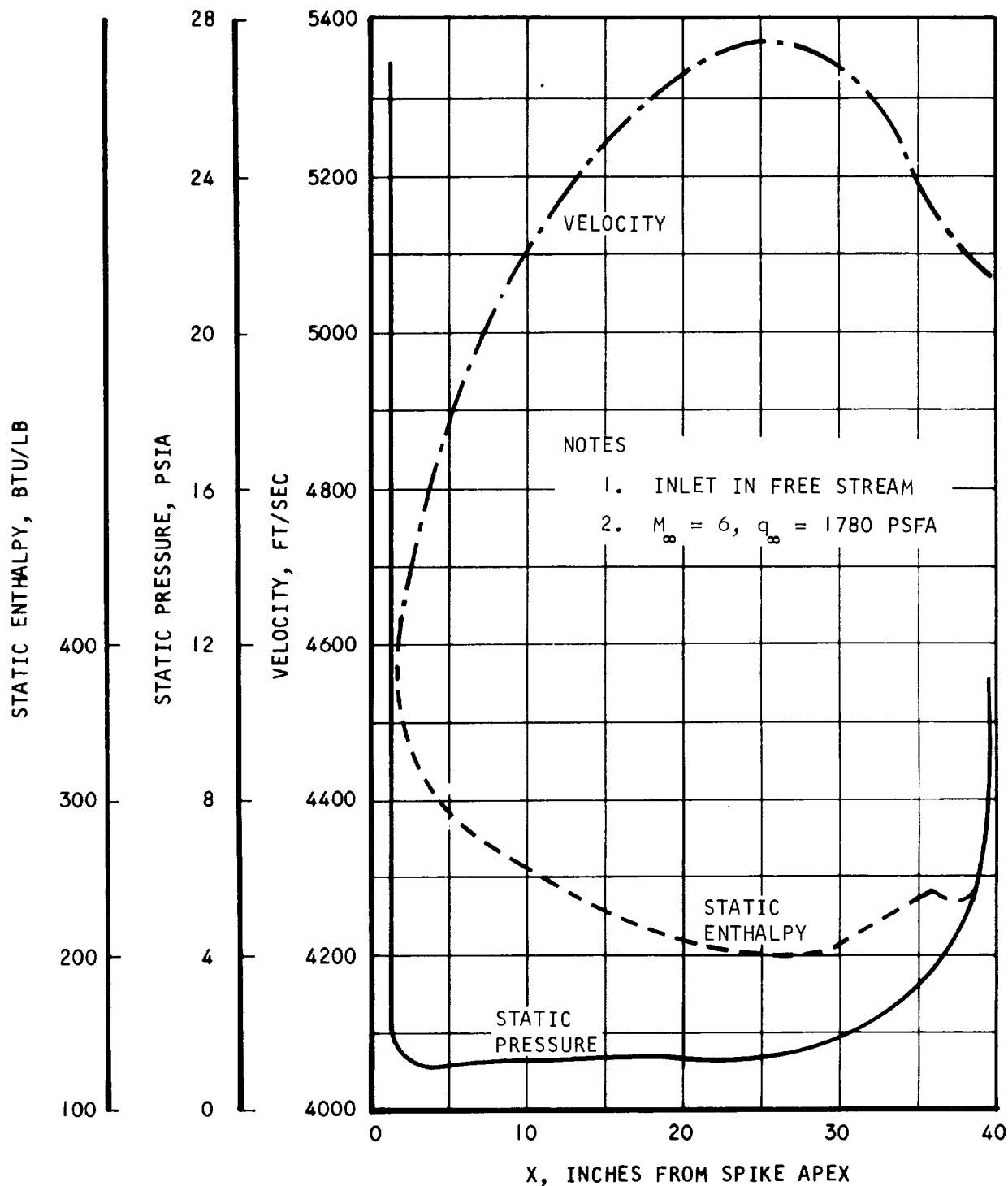


AIRRESEARCH MANUFACTURING DIVISION
Los Angeles, California

UNCLASSIFIED

67-2833
Page 5-6

UNCLASSIFIED



A-32203

Figure 5.1-5. Spike Fore Body Mach 6 Aerodynamic Parameters



AIRESEARCH MANUFACTURING DIVISION
Los Angeles, California

UNCLASSIFIED

67-2833
Page 5-7

UNCLASSIFIED

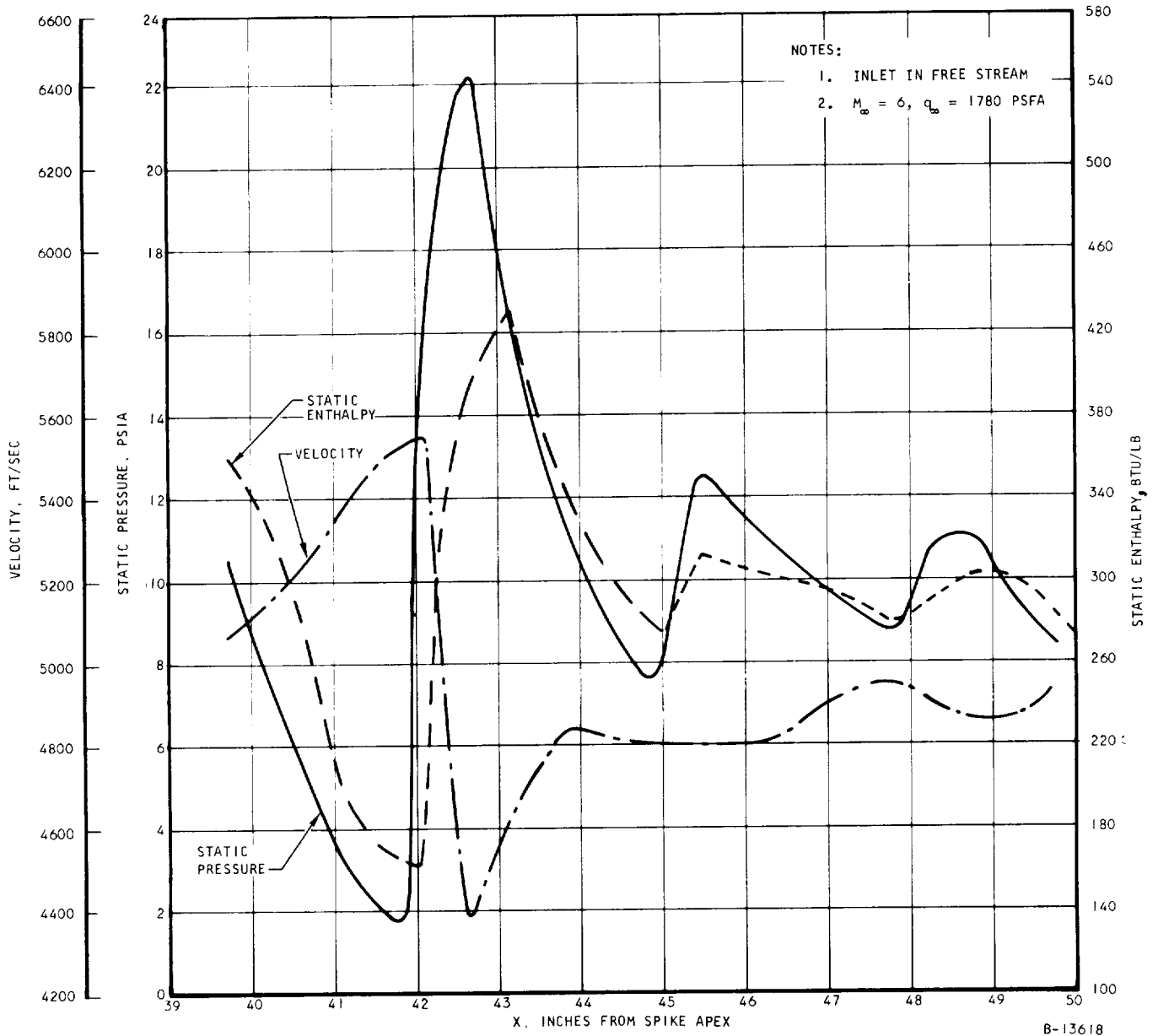


Figure 5.1-6. Spike Aft Body Mach 6 Aerodynamic Parameters



AIRESEARCH MANUFACTURING DIVISION
 Los Angeles, California

UNCLASSIFIED

UNCLASSIFIED

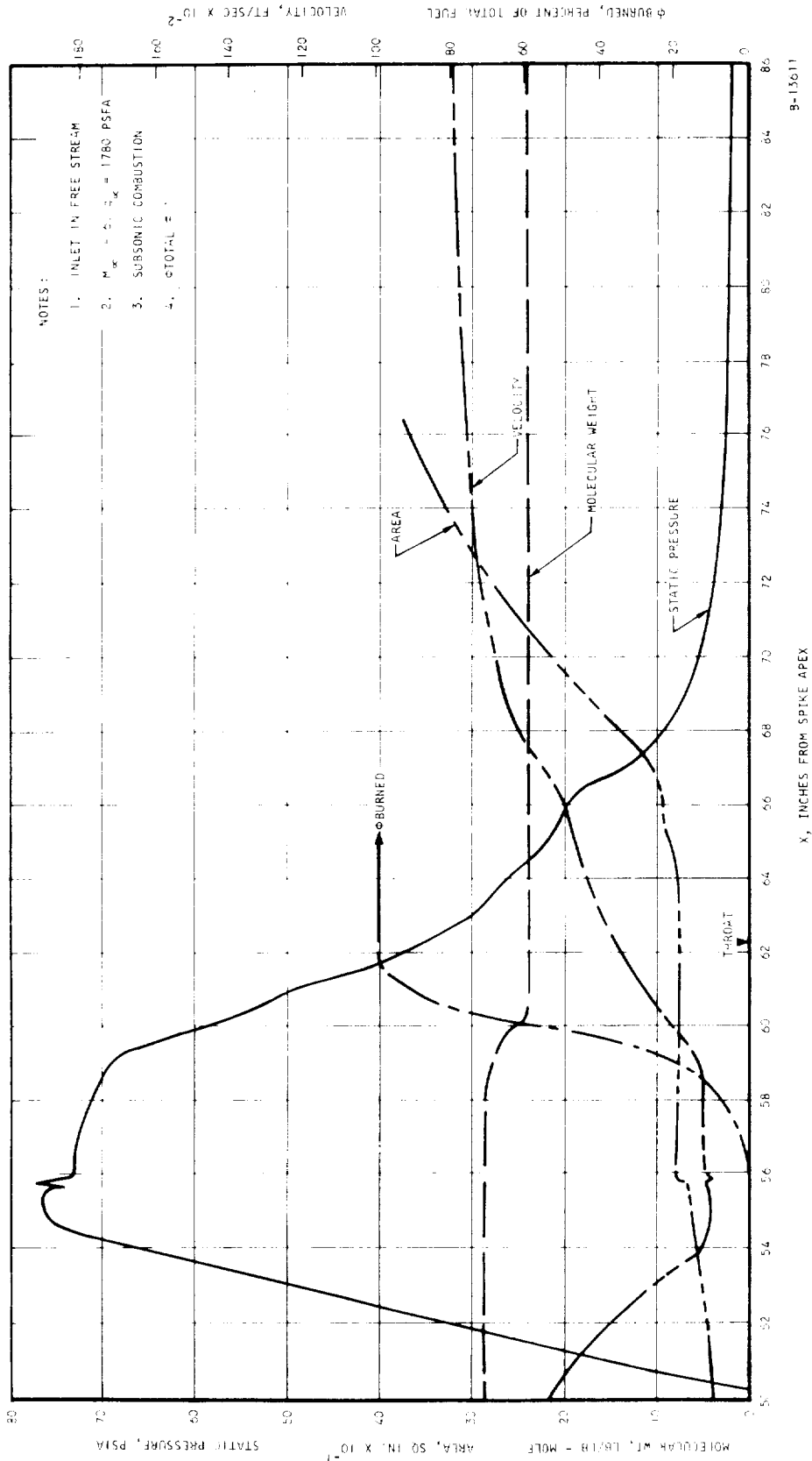


Figure 5.1-7. Inner Body-Outer Shell Mach 6 Aerodynamic Parameters



AIRESEARCH MANUFACTURING DIVISION
Los Angeles, California

UNCLASSIFIED

UNCLASSIFIED

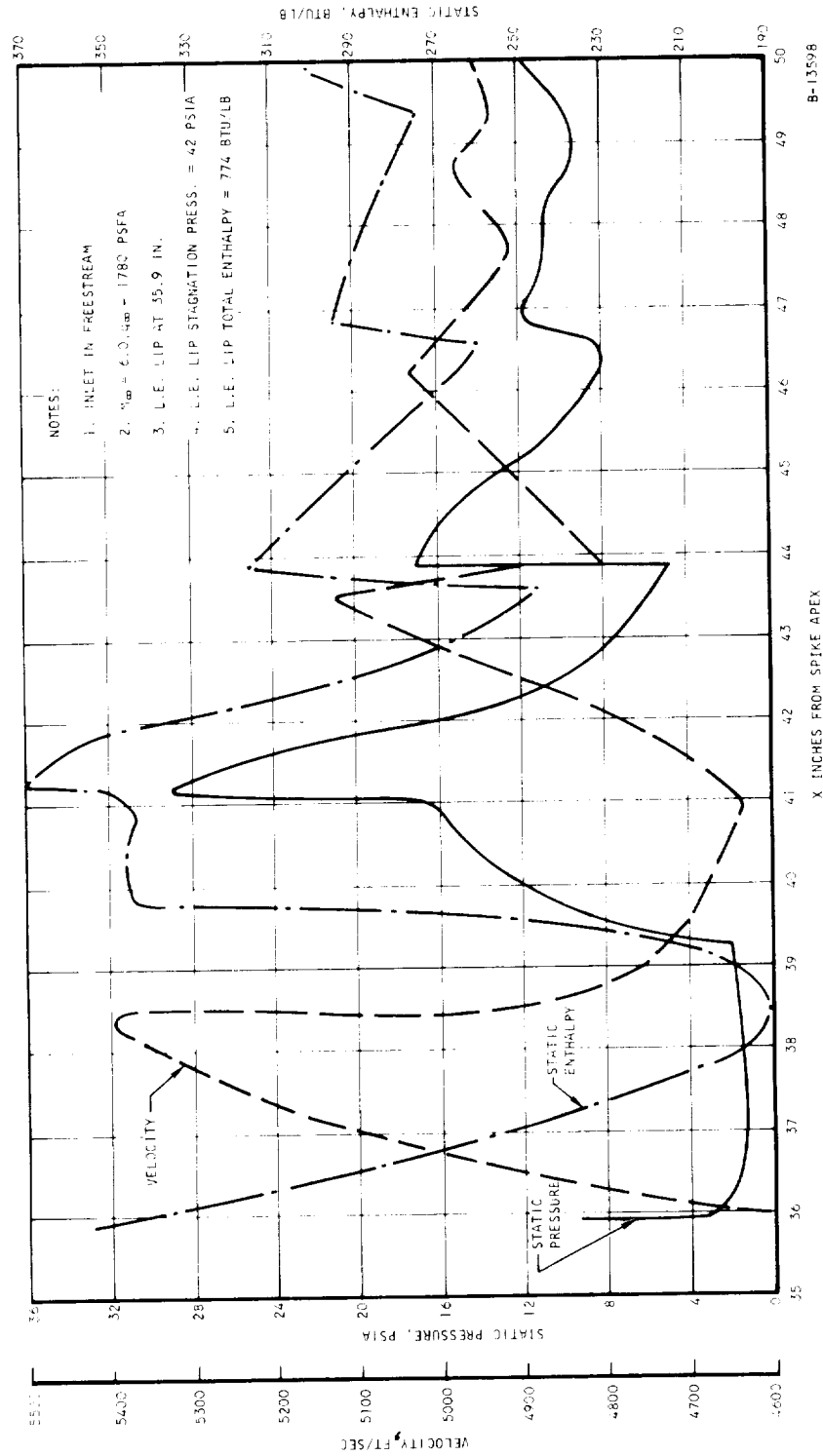


Figure 5.1-8. Outer Shell Mach 6 Aerodynamic Parameters



AIRESEARCH MANUFACTURING DIVISION
Los Angeles, California

UNCLASSIFIED

67-2833

Page 5-10

UNCLASSIFIED

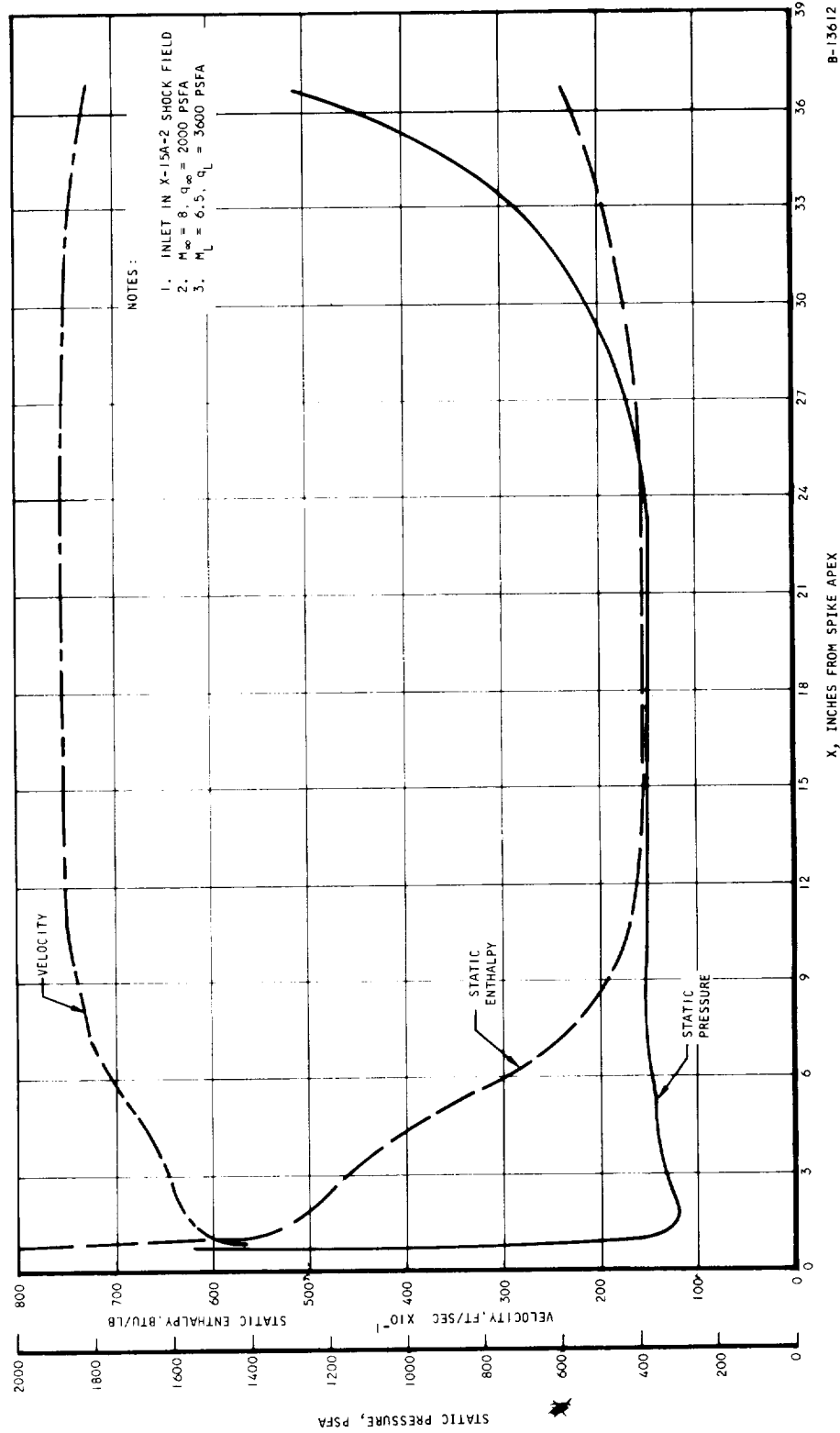


Figure 5.1-9. Spike Fore Body Mach 8 Aerodynamic Parameters



AIRESEARCH MANUFACTURING DIVISION
Los Angeles, California

UNCLASSIFIED

UNCLASSIFIED

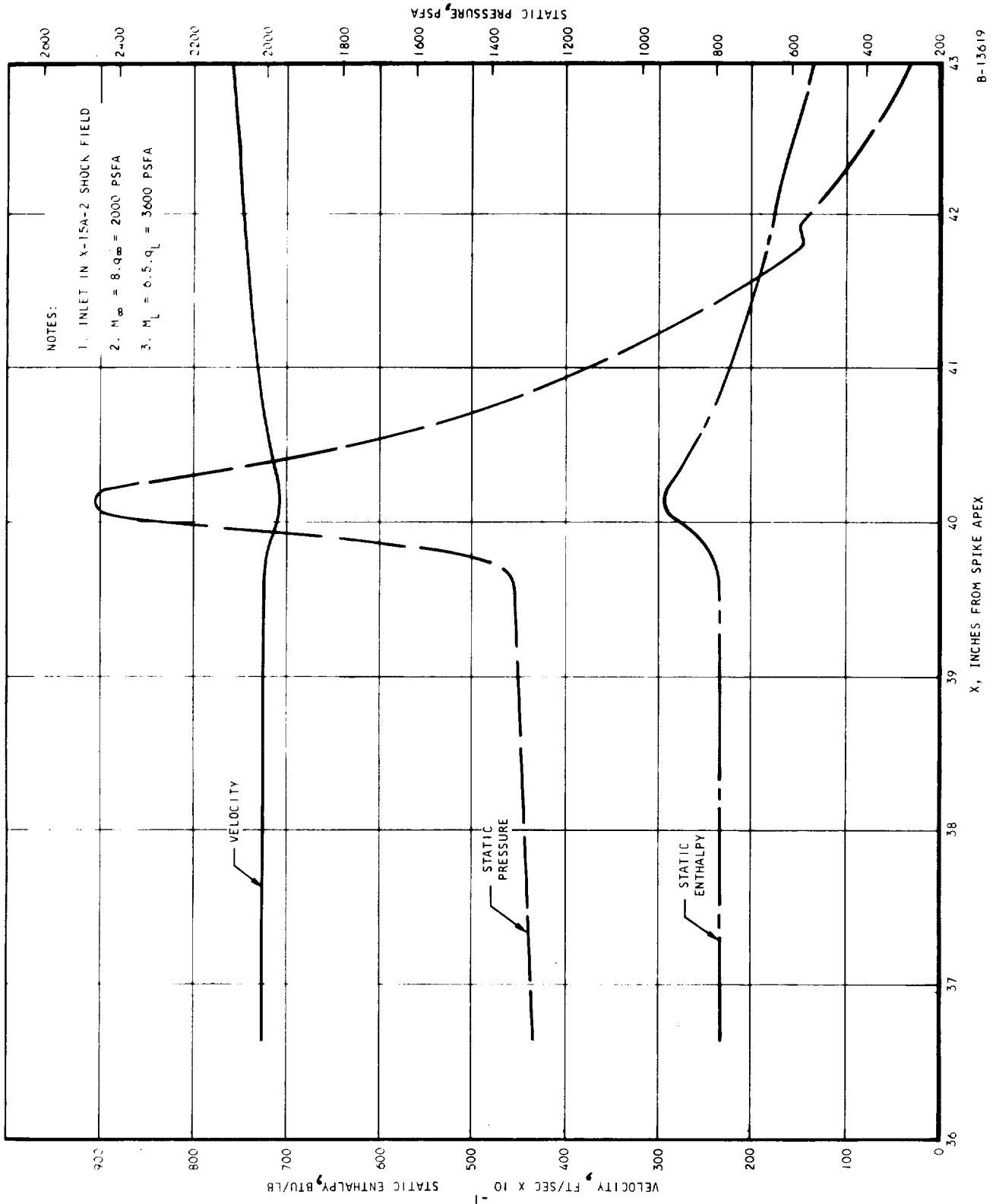


Figure 5.1-10. Spike Aft Body Mach 8 Aerodynamic Parameters

B-13619



AIRSEARCH MANUFACTURING DIVISION
 Los Angeles, California

UNCLASSIFIED

UNCLASSIFIED

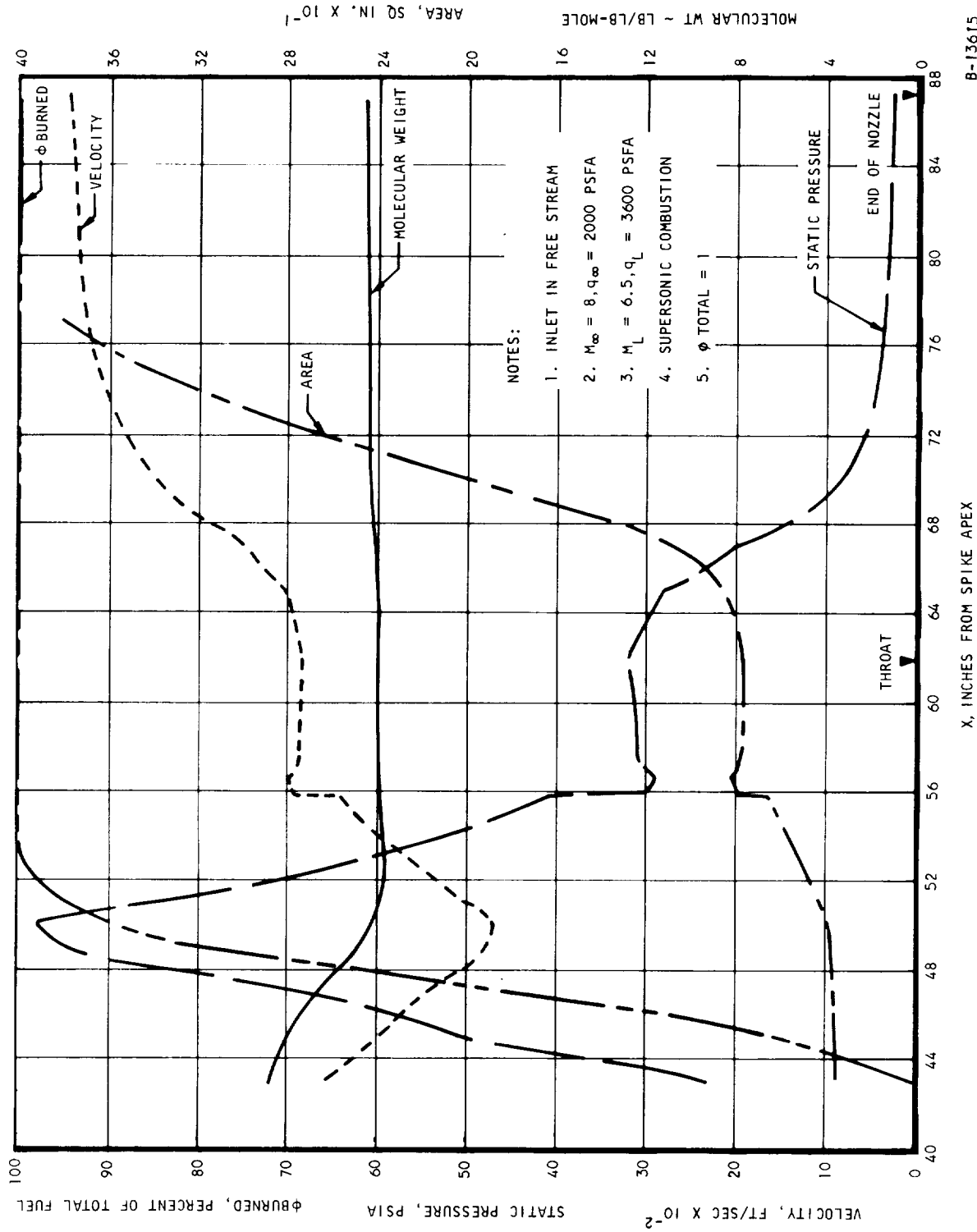


Figure 5.1-11. Inner Body-Outer Shell Mach 8 Aerodynamic Parameters

B-13615

UNCLASSIFIED



AIRESEARCH MANUFACTURING DIVISION
Los Angeles, California

67-2833

Page 5-13

UNCLASSIFIED

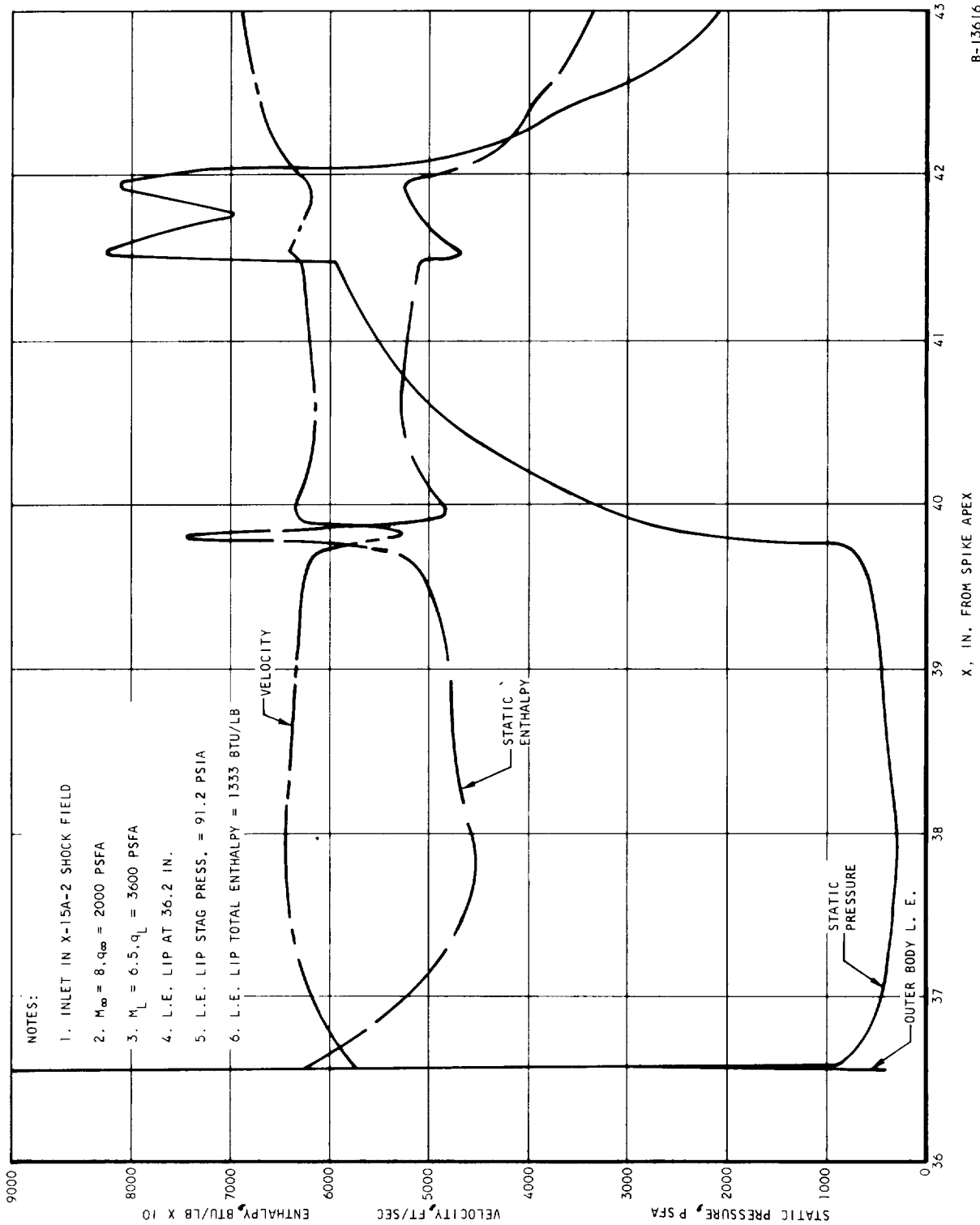


Figure 5.1-12. Outer Shell Mach 8 Aerodynamic Parameters

B-13616



AIRESEARCH MANUFACTURING DIVISION
Los Angeles, California

UNCLASSIFIED

67-2833

Page 5-14

UNCLASSIFIED

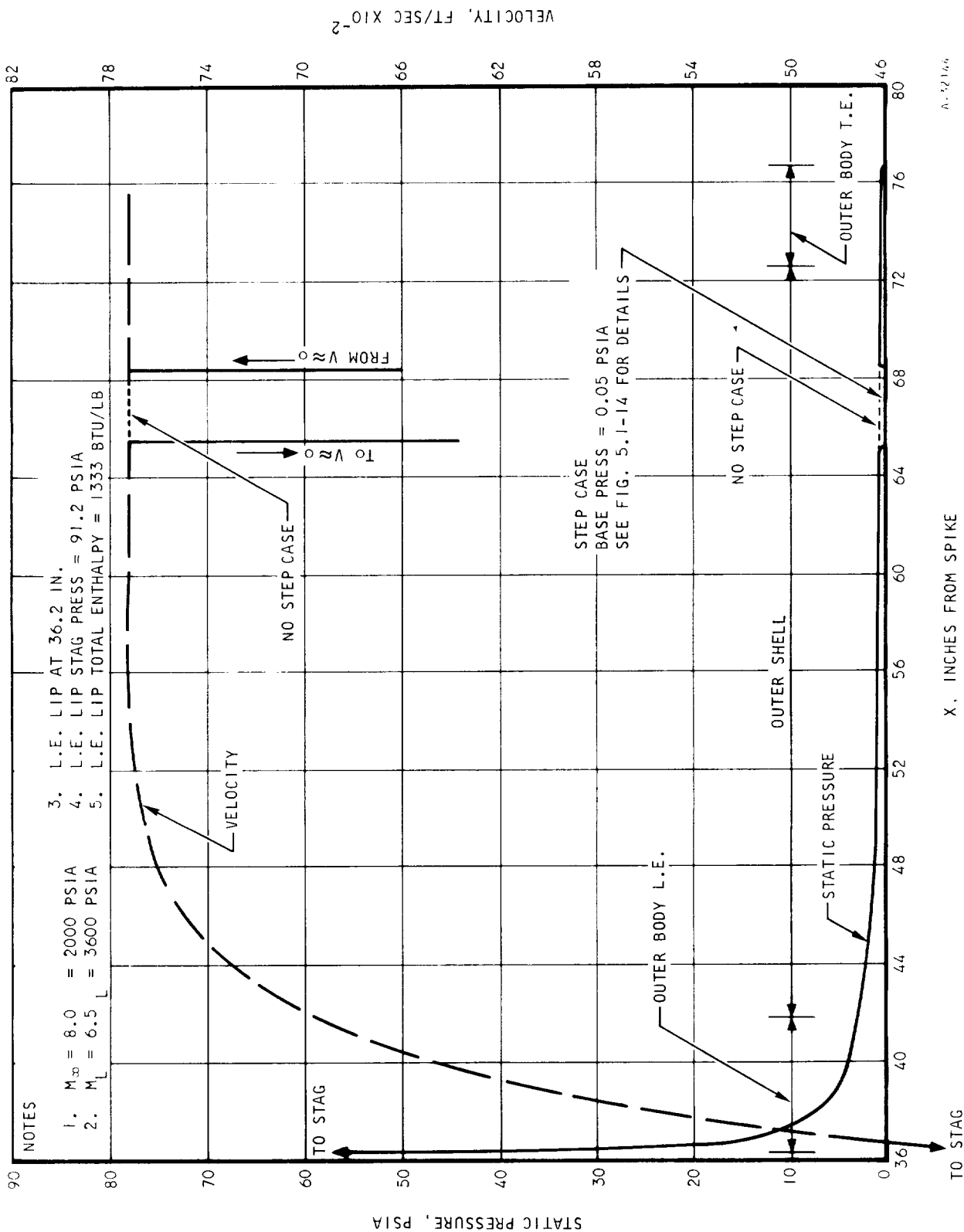


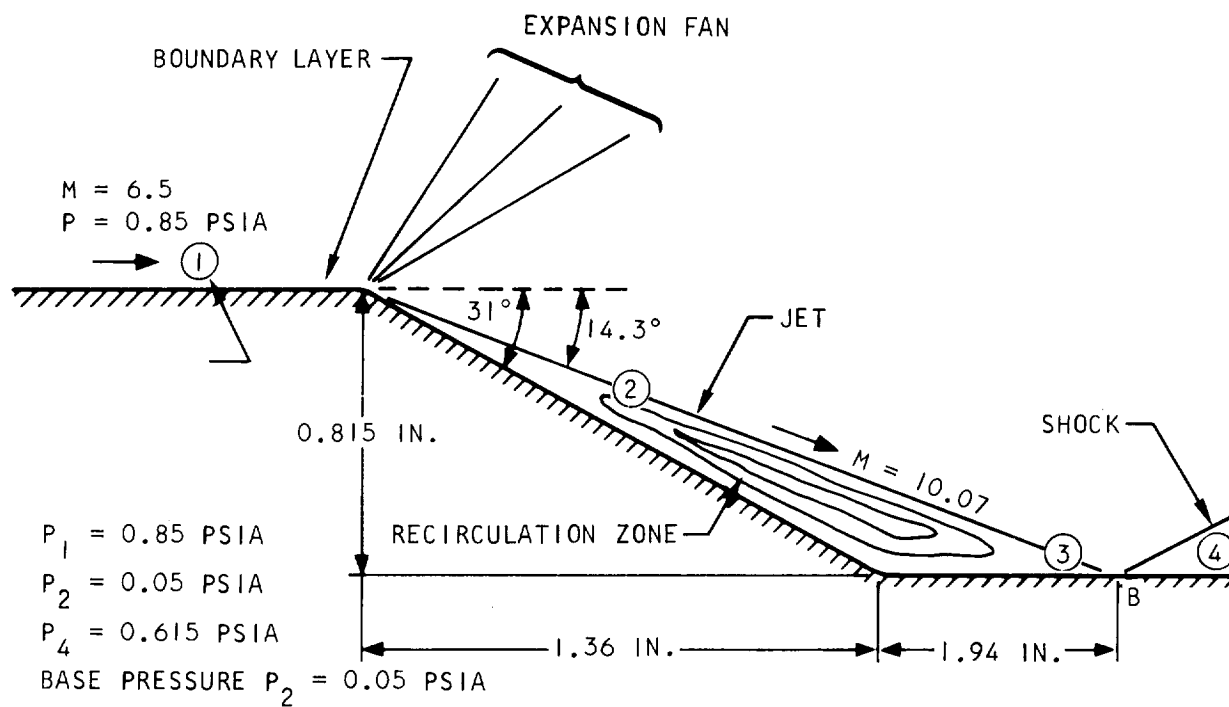
Figure 5.1-13. Estimated Outer Body Mach 8 Aerodynamic Parameters



AIRESEARCH MANUFACTURING DIVISION
Los Angeles, California

UNCLASSIFIED

UNCLASSIFIED



A-32138

Figure 5.1-14. Detailed Flowfield Around the Step Configuration



UNCLASSIFIED

The total enthalpy is calculated by the program using the following relationship.

$$H_T = H_{T_{inlet}} + \frac{52,000 (0.0292) (\phi) (FB)}{1 + 0.0292 (\phi) (FB)}$$

where ϕ , FB and $H_{T_{inlet}}$ are noted on Figures 5.1-1 through 5.1-14 as ϕ total, ϕ burned and, inlet air total enthalpy, respectively. The static enthalpy is calculated from

$$H_S = H_T - \frac{V^2}{2gJ} H_T - \frac{V^2}{64.34 (778)}$$

with the velocity values being taken from the curves. Once the static and total enthalpies have been determined, the static and total temperatures are read from curves or interpolated between the curves shown in Figure 5.2-1.

5.1.2.2 Inlet Operation

Wind tunnel tests using a one-third scale inlet model indicate that an unsymmetrical unstart of the inlet is possible at the maximum design Mach numbers. This condition results in high normal loads when the engine is in the X-15A-2 shock field. Similarly, a symmetrical unstart in the shock field results in high axial loads. The pressure distribution due to either a symmetrical or partial unstart is shown in Figures 5.1-15, 5.1-16, and 5.1-17. The maximum axial load, $P_{xa} = 12,900$ lbs, occurs at $M_\infty = 8$ with a 360° unstarted inlet. At Station 44.6 the pressure is vented into the bellows cavity, and this creates a pressure load, P_{xp} , on the spike, which varies from 400 lbs to 6300 lbs. The time required for the bellows cavity to "fill" to this pressure depends on the rate of mass flow into the cavity compared with its volume. Requirements to minimize the "fill" time will be studied.

Figures 5.1-18 through 5.1-22 indicate pressure distribution on the spike at various Mach numbers, with or without combustion and at various angle of attack conditions.

5.1.3 Qualification Test Vibration Environment

The qualification tests will be performed by applying the sinusoidal and random vibration test levels to the complete engine, while mounted on the thrust measurement system, as specified in the Statement of Work L-4947-B, Paragraph 4.6.2.1.1.

The various component parts of the engine will be designed to withstand the specified input levels. For longitudinal inputs (x-axis), system



UNCLASSIFIED

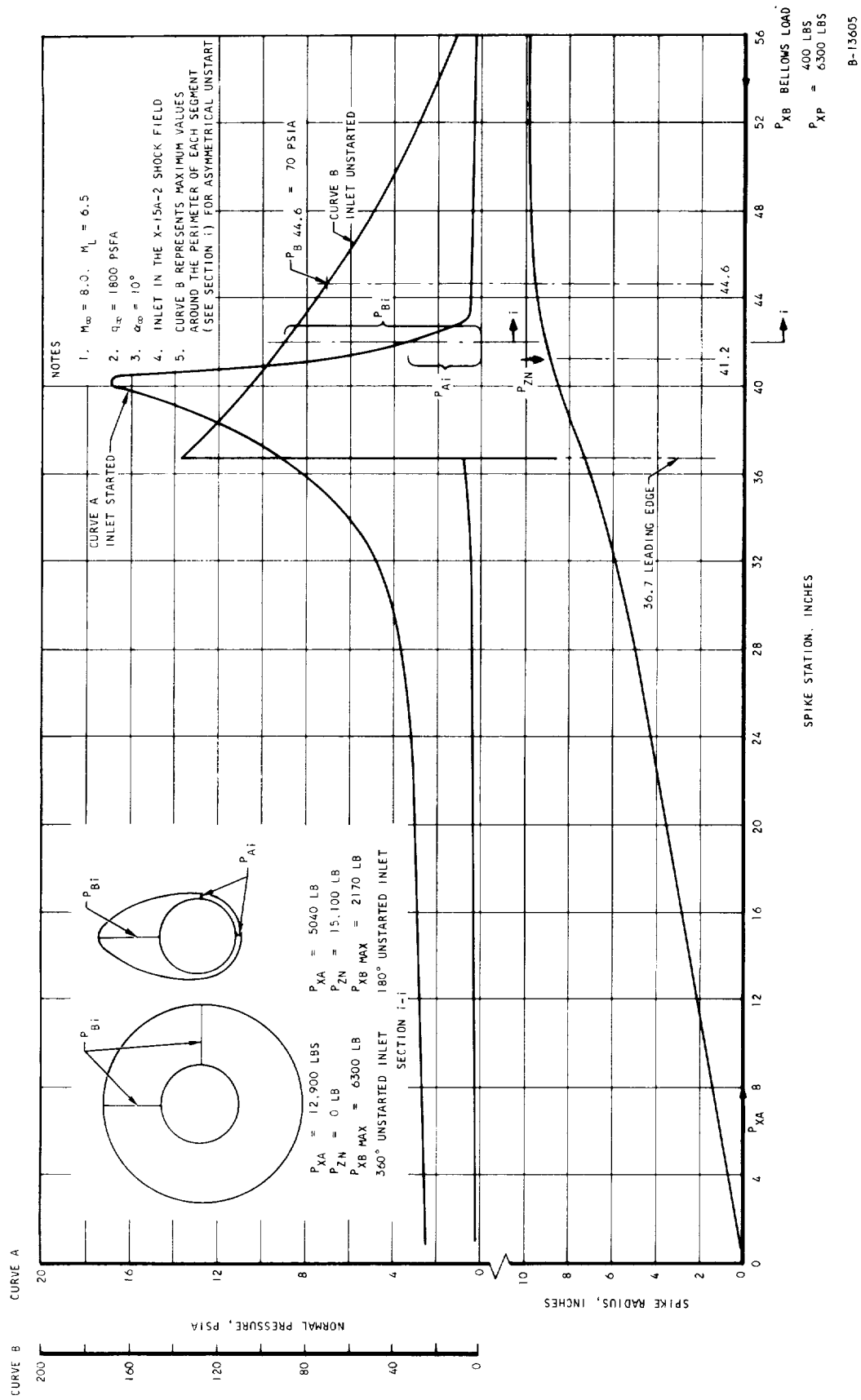


Figure 5.1-15. Spike Pressure Distribution with Unstarted Inlet, $M_\infty = 8$, X-15A-2 Shock Field



UNCLASSIFIED

UNCLASSIFIED

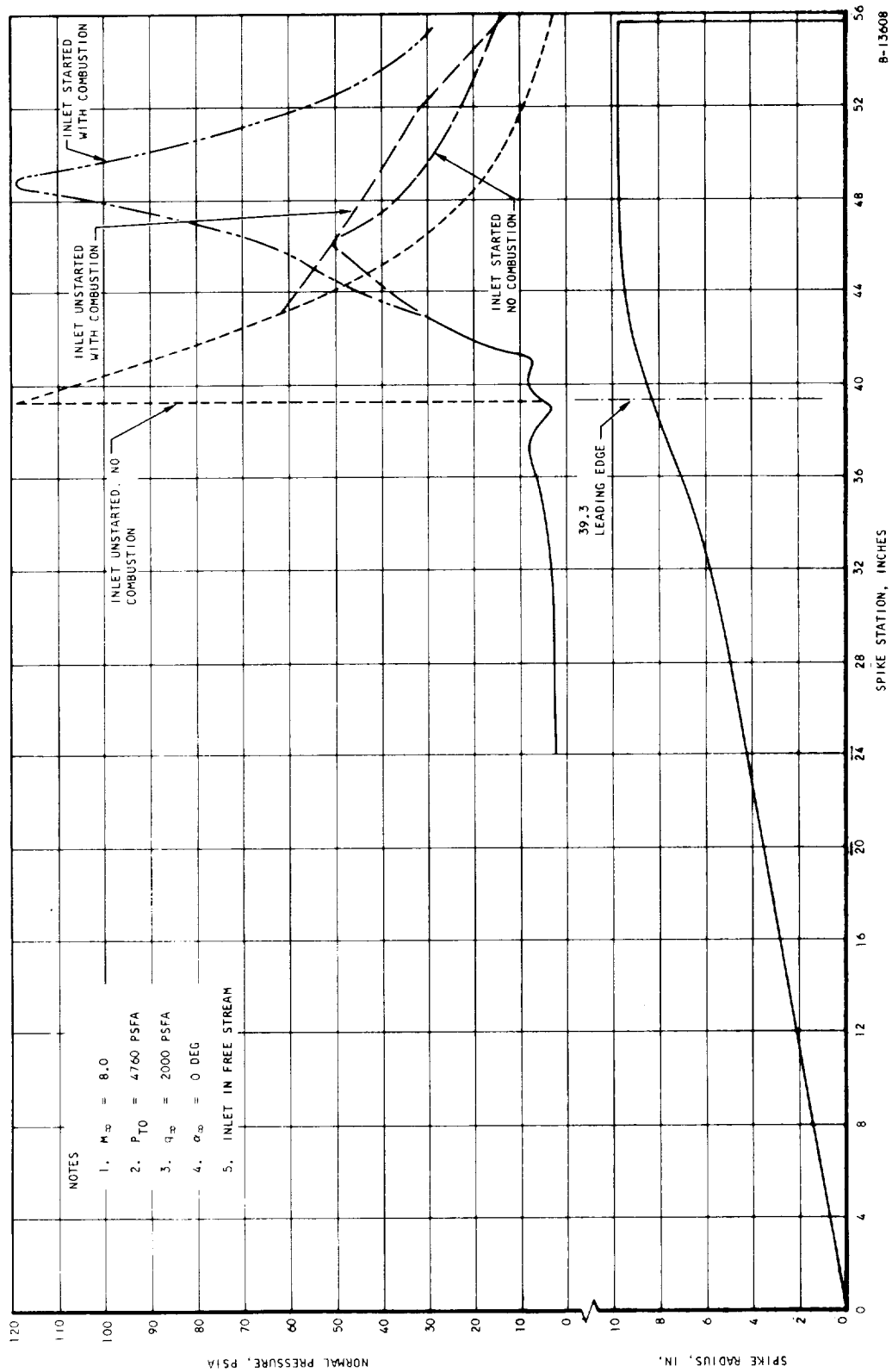


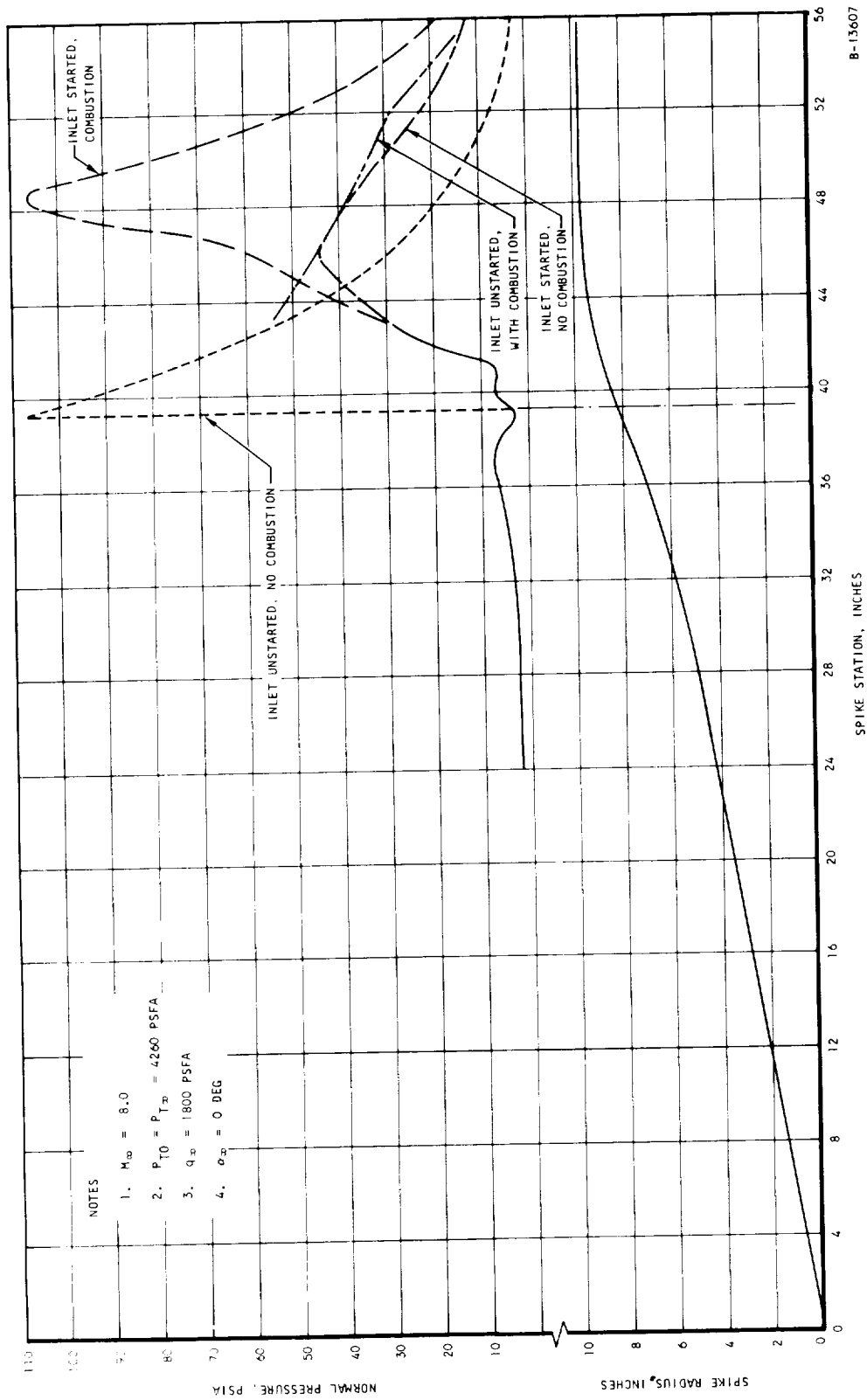
Figure 5.1-16. Spike Pressure Distribution, $M_\infty = 8$, $q_\infty = 2000$ PSFA, Engine in Free Stream



AIRESEARCH MANUFACTURING DIVISION
Los Angeles, California

UNCLASSIFIED

UNCLASSIFIED



B-13607

Figure 5.1-17. Spike Pressure Distribution, $M_{\infty} = 8$, $q_{\infty} = 1800$ PSFA, Engine in Free Stream



AIRESEARCH MANUFACTURING DIVISION
Los Angeles, California

UNCLASSIFIED

UNCLASSIFIED

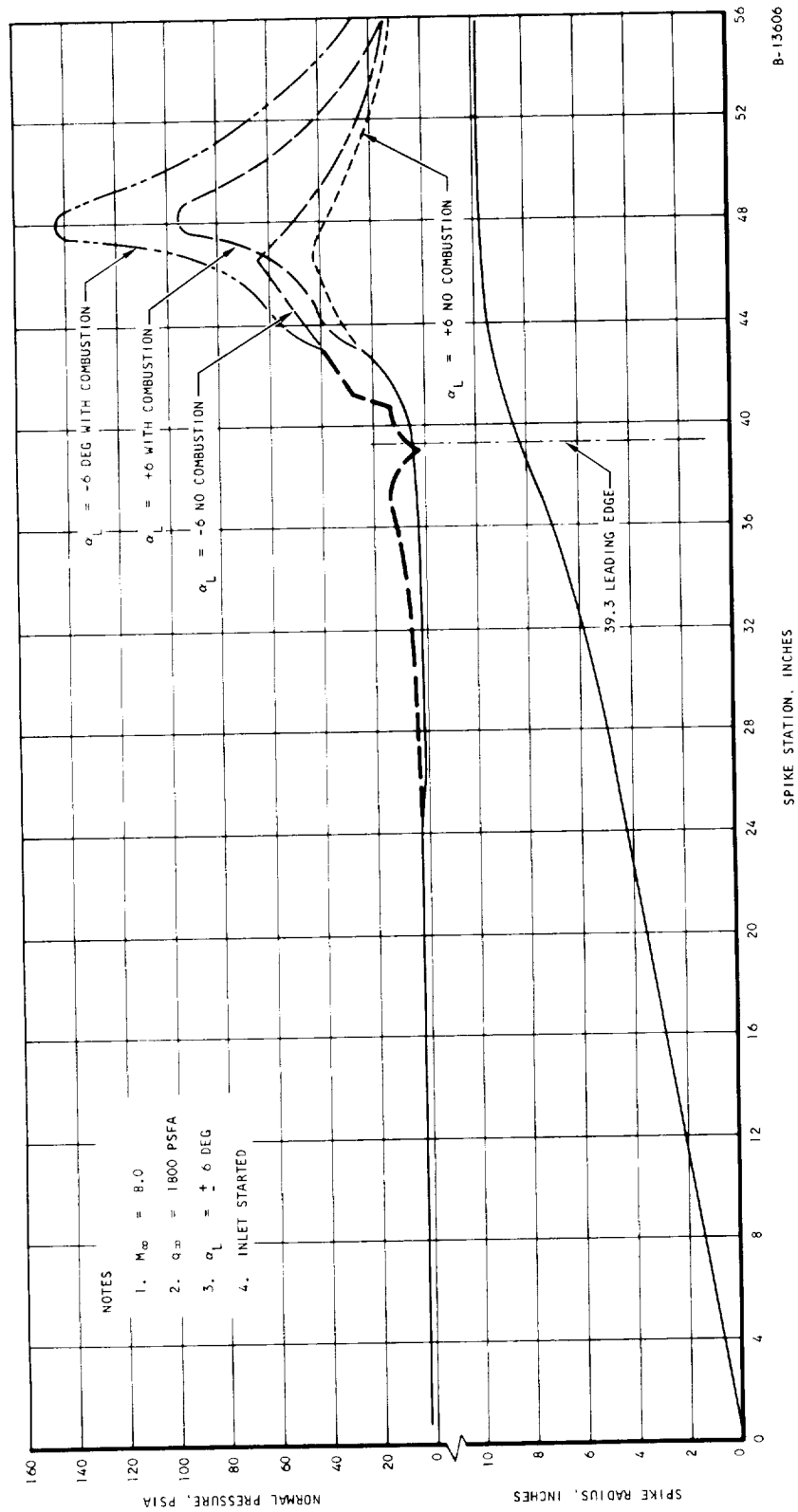


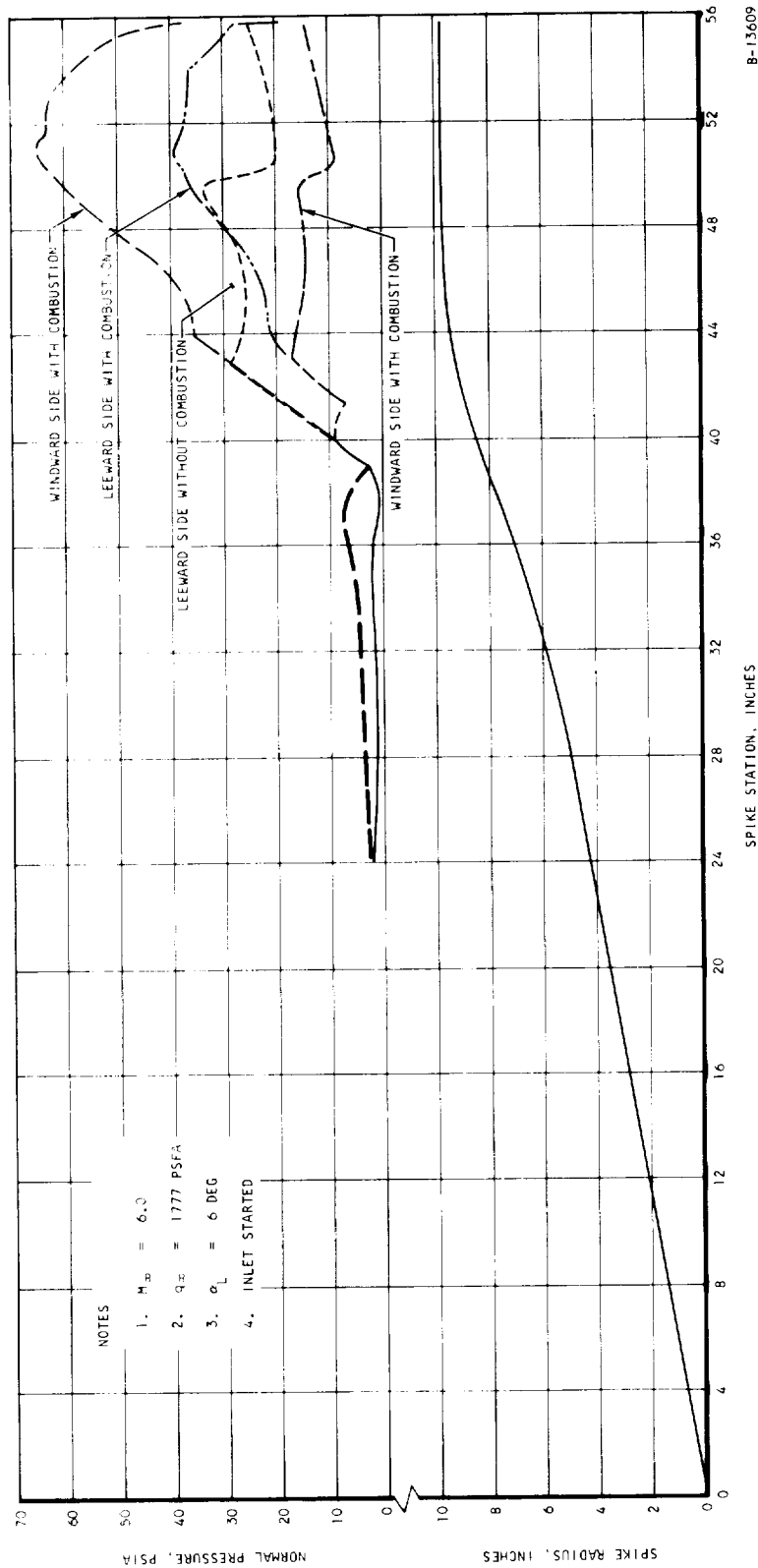
Figure 5.1-18. Spike Pressure Distribution, $M_\infty = 8$, Angle of Attack Condition



AIRESEARCH MANUFACTURING DIVISION
Los Angeles, California

UNCLASSIFIED

UNCLASSIFIED



B-13609

Figure 5.1-19. Spike Pressure Distribution, $M_\infty = 6$, $\alpha_L = 6$ Degrees



AIRESEARCH MANUFACTURING DIVISION
Los Angeles, California

UNCLASSIFIED

UNCLASSIFIED

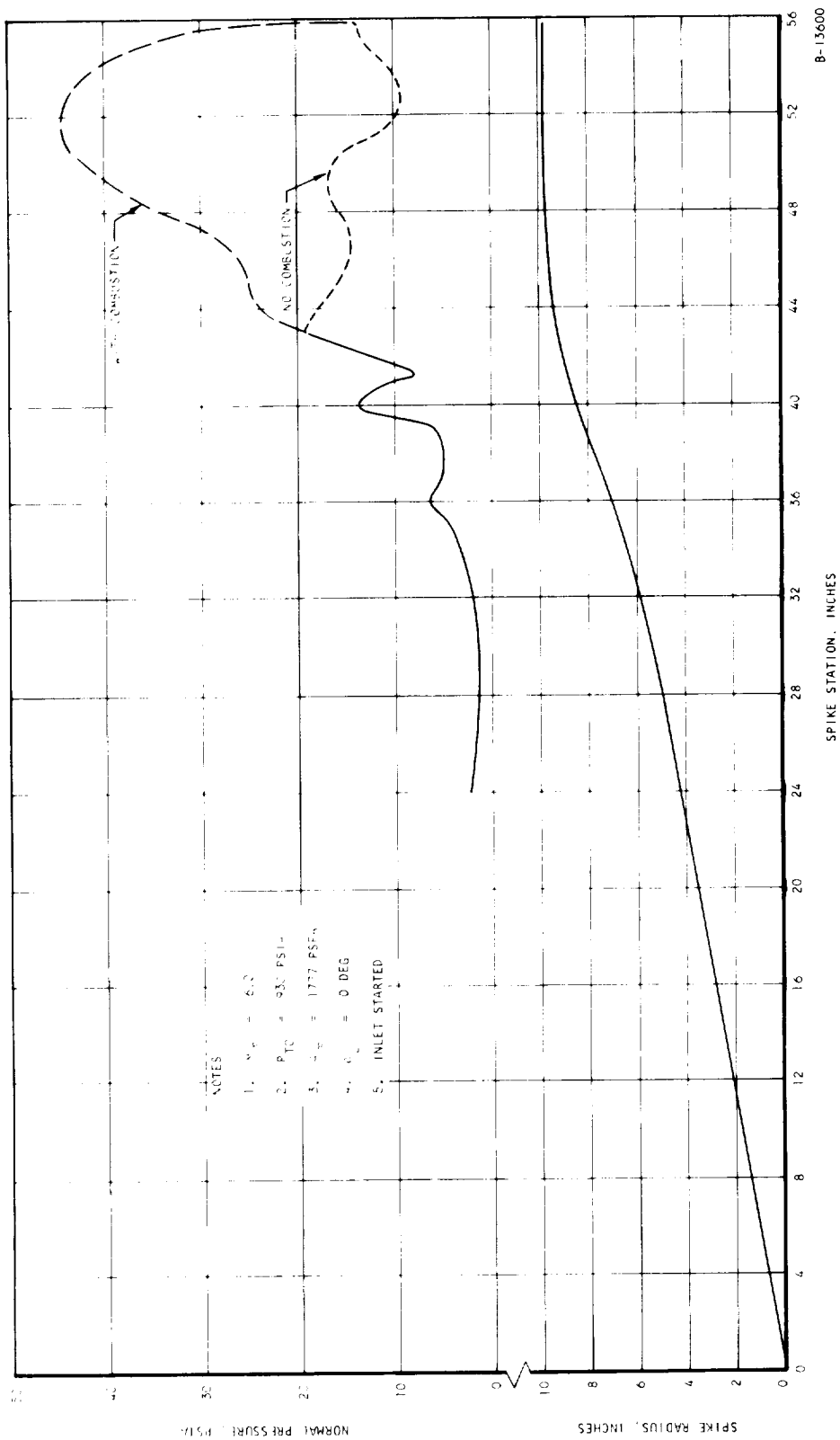


Figure 5.1-20. Spike Pressure Distribution, $M_0 = 6$, Inlet Started



AIRRESEARCH MANUFACTURING DIVISION
Los Angeles, California

UNCLASSIFIED

UNCLASSIFIED

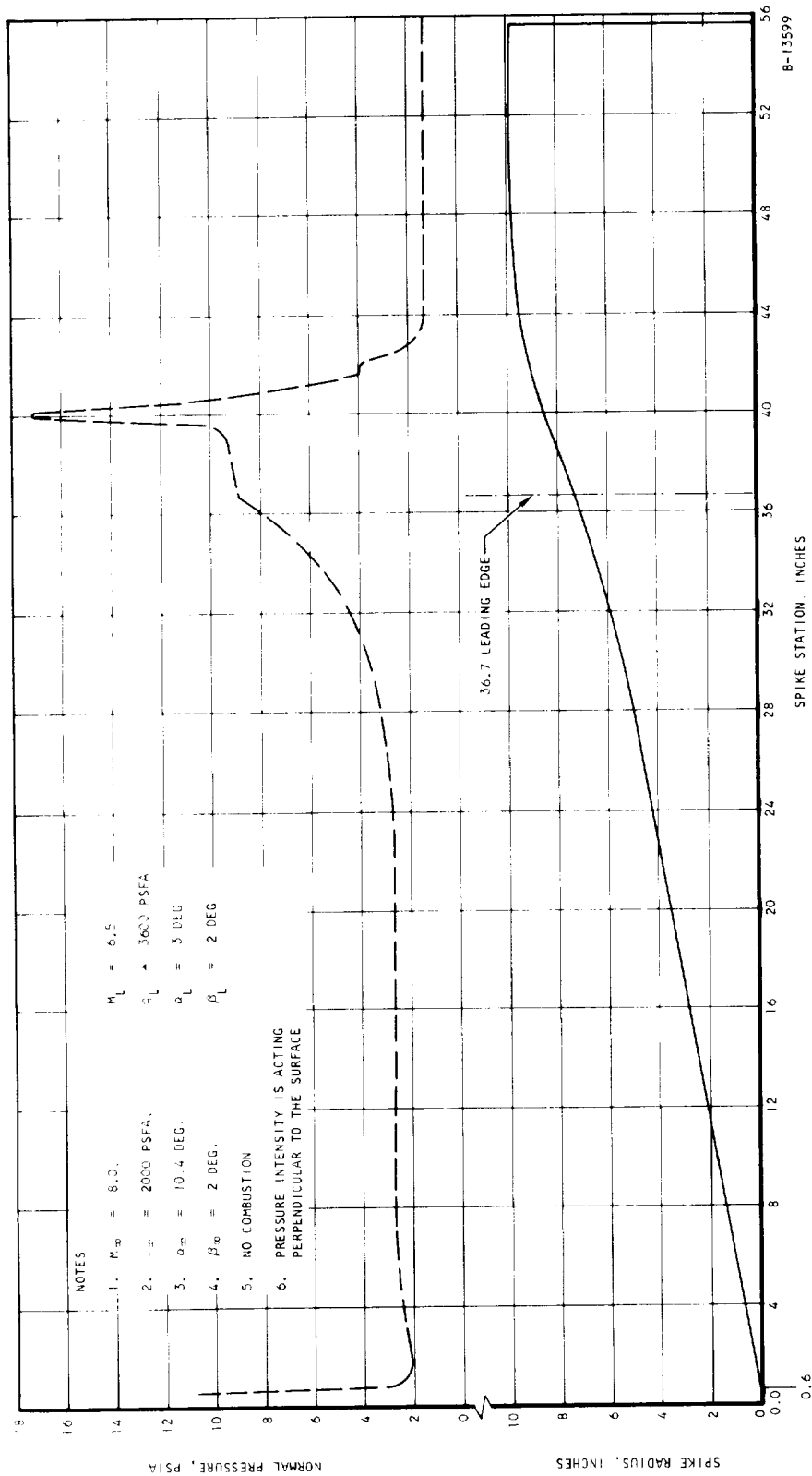


Figure 5.1-21. Spike Pressure Distribution, $M_{\infty} = 8$, Steady State Condition without Combustion



AIRESEARCH MANUFACTURING DIVISION
 Los Angeles, California

UNCLASSIFIED

UNCLASSIFIED

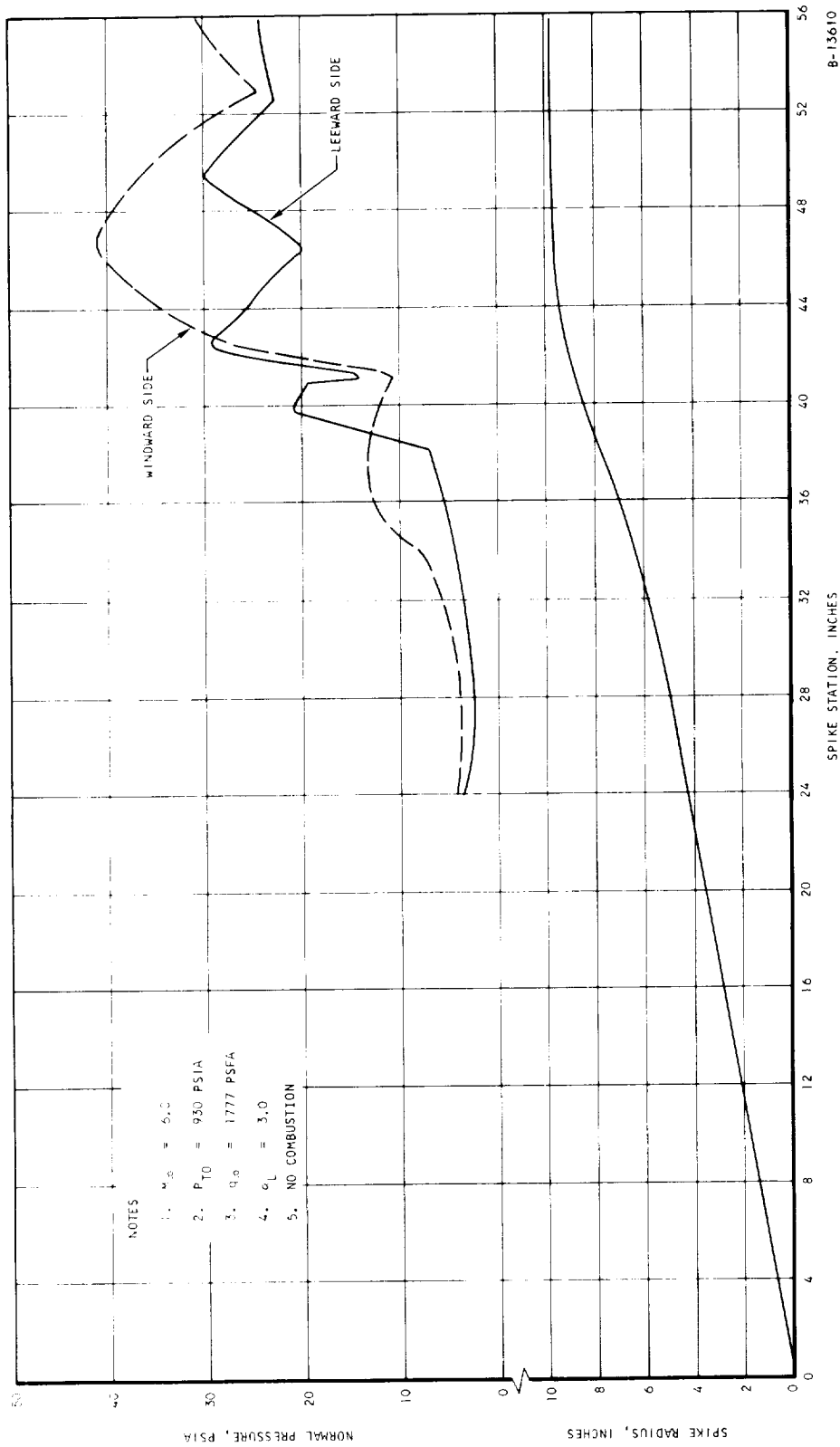


Figure 5.1-22. Spike Pressure Distribution, $M_\infty = 5$, $\alpha_L = 3$ Degrees



AIRESEARCH MANUFACTURING DIVISION
Los Angeles, California

UNCLASSIFIED

amplification will be assumed to produce a 20 g longitudinal response. For transverse loads (y or z axes), the system amplification factor will be assumed to be 2.5/1 for the outer shell, inner body, and spike actuator. The response of the inlet spike will be assumed to be 20 g.

5.1.4

5.1.4.1 Aerodynamic Heating

Figures 5.1-23, 5.1-24 and 5.1-25 indicate the engine heat flux distributions for three flight conditions: (a) Mach 4, 59,000 ft subsonic combustion, (b) Mach 6, 76,000 ft subsonic combustion, and (c) Mach 8, Mach 6.5 local, 88,000 ft supersonic combustion. The heat fluxes indicated are based on (1) the Fay-Riddell correlation for stagnation points (i.e. spike tip and leading edge), (2) laminar flat plate, (3) turbulent flat plate, and (4) realistic wall temperature distributions, i.e., wall temperatures approximating those expected in operation at the various stations.

The Mach 4 and Mach 6 cases have approximately the same maximum heating loads. This is due to two factors, (1) The air flow rates are approximately the same and (2) both cases have a fuel $\phi = 1$ at the second injectors. The most severe heating is experienced at the Mach 6.5 local flight condition.

The outer body has peak heat fluxes of approximately 870 Btu/sec ft² while the 30-mil outside radius leading edge and the 125-mil outside radius spike tip have heat fluxes of 1700 Btu/sec ft² and 815 Btu/sec ft², respectively.

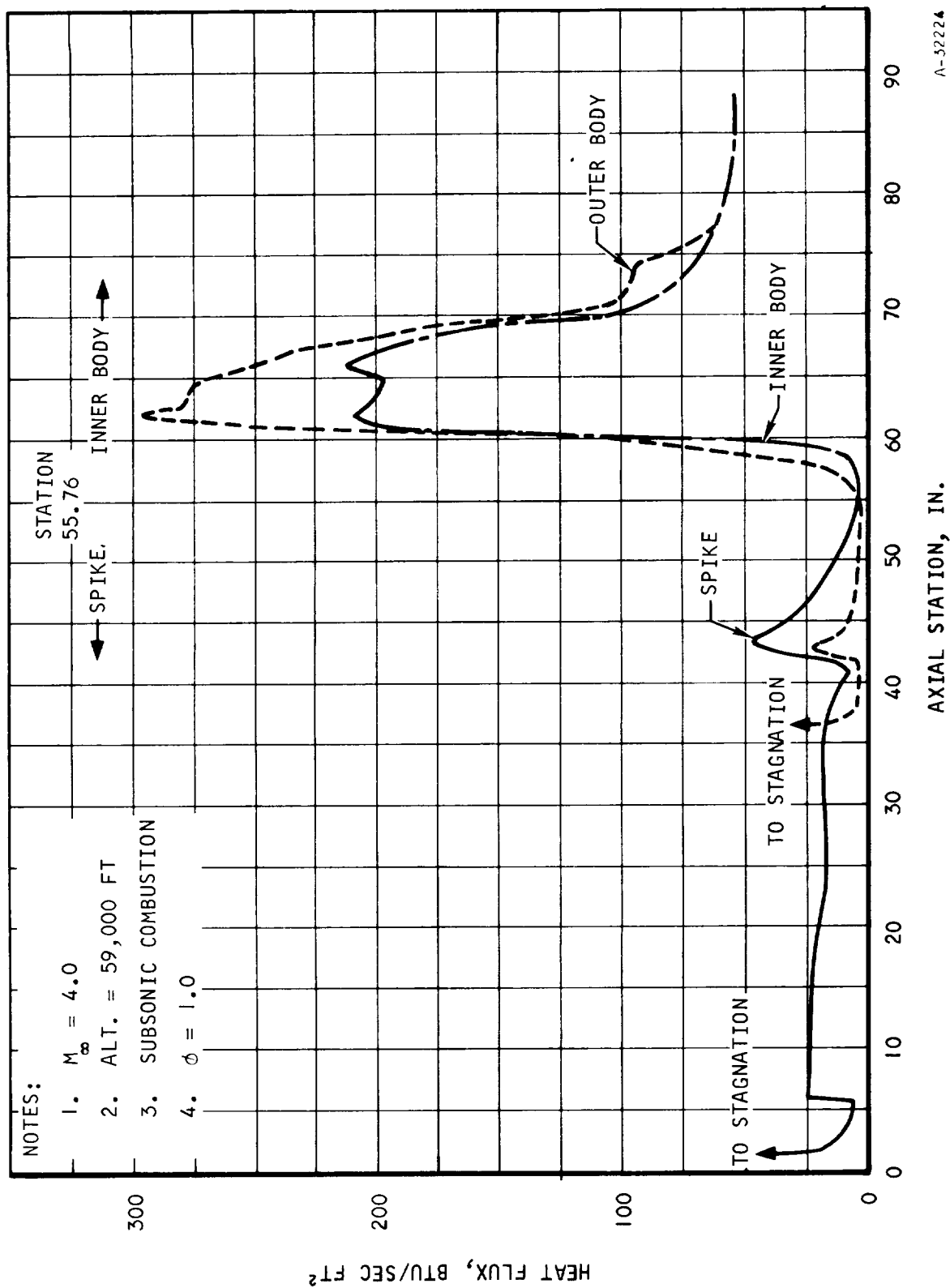
The strut leading edge stagnation line heat flux for $M_L = 6.5$ ($M_\infty = 8$ at 88,000 ft) is 1870 Btu/sec ft² for a leading edge radius of 80 mils. The quoted stagnation heat flux is the average of 2030 Btu/sec ft² for Newtonian flow and 1700 Btu/sec ft² for potential flow. The average was used because the local Mach number of 2 is between the limits of exactness for these two types of flow model. The flow properties and heat flux along the strut sides are shown in Figure 5.1-26. All heat fluxes shown include the gas radiative heating, which varies from 118 Btu/sec ft² at the stagnation line to less than 3 Btu/sec ft² at the strut trailing edge.

No analysis of stagnation heat fluxes for the Mach 4 and Mach 6 cases have been completed pending detail analyses of the cooling jacket flows and temperatures.

Table 5.1-2 provides a comparison of heat flux and heat load calculated by the duct flow and flat plate equations defined in Paragraph 5.2. Significant points of comparison are (1) peak heat fluxes of 800 Btu/sec ft² at station 50 (duct flow calculation) and 716 and 873 Btu/sec ft² (flat plate calculation) on the inner body and outer body, respectively and (2) an overall heat load reduction with pipe flow of about 20 percent, which results from about 23 percent lower heat load on the inner body and about 3 percent lower heat load on the outer body. The hydrogen flow rate would be decreased by more than 20 percent because the allowable cross-section ΔT at Station 50, i.e. the peak heat flux location can affect flow rate as strongly as total heat



UNCLASSIFIED



A-52224

Figure 5.1-23. Engine Heat Flux Distribution, $M_\infty = 4$



AIRESEARCH MANUFACTURING DIVISION
Los Angeles, California

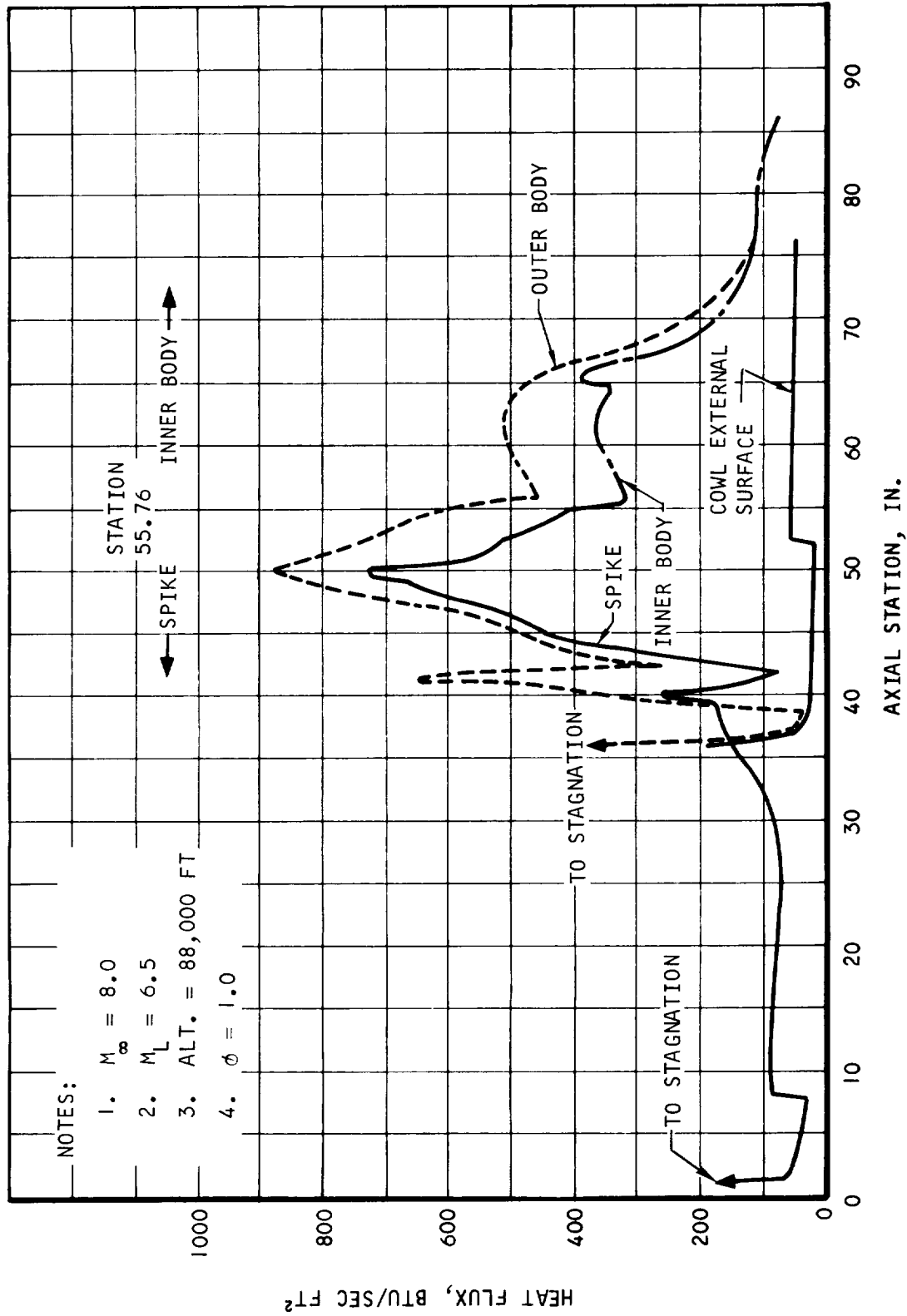
UNCLASSIFIED

UNCLASSIFIED



Figure 5.1-24. Engine Heat Flux Distribution, $M_\infty = 6$

UNCLASSIFIED



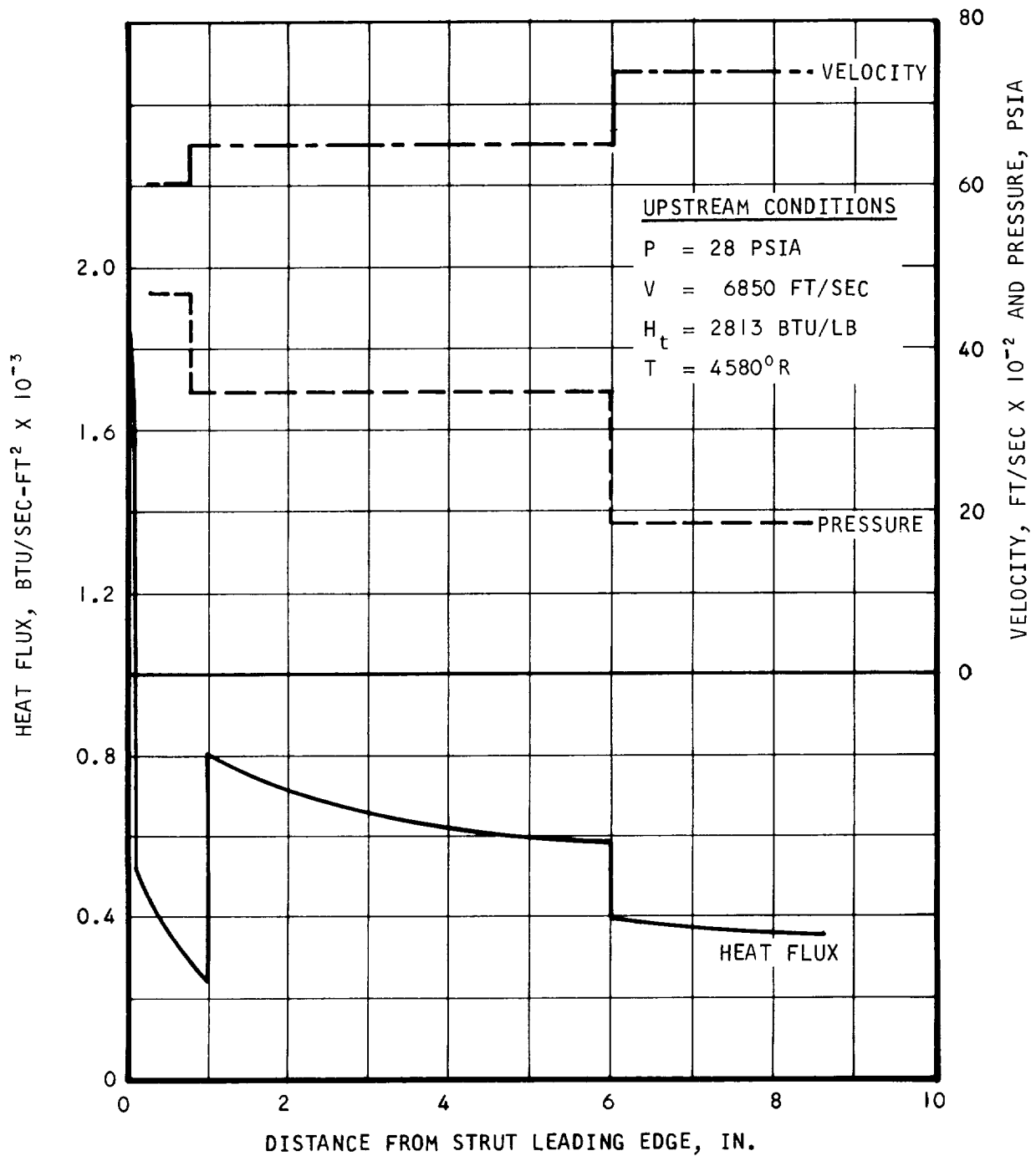
A-52222

Figure 5.1-25. Engine Heat Flux Distribution, $M_\infty = 8$



AIRESEARCH MANUFACTURING DIVISION
Los Angeles, California

UNCLASSIFIED



A-32445

Figure 5.1-26. Strut Heat Flux Distribution, $M_L = 6.5$, 88,000 ft



TABLE 5.1-2
COMPARISON OF DUCT FLOW AND FLAT PLATE
CALCULATIONS

Station, in.	Flat Plate Heat Flux, Btu/sec ft ²		Duct Flow Heat Flux, Btu/sec ft ²
	Spike and Inner Body	Outer Body	
43	263	304	180
45	439	485	360
50	716	873	800
55	415	612	500
60	358	501	380
65	348	476	360
70	187	216	137
75	123	140	77
77	111	113	65

Notes:

1. Duct heat flux \approx flat plate heat flux $\left(\frac{0.023}{0.0296}\right)\left(\frac{S}{D}\right)^{0.2}\left(\frac{T^*}{T^*}\right)$. See Table 5.2-1 for definitions.
2. Mach 6.5 local, Mach 8 free stream, 88,000 ft altitude, 53 lb/sec airflow, $\phi = 1$ at first injector (station 43).
3. Ratio of duct flow heat load to plate heat load
Spike and inner body: 0.97
Outer body: 0.77



load. The flat plate equations have been and will continue to be used for aerodynamic heating calculations, for reasons discussed in Paragraph 5.2.

5.1.4.2 Outer Shell - Engine Mounts

A preliminary review of the structural analysis of the outer shell mounts was conducted in order to check out the aerodynamic pressure load due to a symmetrical unstart with a normal shock at the leading edge lip. This condition was not previously considered in the structural analysis. The review indicated that the symmetrical unstart condition will be critical for the design of the engine mounts.

The bases for the Condition A design load combinations indicated in Table 5.1-3 are given below. Condition A is defined as the maximum axial load (inlet symmetrically unstarted with no combustion).

- (a) The axial load equals 12,100 lb aft acting on the spike. Net aerodynamic force on the outer body is 7210 lb forward. Net aerodynamic load on the outer body leading edge is 1010 lb, aft, and on the six engine struts is 160 lb aft.
- (b) The net internal thrust equals -4240 lb.
- (c) Normal and transverse aerodynamic loads are considered to be negligible for the maximum axial load condition ($\alpha_L = 0$).
- (d) The maximum normal static acceleration that may exist in this condition is equal to + 1.0 g.
- (e) A 3.0 g vibration (response) may be assumed to act in any direction simultaneously with this loading.
- (f) The maximum load may occur with the spike retracted 1.5 to 5.0 in. from the inlet closed position.

5.1.4.3 Outer Body-Inner Body Struts

The outer body-inner body struts and strut attachments are critical for the aerodynamic pressure load due to unsymmetrical unstart with a normal shock at the leading edge lip, which was not previously checked:

The bases for the Condition B design load combinations indicated in Table 5.1-4 is given below. Condition B is defined as the maximum normal load (inlet unsymmetrically unstarted with no combustion).

- (a) The maximum normal load on the spike is equal to 15,100 lb upward. An equal and opposite load, with the same center of pressure exists on the outer body. It is accompanied by an aft load on the spike equal to 5040 lb.



TABLE 5.1-3

CONDITION A - MAXIMUM AXIAL LOAD

$$M_{\infty} = 8, M_L = 6.5$$

	Maximum Load Condition, Force, lb	Design Condition, Force, lb
F_{TX} (Thrust)	0	0
F_{AX} (Aerodynamic press)	-5250	-5250
F_{AZ} (Aerodynamic press)	0 ⁽²⁾	0
F_{AY} (Aerodynamic press)	0 ⁽³⁾	0
F_{IX} (Inertia, static accel)	-1415 +2124	-1415
F_{IY} (Inertia, static accel)	0 ⁽³⁾	0
F_{IZ} (Inertia, static accel)	-707.8 (at $\bar{X} = 55.57$) ⁽⁵⁾	-707.8 ⁽²⁾
F_{YX} (Vibration)	-2124	-2124
F_{BX} (Bellows press)	400-6300 ⁽¹⁾	--- ⁽⁴⁾

Notes:

- (1) Forward on spike, aft on inner body.
- (2) $\alpha_L = 0$ at max axial load, $N_z \cong +1.0$.
- (3) Transverse load is negligible for maximum axial load condition.
- (4) Load is internally balanced, and does not affect outer shell engine mount loads.
- (5) $X = 0$ at apex of spike cone.



UNCLASSIFIED

TABLE 5.1-4

CONDITION B (MAXIMUM NORMAL LOAD)
 $M_L = 6.5$, $q_L = 3240$ PSF, $\alpha_L = 4$ DEG

	MAXIMUM LOAD CONDITION, FORCE, LB	DESIGN CONDITION, FORCE, LB
F_{TX} (Thrust)	0	0
F_{AX} (Aerodynamic press)	-5040	-5040
F_{AZ} (Aerodynamic press)	1167	---(3)
F_{AZI} (Aero press, equal and opposite)	+15,100 ⁽¹⁾	+15,100
F_{AY} (Aerodynamic press)	-862	---(6)
F_{IX} (Inertia, static accel)	+2124 $(\bar{X} = 55.57)$ ⁽⁴⁾ -1415	-1415 $(\bar{X} = 55.57)$
F_{IZ} (Inertia, static accel)	-2124 ⁽⁵⁾	-2124
F_{IY} (Inertia, static accel)	+708	---(6)
F_{YZ} (Vibration)	2124 $(\bar{X} = 55.57)$	2124 $(\bar{X} = 55.57)$
F_{BX} (Bellows press)	2170 (max)	0 ⁽²⁾

Note: Static accel and vibration loads are for total engine. For design of struts and strut attachments, etc., only spike and actuator inertia loads will be considered.

- (1) On spike.
- (2) Critical for strut attachment.
- (3) Considered part of 15,100 load, critical for strut design only.
- (4) $\bar{X} = 55.57$ - engine C.G.
- (5) $\alpha_L = 4$ deg, $N_Z = +3$
- (6) Net transverse load negligible.
- (7) $\bar{X} = 0$ at apex of spike cone.



- (b) The load occurs with $M_L = 6.5$, $q_L = 3240$ psfa, $\alpha_L = 4$ deg. Static acceleration loads that may act simultaneously are indicated in Paragraph 5.1.1.1, (Operating Conditions, $M_L = 6.5$).

Items b, e and f under Condition A Paragraph 5.1.4.2 apply also for Condition B.

5.1.4.4 Actuator

Loads on the actuator will be produced by external aerodynamic forces acting on the spike, bellows spring forces, pressure forces within the bellows cavity, and acceleration forces acting on the spike. These composite loads were reviewed with the inclusion of aerodynamic unstart loads for $M_\infty = 8.0$, $M_L = 6.5$, and X-15 angle of attack = 10 deg. Loads were considered for both symmetrical and asymmetrical unstart conditions.

The maximum aerodynamic axial force is produced by a symmetrical unstart with $M_L = 6.5$, $q_L = 3240$ psfa, and $\alpha_L = 0$. The axial force for this condition is 12,900 lb aft. Normal and transverse aerodynamic loads for this condition are negligible.

The maximum aerodynamic normal force occurs with an asymmetrical unstart with $M_L = 6.5$, $q_L = 3240$ psfa, and a local angle of attack of 4 deg at the engine centerline. The normal force is 15,100 lb upward for this condition, and it is accompanied by an axial force of 5040 lb aft.

The bellows spring force varies from 2500 lb aft for the fully extended spike position to zero with the spike fully retracted. Pressure forces within the bellows cavity vary from 6300 lb forward to 400 lb forward with the spike in the fully retracted position.

Vibrational response acting simultaneously with these loads may be 3.0 g in any direction. The acceleration loads that may occur are listed in Table 5.1-1. Engine thrust forces and external drag forces do not contribute to the actuator loading.

Maximum actuator structural loading occurs for the asymmetrical unstart condition. The various possible load conditions, as derived from Figures 5.1-15 through 5.1-22 are shown in Figures 5.1-27 through 5.1-33. Bellows and internal pressure forces have been incorporated into the figures. The conditions shown are as follows:

- (a) Maximum net axial pressure force, maximum actuator retraction (see Figures 5.1-27 and 5.1-28). Normal forces for these conditions are taken as zero.

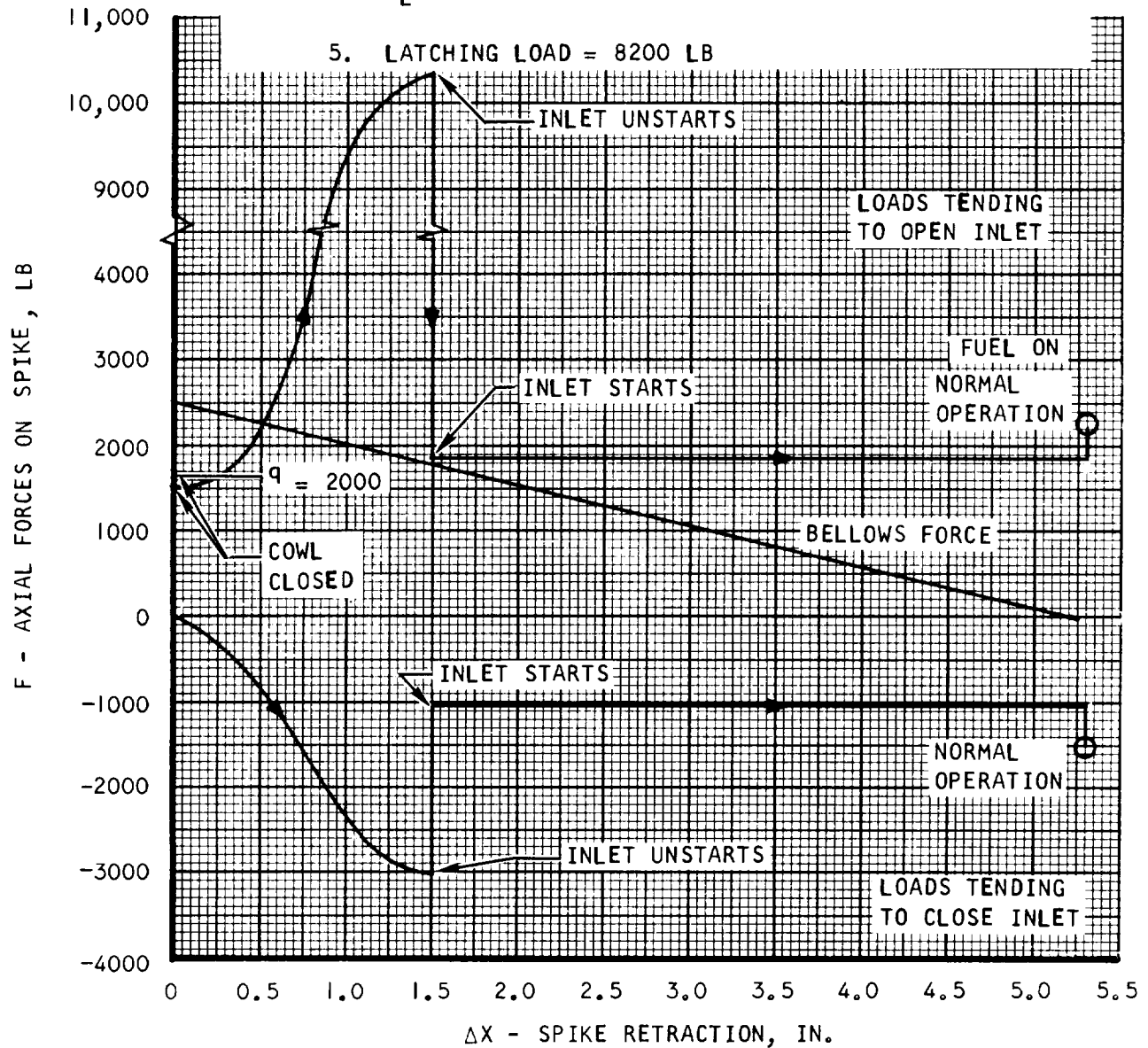
Local Mach number, $M_L = 6.0$

Free stream Mach number, $M_\infty = 7.4$



UNCLASSIFIED

- NOTE: 1. $M_L = 6.0$, $q_L = 3100$ PSFA
 2. $q_\infty = 1800$ PSFA
 3. AT COWL CLOSED POSITION, $q_\infty = 1800$ AND 2000 PSFA
 4. $\alpha_L = 0^\circ$



A-31606

Figure 5.1-27. Estimated Axial Load Profile on Spike During a Typical Inlet Starting Sequence

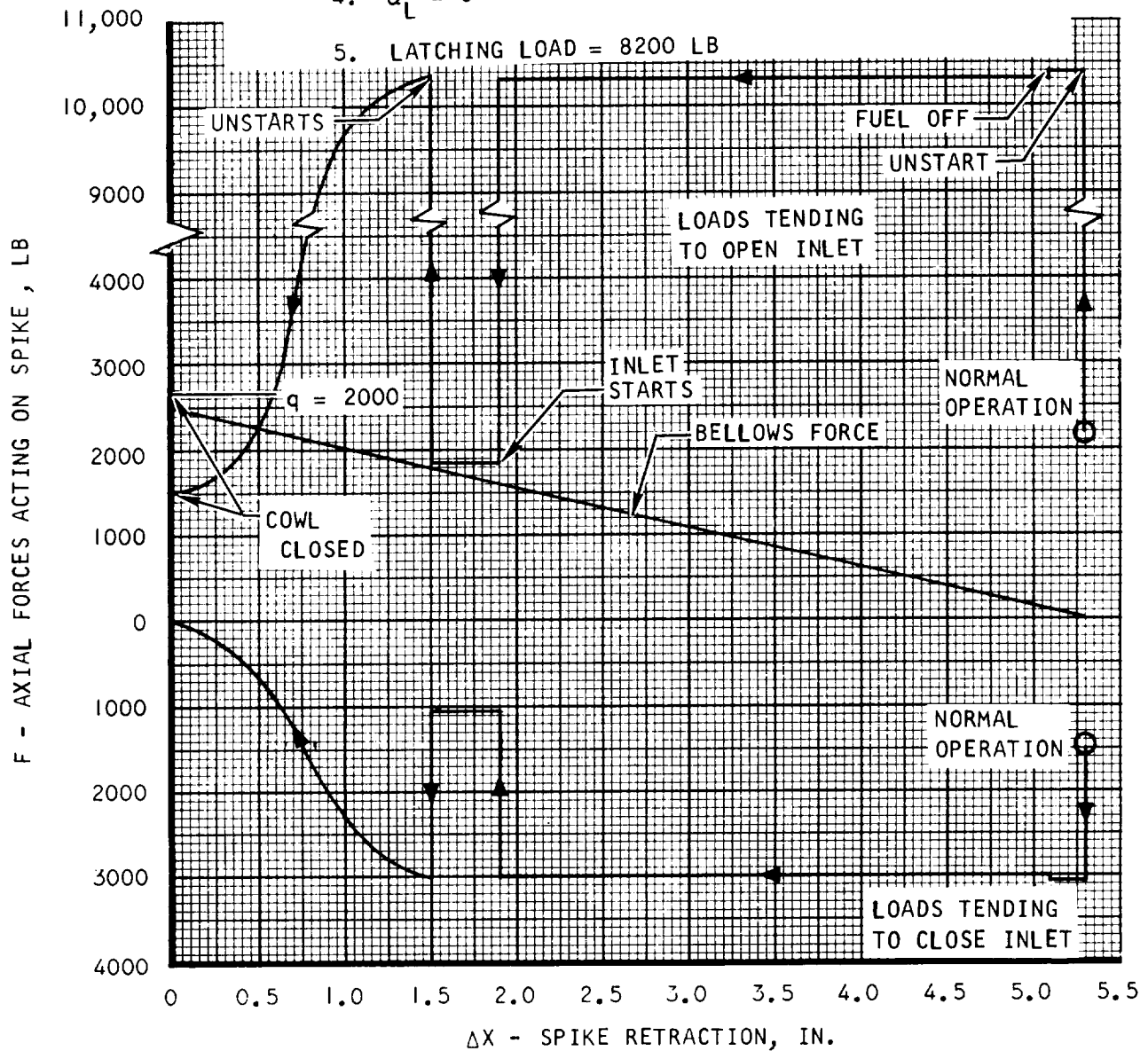


AIRESEARCH MANUFACTURING DIVISION
 Los Angeles, California

UNCLASSIFIED

UNCLASSIFIED

- NOTE: 1. $M_L = 6.0$, $q_L = 3100$ PSFA
 2. $q_\infty = 1800$ PSFA
 3. AT COWL CLOSED POSITION $q_\infty = 1800$ AND 2000 PSFA
 4. $\alpha_L = 0^\circ$
 5. LATCHING LOAD = 8200 LB



A-31605

Figure 5.1-28. Estimated Axial Load Profile on Spike During a Typical Inlet Unstart Sequence (Shock Expelled)



AIRSEARCH MANUFACTURING DIVISION
 Los Angeles, California

67-2833
 Page 5-37

UNCLASSIFIED

UNCLASSIFIED

- NOTE: 1. $M_\infty = 8.0$
 2. $M_L = 6.5$, $q_L = 3240$ PSFA
 3. $q_\infty = 1800$ PSFA
 4. AT COWL CLOSED POSITION $q_\infty = 1800$ AND 2000 PSFA
 5. $\alpha_L = 0^\circ$

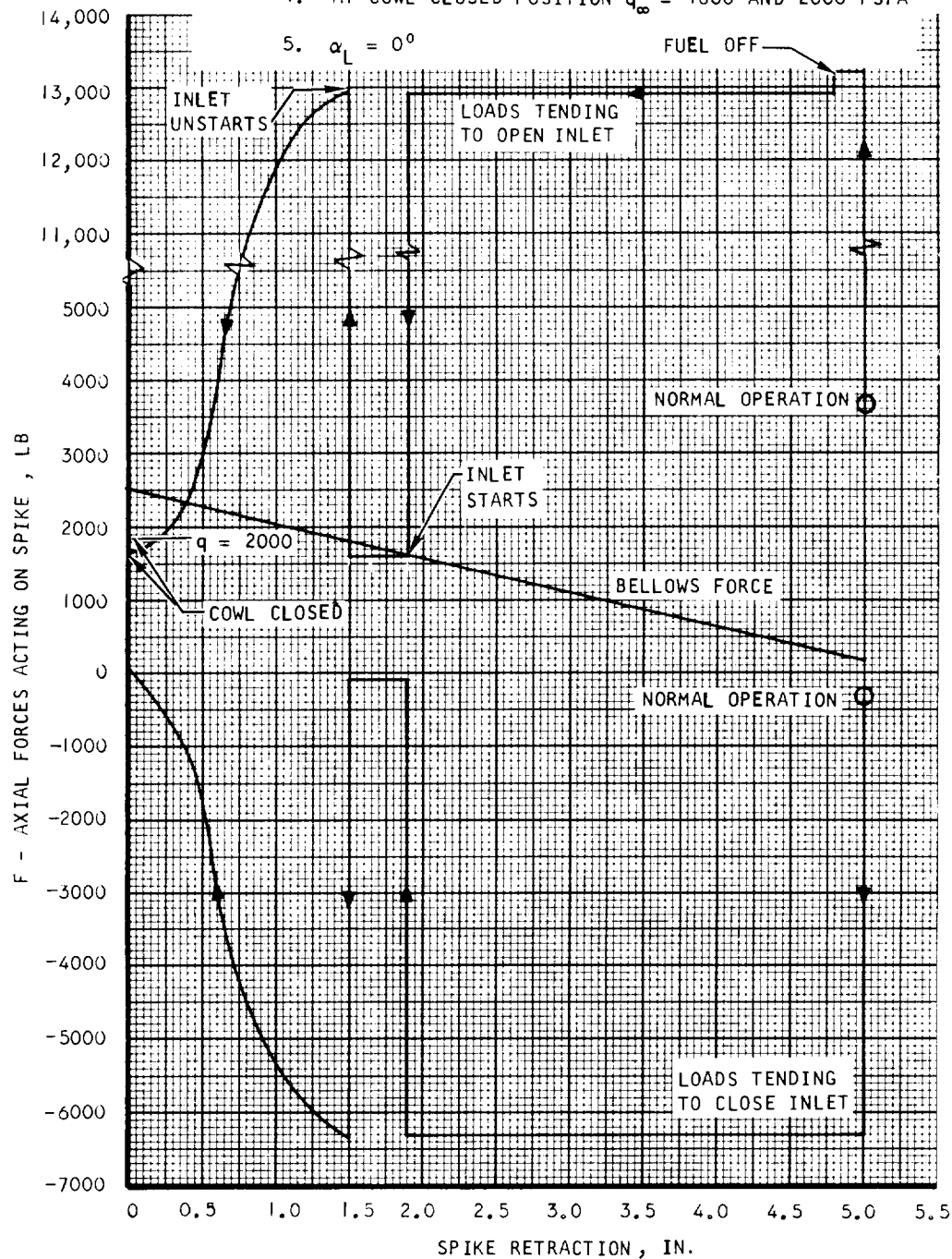


Figure 5.1-29. Estimated Axial Load Profile on Spike During a Typical Inlet Unstart Sequence (Shock Expelled)

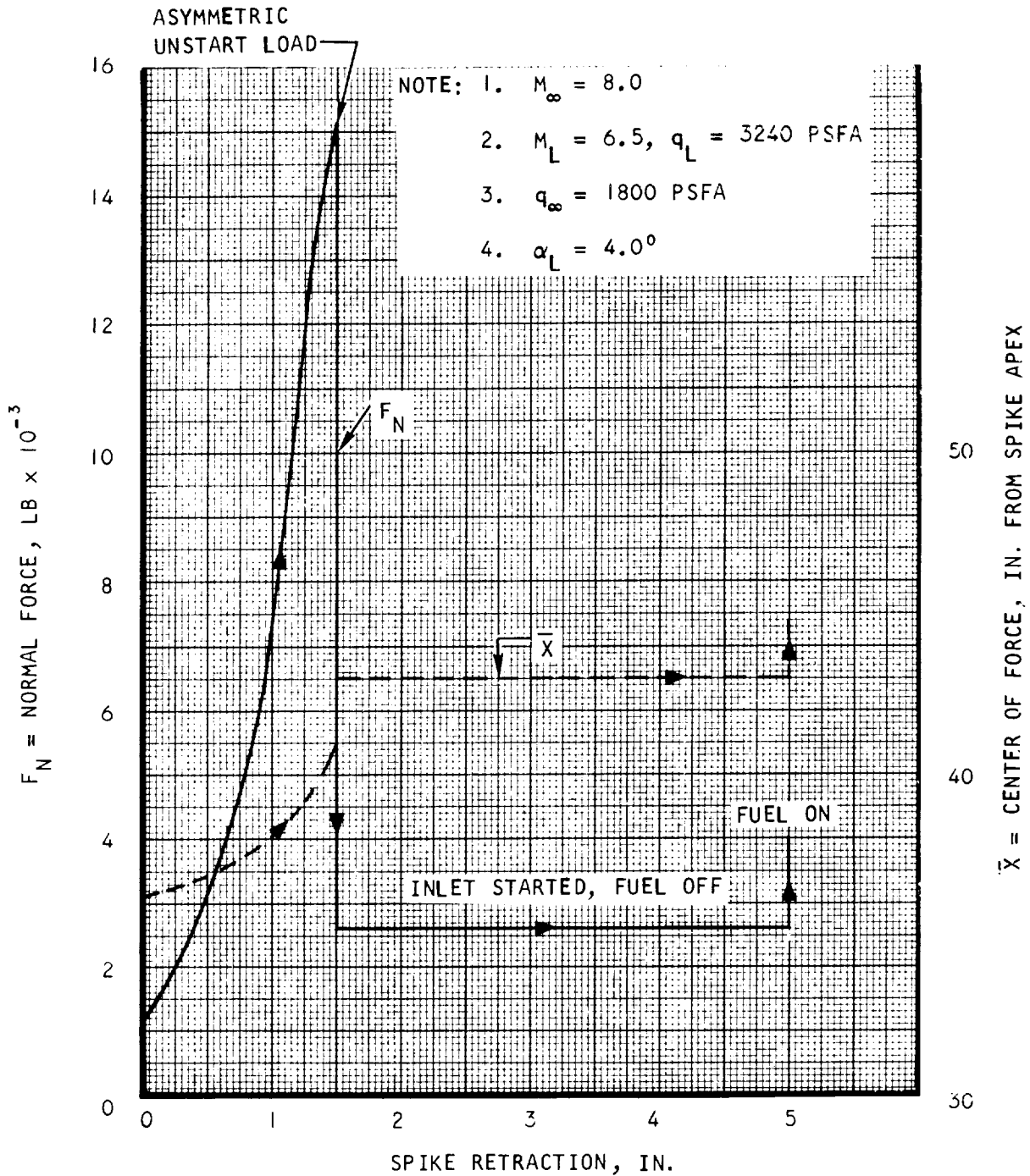
A-31607



AIRESEARCH MANUFACTURING DIVISION
 Los Angeles, California

UNCLASSIFIED

UNCLASSIFIED



A-31608

Figure 5.1-30. Design Normal Load Profile During an Inlet Starting Sequence



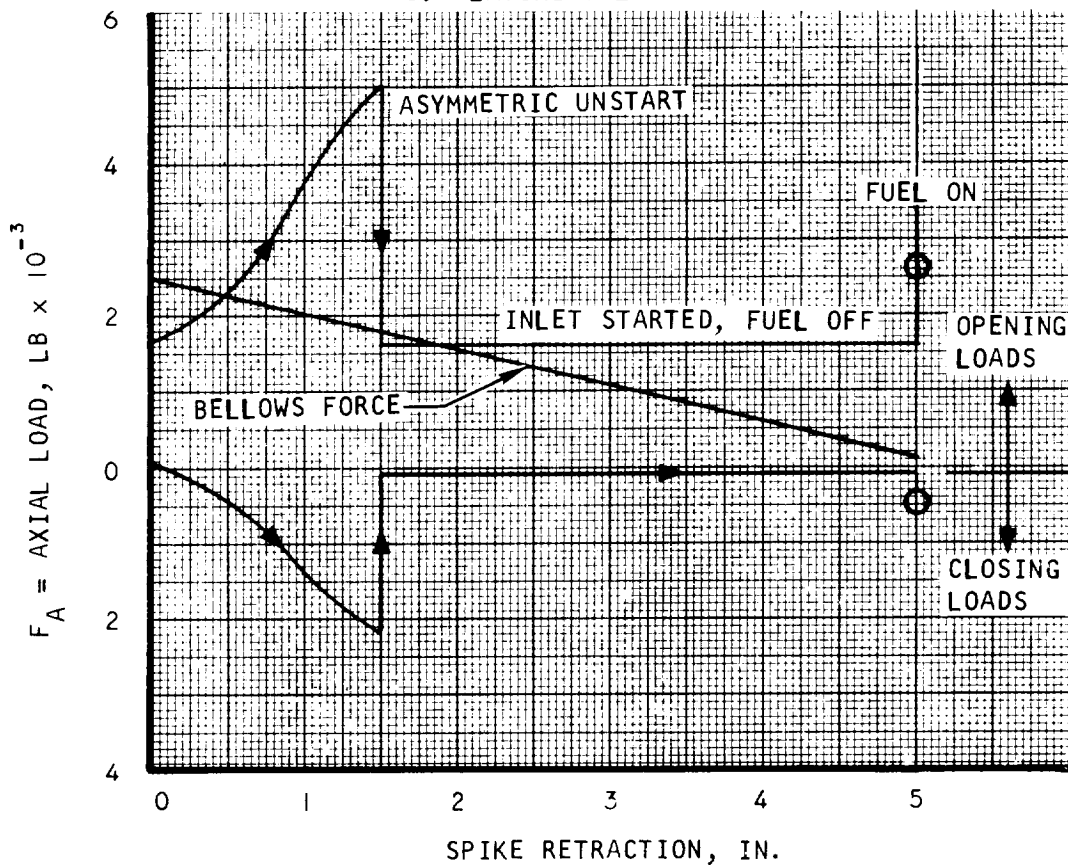
AIRESEARCH MANUFACTURING DIVISION
Los Angeles, California

67-2833
Page 5-39

UNCLASSIFIED

UNCLASSIFIED

- NOTE: 1. $M_\infty = 8.0$
 2. $M_L = 6.5$, $q_L = 3240$ PSFA
 3. $q_\infty = 1800$ PSFA
 4. $\alpha_L = 4.0^\circ$
 5. LATCHING LOAD = 8200 LB



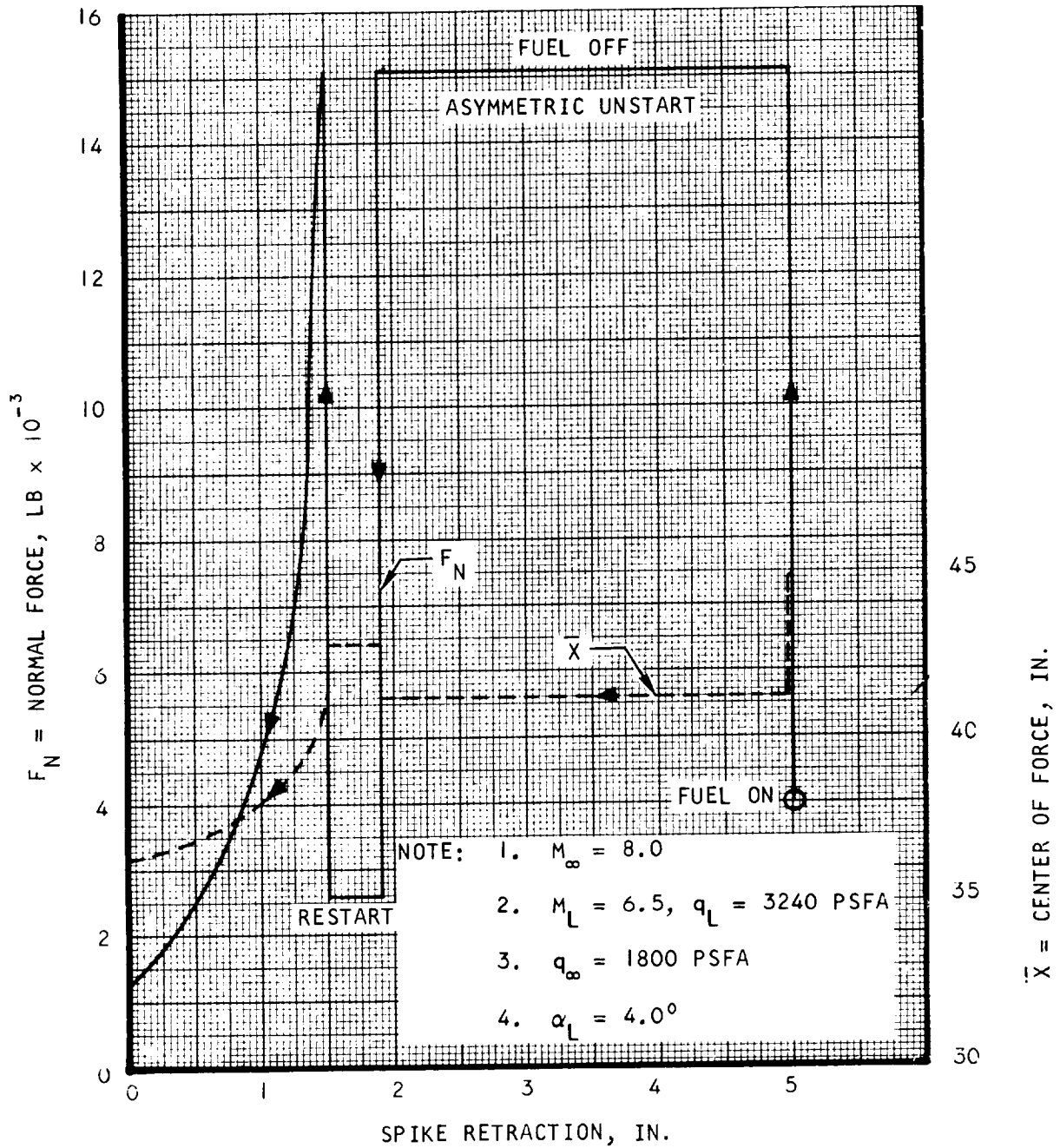
A-31603

Figure 5.1-31. Estimated Axial Load Profile on Spike During a Typical Inlet Starting Sequence



UNCLASSIFIED

UNCLASSIFIED



A-31604

Figure 5.1-32. Estimated Normal Load Profile on Spike During a Typical Inlet Unstart Sequence (Shock Expelled)

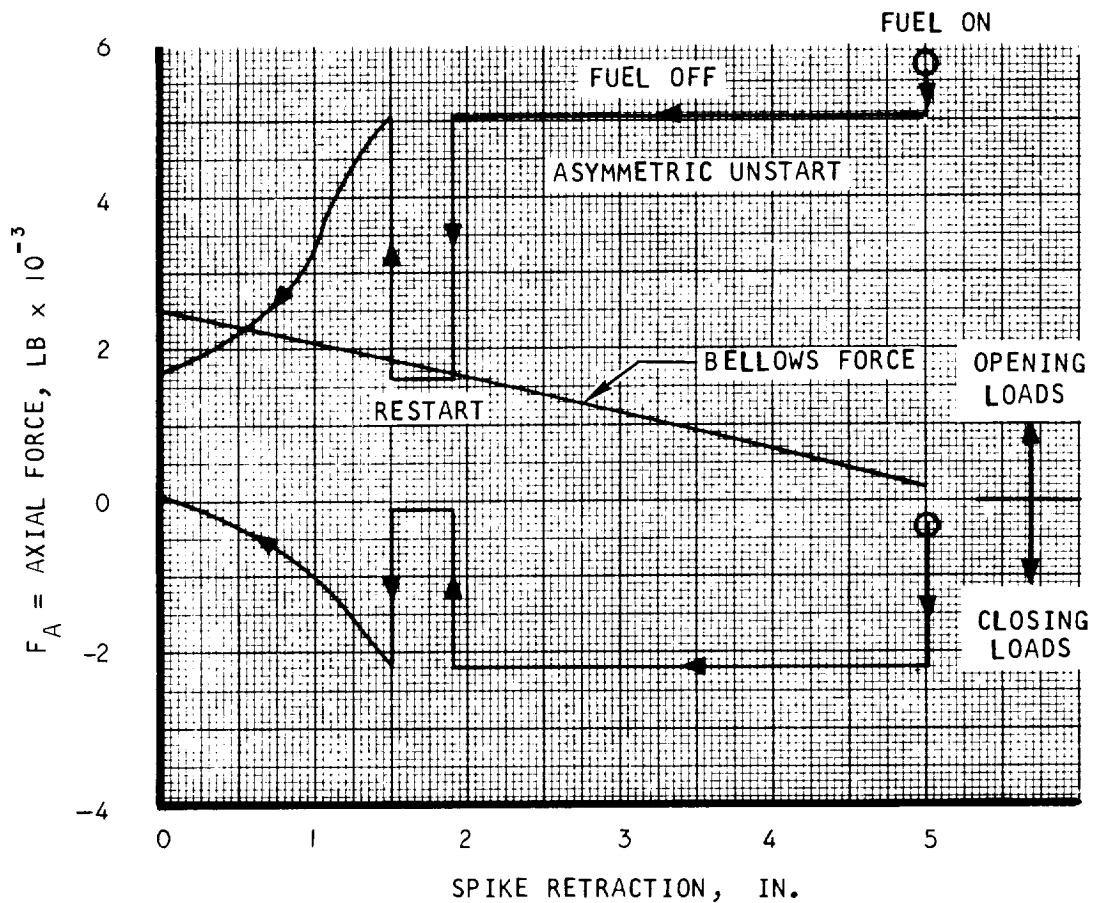


AIRSEARCH MANUFACTURING DIVISION
 Los Angeles, California

UNCLASSIFIED

UNCLASSIFIED

- NOTE:
1. $M_\infty = 8.0$
 2. $M_L = 6.5$, $q_L = 3240$ PSFA
 3. $q_\infty = 1800$ PSFA
 4. $\alpha_L = 4.0^\circ$
 5. LATCHING LOAD = 8200 LB



A-31602

Figure 5.1-33. Estimated Axial Load Profile on Spike During a Typical Inlet Unstart Sequence (Shock Expelled)



AIRESEARCH MANUFACTURING DIVISION
Los Angeles, California

67-2833
Page 5-42

UNCLASSIFIED

UNCLASSIFIED

Local dynamic pressure, $q_L = 3100$ psfa

Free stream dynamic pressure, $q_\infty = 1800$ psfa

Local angle of attack, $\alpha_L = 0$ deg

Local angle of yaw, $\beta_L = 0$ deg

- (b) Maximum normal pressure force, maximum actuator latching load, Figures 5.1-30 through 5.1-33, where the loads occur simultaneously and are to be combined.

Local Mach number, $M_L = 6.5$

Free stream Mach number, $M_\infty = 8.0$

Local dynamic pressure, $q_L = 3240$ psfa

Free stream dynamic pressure, $q_\infty = 1800$ psfa

Local angle of attack, $\alpha_L = 4.0$ deg

Local angle of yaw, $\beta_L = 0$ deg

- (c) Maximum internal pressure force, Figure 5.1-29. Operating conditions are identical to those given in (b), above, except that local angle of attack, $\alpha_L = 0$ deg.

Step changes in aerodynamic loads, as given, are assumed to occur in approximately 0.0002 sec for an inlet start and in approximately 0.002 sec for an inlet unstart. Step changes in internal pressure loads, as given, occur in approximately 0.10 sec, based on bellows cavity size and porting.

In addition to acceleration, vibration, bellows, internal pressure, and aerodynamic loads, friction forces occur in the actuator. These are treated as specific design loads. Both bellows and pressure loads are similarly design variables, but are more uniquely definable and included for completeness.

5.2 AERODYNAMIC HEATING CORRELATION

5.2.1 Summary

The heat transfer data analysis for the test combustor described in Reference 5.2-4 has been completed. Because of simple but effective instrumentation and gas flow property calculation methods, good correlation was obtained between measured and calculated heat flux.

Five of the six analytical methods listed in Table 5.2-1 were used to calculate heat flux for the 26 test points (11 with fuel injection) in Table 5.2-2. Method 6 was not used because of problems in obtaining operational



UNCLASSIFIED

TABLE 5.2-1
HEAT FLUX EQUATIONS AND REFERENCE TEMPERATURES

Method	Heat Flux Equation	Reference Temperature	% Calc / % meas
(1) Duct flow T^*	$q = \frac{0.023 \rho^* u (H_r - H_w)}{(P_r^*)^{2/3} \left(\frac{\rho^* u D}{\mu^*} \right)^{0.2}}$	T^* from enthalpy curve (Figure 5.2-1) $H^* \equiv H + \frac{1}{2}(H_w - H) + 0.22(H_r - H)$ $H_r = H + P_r^{1/3} (H_T - H)$	1.34 \pm 0.18
(2) Duct flow T_r	$q = \frac{0.023 \rho^* u (H_r - H_w)}{(P_r^*)^{2/3} \left(\frac{\rho^* u D}{\mu^*} \right)^{0.2}}$	T_r from enthalpy curve (Figure 5.2-1) $H^* \equiv H + 0.72(H_r - H)$ $H_r = H + P_r^{1/3} (H_T - H)$	0.92 \pm 0.09
(3) Duct flow with bulk density	$q = \frac{0.023 \rho u (H_r - H_w)}{(P_r^*)^{2/3} \left(\frac{\rho u D}{\mu^*} \right)^{0.2}}$	$\rho = \frac{P}{RT}$ P_r^* and μ^* are values corresponding to T^*	1.24 to exceeding 1.6 value increases with X
(4) Flat plate T^*	$q = \frac{0.0296 \rho^* u (H_r - H_w)}{(P_r^*)^{2/3} \left(\frac{\rho^* u X}{\mu^*} \right)^{0.2}}$	Same as in Method (1)	1.16 \pm 0.13
(5) Flat plate T_r	$q = \frac{0.0296 \rho^* u (H_r - H_w)}{(P_r^*)^{2/3} \left(\frac{\rho^* u X}{\mu^*} \right)^{0.2}}$	Same as in Method (2)	0.81 \pm 0.09





TABLE 5.2-1 (Continued)

Method	Heat Flux Equation	Reference Temperatures	% Calc / % meas
(6) Method of Reference 5.2-1	$\frac{dY}{dx} = 1.268 \left\{ \frac{dM}{M_L} \frac{dx}{dx} (1 + g_w H_i) - \frac{jY}{R} \frac{dR}{dx} + B \right\}$		
	$\frac{dH_i}{dx} = - \frac{1}{2 M_L} \left[H_i (H_i + 1)^2 (H_i - 1) \right] \left[1 + (g_w - 1) \frac{H_i^2 + 4 H_i - 1}{(H_i + 1)(H_i + 3)} \right]$		
	$+ \frac{H_i^2 - 1}{Y} \left[H_i - \frac{0.011 (H_i + 1)(H_i - 1)^2}{H_i^2} \frac{T_L}{T^*} \frac{2}{C_f} \right] A$		
6-a	$Y \equiv \left[\frac{M_L A_T \left(\frac{T_L}{T_T} \right)^{\frac{Y+1}{2(Y-1)}}}{\mu_T} \right]^{\frac{1.268}{\theta \delta_T}}$		
6-b	$B \equiv 0.123 e^{-1.561 H_i} \left(\frac{M_L A_T \delta_T}{\mu_T} \right) \left(\frac{T_L}{T_T} \right)^3 \left(\frac{\mu^*}{\mu_T} \right)^{0.268}$		
6-c	$\theta \equiv \int_0^{\delta} \frac{\rho}{\rho_L u_L} \left(1 - \frac{u}{u_L} \right) dy$		

TABLE 5.2-1 (Continued)

Method	Heat Flux Equation	Reference Temperatures	<div><div>% Calc</div><div>% meas</div></div>
6-d	$H = \frac{1}{\theta} \int_0^\delta \left(1 - \frac{\rho u}{\rho_L u_L} \right) dy$		
6-e	$H_i = \frac{H - \frac{Y-1}{2} M_L^2}{g_w \left(1 + \frac{Y-1}{2} M_L^2 \right)}$		





UNCLASSIFIED

TABLE 5.2-2
TEST CONDITIONS AND LOCAL HEAT FLUX

Run	Time, sec	P _{T0'} psia	T _{T0'} °R	$\frac{\Delta T_{T0'}}{\Delta t}$ °R/sec	m, lb/sec	ϕ , Inlet	ϕ_1	ϕ_2	Test Heat Flux, q/A, Btu/sec ft ²				Burning Mode
									X = 6	X = 14	X = 18	X = 22	
6116	62	116	2565	+50	15.9	0.31	0	0	72	39	no data	16	no
	73	109	2605	+7	15.1	0.31	0	0	67	38		15	no
	77	110	2595	-9	15.4	0.29	0.25	0	75	40		17	no
	90	112	2595	< 5	15.6	0.29	0.25	0	75	40		17	no
	302	115	2570	< 5	16.0	0.28	0.15	0	71	39		18	no
	321	114	2570	< 5	16.0	0.28	0.15	0	68	39		16	no
	435	115	3200	+5	14.2	0.51	0.16	0	102	77		30	no
	446	111	3480	< 5	13.5	0.55	0.17	0	111	75		31	no
	465	113	3265	-18	14.1	0.49	0.17	0	114	75		31	no
	560	113	3120	+18	14.3	0.48	0.19	0	97	69		28	no
	583	115	3260	+10	14.0	0.53	0.20	0	114	81		35	no
	612	112	3250	-15	14.0	0.50	0.20	0	107	80		31	no
6040	308	76	1770	---	13.0	0	0	0	26	15	10	6	none
	318	82	2070	---	13.1	0	0	0	34	20	15	9	none
	345	110	2855	---	14.5	0.39	0	0	66	43	24	15	none
	357	122	2920	---	15.9	0.39	0	0	76	45	28	17	none
	369	134	3010	---	17.7	0.42	0	0	87	53	32	19	none

UNCLASSIFIED

supersonic
burning



UNCLASSIFIED

UNCLASSIFIED

TABLE 5.2-2 (Continued)

Run	Time, sec	P _{T0} , psia	T _{T0} , °R	$\frac{\Delta T_{T0}}{\Delta t}$, °R/sec	ϕ , Inlet		ϕ_1	ϕ_2	Test Heat Flux, q/A, Btu/sec ft ²				Burning Mode
					m, lb/sec	ϕ , Inlet			X = 6	X = 14	X = 18	X = 22	
6040	378	142	3090	---	18.4	0.43	0	0	95	59	35	20	none
cont.	386	146	3235	---	18.3	0.48	0	0	103	64	39	23	none
	393	148	3200	---	18.2	0.48	0	0	106	64	38	23	none
	402	149	3165	---	18.1	0.48	0	0	101	64	39	22	none
	436	152	3350	---	18.6	0.53	0.21	0.73	139	198	156	105	subsonic burning
	449	151	3250	---	18.4	0.45	0.20	0.76	123	208	156	106	
	466	150	3235	---	19.3	0.47	0.19	0.73	124	208	156	108	
	486	151	3255	---	18.3	0.50	0.20	0.76	123	211	155	109	
	503	151	3245	---	19.1	0.48	0.18	0.74	122	210	157	107	

Note:

- (1) T_{T0} has been corrected for the radiation and conduction of the total temperature probe by the method of Reference 5.2-4.
- (2) X-station measured from the throat where A = 13 in.²

* $\frac{\Delta T_{T0}}{\Delta t}$ designates the transient nature of the test conditions. Most values for Run 6040 were less than 7°R/sec and none exceeded 10°R/sec.

UNCLASSIFIED

status for the computer program. Three of the five heat flux calculation techniques yielded average ratios of calculated-to-test heat flux between 0.81 and 1.16.

Two factors have led to retention of the flat plate equation with Eckert reference temperature (Method 3 of Table 5.2-1) for aerodynamic heating calculations in the flight engine: (1) limited data are available in the wall-to-total temperature ratio range of greatest interest for the flight engine (0.3 to 0.4); and (2) convergence of correlations by better calculation methods is towards 1.0 for the available data at higher wall-to-total temperature ratios. As more data becomes available in the course of the program, this decision will be reviewed.

With the application of the shock impingement equation, good agreement between calculated and measured heat flux was noted for the region having a shock train in the duct flow with subsonic combustion. The heat transfer coefficient does not increase significantly for supersonic burning without shocks. Because the geometry of the test combustor is an approximate model of the full-scale HRE between the inlet throat and the exit, and because the airflow and enthalpy levels are of the same order, these findings provide greater confidence in the HRE aerodynamic heating analysis.

5.2.2 Objective of Data Analysis

There are three HRE heat transfer areas that require special consideration. The best correlation for heat transfer with high speed turbulent boundary layer flow over a cold wall has not been firmly established (Reference 5.2-2 and 5.2-3). It is pointed out in Reference 5.2-2 that, for a flat plate, the reference temperature technique given by Eckert is less accurate when the wall-to-free stream total temperature ratio is small (T_w/T_T less than 0.6).

Reference 5.2-2 shows that for high supersonic flows, the heat transfer coefficient decreases sharply at $T_w/T_T = 0.2$. Reference 5.2-2 also indicates that improved accuracy will result if the wall temperature is replaced by the recovery temperature in the equation for the reference temperature. Whether this technique is applicable to a duct flow problem is of interest.

A second area of interest is the occurrence of shock trains in a duct. Considerable experimental heat transfer data can be found in the open literature on shock impingement problems. A good survey of this type of flow is found in Reference 5.2-5. However, almost all of these data are for external flows. Whether the external flow solution is applicable to the internal shock remains to be confirmed.

The third area of interest is the effect on surface heating due to combustion, since the flow turbulence level is expected to increase when combustion takes place.



UNCLASSIFIED

5.2.3 Gas Flow Properties

The test combustor involved flows with total enthalpy in excess of 2000 Btu/lb and velocities as high as 7000 fps. These flow conditions are not at the extreme temperatures where gas dissociation and gas radiation effects are important. Nevertheless, the specific heat of the hydrogen-air stoichiometric combustion products which varies from 0.3 to 1 Btu/lb °R in the temperature range of interest, is not a constant value. In the present data analysis, care has been exercised to refine the inlet total temperature interpretation, including the effect of conduction and radiation on the probe (Reference 5.2-4), and to evaluate the flow properties with the assumption of variable specific heat being made. The test data provide the mass flow, inlet total enthalpy, and static pressure along the duct. The duct cross section is known from the measured geometry. To compute the fluid temperature and the flow velocity, a simple method would be the use of a compressible flow table with variable γ and R , or:

$$m = \frac{\gamma g}{R} M \left(1 + \frac{\gamma - 1}{2} M^2 \right) \frac{PA}{\sqrt{T}} \quad (5.2-1)$$

However, this equation is derived assuming constant specific heat. In order to refine the solution, especially in the higher temperature range, a more stringent requirement has to be imposed, i.e., the specific heat is not constant. This requirement can be accommodated by using the basic equations of mass, energy and state.

$$\text{Mass} \quad m = \rho u A \quad (5.2-2)$$

$$\text{Energy} \quad H + \frac{u^2}{2gJ} \quad (5.2-3)$$

$$\text{State} \quad P = \rho RT \quad (5.2-4)$$

To facilitate the calculation, these equations are combined to form the quadratic equation:

$$\frac{u^2}{1000} + \frac{0.348 \text{ HAP}}{mRT} \left(\frac{u}{1000} \right) - \frac{H_T}{20} = 0 \quad (5.2-5)$$

Since A , P , m , H_T are known and H and R are functions of T , Equation (5.2-5) can be solved by trial and error with an assumed value of T . The resulting u and H (a function of T) must also satisfy Equation (5.2-3). This procedure was used in computer program F0020 to calculate enthalpy, temperature, and velocity for the data presented herein.

Shown in Figure 5.2-1 is the gas enthalpy referenced to zero °R (i.e., the enthalpy is zero at zero °R) for pure air and for stoichiometric combustion products of hydrogen and air. These data were based on the equilibrium chemical composition calculated from the method given by Reference (5.2-6). For combustion other than the stoichiometric condition, the enthalpy tables are



UNCLASSIFIED

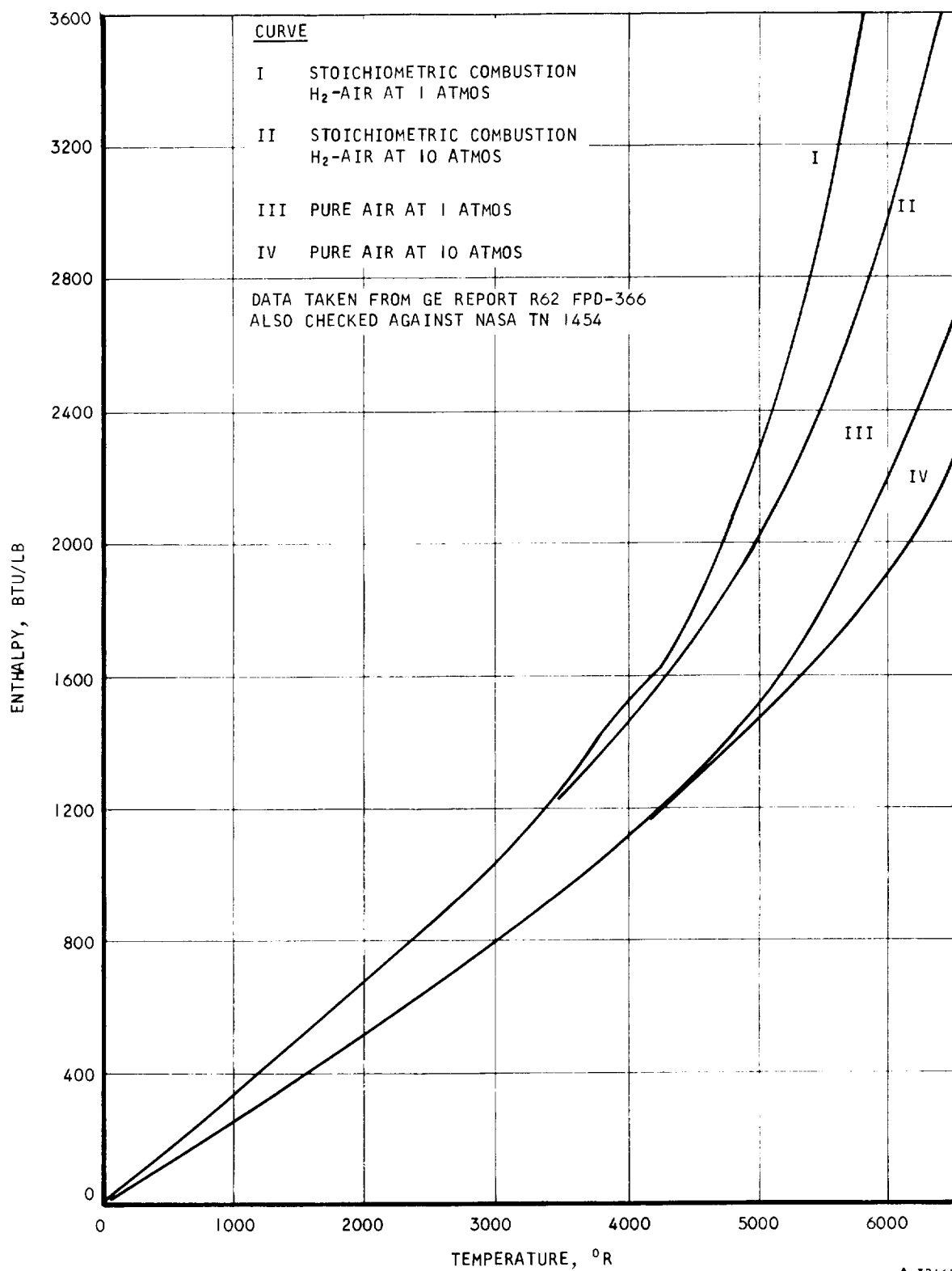


Figure 5.2-1. Equilibrium Enthalpy of Pure Air and Air-H₂ Products

UNCLASSIFIED



AIRESEARCH MANUFACTURING DIVISION
Los Angeles, California

UNCLASSIFIED

interpolated or extrapolated by use of the stoichiometric fraction, ϕ . The validity of this method is demonstrated in Figure 5.2-2, in which the computed enthalpy values for a final temperature of 5400°R at various ϕ are compared with the straight line through the two end points, $\phi = 0$, and $\phi = 1$. The maximum deviation of 3.4 percent occurs where $\phi = 1.3$. The pure air viscosity and Prandtl number are tabulated in Table 5.2-3. The data were assumed to be valid for the combustion products.

TABLE 5.2-3

VISCOSITY OF AIR

$T(^{\circ}\text{R})$	$\mu \times 10^5 \frac{\text{lb mass}}{\text{ft} \cdot \text{sec}}$	$T(^{\circ}\text{R})$	$\mu \times 10^5 \frac{\text{lb mass}}{\text{ft} \cdot \text{sec}}$
400	1.0	3600	4.15
800	1.66	4000	4.4
1200	2.2	4400	4.63
1600	2.58	4800	4.85
2000	2.98	5200	5.03
2400	3.31	5600	5.22
2800	3.6	6000	5.4
3200	3.89		

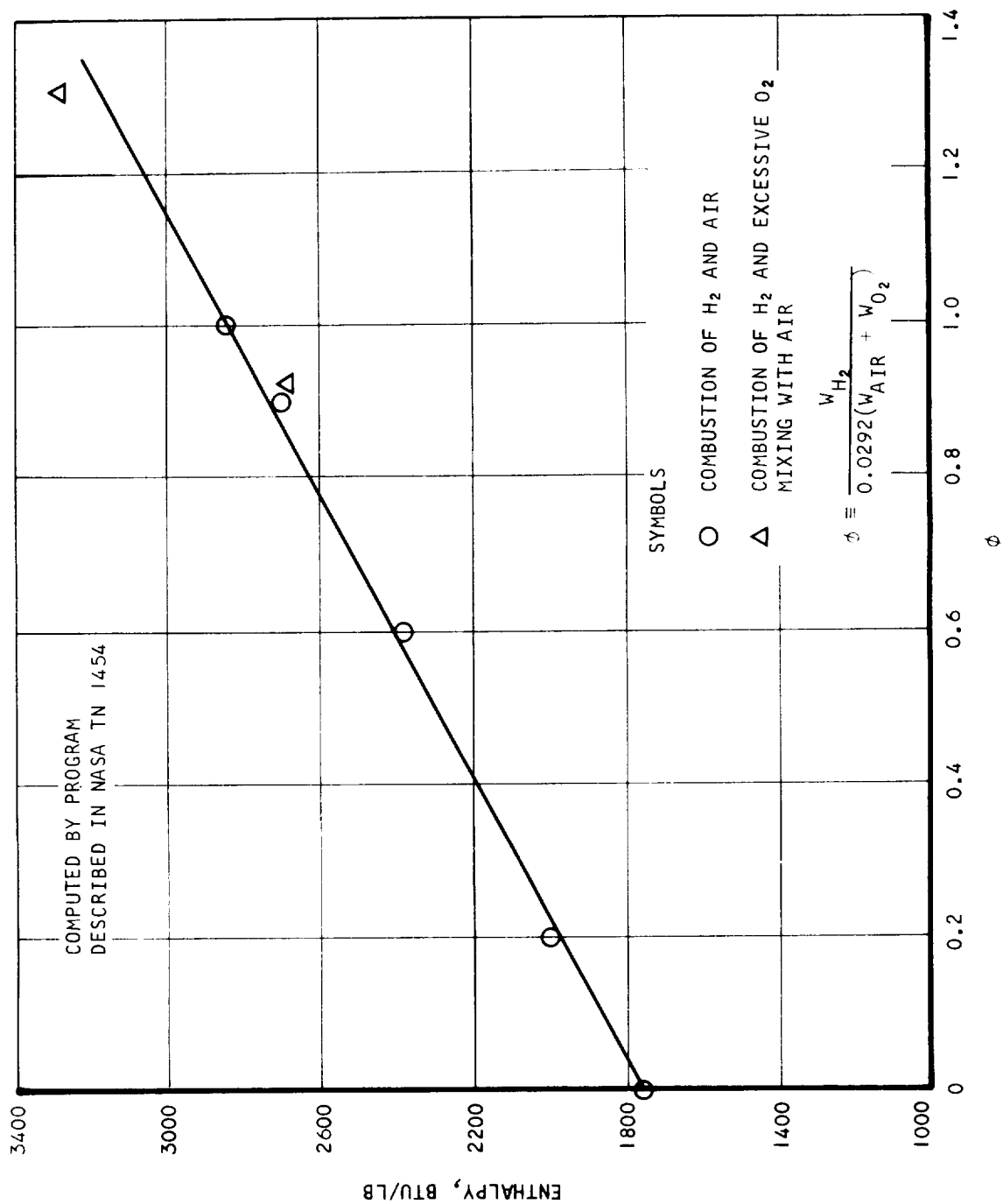
Prandtl Number of Air

$T(^{\circ}\text{R})$	Pr	$T(^{\circ}\text{R})$	Pr
200	0.740	3600	0.773
900	0.738	4500	0.774
1800	0.756	5400	0.774
2700	0.767	6300	0.756

5.2.4 Test Configuration and Instrumentation

The combustor geometry as shown in Reference 5.2-4 is a concentric duct with an inlet area of 13-in.² The annular area increases rapidly to 25-in.²





A-32443

Figure 5.2-2. Enthalpy of Combustion Products at 5400°R and One Atmosphere



UNCLASSIFIED

at a distance one in. from the throat. The geometry aft of this station is very similar to the full scale HRE. The instrumentation consisted of flow metering devices, which measure the airflows and fuel flows before they enter the duct; three inlet total temperature probes, six thermocouples imbedded in the duct wall, and 45 static taps along the duct. After Run 6109, all thermocouples except those located at stations $X = 6, 12, 14, 18, 22$ and 24 were damaged. Data from stations 12 and 24 are not presented here because the pressure levels at $X = 24$ are too low to be reliable, while the thermocouple at $X = 12$ yielded data judged to be erroneous. Additional descriptions are found in Reference 5.2-4.

5.2-5 Test Data

Data from Runs 6040 and 6116 only have been selected for heat transfer analysis. This data is summarized in Table 5.2-2. The total pressure of Run 6116 was essentially at a constant value of 110 psia. The selected data covers an inlet total temperature range from 2500°R to 3400°R which was achieved by burning hydrogen and oxygen upstream of the 13-in.² throat. The total pressure of Run 6040 varies from 60 to 150 psia. Part of the data have no fuel injection in the test combustor, so that the basic turbulent high speed cold wall heat transfer could be examined for the simplest conditions. For the cases with fuel injection, representative data for supersonic burning and subsonic burning were included. The supersonic burning data were taken with small ϕ and with injector only (fuel injected at $X = 1.5$). Pure supersonic burning with fuel injection from both the first and the third injector was not accomplished for the uncoated test combustor (nickel surfaces). The experimental heat fluxes, q_{meas} were computed from the wall thermocouples and the cooling water temperatures by the one-dimensional conduction equation as described in detail in Reference 5.2-4. The typical measured pressure and heat flux distributions are shown in Figures 5.2-3 and 5.2-4.

5.2-6 Method of Analysis

For flows without internal shock, the appropriate heat transfer solution is by a duct equation as indicated in Reference 5.2-6. Reference 5.2-7 indicates that heat transfer in converging-diverging nozzles can be correlated with duct flow equations, even though the boundary layers were very small compared to the duct hydraulic radius and the flow is far from having a fully developed profile. Since the test combustor has a considerably larger L/D ratio than that reported in Reference 5.2-7, the application of the duct flow equation is reasonable. When high adverse pressure gradient occurs in the flow, the duct equation is not expected to yield valid results. For such flows either the integral momentum method of Reference 5.2-8 or the simultaneous solution of the momentum and moment of momentum equations as suggested by Reference 5.2-1 is appropriate. The method of Reference 5.2-1 has been programmed for data reduction. However, this program is not completely operational, and the present data analysis has been restricted to the comparison of the first five of the six methods shown in Table 5.2-1. Computer program H1940 was used to calculate heat flux with the first five methods. These methods are briefly described below.



UNCLASSIFIED

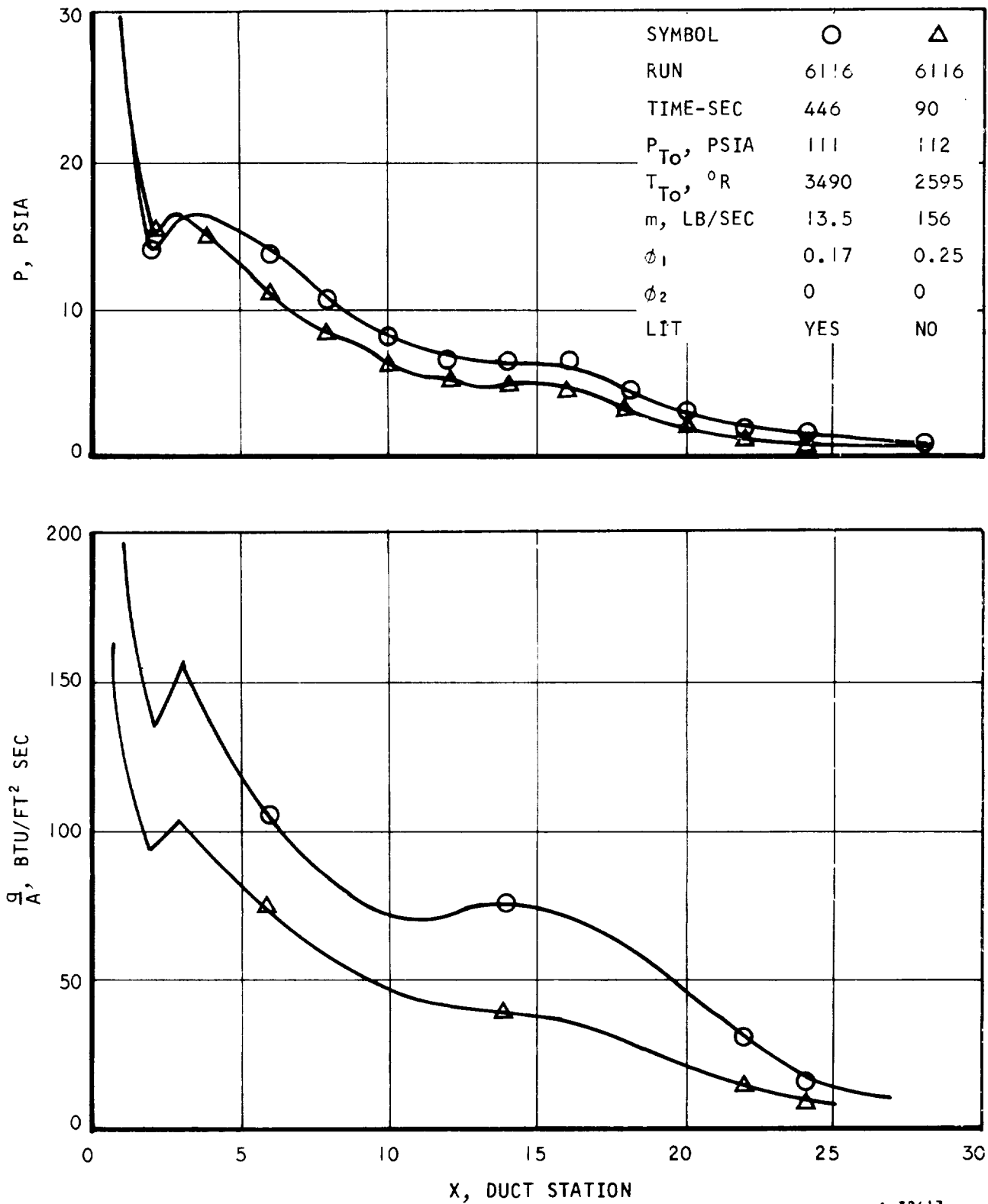
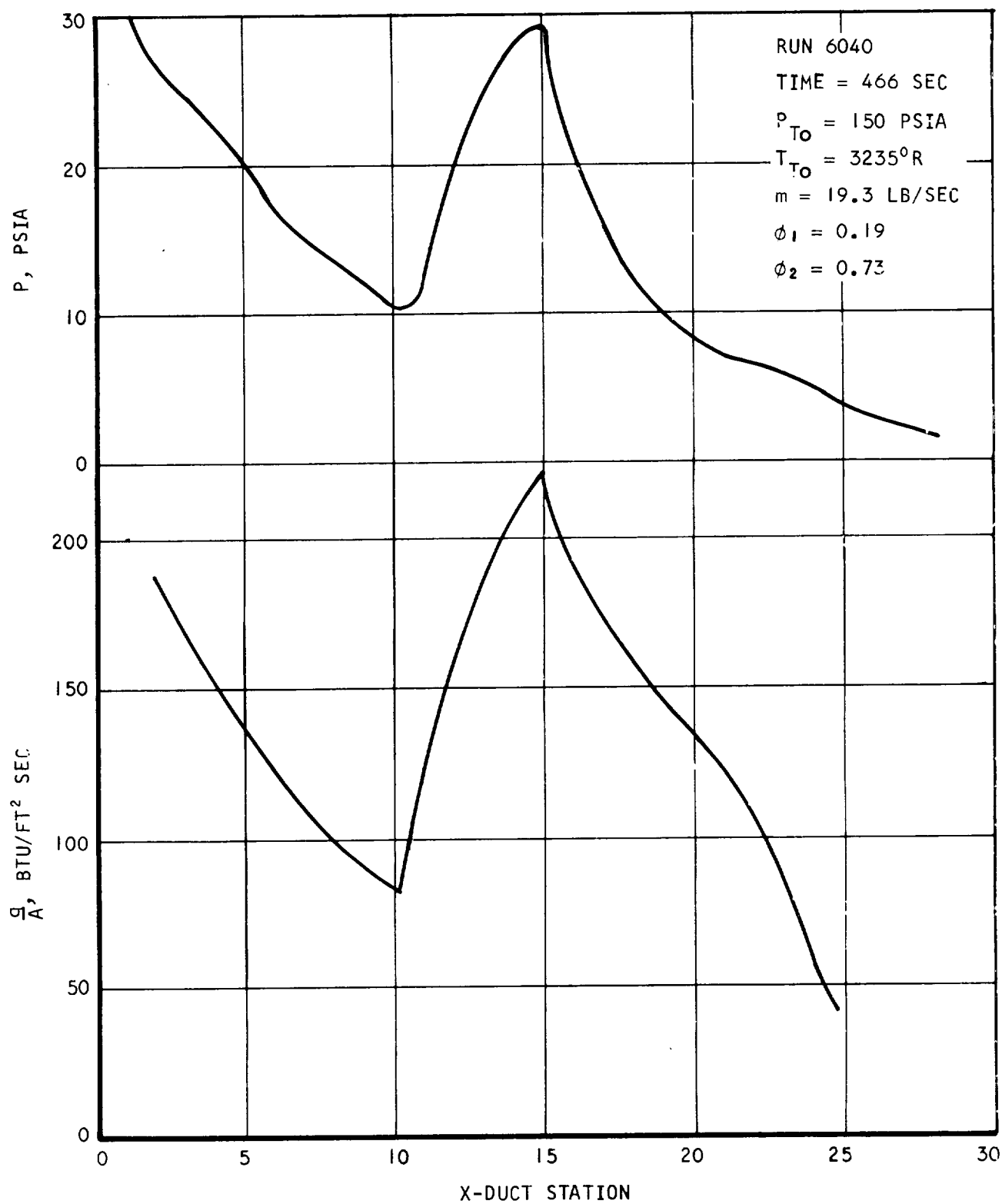


Figure 5.2-3. Test Combustor Typical Pressure and Heat Flux Distribution With and Without Combustion



UNCLASSIFIED

UNCLASSIFIED



A-32420

Figure 5.2-4. Typical Pressure and Heat Flux Distribution With Shock Train and Subsonic Combustion



AIRESEARCH MANUFACTURING DIVISION
Los Angeles, California

UNCLASSIFIED

UNCLASSIFIED

- (1) Duct flow - T^* . This method utilizes the duct flow equation and evaluates all the gas properties based on Eckert's reference temperature.
- (2) Duct flow - T^1 . This method is essentially the same as method (1) except that all gas properties are evaluated at a reference temperature T^1 that is to be computed with Eckert's equation, but the wall temperature (or wall enthalpy) is replaced by the recovery temperature T_r (or the recovery enthalpy).
- (3) Duct flow with bulk density. This method is the same as that of method (1) except that the gas density is to be computed based on the local static temperature.
- (4) Flat plate - T^* . This is the Blasius flat plate turbulent flow equation with the gas properties evaluated at Eckert's reference temperature, T^* .
- (5) Flat plate - T^1 . This is the same as in method (4) except all gas properties are evaluated at T^1 .

5.2-7 Analysis of Results

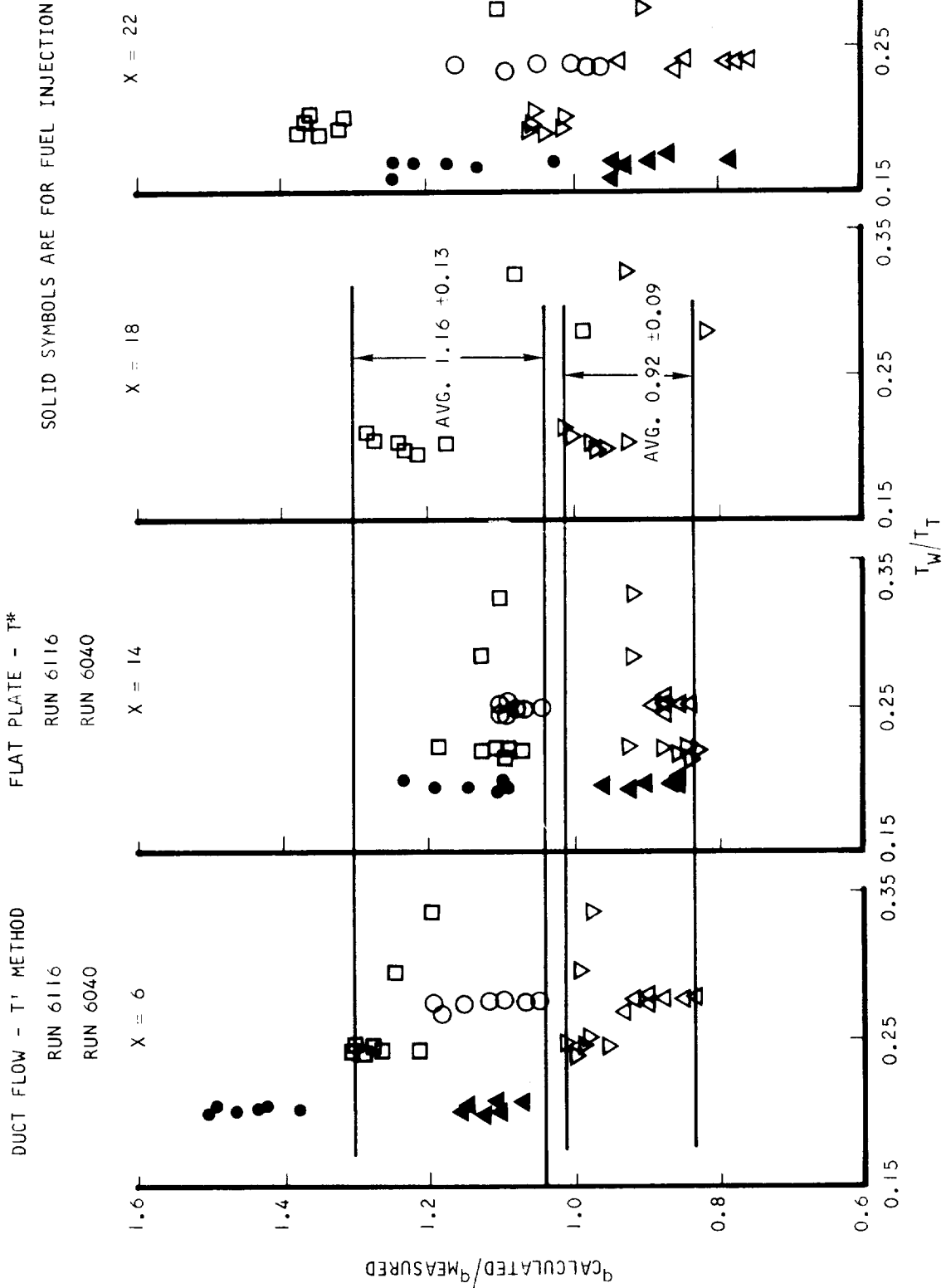
The results are plotted as $q_{\text{calculated}}/q_{\text{measured}}$ vs the wall-to-total temperature ratio at different stations in Figures 5.2-5 through 5.2-10. The data reduced by method 2 of Table 5.2-1 as shown in Figure 5.2-5 appears to be best from the standpoint of data spread and closeness to the measured values.

The calculated values of heat flux are the sum of gas radiation and convection heat fluxes. The gas radiation was usually a negligible fraction of total heat flux. The radiation flux was less than 0.1 percent of the convective flux when no combustion occurred, less than 0.3 percent when supersonic combustion occurred, and less than 3 percent when subsonic combustion occurred.

All fuel injection data of Run 6116 had fuel injected at $X = 1.5$, and was assumed that the combustion was completed at $X = 6$ once the fuel is ignited, for computing the enthalpy of the flow. From the fuel injection data of Figure 5.2-5, the indication is that the combustion has not been completed at Station $X = 6$, and that the computed values are considerably higher than the measured values. For this reason, fuel injection data at station $X = 6$ are excluded from consideration in determining the average heating for these groups of data. Also excluded from consideration are the data from $X = 22$. The measured static pressures at this station are relatively inaccurate, since their absolute values are of the order of 1 to 2 psia, with a possible error of 10 percent or higher. It is seen then that the best two methods are the duct flow solution with the gas properties evaluated at T^1 and the flat plate solution with the gas properties evaluated at T^* . From the geometric consideration and from results of Reference 5.2-7, the duct equation is appropriate. The flat plate solution also offers reasonable agreement because the conversion factor from flat plate flow to duct flow



UNCLASSIFIED



A-32464

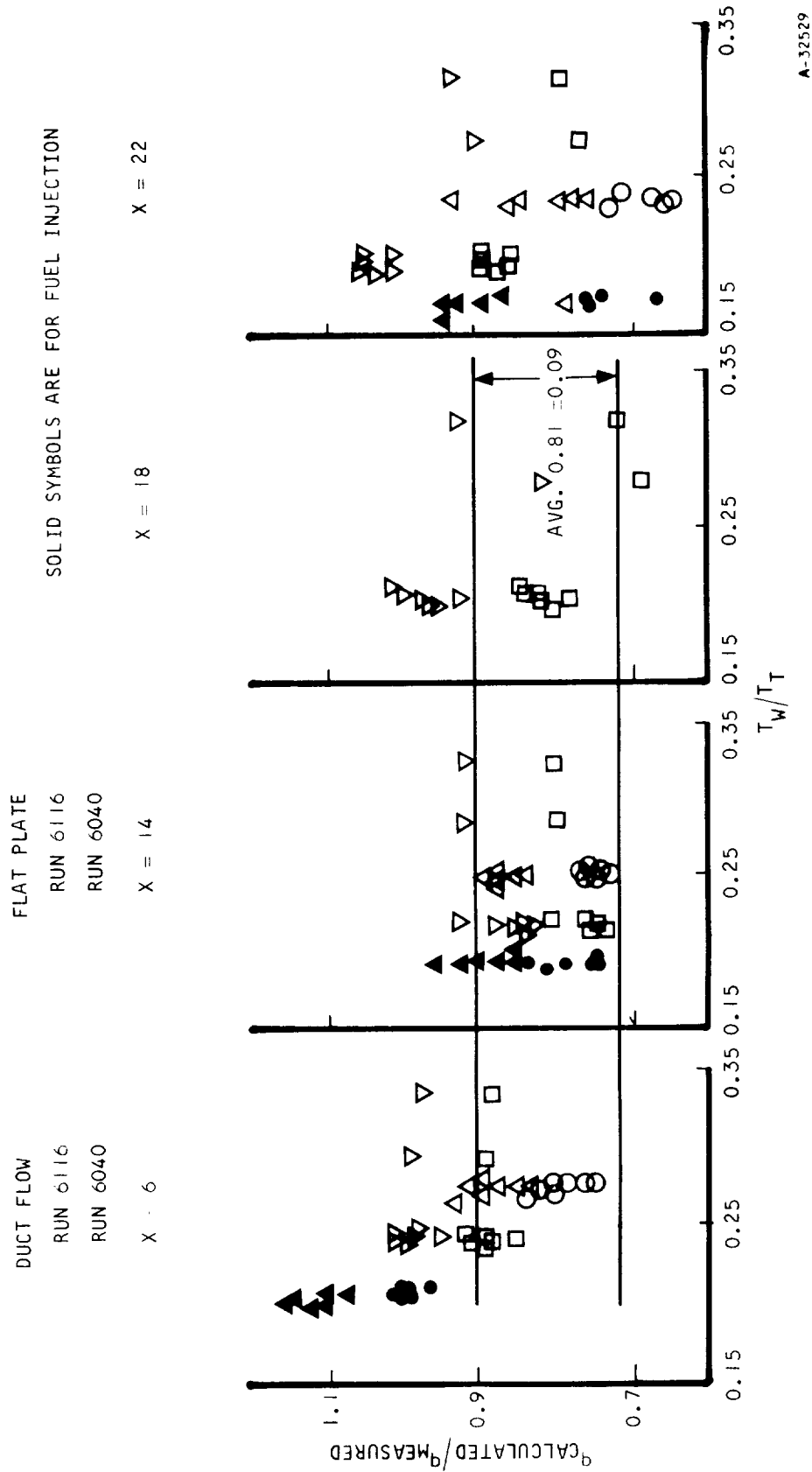
Figure 5.2-5. Comparison of Flat Plate - T* with Duct Flow - T'

UNCLASSIFIED



AIR RESEARCH MANUFACTURING DIVISION
Garrett Corporation

UNCLASSIFIED



A-32529

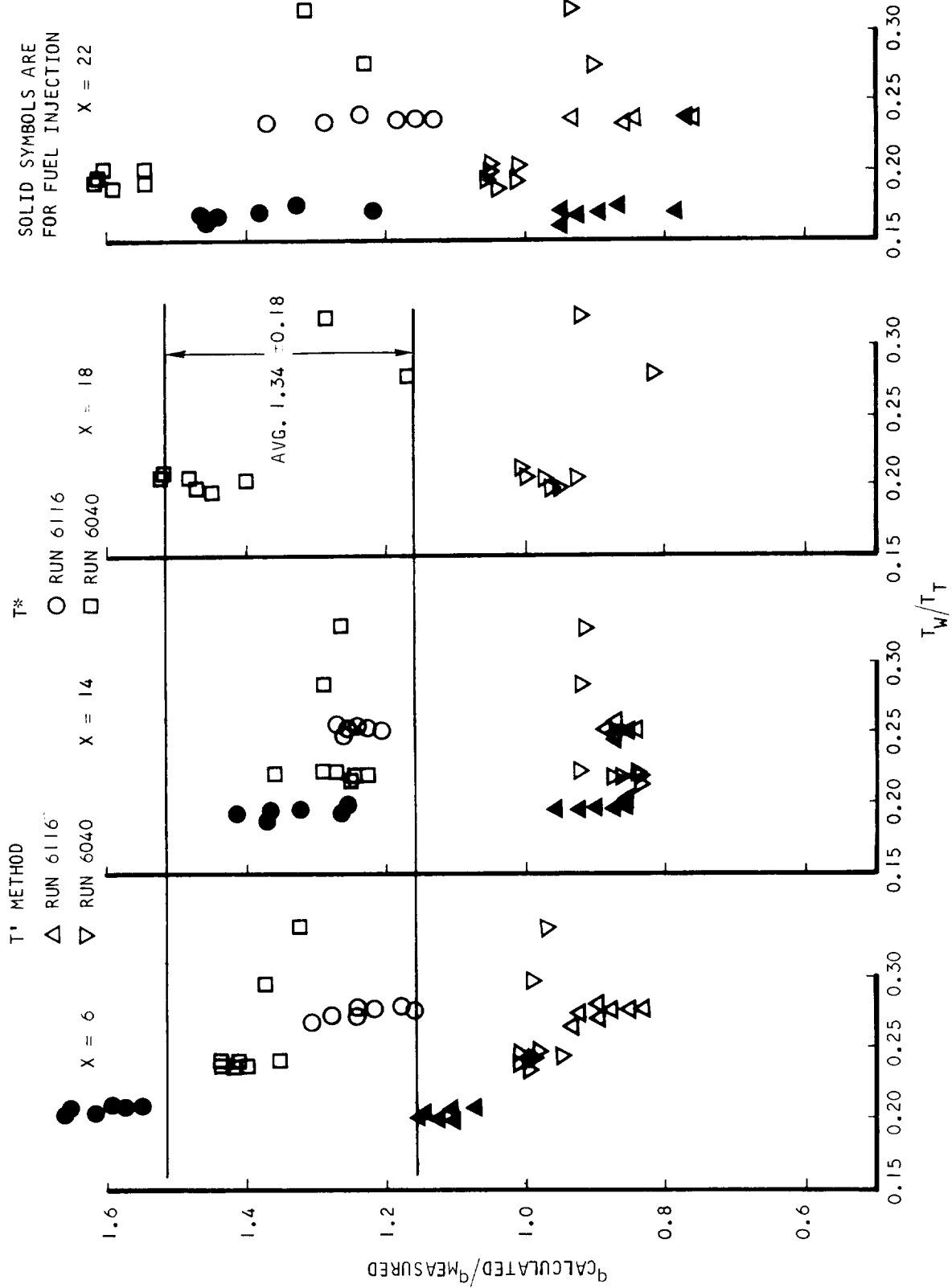
Figure 5.2-6. Comparison of Flat Plate - T' with Duct Flow - T'

UNCLASSIFIED



AIRSEARCH MANUFACTURING DIVISION

UNCLASSIFIED



A-32418

Figure 5.2-7. Comparison of Duct Flow - T^* with Duct Flow - T'

UNCLASSIFIED



AIRSEARCH MANUFACTURING DIVISION
Garrett Corporation



UNCLASSIFIED

DUCT FLOW - T' METHOD

RUN 6116
RUN 6040

X = 6

FLAT PLATE - T*

RUN 6116
RUN 6040

X = 14

X = 18

X = 22

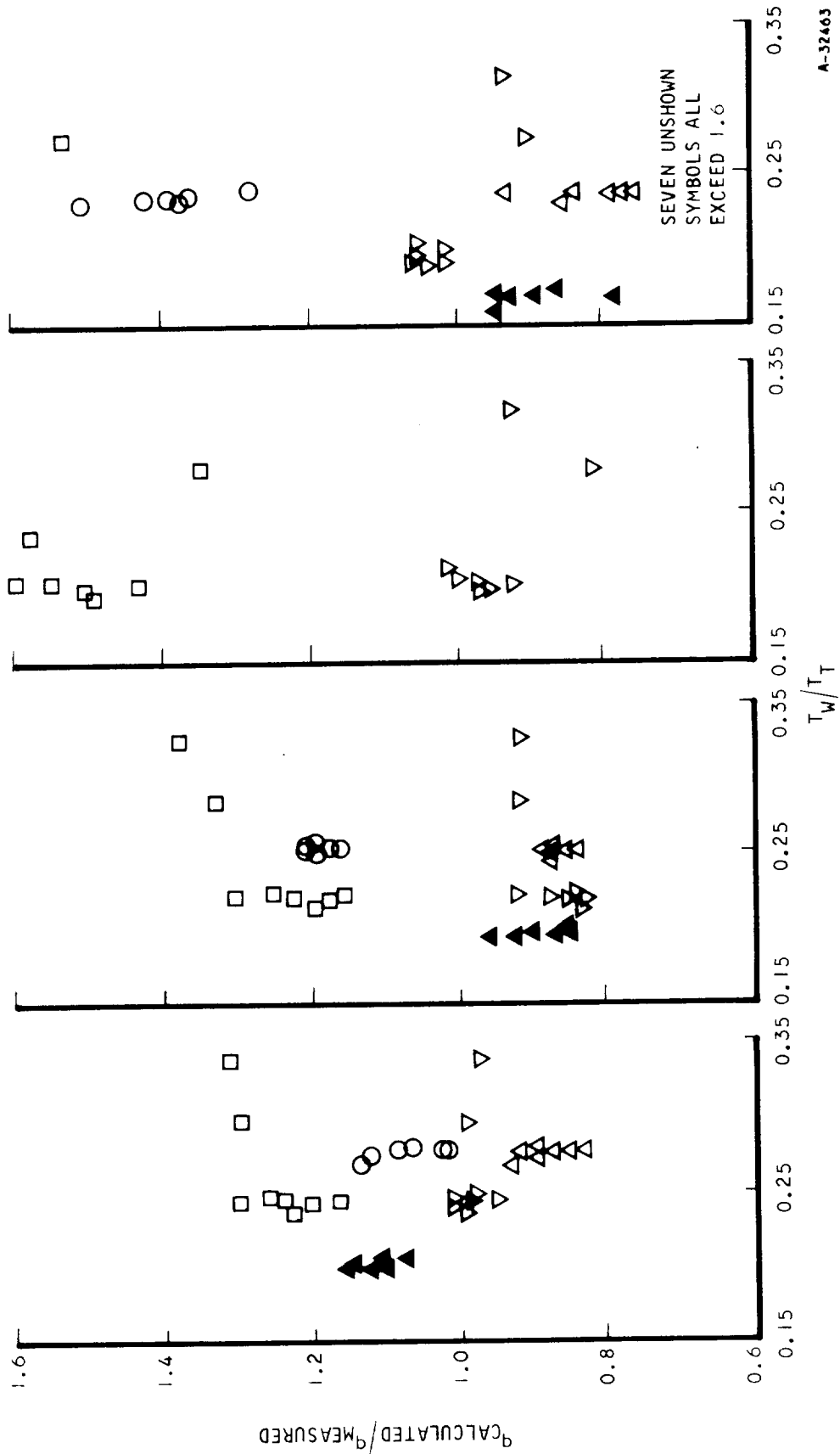


Figure 5.2-8. Comparison of Conventional Duct Flow with Duct Flow - T'

UNCLASSIFIED

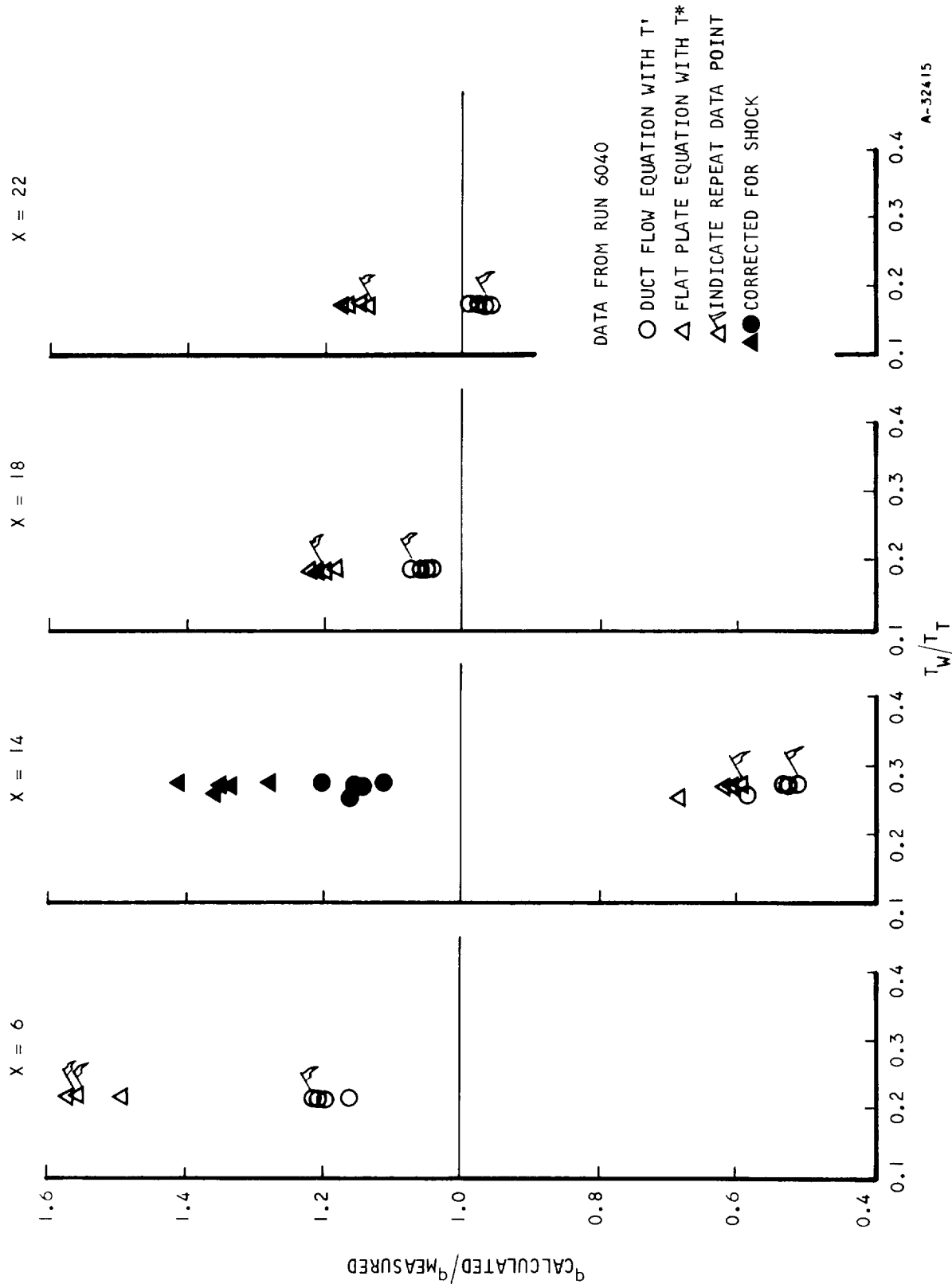


Figure 5.2-9. Heat Transfer with Shock Waves

UNCLASSIFIED



UNCLASSIFIED

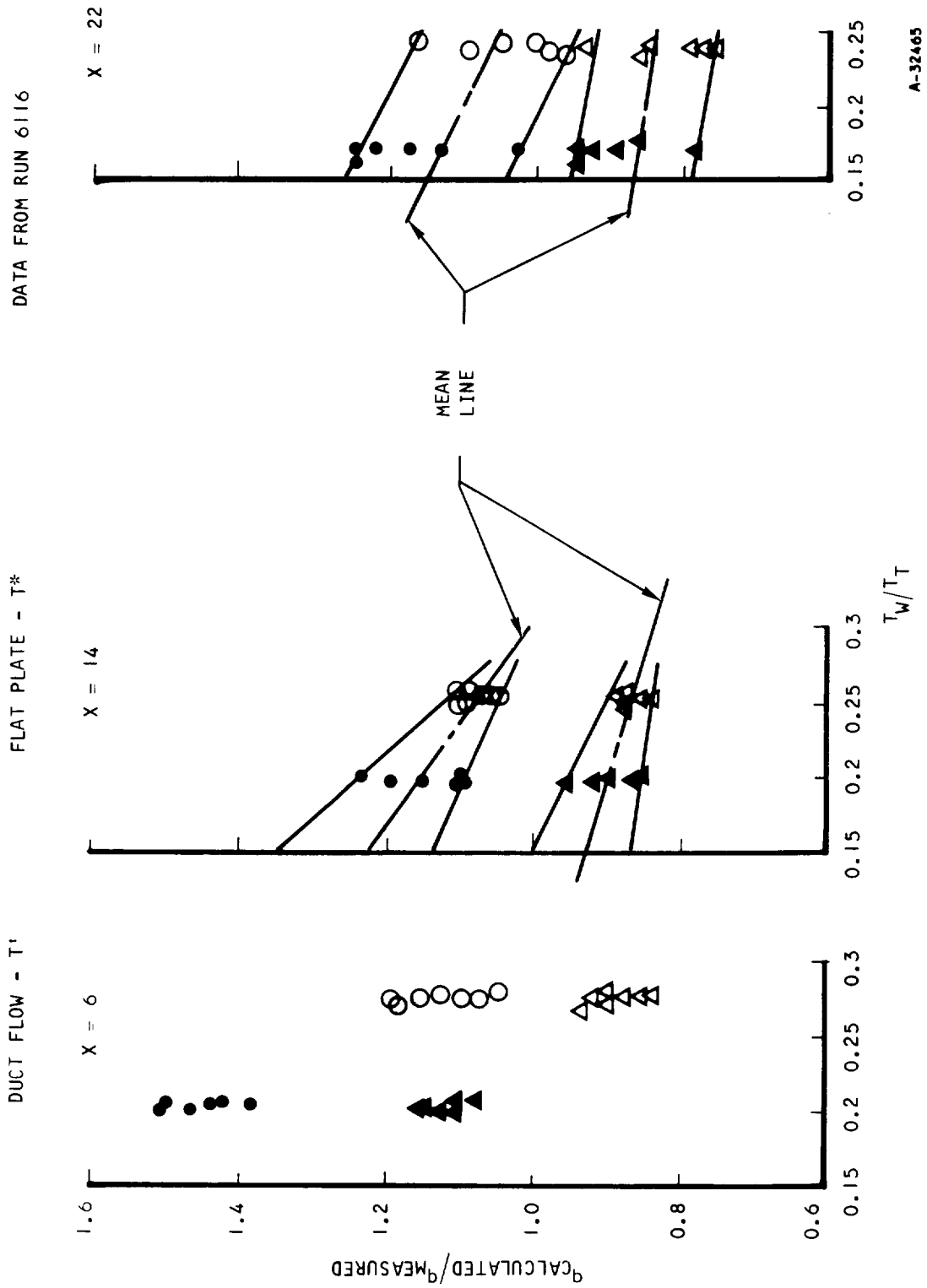


Figure 5.2-10. Comparison of Flat Plate - T* with Duct Flow - T'

UNCLASSIFIED



UNCLASSIFIED

for the combustor geometry is nearly constant. It varies from 1.11 to 1.19 while the ratio $0.0296/0.023 = 1.29$. The conversion ratio is

$$\frac{q_{fp}}{q_{df}} = \frac{0.0296}{0.023} \frac{n}{X} 0.2$$

The ratios at stations where heat flux was measured are:

X, in.	6	14	18	22
Ratio	1.11	1.15	1.19	1.18

Although these two methods yield reasonably good agreement, additional evidences are found which support the T^l method as being a superior one. In order to bring out this point, data from Run 6116 only are plotted in Figure 5.2-10. The T^l method implies that the heat transfer coefficient is independent of the wall temperature. This is supported by the data as the line drawn through the mean T^l data is nearly horizontal. The line drawn through the mean T^* data, inclining at a large angle, indicates that the T^* method yields an erroneous trend insofar as the wall temperature effect is concerned. Perfect correlation would be a horizontal mean line.

5.2.8 Shock Impingement

The effect of shocktrains in subsonic combustion was judged to be similar to shock impingement for the external flow situation. This is seen in Figure 5.2-9 in which the data corresponding to a shockless system are compared with the modified data. The solid symbols are computed for the heat transfer at the shock impingement point (Reference 5.2-4).

$$\frac{h_{max}}{h_{fp}} = \left(\frac{P_{max}}{P_{undisturbed}} \right)^{0.9}$$

To standardize the determination of P_{max} and $P_{undisturbed}$, the calculation was made automatic by the following substitution:

$$\frac{h_{(x=14)}}{h_{(x=10)}} = \left[\frac{P_{(x=14)}}{P_{(x=10)}} \right]^{0.9}$$

The modified calculated values appear to be in good agreement with the measured values although calculated values are generally above measured values. These data have fuel injection from both the first injector and the second injector. One possible reason for the overpredicting trend is that combustion may not have been completed at stations $X = 6$, $X = 14$, and even at $X = 18$ during these runs. Also, and probably more important, the heat of combustion of 52,000 Btu/lb, which was used for computing the total enthalpy, may be slightly high, since combustion occurs at an elevated temperature of several thousand degrees Rankine.



5.2.9 Combustion effect on Heat Transfer

As discussed earlier the combustion was incomplete at $X = 6$. Based on the estimated value of 80 percent completion at $X = 6$ (Reference 5.2-4), the predicted heat flux is still high compared with the measured value. The expected combustion effect as a consequence of higher levels of turbulence is to increase the heat flux. Therefore q_{cal}/q_{meas} is expected to fall well below 1.0. The fact that the predicted heat flux is greater than the measured value suggests little or no contribution to heating due to combustion, at least, when the combustion takes place in supersonic flows.

5.3 ENGINE DYNAMIC ANALYSIS

This section presents the results of work to date on the engine structural model. In order to accomplish this analysis, use has been made of several shell and frame structures computer programs as described in Paragraph 4.2 of this report.

A basic objective of the analysis is to develop a solution that will be applicable to the analysis of structural response for various types of loading. One of the desired outputs is the computation of resonant frequencies and mode shape of the engine structure. The analysis should also allow for computation of response to sustained sinusoidal input, or to transient perturbations produced by external aerodynamic forces, the X-15A-2, or the engine itself. It is also desirable that the resulting structural model permit computation of stresses and deformations due to static forces.

5.3.1 Mathematical Model

Basically, a mathematical model is an acceptable simplified analog that reasonably simulates the behavior of the real structure. Adequate similitude must be attained so that responses of the principal engine component parts are accurately computed. The common approach to a rigorous structural solution is given by

$$[m] \ddot{x} + [c] \dot{x} + [k] x = F(t) \quad (5.3-1)$$

$$m\ddot{x} + c\dot{x} + kx = F(t)$$

where m = the mass-inertia matrix

c = the damping matrix

k = the stiffness matrix

$k^{-1} = [A]$, the flexibility matrix

x = the displacement or deformation vector

\dot{x} = the velocity vector



UNCLASSIFIED

\ddot{x} = the acceleration vector

$F(t)$ = the load vector

From Equation (5.3-1):

- (a) If all elements are not zero, the transient structural response can be calculated
- (b) If $F(t) = 0$ for every t , the steady state vibration response can be obtained.
- (c) If $c = 0$, both former responses are the undamped ones
- (d) If $x = a$ constant which means $\ddot{x} = \dot{x} = 0$, and $\frac{\partial}{\partial t} F(t) = 0$, the static load configuration can be obtained.

Equation (5.3-1), if expressed for one of the degrees of freedom of the system, becomes:

$$m_i \ddot{x}_i + c_i \dot{x}_i + \sum_{j=1}^n k_{ij} x_j = F_i(t) \quad (5.3-2)$$

If the possible perturbation or transient is a general mass or ground perturbation,

$$m_i \ddot{x}_i + c_i (\dot{x}_i - \dot{u}) + \sum_{j=1}^w k_{ij} (x_j - u) = F_i(t) \quad (5.3-3)$$

and the boundary equation becomes:

$$\sum_{k=1}^k c_k (\dot{x}_k - \dot{u}) + \sum_{l=1}^L k_l (x_l - u) = P(t) \quad (5.3-4)$$

where m_i , k_{ij} , c_i (or c_k) = elements of the mass, stiffness and damping matrices

x_i , \dot{x}_i and \ddot{x}_i = components of the displacement, velocity, and acceleration vectors corresponding to the masses

$F_i(t)$ = component of the load vector at the mass i

$P(t)$ = the load, for t , at the base



UNCLASSIFIED

As for any general mathematical model, knowledge of each one of the elements described above is required. If the model is properly chosen, it can be used for both static and dynamic analyses.

5.3.1.1 Analytical Considerations

The double problem (static and dynamic) can be solved by means of parallel and sometimes complementary methods:

- (1) A rigid body model assuming each structural part rigid and attached to each other through elastic springs representing the elastic structural interconnections.
- (2) A structural analysis of each individual structural part in detail, adjusting the boundary conditions as necessary.
- (3) A rigid body model (as stated above), but by using the influence coefficients obtained from the structural analysis, thereby reducing the motions analysis to the normal 6 degrees of freedom for each structural part.
- (4) Integration of the representative matrix of each structural part as submatrices of a total matrix of the structure.

The preferred starting point is the employment of the reduced rigid body model. The accuracy of that model is improved by also applying the procedures indicated in steps 2 and 3 above.

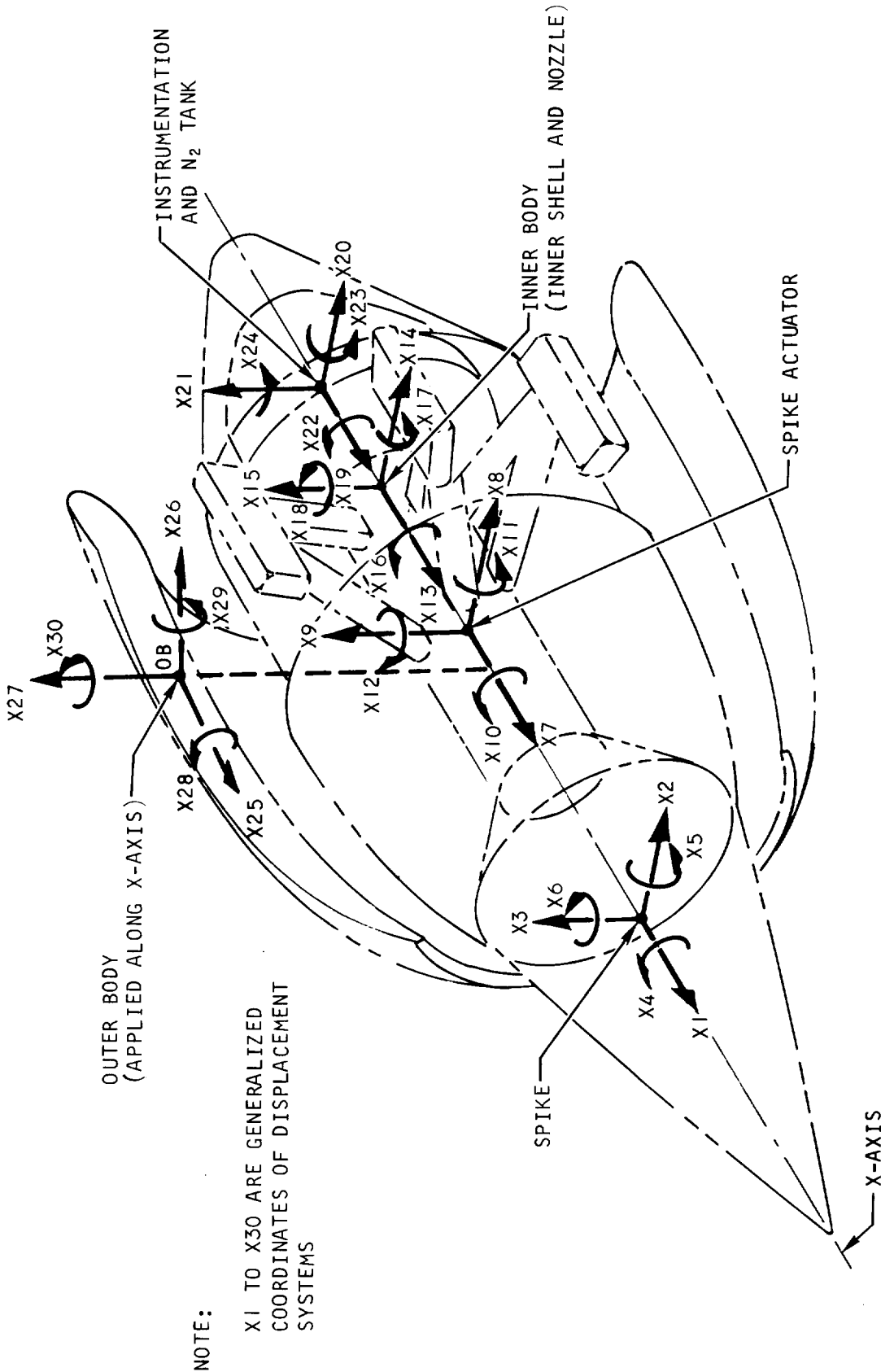
Step 4 represents the total mathematical integration of the total structure. A 30 degree of freedom model was chosen. The 30 degree of freedom system arises by virtue of the flexible coupling of the five rigid mass elements, each one possessing six degrees of freedom. The main masses or parts are: (1) the spike, (2) the spike actuator, (3) the inner body, (4) the instrumentation and N₂ tank, and (5) the outer body. This structural array and the displacement elements are illustrated in Figure 5.3-1. The mass and flexibility interconnections are as shown on Figure 5.3-2.

Computation of the equivalent rigid body mass quantities and the various flexibility coefficients is accomplished as the first step in the analysis. Once these values are established, it is possible to calculate the resonant characteristics of the system. For the present, the pylon is assumed to have infinite rigidity, which is exactly analogous to rigid mounting of the engine from the X-15 side of the thrust sensor. Also, for the present, the wishbone and flexural mounts are not introduced into the model.

The actuator driving mechanism was not defined at the beginning of the analysis, and the internal elastic characteristics for the actuator were not treated in this analysis. The future introduction of those characteristics will influence only the axial modes, and this step can be performed with relative simplicity.



UNCLASSIFIED



A-32166

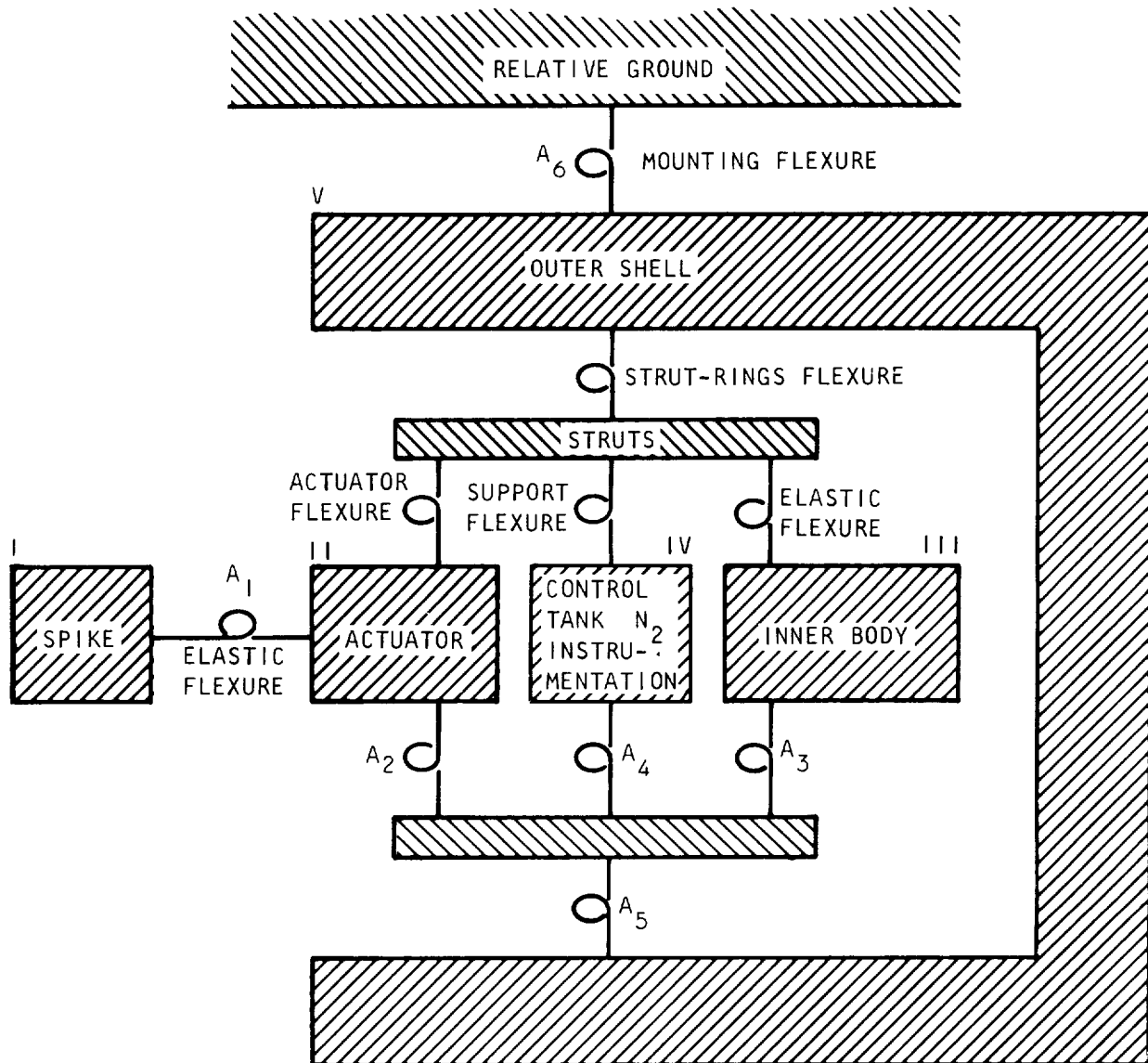
Figure 5.3-1. HRE Structural Model



AIRESEARCH MANUFACTURING DIVISION
Los Angeles, California

UNCLASSIFIED

UNCLASSIFIED



A-32137

Figure 5.3-2. Semi-Rigid Structural Model



AIRESEARCH MANUFACTURING DIVISION
Los Angeles, California

UNCLASSIFIED

UNCLASSIFIED

Some parametric analysis will be carried out with varying damping factors at the various resonant frequencies. It will also be necessary to estimate the magnitudes of the excitation forces to determine estimated response loads for stress analysis purposes.

5.3.1.2 Analysis and Construction of the 30 x 30 Flexibility Matrix

Five structural submatrices were constructed, some of them by parts or integration of other submatrices. Each of the main parts of the total engine was studied as an exact structural replica of the part to be constructed. Once the deformations due to unit loads on each structural element, were found, they were reduced to an equivalent set of displacements and rotations applied to its centroid. Transfer matrices were constructed in order to get cumulative displacements from part to part and obtain the necessary flexibility coefficients.

The first part of the task was devoted to the analysis of the spike, the spike actuator, the inner body, and the N_2 tank instrumentation. Shell structures were analyzed with digital computer shell programs. An Air Force orthotropic shell program for unsymmetrical loads, an AiResearch orthotropic shell program, as well as the Sabor III (MIT) program were utilized to compute shell properties. Frame structural elements within the engine, e.g. actuator double legs, were studied with the STRESS (MIT) computer program. Stiffener rings and ribs were analyzed independently and then integrated into the shell structure.

All four flexibility matrices (denoted as A_1 through A_4 , on Figure 5.3-2) were integrated up to the struts. The struts have been assumed to form a rigid connection between the inner body and the outer body as shown by line M-M on Figure 5.3-3. This resulted in a flexibility matrix of 24 by 24 elements. To "cross" the strut area, a Fourier analysis was performed to take care of the discontinuity effect of the strut loads over both shells, i.e., the inner body and outer shell. Due to the slow convergence--more than fifty harmonics were studied--a convergence analysis was performed. The submatrix, A_5 , which is the flexibility submatrix for the outer shell-strut combined structure, was the end result of this analysis.

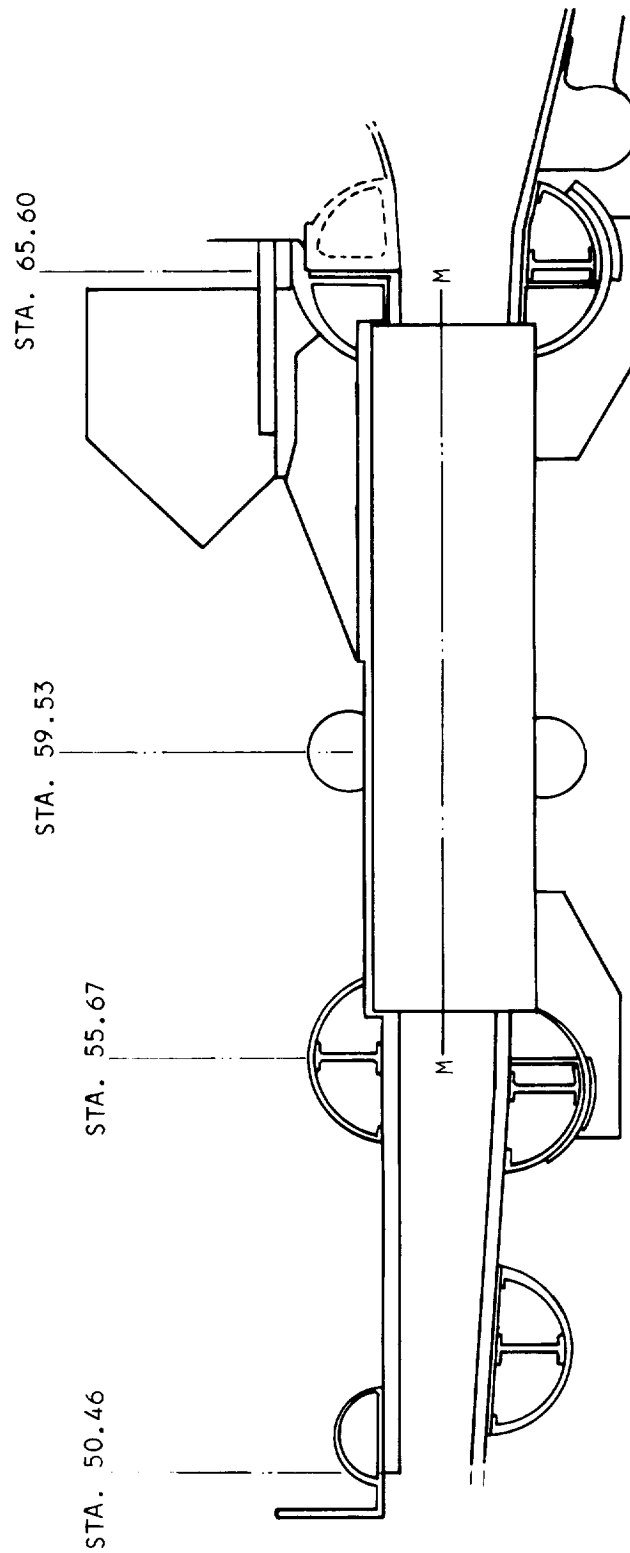
The submatrix A_6 represents the flexibility of the outer shell in relation to the support points. The analysis was performed by hand and checked, including the internal parts of the structure, using the Sabor III computer program. In this way, the total 30 by 30 $[A]$ matrix was obtained. The entire flexibility matrix is given in Table 5.3-1.

5.3.2 Natural Frequencies

Once the total flexibility matrix of the engine was known, the next immediate task was to input the mass and inertia data with that matrix into a computer program, especially developed for the analysis of the natural frequencies and corresponding relative deformation vectors.



UNCLASSIFIED



A-32229

Figure 5.3-3. Strut Connection Between Inner Shell and Outer Body



AIRESEARCH MANUFACTURING DIVISION
Los Angeles, California

UNCLASSIFIED

UNCLASSIFIED

TABLE 5.3-1
30 X 30 FLEXIBILITY MATRIX (Tabulated Flexibility Coefficient ($A_{ij} \times 10^6$))

Row Index	Column Index																																		
	1	2	3	4	5	6	7	8	9	10	11	12	13	14	15	16	17	18	19	20	21	22	23	24	25	26	27	28	29	30					
1	1.995	0	0	0	0	0	0	0.155	0	0	0	0	0.054	0	0	0	0	0	0	0.054	0	0	0	0	0	0.055	0	0	0	0	0				
2	0	6.962	0	0.075	0	0.946	0	3.831	0	0.075	0	0.262	0	0.760	0	0.075	0	0.208	0	2.026	0	0.075	0	0.013	0	2.139	0	0.075	0	0.521	0				
3	0	0	5.759	0	-0.561	0	0	0	2.338	0	-0.314	0	0	0	1.090	0	-0.270	0	0	0	0	0.041	0	-0.101	0	0	0	1.292	0	-0.161	0	0			
4	0	0.075	0	3.215	0	0	0	0.075	0	1.114	0	0	0	0.075	0	0.006	0	0	0	0	0	0.012	0	0	0	0.075	0	0.008	0	0	0	0			
5	0	0	-0.561	0	0.413	0	0	0	-0.836	0	0.023	0	0	0	-0.115	0	0.046	0	0	0	0	0.044	0	0.061	0	0	0	-0.161	0	0.023	0	0			
6	0	0.946	0	0	0	0.418	0	0.236	0	0	0	0.032	0	0.120	0	0	0	0.047	0	0.534	0	0	0	0	0.031	0	0.176	0	0	0	0.027	0			
7	0.155	0	0	0	0	0	0.108	0	0	0	0	0	0.054	0	0	0	0	0	0	0.054	0	0	0	0	0	0.055	0	0	0	0	0	0			
8	0	3.831	0	0.075	0	0.236	0	3.590	0	0.075	0	0.298	0	0.712	0	0.075	0	0.188	0	2.069	0	0.075	0	0.006	0	2.139	0	0.075	0	0.135	0	0			
9	0	0	2.338	0	-0.836	0	0	0	2.852	0	-0.213	0	0	0	1.261	0	-0.163	0	0	0	0	0.713	0	-0.030	0	0	0	1.292	0	-0.161	0	0	0		
10	0	0.075	0	1.114	0	0	0	0.075	0	1.118	0	0	0	0.075	0	0.008	0	0	0	0	0	0	0.013	0	0	0	0.075	0	0.008	0	0	0	0		
11	0	0	-0.561	0	0.028	0	0	0	-0.213	0	0.028	0	0	0	-0.143	0	0.065	0	0	0	0	0.046	0	0.062	0	0	0	-0.161	0	0.023	0	0	0		
12	0	0.262	0	0	0	0.032	0	0.298	0	0	0	0.032	0	0.154	0	0	0	0.069	0	0.047	0	0	0	0	0	0.044	0	0.176	0	0	0.027	0	0		
13	0.054	0	0	0	0	0	0.054	0	0	0	0	0	0.054	0	0	0	0	0	0	0.054	0	0	0	0	0	0	0	0.057	0	0	0	0	0		
14	0	0.760	0	0.075	0	0.120	0	0.712	0	0.075	0	0.154	0	2.167	0	0.075	0	0.183	0	2.215	0	0.075	0	0.058	0	2.139	0	0.075	0	0.075	0	-0.324	0	0	
15	0	0	1.090	0	-0.115	0	0	0	1.261	0	-0.143	0	0	0	1.320	0	-0.168	0	0	0	0	1.210	0	0	0	0	0	1.292	0	-0.161	0	0	0	0	
16	0	0.075	0	0.006	0	0	0	0.075	0	0.008	0	0	0	0.075	0	0.009	0	0	0	0	0	0	0.013	0	0	0	0.075	0	0.008	0	0	0	0	0	
17	0	0	-0.270	0	0.046	0	0	0	-0.163	0	0.065	0	0	0	-0.168	0	0	0.076	0	0	0	0.058	0	0	0	0	0	-0.161	0	0.023	0	0	0	0	
18	0	0.208	0	0	0	0.047	0	0.188	0	0	0	0.069	0	0.183	0	0	0	0.080	0	-0.252	0	0	0	0	0	0	0.176	0	0	0	0	0.027	0	0	
19	0.054	0	0	0	0	0	0.054	0	0	0	0	0	0.054	0	0	0	0	0	0	0.056	0	0	0	0	0	0	0	0	0	0	0	0	0	0	
20	0	2.026	0	0.075	0	0.034	0	2.069	0	0.075	0	0.047	0	2.215	0	0.075	0	-0.252	0	2.329	0	0.075	0	-0.058	0	2.139	0	0.075	0	0.075	0	-0.265	0	0	
21	0	0	0.041	0	0.044	0	0	0	0.715	0	0.046	0	0	0	1.210	0	0.058	0	0	0	0	1.382	0	0.061	0	0	0	1.292	0	-0.161	0	0	0	0	
22	0	0.075	0	0.012	0	0	0	0.075	0	0.013	0	0	0	0.075	0	0.013	0	0	0	0	0	0	0	0	0	0	0.075	0	0.008	0	0	0	0	0	
23	0	0	-0.101	0	0.061	0	0	0	-0.030	0	0.062	0	0	0	0.058	0	0.070	0	0	0	0	0.061	0	0.073	0	0	0	-0.161	0	0.023	0	0	0	0	
24	0	0.013	0	0	0	0.031	0	0.006	0	0	0	0.044	0	-0.049	0	0	0	0.070	0	-0.058	0	0	0	0	0	0.176	0	0	0	0	0.027	0	0	0	
25	0.055	0	0	0	0	0	0.055	0	0	0	0	0	0.057	0	0	0	0	0	0	0.058	0	0	0	0	0	0.060	0	0	0	0	0	0	0	0	
26	0	2.139	0	0.075	0	0.176	0	2.139	0	0.075	0	0.176	0	2.139	0	0.075	0	0.176	0	2.139	0	0.075	0	0.176	0	2.139	0	0.075	0	0.075	0	0.176	0	0	
27	0	0	1.292	0	-0.161	0	0	0	1.292	0	-0.161	0	0	0	1.292	0	-0.161	0	0	0	0	1.292	0	-0.161	0	0	0	1.292	0	-0.161	0	0	0	0	0
28	0	0.075	0	0.008	0	0	0	0.075	0	0.008	0	0	0	0.075	0	0.008	0	0	0	0	0	0	0.008	0	0	0.075	0	0.008	0	0	0	0	0	0	
29	0	0	-0.161	0	0.023	0	0	0	-0.161	0	0.023	0	0	0	-0.161	0	0.023	0	0	0	0	-0.161	0	0.023	0	0	0	-0.161	0	0.023	0	0	0	0	0
30	0	0.621	0	0	0	0.027	0	0.135	0	0	0	0.027	0	-0.324	0	0	0	0.027	0	-0.265	0	0	0	0	0	0	0.176	0	0	0	0	0.027	0	0	0



UNCLASSIFIED

UNCLASSIFIED

5.3.2.1 The Mass-Inertia Matrix

Using weights and moments of inertia referred to the centroids of the main parts, a mass-inertia matrix was produced. Due to the symmetry of the mass array with respect to the x-y-z coordinate system, all of the cross-products of inertias are zero, and the mass-inertia matrix became a diagonal matrix.

5.3.2.2 The EDIE Computer Program

A computer program (V0430) for structural matrix analysis is used to obtain the eigenvalues and eigenvectors of dynamic matrices, created automatically in the computer program. The EDIE program can receive a general square symmetric matrix and obtain its inverted matrix or determinant solution. Also, if a mass-inertia matrix (diagonal or not) is given, the dynamic matrix and the set of eigenvalues and eigenvectors (E; eigenvalues, D: determinant, I: inversion, E: eigenvectors) will be produced. The entire procedure is carried out in double-precision arithmetic on the IBM 360/65 computer.

5.3.2.3 The 30 First Natural Frequencies

A complete map of the first 30 natural frequencies was obtained. These natural frequencies correspond to a flexibility matrix analysis up to the engine side of the thrust sensor and the mounting pads at the outer shell near the mounting ring, which is defined as a "relative ground" at the mounting points. The analysis to date treats all structure above that relative ground (e.g. thrust block, wishbone, and pylon) as being infinitely rigid. Further information about elastic conditions above the relative ground can be easily entered into the flexibility matrix to obtain new frequency-deformation maps.

From the present map, the following comments and conclusions can be made.

- (1) All modes and corresponding frequencies are referred to the maximum temperature condition at $M_{\infty} = 8$. At room temperature, the frequencies, in particular the lower ones, may increase up to 15 percent.
- (2) The lowest mode is a rolling or torsional mode at 22.33 cps producing relative rotational motions in the spike-mounting cone-actuator area. It is not expected that this mode can be excited by externally applied loads. A possible source of excitation can arise due to unsymmetrical mass distribution, and its influence on this mode cannot be completely overlooked.
- (3) The next 13 modes are distinctive in-plane (x-y) or out-of-plane (x-z plane) vibrations, beginning with an x-y in-plane vibration at 26.51 cps--2nd mode--and continuing at 29.89 cps--3rd mode--with an x-z out-of-plane vibration. The 4th through 14th modes fall with the frequency band between 43.53 cps through 203.61 cps.



UNCLASSIFIED

- (4) The first axial mode (longitudinal direction) is the 15th general mode, at 231.67 cps. This axial mode corresponds to the actuator without internal spring characteristics, as mentioned before.
- (5) The following observations may be stated with regard to the first 6 modes:

<u>Mode</u>	<u>Frequency, cps</u>	<u>Main Area of Influence</u>
1	22.33 x	Spike, mount cone, actuator
2	26.51 x-y	Spike, actuator (at supports)
3	29.89 x-z	Struts, mounting rings
4	43.53 x-y	Spike, mount cone
5	47.38 x-z	Actuator
6	54.58 x-y	Struts, outer shell

- (6) The next immediate step will be incorporation of the thrust sensor wishbone flexibility in the overall model. The natural frequencies and mode shapes will be recalculated. The response vibration to qualification test inputs applied at the engine to pylon mounts will be computed.

5.3.3 Shock Loads and Qualification Tests

From inspection of the Equations (5.3-1) and (5.3-3), it can be observed that, there are common sets of coefficients and elements to be used in the perturbation analysis. Three of these sets should be particularly considered.

- (a) Perturbation Forces--This type of force can be applied directly to the masses, i.e., aerodynamic force, internal actuator forces, or to a common ground or "base" i.e., shaking forces in the qualification test or interface forces due to the X-15A-2. These forces can be pulsating, of short or long period, simple sinusoidal function or very complex. They may vary as a function of time.
- (b) The Coordinate System--Depending upon where the forces are acting, it may be convenient to change the absolute system of reference. In general, if the "base" is moving, three new variables will appear--displacement, velocity and acceleration of the "base."
- (c) Damping Coefficients--To obtain the system natural frequencies, the damping coefficients were set equal to zero. Reasonably assuming that the structural damping will give $\xi = C/C_{cr} \leq 0.1$, the frequency shift will be less than 1 percent.



UNCLASSIFIED

UNCLASSIFIED

In order to study the engine response for the frequency spectrum from 10 cps up to 2000 cps, a large number of resonant frequencies will be excited. In order to estimate response amplitudes at these natural frequencies, it will be necessary to make some reasonable assumptions regarding the values of the damping coefficient, C_i .

Not every degree of freedom must have substantial damping. Only a few will require a significant amount of damping (possibly in the order of $\xi = 0.1$), whereas the rest can be adequately damped by structural damping ($\xi < 0.05$).

5.3.3.1 The SHOCK Computer Program

Computer program (V0200) is capable of handling a system with up to 50 degrees of freedom and obtaining the response, through all the 50 degrees combined, under perturbation transient, residual transient, or steady state loads. An optional procedure can be selected to obtain the normal response by a predictor-corrector method or scanning the frequency spectrum to obtain the response at each one of the ω components. An option currently being included in the program will permit consideration of simultaneous perturbations coming from the masses (degrees of freedom) and for the common "base." It also will permit the study of combined perturbations of the engine during flight.

The first problem that will be analyzed with this program, in relation with the HRE, will be the perturbation produced by the asymmetrical unstart at the Mach_L = 6.5 condition.

5.3.3.2 Dynamic Response as a Design Tool

Two types of design areas can be checked or corrected as a consequence of the use of the mathematical model in the EDIE and SHOCK programs. One of them is the mathematical model itself, i.e., whenever an excessive flexibility occurs, it can be pin-pointed and then be adequately reinforced. This type of change will modify the flexibility coefficients producing the flexibility coefficient (a) matrix.

The second area of analysis is the damping matrix. The SHOCK program will allow determination of the precise design area where additional damping may be required.

5.4 ENGINE VIBRATION MODEL

5.4.1 Design Approach and Objectives

An engine vibration model will be constructed using simulated components, i.e., components with inertia properties and flexibility (where applicable) equivalent to those of the full-scale components. Individual structural members (struts, ring manifolds, actuator) will be identical to those used on the full-scale components. This approach permits evaluation of the engine structure during vibration and makes this effort independent of full-scale component development. Early resolution of potential problems under vibration conditions will, therefore, be possible.



UNCLASSIFIED

UNCLASSIFIED

Simulation of components will involve the use of single-wall engine inner and outer shells in place of the sandwich shells that will be used in the final components. Remaining shell assemblies will be suitably modeled, but will not duplicate full-scale component contours or structure. The feasibility of this type of simulation has been investigated and found acceptable in terms of test objectives.

5.4.1.1 Test Objectives

The objectives of the vibration test are to provide the following information as early as possible in the development program:

- (1) Resonant frequencies
- (2) Deflection of the assembly with extrapolation of results to spike tip and throat deflections
- (3) Structural amplifications (and damping)
- (4) Stress in the engine mounts, mount rings, struts, strut attachments, and actuator

The information provided by the test is expected to be sufficiently quantitative to establish a firm basis for the final design of the engine mounting and internal support structures.

5.4.1.2 Test Procedure

The test unit will be connected to the vibration fixture at the "wishbone." Half the time cycling will be conducted at room temperature, and half the time at approximately operating temperature. These temperatures can be achieved by piping hot air into the inner and outer shell manifolds forward of the struts, and cold air into the manifolds aft of the struts, while blowing intermediate temperature air between the inner and outer shells.

A brief outline of the test procedure is given below:

- (1) The assembly will be subjected to sinusoidal vibration levels of 0.06-in. double amplitude at 10 to 31 cps, and at ± 3.0 g from 31 to 2000 cps. The rate of frequency change will be logarithmic with one hour required to proceed from 10 to 2000 cps and back to 10 cps. The cycling test period for each of the three mutually perpendicular axes will be two hours, making a total test time of six hours.
- (2) The specimen will be surveyed for resonance in the 5 to 20 cps range by slowly varying the applied frequency at levels no greater than indicated in step 1 above. This will be accomplished, in turn, along each of two mutually perpendicular axes.
- (3) If resonances are encountered, each resonance will be sustained for a period of one minute. Resonance excitation of the unit directly attributable to the test fixture will be reduced to a level of ± 3 g maximum.



UNCLASSIFIED

UNCLASSIFIED

5.4.2 Assumptions

- (1) The damping contribution of the model single wall inner shell and outer shell will not differ significantly from that of the corresponding engine sandwich shells.
- (2) Resonant amplifications of the test model will approximate those of the engine.
- (3) Lower mode resonant frequencies of the model will not differ significantly from those of the engine.
- (4) A single thickness inner shell and outer shell can be designed which will have approximately the same lower mode dynamic characteristics and load carrying capability as the corresponding engine shells.

5.4.3 Test Configuration

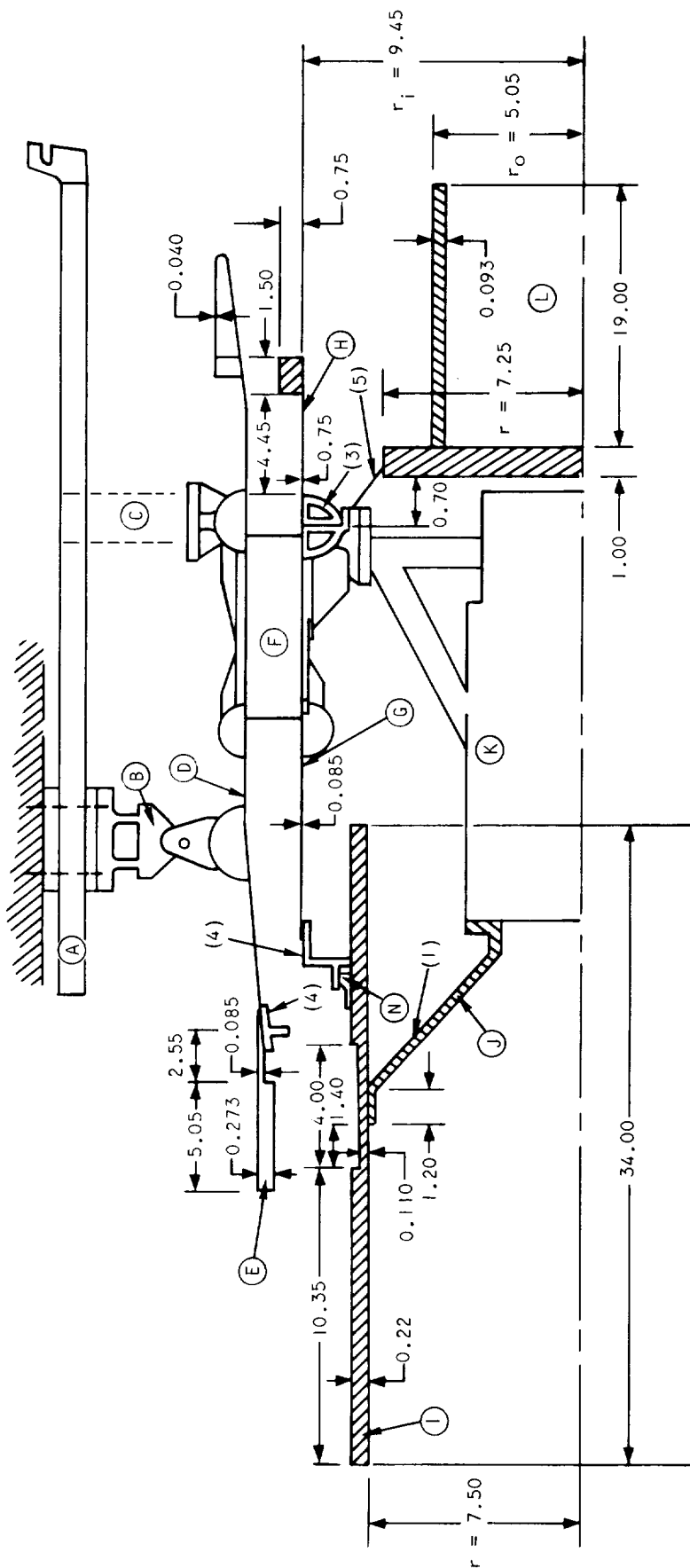
The test engine configuration will consist of the components indicated below. Reference should be made to Figure 5.4-1 for more detailed information.

- (a) Engine mount structure ("wishbone")
- (b) Deflection block (thrust measurement sensor)
- (c) Aft support flexible mount
- (d) Outer shell full-scale component, except that an equivalent thickness shell rather than a sandwich shell will be used.
- (e) Leading edge - a model simulating only the approximate inertia properties will be used
- (f) Six support struts
- (g) Inner shell - same as for (d)
- (h) Nozzle - a model simulating the approximate inertia properties and flexibility will be used
- (i) Spike - same as (h)
- (j) Spike mounting cone - same as (h)
- (k) Actuator full-scale component, except non-structural control elements may be left out
- (l) Fuel control valves and equipment package - same as (e)



UNCLASSIFIED

UNCLASSIFIED



NOTES

1. USE 98119-1 FLANGE ASSEMBLY EXCEPT AS INDICATED ABOVE.
2. INNER SHALL AND OUTER SHELL CONTOURS AS PER ENGINE. SINGLE THICKNESS SHELL TO BE USED. ALL OTHER SHELL COMPONENTS AS PER ENGINE, EXCEPT AS INDICATED ABOVE. NON-STRUCTURAL FUEL INJECTION MANIFOLD ASSY'S NEED NOT BE INCLUDED.
3. PLENUM ASSY AS PER 1980604 EXCEPT ALTERED TO BRAZE TO 9.45 IN. RADIUS CYLINDER.
4. RINGS TO HAVE SAME MOMENTS OF INERTIA AS ENGINE MANIFOLDS.
5. ATTACH IN SIMILAR MANNER AS FOR ENGINE.
6. FUEL CONTROL VALVE SIMULATIONS NOT SHOWN ABOVE.

B-13613

Figure 5.4-1. Test Configuration for Engine Vibration Model



AIRESEARCH MANUFACTURING DIVISION
Los Angeles, California

UNCLASSIFIED

UNCLASSIFIED

- (m) Bellows at spike to inner shell interface will be included for evaluation of bellows (not shown in figure)
- (n) Seal between spike and inner shell will be simulated to duplicate damping properties of engine seal

Masses with simulated inertia properties are used for the cowl leading edge, spike and nozzle. Since these components are relatively rigid from the point of view of primary bending (compared to the joint rigidities), they tend to act as rigid masses when the input frequencies are low. At the higher input frequencies, the flexible joints tend to isolate these components so that primary shell bending modes do not develop. Consequently, the inertia simulation is adequate for these components. The junction flexibilities of these components will be maintained by adjusting the simulated component wall thickness locally at the junction, as required.

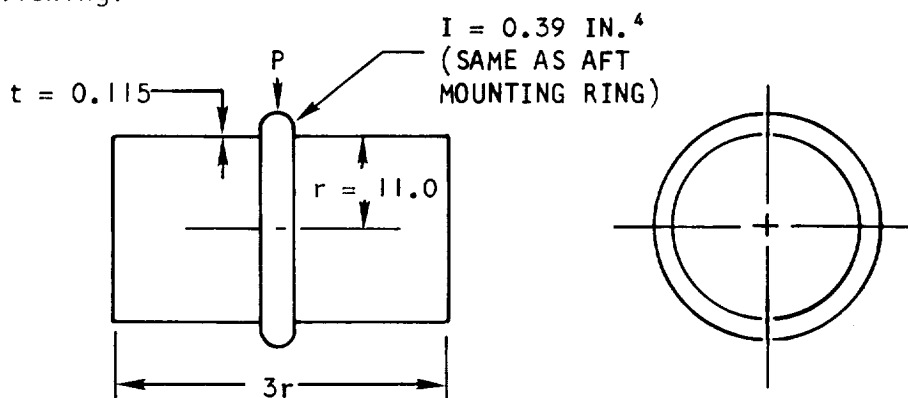
The test assembly will utilize a single wall inner shell and outer shell. For a plate-fin element with a 0.015-in. face sheet, and a 0.060-in. back sheet, separated by a 25R-0.050-0.065-0.006 fin, equivalent single wall thicknesses as indicated below:

For equal moment of inertia 0.114 in.

For equal weight 0.089 in.

For equal section modulus 0.081 in.

No single-thickness shell design can provide a complete simulation of the strut-shell interface. However, because the input levels are constant over most of the frequency range (20-2000 cps) and the resonant amplifications will not change much for small shifts in resonant frequencies, a single equivalent shell thickness was selected, which will give an approximate equal strength, i.e., section modulus. A single wall thickness of 0.085 in. gives very close equivalency for both weight and strength. While some error will be introduced in the natural frequencies, the shell rigidity is mostly in parallel with the rigidities for load being introduced at the struts. This approach is valid if the spring rate of the rings is appreciably higher than that of the shells, so that changes in the magnitude of the shell spring rate do not significantly change the total spring rate. Checking the relative spring rates for the following:



A-32244



AIRESEARCH MANUFACTURING DIVISION
Los Angeles, California

67-2833
Page 5-79

UNCLASSIFIED

UNCLASSIFIED

5.4.3.1 Shell Spring Rate, K_{sh} (based on Bijilaard data)

$$\gamma = \frac{r}{t} = \frac{11}{0.115} = 96 (\approx 100)$$

$$\frac{l}{r} = 3$$

$$\beta = \frac{c}{r} = \frac{1.5}{11} = 0.135 (\approx 1/8)$$

where P is distributed over a $2c \times 2c$ square area

$$\frac{\delta}{(P/Er)} = 15,800$$

$$k_{sh} = \frac{Er}{15,800} = \frac{11E}{15,800} = 6.97 \times 10^{-4} E$$

5.4.3.2 Ring Spring Constant, k_r

$$k_r = \frac{EI}{1075 r^3} = \frac{0.39E}{1075 (11)^3} = 38.9 \times 10^{-4} E$$

For this simple model, the ring contributes about 85 percent of the rigidity.

If k_{sh} becomes $\approx \frac{0.085}{0.115}^3 (6.97 \times 10^{-4} E) = 2.8 \times 10^{-4} E$

5.4.3.3 Total Spring Constants

$$k_{total} \text{ for test model} = (2.8 + 38.9) 10^{-4} E = 41.7 \times 10^{-4} E$$

$$k_{total} \text{ for engine} = (6.97 + 38.9) 10^{-4} E = 45.9 \times 10^{-4} E$$

$$\text{and } \frac{f_{\text{test model}}}{f_{\text{engine}}} = \sqrt{\frac{41.71}{45.9}} = 0.95$$

While the model is of greatly simplified construction, the possible error in resonant frequencies due to changes in shell spring rate will be small and within acceptable limits. This follows from the relative magnitudes of the spring rates for the test model and the engine as well as from the ratio of total spring rates and frequencies for the two. For the actual loading condition, i.e., with loads entering the structure at four points (four of the six struts), the moment distribution is such that the ratio of spring rates (ring to shell) is greater and more favorable than indicated above.



UNCLASSIFIED

5.5 COOLING SYSTEM

5.5.1 Flow Requirements and Pressure Drop

Required hydrogen flow rates and the associated cooling jacket pressure drops with and without the use of zirconia insulation (Rokide Z) have been investigated on a preliminary basis. For Rokide Z, a maximum surface temperature of 3500°R and a maximum thickness of 0.030 in. were used as limits. Figure 5.5-1 summarizes the flow conditions with and without insulation at the $M_\infty = 8.0$, $M_L = 6.5$, altitude = 88,000 ft flight condition. The use of Rokide Z of the thicknesses indicated in Figure 5.5-1 provides an overall flow reduction of 46 percent (3.26 lb/sec to 1.76 lb/sec). Purely on the basis of flow conservation, therefore, the use of insulation is attractive during engine operation. Structural ΔT 's are also significantly reduced. During ascent and descent, flow rate reductions will be relatively less (about 15 percent) as a result of much reduced heat fluxes over most of the engine surfaces. All of the pressure drops are based on a 500 psia cooling jacket outlet pressure.

A detailed summary of the spike flow route 1 is presented in Figure 5.5-2. The use of 0.015 in. thick Rokide for this route aft of Station 35 reduces the required flow rate by 51 percent. The most severe conditions are noted for the 16R fins (without insulation) and 25R fins (with and without insulation). No detailed analysis was completed on the folded flow section with insulation. Because of the low heat fluxes forward of Station 35, little benefit accrues from the use of insulation thicknesses to 0.030 in., which is the maximum being considered as feasible.

The cooling jacket pressure drop for route 1 is 330 psi without insulation and 94 psi with insulation.

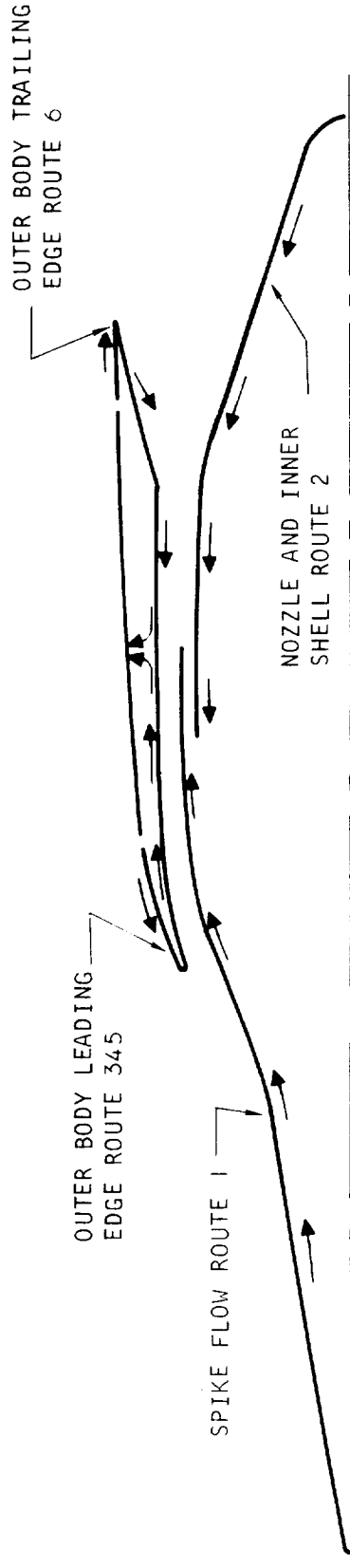
The nozzle and inner shell route 2, is summarized in Figure 5.5-3. The use of 0.015-in. thick Rokide Z reduced the required flow by 24 percent. The two most severe conditions for the 25R fins are noted, with and without insulation. The cooling jacket pressure drop for route 2 is 81 psi without insulation and 45 psi with insulation.

The outerbody leading edge route 345 is summarized in Figure 5.5-4. The use of 0.010-in. thick Rokide Z reduces the required flow rate by 56.5 percent. The maximum and the outlet conditions for the 25R fins are noted, with and without insulation. The cooling jacket pressure drop for route 345 is 148 psi without insulation and 38 psi with insulation.

The outerbody trailing edge route 6 is summarized in Figure 5.5-5. For purposes of comparison, the hydrogen flow is assumed to be constant throughout the route (i.e., no flow split at strut trailing edge to cool struts). Based on this assumption, the use of 0.010-in. thick Rokide Z reduces the required coolant flow by 42 percent. For this route, the maximum conditions for the 25R fins occur near the outlet. The cooling jacket pressure drop for route 345 is 241 psi without insulation and 104 psi with insulation.



UNCLASSIFIED

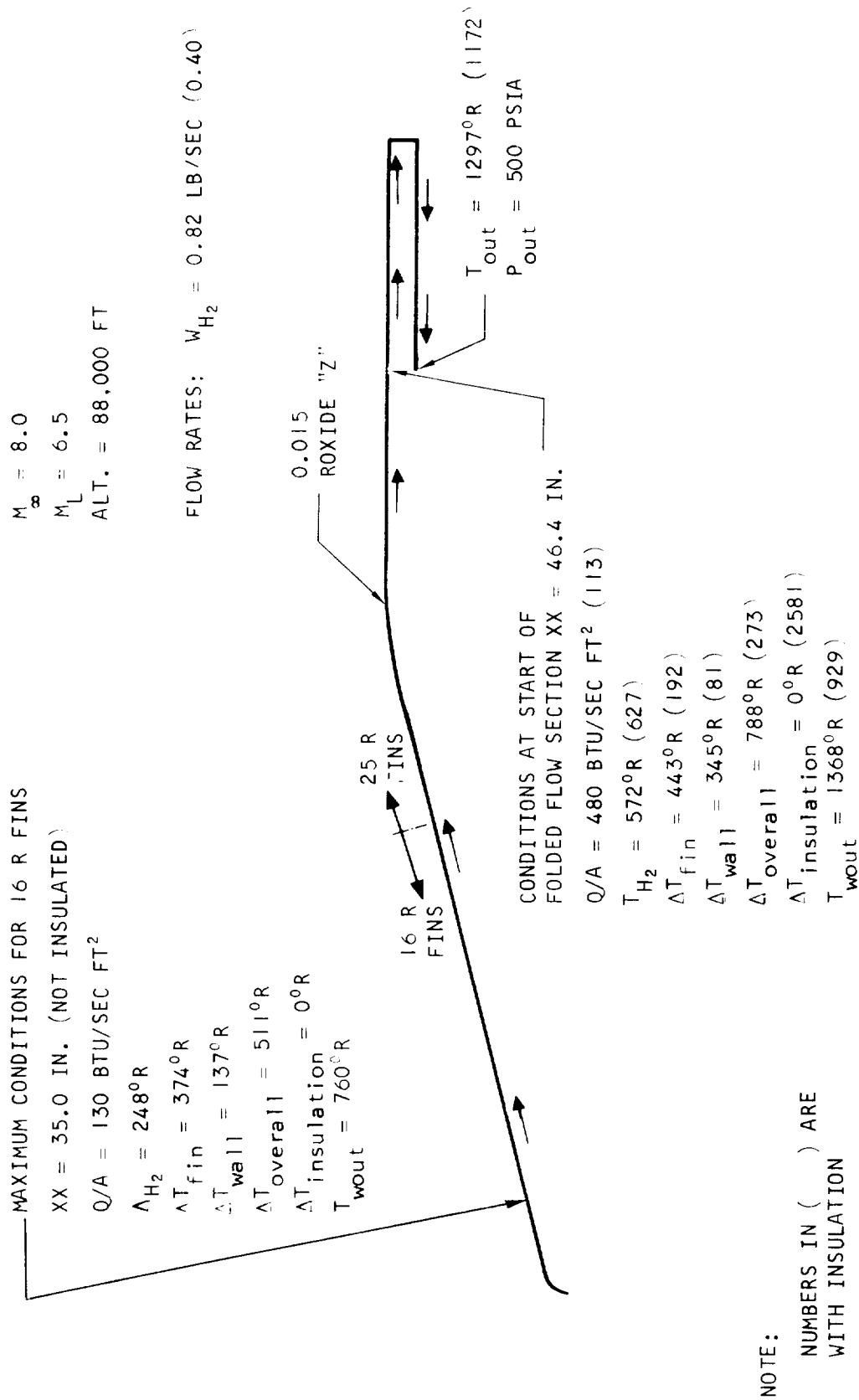


NOTE: ALL OUTLET PRESSURES ARE 500 PSIA
 $M_\infty = 8.0, M_L = 6.5, \text{ALT.} = 88,000 \text{ FT}$

ROUTE	INSULATION THICKNESS, INCHES	HYDROGEN FLOW RATE, LB/SEC	INLET PRESSURE, PSIA	PRESSURE DROP, PSI	INLET TEMP, °R	OUTLET TEMP, °R
1	0	0.82	830	330	100	1297
1	0.015 AFT OF XX-35	0.40	594	94	100	1272
2	0	0.42	581	81	120	1577
2	0.015	0.32	545	45	120	1570
345	0	0.92	648	148	100	1149
345	0.010	0.40	538	38	100	1498
6	0	1.10	741	241	100	1262
6	0.010	0.64	604	104	100	1550

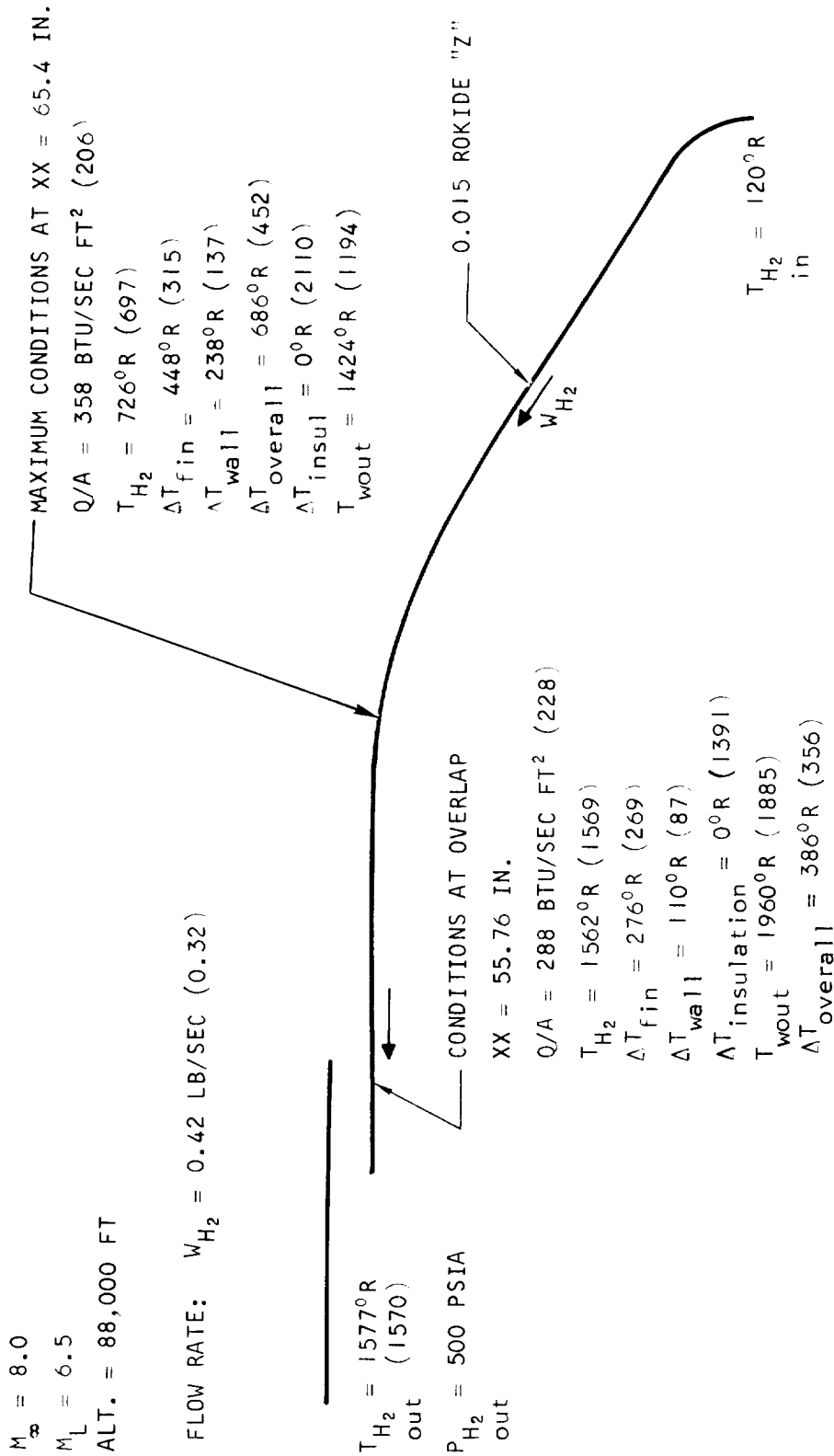
A-32108

Figure 5.5-1. Comparison of Coolant Requirements With and Without Insulation



67-2834

Figure 5.5-2. HRE Spike Flow Route 1



NOTE:

NUMBERS IN () ARE WITH INSULATION

Figure 5.5-3. HRE Nozzle and Inner Shell Route 2



$M_{\infty} = 8.0$
 $M_L = 6.5$
ATL. = 88,000 FT

FLOW RATES: $W_{H_2} = 0.92$ LB/SEC (0.40)

MAXIMUM CONDITIONS FOR 25 R PINS

XX = 49.85 IN.
 $Q/A = 809$ BTU/SEC FT² (342)
 $T_{H_2} = 915^{\circ}\text{R}$ (1246)
 $\Delta T_{fin} = 668^{\circ}\text{R}$ (396)
 $\Delta T_{wall} = 467^{\circ}\text{R}$ (198)
 $\Delta T_{overall} = 1135^{\circ}\text{R}$ (594)
 $\Delta T_{insulation} = 0^{\circ}\text{R}$ (1605)
 $T_{wout} = 2062^{\circ}\text{R}$ (1840)

$P_{out} = 500$ PSIA

$T_{in} = 100^{\circ}\text{R}$

W_{H_2}

0.010 ROKIDE "Z"

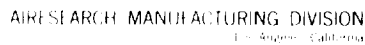
OUTLET CONDITIONS AT XX = 52.0 IN.

$Q/A = 688$ BTU/SEC FT² (367)
 $T_{H_2} = 1149^{\circ}\text{R}$ (1498)
 $\Delta T_{fin} = 520^{\circ}\text{R}$ (397)
 $\Delta T_{wall} = 338^{\circ}\text{R}$ (181)
 $\Delta T_{overall} = 858^{\circ}\text{R}$ (578)
 $\Delta T_{insulation} = 0^{\circ}\text{R}$ (1493)
 $T_{wout} = 2017^{\circ}\text{R}$ (2076)

NOTE:

NUMBERS IN () ARE WITH INSULATION

Figure 5.5-4. HRE Outer Body Leading Edge Route 345

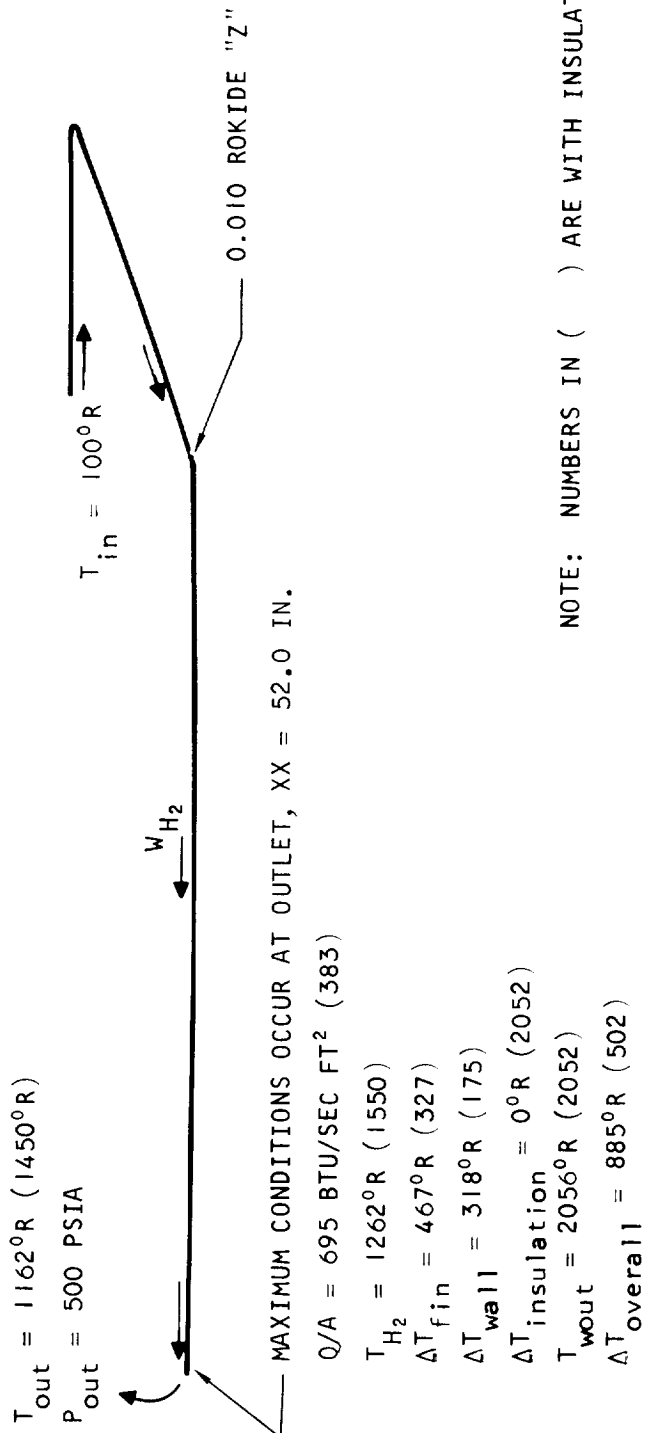


$$\sum^8 = 8.0$$

$$M_L = 6.5$$

ALT. = 88,000 FT

FLOW RATES: $w_{H_2} = 1.10 \text{ LB/SEC (0.64)}$



NOTE: NUMBERS IN () ARE WITH INSULATION

A-32170

Figure 5.5-5. HRE Outerbody Trailing Edge Route 6

UNCLASSIFIED

5.5.2 Structural Temperatures

Figures 5.5-6, -7, and -8 indicate the engine temperature differential and temperature levels for the $Mach_{\infty} = 8$, $Mach_L = 6.5$, 88,000 ft flight condition. The ΔT 's and absolute temperatures are based on the heat fluxes from Figure 5.1-17 and the flow conditions as outlined in Figure 5.5-1 without insulation. The fin geometry used in the calculations is as reported in Paragraph 4.3.2 of Reference 5.5-4.

5.5.3 Outerbody Leading Edge

5.5.3.1 Thermal Design

Results of the HRE cowl leading edge heat flux analysis for Mach 8, 88,000 ft with and without the influences of the X-15 pressure field and for the spike retracted and fully extended positions are shown in Table 5.5-1. Stagnation line heat fluxes were calculated by the use of Reference 5.5-2 using flow properties behind the HRE spike shock where also tabulated in Table 5.5-1. The maximum heat flux of 1550 Btu/sec sq ft was calculated for a 2000°R surface temperature when the spike is at the retracted position and the engine is outside the X-15 pressure field. This heat flux was used to obtain the stagnation line heat transfer coefficient of 0.585 Btu/sec-°R-sq ft used for leading edge passage sizing discussed later in this section.

5.5.3.1.1 Analysis for Spike Extended

The high heat flux of 1000 Btu/sec sq ft when the spike is in the fully extended position results from the presence of a clearance gap of 0.065 in. between the cowl lip and the spike. This gap allows removal of the boundary-layer and thus causes a high energy streamline to impinge at the cowl lip (streamline C in Figure 5.5-9). The air flows through the 0.06-in. gap are 1.1 and 0.85 lb/sec for local engine Mach numbers of 8 and 6.5, respectively.

The Mach 8, 88,000 ft entrance heating for the spike extended position is shown in Figure 5.5-10. These data were computed by the short duct method as outlined in Reference 5.5-3. The heat fluxes for the spike, as shown in Figure 5.5-10, incorporate the flow separation and reattachment upstream of the cowl, which occur because the normal shock at the entrance of the gap is of sufficient strength ($c_p = 1.37$ based on a normal shock from an average of $M = 2.5$ in the boundary layer) to cause boundary-layer flow separation. Because the estimated gap flow is approximately one-third of the mass within the boundary layer, the separated flow will reattach upstream of the gap as indicated in Figure 5.5-10. The total pressure behind the normal shock for the flow model shown in Figure 5.5-10 would not differ greatly from the normal shock shown in Figure 5.5-9. Hence, the simplified flow model of Figure 5.5-9 was used for inlet flow and stagnation flow evaluation.

For evaluation of boundary layer flow properties, both the velocity and temperature profiles are required. Crocco's temperature distribution evaluated for insulated surfaces was used in Equation 5.5-5 only to compute the local



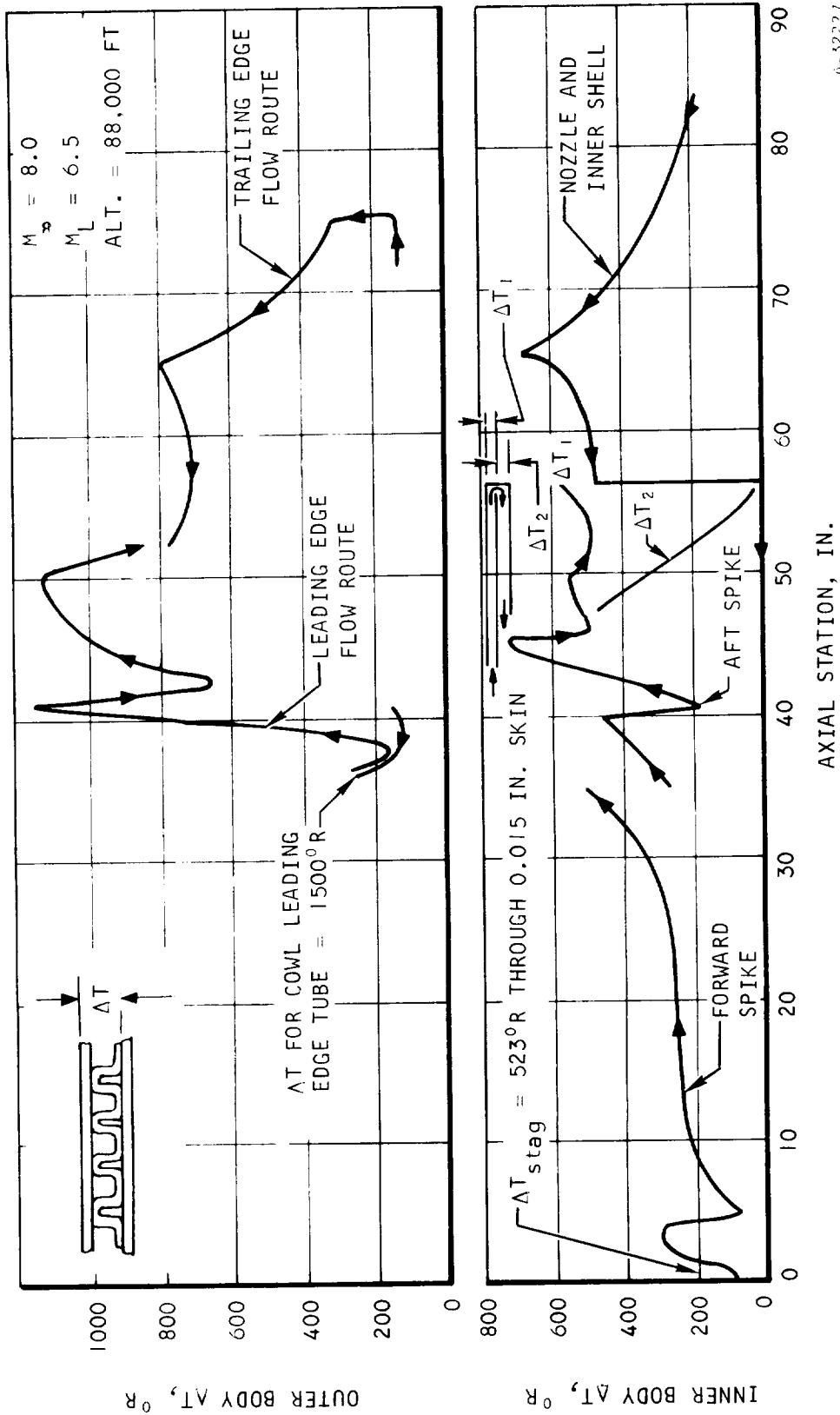


Figure 5.5-6. Engine Temperature Differentials, $M_{\infty} = 8$

A-52227

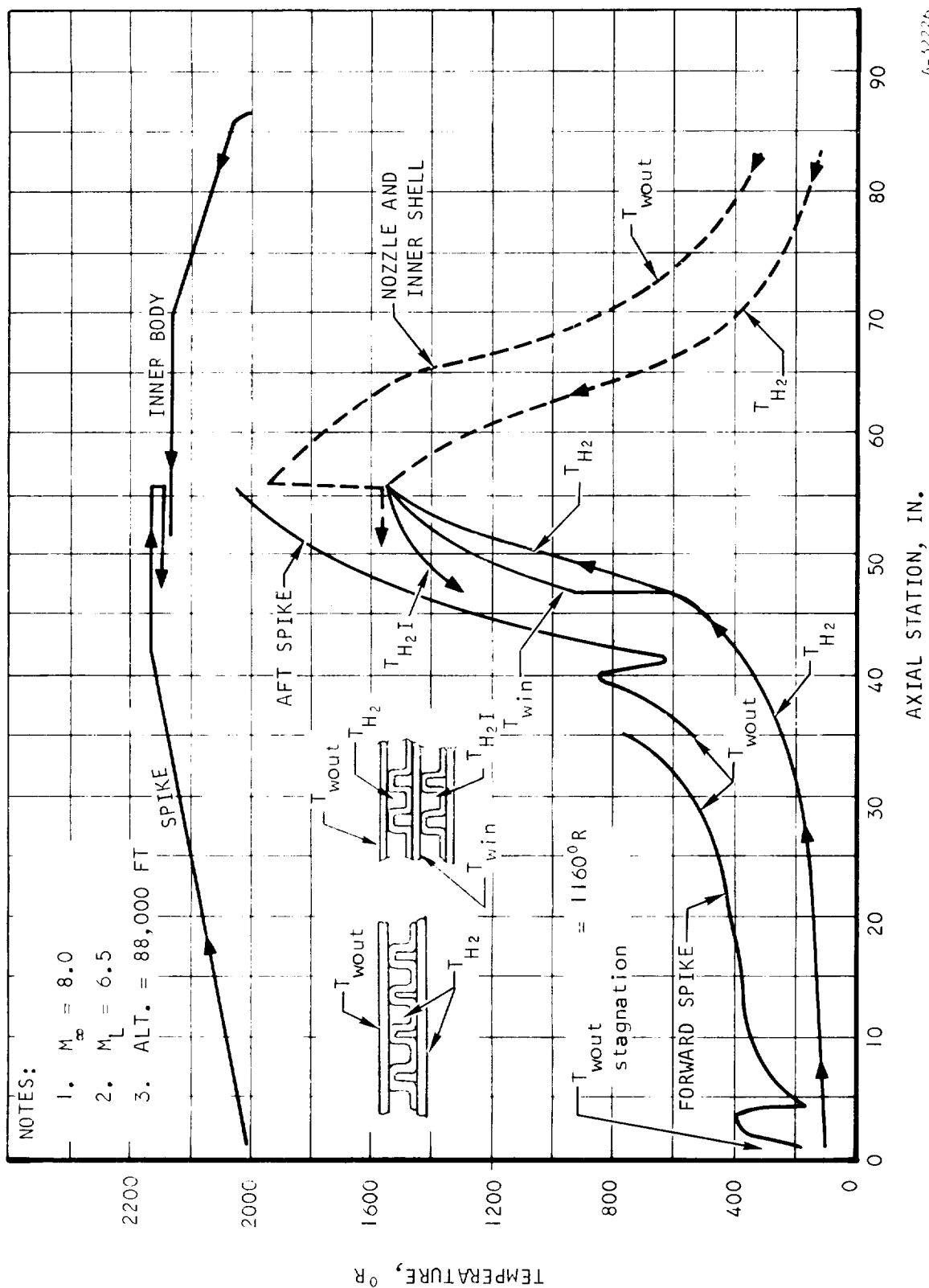
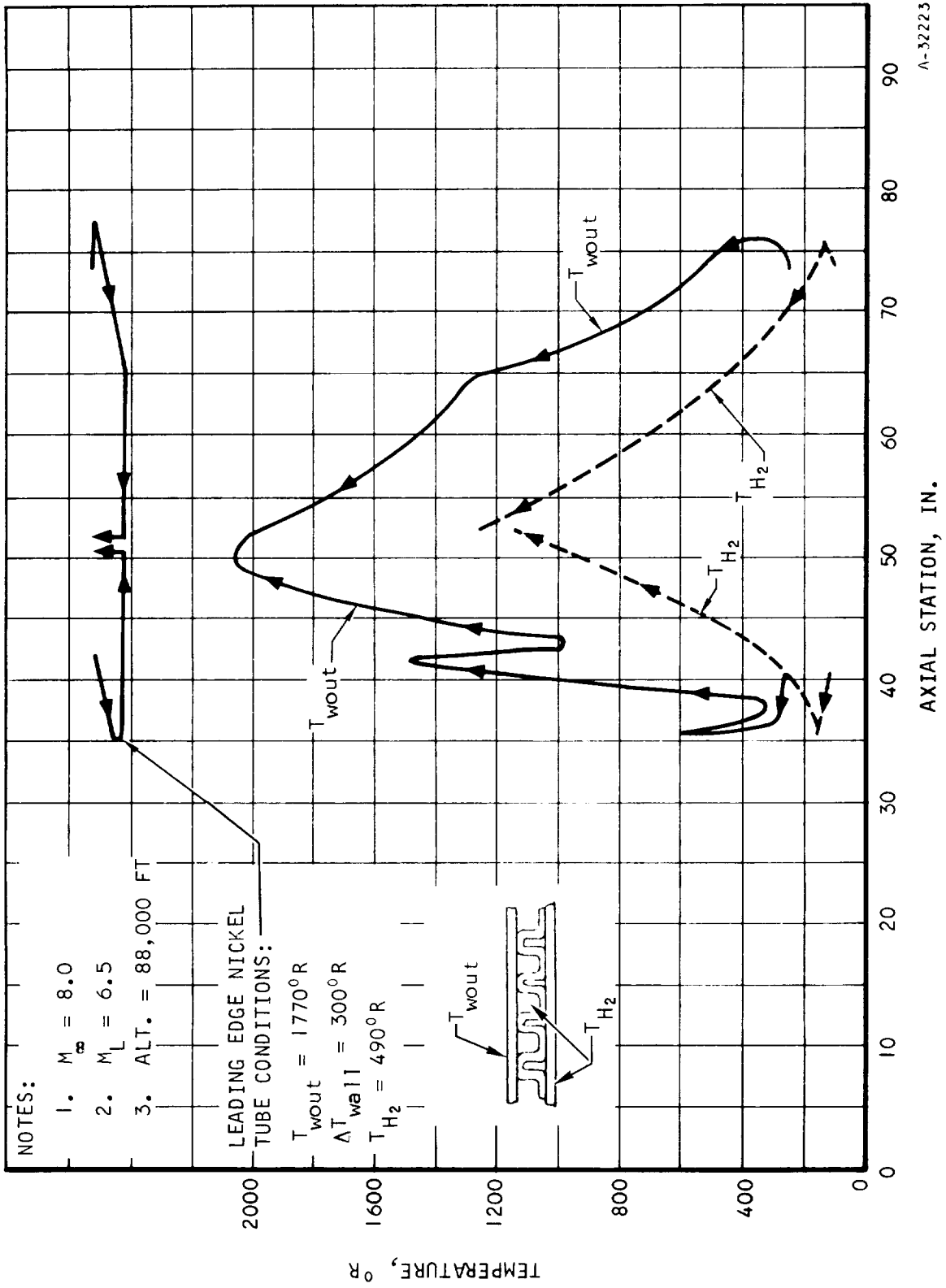


Figure 5.5-7. Spike and Inner Body Temperature Distribution, $M_0 = 8$



A-32223

Figure 5.5-8. Outer Body Temperature Distribution, $M_\infty = 8$

UNCLASSIFIED

TABLE 5.5-1

FLOW PROPERTIES AND HEAT FLUX ON LEADING EDGE FOR FLIGHT M=8, 88,000 FT

Spike Position	Engine Out of X-15 Flow Field ($M_L = 8$)		Engine In X-15 Flow Field ($M_L = 6.5$)		
	Spike Shock Inside LE Lip		Spike Shock Outside LE Lip		
	Retracted	Retracted	Extended	Retracted	Extended
FLOW PROPERTIES					
Upstream of Leading Edge Shock					
Local boundary layer edge Mach No.	8	5	5.69	5.45	5.07
Stagnation Mach No.	8	5.0	5.2	5.45	4.3
Pressure, psfa	40	665	311	307	1110
Static temperature, °R	400	895	820	750	520
Total enthalpy, Btu/lb	1320	1320	1280	1320	1280
Downstream of Leading Edge Shock					
P_{T2} total pressure, psfa	2840	20,500	10,240	11,500	12,200
ρ_{T2} total density, lb/ft ³	0.12	0.093	0.042	0.046	0.05
ρ_{TW} total density at the wall, lb/ft ³	0.028	0.199	0.096	0.108	0.11
γ specific heat ratio	1.3	1.3	1.3	1.3	1.3
Wall temperature, °R	2000	2000	2000	2000	2000
Total temperature, °R	4650	4650	4200	4650	4200
μ_{T2} viscosity at total temperature, lb/sec ft	4.65×10^{-5}	4.65×10^{-5}	4.65×10^{-5}	4.65×10^{-5}	4.65×10^{-5}
μ_w viscosity at wall temperature, lb/sec ft	3.5×10^{-5}	3.5×10^{-5}	3.5×10^{-5}	3.5×10^{-5}	3.5×10^{-5}
Pr_w Prandtl number at wall temperature	0.72	0.72	0.72	0.72	0.72
STAGNATION HEAT FLUX, BTU/SEC FT ² (2000°R wall temperature)	580	1550	1000	1140	100



UNCLASSIFIED

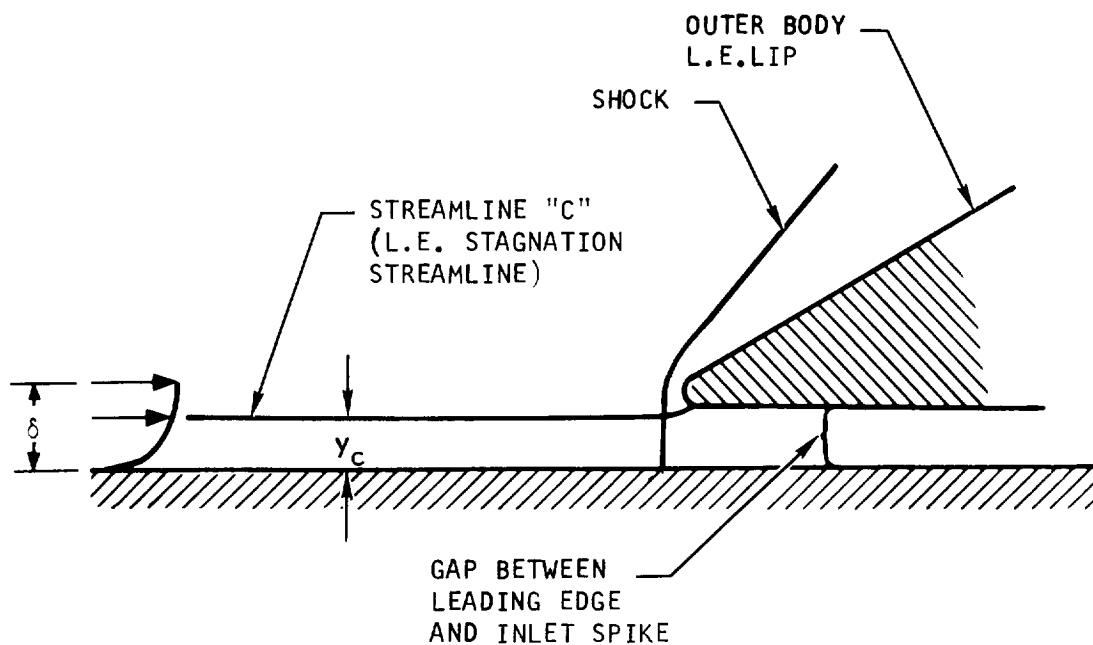
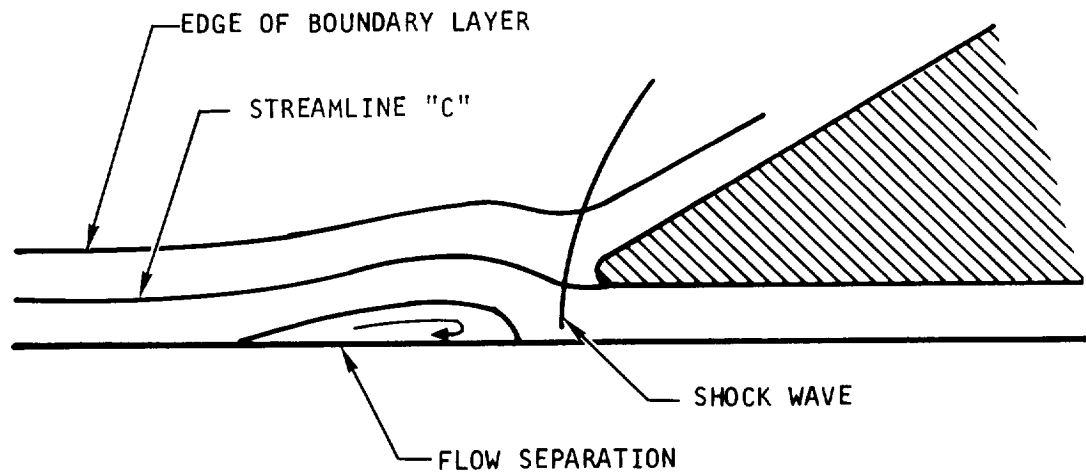
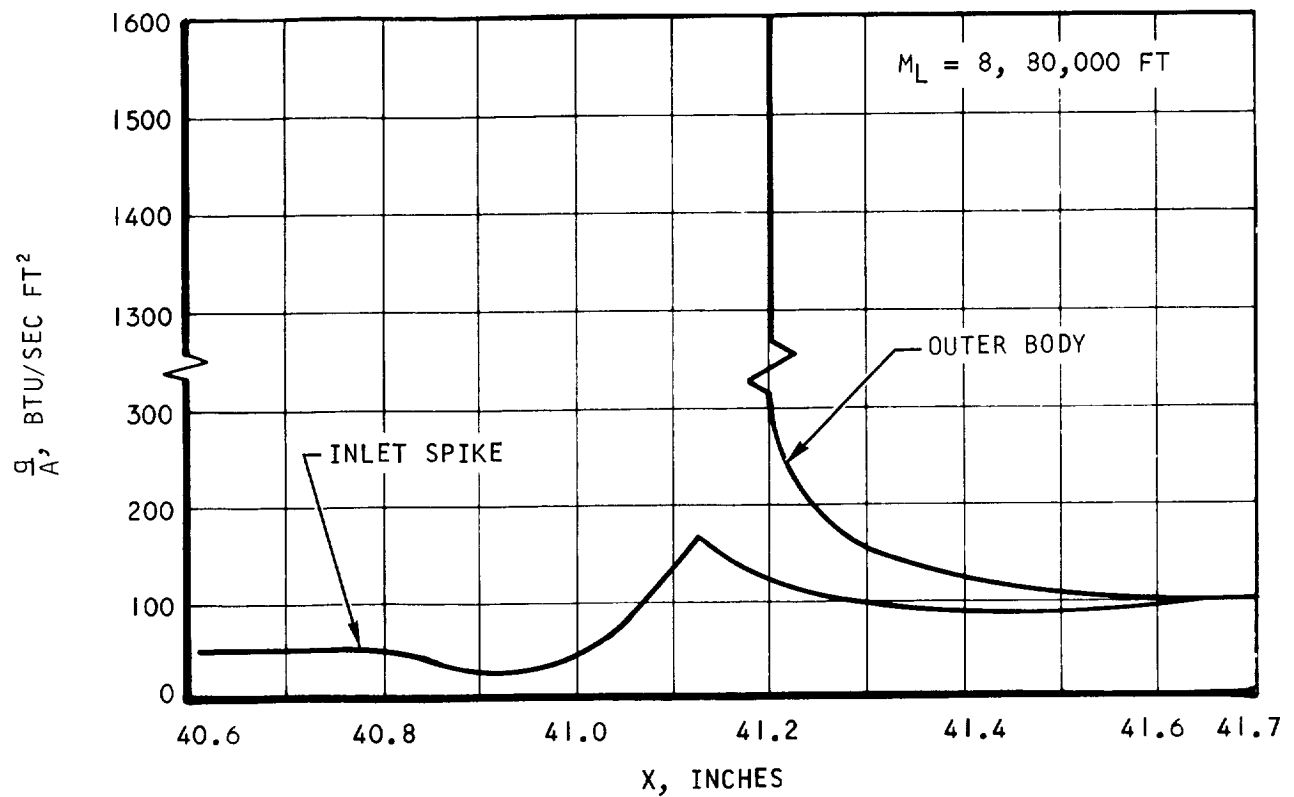


Figure 5.5-9. Idealized Flow Diagram, Spike at Fully Extended Position



UNCLASSIFIED

UNCLASSIFIED



A-32444

Figure 5.5-10. Heat Flux Distribution and Flow Model;
Spike at Fully Extended Position



AIRSEARCH MANUFACTURING DIVISION
Los Angeles, California

UNCLASSIFIED

67-2833
Page 5-93

UNCLASSIFIED

density in order to obtain a closed form solution. This would introduce a slight error in the captured mass. However, for heat transfer calculation the Crocco's temperature distribution evaluated for heat conduction was used. A $1/7$ power velocity distribution was assumed. The choice of Crocco's temperature distribution was for simplicity, although a more accurate temperature profile can be found in Reference 5.5-4. The method of analysis is next discussed in greater detail.

NOMENCLATURE

Symbols

- A = total gap flow area, ft^2
- b = gap height, ft
- h = enthalpy, Btu/lb
- M = Mach No.
- m = mass flow, lb/sec
- q = heat flux, Btu/sec ft^2
- r = distance from centerline to LE lip, ft
- R = gas constant, $\frac{\text{lb}_{\text{force}} \text{ft}}{\text{lb}_{\text{mass}} ^\circ\text{R}}$
- T = temperature, $^\circ\text{F}$
- u = velocity, ft/sec
- y = distance normal to wall surface, ft
- α = mass fraction defined in Equation 5.5-5
- γ = specific heat ratio
- δ^* = displacement thickness, ft
- ρ = density, lb/ft^3



UNCLASSIFIED

Subscripts

- ∞ = edge of boundary layer
- l = gap flow
- T = total or stagnation conditions
- w = wall condition
- C = captured stream tube

When the spike is in the closed position, a clearance gap of 0.06 in. exists between the leading edge and the inlet spike. Because this gap height is of the same order of magnitude as the local boundary-layer height, detailed analysis of the flow property distribution within the boundary layer is required before heat transfer to the cowl lip can be assessed. Specifically, it is desirable to determine, which stream tube stagnates at the cowl lip (see Figure 5.5-9).

This analysis is carried out in two steps. In Step 1, the fractional boundary layer flow entering the gap was determined with the aid of Reference 5.5-5. In Step 2, the boundary layer mass flow was integrated to match the mass fraction entering the gap. For this analysis, the 1/7 power velocity profile was assumed (Equation 5.5-1). In addition, Crocco's temperature profile evaluated for an adiabatic wall was used (Equation 5.5-2) for local density calculations, and Crocco's temperature profile evaluated for the wall conduction (Equation 5.5-3) was used to calculate the local total temperature.

$$\frac{u}{U_{\infty}} = \left(\frac{y}{\delta}\right)^{1/7} \quad (5.5-1)$$

$$\frac{T}{T_{\infty}} = 1 + \frac{\gamma-1}{2} M_{\infty}^2 \left(1 - \frac{u^2}{U_{\infty}^2}\right) \quad (5.5-2)$$

$$\frac{h_{T \text{ local}} - h_w}{h_{T_{\infty}} - h_w} = \frac{w}{U_{\infty}} \quad (5.5-3)$$

Step 1. Determination of the Fractional Boundary Layer Flow Entering Gap

The massflow ratio can be found in Reference 5.5-5. However, it is necessary to distinguish between the definition of mass flow ratio m/m_l , given by Reference 5.5-5, and the term mass flow ratio α used herein. The former refers to the fractional flow compared with the mass flow contained within a stream tube in the free stream having an area of the size of the gap. The term α is defined below:

$$\alpha = \frac{\text{gap flow}}{2\pi r \int_0^{\delta} \rho u dy} = \frac{\text{gap flow}}{2\pi r \rho_{\infty} U_{\infty} (\delta - \delta^*)} \quad (5.5-4)$$



UNCLASSIFIED

$$\frac{(m/m_\ell) 2\pi r b (\rho_\infty U_\infty)}{2\pi r \rho_\infty U_\infty (\delta - \delta^*)} = \frac{b}{(\delta - \delta^*)} \frac{m}{m_\ell} \quad (5.5-4)$$

By way of illustration, for $M = 5$ (representative of boundary layer edge Mach number, spike extended, Table 5.5-1), 1/7 power velocity profile, and gap to boundary layer ratio of 1/2, the mass flow ratio m/m_ℓ is 0.31 taken from Reference 5.5-5. The gap flow so calculated is 34 percent of the total boundary layer mass flux.

Step 2. Evaluation of the Stagnation Line Flow Properties

From the above established gap flow, m , the value of y_c can be determined such that the integrated mass flux from $y = 0$ to $y = y_c$ would yield m .

$$\begin{aligned} \frac{m}{2\pi r} &= \int_0^{y_c} \rho u dy = \rho_\infty V_{as} \int_0^{y_c} \frac{\rho u}{\rho_\infty V_{as}} dy \\ &= \rho_\infty V_{as} \delta \int_0^{y_c/\delta} \frac{\rho}{\rho_\infty} \frac{u}{U_\infty} d\left(\frac{y}{\delta}\right) \\ &= \rho_\infty U_\infty \delta \int_0^{y_c/\delta} \frac{T_\infty}{T} \frac{u}{U_\infty} d\left(\frac{y}{\delta}\right) \end{aligned} \quad (5.5-5)$$

Assuming Crocco's temperature profile for adiabatic wall,

$$\frac{m}{2\pi r} = \rho_\infty U_\infty \delta \int_0^{y_c/\delta} \frac{u/U_\infty}{1 + \frac{\gamma-1}{2} M_\infty^2 \left(1 - \frac{u^2}{U_\infty^2}\right)} d\left(\frac{y}{\delta}\right) \quad (5.5-6)$$

Introducing the 1/7 power velocity profile,

$$\begin{aligned} \frac{m}{2\pi r} &= \rho_\infty U_\infty \delta \int_0^{y_c/\delta} \frac{(y/\delta)^{1/7} d(y/\delta)}{1 + \frac{\gamma-1}{2} M_\infty^2 - \frac{\gamma-1}{2} M_\infty^2 (y/\delta)^{2/7}} \\ &= 0.34 \rho_\infty U_\infty (\delta - \delta^*) \end{aligned} \quad (5.5-7)$$

Equation (7), upon integration, yields $y_c/\delta = 0.71$.



UNCLASSIFIED

The velocity and total enthalpy corresponding to this streamline, $y_c/\delta = 0.71$ are:

$$\frac{u}{U_\infty} = \left(\frac{y_c}{\delta}\right)^{1/7} = 0.95 \quad (5.5-8)$$

$$\frac{h_t}{h_{t_\infty}} = \frac{h_w}{h_{t_\infty}} + \left(1 - \frac{h_w}{h_{t_\infty}}\right) \left(\frac{y_c}{\delta}\right)^{1/7} = 0.96 \quad (5.5-9)$$

Equation 5.5-9 is derived by rearranging of Equation 5.5-3.

The rest of the properties corresponding to this streamline can be determined once U and h_t are established.

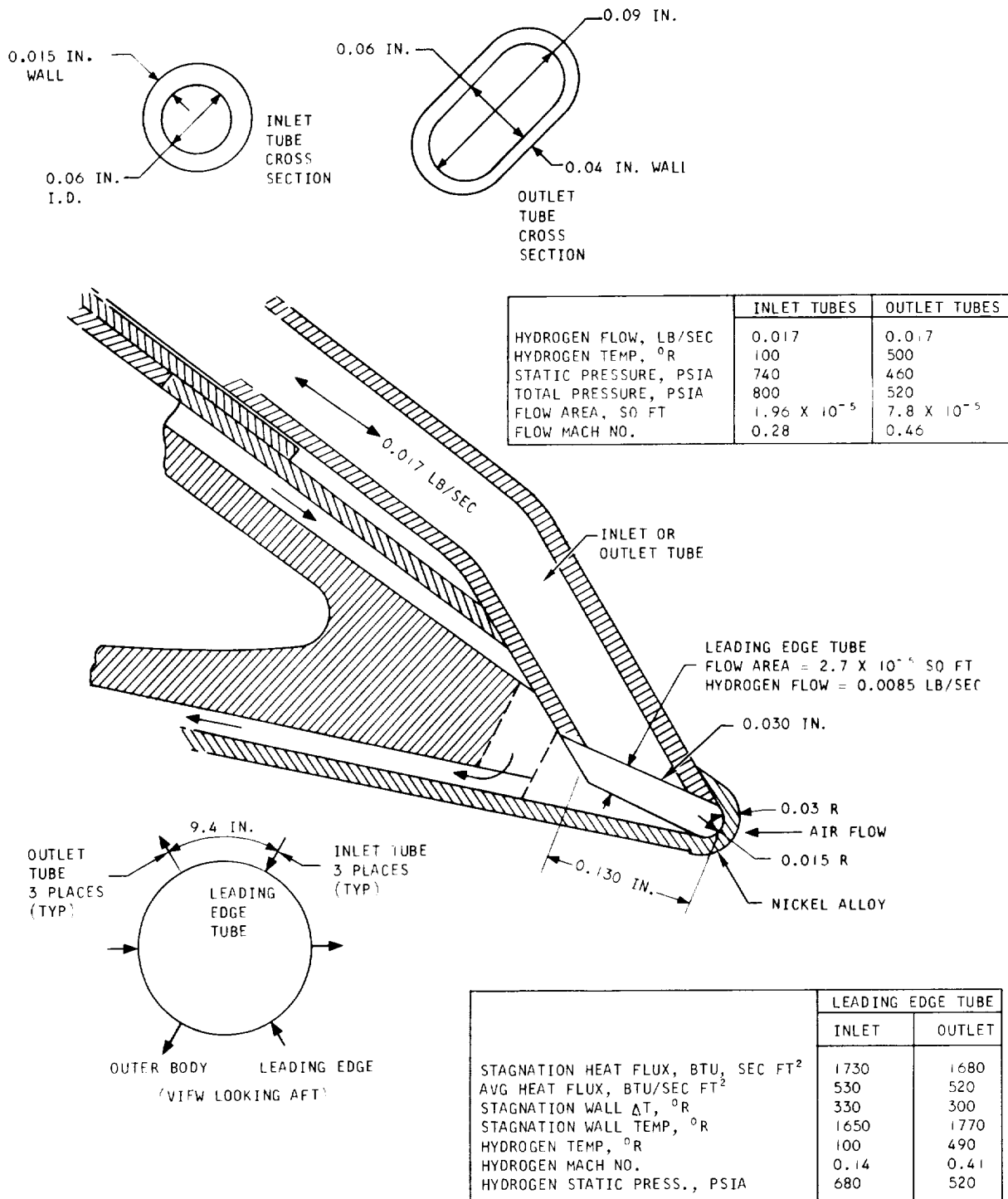
5.5.3.1.2 Cooling Passage Heat Transfer Design

The tubular leading edge design, shown schematically in Figure 5.5-11, is the basis for current work in design of the leading edge. Previous leading edge cooling passage design was based on forward outer shell flow that was perpendicular to the leading edge through a clearance (Figure 5.5-12) sized to maintain the stagnation line temperature at 1660°R and the maximum overall difference between stagnation line and hydrogen temperatures at 1200°R. These limitations were selected to provide adequate cycle life for thermal fatigue. With the 1750 Btu/sec ft² stagnation line heat flux (Table 5.5-1, $M_L = 8$, spike retracted, 1660°R wall temperature), the required clearance is 6 mil for a Hastelloy X wall and the hydrogen conditions shown in Figure 5.5-12 for the retracted spike. Greater certainty of achieving acceptable hardware can be obtained by using nickel instead of Hastelloy X for the skin. The higher conductivity of nickel results in a reduced wall ΔT and hydrogen heat transfer coefficient, which in turn permit a clearance increase from 6 mil to about 12 mil. However, the problem with the extended spike is critical because coolant conservation requirements result in comparable clearances for Hastelloy X and nickel of 1.15 mil and 2 mil respectively. Specifically, these minute clearances are required to obtain coolant conservation during ascent-descent, with maximum closed spike stagnation heat flux of 1000 Btu/sec ft² and hydrogen conditions noted in Figure 5.5-12. The noted stagnation region hydrogen conditions result with a heat load of 373 Btu/sec which occurs at Mach 8 and 88,000 ft altitude with an outlet temperature of 1600°R for flow rate route 345 on the leading edge and forward outer shell.

Because the above-mentioned leading edge clearances are too small for practical construction, the design with flow parallel to the leading edge was reconsidered. Although the design features summarized in Figure 5.3.3 are for use of inlet and outlet tubes on the outside surface of the leading edge, other manifolding methods are being investigated. The indicated manifolding has 3 inlet and 3 outlet tubes interspersed around the leading edge circumference at 60 degree intervals. An outlet hole of 100 mil diameter may be substituted for the oval tube shown in Figure 5.5-11, if dumping the leading edge flow to ambient proves acceptable.



UNCLASSIFIED



B-13623

Figure 5.5-11. Outer Body Leading Edge Cooling Configuration

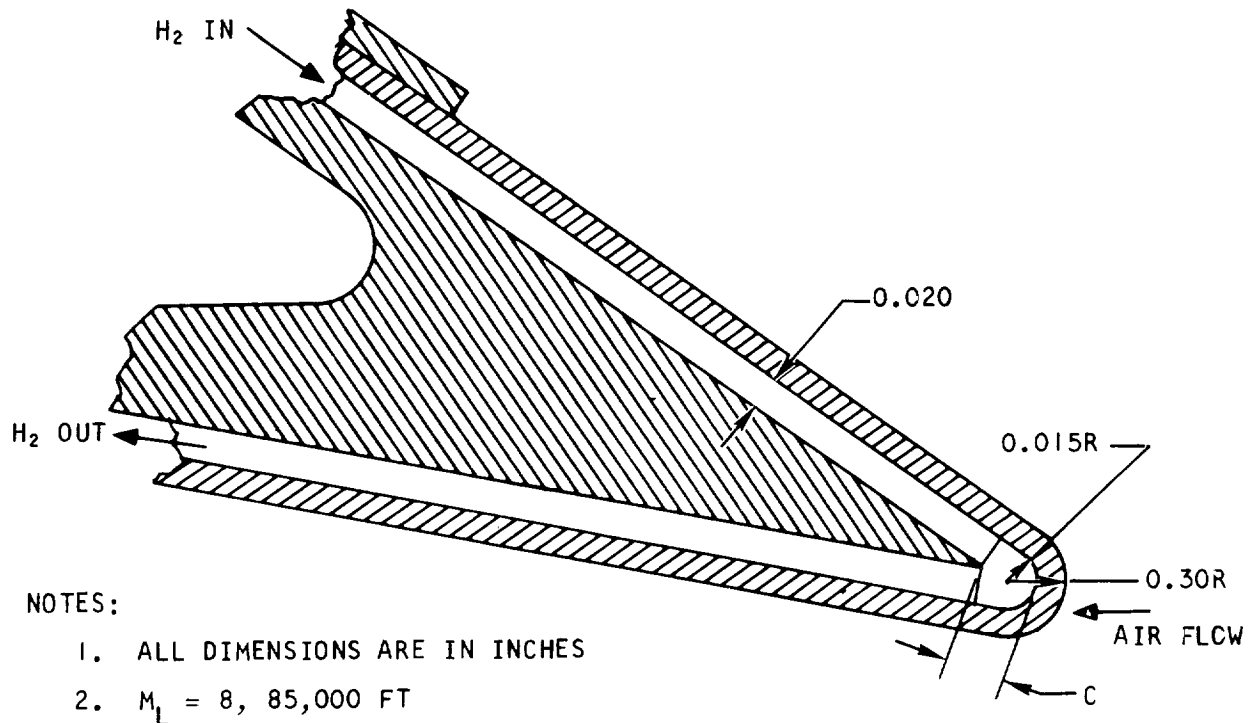
UNCLASSIFIED



AIR RESEARCH MANUFACTURING DIVISION
Los Angeles, California

67-2833
Page 5-98

UNCLASSIFIED



NOTES:

1. ALL DIMENSIONS ARE IN INCHES
2. $M_L = 8, 85,000$ FT

A-32234

Engine Condition	Lit		Ascent-Descent	
Wall Material	Nickel	Hastelloy X	Nickel	Hastelloy X
Stagnation heat flux, Btu/sec-ft ²	1750	1750	1000	1000
Stagnation wall T, °R	1660	1660	1660	1660
Stagnation wall ΔT, °R	240	880	190	500
Hydrogen flow, lb/sec	0.92	0.92	0.069	0.069
Hydrogen T, °R	164	164	486	486
C, mils	12	6	2	1.15

Figure 5.5-12. Flow Perpendicular to Leading Edge

UNCLASSIFIED



AIRSEARCH MANUFACTURING DIVISION
Los Angeles, California

UNCLASSIFIED

The passage dimensions are large enough to ensure avoiding blockage during fabrication or use. The use of nickel as the wall material permits use of a maximum stagnation line temperature of 1770°R and a wall ΔT of only 300°R at the corresponding local heat flux of $1680 \text{ Btu/sec ft}^2$. Use of a round tube of 30 mil ID and 60 mil OD was rejected because of excessive Mach number with a practical number of inlets and outlets. The use of an oval leading edge tube permits more than a three-fold reduction in hydrogen temperature change per inch of flow. An acceptable outlet Mach number is thus achieved. The stagnation region ΔT values are 85 percent of the ΔT calculated by a one dimensional analysis. The 85 percent factor was obtained by comparison of several one and two dimensional temperature distribution analyses of the strut leading edge.

5.5.3.2 Structural Analysis

A modified leading edge design was investigated in some detail to determine thermal fatigue performance and structural capability for pressure containment. The configuration that was studied was depicted in Figure 5.5-11. The inside flow channel is 0.030 in. wide x 0.130 in. long with a 0.015 in. radius at each end.

5.5.3.2.1 Thermal Fatigue Analysis

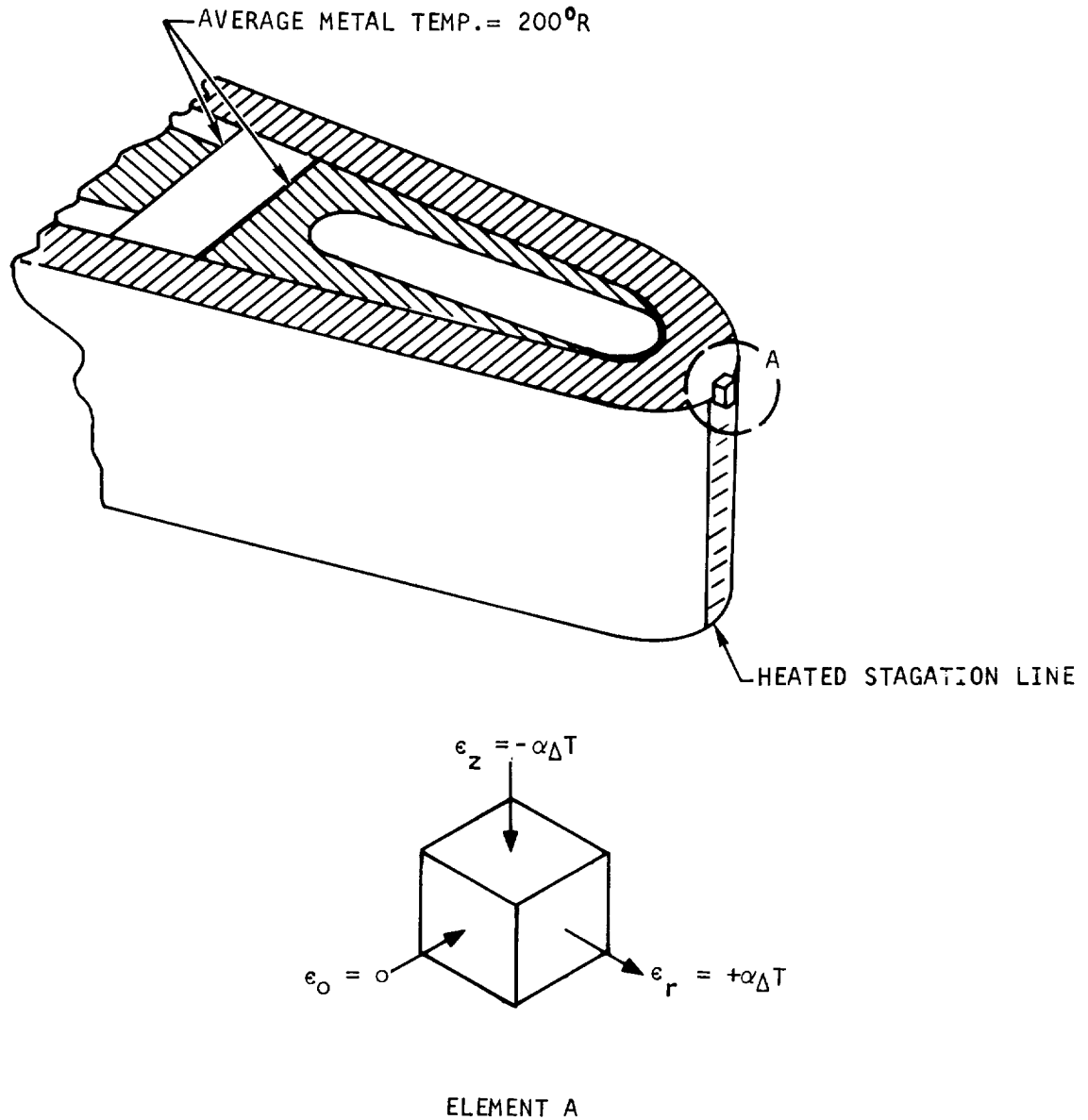
The use of Ni-200 sheet for the leading edge offers the two-fold advantages of higher thermal conductivity and appreciably greater ductility than Hastelloy X over the entire range of temperature that may be experienced. The material is not as strong as Hastelloy X, particularly at higher temperatures, so that some investigation was needed to establish limits in metal temperatures and temperature differences.

The increased thermal conductivity for Ni-200 decreases the wall ΔT at the leading edge stagnation point to approximately 300°R , as compared to a value in excess of 600°R for Hastelloy X. For this reason, the effect of the ΔT through the thickness becomes a relatively small factor for thermally induced plastic strain. The primary determining number is the relative ΔT between the metal temperature at the outside wall stagnation line and the metal temperature for the bulk of the material in the cowl leading edge. For all interests and purposes this is equal to the structural wall temperature in the vicinity of the leading edge, which is in turn equal to the coolant temperature of the main cooling stream. This temperature is approximately 200°R . The maximum stagnation point metal temperature occurs at the hydrogen exhaust ports for the leading edge, and this is shown to be 1770°R in Figure 5.5-11. Hence, the metal ΔT to be used for the thermal fatigue analysis is 1570°R ($1770^{\circ}\text{R} - 200^{\circ}\text{R}$).

The thermal fatigue analysis was carried out for stagnation point temperatures of 1460°R , 1660°R and 1860°R . The small structural element at the stagnation line was assumed to be laterally restrained from dimensional change by the surrounding leading edge structure, which operates at a much lower metal temperature. The differential thermal expansion between the stagnation fiber and the bulk metal temperature was therefore assumed to produce a stress distribution that was consistent with the applied strains. This is shown on Figure 5.5-13. The total axial strain, ϵ_z , is equal to $-\alpha \Delta T$ ($-\alpha_{\text{hot}} T_{\text{hot}} + \alpha_{\text{cold}} T_{\text{cold}}$). The tangential strain is zero, and by virtue of the constant



UNCLASSIFIED



A-32231

Figure 5.5-13. Plastic Strains at Leading Edge Stagnation Point



UNCLASSIFIED

UNCLASSIFIED

volume rule for plastic flow, the radial total strain is equal and opposite to the axial strain. In summary,

$$\epsilon_{\theta t} = 0$$

$$\epsilon_{rt} = + (\alpha_{\text{hot}} T_{\text{hot}} - \alpha_{\text{cold}} T_{\text{cold}})$$

$$\epsilon_{zt} = - (\alpha_{\text{hot}} T_{\text{hot}} - \alpha_{\text{cold}} T_{\text{cold}})$$

The stresses associated with these strain values are

$$\sigma_{\theta} = 0$$

$$\sigma_r = 0.577 \sigma_{\text{yield}}$$

$$\sigma_z = - 1.155 \sigma_{\text{yield}}$$

The elastic strains are

$$\epsilon_{\theta e} = \frac{1}{E} (\sigma_{\theta} - \nu \sigma_z) = + \frac{0.35 \sigma_{\text{yield}}}{E}$$

$$\epsilon_{re} = \frac{1}{E} (\sigma_r - \nu \sigma_z) = - \frac{0.22 \sigma_{\text{yield}}}{E}$$

$$\epsilon_{ze} = \frac{1}{E} (\sigma_z - \nu \sigma_r) = - \frac{0.96 \sigma_{\text{yield}}}{E}$$

The plastic strain quantities in the principal directions become:

$$\epsilon_{\theta p} = \epsilon_{\theta t} - (\epsilon_{\theta e})_{\text{hot}} - (\epsilon_{\theta e})_{\text{cold}}$$

$$\epsilon_{rp} = \epsilon_{rt} - (\epsilon_{re})_{\text{hot}} - (\epsilon_{re})_{\text{cold}}$$

$$\epsilon_{zp} = \epsilon_{zt} - (\epsilon_{ze})_{\text{hot}} - (\epsilon_{ze})_{\text{cold}}$$

Since the elastic contributions will be relatively small as compared to the plastic strains, it will be sufficiently accurate to make the following approximations:

$$\epsilon_{\theta p} = 0$$

$$\epsilon_{rp} = - \epsilon_{zp}$$

$$\epsilon_{zp} = - (\alpha_{\text{hot}} T_{\text{hot}} - \alpha_{\text{cold}} T_{\text{cold}}) + \frac{0.96}{E} \sigma_{\text{yield hot}} + \sigma_{\text{yield cold}}$$



UNCLASSIFIED

The following material properties were used to obtain the elastic components of strain:

Temperature	σ_{yield} , ksi	E, psi	$0.96 \sigma_y / E$
200°R (-260°F)	25	30×10^6	0.00080
1460°R (1000°F)	13.5	27×10^6	0.00048
1660°R (1200°F)	11.0	24×10^6	0.00044
1860°R (1400°F)	8.0	20×10^6	0.00035

The effective plastic strain due to multiaxial deformations is computed as follows:

$$\epsilon_{\text{eff}} = \sqrt{\frac{2}{3}} \left[\left(\epsilon_{\theta\rho} - \epsilon_{r\rho} \right)^2 + \left(\epsilon_{r\rho} - \epsilon_{z\rho} \right)^2 + \left(\epsilon_{z\rho} - \epsilon_{\theta\rho} \right)^2 \right]^{1/2} = \frac{2}{\sqrt{3}} \epsilon_{z\rho}$$

The number of operating cycles to produce plastic failure is

$$N = \left(\frac{C}{\epsilon_{\text{eff}}} \right)^2$$

where the constant, C, is related to material ductility. The minimum reduction of area for Ni - 200 over the temperature range from 200°R to 1800°R is in excess of 60 percent. The value for C based upon this RA is 0.75. In order to allow for the loss in ductility that is encountered in thin sheet, a value of C = 0.375 is used in the following computation of cycle life. Furthermore, a plasticity strain concentration factor of two is also used as a multiplier for ϵ_{eff} in order to allow for localized strain concentration and creep effects.

The cycle life calculations are performed in Table 5.5-1.

TABLE 5.5-1

LOW CYCLE FATIGUE CALCULATIONS

T _{stagnation}		ΔT	α	αΔT	(ε _{ze}) _{hot}	(ε _{ze}) _{cold}	ε _{zp}	ε _{eff}	N
°R	°F								
1460 ⁰	1000 ⁰	1260 ⁰	8.5	0.01070	0.00048	0.00080	0.00948	0.01095	296
1660 ⁰	1200 ⁰	1460 ⁰	8.7	0.01270	0.00043	0.00080	0.01147	0.01325	200
1860 ⁰	1400 ⁰	1660 ⁰	8.9	0.01480	0.00037	0.00080	0.01363	0.01575	142



UNCLASSIFIED

For the 1770°R design temperature, expected cycle life will be 170. Since reduced ductility and localized strain concentrations have been accounted for, this appears to be a satisfactory design.

5.5.3.2.2 Pressure Containment Stresses

Pressure stresses were computed by treating the leading edge structure as a closed, tapered arch. The analysis was performed by using the elastic center method. The leading edge was first cut at the tip, and deflections on the free cantilever caused by the pressure forces were determined. The reactions needed to restore the deflections were then computed. The resulting moment distribution is plotted along the neutral line of the arch structure on Figure 5.5-6. The stresses are primarily due to bending, and these are tabulated along the arch neutral line on Figure 5.5-14.

The metal temperatures at the tip will be 1310°F at the outer skin stagnation line and approximately 1000°F at the inside wall.

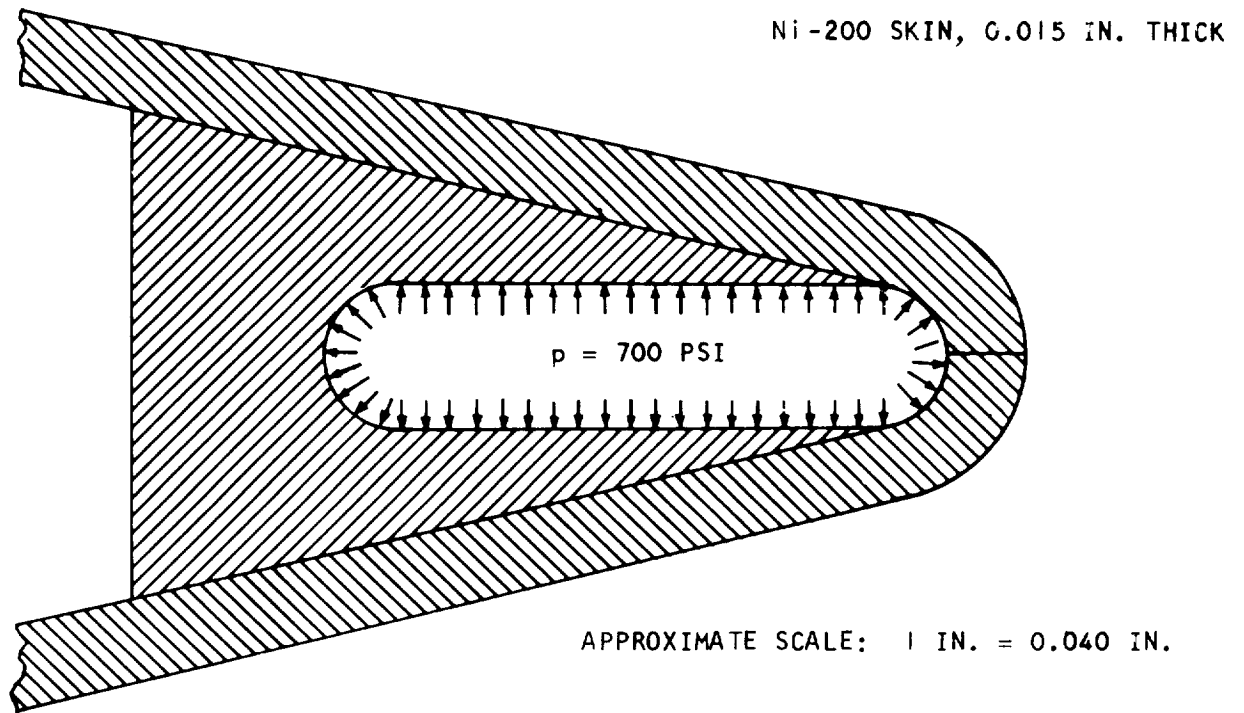
The bending moments and bending stresses at the node points shown in Figure 5.5-14 are presented in Table 5.5-2. Positive values indicate positive bending moments and tensile bending stresses at the inner surface. Bending stresses are at their maximum value at the tip, and they remain quite high over an arc distance of approximately 45 deg from the tip (stagnation line). The peak stress level is 11,800 psi due to bending. There is also a direct tensile stress of 2600 psi acting at the leading edge tip. Therefore, the total stresses are 14,400 psi at the inner fiber and 9200 psi at the outer fiber at the stagnation line. These stress levels are slightly higher than the material yield strength properties at these locations for operation at 1000°F inside temperature and 1310°F outside temperature. These results indicate that a small amount of localized yielding would be produced by internal pressure.

Sustained pressure loading will also cause localized creep at the tip. This will in turn cause stress relaxation at the tip with a transferral of load to the remaining structure. In order to assess the potential effects of creep relaxation, a second analysis was carried out, in which it was assumed that a plastic hinge is formed at the tip. The redistribution of moments and stresses for this conditions are also shown in Table 5.5-2. Tip loading is decreased to 32.3 lb, and tip tensile stress is therefore reduced to 2150 psi. Bending stresses in the heated zone drop to well below the material yield strength properties near the tip. Stresses are increased away from the tip to a peak value of -12,400 psi at node point 6 (per Figure 5.5-14). Metal temperature is greatly reduced at this location to 200°F or less, at which the yield strength exceeds 20,000 psi.

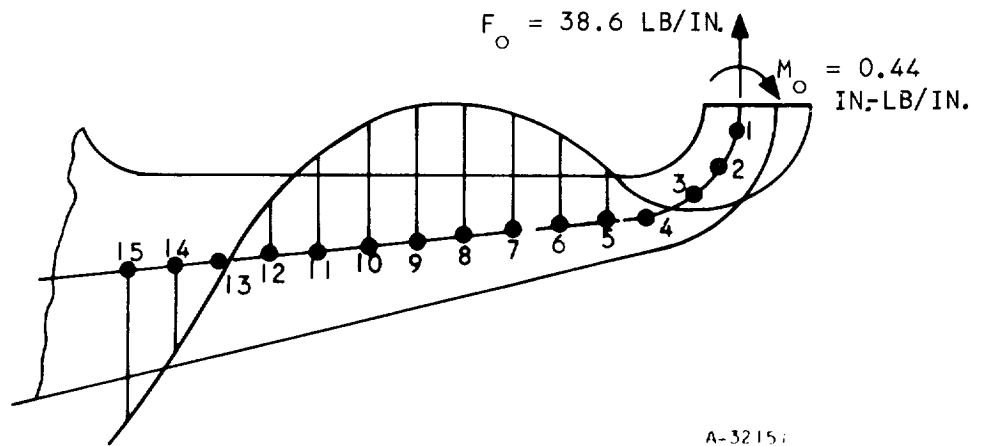
It is therefore concluded that even with complete relaxation of the bending moment at the leading edge stagnation line, the change in leading edge configuration will be very small. Also, stress relaxation at the stagnation line does not tend to produce yield hinges elsewhere in the structure. These results indicate that this leading edge design should operate successfully.



UNCLASSIFIED



a. Leading Edge Configuration



b. Moment Distribution along Neutral Line

Figure 5.5-14. Leading Edge Pressure Loading and Moment Distribution



UNCLASSIFIED

UNCLASSIFIED

TABLE 5.5-2

LEADING EDGE PRESSURE STRESSES

Node Point	Built in at Tip		Yield Hinge at Tip	
	Bending Moment in.-lb/in.	Stress* psi	Bending Moment in.-lb/in.	Stress* psi
0	+0.440	+11,800	0	0
1	+0.420	+11,200	-0.0117	-300
2	+0.330	+8,800	-0.0800	-2,130
3	+0.160	+4,270	-0.217	-5,800
4	-0.080	-2,140	-0.392	-11,400
5	-0.310	-6,240	-0.577	-11,600
6	-0.520	-9,110	-0.710	-12,400
7	-0.630	-7,800	-0.780	-9,700
8	-0.700	-7,000	-0.775	-7,750
9	-0.690	-5,700	-0.700	-5,710
10	-0.620	-4,430	-0.560	-4,000
11	-0.460	-2,700	-0.340	-2,000
12	-0.240	-1,250	-0.060	-310
13	+0.060	+440	+0.300	+2,200
14	+0.420	+1,660	+0.720	+2,850
15	+0.840	+2,730	+1.240	+4,020



UNCLASSIFIED

UNCLASSIFIED

5.6 MISSION COOLANT REQUIREMENTS

Analyses were performed to determine minimum hydrogen coolant requirements for ascent and descent to and from a Mach 8 (flight and engine local) 88,000-ft flight profile. These results established requirements for control of flow in each of the four flow routes as a function of time during mission. Ascent and descent coolant requirements for three methods of flow control are presented in Figure 5.6-1.

The thermodynamic minimum coolant weight for ascent and descent is 28.2 lb and is based on a 100°R inlet and 1600°R outlet coolant temperature for the calculated heat loads on each flow route. The thermodynamic minimum coolant consumption can be further reduced to 24.3 lb if the external surfaces of the spike and outer body leading edge flow routes are coated with Rockide Z (zirconium oxide). These coolant expenditures during non-lit ascent and descent can be approached if the flow rate in each of the flow routes is individually modulated for a 1600°R outlet temperature. If the coolant flow in the four routes is established by fixed geometry orifices selected to give best coolant usage during combustion, the ascent and descent coolant consumption is 73 lb. However, the above two non-lit coolant consumptions do not provide for adequate cooling of the spike and outer body leading edge designs presented in Reference 5.5-1. The time dependent flow rates associated with the non-lit consumptions were calculated by matching the hot gas heat load to the heat absorbed by the coolant to give a 1600°R outlet temperature.

In two routes, outlet temperature measurement does not reflect localized metal surface hot spots in the stagnation regions. During ascent and descent, the spike and outer body leading edge heat fluxes are a higher percentage of their design point combustion period levels than are the overall heat loads on each flow route. If a thermocouple mounted in the outer body leading edge regulated coolant to all flow routes with fixed geometry orifices such that the outer body leading edge temperature was maintained at 1500°R, the ascent and descent coolant expenditure would be 150 lb. Table 5.6-1 summarizes flow requirements for the various conditions noted above.

Alternate flow routing systems were investigated as a means of improving utilization of the hydrogen thermal capacity and, thereby, reducing coolant consumption. The maximum reduction obtainable by this means was about 11 percent. All considered flow routings introduced unacceptable strut structural temperature differences and/or excessive coolant pressure drops. Manipulation of flow routing, therefore, was abandoned because significant improvements were not offered.

There are several factors that will further increase the ascent and descent coolant consumption above the values reported herein. These factors, which will be further investigated, are:

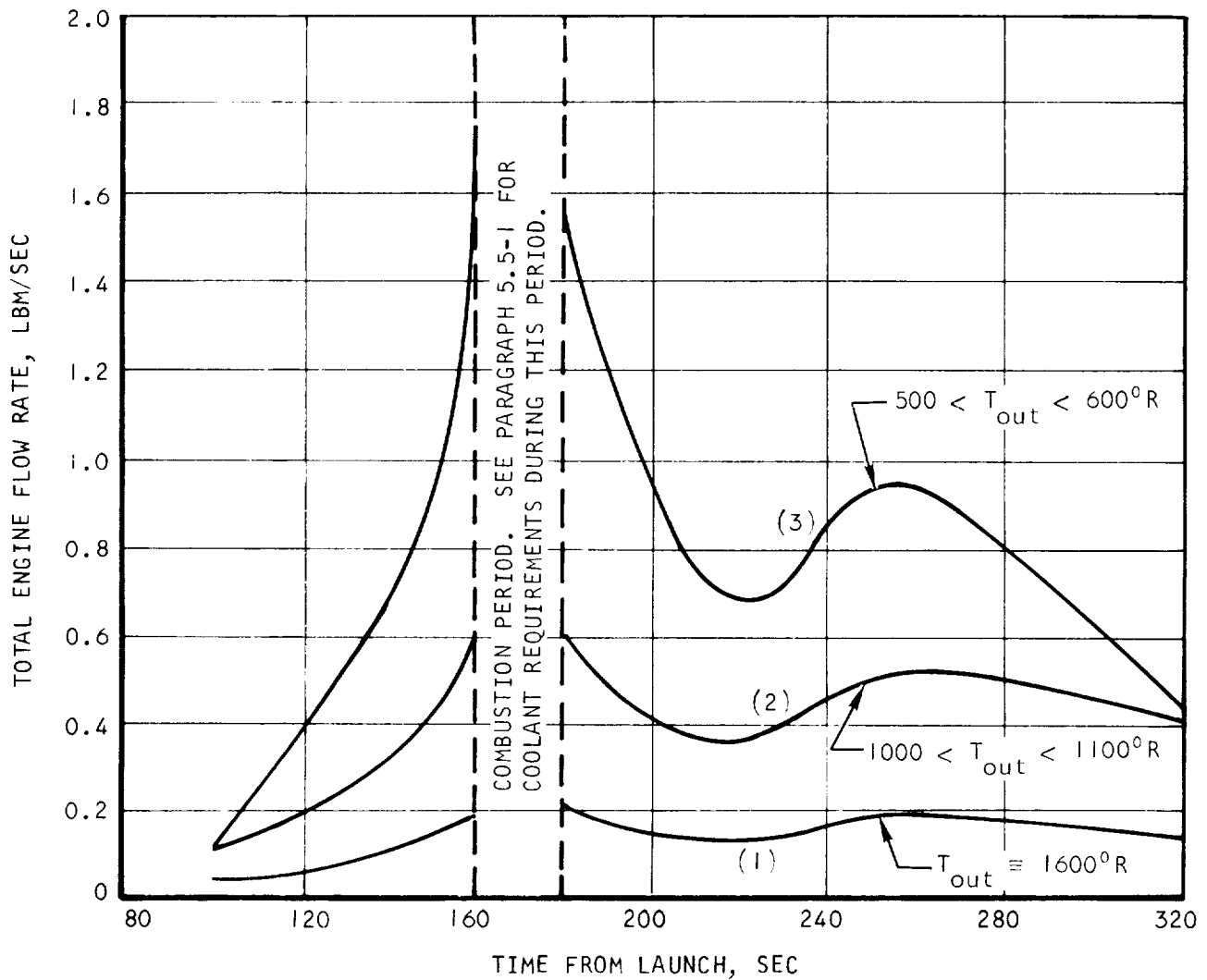


CURVE IDENTIFICATION

- (1) THERMODYNAMIC MINIMUM COOLANT RATE FOR 1600°R COOLANT OUTLET TEMPERATURE IN ALL FLOW ROUTES. ASCENT AND DESCENT COOLANT CONSUMPTION IS 28.2 LB.
- (2) COOLANT FLOW RATE FOR FIXED ORIFICE FLOW CONTROL. ORIFICES SIZED FOR REQUIRED FLOW SPLIT DURING COMBUSTION. SPIKE COOLANT OUTLET TEMPERATURE OF 1300°R CONTROLLING. ASCENT AND DESCENT COOLANT CONSUMPTION IS 73 LB.
- (3) OUTER BODY LEADING EDGE TIP TEMPERATURE OF 1500°R CONTROLLING WITH FIXED ORIFICE FLOW AS IN (2). ASCENT AND DESCENT COOLANT CONSUMPTION IS 150 LB.

NOTE:

COOLANT RATES CORRESPOND TO HEAT RATES DETERMINED FROM FLIGHT PROFILE SHOWN IN FIGURE 5.6-2.



A-52241

Figure 5.6-1. Ascent and Descent Coolant Requirements



UNCLASSIFIED

TABLE 5.6-1

SUMMARY OF ASCENT AND DESCENT COOLANT REQUIREMENTS

Case 1: No Insulation on Engine Surfaces

Thermodynamic minimum consumption	28.2
Increase in consumption due to 1300°R spike outlet coolant temperature	3.2
Increase due to separate cooling of outer body leading edge tip	<u>6.0</u>
Total	37.4 lb

Case 2: Rockide Z Insulation on Spike

Thermodynamic minimum consumption	24.3
Increase in consumption due to 1300°R spike outlet coolant temperature	2.6
Increase due to separate cooling of outer body leading edge tip	<u>6.0</u>
Total	32.9 lb

Case 3: Fixed Orifice Flow Control 73.0 lb

Case 4: Leading Edge Tip Temperature of 1500°R with Fixed Orifice Flow Control 150.0 lb



UNCLASSIFIED

1. Effect of Engine Envelopment in X-15 Flow Field--The analytical results reported herein correspond to flight conditions where the engine is not enveloped in the X-15 flow field. Steady state design conditions at the Mach 8 (Mach 6.5 local), 88,000 ft condition results in higher heat loads than at Mach 8 local conditions. Heat loads and coolant requirements will also increase for ascent and descent.
2. Outer Body Leading Edge Cooling--Cooling design revision of leading edges will provide for small cross section area coolant passages in parallel with the four major flow routes and was discussed in Paragraph 5.5.3. The coolant required for these passages was not included in this analysis, but it is estimated to be a maximum of 20 percent of the total ascent-descent coolant consumption, or an increase of about 6 lb in the total hydrogen required. A six-lb increase is associated with connection of the leading edge passages in parallel with the spike flow route as discussed in Paragraph 5.6.2. Turbopump bearing coolant may be used for leading edge cooling at no increase in required coolant, if bearing coolant discharge pressure is high enough to force bearing coolant through the leading edge.
3. Temperature Sensing Versus Programmed Coolant Control--The results reported herein indicate coolant consumption based on required hot gas heat load absorption by the coolant. This assumes that all valves have instantaneous response to a near step change in hot gas heat load, when the spike is unlatched and combustion starts. The increase in required coolant from spike latched to spike open with combustion at the design point could be as high as sixfold. It may be necessary to preprogram the engine coolant above that required for adequate cooling just prior to combustion so that transitional effects in the coolant control system from spike latched to spike open with combustion conditions will be reduced. Preprogramming coolant rate will have the effect of adding coolant consumption at the start and finish of the combustion period.

Heat loads on all engine surfaces during ascent and descent were calculated using the modified Mach number--altitude history presented in Figure 5.6-2. The solid line curves in Figure 5.6-2 were provided by North American Rockwell and reported in NAR Report No. NA-67-401-2, Figure 17. The dashed line curves are modifications made by AiResearch to include 20 seconds of constant Mach (8) and constant altitude (88,000 ft) for combustion. The calculated heat loads are for approaching free stream conditions immediately upstream of the spike bow shock wave and do not take into account engine envelopment in the X-15 flow field. Heat loads on spike and internal outer body surfaces exposed to the free stream were calculated for several points on the flight profile, using axial averaged hot gas conditions adjacent to these surfaces. Results of using this method for the spike surface at Mach 8, 88,000 ft agree within 3 percent with the corresponding surface heat load determined from computer analysis in Reference 5.5-1.



UNCLASSIFIED

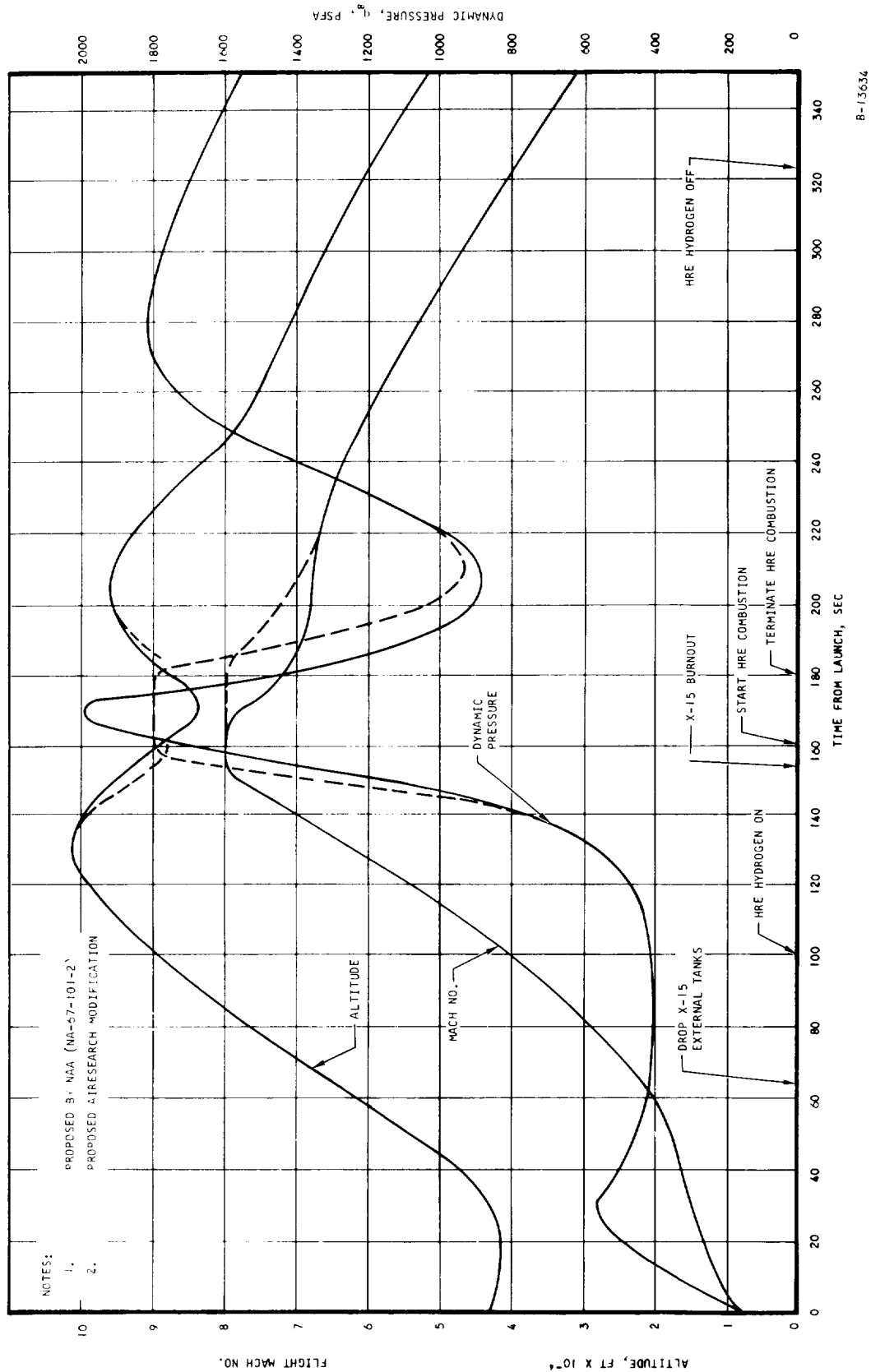


Figure 5.6-2. Proposed X-15A-2 Trajectory for HRE Mission to Mach 8



AIRESEARCH MANUFACTURING DIVISION
Los Angeles, California

67-2833
Page 5-111

UNCLASSIFIED

UNCLASSIFIED

Heat loads on internal surfaces of the spike and outer body leading edge were calculated from estimated hot gas leak flow rates (1 lbm/sec at Mach 8, 88,000 ft) through the 0.060 inch gap between the spike and leading edge when the spike is in the closed (extended) position. At Mach 8, 88,000 ft with spike closed, the internal leak flow heat load is 33 percent of the total spike heat load and 73 percent of the total leading edge heat load.

A breakdown of loads on engine surfaces with the spike in the closed position at Mach 8, 88,000 ft alt is presented in Figure 5.6-3. Heat loads in parentheses indicate the corresponding heat load when the spike is open with design point combustion and, also, do not reflect engine envelopment in the X-15 flow field.

The sequence of events for the mission to Mach 8 is indicated in Figure 5.6-2. Assumptions are as follows: during flight, hydrogen will flow through engine surface coolant passages when the free stream Mach number is 4 and greater and when the free stream total temperature is 1140°F (1600°R) and greater. A temperature of 1600°R is the thermal limit of the structure. For the results described herein, it was assumed that coolant rate increases with increasing Mach number from the initial value at Mach 4. When Mach 8, 88,000 ft is reached, the spike is instantaneously unlatched to the required position and design point combustion commences. Correspondingly, the coolant flow rate instantaneously increases from the value at Mach 8 with the spike closed to the design point value with the spike open and combustion. After the 20-sec combustion period, the spike is instantaneously closed and coolant rate decreases to the Mach 8 precombustion value. Coolant rate decreases with decreasing Mach number until Mach 4 is reached, at which time the coolant is turned off.

5.6.1 Outlet Temperature Control

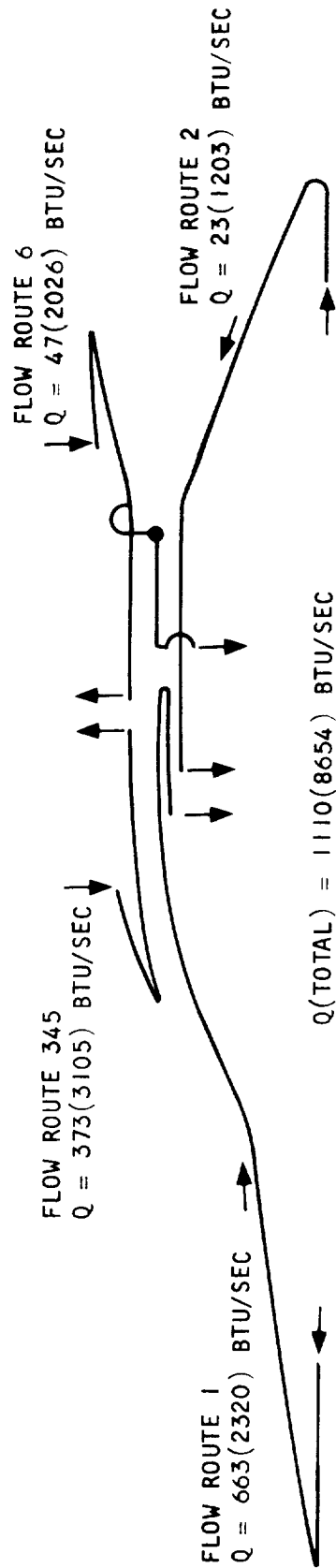
Coolant flow rate scheduling to flow route passages can be controlled by either maintaining the maximum allowable structural temperature at 1600°R or the maximum allowable skin surface temperature at 2060°R, or both. When only one thermal limit is maintained, it must be verified that the other thermal limit is never exceeded. This analysis is concerned with maintaining the maximum structural temperature at 1600°R. It is assumed that the maximum allowable surface skin temperature is never exceeded during flight.

The structural temperature at any location in coolant circuit is very nearly equal to the coolant temperature at that location. The thermal effectiveness of the fins in the coolant jackets is so low that the ΔT from inside skin to structural wall is effectively equal to the ΔT from inside skin to coolant. The outlet coolant temperature is nearly a direct measure of the maximum structural temperature in a flow route. In turn, the heat load on metal surfaces of a flow route is a measure of the coolant flow rate in that flow route to maintain the outlet coolant temperature (and maximum structural temperature) at 1600°R.

A hydrogen consumption of 28.2 pounds can be approached if four separate modulating valves regulate flow in each of the four flow routes so that an outlet coolant temperature of 1600°R is maintained. A 1600°R outlet coolant



UNCLASSIFIED



A-32201

NOTES:

1. VALUES NOT IN PARENTHESES ARE FOR SPIKE LATCHED CONDITIONS.
2. VALUES IN PARENTHESES ARE FOR SPIKE UNLATCHED COMBUSTION CONDITIONS.

Figure 5.6-3. Comparison of Engine Flow Route Head Loads,
 $M_L = 8$; 88,000 ft



AIRESEARCH MANUFACTURING DIVISION
Los Angeles, California

UNCLASSIFIED

UNCLASSIFIED

temperature can be achieved in all but the spike flow route. In the double sandwich plate-fin section of the aft spike, coolant is heated to 1600°R at the end of the passage adjacent to the hot gas, but is cooled below 1600°R after making a 180 deg turn and flowing through the inner passage of the double sandwich section. The coolant outlet temperature of the spike for design combustion conditions is 1300°R. During non-lit, spike closed conditions, the outlet coolant temperature can be slightly higher than 1300°R, but to have a single value of spike outlet temperature, a 1300°R spike coolant outlet appears desirable for all flight phases. For 1600°R outlet coolant temperature in three of the four routes and 1300°R in the spike route, the hydrogen consumption for non-lit, spike closed conditions is 31.4 pounds.

Application of Rockide Z (zirconium oxide) to external surfaces of the spike and outer body leading edge flow routes (0.030 inch thick on the spike fore body, 0.015 inch on the spike aft body, and 0.020 inch on the outer body) can reduce the uninsulated thermodynamic minimum for ascent and descent from 28.2 lb to 24.3 lb. Rockide Z insulation can reduce hot gas heat absorption in metal surfaces by (1) creating an additional thermal conduction resistance in the heat path from hot gas to coolant and (2) dissipating hot gas heat input by radiation because Rockide Z surface temperatures of up to 3500°R appear feasible. The reduction in coolant consumption on internal surface during combustion is much greater than on external surfaces because internal combustion heat fluxes are much greater. The net combustion coolant rate could be 50 percent lower than for uninsulated surfaces because of the large ΔT in Rockide Z with metal surfaces maintained at 2060°R maximum. On external surfaces, the heat flux is lower, the ΔT through Rockide Z is correspondingly lower, and the net reduction in coolant consumption is only 15 percent (28.2 to 24.3 lb).

Fixed geometry orifices in all but the pressure drop controlling route was investigated as a means of coolant flow control. This method eliminates the use of modulating valves at the route inlets, but results in a considerable increase in hydrogen consumption during non-lit, spike closed conditions. Outlet temperature sensors adjust the flow rate in all four routes, so that the maximum allowable coolant outlet temperature in any route is never exceeded. The orifice sizes would be selected to give best coolant usage during design combustion conditions. Under these conditions, the coolant consumption for non-lit spike closed conditions is 73 pounds. This more than twofold increase in coolant consumption over individual flow control results from the relationship of the heat load on each flow route during non-lit, spike-closed conditions and during combustion at Mach 8, 88,000 ft. During design combustion conditions, the inner shell, outer shell, trailing edge, and nozzle, receive 37 percent of the total heat load (Reference 5.5-1). During non-lit, spike closed conditions, these surfaces receive less than 10 percent of the total heat load. Because fixed orifice flow regulation will give approximately the same flow split for all heating conditions, the inner shell, outer shell, trailing edge, and nozzle will be overcooled during non-lit, spike closed conditions. In fact, the coolant in the highly heated routes will be more dense and a higher percentage of the total coolant will flow through these routes during non-lit conditions than during combustion.



UNCLASSIFIED

UNCLASSIFIED

5.6.2 Hot Spot Temperature Control

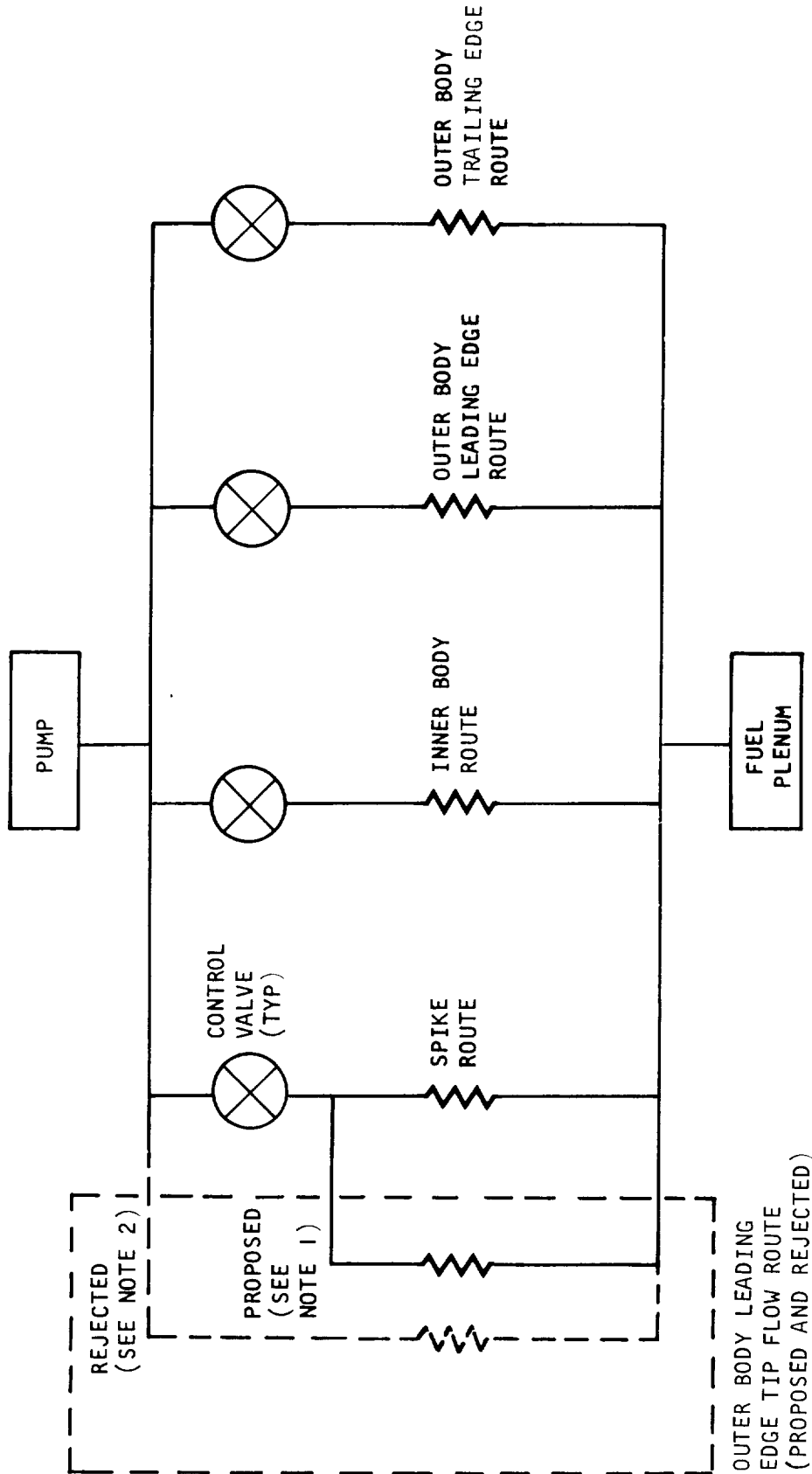
Results of the non-lit, spike closed coolant consumption analysis, when coolant flow rate is controlled by stagnation region requirements, show that localized high heat fluxes exist during engine non-lit on the leading edges of the spike and outer body. During non-lit, spike closed conditions at Mach 8, 88,000 ft, the coolant demand is 0.57 lb/sec (Case 2 in Figure 5.6-1) for fixed orifice flow control and 0.22 lb/sec (Case 1) for four-valve flow control. However, the spike and outer body leading edges receive approximately the same heat flux regardless of whether the spike is open with combustion or closed. With an engine total coolant flow rate of either 0.57 lb/sec or 0.22 lb/sec, the outer body leading edge temperatures and temperature differences will be above the structural limits, as discussed in Paragraph 5.5.3.

The ascent and descent coolant consumption required to maintain outer body leading edge temperatures at acceptable levels was determined for the fixed orifice flow control method. It was assumed that the outer body leading edge temperature was maintained at 1500°R. The resulting ascent and descent coolant consumption is 150 pounds. This coolant consumption is higher than determined in the preceeding analysis because the consumption reflects a hydrogen conductance at the outer body leading edge that was increased by increasing leading edge passage flow rate and thereby increasing flow rate in all engine flow routes. Hydrogen conductance at this leading edge could also be increased by decreasing the hydrogen passage height at the outer body leading edge so the leading edge would be adequately cooled during ascent and descent. However, during combustion the increased flow rate required in the leading edge flow route would result in a large pressure drop in this reduced clearance region. The coolant flow routing schematic for outer body leading edge cooling (based on the revised design discussed in Paragraph 5.5.3) in relation to the four major flow routes is shown in Figure 5.6-4. The solid line leading edge tip schematic is presently considered for design because this method can reduce the leading edge coolant consumption over the dashed line schematic by as much as 45 percent. The dashed line route schematic will deliver a constant coolant rate to the leading edge throughout the entire period that coolant flows through the engine. The flow rate required to cool the leading edge tip adequately during combustion is 0.05 lb/sec (dashed line route), so that coolant consumption in this route is 11 lb. The solid line route schematic is regulated by the spike control valve. The fixed flow split between spike and leading edge tip can be set so that the tip will be adequately cooled during the entire flight. Thus, will require that the tip be overcooled during combustion. The estimated tip flow route consumption for the solid line route schematic is 6 lb plus the flow rate overcooling the tip during combustion.

The spike leading edge tip design will be modified to a minor extent. The hole diameter that controls coolant flow to the spike tip has been adjusted to increase the coolant rate and therefore the coolant conductance, and thus keep the spike tip temperature to an acceptable level throughout the entire mission. There is no increase in total coolant consumption due to an increase in coolant supply to the spike tip.



UNCLASSIFIED



A-32242

NOTES:

1. FLOW ROUTING PROPOSED FOR DESIGN. ASCENT-DESCENT COOLANT CONSUMPTION IS 6 L.B., PLUS APPROXIMATELY 1.5 LB DURING COMBUSTION.
2. FLOW ROUTING REJECTED. TOTAL FLIGHT COOLANT CONSUMPTION IS 11 L.B AT A CONSTANT FLOW RATE OF 0.050 LBM/SEC.

Figure 5.6-4. Revised Route Schematic



AIRSEARCH MANUFACTURING DIVISION
Los Angeles, California

UNCLASSIFIED

UNCLASSIFIED

5.6.3 Alternate Flow Routing

In Paragraph 5.6.1 it was indicated that the spike coolant outlet temperature is 1300°R instead of the maximum allowable of 1600°R during combustion, which results in as much as an 11 percent increase in coolant consumption (28.2 to 31.4 lb) during ascent and descent, plus a similar percentage increase during combustion. An investigation aimed at utilizing this 300°R of previously unused coolant thermal capacitance and reducing the number of coolant control valves was performed.

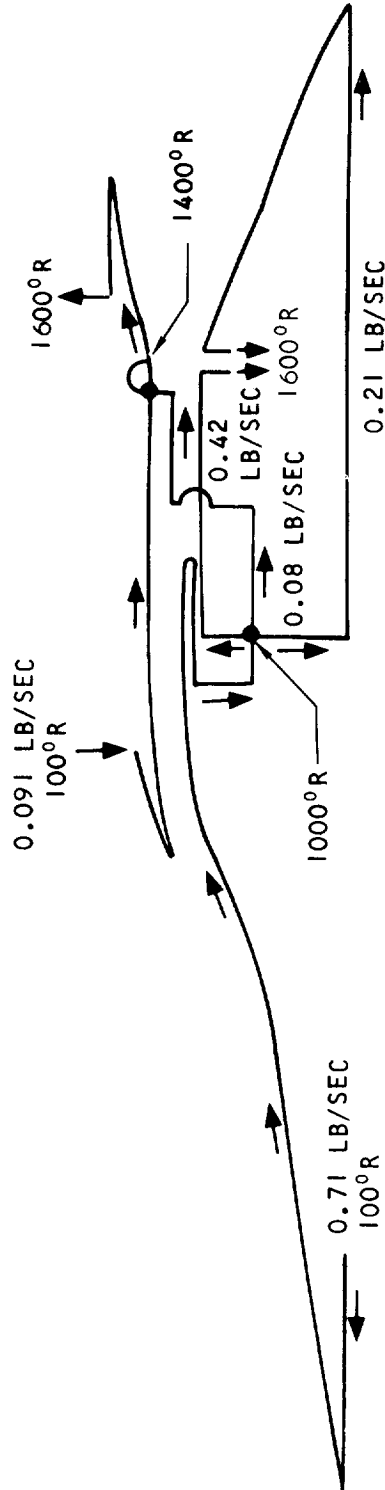
Several flow route schematics were analyzed, but were rejected because of one or more disadvantages relative to the present flow routing. The flow routings investigated and the reasons for rejection are summarized below:

- (1) Four Flow Route Systems--The present design has four major flow routes. Systems investigated in this category had small modifications from the present design and offered no advantage over the present design or introduced unacceptable structural temperature differences across the strut. Strut temperature differences are caused by unequal coolant temperatures in the inner and outer shell adjacent to the strut.
- (2) Three Flow Route Systems--The three flow route systems that were investigated characteristically had an outer body leading edge flow route that extended to the aft end of the strut or the trailing edge of the outer body. Also the coolant at spike outlet was routed into the inner shell and exited at the bolted flange/manifold. These systems were rejected because of unacceptable structural temperature difference across the strut and larger coolant pressure drop than the two flow route systems discussed below.
- (3) Two Flow Route Systems--The two flow route systems that were investigated have acceptable structural temperature difference across the strut and gave lower coolant pressure drop than the three flow route systems. Though lower than the three flow route systems pressure drop, the pressure drop in the best two route system exceeds turbopump capabilities. The structural temperature of the bolted flange/manifold for the best two route system is 1600°R as compared with 600°R for the present flow routing design.

The best two route system considered is presented in schematic form in Figure 5.6-5 (the number of routes as used herein is equal to the number of 100°R coolant inlets). The coolant flow rates and temperatures indicated in Figure 5.6-5 correspond to the combustion heating loads at Mach 8, 88,000 ft. The spike and outer body leading edge structures will operate colder than the present design, but the aft structures of the engine will operate hotter. The maximum strut structural temperature difference is approximately 400°R as compared with 250°R for the present design, and the temperature of the bolted flange/manifold is 1600°R . There is a total coolant rate reduction from 1.72 lb/sec to 1.62 lb/sec or a 6.4 percent decrease. During ascent and descent, the coolant consumption would be 30 lb, which will not provide



UNCLASSIFIED



NOTES:

1. COOLANT TEMPERATURES AND FLOW RATES CORRESPOND TO $M_L = 8$, 88,000 FT COMBUSTION CONDITIONS.
2. TOTAL FLOW RATE = 1.62 LB/SEC.
3. A MINIMUM INLET COOLANT PRESSURE OF 1000 PSIA IS REQUIRED TO OBTAIN A PRESSURE OF 400 PSIA AT THE FUEL PLENUM.

A-32200

Figure 5.6-5. Two-Flow Route Alternate Schematic



AIRESEARCH MANUFACTURING DIVISION
Los Angeles, California

UNCLASSIFIED

UNCLASSIFIED

adequate cooling for the outer body leading edge with leading edge modifications discussed in Paragraph 5.5.3. The inlet coolant pressure required to provide 400 psia hydrogen to the fuel plenum was estimated at 965 psia minimum. The estimate considered only pressure drops in the plate-fin jackets and neglected line losses. When line losses are considered, the required inlet pressure is over 1000 psia, which is above the current pump design outlet pressure of 800 psia.

5.7 ABLATIVELY COOLED COWL

The HRE outer shell is covered with an ablatively cooled cowl. It is planned to attach this cowl to the engine mounting structure (wishbone) directly and transmit all aerodynamic and inertia loads directly to the mounting structure.

The available envelope allows very little space for this cowl. Several alternative designs were conceived and investigated in order to develop a workable solution for the design of the cowl. The following configurations were studied:

- (1) 0.06 in. thick Hastelloy X shell with no reinforcing
- (2) 0.06 in. thick Hastelloy X shell with two stiffener rings. These rings were to be attached to the mounting structure
- (3) Same as 2 with three rings
- (4) Beaded shell of optimum thickness with two stiffening rings
- (5) Same as 4 with three rings
- (6) Double walled shell with corrugated core

These configurations are shown on Figure 5.7-1.

5.7.1 Applied Loads

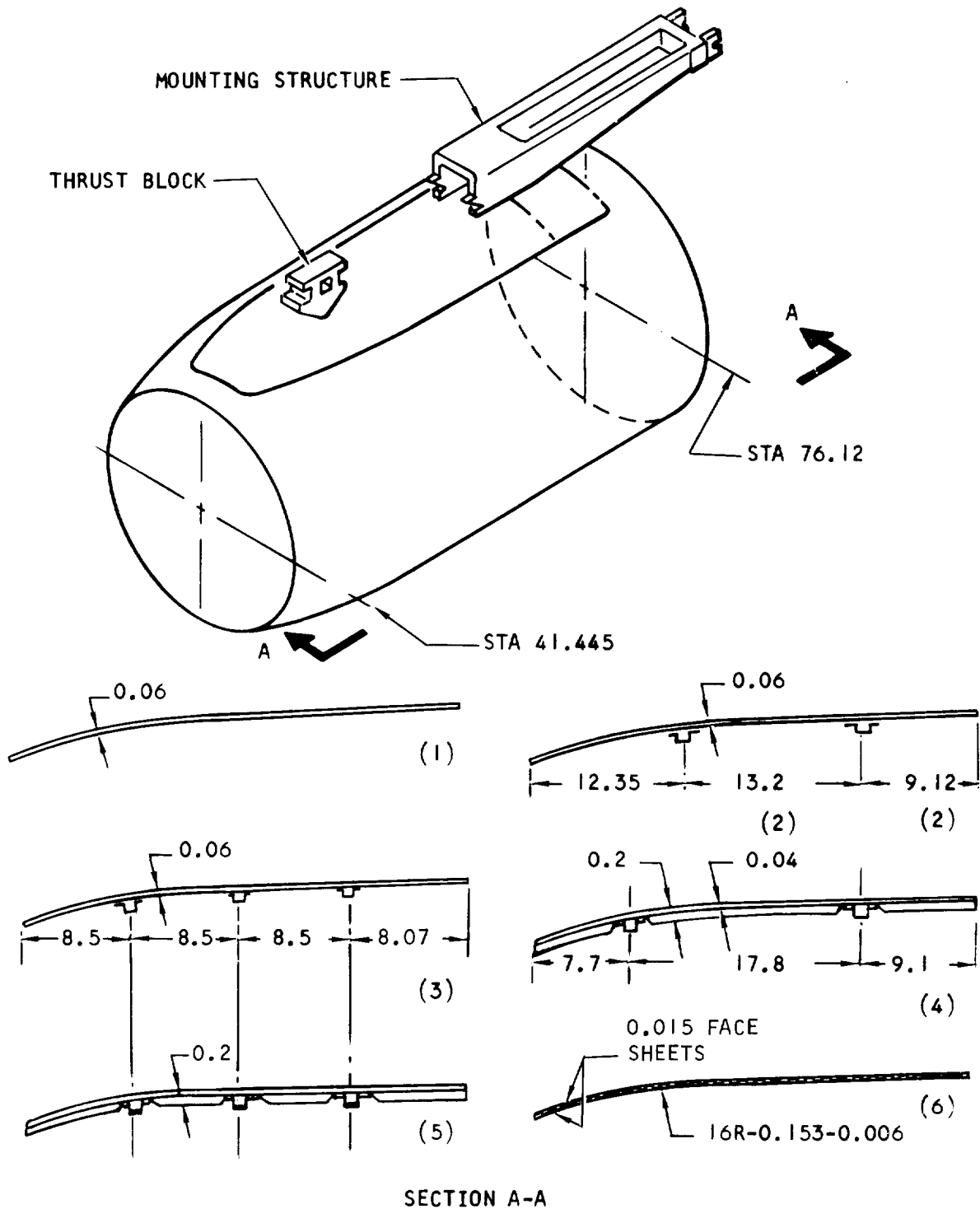
The aerodynamic loads governing the desing of the cowl occur with the spike fully extended. Table 5.7-1 shows the three most significant load conditions.

A shock wave starting from the leading edge of the X-15 lower vertical stabilizer (pylon) creates a high pressure ridge on the top of the cowl. Pressure distribution due to this shock wave is shown on Figure 5.7-2. It is assumed that the temperature of the cowl will not exceed 600°F. For the purpose of computer analysis the aerodynamic loads were simulated as the sum of a uniformly distributed 2.0 psi external pressure and a cosine series pressure of 1.0 psi intensity.

The weight of Configuration 1 is 64.8 lb with the Martin Company MA-25S ablative coating, while the weight of the most feasible alternate (Configuration 4) is 65.45 lb.



UNCLASSIFIED



A-32202

Figure 5.7-1. Cowl Design Configurations



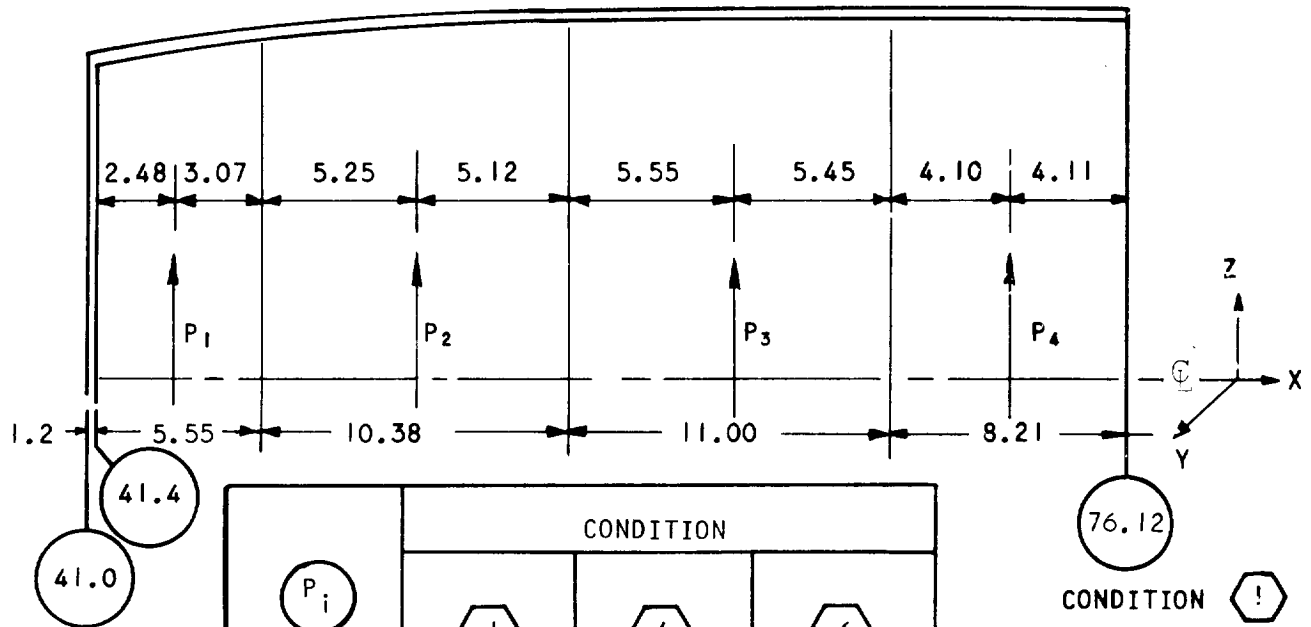
AIRESEARCH MANUFACTURING DIVISION
Los Angeles, California

UNCLASSIFIED

67-2833
Page 5-120

UNCLASSIFIED

TABLE 5.7-1. COWL AERODYNAMIC LOADS



		CONDITION		
		1	4	6
P_1	P_{1x}	365	688	283
	P_{1y}	134	171	249
	P_{1z}	486	258	106
P_2	P_{2x}	45	83	34
	P_{2y}	113	145	211
	P_{2z}	396	218	89
P_3	P_{3x}	78	146	60
	P_{3y}	82	104	150
	P_{3z}	284	144	59
P_4	P_{4x}	0	0	0
	P_{4y}	9	18	35
	P_{4z}	118	8	7

CONDITION !

$M_\infty = 8.0$, $q_\infty = 2000$ PSFA
 $M_L = 8.0$, $q_L = 2000$ PSFA
 $\alpha_\infty = 10.4$ DEG, $\beta_\infty = 2.9$ DEG
 $\alpha_L = 10.4$ DEG, $\beta_L = 2.9$ DEG

CONDITION 4

$M_\infty = 8.0$, $q_\infty = 2000$ PSFA
 $M_L = 6.5$, $q_L = 3600$ PSFA
 $\alpha_\infty = 10.4$ DEG, $\beta_\infty = 2$ DEG
 $\alpha_L = 3$ DEG, $\beta_L = 2$ DEG

CONDITION 6

$M_\infty = 8.0$, $q_\infty = 835$ PSFA
 $M_L = 6.5$, $q_L = 1500$ PSFA
 $\alpha_\infty = 10$ DEG, $\beta_\infty = 7$ DEG
 $\alpha_L = 3$ DEG, $\beta_L = 7$ DEG

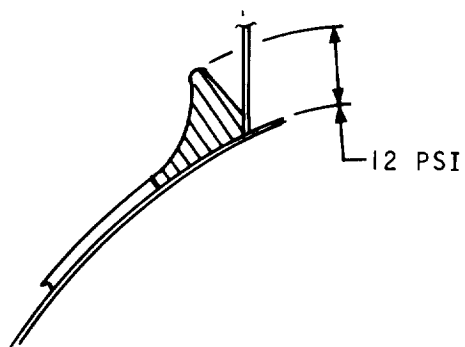
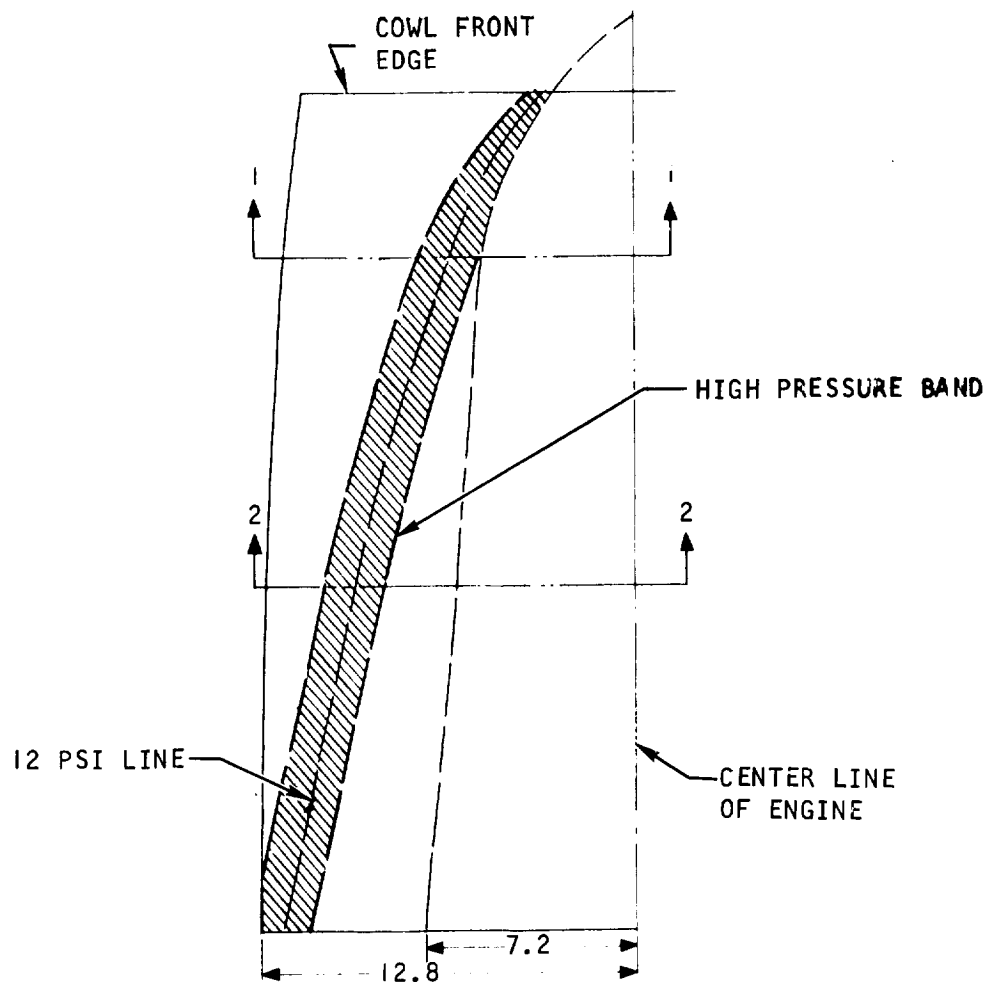
A-32173



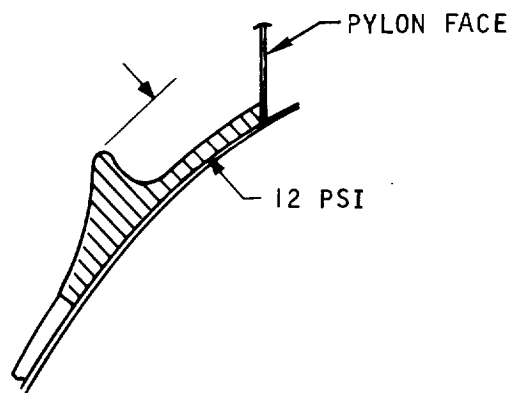
AIRESEARCH MANUFACTURING DIVISION
Los Angeles, California

UNCLASSIFIED

UNCLASSIFIED



PRESSURE DISTRIBUTION 1-1



PRESSURE DISTRIBUTION 2-2

A-32194

Figure 5.7-2. High Pressure Band Acting on Cowl, Mach 8



AIRESEARCH MANUFACTURING DIVISION
Los Angeles, California

UNCLASSIFIED

67-2833
Page 5-122

UNCLASSIFIED

5.7.2 Structural Design

The stress analysis of the different cowl design configurations shown on Figure 5.7-1 revealed that the selection of the proper design configuration is primarily governed by deflection limitations.

Calculations indicate that the Configuration 1 is totally unacceptable. The magnitude of the deformations is such that the shell would rest on the outside shell ($\Delta > 5.0$ in.). Critical buckling pressure is 0.75 psi, one third of the actual pressure.

Configuration 2, although an improvement over 1, will deform excessively at the aft end of the straight cylinder section. Also, the location of the front stiffening indicated on Section A-A of Figure 5.7-1 cannot be used due to interference with the outer body piping. This ring must be located substantially forward (to a position 7.7 in. from the front edge of the cowl), and once this is done, deflections of the shell between the stiffening rings become excessive. In conclusion, Configuration 2 cannot be used.

The three-ring configurations, 3 and 5, would be structurally advantageous. However, accommodation of the middle ring would require large changes in cowl contour and lead to a reduced ground clearances. These configurations, therefore, are considered unusable.

Configuration 4 is the recommended geometry. Due to the length of the span between the two stiffening rings, the shell must be beaded to prevent excessive shell deflections. The details of the beads and the stiffening rings are shown on Figure 5.7-3, Sections B-B and C-C. Flange rings, as shown on Section D-D, are used at the front and aft end of the cowl. These are needed to prevent local buckling of the cowl shell from the front edge to the front stiffening ring and from the aft stiffening ring to the aft edge of the cowl.

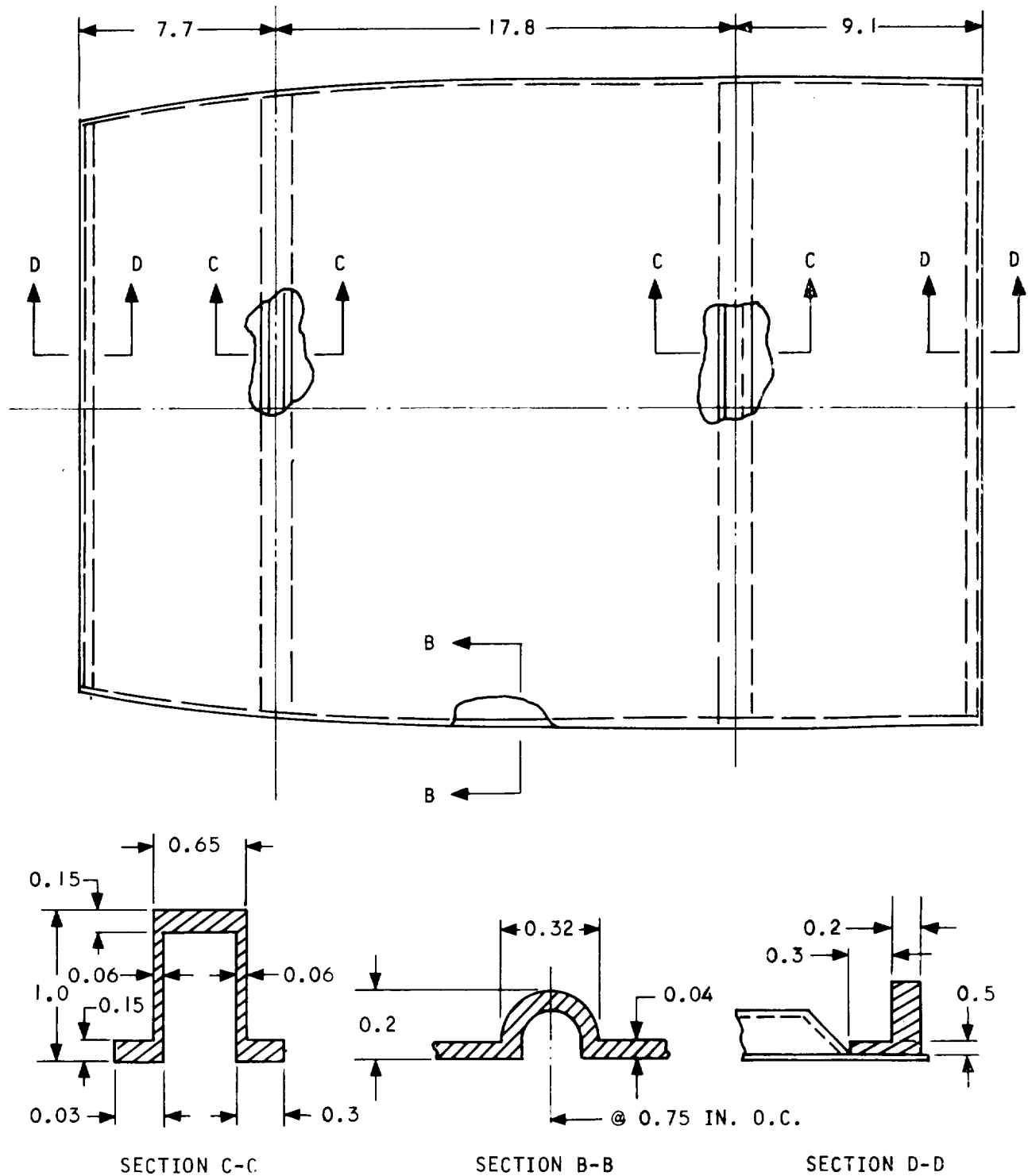
The maximum deflection of the beaded panels between the rings will be 0.1 in. The load on the stiffening ring is shown on Figure 5.7-4 together with the moment diagram. The design of the ring is governed by the deflection criteria and the stresses are quite low ($\sigma_{\text{bending}} = 7400$ psi, $\sigma_{\text{axial}} = 1600$ psi). All of these values were computed using elastic properties of the materials at 600°F and neglecting the stiffness contribution of the ablative coating.

Configuration 6, although its moment of inertia substantially exceeds the moment of inertia of Configuration 1, will deform more than 1.0 in. If two 0.020 in. facing sheets are used, then the depth of the section would have to be 0.6 in. to give sufficient stiffness. This dimension infringes on the currently available envelope.

Flutter and vibration analysis of the cowl will be performed when the basic design details have been finalized.



UNCLASSIFIED



A-32153

Figure 5.7-3. Structurally Feasible Design Configuration of Cowl



AIRESEARCH MANUFACTURING DIVISION
Los Angeles, California

UNCLASSIFIED

67-2833
Page 5-124

UNCLASSIFIED

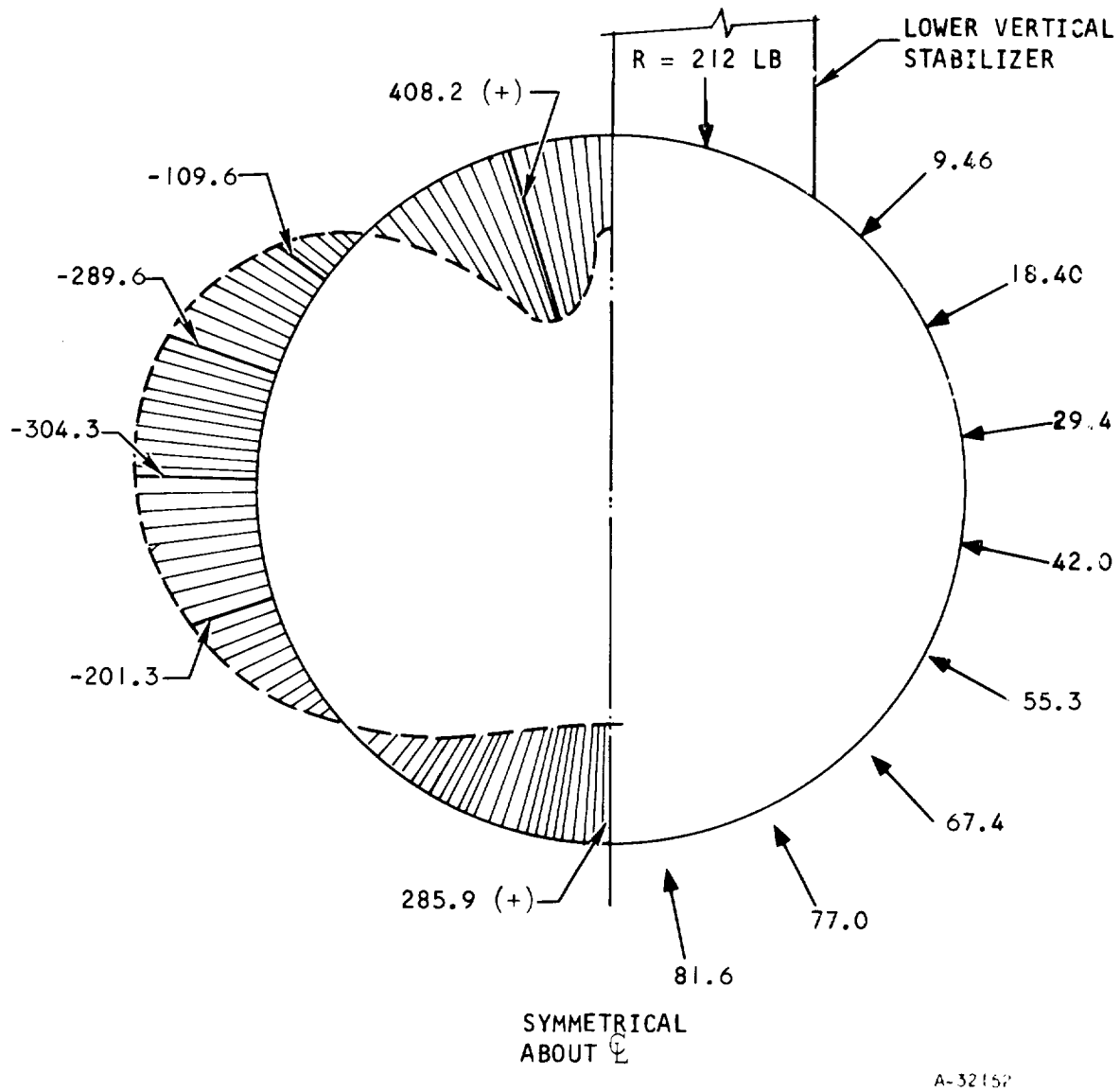


Figure 5.7-4. Cowl-Stiffening Mounting Ring Analysis



UNCLASSIFIED

UNCLASSIFIED

5.7.3 Thermal Design

An initial thermal study of the ablatively-cooled cowl surface has been made. The aerodynamic data from Figure 5.1-13 for the contours of the cowl shown in Drawing L980615 were used to calculate the loads summarized in Table 5.7-2. The thicknesses associated with turbulent flow are recommended. Further refinement of these results will be accomplished, but is being delayed because (1) the final cowl contours have not been defined, but are pending reevaluation of the outer shell design for revised load conditions and (2) the Martin ablative coating analysis computer program, although requested, has not been received.

Some temperature and pressure test data for the dummy HRE X-15 flight have become available from NASA-FRC. Other important data, such as flight trajectory, dummy HRE skin thickness and material, ablator thickness and material are required for comparison between flight test data and analytical prediction. A request for the necessary information on the flight test has been made.

5.7.3.1 Heat Load

Based on the aerodynamic data at $M = 8$ and 85,000 ft (Figure 5.1-13) and the proposed X-15A-2 flight trajectory for the HRE mission to Mach 8 shown in Figure 5.7-5, the heat flux was calculated on the cowl surface using the Eckert flat plate heat transfer equation. The contour of the ablative surface was obtained from Drawing L980615. The variation of the heat flux with the flight time is shown in Figure 5.7-5 at the beginning and end points of the cowl surface (Station 45 and 76). The local heat load, which is the result of numerical integration of local heat flux over the entire flight time is tabulated in Table 5.7-2 at various locations on the cowl surface. Both laminar and turbulent flow fields were assumed. The heat loads on the entire ablative cowl surface at Mach 8 and 85,000 ft are 120 and 600 Btu/sec for laminar and turbulent flows, respectively. It is noted that the heat fluxes or heat loads are so-called "cold wall" values using a base temperature of 0°R .

5.7.3.2 Ablator Thickness

The appropriate thickness of the ablative material depends on the properties (mechanical, thermal, and ablative) of the ablator and base material as well as the heat load. The MA-25S, a sprayable ablator developed by the Martin Company, which is also applied to the X-15A-2 fuselage surfaces, was selected for compatibility with the airplane. Its important properties from Reference 5.7.3-1 are tabulated in Table 5.7-3. The design curves of MA-25S for the X-15 Mach 8 trajectory from Reference 5.7-1 are shown in Figure 5.7-6. Inconel was used as a base material in developing Figure 5.7-6, while Hastelloy X is a candidate for the HRE cowl. However, two base materials have similar physical properties of density, specific heat, and thermal conductivity that enter the ablation calculation, as shown in Table 5.7-4. Therefore, Figure 5.7-6 was used for an estimation of the ablator thickness for the present cowl. As can be seen from Figure 5.7-6, the ablator thickness is a function of the base material thickness in addition to the heat load and other





UNCLASSIFIED

UNCLASSIFIED

TABLE 5.7-2
REQUIRED THICKNESS OF ABLATOR MA-25S
FOR 0.04-IN. THICK HASTELLOY X AS A BASE MATERIAL

Station No.	Reynolds Number, $Re, \times 10^{-6}$	Flow Pattern	Heat Flux, $q/A,$ $Btu/sec\ ft^2$	$QT = (q/A)dt,$ Btu/ft^2	Ablator MA-25S Thickness, in.
45 (Beginning of ablative cowl)	0.75	Laminar Turbulent	20.8 102	3,700 20,500	0.31 0.47
49	2.5	Laminar Turbulent	11.7 59.0	2,080 11,900	0.26 0.42
65	5.2	Laminar Turbulent	5.7 33.6	1,010 6,500	0.17 0.37
72 (Position of bump-induced shock)	---	Laminar Turbulent	47 304	8,350 58,200	0.39 0.57
76 (End of ablative cowl)	7.5	Laminar Turbulent	4.64 31	830 5,930	0.14 0.36

NOTES:

(1) $Re = \frac{\rho V \times}{\mu}$

(2) Re and q/A , as shown, are based on $M_{\infty} = 8, 85,000\ ft$

UNCLASSIFIED

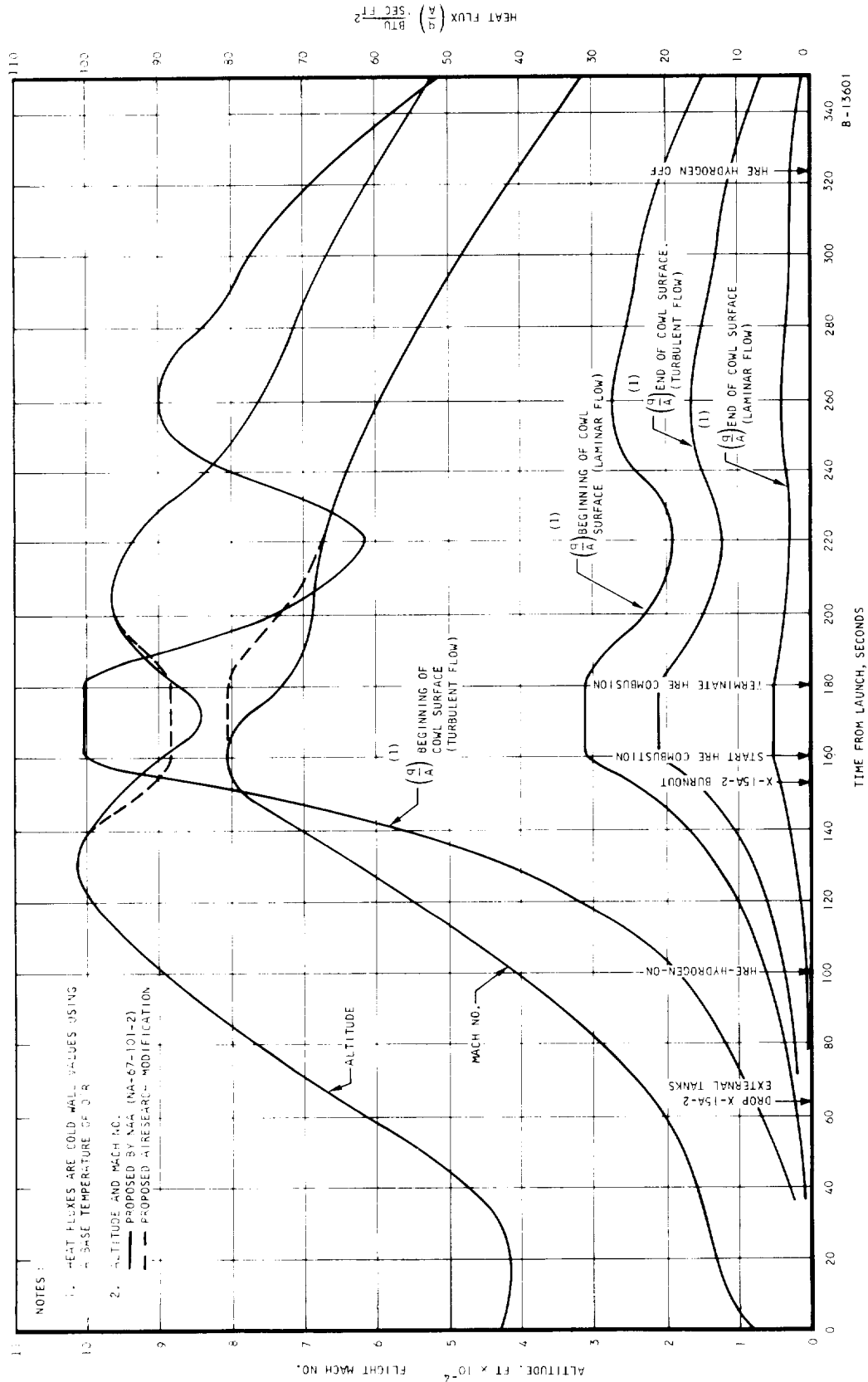


Figure 5.7-5 . Ablative Cowl Heat Loads at Mach 8



AIRESEARCH MANUFACTURING DIVISION
Los Angeles, California

UNCLASSIFIED

UNCLASSIFIED

TABLE 5.7-3

PROPERTIES OF MARTIN COMPANY ABLATOR MA-25S

Temperature, °R	Thermal Conductivity, Btu/in, sec °F x 10 ⁶		Specific Heat, Btu/lb °F		Emissivity	
	Virgin	Char	Virgin	Char	Virgin	Char
400	1.180	---	0.280	---	0.720	---
600	---	---	---	---	---	0.643
700	1.350	---	0.316	---	---	---
800	---	---	---	---	0.786	---
950	---	---	0.208	---	---	---
1000	1.440	2.430	---	0.210	---	---
1200	---	---	---	---	0.815	0.685
1500	---	2.960	---	0.280	---	---
1800	---	---	---	---	---	0.665
2000	---	3.710	---	0.300	---	---
2400	---	---	---	---	---	0.631
3000	---	---	---	---	---	0.600

NOTES:

- (1) Virgin density = 28 lb/ft³
- (2) Char density = 9.8 lb/ft³
- (3) Heat of pyrolysis = 75 Btu/lb



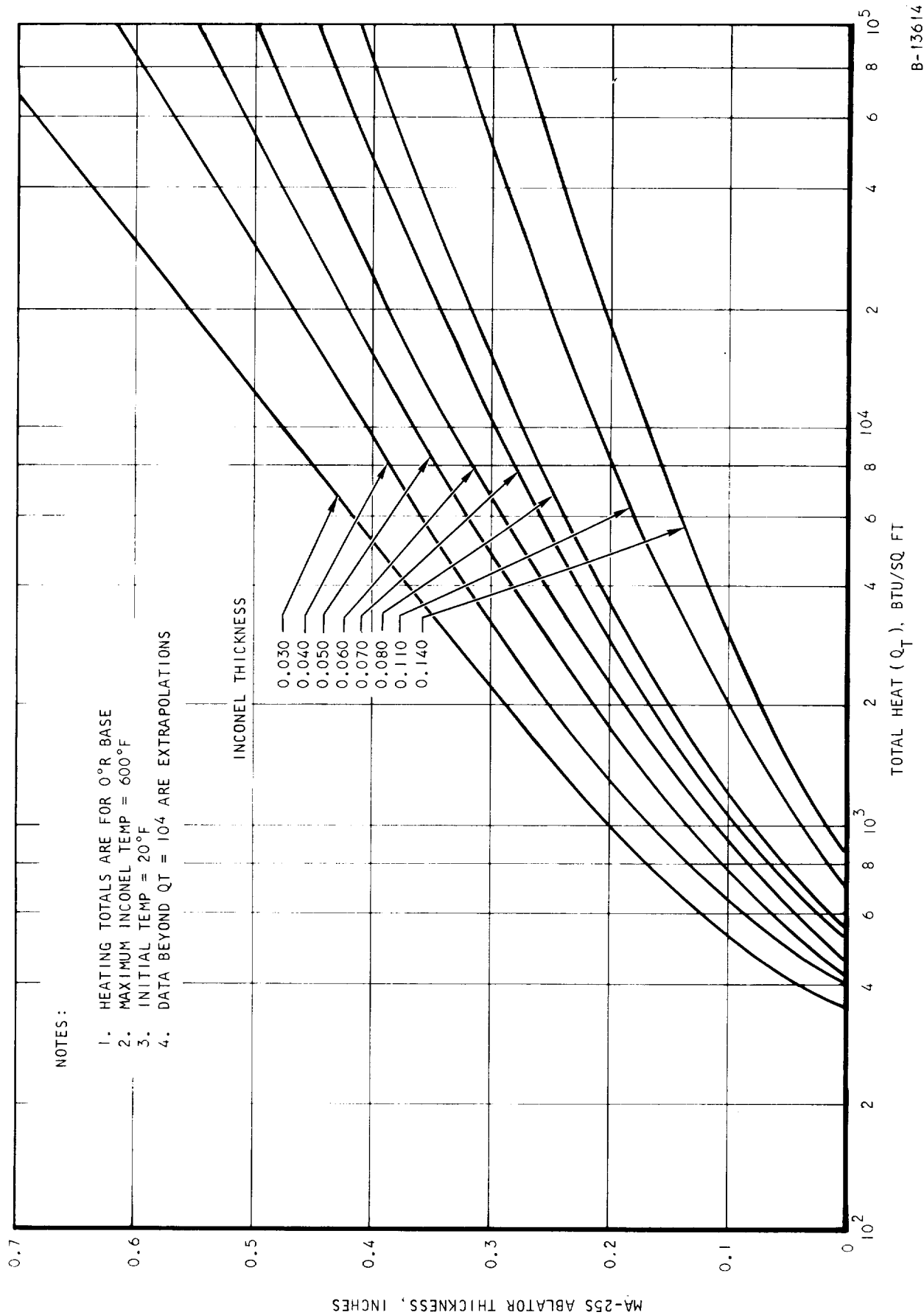


Figure 5.7-6. Ablator Design Curves for Mach 8 Conditions

B-13614



UNCLASSIFIED

TABLE 5.7-4

COMPARISONS OF PROPERTIES OF INCONEL AND HASTELLOY ALLOY X

	Density, lb/in. ³	Specific Heat, Btu/lb °F	Thermal Conductivity, Btu/ft ² hr °F		
			200°F	400°F	600°F
Inconel (718)	0.296	0.10	86	98	111
Hastelloy, Alloy X	0.297	0.105	76	88	100

factors. Since the thickness of the Hastelloy X base material currently under consideration is 0.04 in., the required MA-25S thicknesses at various locations and heat load conditions, as tabulated in Table 5.7-2, were obtained with use of this value.

5.7.3.3 Flow Field

Flow field results were determined for both laminar and turbulent flows. Marked differences occur. The local Reynolds number along the cowl contour at M = 8 and 85,000 ft in Table 5.7-2 indicates that the flow in the forward portion of the cowl may be laminar, while the flow in the aft region of the cowl may be turbulent. Figure 5.7-7 shows that as the free stream Mach number decreases, Reynolds number increases, and hence the flow is more likely to be turbulent for most of the flight time. Also, for the range of the Reynolds number under discussion, free stream disturbance, local discontinuities on the cowl contour, and surface roughness due to char formation of the ablative material may produce early transition to turbulent flow. To insure against local overheating, the results based on turbulent flow are being used.

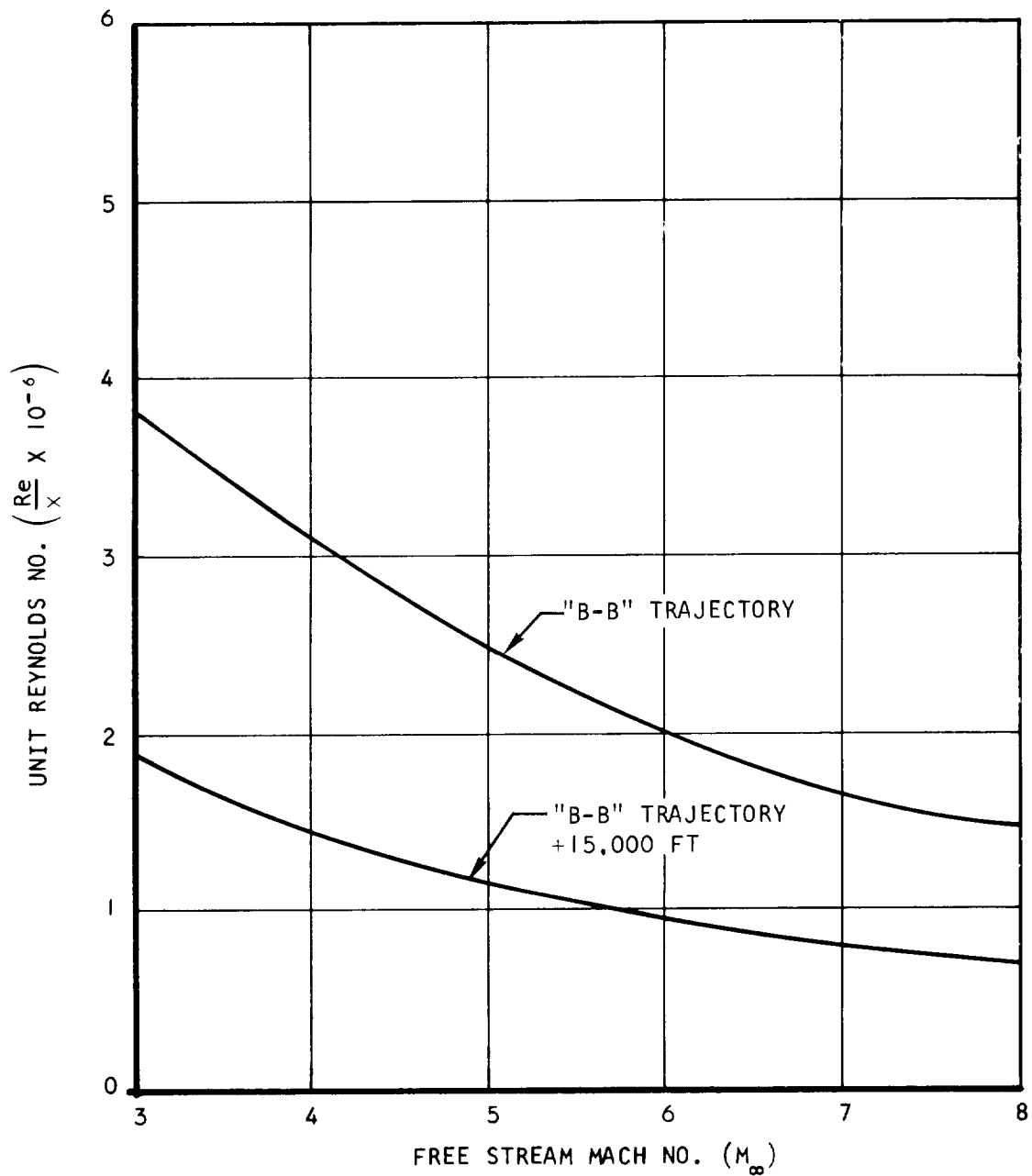
5.7.3.4 Local Protuberances

Local protuberances are shown on the cowl surface in Drawing 980615. These protuberances induce boundary layer separation and a shock near station 72. The aerodynamic analysis (Figure 5.1-14) indicates that the ratio of the pressure rise across this shock is 12.3 at M = 8 and 85,000 ft. The associated rise in heat flux may be determined by the relation

$$\frac{(q/A)_{\max}}{(q/A)_0} = \left(\frac{P_2}{P_1}\right)^n$$



UNCLASSIFIED



A-32112

Figure 5.7-7. Unit Reynolds Numbers for HRE Missions



AIRSEARCH MANUFACTURING DIVISION
Los Angeles, California

UNCLASSIFIED

UNCLASSIFIED

where $(q/A)_0$ is the heat flux in the shockless system, P_1 and P_2 are the upstream and downstream pressures of the shock, and n is a constant with a value between 0.80 and 0.93. With use of $n = 0.9$, the local maximum (or peak) heat flux becomes approximately 10 times as great as the heat flux in the corresponding shockless system. This requires thickening of the ablative material in the region, as shown in Table 5.7-2.

5.8 INLET SPIKE

The inlet spike is shown on Drawing L980612. Basically it consists of three ring-stiffened truncated sandwich cones. The facing of the forward position, from Station 0.6 to Station 35 is 0.015 in. sheet, while the core consists of 0.153-in.-high fins. Exterior facing of the middle portion, between Stations 35.0 and 46.0 is 0.015 in. while the interior facing is 0.06, and the fin height is 0.050 in. The last, almost cylindrical portion is a sandwich with two cores and three facing sheets. The cores are 0.050 in. high fins, while the two exterior facing sheets are 0.015-in. thick. The interior facing is 0.060 in. thick.

The spike is attached to the actuator by a mounting cone.

The weight of the inlet spike shell with the mounting cone and the stiffening ring is 90.1 lb. The center of gravity of the spike is located at Station 43.0 on the X-axis.

5.8.1 Design Loads

The inlet spike is exposed to the following loads:

(a) Aerodynamic loads:

Pressure

Heating

(b) Inertia loads

(c) Environmental loads due to ground handling, fabrication, storage, etc.

The aerodynamic loads acting on the spike are shown on Figures 5.1.2.2-1 through 5.1.2.2-3. The governing load occurs in case of inlet unstart conditions at $M_\infty = 8$ in the shock field of the X-15, with a normal shock at the leading edge.

Maximum axial load occurs at free stream Mach 8, BB line trajectory, corresponding to shock field conditions surrounding the engine of $M_\ell = 6.5$, $q_\ell = 3240$ psf. Maximum axial load tending to open the inlet for this case



UNCLASSIFIED

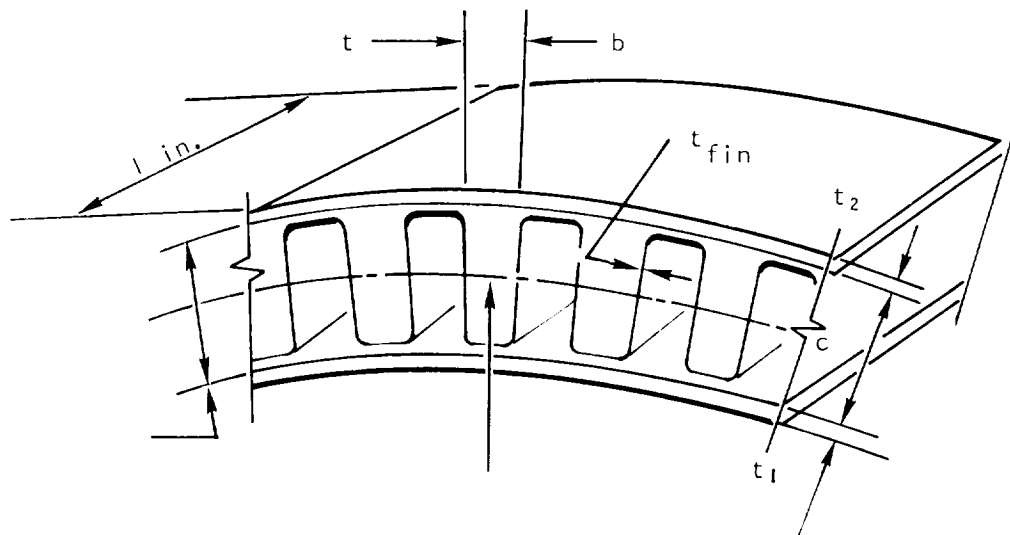
UNCLASSIFIED

is 12,900 lb. There is an opposing axial load which varies from 400 lb to 6300 lb due to pressure forces on the bellows. Maximum normal load occurs with an asymmetrically unstated inlet at $M_{\ell} = 6.5$, $q_{\ell} = 3240$ psf. Axial load for this case is 5040 lb, while the load due to pressure loading on the bellows is 2170 lb. Spike temperatures at $M_{\ell} = 6.5$ are shown on Figure 5.8-1. Spike geometry and pertinent design details are also shown on Figure 5.8-1.

5.8.2 Structural Design

The modified normal pressures acting on the spike shell have increased from the ones used in earlier analysis. Also, the location of the pressure peaks have changes substantially.

In this updated analysis, critical buckling pressures have been calculated for three segments of the spike. These segments were treated as straight, finite length sandwich cylinders with isotropic faces and an orthotropic core. The geometry has been considered uniform for each of these sections. The following sketch depicts the basic cross-sectional geometry of the shells under consideration.



Basic Shell Element

In this sketch:

- t_1, t_2 face plate thicknesses (not necessarily equal)
- t_{fin} fin thickness
- c fin height
- b fin spacing



UNCLASSIFIED

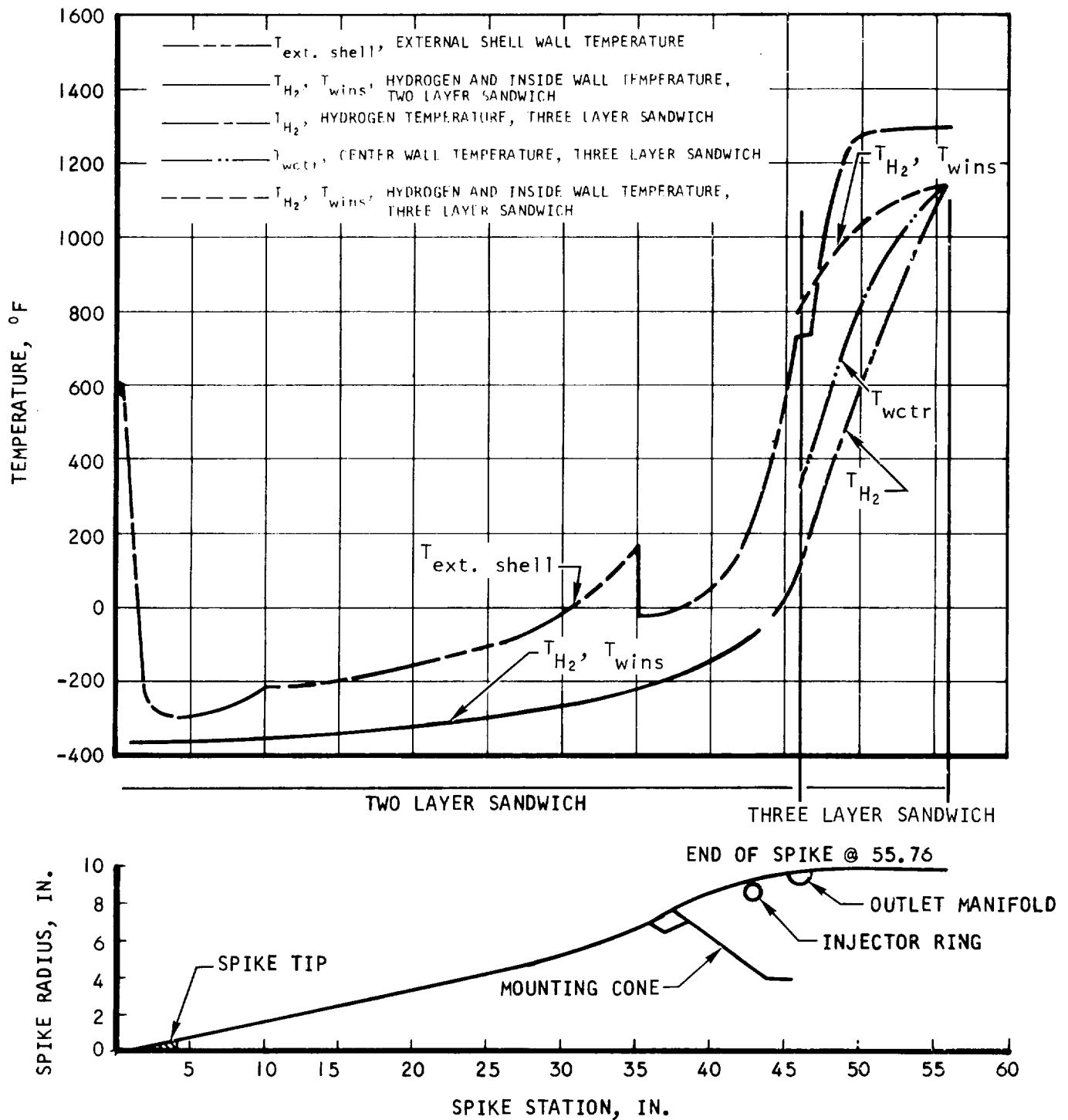


Figure 5.8-1. Spike Temperatures and Details versus Spike Axial Station



UNCLASSIFIED

UNCLASSIFIED

5.8.2.1 Buckling Analysis

Buckling pressure for a finite length sandwich cylinder with isotropic face sheets and an orthotropic core is given in Reference 5.8.2-1. The ends of the cylinder are simply supported and held circular. The critical buckling pressure is given by the formula

$$P_{cr} = \frac{2 Et}{(1 - \nu^2)R} K$$

The buckling coefficient, K , is computed from the expression

$$K = \frac{\frac{8}{9} + \frac{\alpha^2 n^2}{\beta} (n^2 - 1) \left(3 + \frac{n^2}{\beta}\right) (n^2 - 1 + \beta) + \frac{32}{9} V \alpha n^2}{(n^2 - 1) \left(1 + \frac{n^2}{\beta}\right)^2 (1 + 4 V \alpha n^2)}$$

The several parameters in this equation are computed as follows:

$$\alpha = \frac{h}{2R}, \quad \beta = \left(\frac{\pi R}{a}\right)^2 \quad \text{and} \quad V = \frac{Et}{4(1 - \nu^2) R G_{cy}}$$

where E = face sheet elastic modulus

t = face sheet thickness

R = shell radius

n = number of circumferential full waves of shell

ν = face sheet Poisson ratio

h = centerline spacing between face sheets

a = shell length between stiffening rings

G_{cy} = shear modulus of orthotropic core in circumferential direction

The expression for shear stiffness of the fin core is

$$S = \frac{n c^2 E_{fin}}{\left(\frac{c}{t_{fin}}\right)^3 \left[1 + 2 \left(\frac{b}{c}\right) \left(\frac{E_{fin}}{E_t}\right) \left(\frac{t_{fin}}{t}\right)^3\right]}$$



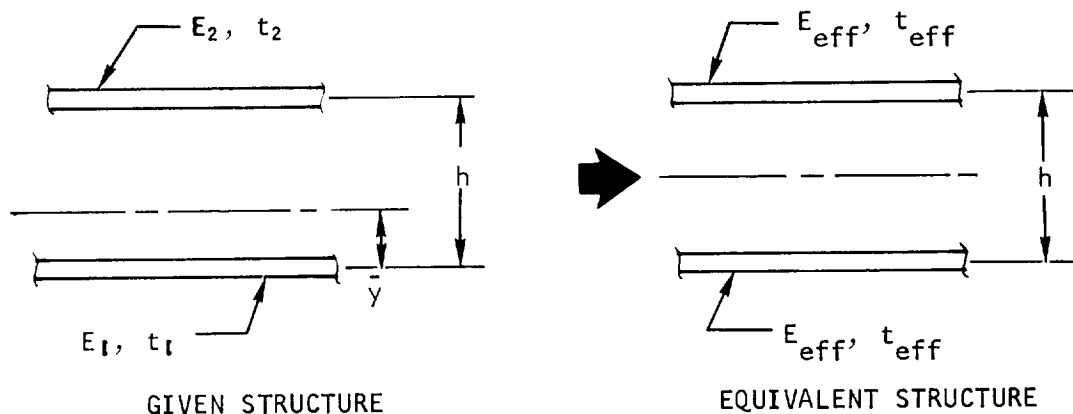
UNCLASSIFIED

The shear modulus for the core is then calculated by the formula

$$G_{cy} = \frac{c S}{h^2}$$

These equations are specifically applicable to sandwich shells with equal thickness face sheets and the same elastic modulus in both sheets. Only the front portion of the spike has equal thickness in the two sheets (both faces are 0.015 in. thick). Due to temperature differences between the two sheets, the properties will be different. The prestressing due to the ΔT also forces the material into the inelastic portion of the stress-strain range. The buckling formula makes use of the quantity Et . It is necessary to determine the equivalent value for $E_{eff} t_{eff}$ that is applicable to sandwich construction with unequal face sheets and dissimilar elastic properties.

Since the buckling capability is inherently related to the bending stiffness of the sandwich, it is required to determine the plate thickness that produces the same value for EI as the actual sandwich. This is illustrated by the following sketch:



For the given structure

$$\bar{y} = \frac{\sum EAY}{\sum EA} = \frac{E_2 t_2}{E_1 t_1 + E_2 t_2} h = \left(\frac{\gamma}{\gamma + 1} \right) h$$

where $\gamma = \frac{E_2 t_2}{E_1 t_1}$

From this

$$EI = \frac{E_1 t_1^3}{12} + \frac{E_2 t_2^3}{12} + E_1 t_1 h^2 \left(\frac{\gamma}{\gamma + 1} \right)^2 + E_2 t_2 h^2 \left(\frac{1}{\gamma + 1} \right)^2$$



UNCLASSIFIED

$$EI = E_1 t_1 \frac{h^2}{2} \left[\left(\frac{t_1}{h} \right)^2 \left(\frac{1 + \gamma \left(\frac{t_2}{t_1} \right)^2}{6} \right) + \frac{2\gamma}{\gamma + 1} \right]$$

also

$$E_{\text{eff}} I_{\text{eff}} = E_{\text{eff}} t_{\text{eff}} \frac{h^2}{2} \left[\frac{1}{3} \left(\frac{t_{\text{eff}}}{h} \right)^2 + 1 \right]$$

Since h is common to both expressions, the quantity $E_{\text{eff}} t_{\text{eff}}$ is computed as follows:

$$E_{\text{eff}} t_{\text{eff}} \left[\frac{1}{3} \left(\frac{t_{\text{eff}}}{h} \right)^2 + 1 \right] = E_1 t_1 \left[\left(\frac{t_1}{h} \right)^2 \left(\frac{1 + \gamma \left(\frac{t_2}{t_1} \right)^2}{6} \right) + \frac{2\gamma}{\gamma + 1} \right]$$

Actually, E_{eff} and t_{eff} cannot be precisely computed individually, because the t_{eff} appears both inside and outside of the brackets. Since t_{eff}/h is generally much less than unity, a very good estimate can be obtained by assuming the $t_{\text{eff}}/h \leq 0.25$. The quantity inside the bracket takes the numerical value of 1.02. This has been used for the spike buckling analysis. As a check on this approach the equivalent single sheet thickness was also computed to produce the same EI , and this thickness was then placed into the buckling formula for short cylinders with simply supported, circular ends. The results agreed within 5 percent, which serves as a satisfactory verification of this approach.

As already noted, the ΔT between the face sheets produces appreciable thermal stresses in both face sheets, and these stresses are usually well above the proportional limit. In order to cope with this effect, stress-strain curves were generated for Hastelloy X from room temperature to 1000°F at 200° intervals. Since the ΔT constraint is biaxial, a modified set of stress-strain curves were obtained for the condition of equal biaxial stresses. The differential thermal expansion due to the ΔT was computed, and from the equibiaxial stress strain curves, a direct calculation of thermal stress was made. Curves were also prepared in which tangent modulus was plotted versus applied stress at the above mentioned temperature intervals. The tangent modulus on one sheet was used in conjunction with the elastic modulus on the other sheet to obtain the composite EI , and then the numerical value for $E_{\text{eff}} t_{\text{eff}}$. The buckling formulas were then used to calculate the critical buckling pressures of the different shell elements in the spike. In this computation, successive values of circumferential waves, n , are placed into the formula for the buckling coefficient k until k_{min} is found. Then the values for k_{min} and $E_{\text{eff}} t_{\text{eff}}$ are used to obtain buckling pressure. This value for buckling pressure is then applied to the sandwich shell structure in combination with the ΔT effects. Since the structure is inelastic, this will obviously lead to



UNCLASSIFIED

reduced tangent modules values for the face sheets, and hence a better estimate of buckling pressure. The buckling pressure obtained from the second iteration is therefore lower than the applied pressure (based upon the first iteration), and the second result is a somewhat conservative estimate of buckling pressure. The iterative process can be repeated until an exact match is obtained. Results from the second iteration were approximately 10 to 15 percent less than the first, which means that further iterations will not greatly change the ultimate value for buckling pressure. It is believed that these refinements will produce valid computed estimates of shell buckling pressures. The design objective is a safety factor of not less than 1.5 between calculated buckling pressure and applied pressure.

5.8.2.2 Calculated Results

The spike was broken into four distinct shell elements. Section I is the shell length from the spike front section at Station 4.0 to Station 36.5 where the mounting core attaches to the spike. Section II begins at the aft end of the mounting core joint with the spike at Station 37.8 and it ends at the injector ring, Station 43.0. Section III is the shell element from the ejector ring, Station 43.0 to the front edge of the spike exhaust manifold ring, Station 45.3, Section IV is the shell element from the aft end of the exhaust manifold ring, Station 46.8 to the end of the spike, Station 55.8. Average metal temperatures and ΔT 's over each section of the spike were used. The critical applied pressure condition is the $M_1 = 6.5$ symmetrical unstart which produces a peak steady pressure of 138 psi at the cowl lip and reduces to 22 psi at the aft end of the spike. The applied pressure was taken to be the mean pressure over each shell section. A condensed summary of these results and operating conditions for each shell section is provided in the following discussion.

Spike Section I - Station 4.0 to Station 36.5

Section length = 32.5 in.

Radius at Station 4.0 = 0.75 in.

Radius at Station 36.5 = 7.25 in.

Mean radius = $2/3 (0.75 + 7.25) = 5.33$ in. (use 5.5 in.)

Temperature - less than room temperature

Mean $\Delta T = \leq 200^\circ\text{F}$

The minimum buckling coefficient for the first iteration occurred with $n = 3$ (three full circumferential waves), and the computed buckling pressure was 72.0 psi. The second iteration yielded a buckling pressure of 66.5 psi.



UNCLASSIFIED

Applied pressures vary from 2 psi at Station 4.0 to a maximum of 10 psi at Station 36.5. Based upon a uniform pressure of 10 psi, the safety factor is

$$S.F. = \frac{66.5}{10.0} = 6.65$$

Spike Section II - Station 37.8 to Station 43.0

Section length = 5.20 in.

Mean radius = 8.60 in.

Mean inner sheet temperature = -140°F

Mean outer sheet temperature = 100°F

Mean ΔT = 240°F

Inner shell thickness = 0.060 in.

Outer shell thickness = 0.015 in.

The first iteration yielded a buckling pressure of 184 psi. The second iteration with the imposed 184 psi produced a calculated buckling pressure of 169 psi with 11 circumferential waves. The applied pressure ranges from 124 psi at Station 37.8 to 84 psi at Station 43.0 with a mean pressure of 102 psi. The buckling safety factor is

$$S.F. = \frac{169}{102} = 1.66$$

Spike Section III - Station 43.0 to Station 45.3

Section length = 2.3 in.

Mean radius = 9.25 in.

Mean inner sheet temperature = -20°F

Mean outer sheet temperature = 420°F

Mean ΔT = 440°F

Inner shell thickness = 0.060 in.

Outer shell thickness = 0.015 in.

The buckling pressure from the first iteration was 219 psi. The second iteration produced a computed buckling pressure of 211 psi. Pressure varies from 84 psi at Station 43.0 to 64 psi at Station 45.3. Average applied pressure is 74 psi. The safety factor is

$$S.F. = \frac{211}{74} = 2.85$$



UNCLASSIFIED

Spike Section IV - Station 46.8 to Station 55.8

Section length = 9.0 in.

Mean radius = 9.75 in.

Mean inner sheet temperature = 1040°F

Mean outer sheet temperature = 855°F

Mean ΔT = 185°F

Inner sheet thickness = 0.60 in.

Outer sheet thickness = 0.015 in.

This shell has a stiffening ring at Station 46.8 and is free at the aft end, Station 55.8. The effective shell length has been taken as 18.0 in. for the buckling calculations. The first iteration produced a buckling pressure of 58 psi, and the second iteration resulted in a buckling pressure of 55 psi.

Applied external pressure varies from 63 psi at Station 46.8 to 22 psi at Station 55.8. With the spike in the $M_L = 6.5$ operating position; there is a balancing pressure of 3 psi in the bellows cavity (Station 46.8 to 50.5), and a balancing pressure of 14 psi on the underside of the spike from the seal at Station 50.5 to the end of the spike. The average applied pressure due to this loading is 36.4 psi. The safety factor is

$$S.F. = \frac{55}{36.4} = 1.51$$

5.9 INLET SPIKE ACTUATOR

5.9.1 Revised Operating Requirements

The load profiles for critical actuator operating conditions given in Paragraph 5.1.4 herein differ significantly from those presented in the previous TDR (Reference 5.5-1, Paragraph 4.8). Other operating requirements for the actuator remain essentially unchanged from those presented in the referenced report with two exceptions:

- (a) Positioning accuracy at $M_\infty = 8$ has been changed from ± 0.144 in. to ± 0.058 in.
- (b) The environmental temperature has been changed to 300°F maximum from 450°F maximum, which is the soak temperature of the actuator mass.



UNCLASSIFIED

As a result of the changes in actuator load profile, a hydraulic actuation system is currently being investigated as a substitute for the pneumatic system previously planned. The design loads and the structural design for the actuator, as discussed in the following paragraphs, are not expected to be affected by this change in driving fluid; however, means of reducing the bearing loads that result from the increased normal loading on the actuator are also being investigated and would affect detail results for this aspect of the problem.

5.9.2 Design Loads

Analysis of aerodynamic loads acting on the spike due to symmetrical and asymmetrical engine unstart operation at $M_\infty = 8.0$, $M_L = 6.5$ has produced the modifications of loads acting on the actuator relative to the previous design. The maximum aerodynamic loads occur with inle unstart and are as follows (see Paragraph 5.1.4):

Symmetric Unstart ($\alpha_L = 0 \text{ deg}$)

$M_\infty = 8.0$	Axial load = 12,900 lb
$M_L = 6.5$	Normal load = Zero
$q_\infty = 1800 \text{ psfa}$	
$q_L = 3240 \text{ psfa}$	
X-15 angle of attack = 10 deg	

Asymmetric Unstart ($\alpha_L = 4.0 \text{ deg}$)

$M_\infty = 8.0$	Axial load = 5040 lb
$M_L = 6.5$	Normal load = 15,100 lb
$q_\infty = 1800 \text{ psfa}$	
$q_L = 3240 \text{ psfa}$	

The remaining loads, such as those produced by the bellows extension and internal pressure loads, are as outlined in Paragraph 5.1.4. The resulting net design loads on the actuator are:

Symmetric Unstart

Axial load = 12,500 lb
Normal load = Zero



UNCLASSIFIED

Asymmetric Unstart

Axial load = 2800 lb

Normal load = 15,100 lb

(Center of pressure at Sta 41.2)

5.9.3 Structural Design

The actuator material used in this design is 17-4 PH, heat treated for a yield stress greater than 125,000 psi (1150°F aging temperature). Previous design work had been accomplished with Type 347 CRES.

5.9.3.1 Deflection Analysis

Actuator deflections were determined over the entire range of actuator travel at the spike mounting plane. These were transformed into spike deflections under the cowl lip and at the extreme aft end of the spike, as illustrated on Figure 5.9-1. The computed deflections for the spike at the cowl lip and at the spike aft end are plotted vs spike travel on Figure 5.9-2. Finally, the results are presented in Table 5.9-1 for net operating clearances of the spike relative to the leading edge lip and the spike aft end relative to the inner body. The results indicate that there is sufficient initial clearance to absorb the deflections due to applied loads.

5.9.3.2 Stresses Due to Applied Loads

The stresses due to the increased loads was determined by reference to the work reported in Reference 5.5-1. This was accomplished by directly scaling the previously computed results with the new loads. Due to the change in material to 17-4 PH, the safety margins with the new loads were found to be even larger than for Type 347 CRES. Essentially, the design is deflection limited, and the structural configuration required to satisfy the allowable displacements will invariably be adequate for stresses.

5.9.3.3 Friction Loads and Bearing Stresses

A study of friction forces and bearing stresses was carried out for the most critical condition, which is an asymmetrical unstart. Total friction force vs spike retraction position is plotted on Figure 5.9-3. A peak value of nearly 6000 lb occurs at a spike retraction position between 1.5 and 2.0 in. Maximum bearing stress was computed to be 2020 psi. This bearing stress makes the use of chrome-plated 17-4 PH sliding surfaces somewhat doubtful. Alternate bearing surfaces and designs using an increased L/D will be investigated with the aim of increasing confidence in actuator operation.



UNCLASSIFIED



UNCLASSIFIED

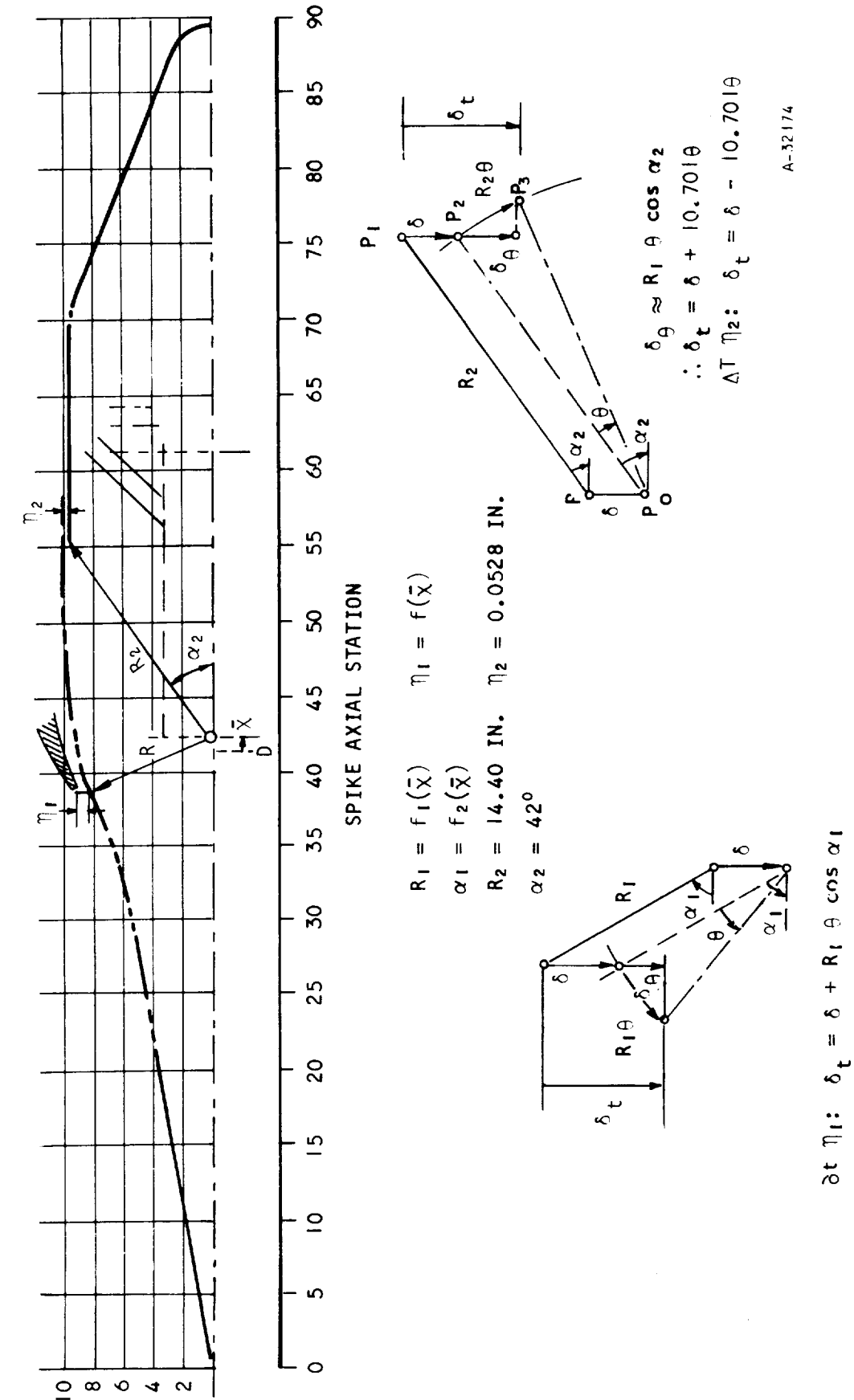
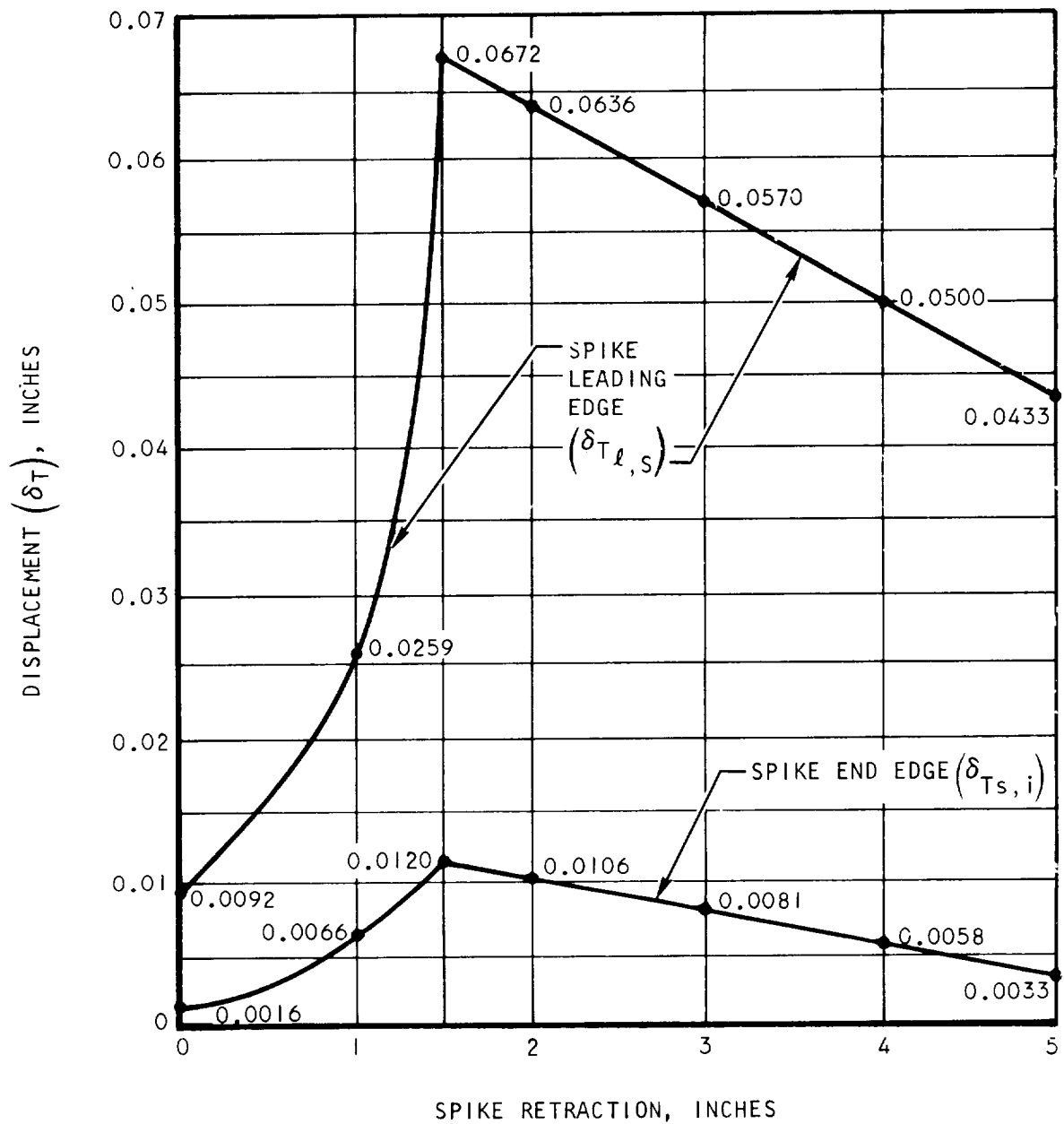


Figure 5.9-1. Spike Clearance Analysis

UNCLASSIFIED



A-32141

Figure 5.9-2. Maximum Spike Displacement at Leading Edge and End Edge



AIRESEARCH MANUFACTURING DIVISION
Los Angeles, California

UNCLASSIFIED

UNCLASSIFIED

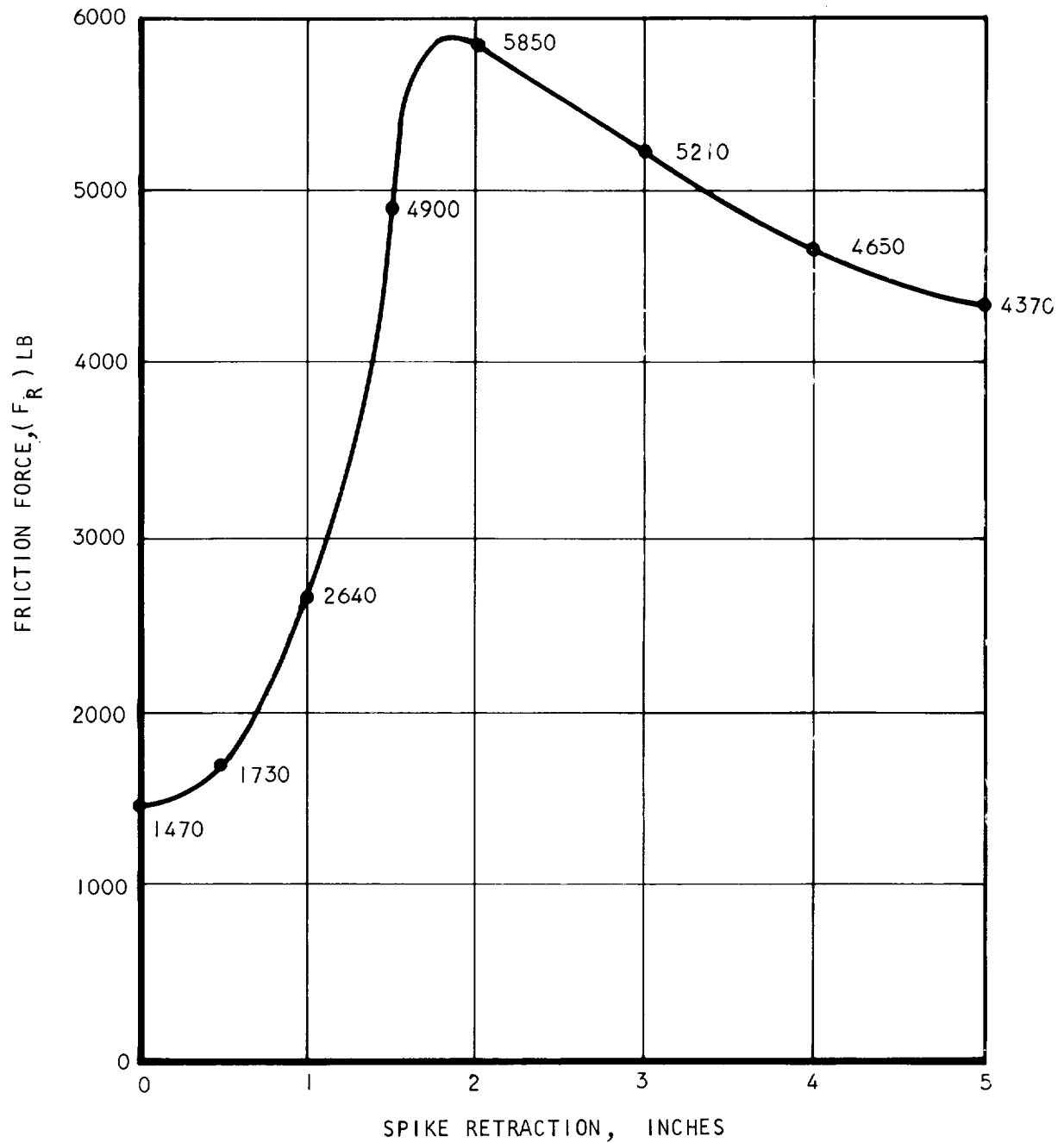
TABLE 5.9-1

SPIKE CLEARANCES RELATIVE TO COWL LEADING EDGE AND INNER BODY

X	δ_T , in.	Leading Edge/Spike			Spike/Inner Body	
		Geometric (Δ) Radial Clearance, With No Load, in.	Net Clearance, in.	δ_T , in.	Geometric (γ) Clearance, in.	Net Clearance, in.
0.0	0.009	0.060	0.051	0.002	0.053	0.051
1.0	0.026	0.350	0.324	0.007	0.053	0.046
1.5	0.068	0.520	0.452	0.012	0.053	0.041
2.0	0.064	0.690	0.626	0.011	0.053	0.042
3.0	0.057	1.070	1.013	0.008	0.053	0.045
4.0	0.050	1.430	1.380	0.006	0.053	0.047
5.0	0.043	1.790	1.747	0.003	0.053	0.050



UNCLASSIFIED



A-32142

Figure 5.9.3. Friction Forces Due to Actuator Movement Under Maximum Load Condition



AIRESEARCH MANUFACTURING DIVISION
Los Angeles, California

UNCLASSIFIED

UNCLASSIFIED

5.10 OUTER BODY-INNER BODY STRUTS

5.10.1 Design Loads

The design load for the struts and strut attachments are indicated in Figure 5.10-1. This diagram indicates the maximum strut load resulting from the design condition forces discussed in Paragraph 5.1.4. A comparison with the previous design loads in Reference 5.5-1 indicates an increase of approximately 200 percent in the longitudinal component to 15,570 lb, and an increase of approximately 65 percent for the radial component to 4370 lb.

5.10.2 Structural Design

The detail structural design for the design loads indicated above is currently in process.

5.11 INNER BODY TEST ASSEMBLY

5.11.1 Aerodynamic Heating and Cooling Design

Heat transfer analyses were performed to determine hot gas aerodynamic heating and cooling hydrogen test conditions required to obtain design point metal temperatures and metal temperature differences on the inner body (inner shell and nozzle) for test with air-oxygen hydrogen combustion products in subsonic flow. Results are shown in Table 5.11-1. Two design points for the test setup were investigated. These are the temperature and ΔT conditions predicted (1) in Paragraph 5.5.2 for combustion at Mach 6.5 local (Mach 8 free stream) and 88,000 ft, and (2) Mach 8 local and freestream at 88,000 ft. These design points were investigated because the thermal design of the inner body was performed at Condition 2, above, while the revised operating environment is for Condition 1. Thus, the cycling portion of the flow test will consist of two phases:

- (a) At Condition 2 for 100 cycles or until failure.
- (b) Following survival of phases above, at Condition 1 for 100 cycles or until failure.

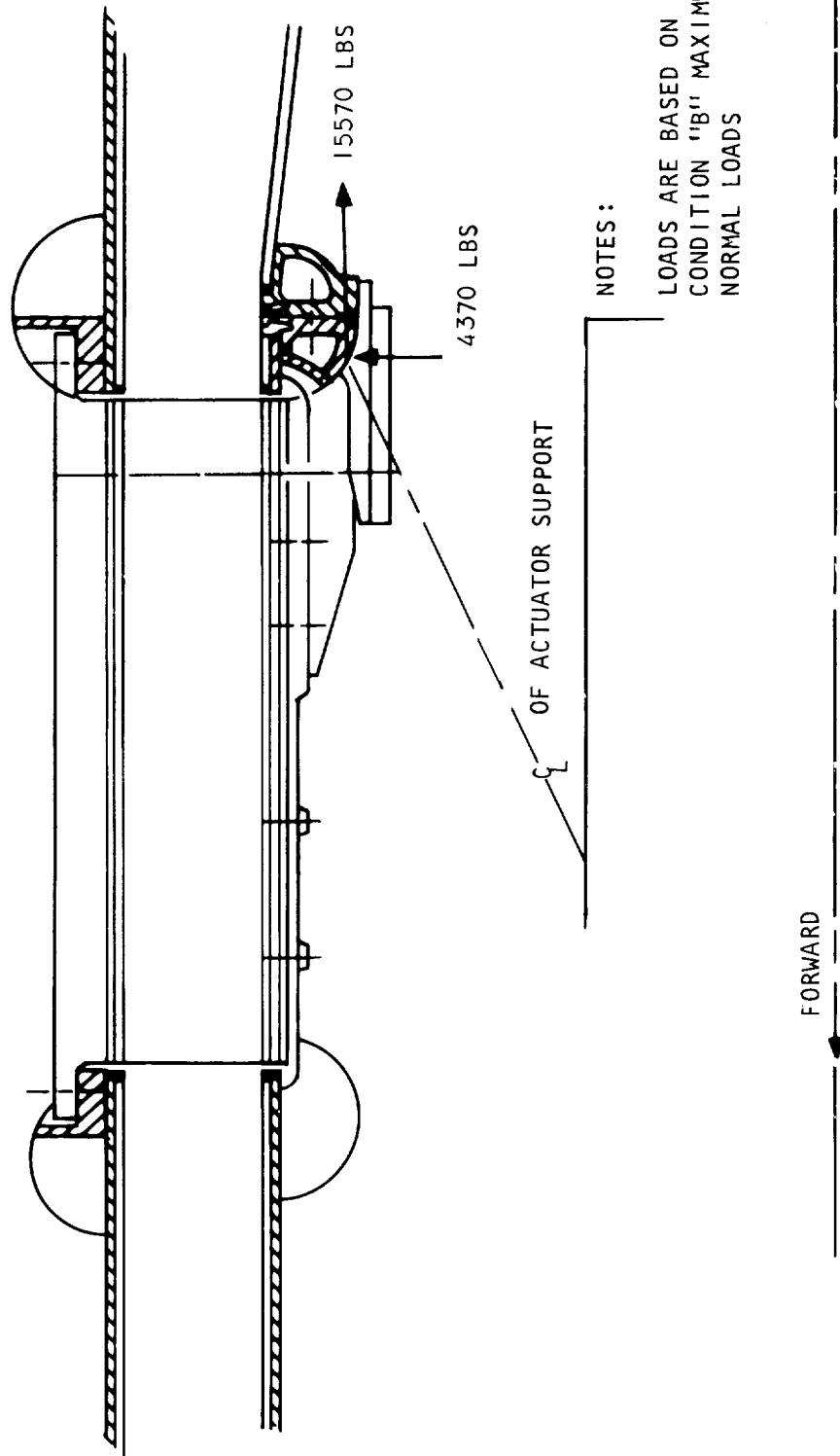
The following discussion centers on simulation of Condition 1, because this condition will determine the designs of the test adapter and is the more difficult to meet. As shown in Figure 5.10-1, adequate simulation of Condition 2 is obtainable with a configuration designed for Condition 1.

The objectives of inner body thermal simulation are:

- (a) A cross section ΔT distribution in the plate-fin cooling jackets that is $\pm 50^\circ\text{R}$ of the predicted design values (the cross section ΔT is the sum of the ΔT 's through the 0.015-in. thick skin and the 0.050-in. high fins).



UNCLASSIFIED



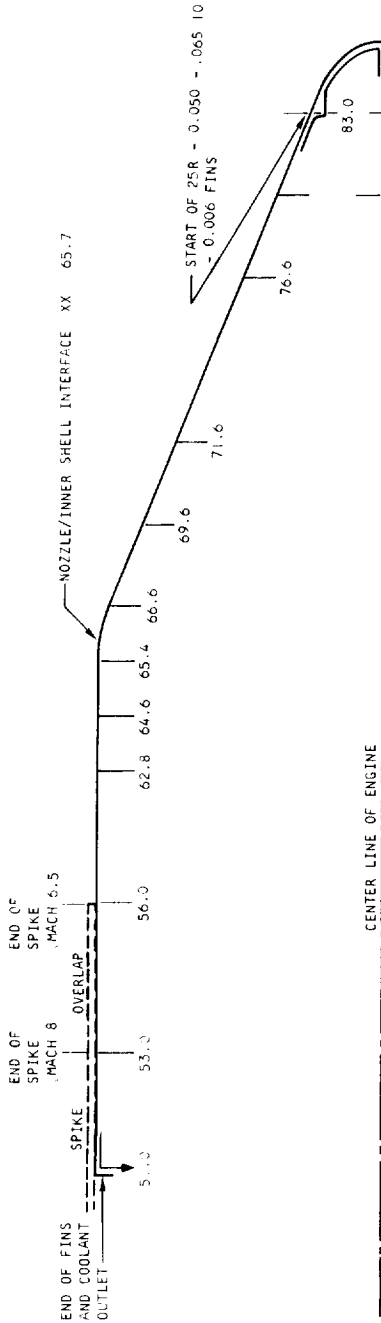
A-32136

Figure 5.10-1. Outer Shell/Inner Body Strut Design Loads



AIRESEARCH MANUFACTURING DIVISION
Los Angeles, California

UNCLASSIFIED



Test or Flight Condition	Test Parameter	Axial Distance From Spike Apex with Spike at M _{6.5} Position													
		51.0	53.0	56.0	62.3	64.6	65.4	66.6	69.6	71.6	76.6	83.0			
Mach 6.5 local, 88000 ft altitude predicted flight conditions, Coolant flow rate 0.42 lb/sec Inlet coolant temperature 120°R	Fin ΔT , °R	0	0	276	387	397	448	424	288	231	154	69			
	Wall ΔT , °R	0	0	110	188	202	238	232	176	151	127	117			
	Gross Sectional ΔT , °R	0	0	386	575	599	686	656	464	382	281	186			
	Outer Wall Temperature, °R	1578	1578	1960	1552	1447	1424	1318	884	735	503	307			
	Structural Wall Temperature, °R	1577	1577	1962	1552	1447	1424	1318	884	735	503	307			
	Heat Flux, Btu/sec ft ²	0	0	288	338	329	358	331	203	162	116	94			
Test Unit, Mach 6.5 simulation Hot gas rate 12 lb/sec Inlet hot gas temperature 4500°R Coolant rate 0.44 lb/sec Inlet coolant temperature 120°R Coolant P (in) = 700 psia, P = 275 psid Tunnel Wall/Inner Shell Clearance 0.30 in.	Fin ΔT , °R	184	204	237	340	375	400	446	180	137	100	31			
	Wall ΔT , °R	75	86	106	180	207	230	258	114	93	81	46			
	Gross Sectional ΔT , °R	259	290	343	529	582	630	704	294	230	181	77			
	Outer Wall Temperature, °R	1835	1760	1640	1350	1278	1230	1200	671	559	431	278			
	Structural Wall Temperature, °R	1861	1455	1279	820	675	580	474	368	322	247	200			
	Heat Flux, Btu/sec ft ²	196	211	235	290	302	310	320	126	97	77	41			
Test Unit, Mach 6.5 simulation Same hot gas conditions as above. Coolant rate 0.38 lb/sec Inlet coolant temperature 200°R Coolant P (in) = 700 psia, P = 205 psid Inner shell is coated with 0.015 in. Rockide Z from XX 51.0 to XX 56.0 to simulate spike overlap	Fin ΔT , °R	92	102	231	353	383	407	453	190	145	107	35			
	Wall ΔT , °R	38	43	92	166	192	211	245	110	91	80	46			
	Gross Sectional ΔT , °R	130	145	323	518	575	618	698	300	236	187	81			
	Outer Wall Temperature, °R	1715	1645	1763	1423	1347	1298	1240	703	583	445	282			
	Structural Wall Temperature, °R	1585	1500	1420	880	748	656	562	394	340	254	200			
	Heat Flux, Btu/sec ft ²	98	106	222	282	296	304	317	125	97	77	41			
Mach 6 local, 88000 ft altitude predicted flight conditions. Coolant flow rate = 0.22 lb/sec Inlet coolant temperature 120°R	Fin ΔT , °R	0	196	185	268	268	---	261	---	139	81	52			
	Wall ΔT , °R	0	58	57	99	105	---	107	---	68	49	54			
	Gross Sectional ΔT , °R	0	254	232	367	373	---	368	---	207	130	106			
	Outer Wall Temperature, °R	1624	1891	1647	1220	1077	---	916	---	504	274	226			
	Structural Wall Temperature, °R	1624	1624	1393	840	692	---	538	---	334	224	120			
	Heat Flux, Btu/sec ft ²	0	155	135	161	154	---	139	---	65	43	43			
Test Unit, Mach 8 simulation Hot gas rate 9.5 lb/sec Inlet hot gas temperature 4500°R Coolant rate 0.40 lb/sec Inlet coolant temperature 520°R Coolant P (in) = 700°R, P = 380 psid Tunnel Wall/Inner Shell Clearance 0.30 in.	Fin ΔT , °R	132	141	158	199	214	---	231	---	104	71	29			
	Wall ΔT , °R	51	56	65	92	102	---	115	---	62	51	30			
	Gross Sectional ΔT , °R	183	197	223	291	316	---	346	---	166	122	59			
	Outer Wall Temperature, °R	1786	1714	1612	1343	1275	---	1197	---	815	691	580			
	Structural Wall Temperature, °R	1596	1510	1375	1045	951	---	845	---	646	567	520			
	Heat Flux, Btu/sec ft ²	136	143	152	175	181	---	188	---	88	68	38			

TABLE 5.10-1. COMPARISON OF INNER BODY THERMAL CONDITIONS BETWEEN PREDICTED FLIGHT AND TEST



UNCLASSIFIED

- (b) A maximum metal surface temperature within 50°R on the low side of 2060°R .
- (c) A structural temperature distribution within 100°R of flight conditions, but not exceeding 1600°R .

Wall ΔT can only be obtained by determining a particular level of heat flux. Also, heat flux and overall cross section ΔT are almost linearly related, so that heat flux comparisons made in the following discussion indicate an approximate overall ΔT .

The test unit, the support structure, and the aft tunnel wall are shown in Drawing 980614. The forward tunnel wall will be cylindrical and is scheduled for detail design later in the program. The test conditions that gave the best simulation of the Mach 6.5 local conditions within the stated objectives were:

- (a) A hot gas flow rate of 12 lb/sec in the test tunnel
- (b) A hot gas inlet temperature of 4500°R
- (c) A hydrogen coolant flow rate of 0.44 lb/sec at an inlet temperature of 200°R
- (d) A clearance between tunnel wall and inner shell of 0.30 in. while operating hot.

Hot gas heat transfer rates on the nozzle surfaces were calculated from the flat plate equations for laminar and turbulent flow. The heat transfer rates were modified for the conical shape nozzle because test flow is opposite to the direction of design flow. A low transition Reynolds number of 100,000 based on nozzle surface length from the nozzle cap was used because the hot gas flow is subsonic and the flow approaching the nozzle in the duct is turbulent. For 12 lb/sec of hot gas flow, the laminar to turbulent transition occurs at about 5 in. aft of the nozzle cap. Heat transfer rates on inner shell surfaces were calculated from duct flow correlations. The hydraulic diameter for an annulus that is twice the clearance between inner shell and tunnel wall was used. At the nozzle/inner shell interface, the heat flux distributions from the flat plate method on the nozzle and the duct flow method on the inner shell were faired to give a smooth transition between methods. The heat flux difference between the two methods at the nozzle/inner shell interface was about 10 percent, with the flat plate method being lower. Neither gas radiation or wall radiation was considered in the analysis. In addition, the enthalpy of stoichiometric combustion products of hydrogen and air (Figure 5.2-1) were used. During the test, however, a hot gas composition of 50 percent H_2O and 50 percent N_2 is more probable. The effects of radiation and hot gas composition on the enthalpy temperature relation will be determined before testing and will be reflected in changes in hot gas flow rates from values reported in Table 5.11-1.



UNCLASSIFIED

The test unit metal temperatures and cross-section temperature differences predicted for the above test conditions are presented in Table 5.11-1. Cross sectional ΔT 's are in close agreement with flight ΔT 's predicted for the inner shell. For example at the nozzle/inner shell interface, Station 65.4 (axial location for Mach 6.5 spike position), the predicted flight ΔT is 686°R while the predicted test ΔT is 630°R , or 56°R lower than flight. At Station 66.6 the predicted flight is 656°R , while the predicted test ΔT is 704°R , or 48°R higher than flight. At Station 56.0 the predicted flight ΔT is 386°R , while the predicted test value is 343°R , or 43°R lower. Generally, the test objectives on the inner shell can be met with the stated test conditions.

On the nozzle, the predicted test ΔT 's are lower than predicted for flight. At the fin entrance, Station 83.0, the predicted flight ΔT is 186°R , compared with 77°R predicted for test, or 109°R lower. The largest difference between predicted flight and test ΔT 's on the nozzle occurs at Station 69.6, where the test cross section is 170°R lower than flight. These differences can be tolerated, however, because structural temperatures on the nozzle predicted for design combustion flight conditions are equal to or less than room temperature (650°R maximum) and ΔT 's are low in any event and not design limiting. An increased test heat flux on the nozzle surfaces (due to tunnel wall and hot gas radiation) will produce slightly higher ΔT 's than reported in Table 5.11-1.

The 5-in.-long section of the inner shell nearest to the hydrogen outlet manifold is protected from exposure to hot gas heating on the flight engine because the spike overlaps the inner shell in this region. A better simulation is achieved in this region if the test heat flux and temperature differences are reduced. The critical section is the braze joint between the 0.015-in.-thick skin and the 0.050-in.-high fins at the end of the finned section at Station 51.0. The heat flux in this region can be reduced by using either or both a coating of Rockide Z (zirconium oxide) or an abrupt increase in tunnel diameter.

If 0.015 in. of Rockide Z is coated on the last 5 in. of the inner shell, the heat flux will be reduced in half. This case was considered in the analysis and results are included in Table 5.11-1. Because the heat load is reduced locally, the test unit coolant flow rate can be reduced from 0.44 lb/sec to 0.38 lb/sec. The cross section ΔT in the coated section of the inner shell is approximately 130°R , compared with 320°R for the adjacent uncoated section at Station 56.0.

Reducing heat flux by abruptly changing the free flow area of the hot gas passage was also considered. If the clearance between the tunnel wall and the inner shell is increased from 0.30 in. to 0.75 in. in the spike overlap region the heat flux will be approximately halved, and the same effect as applying a 0.015-in.-thick coating of Rockide Z would be accomplished.

The 0.30 in. clearance between the inner shell and tunnel is necessary in order to increase heat flux and, therefore, metal cross section. The location at which the 0.30-in. clearance is required during hot test operation is at the nozzle/inner shell interface, where the inner body hot gas heat flux



UNCLASSIFIED

and cross section ΔT is a maximum. The thermal expansion at the nozzle/inner shell interface will be negligible during the test because the design structural temperature at this location is slightly above room temperature. However, it is estimated that the inner shell diameter increase will be 0.10 in. at the hydrogen outlet due to thermal expansion, for the reason that the design operating structural temperature at this point is 1600°R. If the test unit and tunnel wall are assembled as that a constant clearance of 0.30 in. is maintained along the inner shell, the clearance will decrease linearly from 0.30 in. at nozzle/inner shell interface to 0.25 at the hydrogen outlet during the hot test. The tunnel walls will expand negligibly if they are water cooled as anticipated. Water-cooled walls will operate at a cross section average temperature of approximately 850°R. The axial variation in tunnel wall temperature will be less than 100°R. The values of predicted test hot gas heat flux in Table 5.11-1 were determined for a constant clearance of 0.30 in. The indicated test heat flux decreases from 320 Btu/sec sq ft at the nozzle/inner shell interface to 235 Btu/sec sq ft at Station 56.0 (end of spike overlap on the flight engine). This is caused by a decrease in hot gas temperature from 4500°R at the inlet to 3700°R at Station 51.0. There is also a decrease in predicted flight heat flux from the nozzle/inner shell interface (358 Btu/sec sq ft) to Station 56 (288 Btu/sec sq ft), but not as much as predicted for the test. However, when the thermal expansion of the inner shell diameter is considered, the test heat flux will increase to approximately 260 Btu/sec sq ft at Station 56.0 which more closely approaches the predicted flight heat flux of 288 Btu/sec sq ft.

Hot gas in the tunnel is subsonic and at low velocity. For a hot gas flow rate of 12 lb/sec at 4500°R and 300 psia, the approaching velocity in the 20 in. dia duct is approximately 40 ft/sec. Along the 0.30 in. clearance between tunnel wall and inner shell, hot gas velocity will be about 400 ft/sec and the Mach number will be about 0.15, so the flow was considered incompressible.

The selected hot gas conditions give a stagnation point heat flux on the nozzle cap of about 50 Btu/sec sq ft. The corresponding nozzle cap heat flux predicted for flight when hot gas flows in the opposite direction is 40 Btu/sec sq ft. This increase in nozzle cap heat flux for test will not increase cap metal temperatures above acceptable limits because the maximum reported temperature on the nozzle cap predicted for flight was 1160°R and occurred on the bolt. Due to the increased heat flux and increased coolant temperature (to 200°R, 120°R for flight), the bolt temperature will be 1460°R (1000°F).

An attempt was made in the analyses to simulate Mach 6.5 local metal temperatures and temperature differences using 520°R inlet hydrogen. Hydrogen at 520°R is preferred for testing because it is more economical and is easier to use than cryogenic hydrogen at 200°R. However, predicted flight (Mach 6.5 local) temperatures and temperature differences cannot be achieved with 520°R inlet hydrogen. To simulate the maximum cross section ΔT , which occurs in the vicinity of the nozzle/inner shell interface, the combination of a low hydrogen temperature and a high heat flux must exist at this location. If the 520°R inlet hydrogen flow rate is increased to decrease hydrogen



UNCLASSIFIED

temperature at this location and the hot gas heat flux is increased by increasing hot gas flow rate and/or decreasing hot gas passage clearance, the following will occur:

- (a) The maximum available hydrogen flow rate of 0.50 lb/sec will be exceeded.
- (b) The required hydrogen pressure drop through the test unit will exceed the inlet pressure of 700 psia.
- (c) The clearance between inner body and tunnel wall will decrease below 0.30 in., or the required hot gas flow rate will be above 15 lb/sec. (A clearance of 0.30 in. is considered the feasible minimum for design; 15 lb/sec is the maximum hot gas flow rate available.)

The inner body test unit is connected to a support structure that has a diameter slightly less than the inner shell. The support structure is anchored to the aft tunnel wall by four struts that also serve as conduits for water, hydrogen, nitrogen, and pressure and for temperature instrumentation leads. The support structure, struts, and aft tunnel are fabricated from low carbon steel and are cooled with water flowing in plain annular passages beneath the metal surfaces.

During inner body testing, the inner shell strut mounting sockets will be covered with six, double-sandwich plate-fin panels that are water cooled. The panels provide a pressure seal between the hot gas in the annular clearance and the nitrogen in the interior of the test section.

The water flow rates in the support structure, test support struts, aft tunnel wall, and plate-fin panels covering the strut mounting holes were selected to give wall inner surface temperatures not exceeding the saturation temperature of 300°F at a pressure of 70 psia. This pressure will exist at the support structure annulus water outlet with a 50 psia test unit outlet pressure. Resulting hot surface metal temperatures in the water-cooled routes will be 900°R maximum and wall ΔT 's will be 150°R maximum. The required water flow rates and pressure drops for the water flow routes are:

<u>Flow Route</u>	<u>Flow Rate, gpm</u>	<u>Pressure Drop, psi</u>
Support structure and four struts	43 per strut	60
Six double sandwich plate-fin panels	5 (total for all 6 panels)	60
Outer duct	30	40

The available water supply for this test will be 1000 gpm at 110 psia, so both the test unit flow rates and pressure drops are acceptable. The reported water pressure drop reflects an increase by 20 percent from calculated values for the test unit, to include allowance for external line losses.



UNCLASSIFIED

5.11.2 Structural Design

5.11.2.1 Design Conditions

The inner body test adapter is designed to meet the following operating conditions and proof conditions. Factors of safety are listed in Paragraph 5.11.2.3.

(a) Operating Conditions

Temperatures

Tunnel flowing combustion gas: up to 4500⁰R

Cooling hydrogen: in, 200⁰R; out, 1600⁰R

Cooling water (main circuit): in, 70⁰F; out, 100⁰F

Cooling water (strut housing plate circuit): in, 70⁰F;
out, 200⁰F

Pressurizing nitrogen: 100⁰F

Pressures

Tunnel flowing combustion gas: 300 psi

Cooling hydrogen: in, 700 psi

Cooling water: in, 100 psi

Pressurizing nitrogen: 320 psi

Pressure differential, nitrogen-hot gas: 30 psi max

(b) Proof Conditions

Room Temperature

Water Pressure: 300 psi



UNCLASSIFIED

5.11.2.2 Material

The entire structure will be made of SAE-1020 steel, except for the pipes and tubes, which will be 321 CRES steel. The mechanical properties of these materials are as follows:

SAE-1020 (T < 200°F)

$$E = 28 \times 10^6$$

$$F_{tu} = 55,000 \text{ psi}$$

$$F_{ty} = 36,000 \text{ psi}$$

$$\alpha = 6.5 \times 10^{-6} \text{ } ^\circ\text{F}$$

321 CRES

$$F_{ty} (\text{at RT}) = 40,000 \text{ psi}$$

$$F_{ty} (\text{at } 200^\circ\text{R}) = 35,000 \text{ psi}$$

$$F_{ty} (\text{at } 1600^\circ\text{R}) = 30,000 \text{ psi}$$

$$F_{tu} (\text{at RT}) = 70,000 \text{ psi}$$

5.11.2.3 Factors of Safety

The maximum allowable mechanical stress was taken as $1/2 F_{tu}$ or $3/4 F_{ty}$, whichever is less, i.e., 27,000 psi for the structure and the colder pipes, and 22,500 psi for the hydrogen outlet pipes and tubes.

5.11.2.4 Structural Analysis

a. Two-Plate Door Assembly

Under operating conditions, this assembly, consisting of two parallel plates, is designed to resist a 30 psi ΔP across the door. The internal water pressure being 50 psi, the assembly must simultaneously resist a $300 - 50 = 250$ psi ΔP across each plate. It must also resist a 300 psi internal proof pressure at room ambient pressure and temperature.

Pins and, whenever necessary for assembly and disassembly, short tubes are used to maintain plate spacing and to maintain the bending stresses, due to the ΔP between the coolant and the external gases, within allowable limits. The maximum allowable distance between the pins, if these were placed in the common square pattern, would be about twice the mean pin distance that is being used in an axisymmetrical pattern. This provides a high margin of safety. The door assembly will assume some bowing under the 30 psi ΔP , but the stresses due to this effect will remain within allowable limits.

b. Duct Assembly

The flanges of the duct assembly are bolted to the test tunnel with 24 bolts, preloaded to 10,000 lbs per bolt, which is considered adequate to prevent separation of the duct assembly from the tunnel under a 300 psi pressure.



UNCLASSIFIED

c. Pipes and Tubes

Of all pipes and tubes, the hydrogen outlet central tube, which operates at 1600°R and 700 psi, experiences the highest loading, resulting in a stress of 15,000 psi. The margin of safety equals $\frac{22,500}{15,000} - 1 = 0.5$.



UNCLASSIFIED

REFERENCES

- 5.2-1 Sasman, Phillip; Cresci, Robert "Compressible Turbulent Boundary Layer with Pressure Gradient and Heat Transfer" Brooklyn Polytechnics Report ARL 6565
- 5.2-2 Quinn, Robert D. and Palitz, Murray "Comparison of Measured and Calculated Turbulent Heat Transfer on the X-15 Airplane at Angles of Attack up to 19.0° . NASA TMX-1291 (Confidential)
- 5.2-3 G. Drougge "Measurement of Heat Transfer In a Highly Cooled Turbulent Boundary Layer at $M = 4.6$ & 7 FFA AU-120:4 Del II NASA Accession No. N67-25580
- 5.2-4 AiResearch Report AP-67-2536, "HRE Phase I Boiler Plate Engine Tests Final Technical Data Report (Confidential)"
- 5.2-5 J. E. Wnerer and F. I. Clayton "Flow Separation in High Speed Flight a Review of the State-of-the Art" Douglas Report SM-46429
- 5.2-6 Frank J. Zelezenik and Sanford Gordon "A General IBM 704 or 7090 Computer Program For Computation of Chemical Equilibrium Compositions Rocket Performance, and Chapman-Jouguet Detonations." NASN TND-1454
- 5.2-7 L. H. Back, P. F. Massier & H. L. Gier" Convective Heat Transfer in a Convergent-Divergent Nozzle" JPL Technical Report 32-415
- 5.2-8 Eli Reshotko and Maurice Tucker "Approximate Calculation of the Compressible Turbulent Boundary Layer With Heat Transfer and Arbitrary Pressure Gradient" NACA TN 4154
- 5.5-1 AiResearch Report AP-67-2537, HRE Structures and Cooling Development, Second Interim Technical Data Report (Confidential)
- 5.5-2 J. A. Fay and F. R. Riddell, "Theory of Stagnation Point Heat Transfer In Dissociated Air" Journal of Aeronautical Sciences, Vol. 25 Na 2, Feb 1958
- 5.5-3 Kreith, "Principles of Heat Transfer" 2nd Edition, 1966, International Textbook Co., Scranton, Penn.
- 5.5-4 Pinckney, "Flat-Plate Compressible Turbulent Boundary-Layer Static Temperature Distribution with Heat Transfer", 25, 1967 AIAA Paper No. 67-195



UNCLASSIFIED

REFERENCES (Continued)

- 5.5-5 Simon and Kowalski, "Charts of Boundary-Layer Mass Flow and Momentum for Inlet Performance Analysis Mach Number Range 2 to 5.0", TN 3583
- 5.7-1 Martin Company Report ER-14535,, "Design of X15A-2 Thermal Protection System"
- 5.8.2-1 Plantena, F. J., Sandwich Construction, John Wiley and Sons, 1966



AIRESEARCH MANUFACTURING DIVISION
Los Angeles, California

UNCLASSIFIED

This material contains information affecting the national defense of the United States within the meaning of the espionage laws, Title 18, U.S.C., Sections 793 and 794, the transmission or revelation of which in any manner to an unauthorized person is prohibited by law.

Downgraded at 3 year intervals.
declassified after 12 years
DOD DIR 5200.10

6. DESIGN EFFORT

During the reporting period, the revised aerodynamic loads have caused changes in the design of the leading edge, the outer shell, and, to a lesser extent, the inlet spike and its mounting cone. In addition, the inlet spike actuator mechanical design is being reviewed and is expected to undergo revision. Work associated with these design revisions is currently in process.

In addition to the layout design effort discussed in this section, a large portion of the design effort was devoted to preparation of detailed drawings for the nozzle, the inner shell, the leading edge, and the inlet spike. In the case of the leading edge and the inlet spike, drawings prepared and released for manufacture were for those areas not expected to be affected by design revisions. Only limited detail design drawings for the outer shell had been started before all effort was stopped pending evaluation of the impact of new loads on the design. In all cases, the much earlier released drawings for the component shells remained active and fabrication of shell tooling and of shells themselves is proceeding. This is entirely feasible since possible changes in shell strength requirements can be readily accommodated by ring stiffening.

The layout design effort during the reporting period included work in the following areas:

- a. Qualification test engine
- b. Inner body test assembly and adapter.
- c. Inlet spike actuator

6.1 QUALIFICATION TEST ENGINE

Layout design of the qualification test engine, aimed at establishing a preliminary configuration, was continued and completed even though details for various components would be revised as a result of the load changes previously discussed. In general, the validity of the work performed on engine layout is not expected to be affected by changes in component detail design. Rather, the layout constitutes the basis for establishing component interfaces, packaging of subsystems and components, assembly and disassembly procedures, and plumbing arrangements.



UNCLASSIFIED

6.1.1 Design Ground Rules

Layout Drawing L980615, Sheets 1 and 2, shows the completed layout for the qualification test engine, configuration No. 1. This drawing reflects the following considerations:

- a. The engine operates in the free stream, not in the shock field of the X-15A-2, at $M = 8$, 88,000 feet, dynamic pressure = 1800 psfa.
- b. Inlet unstarts are symmetrical and produce no normal loads in addition to those encountered in normal engine operation.
- c. The interface of the engine with the thrust measuring system, that is with pylon-mounted structure, occurs on the engine side of the engine mounts, as shown in the layout drawing. This interface is arbitrary and is used only to define the interface of the Structures and Cooling Development effort. The design of the thrust measuring system and of the engine mounting system is necessarily closely related to design of the engine structures. Thus, dynamic analysis of the engine will be carried through the thrust measuring system, the mounting structure, and to the air frame, since the flexibility and the response of this equipment directly influences the dynamic performance of the engine and is, in turn, influenced by the engine. Similarly, design of the thrust measuring and mounting systems are coordinated with the design of the engine, starting at the preliminary stages. In summary, the interface arrangement is arbitrary and reflects a drawing rather than a functional arrangement.
- d. As an objective, all hydrogen plumbing connections are made by either welding or brazing. The use of seals and threaded fasteners is limited to the minimum required for assembly and disassembly of major components, and access to the various subsystems. Replacement of certain of the components is complicated by this approach, but the chance for hydrogen leakage is considerably reduced. The latter is considered the more important objective.
- e. Hastelloy X is used on all regeneratively cooled structures. Inconel 718 and Type 347 corrosion resistant steels are used in selected areas. Specifically, all connecting tubing used in the engine is made from CRES, since the maximum temperature expected in any of the tubing lines is below 1200°F. The actuator is fabricated from 17-4 pH steel and the nitrogen storage tank from Inconel 718, as is the bellows that seals the interface between the inlet spike and the inner shell.

6.1.2 Features

The engine layout drawing shows the arrangement of equipment in the engine. Sheet 2 of the layout drawing shows sections through the inner body cavity that were used to establish packaging configuration and plumbing arrangements. In the following discussion, reference will be to Sheet 1 of the drawing. Figure 6.1-1 shows the flow routes and temperatures used to design the engine. The



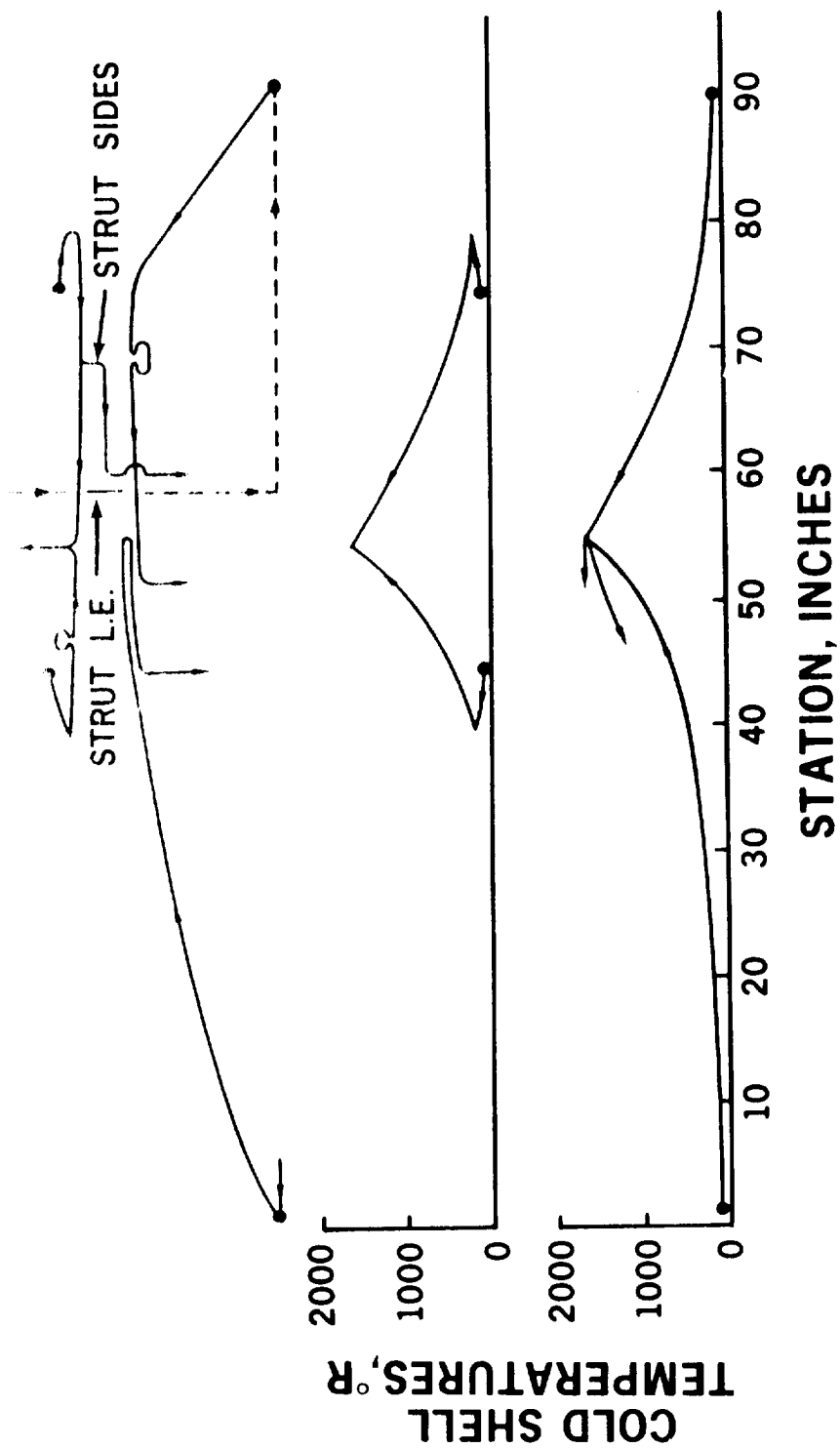


Figure 6.1-1. Engine Flow Routes and Temperatures

UNCLASSIFIED

temperatures shown in the figure are important as they directly affect the mechanical design aspects. The cold shell temperatures shown are identical for all practical purposes to the hydrogen temperatures at the appropriate stations.

The engine assembly procedure of completed full-scale components and the various features of the engine are described in the following steps:

- Step 1. The outer shell is positioned over the inner shell and the strut cutouts are aligned. After this, the struts are installed with their gasketing (nickel) and bolted in place. This assembly constitutes the backbone for all subsequent assembly work.
- Step 2. The fuel valves are installed as an assembly and bolted to individual mounting brackets on the manifold serving the second injector station. These valves are interconnected by tubing which forms the fuel plenum. This tubing is provided with bellows corrugations between the valves to allow for differential expansion between the inner shell and the valve assembly. Connecting lines to the fuel plenum and the valve outlets are welded in place as part of the valve assembly.
- Step 3. All plumbing lines connecting the outer shell to the fuel plenum and valves are installed through the struts and fitted up to the mating lines. Lines from the inner shell to the fuel plenum are similarly fitted. All lines have brazed sleeves preinstalled with braze rings in place. Connections are then bonded using a hand held induction brazing tool.
- Step 4. The asbestos packing on the forward end of the inner shell is installed.
- Step 5. The inlet spike is installed in place over the inner shell. The sealing bellows flange is bolted to the inner shell. Bellows serving the spike (spike coolant inlet, spike coolant outlet, and injector manifold) will have been preinstalled in the inlet spike and are now connected to the fuel plenum or valve, as required, using a clamped connection ("conoseal" type).
- Step 6. The inlet spike actuator is bolted to the inner shell mounting pads and the inlet spike mounting cone is bolted to the actuator flange. At this time, the position of both the inlet spike and the actuator itself are adjusted to assure concentricity between the inlet spike and inner shell and to true the axial travel of the inlet spike and actuator relative to the inner shell. Shims are used to accomplish this at the actuator mounting pads, while the spike adjustment relative to the actuator is accomplished by providing suitable clearance holes in the mounting flanges. The instrumentation package shown at the forward end of the actuator is preinstalled.



UNCLASSIFIED

UNCLASSIFIED

- Step 7. The leading edge assembly is bolted to the outer shell and the tubing connections from the leading edge to the manifolds provided in the outer shell are braze-joined.
- Step 8. The nitrogen storage tank is bolted to the mounting ring provided on the inner shell and the nitrogen supply and pressure regulator lines are connected to the tank.
- Step 9. The controls components are installed on the mounting plate provided on the nitrogen tank.
- Step 10. The nozzle is bolted to the inner shell using the access provided through the nozzle cap. At this time, the nozzle instrumentation connections (connector installation not shown) also are made.
- Step 11. The nozzle components are installed.

Upon completion of these operations, the engine is ready for mounting to the thrust measuring system and for joining the hydrogen lines to pump discharge line, and the turbine inlet and dump lines. Electrical lines will already be installed with quick disconnect fittings for attachment to aircraft wiring. All required wiring must pass through the strut cavity and is installed simultaneously with the plumbing (step 3). Leakage tests at proof pressure follow all hydrogen circuit joining operations. (These tests were not separately noted in the step-by-step discussion.) Both electrical and mechanical systems will be exercised following their installation to insure satisfactory functioning to established specification requirements prior to continuation of assembly operations.

The ablatively cooled cowl is installed after mounting the engine to the thrust measuring system. The cowl is mounted directly to the structure above the thrust measuring system to avoid drag inputs to thrust measurements. The cowl outline is indicated on the drawing for reference, but is not considered to represent a final configuration. Cowl contours and mounting details will be strongly influenced by the outer shell envelope. This envelope, in turn, will change as a result of the revised load conditions. Since layout design of the cowl had not been initiated when the revision of loads became known, only a preliminary structural analysis was performed as reported in Section 5.

Details of the routing of hydrogen lines through the struts are shown in the drawing for each of the six struts. The remaining space in the struts has been reserved for wiring. The reserved area is near the coolant inlet to the strut and is, therefore, the coolest area, with metal temperatures near room temperature at design conditions. Wiring is run here to reduce the need for thermal shielding.

The interface of the engine with the pylon leading edge is indicated in the drawing. The joint between the pylon and adjacent structure requires sealing and ablative protection. Restraint on the engine due to this joint would introduce inaccuracies into the thrust measurement and must be avoided.



UNCLASSIFIED

Alternatively, the pylon leading edge could be repositioned relative to the engine to intersect the ablatively cooled cowl. Because of the envelope restrictions that exist for the leading edge, the most desirable approach to repositioning is to move the engine forward by several inches on the pylon relative to the position shown. The possibility of doing this is being investigated. Shortening of the external leading edge surface is unattractive because of the space requirements for a smooth interface between the leading edge external surface and the ablatively-cooled cowl external surface. Since both engine X-15 integration studies and engine structures design were being carried on at the same time, this interface problem was deferred pending resolution of the overall pylon packaging problem.

6.1.3 Maintenance and Refurbishment

The basic approach to engine assembly and disassembly has assumed that refurbishment and maintenance of the type requiring replacement of hydrogen system components generally will be accomplished at the factory level. This assumption is based on a coordination meeting conducted at Edwards Air Force Base with NASA Flight Research Center personnel. Access to all electrical components, however, is possible in the field. The procedures involved in replacement or maintenance of various components are described in the following paragraphs:

- a. Refurbishment of the leading edge. Inlet and outlet lines must be cut (brazed connections) and the leading edge removed after unbolting of the flange connection with the outer shell. Installation of a new leading edge requires that new braze connections to the manifolds be made. The induction brazing operation required here can be accomplished with relative ease using portable equipment and could be done in the field, if necessary.
- b. Replacement of strut. This requires that lines and electrical wires passing through the strut be cut or unsoldered, as required, and removed. To permit cutting of the lines in the inner body, disassembly of the control equipment, the nitrogen tank, and the actuator is required. This work would be performed at the factory level.
- c. Access to instrumentation mounted in the spike. The control and instrumentation packages mounted in the nozzle area, the nitrogen tank, and the inlet spike actuator must be removed. No cutting of hydrogen lines is required. This work can be performed in the field.
- e. Removal of the inlet spike. The leading edge must be removed, as described above, the inlet spike actuator must be removed along with equipment to the rear of the actuator, the bellows clamps connecting spike hydrogen lines to the fuel plenums and valves must be removed, and the sealing bellows must be unbolted. All joints involved in this operation, except the leading edge hydrogen lines, are mechanical.



UNCLASSIFIED

UNCLASSIFIED

- e. Replacement of inner or outer shells. As may be deduced from the description of the assembly sequence, this requires complete stripping of the engine and involves a more or less rebuilding operation.

All operations requiring access to the center body cavity are performed with the nozzle removed in a sequence which is the reverse of that used on assembly. No lines must be cut to accomplish this and standard wrenches only are required for assembly or disassembly.

6.2 INNER BODY TEST ASSEMBLY

The inner body full-scale components, as fabricated, are suitable for static burst and creep-rupture testing. A special adapter is required for installation of the inner body assembly in the flow test ducting. Layout design of this assembly and the test adapter has been completed and is shown in Drawing L980614.

6.2.1 Design Ground Rules

The principle objective in design of the test assembly was to form a single deliverable unit (the innerbody and its adapter) ready for installation in the test ducting, with only external water, hydrogen, and instrumentation connections required. This objective has been accomplished. A equally important requirement in terms of evaluating test results was that the restraints imposed on the innerbody component approximate those encountered in the engine installation. For this reason, the actuator support structure is simulated. Because the test is performed with subsonic flow, full-scale struts will not be used. Such struts would not contribute to shell evaluation are themselves already being evaluated with supersonic flow at appropriate Mach numbers and with panels that simulate the inner shell. The strut openings in the inner shell are capped for purposes of the flow tests. Because the test assembly constitutes a confined space at high absolute pressure during testing, hydrogen leakage into the cavity must be assumed to result either in burning or detonation in the presence of air. Inerting of the inner cavity was therefore an important objective.

6.2.2 Features

With reference to layout drawing L980614, the following features of the test assembly are noted:

- a. Flow over the innerbody is reversed relative to the engine installation, so that flow is from the nozzle cap over the nozzle and the inner shell. The possibility of testing in this manner was investigated to minimize extraneous development effort associated with the seal at the interface between the adapter and the inner body. The large temperature differential at this point results in an awkward sealing problem. On the other hand, leakage of the inerting gas into the flow stream, with the adapter located upstream of the inner body, would be objectionable because of its effect on data correlation.



UNCLASSIFIED

UNCLASSIFIED

Hot gas flow reversal was investigated in terms of the absolute temperatures that result on the shells, the temperature gradients on the metal, and the metal temperature differences. The objectives of the tests in terms of these temperatures could be met with reversed hot gas flow and without introduction of extraneous loads on the structure. Consequently, this test arrangement was adopted.

- b. The inner body is structurally mounted to the adapter in a way simulating the installation of the inlet spike actuator in the inner-body. This is done to provide the restraint offered by the actuator mounting struts on the inner body.
- c. A spring seal is used between the adapter and the inner body. This seal will leak inerting gas into the hot gas stream. This method will be acceptable with the current arrangement.
- d. A relief valve is provided to vent inner body cavity pressure to the hot gas duct at a preset limit. It is expected that during normal operation, positive cavity-to-duct pressure differentials between two and five psi will be maintained by introduction of nitrogen gas into the cavity. The relief valve is provided to limit the pressure differential to 30 psig in the cavity during hot gas duct transient conditions. The test abort procedure will be programmed to first shut down the hydrogen supply to the in-line combustor and to the test unit, in sequence, and purge each of the hydrogen systems. Only after this has occurred is the airflow to the unit reduced; the relief valve is sized to accommodate this situation rather than instantaneous shutdown of the air also. During normal shutdown, hydrogen flow is gradually reduced to the combustor and pressure changes are mild and controllable. Similarly, during test startup, pressure buildup is controllable. The combination of a spring-loaded seal and the relief valve are expected to be adequate to prevent overloading of the inner body due to internal pressures.
- e. The hydrogen inlet line (View A of Drawing L980614) is enclosed by a second tube to prevent water freezing in the strut under the planned cryogenic conditions.
- f. The end plate of the test adapter has been made removable. This has been done to permit use of this adapter for testing of the inlet spike. For testing of the innerbody, access is provided through the nozzle. Access from one end only is available in the spike. For the same reason, the inner body mounting structure has been flanged and bolted to the adapter to permit removal and replacement of a fitting for attachment of the inlet spike mounting cone.
- g. The strut holes in the inner shell are blanked off with water-cooled panels shaped to the hole outline. An asbestos seal is provided between the blanked off panel and the strut socket to prevent the escape of inert gas into the hot gas stream. Mounting bolts for the water-cooled panels have been made long and are fitted through clearance holes to allow for differential growth between the panel and the shell and to avoid damage to the water-cooled panel.



UNCLASSIFIED

UNCLASSIFIED

- h. The material used for the test adapter is 1020 carbon steel. This material has approximately three times the thermal conductivity of CRES and simplifies the cooling problem for the test adapter. Corrosion protection will be provided using commercially-available coatings.

6.2.3 Assembly

The test adapter will be fabricated as a complete unit. All water, hydrogen, pressure sensing, and thermocouple lines will be installed. The end plate of the adapter is removed. Starting with the inner shell by itself, the mounting structure is placed in position and bolted to the inner shell mounting pad. Inner shell line connections and instrumentation connections are then made. The assembled inner shell is then bolted to the mounting flange in the adapter, through the adapter end opening, and the adapter end plate is bolted in place.

Before installation, the nozzle is brought to within approximately one foot of the inner shell and instrumentation connections are made. Instrumentation lines will be left sufficiently long to provide the necessary flexibility. The nozzle is then assembled to the inner shell in the same manner as used for normal engine installation and the nozzle cap close-out is made.

The assembly as shown in the layout drawing is delivered as a unit to the test facility for direct installation into the test ducting. Threaded connections are used for all internal and external hydrogen lines to facilitate assembly and disassembly. Accessibility of the fittings and the relative ease of reworking a fitting are expected to permit leak-free operation with this arrangement.

6.3 INLET SPIKE ACTUATOR

A discussion of the inlet spike actuator as shown on Layout Drawing LI09528, Sheet 4, was presented in the previous TDR (Reference 6-1). Layout Drawing LI09528, Sheet 5, presents the final configuration of the actuator. The design of the actuator, as shown in this drawing, was formally reviewed on 11 October 1967, during the Preliminary Design Review. None of the features and details of the actuator have been changed relative to the description contained in the reference report. Drawing PI09528-1 (3 sheets) is a schematic diagram and description of the actuator.

As discussed elsewhere, the design of the inlet spike actuator is currently being reviewed with a view toward substituting an hydraulic system for the pneumatic system presented in the layout drawing. The revised and much higher loads make the hydraulic system more attractive. If feasible, the hydraulic system is expected to lead to considerable simplification in design of the actuator itself. Overall system complexity, however, may be greater or less and cannot be assessed until the design work currently in process has been completed.

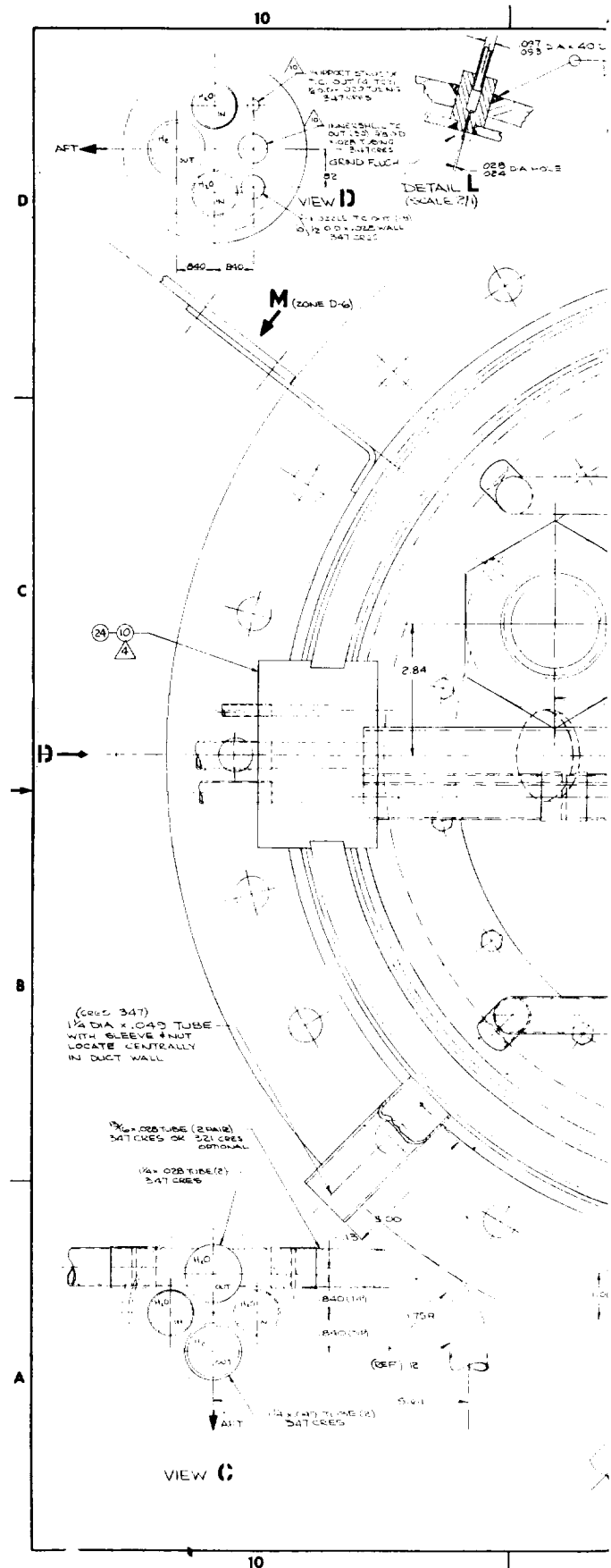


UNCLASSIFIED

The bearing loads resulting on the sliding surface between the two actuator sleeves have been increased to approximately 2000 psi for the revised normal-loading conditions. This is approximately three times higher than the previous bearing loads. The length-to-diameter ratio of the actuator shown in Drawing L109528, as well as the use of chrome-plated 17-4 pH steel, appear doubtful with the increased bearing loads. Consequently, consideration is being given to the following design changes:

- a. Increase in length-to-diameter ratio by fixing the actuator sleeve to the struts, fixing the piston, and translating the inner sleeve. (As shown in Drawing L109528, Sheet 5, the outer sleeve and piston translate while the inner sleeve is fixed.) By this means, the length-to-diameter ratio can be approximately doubled.
- b. Use of Teflon-impregnated fiberglass bearings on the inner sleeve. Preliminary information indicates that such bearings can sustain bearing pressures up to 13,000 psi at temperatures up to 450°F, if properly precompressed.





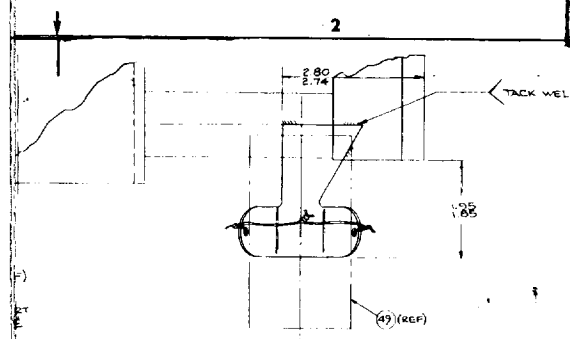
FOLDOUT FRAME /



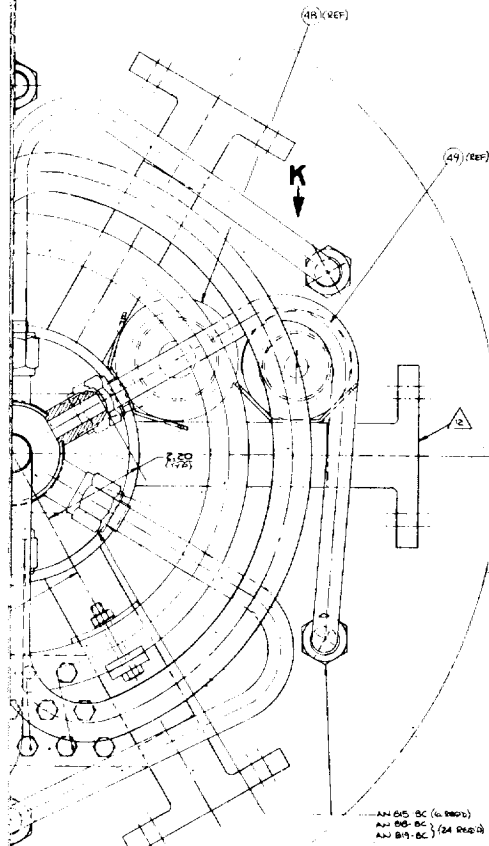
AIRESEARCH MANUFACTURING DIVISION
Los Angeles, California



UNCLASSIFIED



VIEW ON K
SHOWING BRACKET



QTY	PART NUMBER	DESCRIPTION	UNIT	MATERIAL	REMARKS	DATE	BY	APPROVED
57	980543-1	TERMINAL BOARD ASSY	1					
56	980020-1	INNER BODY ASSY	1					
55	482 255-1	CHECK VALVE	1					
54	0507-378	CONNECTOR - PLUG	1					
53	0504-378	CONNECTOR - RECEPTACLE	1					
52	0507-615	CONNECTOR - PLUG	1					
51	0504-615	CONNECTOR - RECEPTACLE	1					
50	980542-1	BRACKET	2					
49	980541-1	HOUSING - CONNECTOR	2					
48	980540-1	HOUSING - CONNECTOR	2					
47	980539-1	BRACKET	12					
46	980538-1	BRACKET	6					
45	980537-1	BRACKET	6					
44	980536-1	TUBE ASSY	1					
43	980535-1	TUBE ASSY	1					
42	980534-1	TUBE ASSY	6					
41	980533-1	TUBE ASSY	6					
40	980532-2	MANIFOLD ASSY	1					
39	980531-1	MANIFOLD ASSY	1					
38	980530-1	GASKET	6					
37	980529-1	PLATE PIN ASSY	6					
36	980528-1	DOOR ASSY	1					
35	980527-1	MANIFOLD ASSY	2					
34	980526-1	SHM - LAMINATED	1					
33	980525-1	TUBE ASSY	1					
32								
31								
30	980524-1	TUBE ASSY	2					
29								
28								
27								
26	980523-1	TUBE ASSY	2					
25	980522-1	STRUT BODY	8					
24	980521-1	STRUT BODY	3/6					
23	980520-1	SEAL	1					
22								
21								
20								
19								
18	980519-1	TUBE ASSY	1					
17								
16								
15								
14								
13	980518-2	2 TUBE (OPR ITEM 12)	11					
12	980518-1	2 TUBE	11					
11	980517-1	MANIFOLD ASSY	5					
10	980516-1	STRUT N1.4 ASSY	2					
9	980515-1	STRUT N1.5 ASSY	2					
8	980514-1	STRUT N1.2 ASSY	2					
7	980513-1	STRUT N1.1 ASSY	2					
6	980512-1	DUCT ASSY	2					
5	980511-1	FWD SUPPORT ASSY	2					
4	980510-1	AFT SUPPORT ASSY	1					
3								
2	980506-1	FWD TEST ASSY	1					
1	980505-1	TEST ASSY	1					

THESE TUBES TO EXTEND OUT OF STRUT SUFFICIENTLY TO RECEIVE A NUT & SLEEVE
INDIVIDUAL DEPTS TO BE DETERMINED DURING DETAILING. MGO-TC5 TO BE DRILLED IN AN
EXTERNAL TUBE (PER DEPT 94-4) PROVIDING A MATING SLEEVE & NUT FOR ASSY

FURNACE BRAZE PER AIRRESEARCH SPEC WBS-27 USING
FURNACE 7 BRAZING ALLOY
ADDITIONAL THERMOCOUPLE READINGS TO BE TAKEN AT EACH END OF CONNECTOR
TO CHECK DESIRED UNIFORM TEMPERATURE AROUND CONNECTOR PER DEPT 94-4

FINISH ON SUPPORT STRUCTURE (INTERNAL WATER SURFACES ALSO)
ALL CARBON STEEL PARTS:- SANDBLAST, WELD, DEGREASE
BLOW DRY, APPLY 2 COATS OF EPOXY PRIMER PER AIRRESEARCH SPEC
PR25 TYPE I, C, C, BAKE AT 300°F FOR 1HR AFTER SECOND COAT

TORCH BRAZE PER AIRRESEARCH SPEC WBS-27 USING SILVER
BRAZING ALLOY PER QQ-S-561 CLASS B

THIS GAP MUST BE KEPT TO A MINIMUM TO ACCOMMODATE
EXPANSION OF STRUT HOUSING

EXTERNAL TUBES EMERGING FROM STRUTS TO EXTEND 1" THEN BEND
AWAY FROM STRUT CENTER 2" OR +45° (SEE DRAWING 9) WHERE NECESSARY
TO ADD SLEEVE & NUT FOR EXTERNAL CONNECTION INDIVIDUAL REQUIREMENTS
TO BE DETERMINED DURING DETAILING

FURNACE BRAZE PER AIRRESEARCH SPEC WBS-27 USING
N1000 PER ASTM B-260 BAY-4 BRAZING ALLOY

PENETRATION WELD 20%-40%

WELD PER AIRRESEARCH SPEC WBS-18

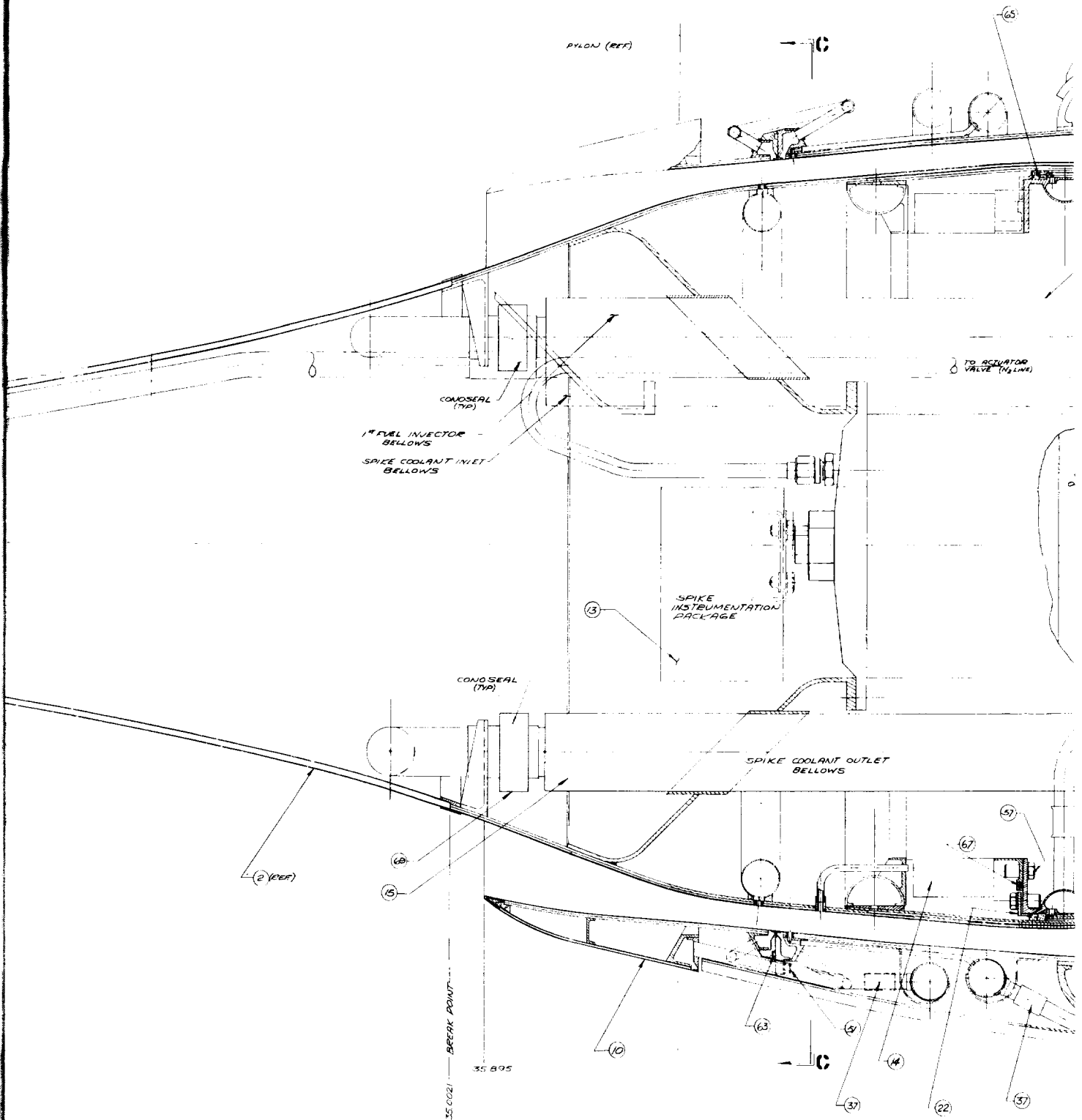
NOTES UNLESS OTHERWISE SPECIFIED

FOLDOUT FRAME 5

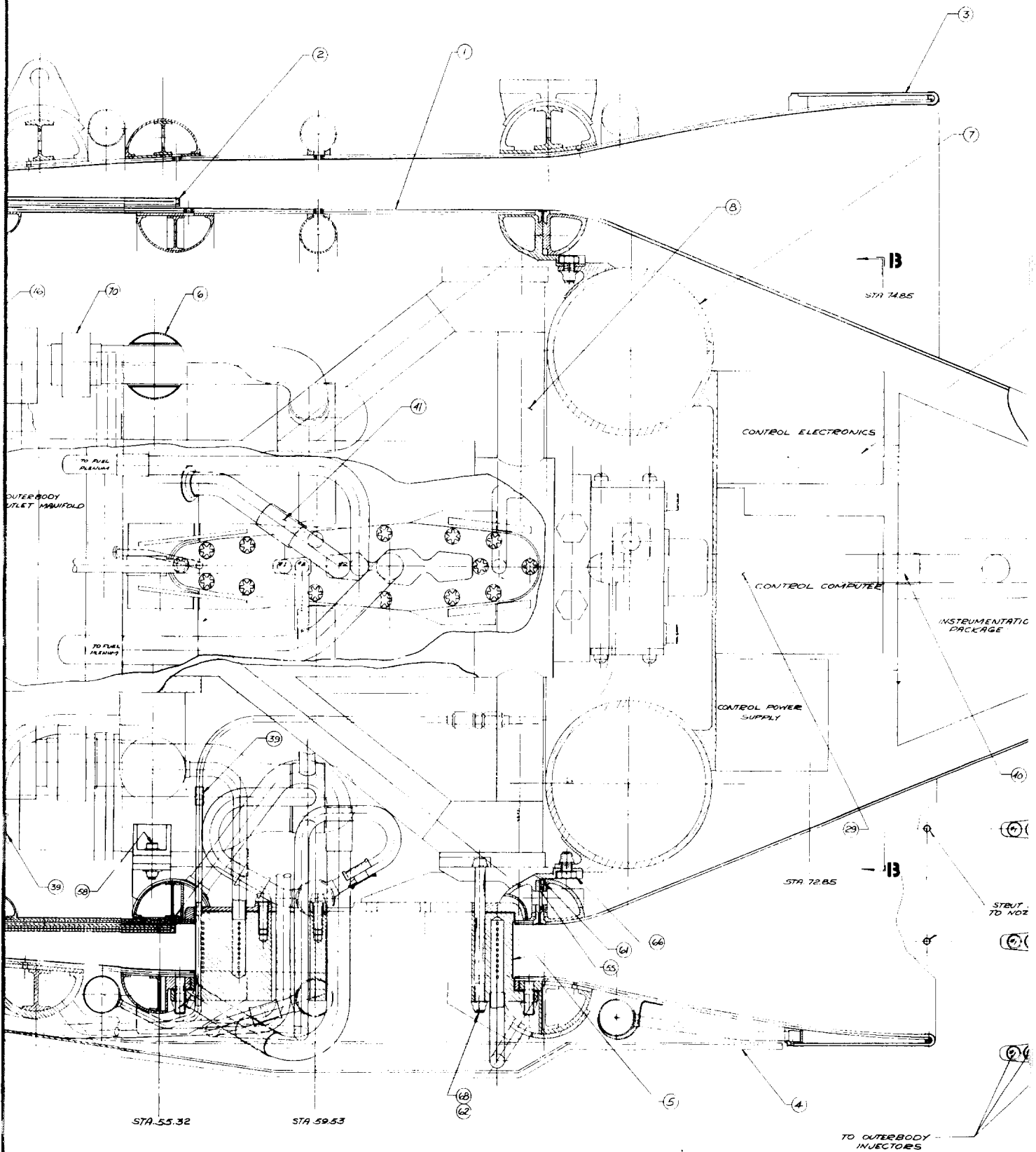
C-2431

STA 000

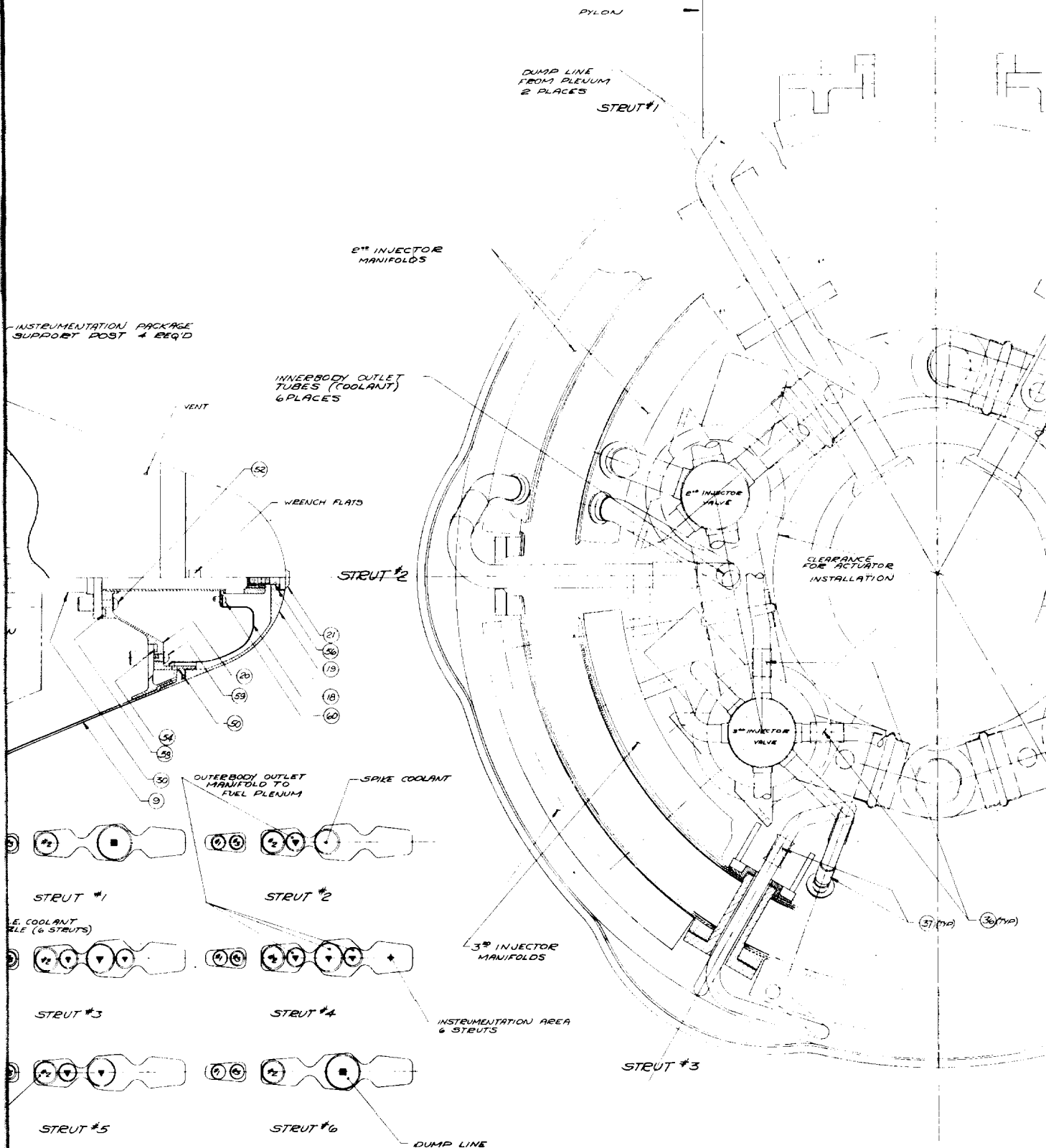
FOLDOUT FRAME 1



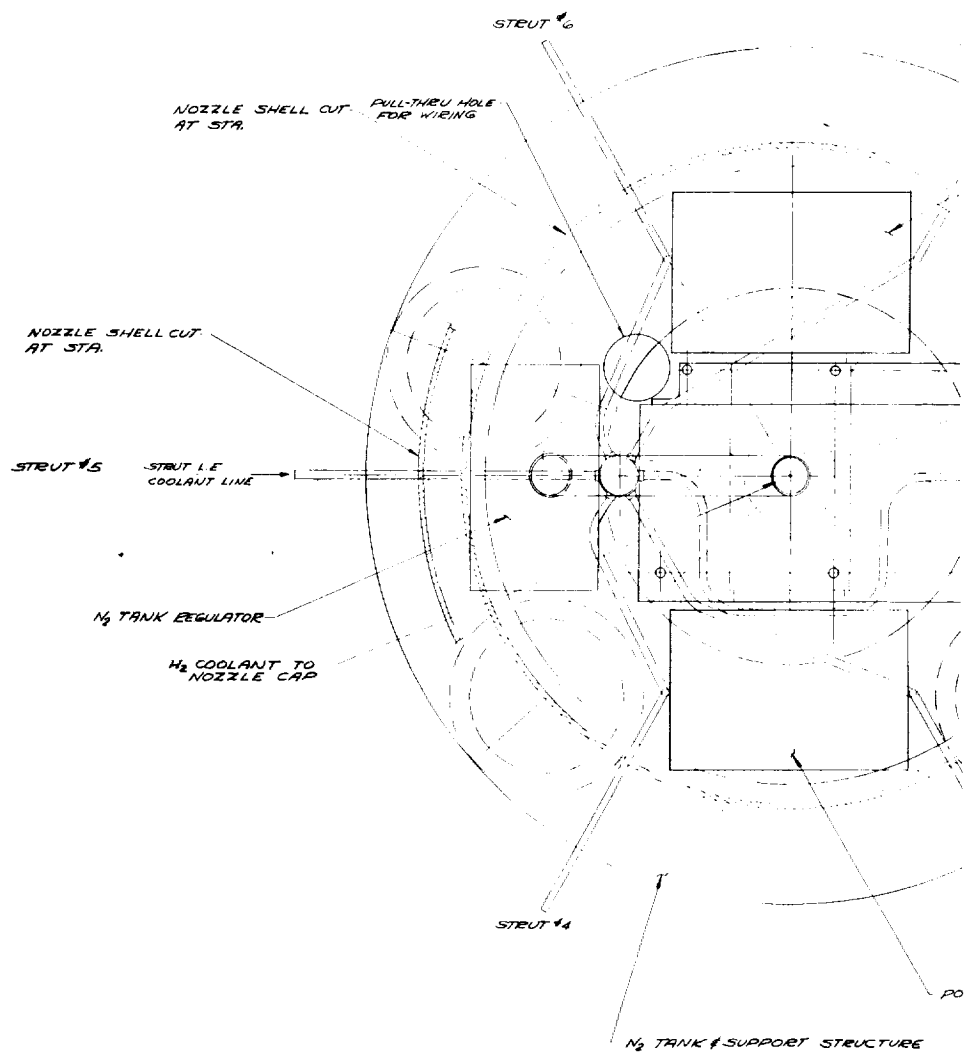
FOLDOUT FRAME 2



FOLDOUT FRAME 3

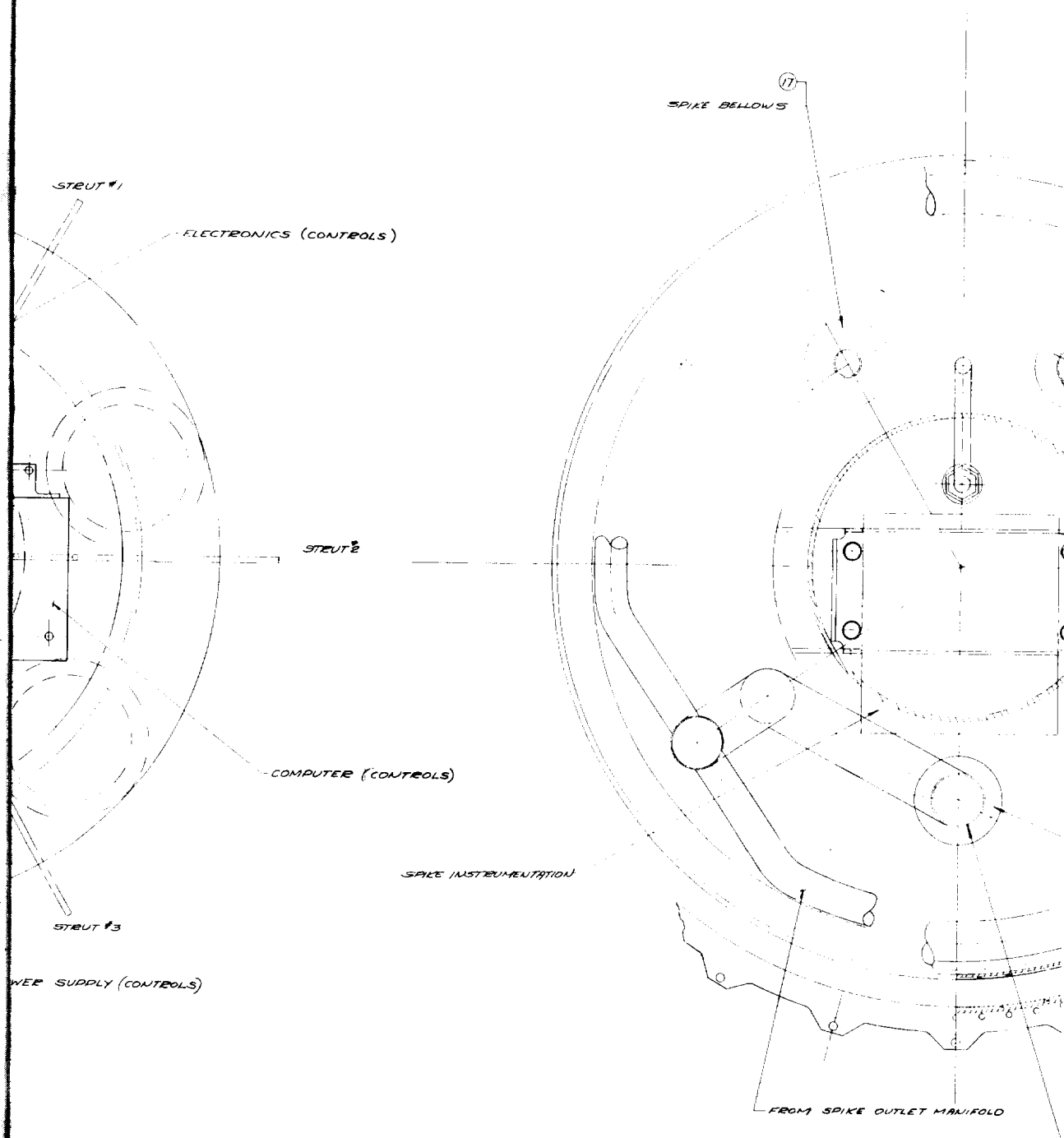


FOLDOUT FRAME 4



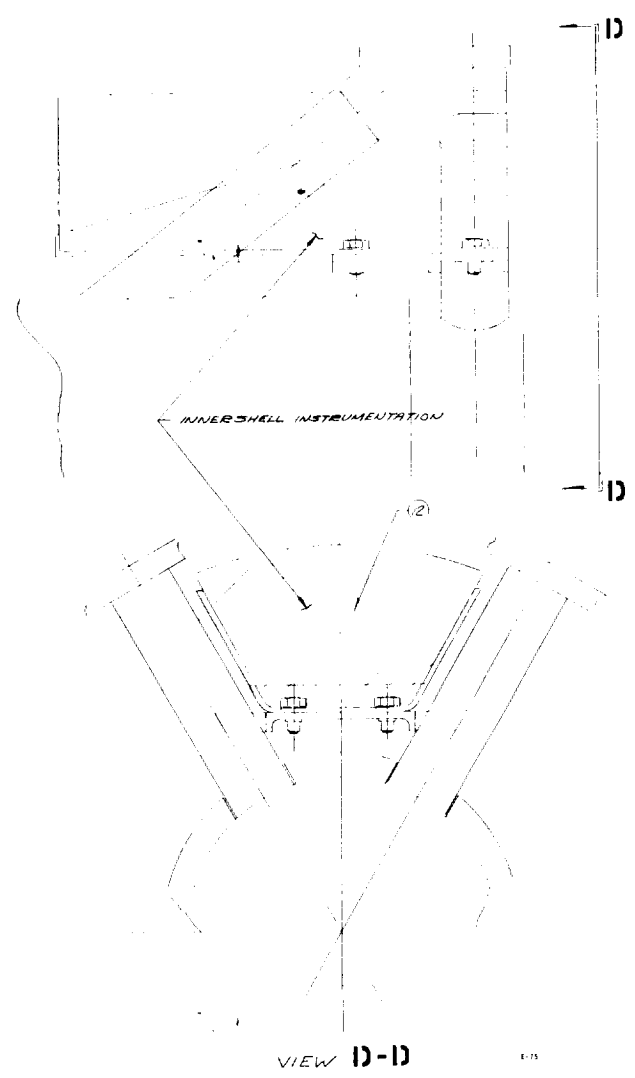
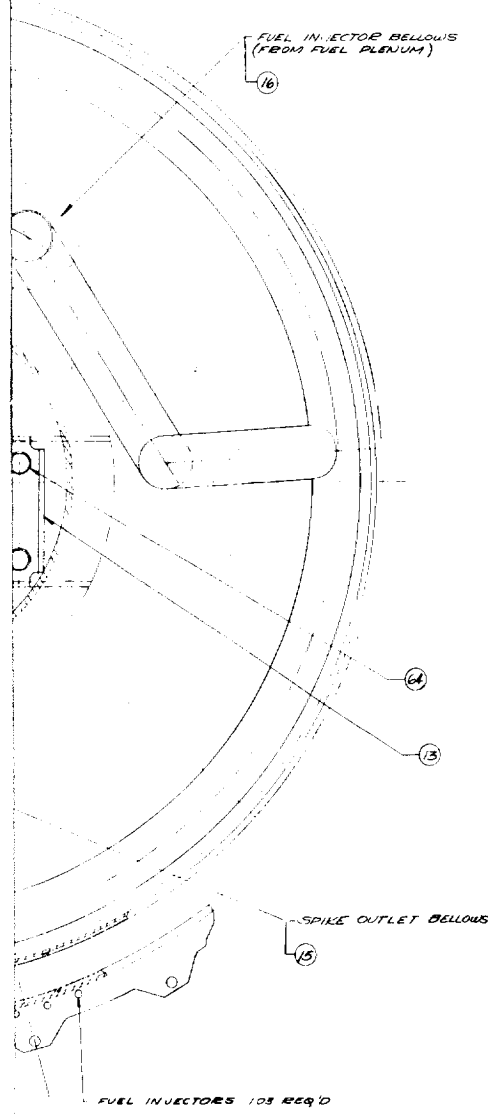
SECTION 13-13

FOLDOUT FRAME



SECTION C-C

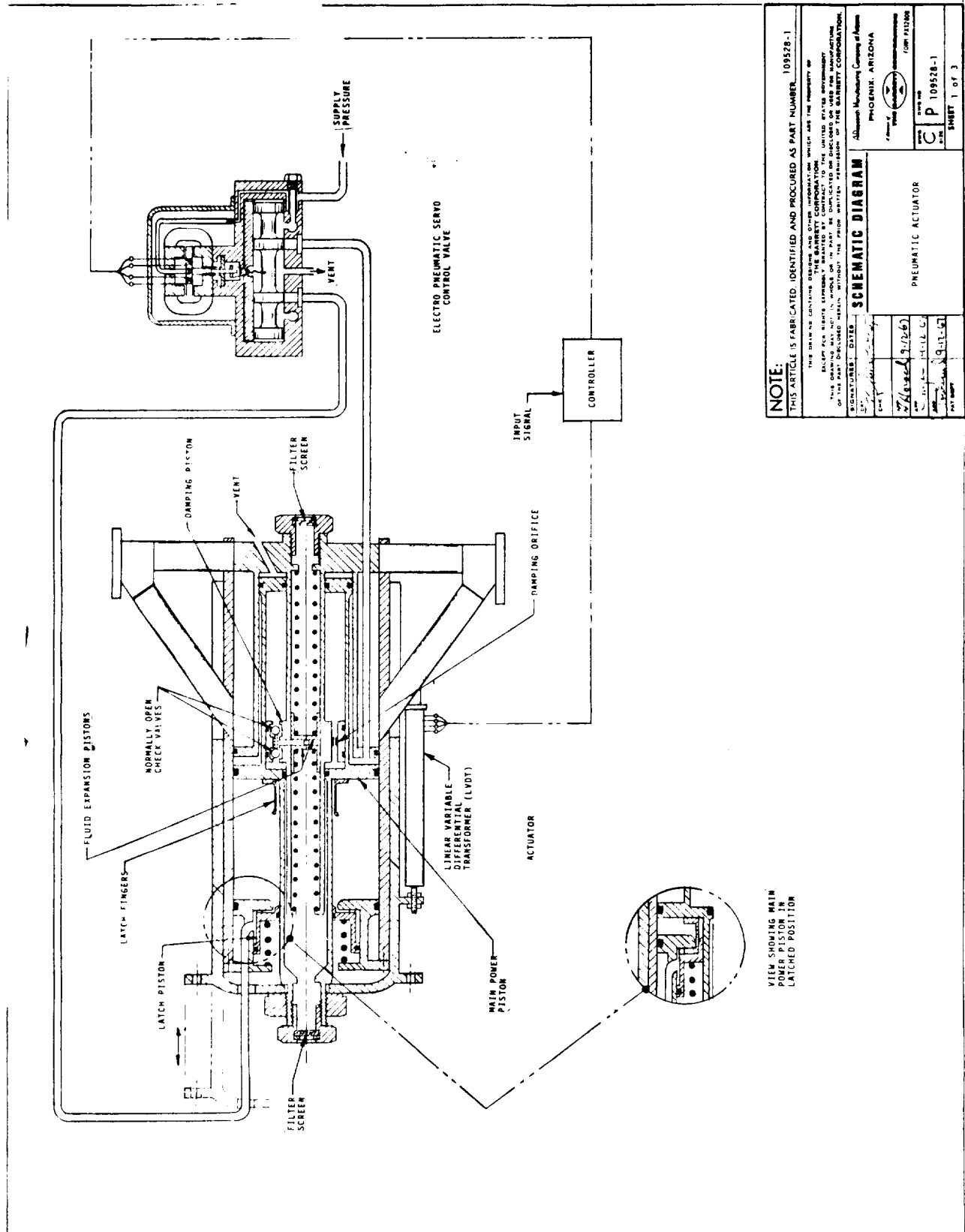
UNCLASSIFIED



AIR RESEARCH MANUFACTURING COMPANY <small>A DIVISION OF THE AIRCRAFT MANUFACTURING COMPANY</small>			
LAYOUT			
QUALIFICATION TEST ENGINE			
CONFIGURATION N° 1			
HSE			
REV	DATE	BY	CHK
70210		L	980615
SCALE FULL	WT		SHEET 2 OF 2

FOLDOUT FRAME 3

UNCLASSIFIED



AIRESEARCH MANUFACTURING DIVISION
Phoenix, Arizona

UNCLASSIFIED

UNCLASSIFIED

THIS DRAWING CONTAINS DESIGNS AND OTHER INFORMATION WHICH ARE THE PROPERTY OF
THE GARRETT CORPORATION.
EXCEPT FOR RIGHTS EXPRESSLY GRANTED BY CONTRACT TO THE UNITED STATES GOVERNMENT
THIS DRAWING MAY NOT, IN WHOLE OR IN PART, BE DUPLICATED OR DISCLOSED OR USED FOR MANUFACTURE
OF THE PART DISCLOSED HEREIN, WITHOUT THE PRIOR WRITTEN PERMISSION OF THE GARRETT CORPORATION.

Description:

This unit is an electro-pneumatic servo controlled pneumatic powered, piston type, hydraulically damped, linear actuator. The unit consists of three primary elements, the electro-pneumatic servo control valve, the pneumatic linear actuator, and a linear, variable, differential transformer. Also required but not included with the unit, is an electrical controller which will provide the electrical signal necessary to satisfy the actuator position.

With actuator supply pressures above the minimum operating pressure to overcome the actuator load requirements, the actuator is positioned by supplying an input signal to the electrical controller. The controller, in turn, supplies an electrical error signal to the electro-pneumatic servo control valve which converts the electrical signal to a delta pressure output. The pressure output then is supplied across the main actuator power piston. The control valve either pressurizes or vents the respective sides of the power piston as required by the electrical controller.

The position of the actuator is sensed by the linear, variable, differential transformer (LVDT) and converted into an electrical signal and fed back to the electrical controller to reduce the error signal which, in turn, modulates the servo control valve until the actuator reaches the desired position.

The pneumatic actuator incorporates several design features which enhance the performance of the unit. These features are: (1) Hydraulic damping, (2) Hydraulic fluid expansion compensation, and (3) A mechanical latch mechanism for the extended position.

A piston type dash pot is provided for hydraulic damping. Under static conditions the normally open check valves allow fluid flow in and out of the fluid expansion chamber. As the fluid expands, the static pressure increases and overcomes the spring load behind the expansion pistons and the position of the piston adjusts to compensate for the fluid expansion.

NOTE:

THIS ARTICLE IS FABRICATED, IDENTIFIED AND PROCURED AS PART NUMBER 109528-1

SIGNATURES		DATES	SCHEMATIC DIAGRAM	AirResearch Manufacturing Company of Arizona	
DRF	<i>T. H. H. H.</i>	9-12-67		PHOENIX, ARIZONA	
CHK				A division of THE GARRETT CORPORATION	
APP	<i>H. H. H.</i>	9-12-67		PNEUMATIC ACTUATOR	
APP	<i>J. H. H.</i>	9-12-67		UNCLASSIFIED	
APP	<i>J. H. H.</i>	9-12-67	DWG NO. P 109528-1		
PAT DEPT.			SHEET 2 of 3		

UNCLASSIFIED

THIS DRAWING CONTAINS DESIGNS AND OTHER INFORMATION WHICH ARE THE PROPERTY OF
THE GARRETT CORPORATION.
EXCEPT FOR RIGHTS EXPRESSLY GRANTED BY CONTRACT TO THE UNITED STATES GOVERNMENT
THIS DRAWING MAY NOT, IN WHOLE OR IN PART, BE DUPLICATED OR DISCLOSED OR USED FOR MANUFACTURE
OF THE PART DISCLOSED HEREIN, WITHOUT THE PRIOR WRITTEN PERMISSION OF THE GARRETT CORPORATION.

Description: (Continued)

The mechanical latch mechanism consists of a number of flexible fingers produced by longitudinal cuts on the cylinder parallel to the axis of the cylinder. The end of the cylinder (or the end of the fingers) incorporates a latch contour which when engaged enters a matching latch bore. The fingers deflect inward as the latch cylinder enters the latch bore. As the latch completes the stroke the latch fingers spring back (outwardly) to their natural position. After reaching the forward position and as the pressure decreases, the latch piston is driven forward by a return spring and the forward lip on the piston enters under the fingers and engages the latch.

The actuator is unlatched in a reverse manner.

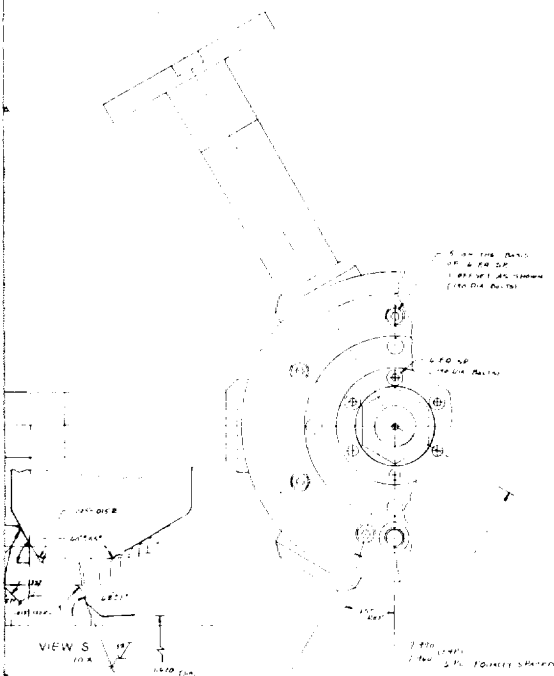
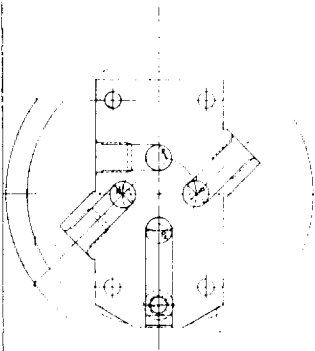
NOTE:

THIS ARTICLE IS FABRICATED, IDENTIFIED AND PROCURED AS PART NUMBER 109528-1

SIGNATURES		DATES	SCHEMATIC DIAGRAM	A/R Research Manufacturing Company of Arizona	
DRC	<i>T. J. [Signature]</i>	9-12-67		PHOENIX, ARIZONA	
CHK				A division of THE GARRETT CORPORATION	
APP	<i>R. H. [Signature]</i>	9-12-67		PNEUMATIC ACTUATOR	
APP	<i>J. [Signature]</i>	9-12-67			
APP	<i>U. [Signature]</i>	9-12-67			
PAT DEPT.			UNCLASSIFIED	DWG SIZE A	DWG NO. P 109528-1
				SHEET 3 of 3	



		REVISIONS				
		ZONE	LTR	DESCRIPTION	DATE	APPROVED
<p>This drawing contains information and other communications that are the property of THE GASSETTY CORPORATION. It is to be used only for the purpose for which it was prepared. It is not to be reproduced, copied, or otherwise used for any other purpose without the written consent of THE GASSETTY CORPORATION.</p>						

[illegible]

(A) - HARD CHROME PLATE
 (A) - DRY FILM TUBE
 (B) - CLEAN Pk 1/2 INCH 1/2 INCH
 (A) - HARD ANODIZED Pk 1/2 INCH 1/2 INCH
 1/2 INCH 1/2 INCH

PROPRIETARY NOTICE This layout contains information that is the property of the U.S. Government and is not to be distributed outside the U.S. Government.		LAYOUT PRODUCTION LAYOUT		
DRAWING NO. 28-1467 DATE 1-28-67	AUTH. 1-28-67 DATE 1-28-67	NAME INLET SPIKE ACTUATOR		DESK L-105510 DATE 8 OF 8

FOLDOUT, FRAME 3

7. MANUFACTURING

7.1 COMPOUND-CURVED MODELS

The compound-curved shell model shown on Figure 7.1-1 was designed to simulate in reduced scale the finned structure typical of the engine. To some degree, it incorporates the compound-curved contour characteristics of all HRE sections and, specifically, the inlet spike. The model was constructed to gain experience in fabrication, assembly, and brazing of compound-curved shell structures.

7.1.1 Shell Fabrication

The two most important considerations in fabricating the compound-curved models are: (1) to maintain the desired contour and size, after completion of assembly, and (2) to control shell thickness closely because of brazing fitup and heat transfer requirements.

To achieve these goals the following major operations were performed during the fabrication process:

1. Blanking and forming of frustro-conical shells, using slightly thicker material than required for the finished part, to allow for thinning during forming operations.
2. Welding and planish rolling of the butt joint in the formed cone.
3. Preforming to a size approximately one percent smaller in diameter than the finish dimensions.
4. Stress relief annealing.
5. Chem milling of the outside shell wall to a uniform thickness, which is 0.001 to 0.002-in. more than the finished dimension.
6. Abrasive polishing of the outside surface to remove material subject to intergranular attack during chem milling and to produce the final thickness.
7. Finish forming by the "Electroshape" electrohydraulic technique.



UNCLASSIFIED



Figure 7.1-1. Compound-Curved Model (Manifolds Omitted)



AIRESEARCH MANUFACTURING DIVISION
Los Angeles, California

UNCLASSIFIED

67-2833
Page 7-2

UNCLASSIFIED

Experience in forming approximately 20 shells has indicated two factors of direct bearing on full-scale component fabrication (1) the interrelationship of the preforming-annealing-chem milling sequence on subsequent material properties and (2) the special restraint requirements for the parts during Electroshape forming.

7.1.1.1 Preforming-Anneal-Chem Milling Interrelationship

A portion of the shells, particularly those fabricated from 0.020-thick material, exhibited reduced ductility after the chem-milling operation. Metallography samples showed dicated pronounced intergranular attack on the surface.

The chem-milling operation used for reducing the shell thickness after preforming utilizes an acid solution to dissolve metal from the surface. The quantity of metal removed is controlled by adjusting the time that the surface is exposed to the solution. The actual removal of metal, however, does not occur just on the outside surface, but also penetrates into the metal along the grain boundaries that are exposed to the surface. If grains are uniform and small, the attack into the metal is insignificant. However, if grain size is large, the intergranular attack is more pronounced. Under these circumstances, it is necessary after chem milling to remove more surface metal mechanically to avoid apparent reduction in strength and ductility because of the numerous points of stress concentration at the bottom of the attacked zone.

At the conventional annealing temperature of 2150°F, Hastelloy X that has been previously cold worked greater than 10 percent exhibits excellent return of ductility and uniform small grain size. Material that has been previously cold worked less than 10 percent, however, when annealed at 2150°F, tends to produce a duplex grain structure consisting of small and very large grains. By itself this type of grain structure does not have any marked effect on strength, but, as described above, is adversely affected by the chem milling operation. Preliminary work done by Haynes Stellite on the effect of annealing temperatures on grain size of partially cold worked Hastelloy X indicates that a degree of control can be achieved by reducing the annealing temperature. A limited annealing effect investigation, with the objective of achieving better control of grain size and post chem-milling properties, is currently in process.

7.1.1.2 "Electroshape" Requirements

A typical setup for "Electroshape" forming of a compound-curved shell is shown schematically by Figure 7.1-2. Success of the forming sequence depends on clamping the part securely between the seal surfaces at the top and bottom, filling the inside of the part with water, and evacuating the space between the part and the die cavity before discharge. Top and bottom sealing is achieved by clamping the trimmed edges of the shells into resilient gaskets. The technique is satisfactory for the duration of a single discharge; but, apparently because of the heavy lateral forces during discharge due to diameter differences, the small end of the shell buckles inward sufficiently to destroy the seal. It has been found necessary in a large percentage of the shells to



UNCLASSIFIED

UNCLASSIFIED

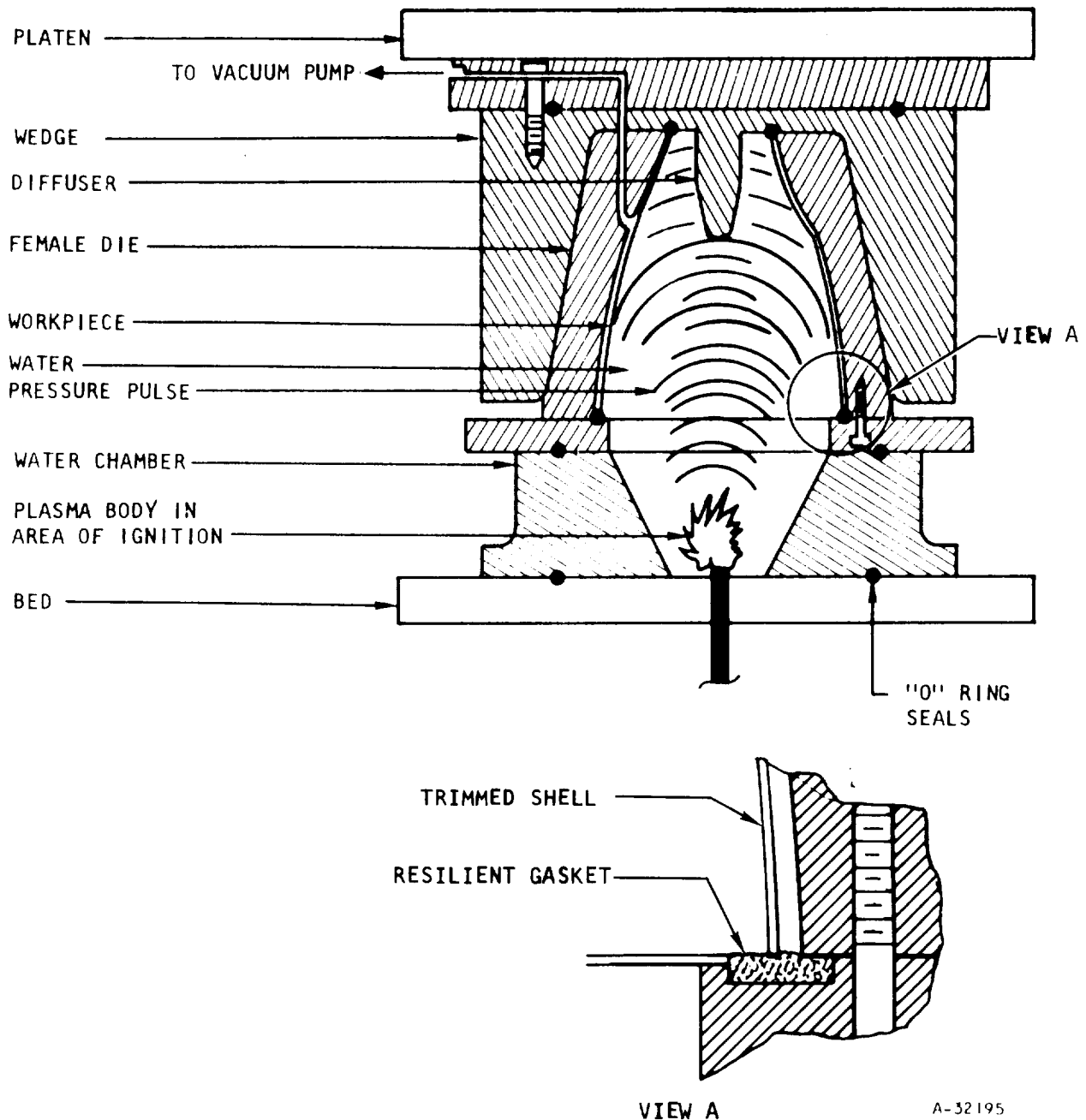


Figure 7.1-2. Electrohydraulic Forming of Shell



UNCLASSIFIED

UNCLASSIFIED

straighten the rim on the small end and to perform a second "Electroshape" operation in order to achieve the required final size and smooth contour. Restraint of the full-size, frustro-conical shapes by means of an added flange clamped under the die pocket has been incorporated in the fabrication procedure.

7.1.2 Brazing Evaluation

The objective of the brazing evaluation activity was the development of techniques and tooling for producing completely continuous fin-skin joints required for structural integrity, while maintaining precise surface contour and size. The size and shape of the shells before assembly can be controlled within close tolerances to provide the correct space for the fins; but, it is necessary to apply compressive loading on the fins to insure optimum joint conditions. The finished size and contour of the braze assembly is insured by using a graphite mold, machined to the exact size of the finished part at the selected braze temperature, and supplying sufficiently controlled internal pressure to the brazement to cause contact at the brazing temperature.

The assembly procedure prior to the actual brazing operation consists of the following major steps:

1. Thorough degreasing and chemical cleaning of all detail parts.
2. Attachment of a layer of braze alloy foil to the inner shell.
3. Attachment of the fins in the form of narrow circumferential strips and the headers.
4. Attachment of a layer of braze alloy foil to the outside of the fins.
5. Assembly of the outer shell.

Two methods of fixturing are being evaluated: one using a segmented expanding graphite plug to force the inner shell outward; the other, using pneumatic pressure to force the inner shell outward. Both methods employ the same external graphite form to control the final size and shape.

7.1.2.1 Segmented Graphite Plug

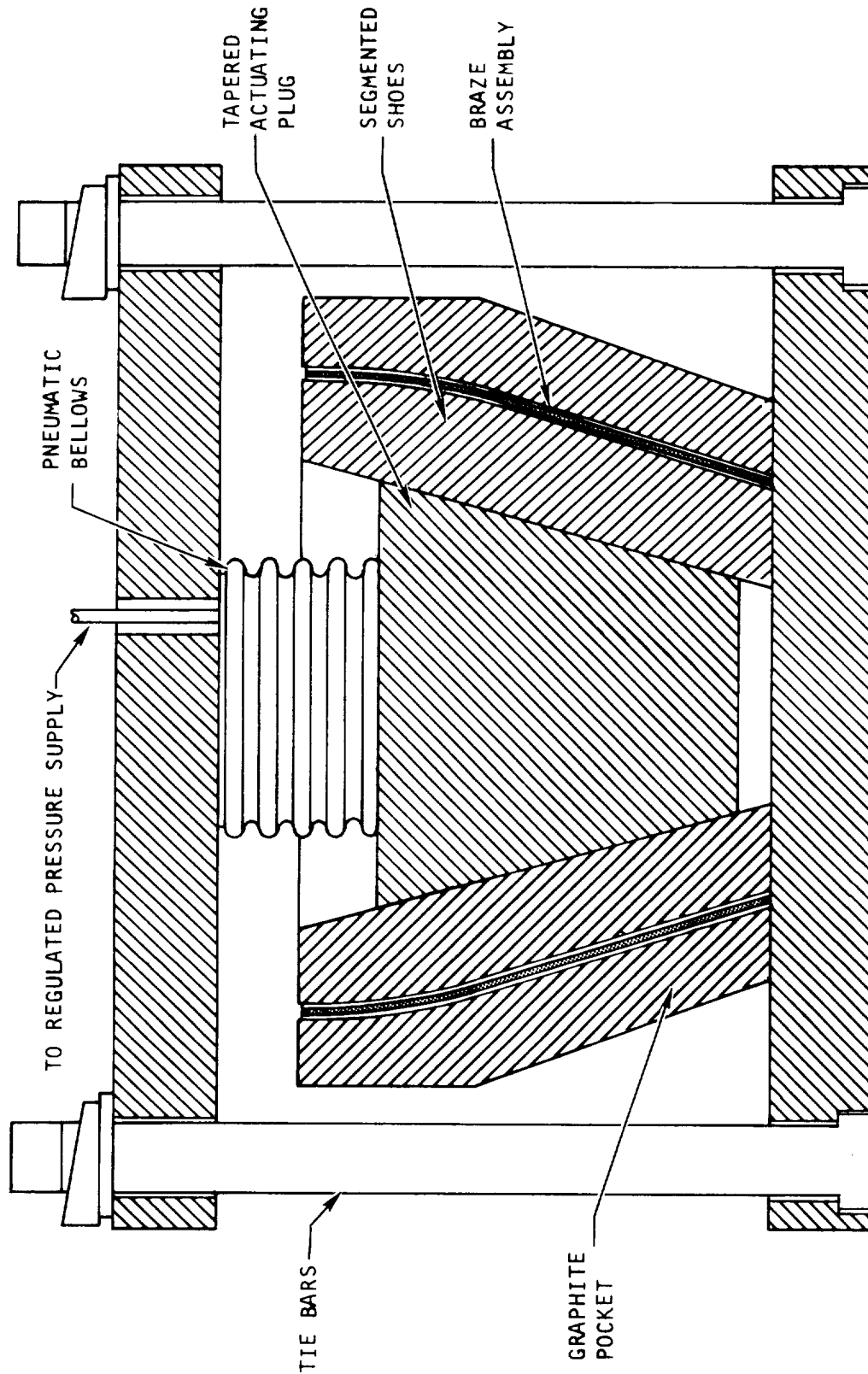
Two assemblies have been assembled and brazed, using the expanding plug technique. Figure 7.1-3 shows diagrammatically the major components of this setup, which include the graphite pocket outside, the braze assembly, the segmented shoes bearing against the inner shell, the tapered actuating plug, and the pneumatic bellows for applying the driving force to the plug.

Both assemblies were brazed in a vacuum furnace, using Palniro I alloy at a brazing temperature of 2070°F.

The first assembly, utilizing shells without headers that had been rejected for being slightly less the minimum allowable thickness, was brazed to tryout the setup. The appearance of the braze joints was good, and the assembly was pressure tested at room temperature.



UNCLASSIFIED



A-32193

Figure 7.1-3. Brazing Setup, Segmented Plug



AIRESEARCH MANUFACTURING DIVISION
Los Angeles, California

UNCLASSIFIED

UNCLASSIFIED

The second assembly setup featured refinements in bellows pressure control and additional tie bars. In-tolerance shells were used for this assembly. This unit was proof pressure tested at room temperature and later subjected to elevated temperature burst tests.

7.1.2.2 Pneumatically-Loaded Inner Shell

The second method of applying the internal loads to the inner shell to cause it to expand against the graphite outer pocket is shown diagrammatically in Figure 7.1-4. It consists of the graphite outer pocket and the braze assembly, which incorporates plates or an insert welded to the inner shell to permit pressurization.

The first assembly, using shells slightly below the minimum allowable thickness and no headers, incorporated plates welded to the inner shell at the top and bottom. Three internal straps were welded to the plates to resist bulging. The assembly was brazed in a vacuum furnace at 2070°F using Palniro I braze alloy. The applied internal pressure during brazing was 28 psia. The assembly appeared to be brazed satisfactorily and was dimensionally within tolerance.

The second assembly utilized a frustro-conical insert welded to the inner shell, and in-tolerance shells, and headers. This unit was brazed in a vacuum at 2070°F using Palniro I alloy. A pressure of 28 psia again was applied during brazing. Except for slight local bulging of the insert, the brazing cycle was completed without incident. The unit was room temperature proof pressure tested and later subjected to a high temperature burst test.

7.1.3 Current Status

Further developmental activities on the graphite insert fixture approach to compound curved model brazing are being discontinued. Remaining evaluation activities will be concentrated on improving techniques for pneumatically pressurizing the inner shells.

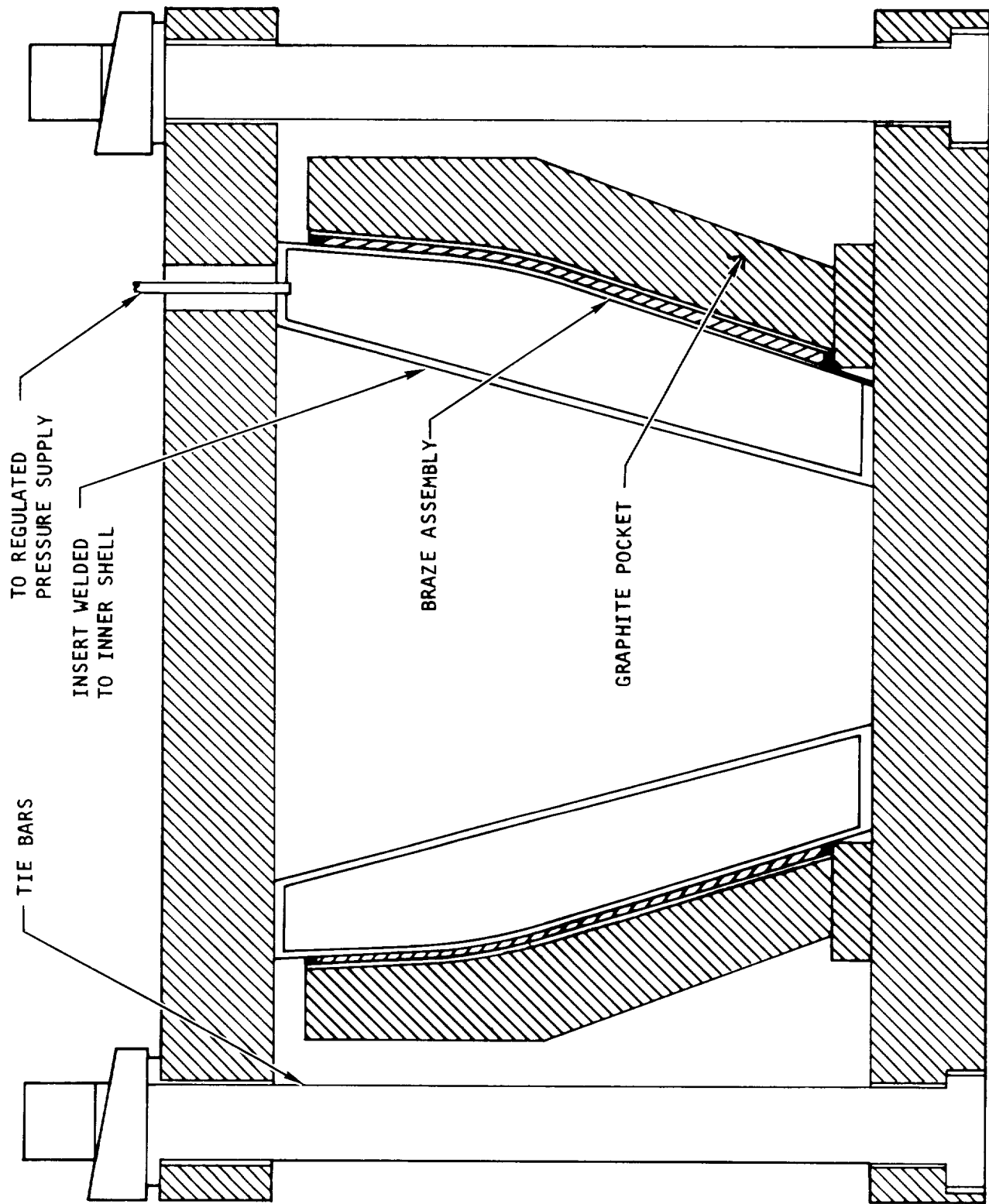
The design of the graphite insert has been modified to incorporate internal reinforcement to prevent movement during brazing. Modifications in the setup are being incorporated to permit brazing with Palniro 4 alloy at 2170°F. A shift from vacuum to atmosphere brazing is planned in recognition of the increased availability of this capability for brazing the much larger full-scale engine assemblies.

7.2 FLAT PANELS

Two configurations of continuous joint panels were fabricated and tested one simulating the continuous manifold joint between the inner shell and nozzle and the other simulating the built-in gap between fins required at the outlet manifold of the outer shell. In addition to these panels, a basic flat panel configuration incorporating a different fin was fabricated. Manufacturing details for these specimens are described below.



UNCLASSIFIED



A-32187

Figure 7.1-4. Brazing Setup - Pneumatically Expanded Inner Shell



UNCLASSIFIED

7.2.1 Inner Shell-Nozzle Joint Panels

The inner shell-nozzle joint panel specimens simulate the relatively complex fabrication sequence required for assembly of full scale components. Figure 7.2-1 shows the detail components required for one half of the assembly. First, a welding operation and a machining operation were made on one sub-assembly; then, two brazing operations were made simultaneously on the sub-assemblies; and, finally, following a machining operation on one of the sub-assemblies, the brazing and machining operations were completed.

The first welding operation, which was performed on the manifold, utilized the electron beam technique. However, excessive discharge of molten metal on the back side of the joint has led to substituting TIG welding for full-scale hardware. After machining the manifold weldment to insure braze joint flatness (0.001 to 0.003 clearance), the weldment was brazed to the flange plate, using Palniro 4 alloy at 2170°F. Simultaneously, the fin-skin assembly was prepared and brazed using the same alloy. The manifold-flange assembly was then machined to fit the fin-skin assembly, and the holes for bolt inserts were machined. The fins, inserts, and caps were joined to the manifold in the final braze assembly, using Palniro 1 alloy at 2070°F. The final machining operation was performed on the seal pocket flange faces. The completed inner shell-nozzle joint panels are shown in Figure 7.2-2 prior to assembly.

7.2.2 Continuous Fin Gap Panels

The fabrication procedure for the continuous fin gap panel specimens, shown schematically in Figure 7.2-3, included, first, a braze operation for the skin-fin joints; then a machining operation for the holes in the skin; and finally a braze operation to attach the manifolds, tubes, and reinforcing doublers to the specimens. Palniro 4 braze alloy at 2170°F was used to braze the fins to the skins, and Palniro 1 braze alloy at 2070°F was used to braze the manifolds and doublers.

7.2.3 Basic Panels

During the previous reporting period, the first three flat panel fin geometries tested below were fabricated.

During the present reporting period, the last fin geometry listed below was installed in six specimens of basic two-by-three inch flat panels and brazed. Hastelloy X was used for all four configurations. Palniro 4 braze alloy foil (0.001 inch thick) was used between fins and skin, and the units were brazed at 2170°F in a vacuum.

<u>Fins per in.</u>	<u>Fin Height, in.</u>	<u>Fin Offset, in.</u>	<u>Fin Thickness, in.</u>
34	0.025	0.050	0.002
20	0.076	0.100	0.004
16	0.153	0.143	0.006
20	0.050	0.100	0.006



UNCLASSIFIED



60892

Figure 7.2-1. Detail Components for Inner Shell-Nozzle Joint Flat Panel

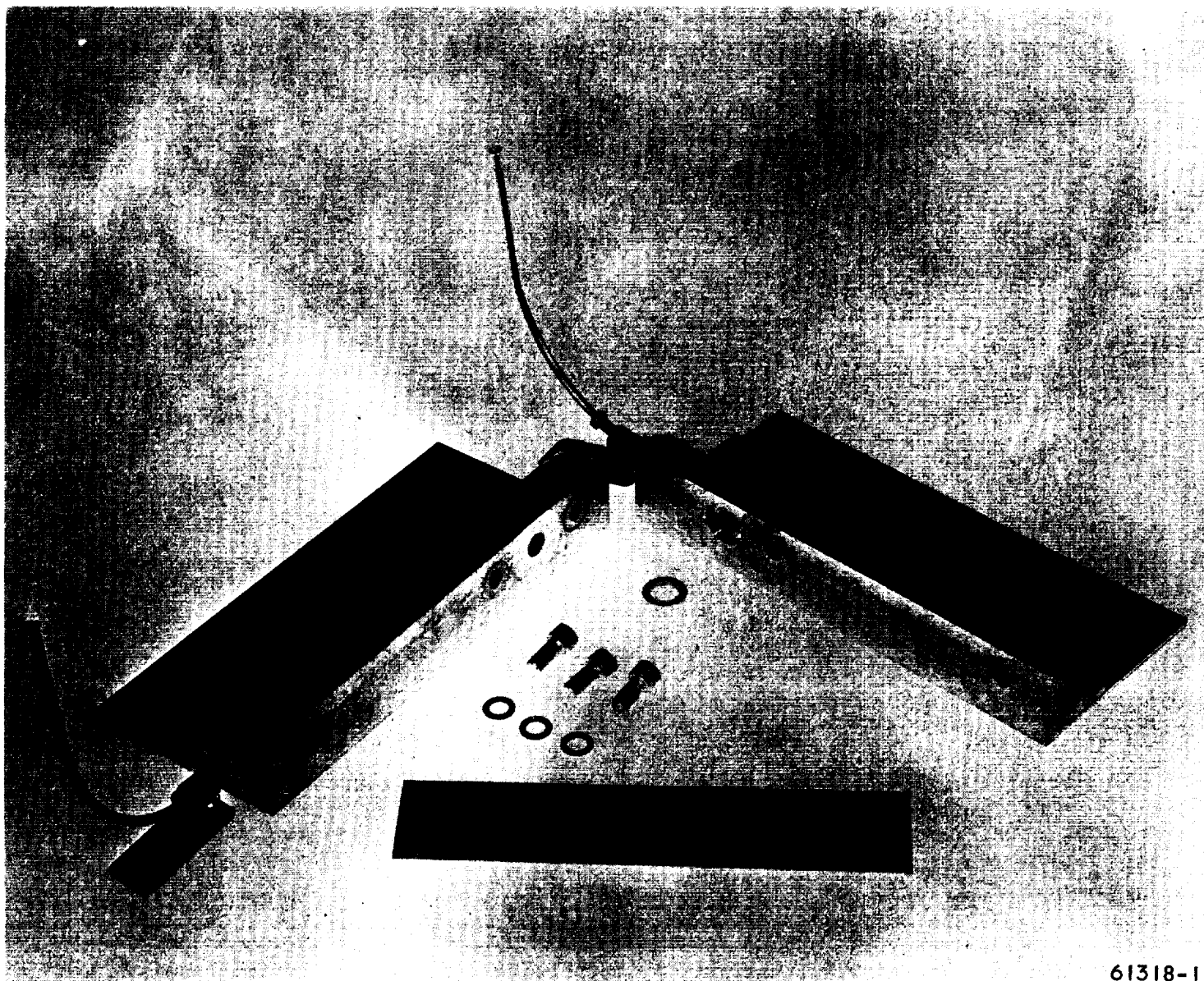


AIRESEARCH MANUFACTURING DIVISION
Los Angeles, California

67-2833
Page 7-10

UNCLASSIFIED

UNCLASSIFIED



61318-1

Figure 7.2-2. Inner Shell-Nozzle Joint Panels, Unassembled



AIRESEARCH MANUFACTURING DIVISION
Los Angeles, California

UNCLASSIFIED

67-2833
Page 7-11

UNCLASSIFIED

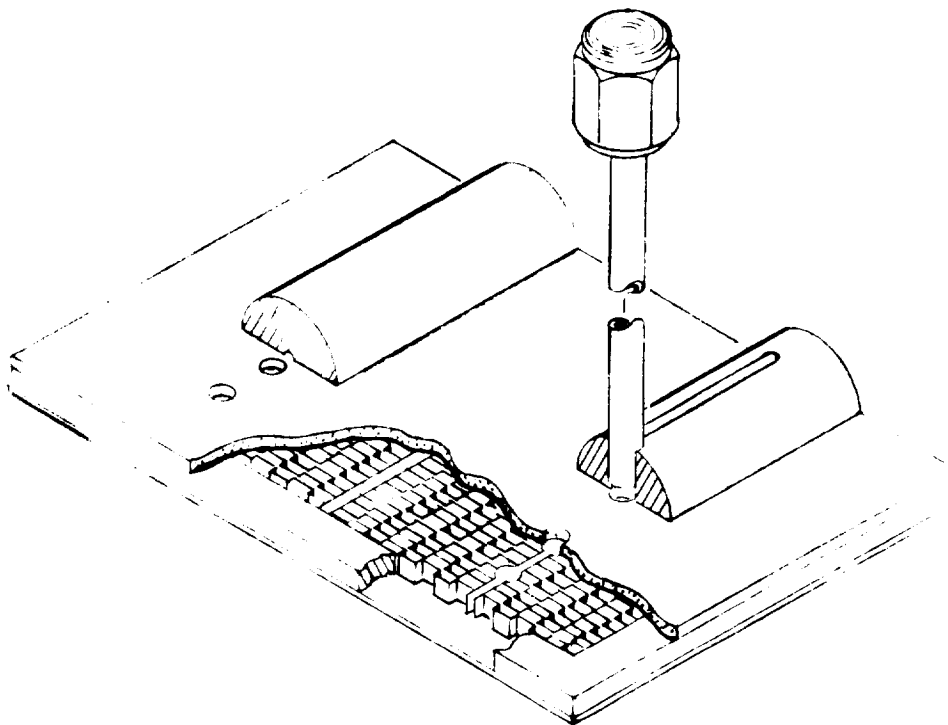


Figure 7.2-3. Coolant Exhaust Continuous Joint Flat Panel



AIRESEARCH MANUFACTURING DIVISION
Los Angeles, California

67-2833
Page 7-12

UNCLASSIFIED

UNCLASSIFIED

7.3 OUTER BODY LEADING EDGE STRAIGHT SECTION

7.3.1 Purpose

The leading edge straight section shown in Figure 7.3-1 will be used to evaluate structural and performance characteristics and to develop a leading edge configuration meeting engine design operating requirements. A detailed description of the manufacturing and assembly procedures was given in the previous report TDR (Reference 7-1).

7.3.2 Approach

The two alternate configurations shown in Figure 7.3-2 were considered for the plate-fin braze assembly, which is the basic section of the leading edge. Figure 7.3-2A shows the single skin assembly approach, and Figure 7.3-2B shows the separate leading edge tip approach. The single outer skin configuration was selected as the first option because it is simple to construct and needs only one braze cycle to complete the plate-fin braze assembly, as compared to a two-stage braze operation needed to complete the assembly of the alternate three-piece configuration.

7.3.3 Development Effort

7.3.3.1 Single Outer Skin Configuration

The first assembly, S/N 1, was processed through the second stage brazing cycle, but failed during the leakage and proof pressure inspection performed as part of the manufacturing procedure. Bulging of the outer skin occurred at an applied pressure of 300 psig on both sides for a distance of approximately 0.5 in. back from the leading edge. A lack of braze joint strength between the skin and the fins, which was attributed to inadequate fixture loading at the tip section and non-uniform fin height, was subsequently found to be the source of this condition. Figure 7.3-3 is an enlarged section of the bulged area and shows poor fitup due to non-uniformity in fin height. Fin details were made for subsequent assemblies to correct this condition.

In order to pressure test the plate-fin assembly before it is used as a component in the next assembly, the design was modified to a closed assembly, which could be pressure tested and then machined to conform to the original configuration. The modifications are shown in Figure 7.3-4, and the pressure test clamping arrangement is shown in Figure 7.3-5.

Fabrication of plate-fin braze assembly S/N 2 was completed and pressure tested. At 600 psig bulging in a small area, as shown in Figure 7.3-6 was noted. A clamping arrangement was provided for the area, and the pressure test was continued to 1050 psig. No other evidence of bulging was found. The poor braze joint in the tip area between the fin and skin was in this case directly attributable to the brazing fixture, which did not apply adequate and uniform pressure to the component details during the brazing cycle, particularly at the tip section. Because this condition would not have occurred if the same fixture was used for the alternate configuration of separate tip and side panels, it was decided to use the alternate configuration for the next plate-fin braze assembly.



UNCLASSIFIED

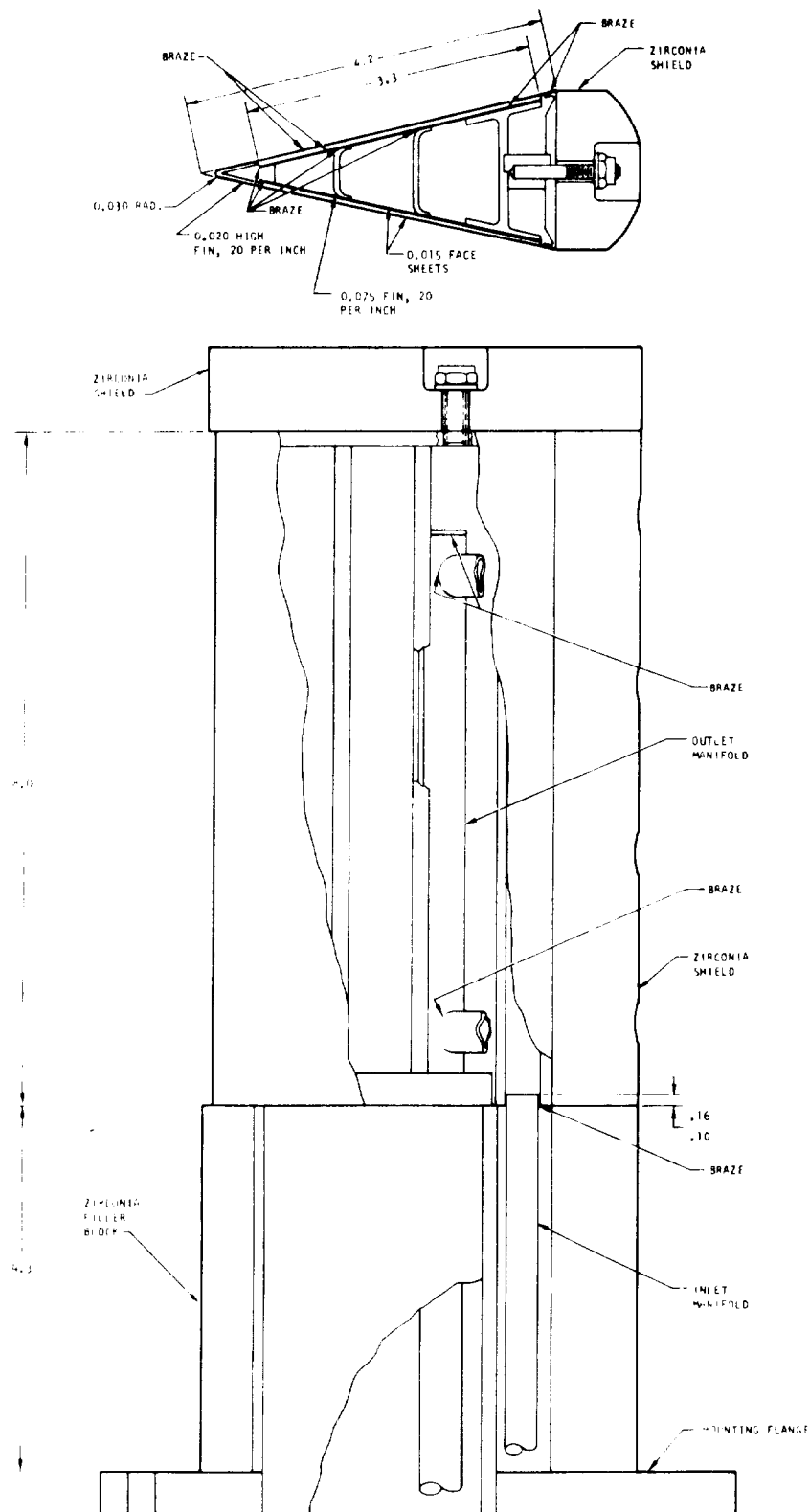


Figure 7.3-1. Outer Body Leading Edge
Straight Section

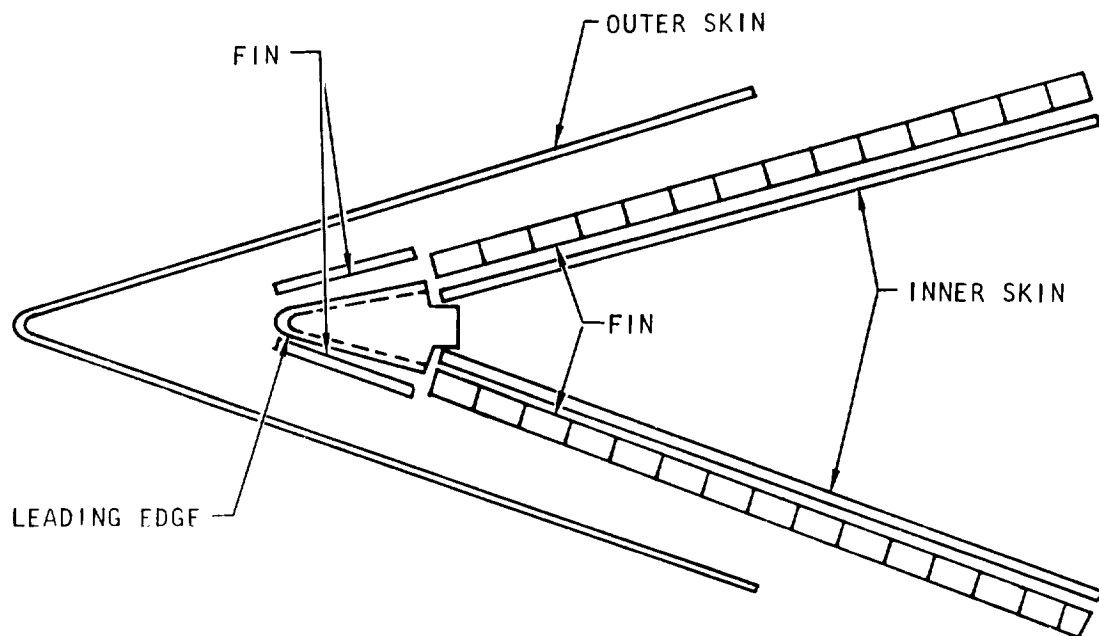


AIRESEARCH MANUFACTURING DIVISION
Los Angeles, California

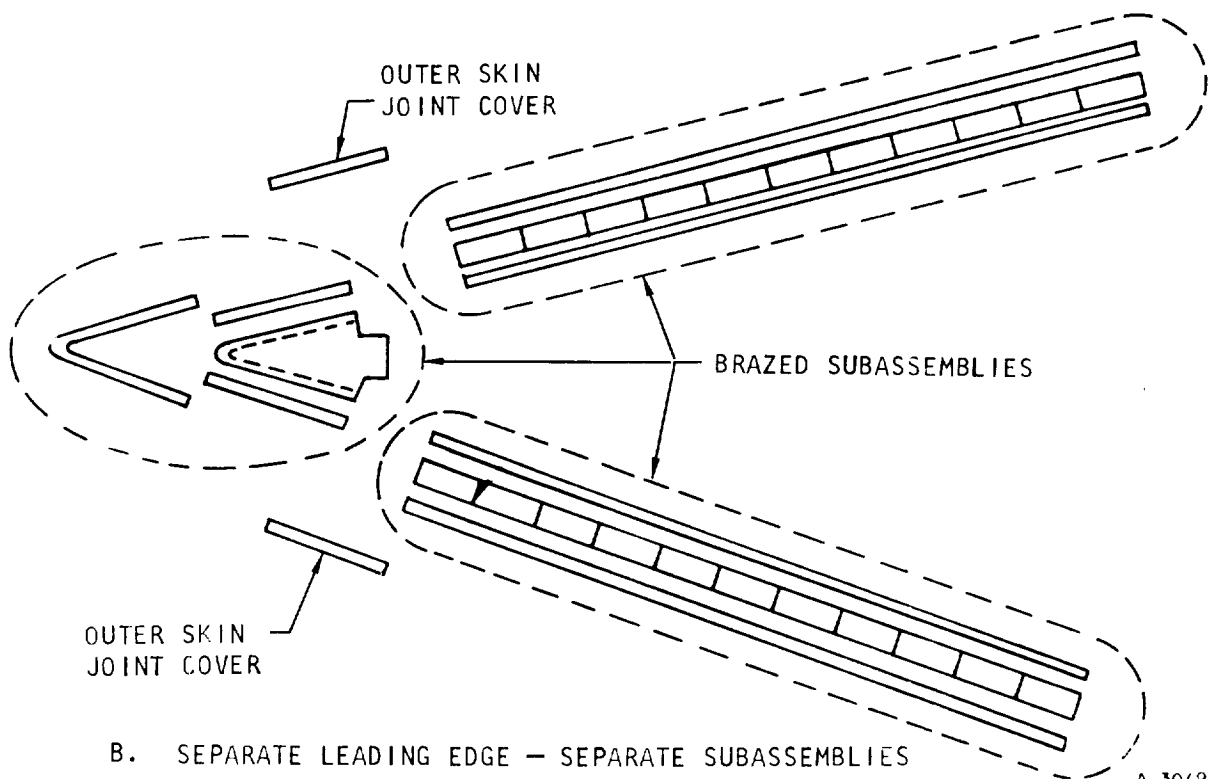
67-2833
Page 7-14

UNCLASSIFIED

UNCLASSIFIED



A. SINGLE OUTER SKIN - SINGLE ASSEMBLY



B. SEPARATE LEADING EDGE - SEPARATE SUBASSEMBLIES

A-30499

Figure 7.3-2. Plate Fin Braze Assembly

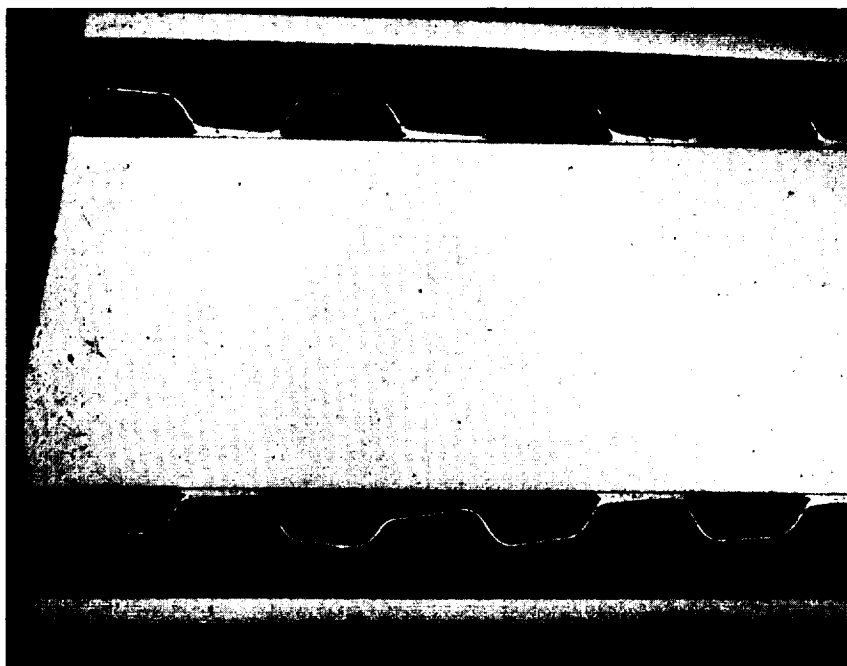


AIRESEARCH MANUFACTURING DIVISION
Los Angeles, California

67-2833
Page 7-15

UNCLASSIFIED

UNCLASSIFIED



F-8358

Figure 7.3-3. Unbrazed Section of Plate Fin
Braze Assembly S/N 1

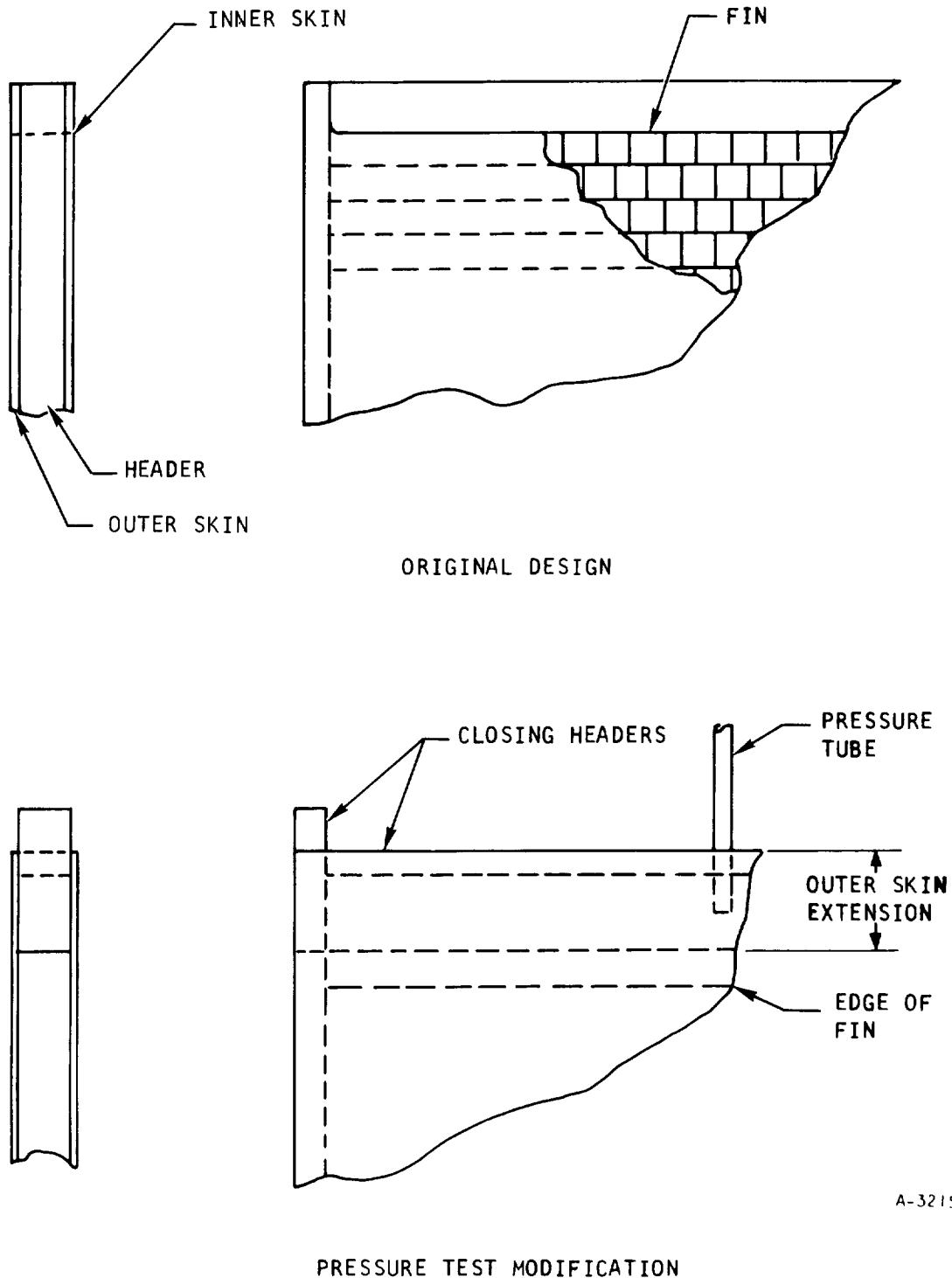


AIRSEARCH MANUFACTURING DIVISION
Los Angeles, California

UNCLASSIFIED

67-2833
Page 7-16

UNCLASSIFIED



A-32157

Figure 7.3-4. Modification of SK51287-7 Plate Fin Assembly for Pressure Test

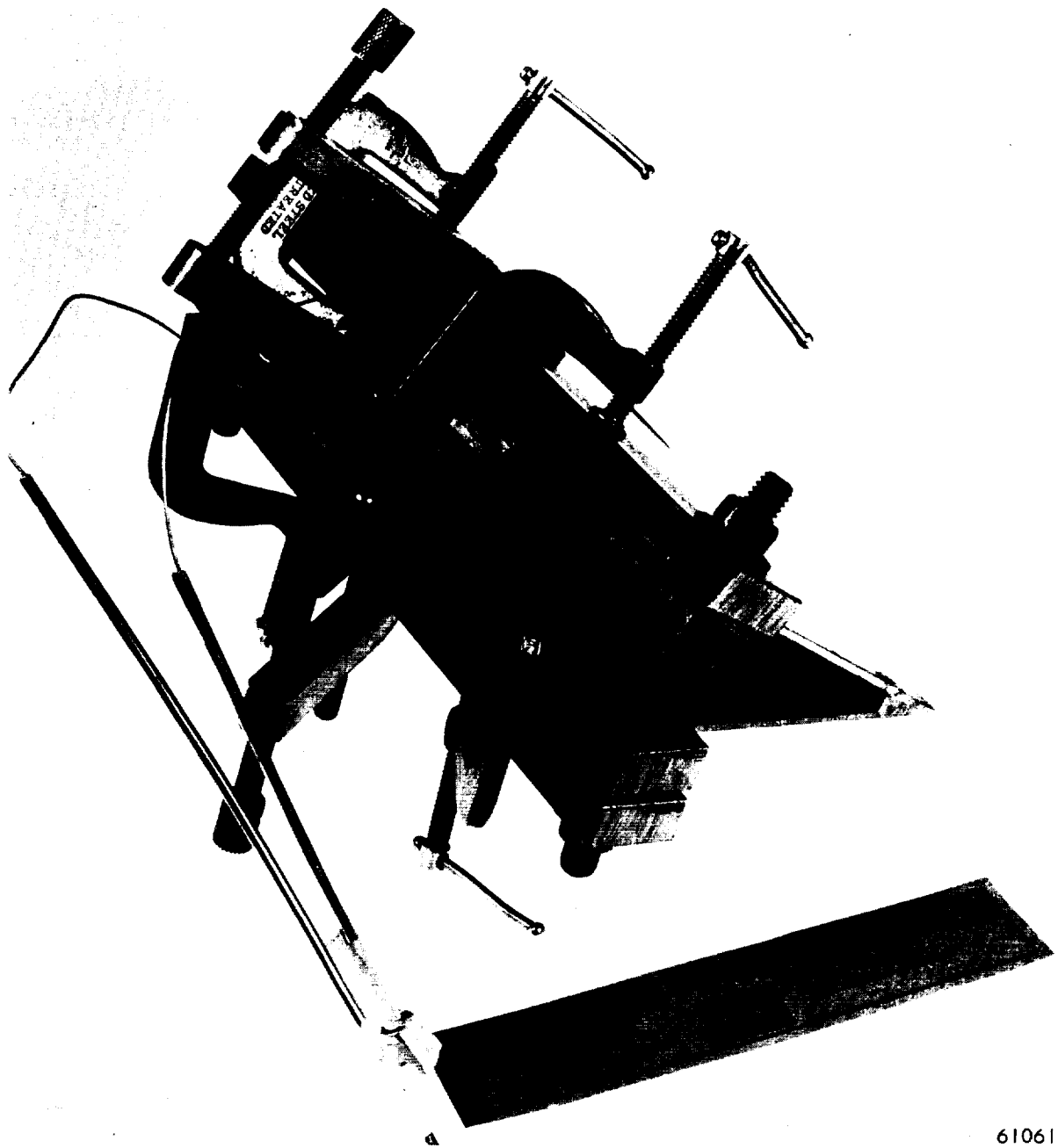


AIRESEARCH MANUFACTURING DIVISION
Los Angeles, California

UNCLASSIFIED

67-2833
Page 7-17

UNCLASSIFIED



61061

Figure 7.3-5. Plate-Fin Assembly Pressure Test Clamping Arrangement

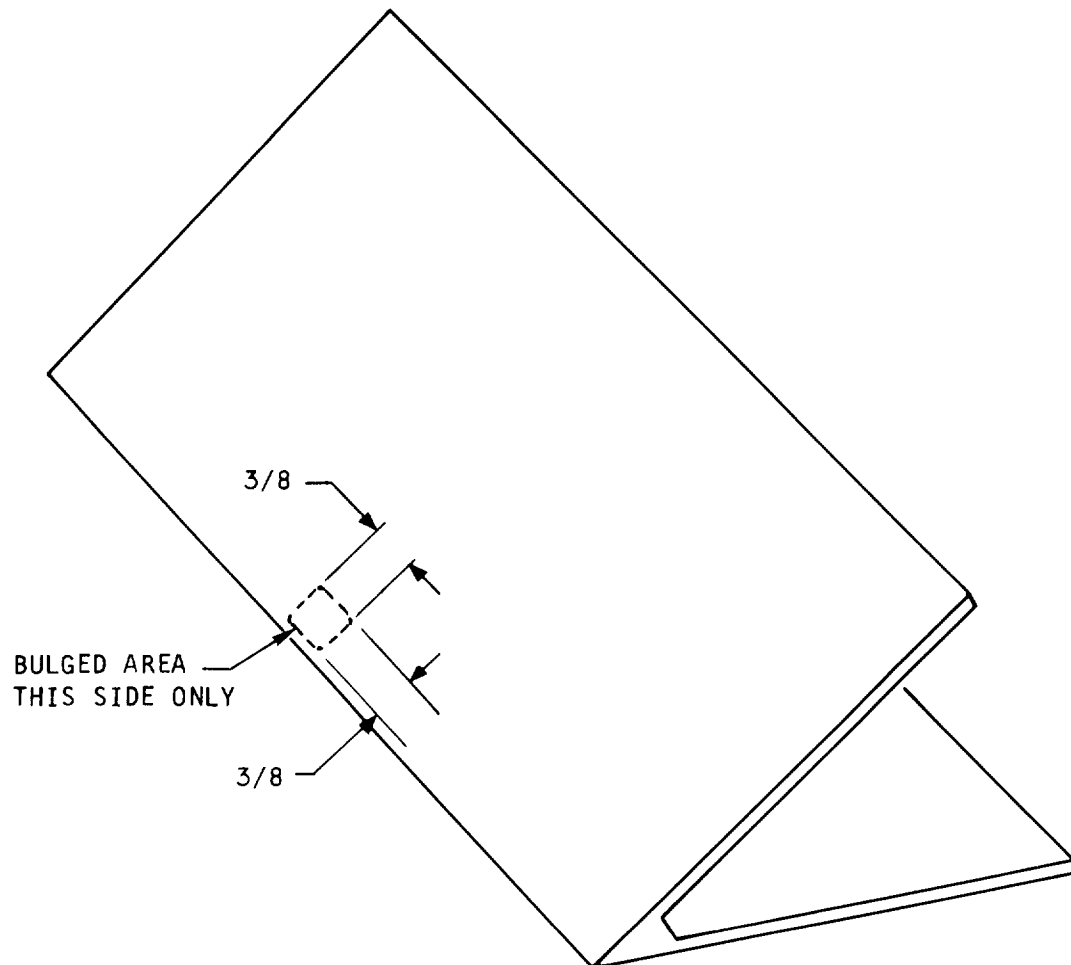


AIRESEARCH MANUFACTURING DIVISION
Los Angeles, California

UNCLASSIFIED

67-2833
Page 7-18

UNCLASSIFIED



A-32155

Figure 7.3-6. S/N 2 Plate-Fin Braze Assembly
Pressure Test Failure



AIRESEARCH MANUFACTURING DIVISION
Los Angeles, California

UNCLASSIFIED

67-2833
Page 7-19

UNCLASSIFIED

7.3.3.2 Separate Leading Edge Tip

Plate-fin braze assembly S/N 3 with separate leading edge tip and plate subassemblies was brazed successfully and proof pressure tested satisfactorily to 1050 psig. No fixture modifications were needed, except for adding two removable guides to position the load-applying "V" block when brazing the separate leading edge. A sketch of the leading edge and fixturing arrangement is shown in Figure 7.3-7. Plate subassemblies were brazed using flat blocks for support and loading. The brazed subassemblies are shown in Figure 7.3-8 and the completed assembly before machining is shown in Figure 7.3-9. Machining was completed and the finished part was used for leading edge assembly S/N 2.

7.3.3.3 Leading Edge Assembly

Leading edge assembly S/N 2, shown in Figure 7.3-10, was satisfactorily processed through the two successive brazing cycles needed to complete the assembly, except for the mechanical work of connecting the instrumentation and the insulating blocks. A proof pressure test at 700 psig showed no evidence of leakage or deformation, and the unit was installed in the pressure drop and flow test setup. During the test instrumentation check out, leaks were observed in the small dia (0.041) pressure tubing. Attempts to repair the leaks were unsuccessful, since new leaks appeared to develop as soon as the known leaks were repaired.

Several leaking tube sections were removed and a metallurgical investigation was made to determine the cause of the leaks. Examination of tube sections showed cracks along the grain boundaries, due to carbide precipitation, as shown in Figure 7.3-11. In view of these findings, a comprehensive investigation was made to determine the cause of the cracks and the corrective action needed to repair the test unit and prevent recurrence on subsequent assemblies. This investigation definitely determined that the cracks were due to carburizing of the type 304 CRES tubes during the second stage brazing cycles, when the assembly was brazed in a hydrogen atmosphere furnace using graphite fixtures. During cool down in this stage and the following third stage braze cycle, excessive carbide precipitation occurred, followed by development of cracks along the weakened grain boundaries.

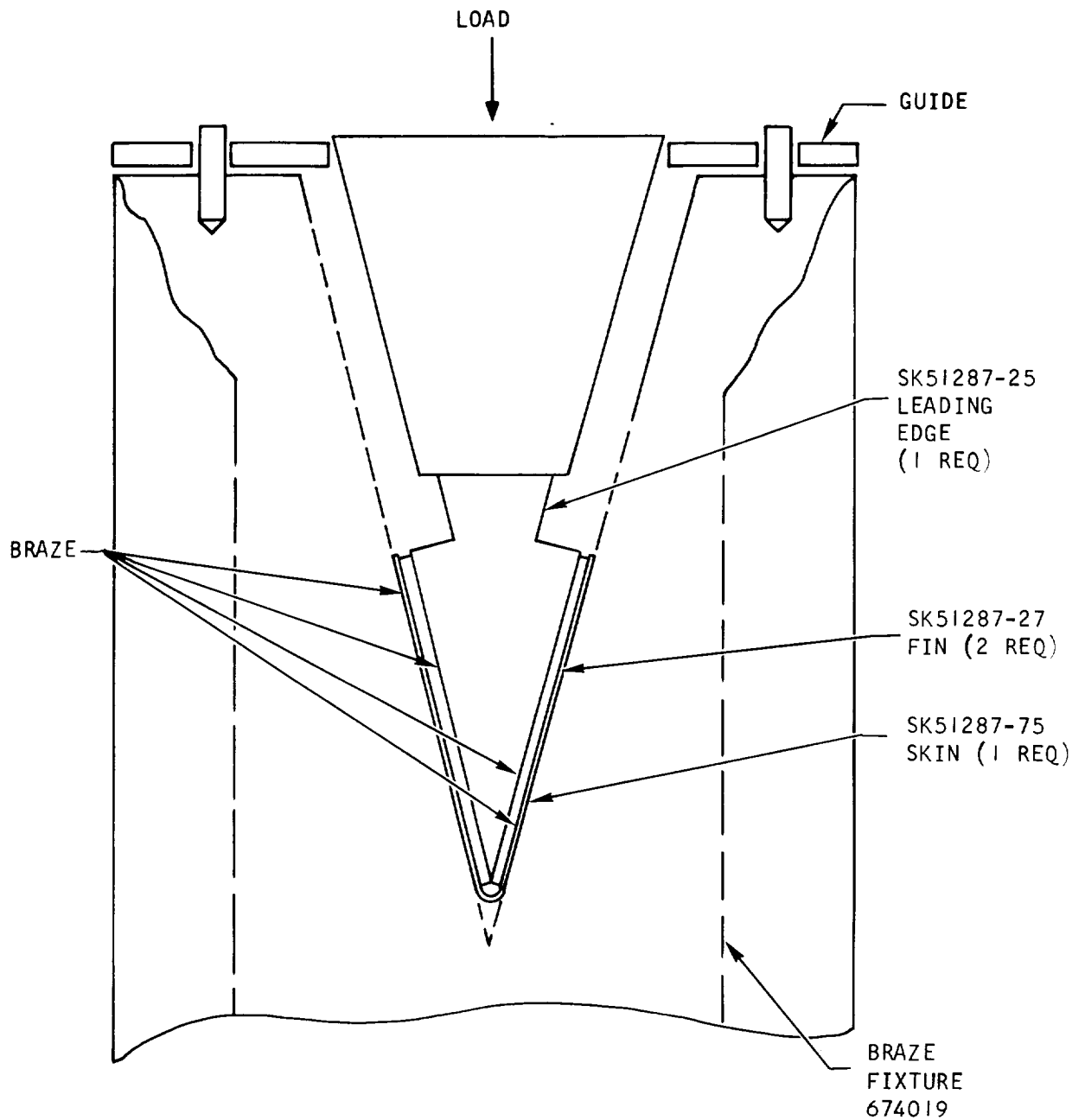
Repair of the unit was made by blocking the tubes at the points where the tubes are connected to the unit. Elimination of these pressure taps, which sense coolant inlet and outlet manifold pressures, will restrict the data that will be obtained for coolant flow distribution in the manifolds, but will not prevent using the unit for flow and heat transfer tests.

The following corrective action was taken to prevent recurrence of this condition in subsequent assemblies: (1) brazing operations with graphite fixtures will be done only in vacuum or inert gas atmosphere furnaces to eliminate the possibility of carburizing the tubing, and (2) the tubing material will be changed to Type 347 CRES, which is less susceptible to both carburizing and carbide precipitation during cooling.



UNCLASSIFIED

UNCLASSIFIED



A-32154

Figure 7.3-7. Separate Leading Edge Assembly and Braze Fixture

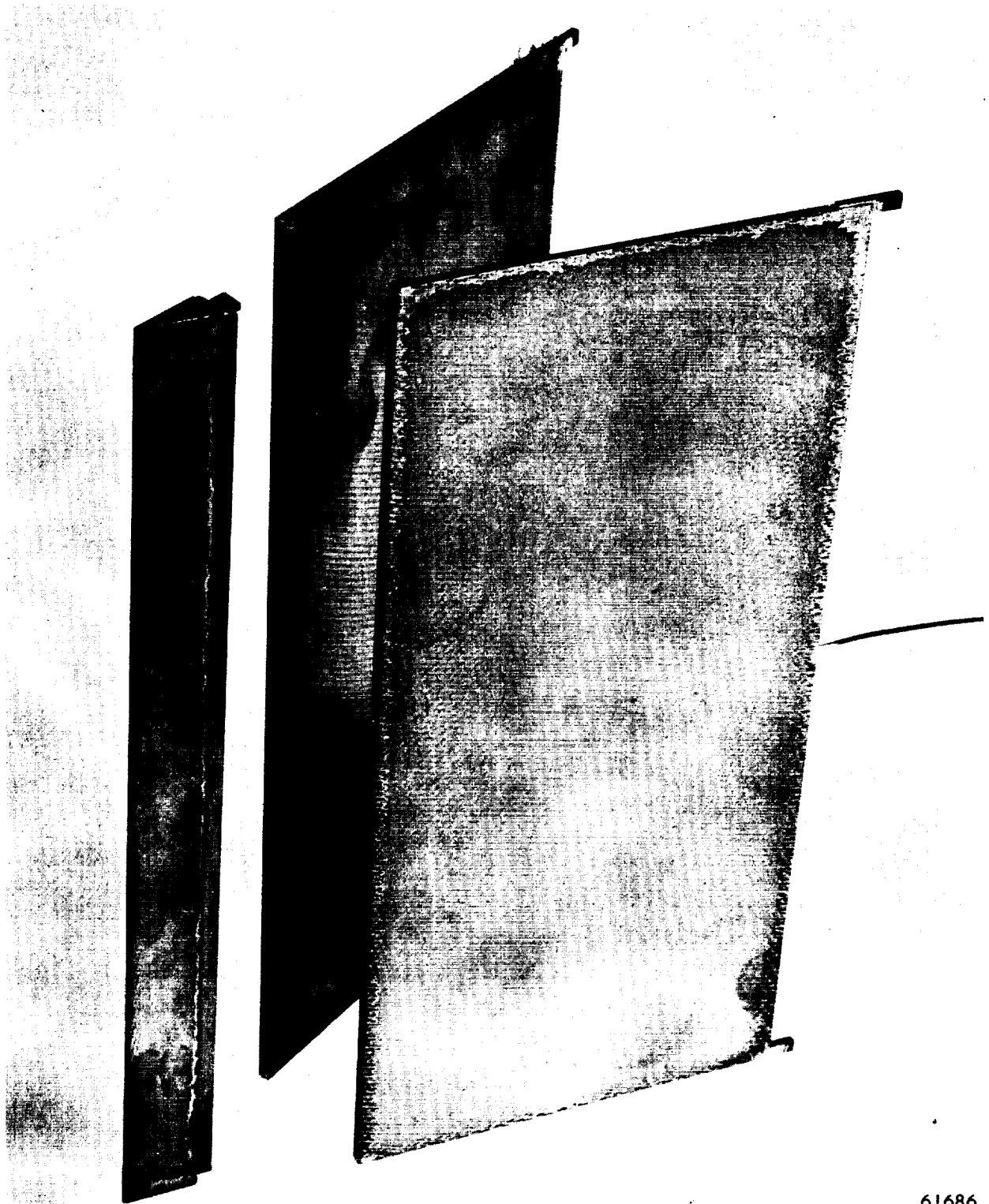


AIRSEARCH MANUFACTURING DIVISION
Los Angeles, California

UNCLASSIFIED

67-2833
Page 7-21

UNCLASSIFIED



61686

Figure 7.3-8. Leading Edge and Panel Subassemblies for Plate-Fin Braze Assembly

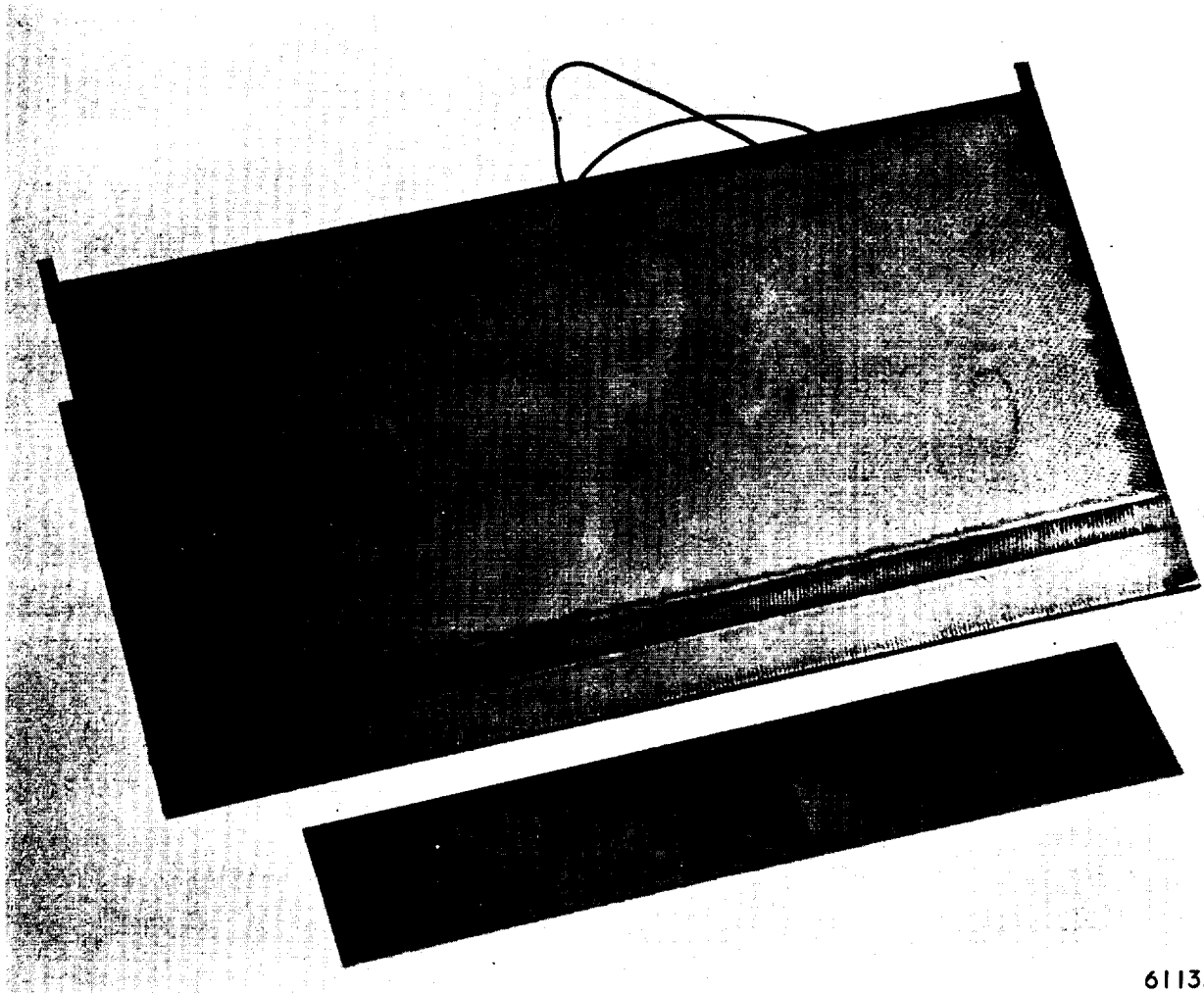


AIRSEARCH MANUFACTURING DIVISION
Los Angeles, California

UNCLASSIFIED

67-2833
Page 7-22

UNCLASSIFIED



61135

Figure 7.3-9. Plate-Fin Braze Assembly Before Machining

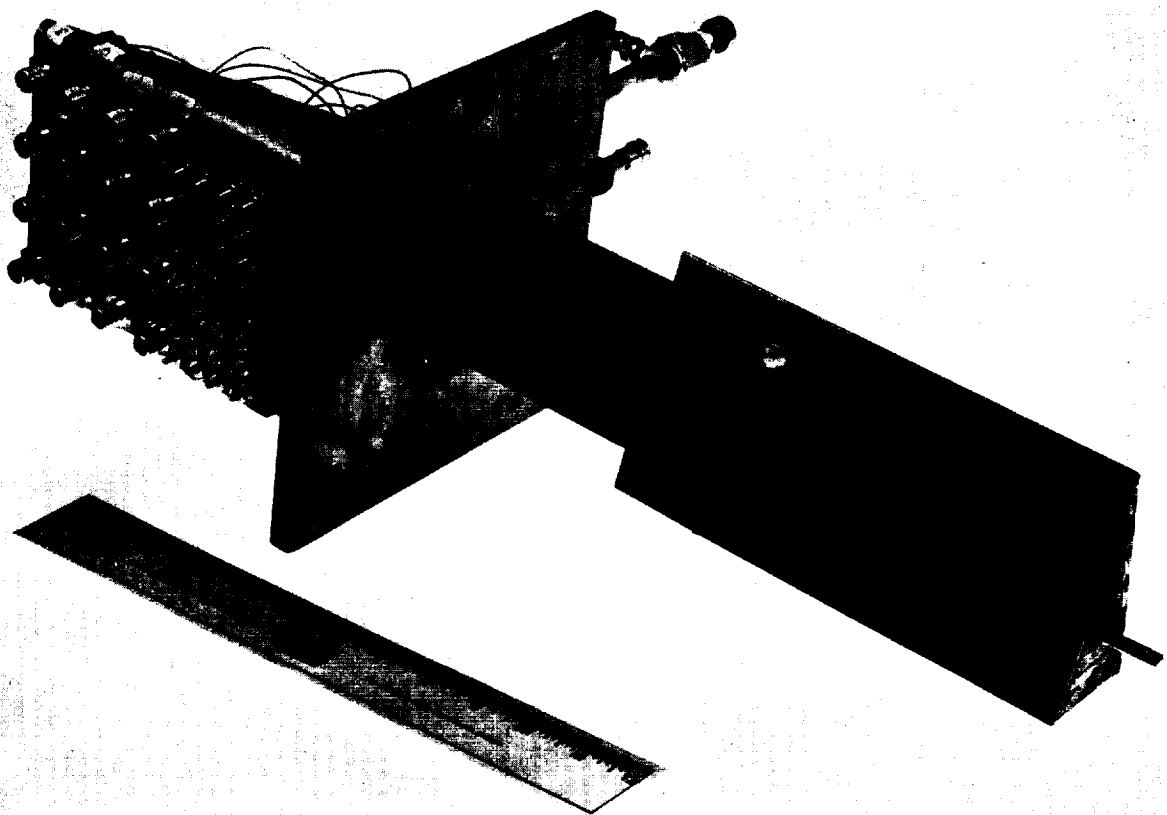


AIRESEARCH MANUFACTURING DIVISION
Los Angeles, California

UNCLASSIFIED

67-2833
Page 7-23

UNCLASSIFIED



61512-1

Figure 7.3-10. Leading Edge Test Specimen S/N 2



AIRESEARCH MANUFACTURING DIVISION
Los Angeles, California

UNCLASSIFIED

67-2833
Page 7-24

UNCLASSIFIED



F-8360

Figure 7.3-11. Crack Through Wall of Instrumentation Tube
(Magnified 250 x)



AIRESEARCH MANUFACTURING DIVISION
Los Angeles, California

UNCLASSIFIED

67-2833
Page 7-25

UNCLASSIFIED

7.3.4 Current Status

Two additional plate-fin braze assemblies, S/N 4 and S/N 5, have been fabricated satisfactorily. Subassemblies for S/N 6 were completed and are in process of assembly for the next braze operation. No problems were experienced with these assemblies. Leading edge assembly S/N 2 is being installed at the NAR test facility for flow and temperature distribution testing and performance testing. Leading edge assembly S/N 3 is in process of assembly using plate-fin braze assembly S/N 4.

7.4 STRUT TEST SECTION

7.4.1 Purpose and Approach

The strut test section shown on Drawing SK-51321 will be used to evaluate manufacturing methods, structural strength, flow distribution, and thermal characteristics for the full-scale inner body-outer body struts. Since the test strut is identical to the full-scale struts, development of manufacturing methods will be directly applicable.

7.4.2 Development Effort

To evaluate problems in the use of the strut assembly brazing fixture, shown in Figure 7.4-1 with the strut installed for brazing, the first brazing operation was run without using brazing alloy. This procedure permitted salvaging of details, particularly the strut body, in the event the fixturing did not provide suitable loading during the brazing cycle. Non-uniform loading was, in fact, experienced, as evidenced by buckling of the skin at the trailing end and at the transition line along the side, as shown in Figures 7.4-2 and 7.4-3, respectively. During the brazing cycle diffusion bonding occurred between the skin, fins, and body. The skin and fins were damaged in removal and were scrapped, but the strut body was undamaged and reusable. Shims were used between the outer ring and the four segments of the braze fixture to control the loading during brazing.

For the braze cycle on the strut assembly S/N 1, shimming was revised to reduce the loading on the ends. The assembly showed uniform loading during the braze cycle. Although some wrinkling still occurred at the trailing edge, the unit as shown in Figure 7.4-4, appeared acceptable. A subsequent leakage check showed several leaks between the skin and body at the top and bottom joints of the skin and body. These leaks were repaired in the second braze cycle, in which the doubler strips were brazed to the body and skin. After the second braze cycle, the assembly, shown in Figure 7.4-5, was proof tested to 700 psig and showed no evidence of leakage or deformation. Figure 7.4-6 shows the assembly installed in the pressure test fixture. No problems were experienced with the other components for the strut test section, which are all in process of assembly.



UNCLASSIFIED



F-8360

Figure 7.4-1. Strut Assembly S/N 1 in Braze Fixture After Brazing

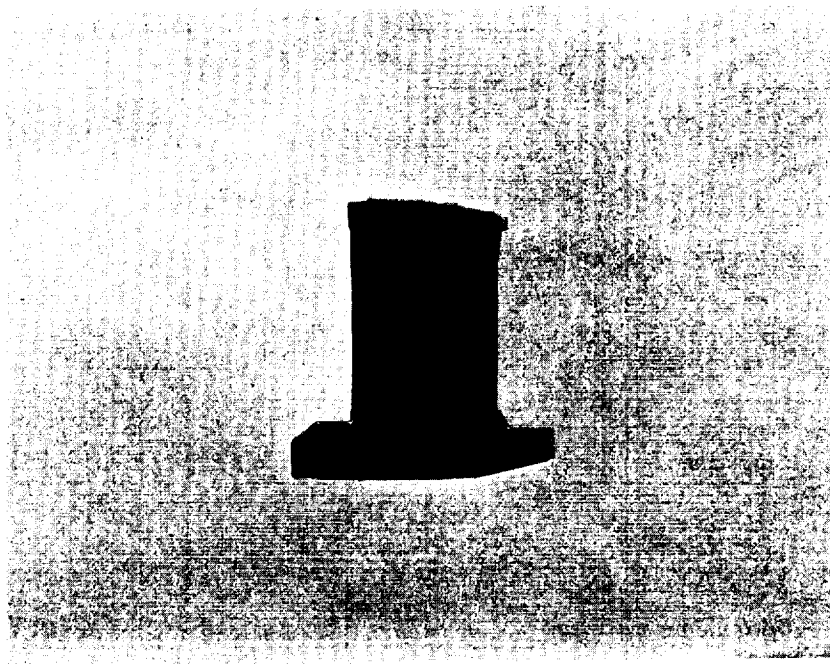


AIRESEARCH MANUFACTURING DIVISION
Los Angeles, California

UNCLASSIFIED

67-2833
Page 7-27

UNCLASSIFIED



F-8359

Figure 7.4-2. Wrinkled Skin at Trailing Edge of Strut Assembly
After Dummy Braze Cycle



AIRSEARCH MANUFACTURING DIVISION
Los Angeles, California

UNCLASSIFIED

67-2833
Page 7-28

UNCLASSIFIED

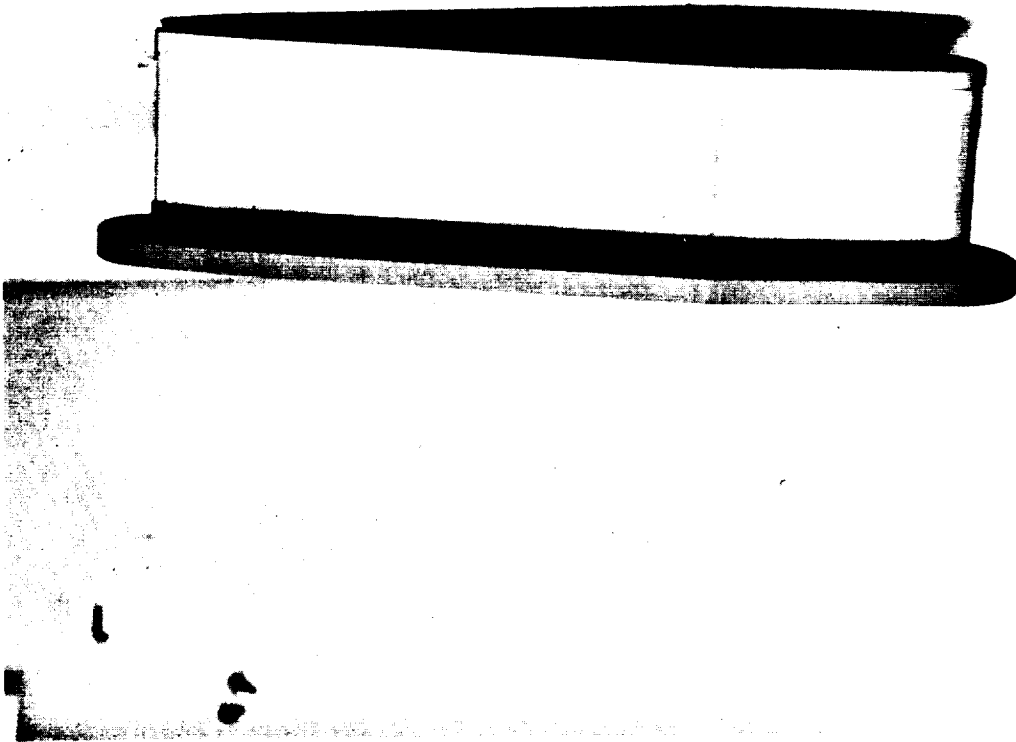


Figure 7.4-3. Wrinkled Skin at Side of Strut Assembly
After Dummy Braze Cycle



UNCLASSIFIED

UNCLASSIFIED

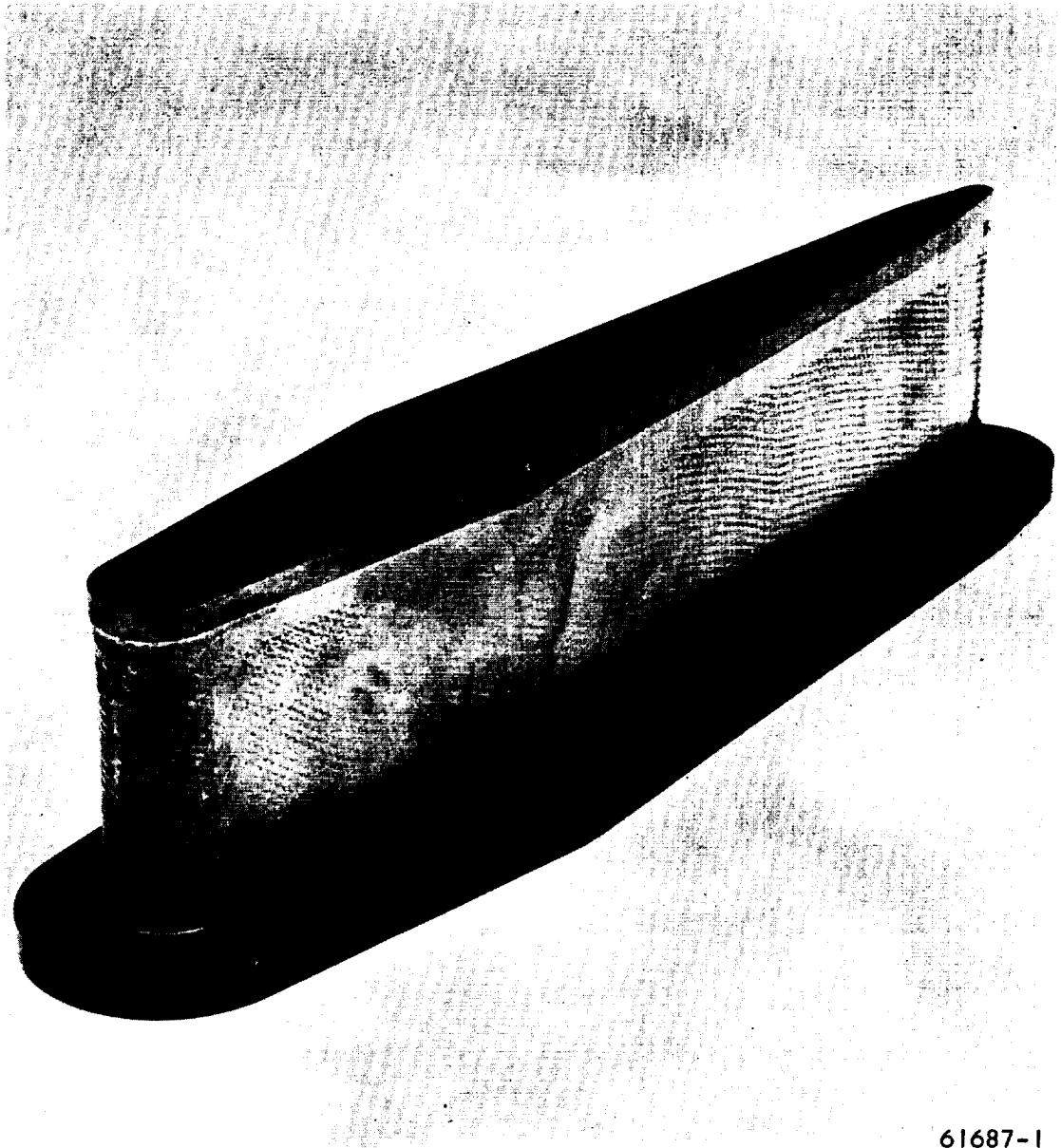


Figure 7.4-4. Strut Assembly, S/N 1, First Braze Cycle

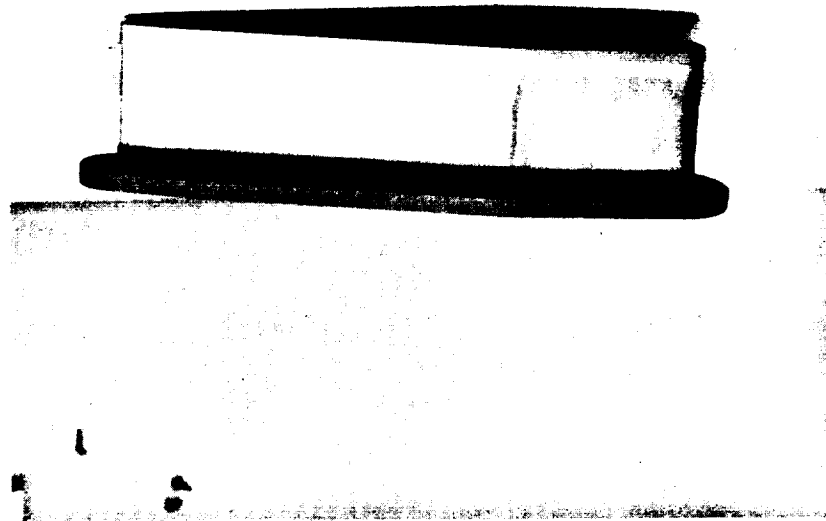


AIRESEARCH MANUFACTURING DIVISION
Los Angeles, California

UNCLASSIFIED

67-2833
Page 7-30

UNCLASSIFIED



F-8368

Figure 7.4-5. Strut Assembly, S/N 1, Second Braze Cycle

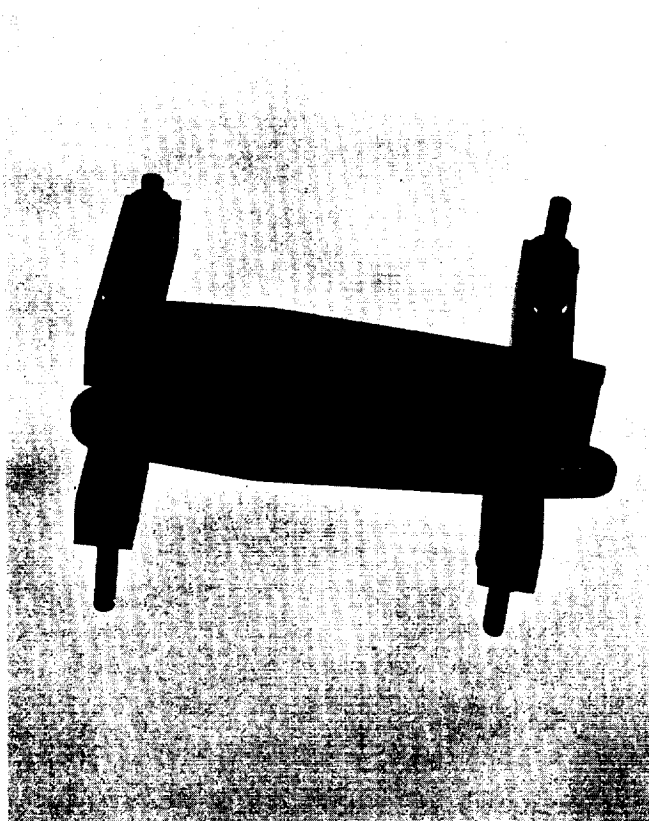


AIRESEARCH MANUFACTURING DIVISION
Los Angeles, California

UNCLASSIFIED

67-2833
Page 7-31

UNCLASSIFIED



F-8364

Figure 7.4-6. Strut Assembly, S/N 1, Pressure Test Fixture



AIRESEARCH MANUFACTURING DIVISION
Los Angeles, California

UNCLASSIFIED

67-2833
Page 7-32

UNCLASSIFIED

7.3.3 Current Status

Strut S/N 1 is being machined in preparation for the final braze cycle to incorporate studs and tubing connections. A second assembly, S/N 2, is being prepared for brazing. This assembly will be brazed with the doubler strips installed for the first braze cycle. No fixture modification will be necessary, because the fixture was designed to accommodate chem-milled skins, which have thicker end sections (equal to the combined skin and doubler).



AIRESEARCH MANUFACTURING DIVISION
Los Angeles, California

67-2833
Page 7-33

UNCLASSIFIED

8. TESTING

8.1 FLAT PANEL RUPTURE

8.1.1 Continuous Joint Rupture Panels

The highest metal temperatures in the outer shell exist at the exit manifold. Also, at this manifold, the sandwich shell has been considerably thinned locally in providing exit passages between the manifold and the shell coolant passage (Reference 8-1, page 4-81). Because of these two adverse conditions, a creep-rupture test was instituted in order to verify the design. The critical operating conditions are indicated below:

Maximum Thermal Wall Temperature	1600°F
Maximum Fin Temperature	1423°F
Coolant Pressure	628 psig
Coolant Temperature	793°F

The test specimens consisted of Hastelloy X flat panels brazed to 20R-.100-.050-.006 fins. The fins were spaced between the panels so that two gaps, 0.055-in. wide, were incorporated. A series of holes were EDM machined through the structural skin and into the fins to simulate the outer shell arrangement (see Figure 7.2-3).

8.1.2 Flat Plate and Fin Panels

A creep-rupture test was instituted in order to test the strength of the 20R-.050-.100-.006 Hastelloy X fins under various conditions. Both face sheet thicknesses were 0.015 in.

8.1.3 Test Results

8.1.3.1 Continuous Joint Rupture Panels

The tests performed on the two specimens consisted of first a room temperature proof pressure test to 2200 psig, which both panels survived without incident. A creep-rupture test was then performed on both units with conditions and results as tabulated below:



UNCLASSIFIED

UNIT	TEMPERATURE, °F	PRESSURE, psig	TIME TO RUPTURE, hr
1	1600	650	5.66
2	1550	600	25.25

Post test observation indicated that both specimens failed in the fin-joint areas, parting at the braze joints rather than thru the fins. Figure 8.1-1 shows the panels following the test.

8.1.3.2 Flat Plate and Fin Panels

The test conditions and results are tabulated below:

UNIT	TEST	TEMPERATURE, °F	PRESSURE, psig	TIME
1	Burst	1600	2750	--
2	Burst	1600	2825	--
3	Creep-Rupture	1600	650	15 hr - 22 min
4	Creep-Rupture	1600	700	12 hr - 37 min
5	Creep-Rupture	1600	750	11 hr - 30 min

In all cases, the rupture occurred in the fins.

8.1.4 Data Reduction

8.1.4.1 Continuous Joint Rupture Panels

Unit 1

6.55-hr creep-rupture stress at 1600°F equals 15,000 psi for Hastelloy X.

$$P/\sigma_r = 650/15,000 \quad (\text{Assuming braze strength equal to that of sheet})$$

$$P/\sigma_r = 0.0432$$

Unit 2

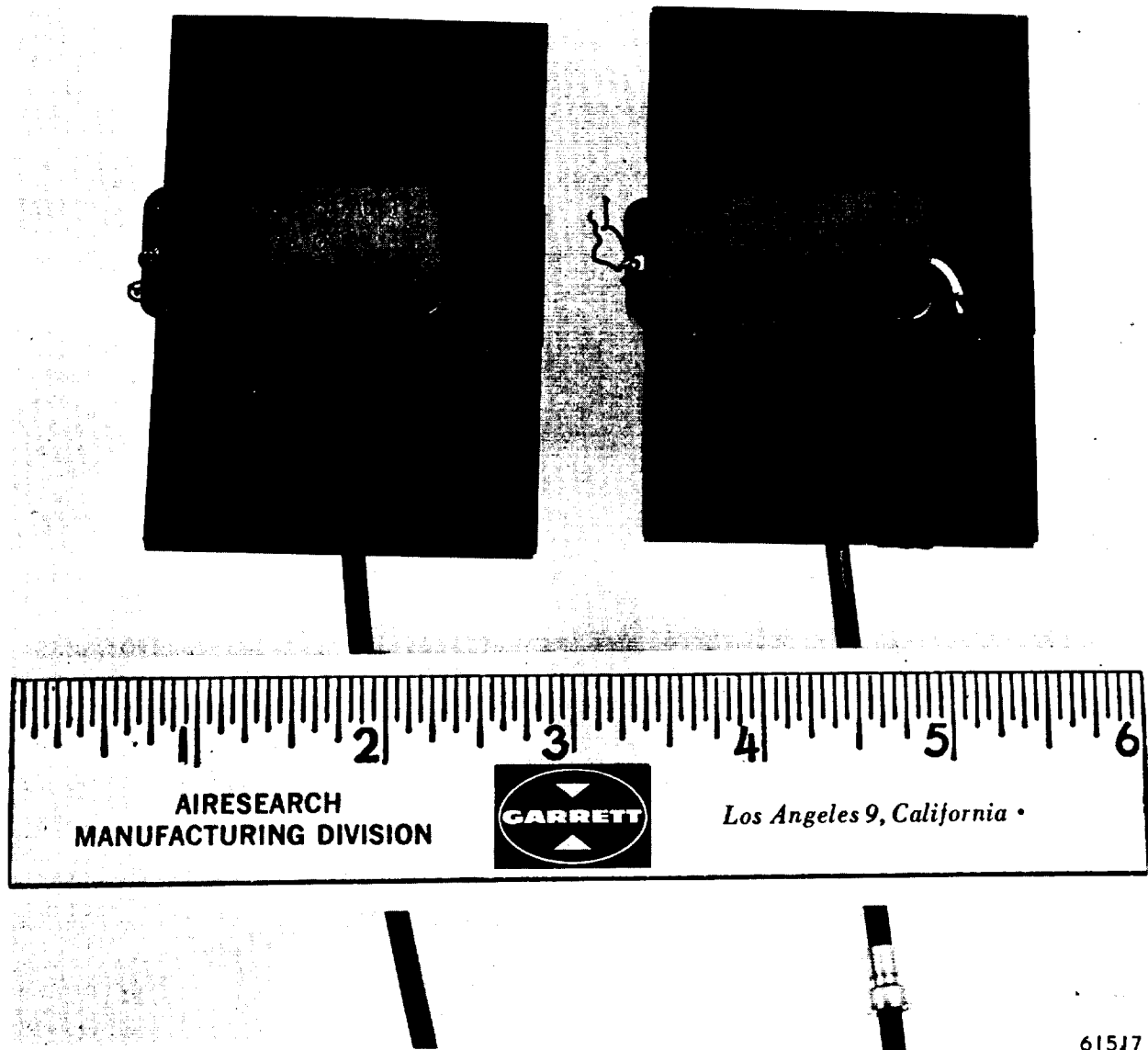
25.25-hr creep-rupture stress at 1550°F equals 15,000 psi for Hastelloy X.

$$P/\sigma_r = 600/15,000 = 0.040$$

$$P/\sigma_{r \text{ avg.}} = \frac{0.040 + 0.0432}{2} = 0.0416$$



UNCLASSIFIED



61517

Figure 8.1-1. Continuous Fin Joint Specimens After Rupture



AIRESEARCH MANUFACTURING DIVISION
Los Angeles, California

UNCLASSIFIED

67-2833
Page 8-3

UNCLASSIFIED

For Operating Conditions

$$T_{\text{braz}} = T_{\text{max fin}} = 1423^{\circ}\text{F}$$

$$T_{\text{design}} = T_{\text{braz}} + 100 = 1523^{\circ}\text{F}$$

$$10\text{-hr creep-rupture stress} = 20,000 \text{ psi}$$

$$S (\text{allowable stress}) = \frac{20,000}{1.5} = 13,300 \text{ psi (Ultimate factor of safety} \\ = 1.5)$$

Correcting for relief provided by ΔT in fins

$$P_{\text{equiv}} = \frac{-E \alpha \Delta T t}{r}$$

$$T_a \text{ in thermal wall} = 1512^{\circ}\text{F}$$

$$E_{1512} = 21 \times 10^6 \text{ psi}$$

$$\alpha_{1512} = 9.1 \times 10^{-6} \text{ in/in } ^{\circ}\text{F}$$

$$t = \text{thermal wall thickness} = 0.015 \text{ in.}$$

$$r = 11.0 \text{ in.}$$

$$\Delta T = 1512 - 793 = 719^{\circ}\text{F}$$

$$P_{\text{equiv}} = \frac{-21 \times 10^6 (9.1 \times 10^{-6}) (719) (0.015)}{11.0} = -188 \text{ psi}$$

$$P_{\text{tot}} = 628 - 188 = 440 \text{ psi}$$

$$P_{\text{allow}} = P \sigma_{r_{\text{avg}}} \times S = 0.0416 (13,000) = 540 \text{ psi}$$

$$MS = \frac{540}{440} - 1 = 0.23$$

8.1.4.2 Flat Plate and Fin Panels

Using the fin stress formula,

$$\sigma_{\text{fin}} = \frac{P}{f} \left(\frac{b}{t_f} - 1 \right)$$

the test results yield the following indicated fin efficiencies.



UNCLASSIFIED

<u>Unit</u>	<u>Fin Stress, psi</u>	<u>Material Rupture Stress, psi</u>	<u>Fin Efficiency, Percent</u>
1	20,200	36,500	56.4
2	20,700	36,500	56.8
3	4,770	13,800	34.6
4	5,200	14,200	36.6
5	5,500	14,400	38.2

8.1.5 Conclusions

8.1.5.1 Continuous Joint Rupture Panels

Based on the aforementioned design conditions, the outer shell coolant exit structural design is satisfactory with a margin of safety of 23 percent.

8.1.5.2 Flat Plate and Fin Panels

Results appear consistent and are in agreement with data reported for other fin geometries. The average fin efficiency for short time burst at 1600°F equals 56.6 percent, while for creep-rupture it drops to 36.4 percent. These values have been shown to be satisfactory for structural design based on creep-rupture allowables.

8.1.6 Future Action

8.1.6.1 Continuous Joint Rupture Panels

No further testing of this joint is planned. The design, however, will be rechecked analytically for any new design conditions that may appear as the development effort progresses.

8.1.6.2 Flat Plate and Fin Panels

A creep-rupture test will be conducted in the near future on a series of panels with 28R-.050-.100-.006 fins, using 1.4 mils of braze foil rather than the 1.0 mils used in this series of panels. For comparison with data reported above, 20R-.050-.100-.006 fins will also be brazed using 1.4 mils of braze foil.

8.2 THERMAL CYCLE PANELS

Thermal cycle testing is being conducted to evaluate the low cycle fatigue performance of finned structures subjected to thermal differential loading. A typical test setup is shown in Figure 8.2-1. Figure 8.2-2 shows a close-up view of the specimen installed in the test setup with the lamp and shield orientation. Heated nitrogen was substituted for air for the support panel coolant. The control and flow measurement console for the hot nitrogen supply is shown in Figure 8.2-3. The data track thermal cycle function generator for the quartz lamp heat source Ignition Temperature Controller is shown in Figure 8.2-4.



UNCLASSIFIED

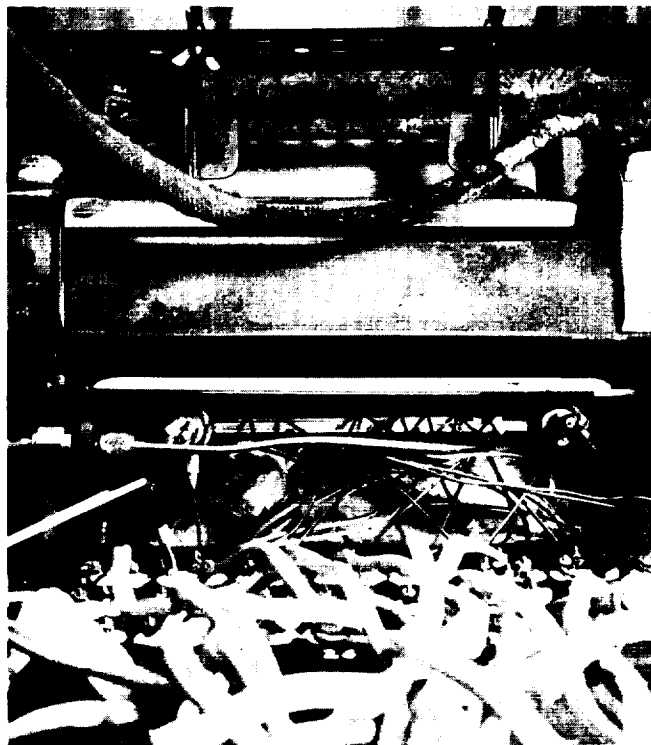
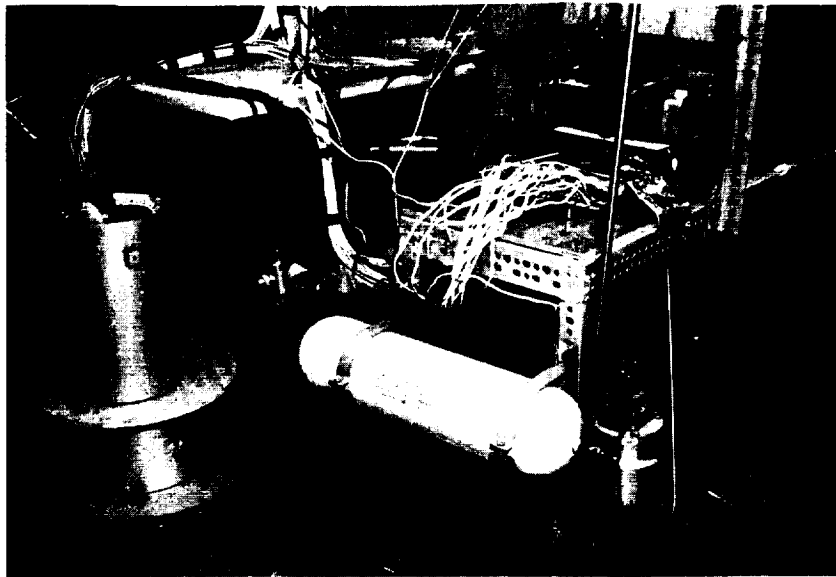


Figure 8.2-1. Temperature Distribution and Thermal Cycle Test Setup



AIRSEARCH MANUFACTURING DIVISION
Los Angeles, California

UNCLASSIFIED

67-2833
Page 8-6

UNCLASSIFIED

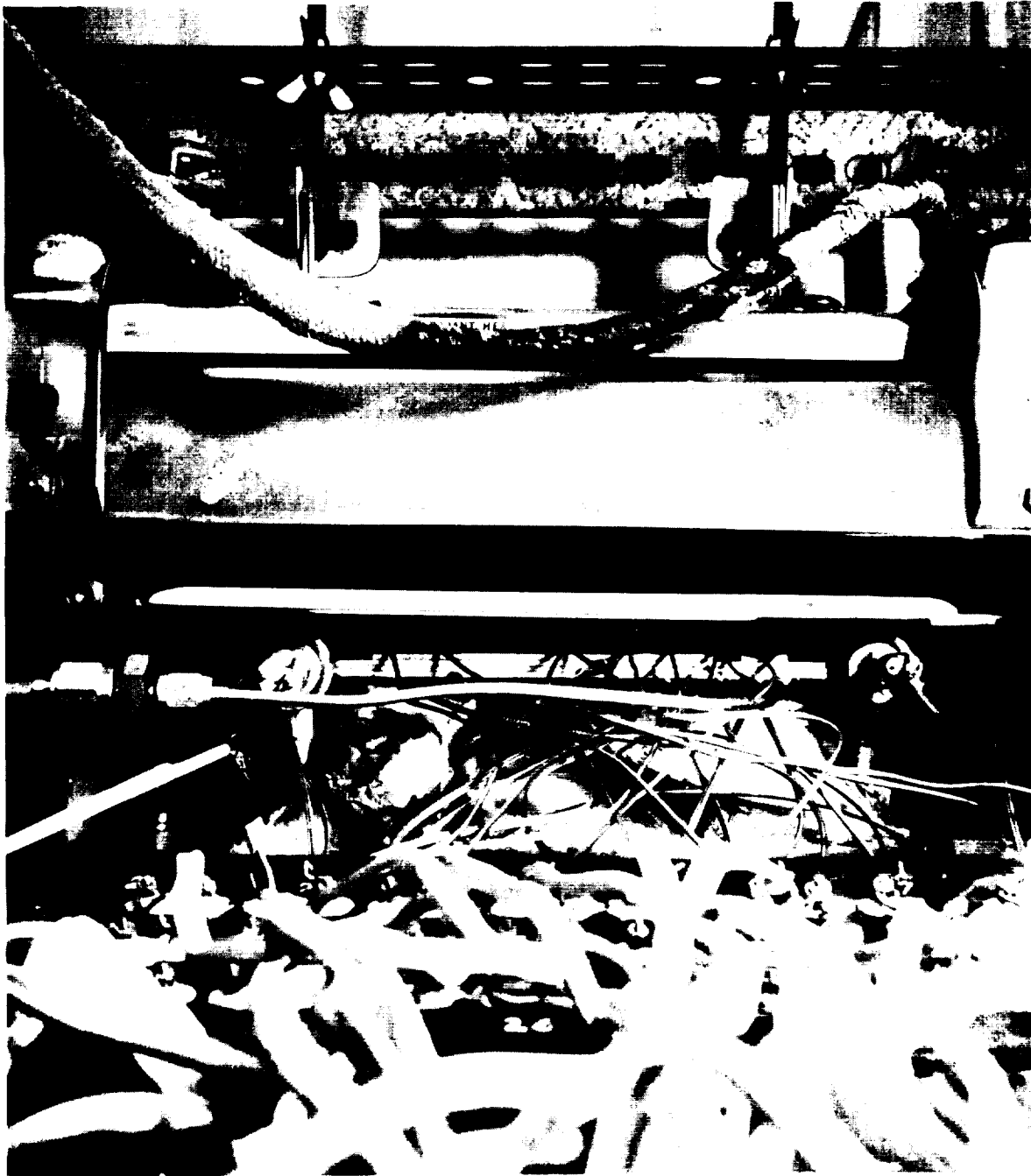


Figure 8.2-2. Flat Panel Test Specimen Installation

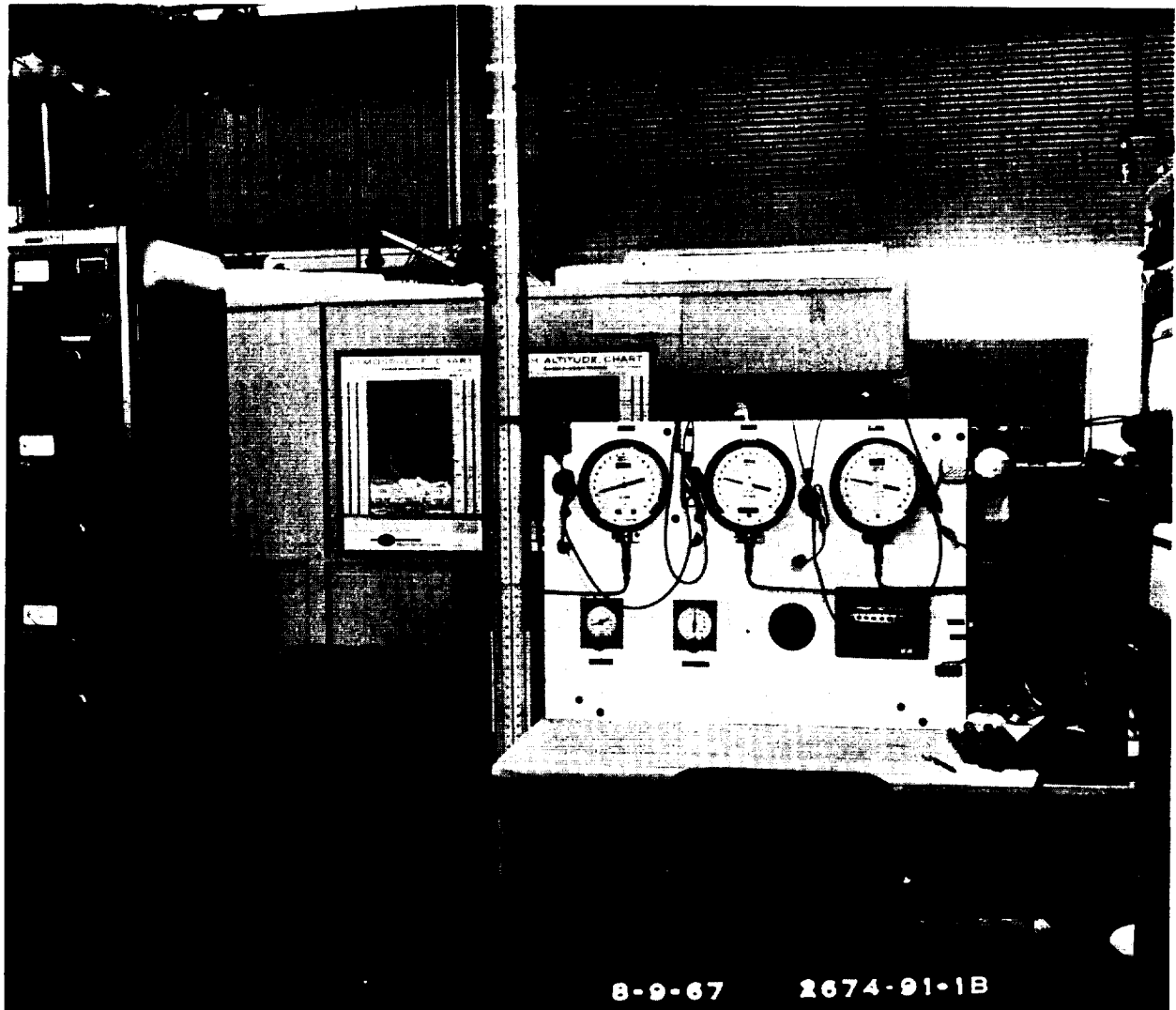


AIRESEARCH MANUFACTURING DIVISION
Los Angeles, California

UNCLASSIFIED

67-2833
Page 8-7

UNCLASSIFIED



F-8371

Figure 8.2-3. Coolant Heating and Flow Controls for Flat Panel Tests

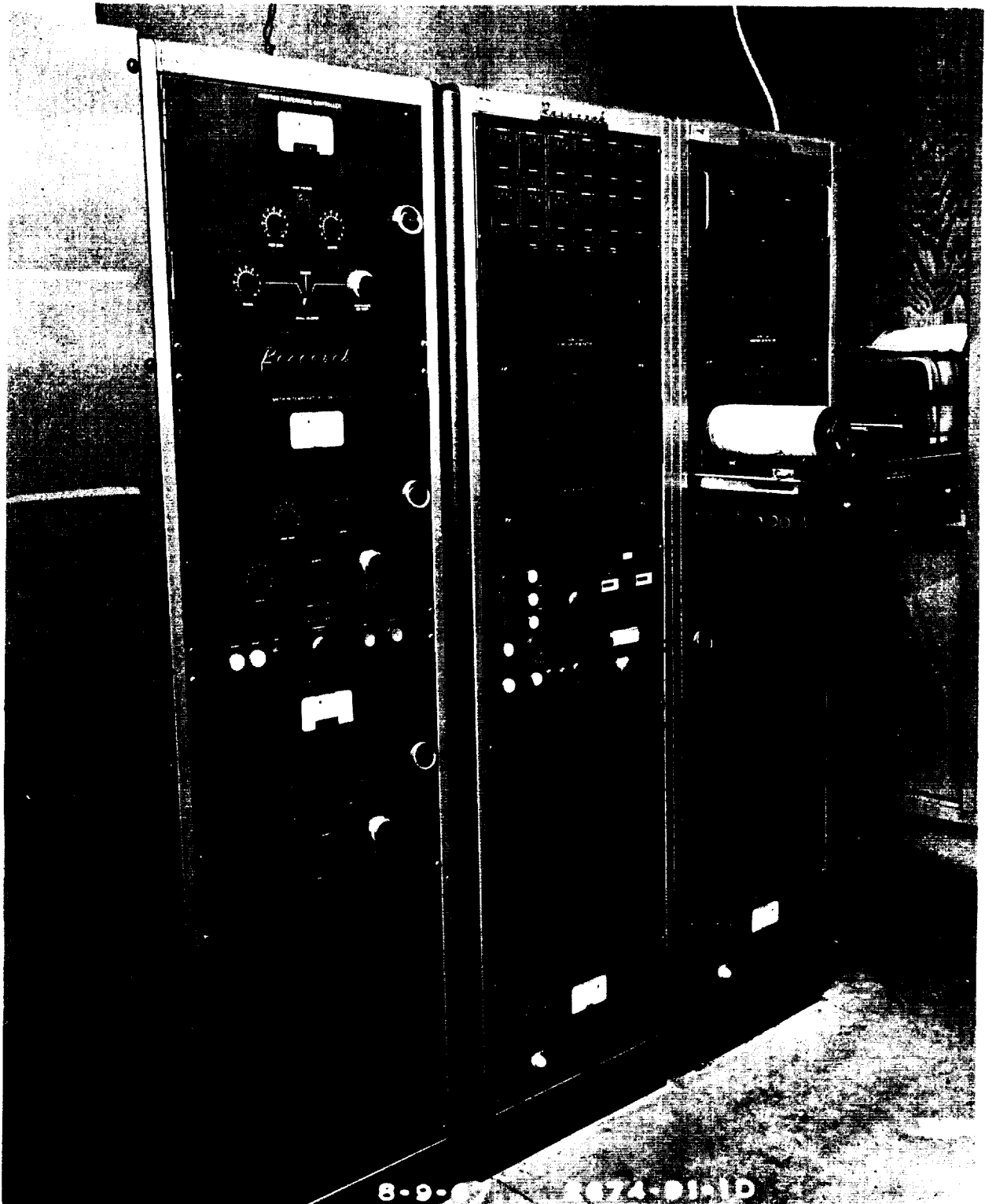


AIRSEARCH MANUFACTURING DIVISION
Los Angeles, California

UNCLASSIFIED

67-2833
Page 8-8

UNCLASSIFIED



F-8369

Figure 8.2-4. Quartz Lamp Heat Source Controls



AIRESEARCH MANUFACTURING DIVISION
Los Angeles, California

UNCLASSIFIED

67-2833
Page 8-9

8.2.1 Test Results

Six test specimens have been run to date. Test results are tabulated in Table 8.2-1. In the initial setup, the test conditions were maintained until the test panel attained equilibrium as indicated by nitrogen coolant outlet temperature stability. The test conditions were then verified and the panels were cycled at the specified structural fin thermal differential.

The initial setup had to be changed somewhat to obtain more uniform heating of the top surface of the structural panel. The original quartz lamp reflector assembly containing eight lamps in a single row was changed to a double staggered row quartz lamp assembly using only 10 of the lamps concentrated in the center of the holder. This greatly improved the overall top surface heating uniformity. In addition, the original stainless water cooled shield was replaced with an inert "Glass Rock" thermal insulation material.

Specimen S/N 4 showed the results listed in Table 8.2-1. These results were considerably different from those experienced with the previous three specimens, leading to the conclusion that there may have been some significant discrepancy in the fabrication of this specimen. This specimen will be physically examined in order to obtain more detailed data.

8.2.2 Test Data Reduction

8.2.2.1 Heat Transfer Analysis

Runs 1, 2, and 3 on flat panel S/N 4 verified the analytical procedures used to calculate the overall unit ΔT 's, the insulating fin ΔT 's, and the average center plate temperatures. For the three test runs, the ratio of steady state test ΔT to the steady state calculated ΔT was an average of 1.041 or about a 4 percent deviation. The various ΔT 's for the three tests are summarized in Table 8.2-2. The last column showing maximum transient ΔT 's above the nominals is the most significant.

The calculated steady state temperatures for the center plate were higher than the corrected center plate temperatures, as shown in Figures 8.2-5, 8.2-6 and 8.2-7, by 15 to 50°F maximum. These minor deviations are well within the limitations of the test apparatus and the analytical assumptions. Thermocouple locations on the unit are shown in Figure 8.2-8.

In order to determine the validity of the heat transfer technique used to determine the temperature distribution through flat panel S/N 4 had the center plate, as well as the upper and lower surfaces, instrumented to record the temperatures during the transient cycles. The schematic in Figure 8.2-5 indicates the relative locations of the temperatures obtained from the tests. Figures 8.2-5, 8.2-6, and 8.2-7 also indicate the analytical versus the test results for three typical cycles. In each case a comparison of theory to test was completed for thermocouple pair 2 and 10. Thermocouple 25 (center plate), one in. downstream of TC pair 2-10, as shown in the above figures, was corrected for position to coincide with TC pair 2-10.



TABLE 8.2-1
FLAT PANEL TEST RESULTS

Specimen Part Number	Structural Panel Pressure, psig	Coolant Inlet Temp, °F	Coolant Flow Rate, lb/min	Total Cycles at Nominal ΔT					Remarks
				600°F	700°F	800°F	900°F		
SK51315-1 #1	290	415	1.39	202(2)	--	--	--	--	--
		332	2.18	--	--	19(2)	--	--	Changed heat lamp to higher intensity unit for rest of tests.
SK51315-1 #2	290	415	1.40	--	--	94(2)	--	--	--
SK51370-1 #1	290	411	1.35	--	--	73(7)	--	--	--
SK51370-1 #2	200	428	1.38	--	--	187(1)	--	--	--
SK51315-1 #3	200	519	1.40	--	131(1)	--	--	--	--
SK51315-1 #4	50	642	1.34	102(2)	--	--	--	--	--
		535	1.46	--	2(2)	--	--	--	--
		427	1.33	--	--	1(1)	--	--	--

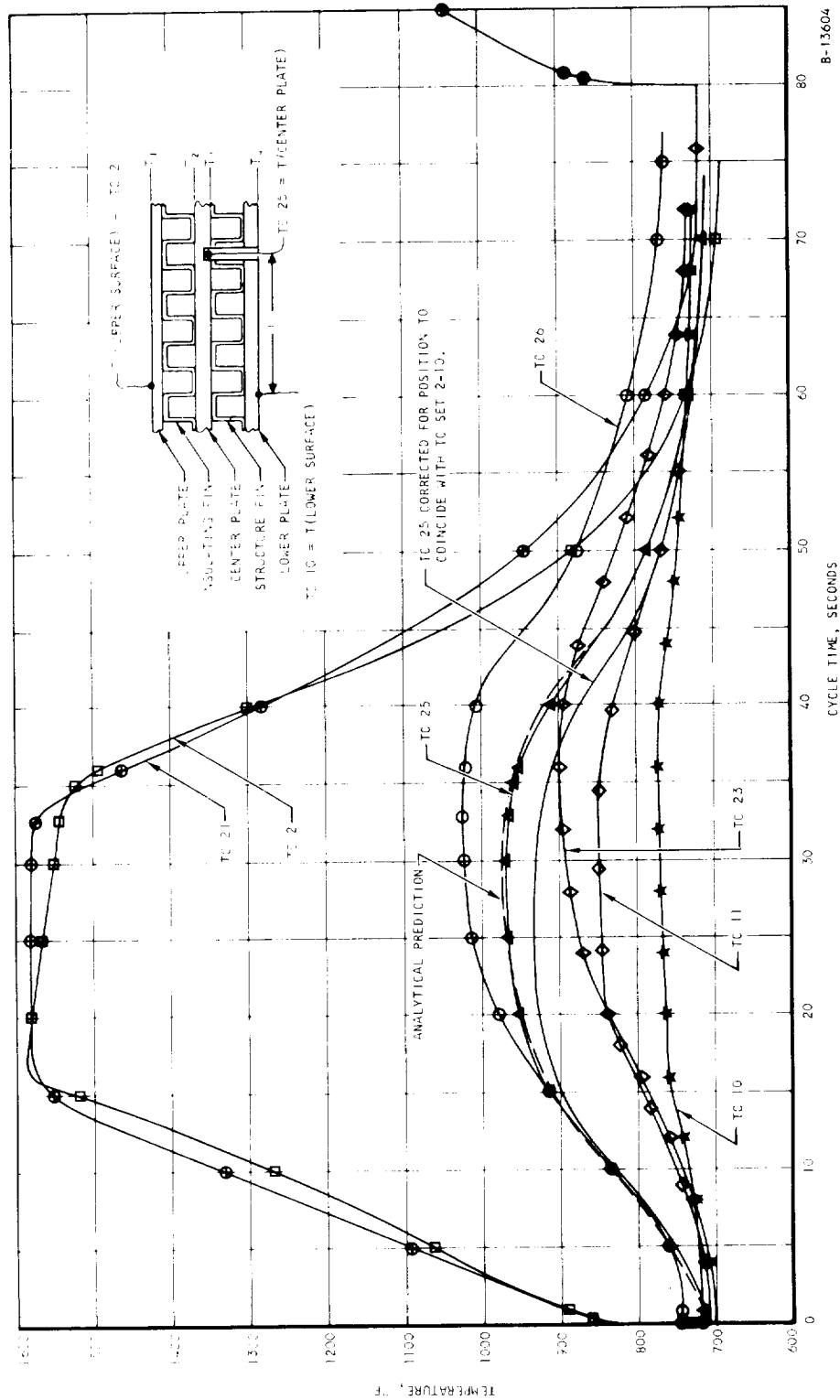
() Indicates number of steady runs in total cycles.

TABLE 8.2-2
DELTA T SUMMARY FOR THERMAL CYCLE FLAT PANELS

Test Run No.	Coolant Parameters		Heat Fluxes (SS)		Steady State (SS)				$\Delta T_{\text{Transient}}$	
	$T_{N2-in},$ $^{\circ}F$	$T_{N2-out},$ $^{\circ}F$	N_2 Flow, lb/min	$(Q/A)_{avg},$ Btu/sec ft ²	$(Q/A)_{local},$ Btu/sec ft ²	$\Delta T_{nom},$ $^{\circ}F$	$\Delta T_{calc},$ $^{\circ}F$	$\Delta T_{Test},$ $^{\circ}F$	$\frac{\Delta T_{Test}}{\Delta T_{calc}}$	$\Delta T_{\text{Transient}}$ max $^{\circ}F$
1	727	917	1.40	17.2	30.0	600	575	625	1.085	680
2	530	818	1.30	23.6	32.8	700	755	770	1.02	835
3	425	752	1.39	28.6	37.4	800	820	840	1.02	925



UNCLASSIFIED



B-13604

Figure 8.2-5. Typical Flat Panel Thermal Cycle Test Results for 600°F Nominal Steady State AT



AIRESEARCH MANUFACTURING DIVISION
Los Angeles, California

UNCLASSIFIED

67-2833

Page 8-13

UNCLASSIFIED

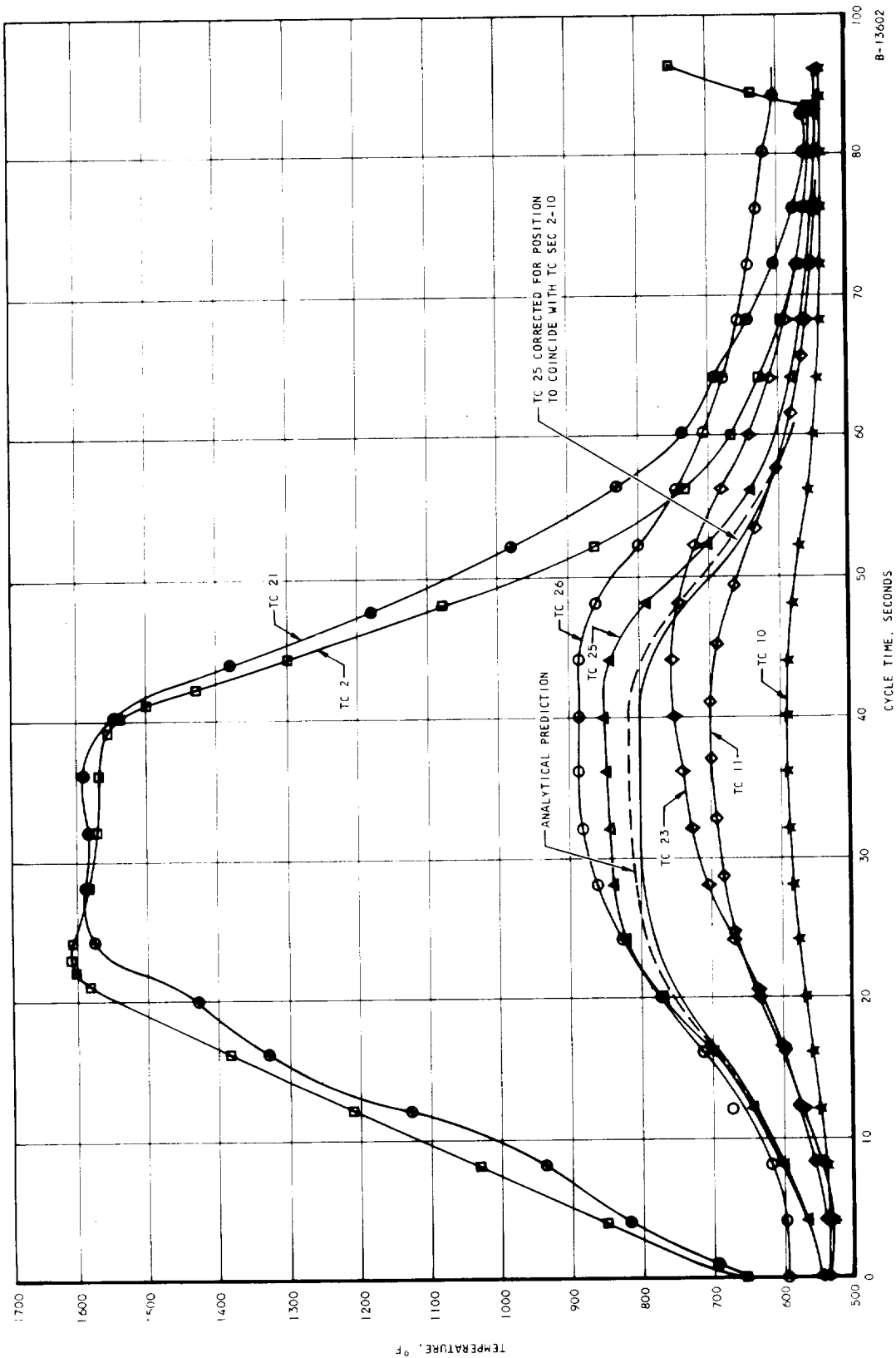


Figure 8.2-6. Typical Flat Panel Thermal Cycle Test Results for 700°F Nominal Steady State ΔT



AIRESEARCH MANUFACTURING DIVISION
Los Angeles, California

UNCLASSIFIED

67-2833

Page 8-14

UNCLASSIFIED

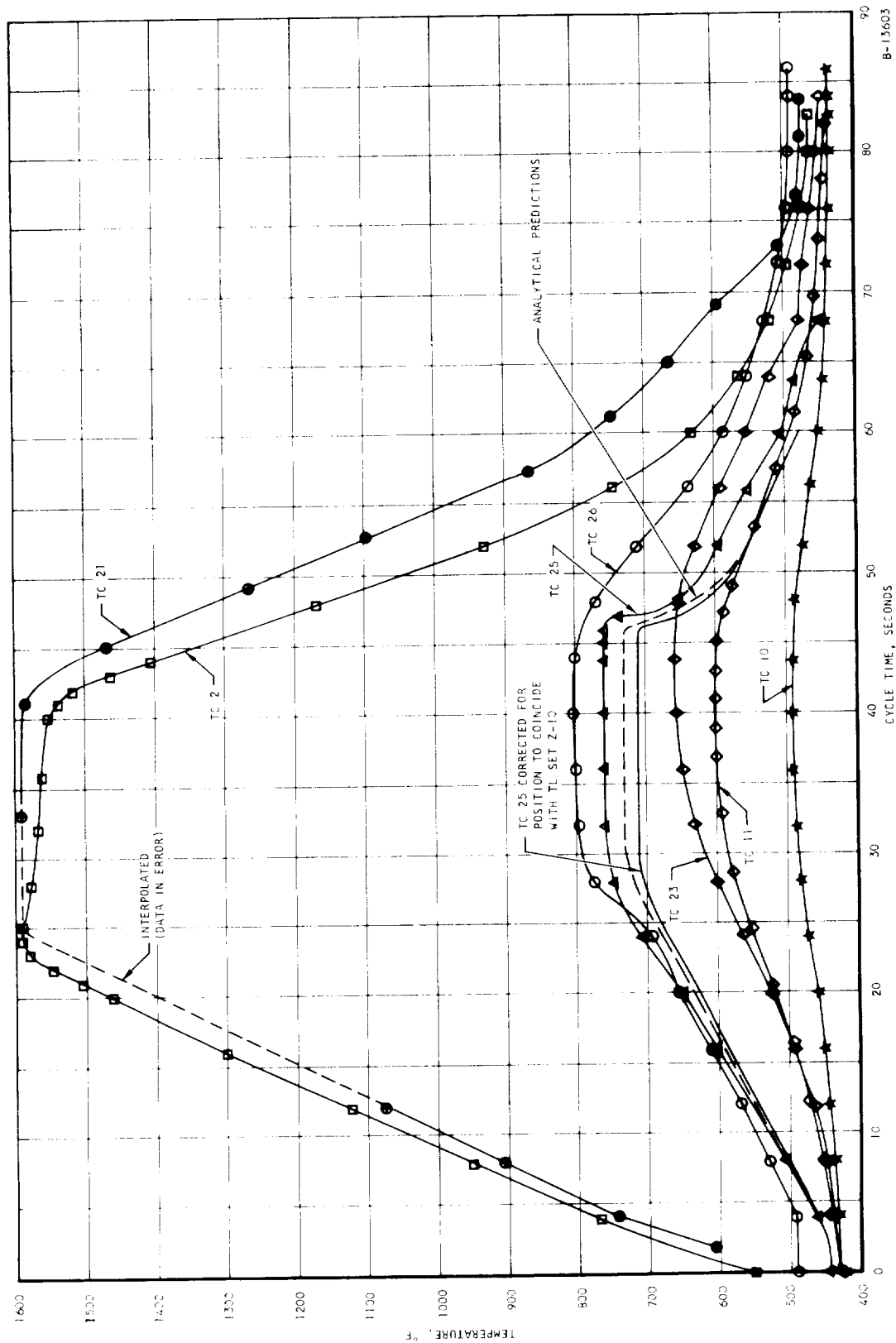


Figure 8.2-7. Typical Flat Panel Thermo Cycle Test Results for 800°F Nominal Steady State ΔT



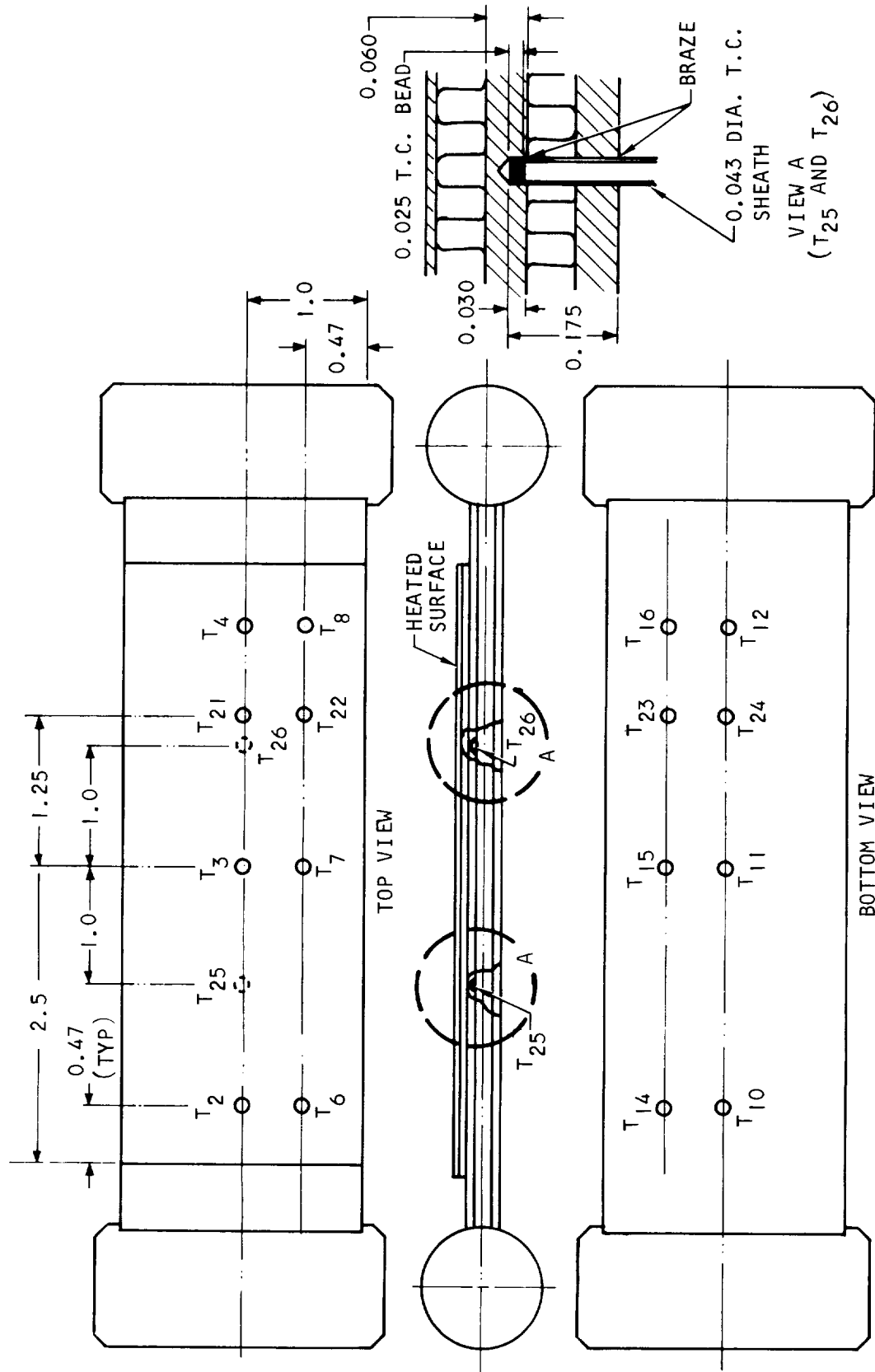
AIRESEARCH MANUFACTURING DIVISION
Los Angeles, California

UNCLASSIFIED

67-2833

Page 8-15

UNCLASSIFIED



A-32230

Figure 8.2-8. Flat Panel S/N 4 Metal Surface Thermocouple For Thermal Cycle Test



AIRESEARCH MANUFACTURING DIVISION
Los Angeles, California

67-2833
Page 8-16

UNCLASSIFIED

In order to obtain the corrected curve for TC 25, the difference in temperature due to location was estimated by assuming that the center plate temperature increase per in. of length was equal to the nitrogen temperature increase per in. of length. The $\Delta T/\text{in.}$ was derived for various time increments from curves similar to 8.2-9.

From Figure 8.2-9, the nitrogen heat-up per in. is

$$\frac{TC\ 23 - TC\ 10}{X_{23} - X_{10}} = \frac{735 - 585}{4.25 - 1.00} = 46^\circ\text{F/in.}$$

TC 25 is one in. downstream of TC pair 2-10. Therefore, the corrected temperature for TC 25 vs

$$(TC25)_{\text{corrected}} = 845 - 46 = 799^\circ\text{F}$$

This is shown on Figure 8.2-6 at 32.5 sec.

8.2.2.2 Stress Analysis

The temperatures in the upper surface, the center plate, and the lower plate must be considered in the stress analysis in order to evaluate the plastic strain in the upper surface. The maximum condition always occurs during the heat-up portion of each cycle at the instant of time that the upper surface temperature levels off. These temperatures are summarized for thermocouples No. 2, 10, and 25 (corrected) in Table 8.2-3 for the nominal 600°F, 700°F, and 800°F tests that were conducted. The conditions shown in the table were obtained from a single test unit. Because of the duplication of test conditions, however, they are equally applicable to the other five units that were tested.

TABLE 8.2-3

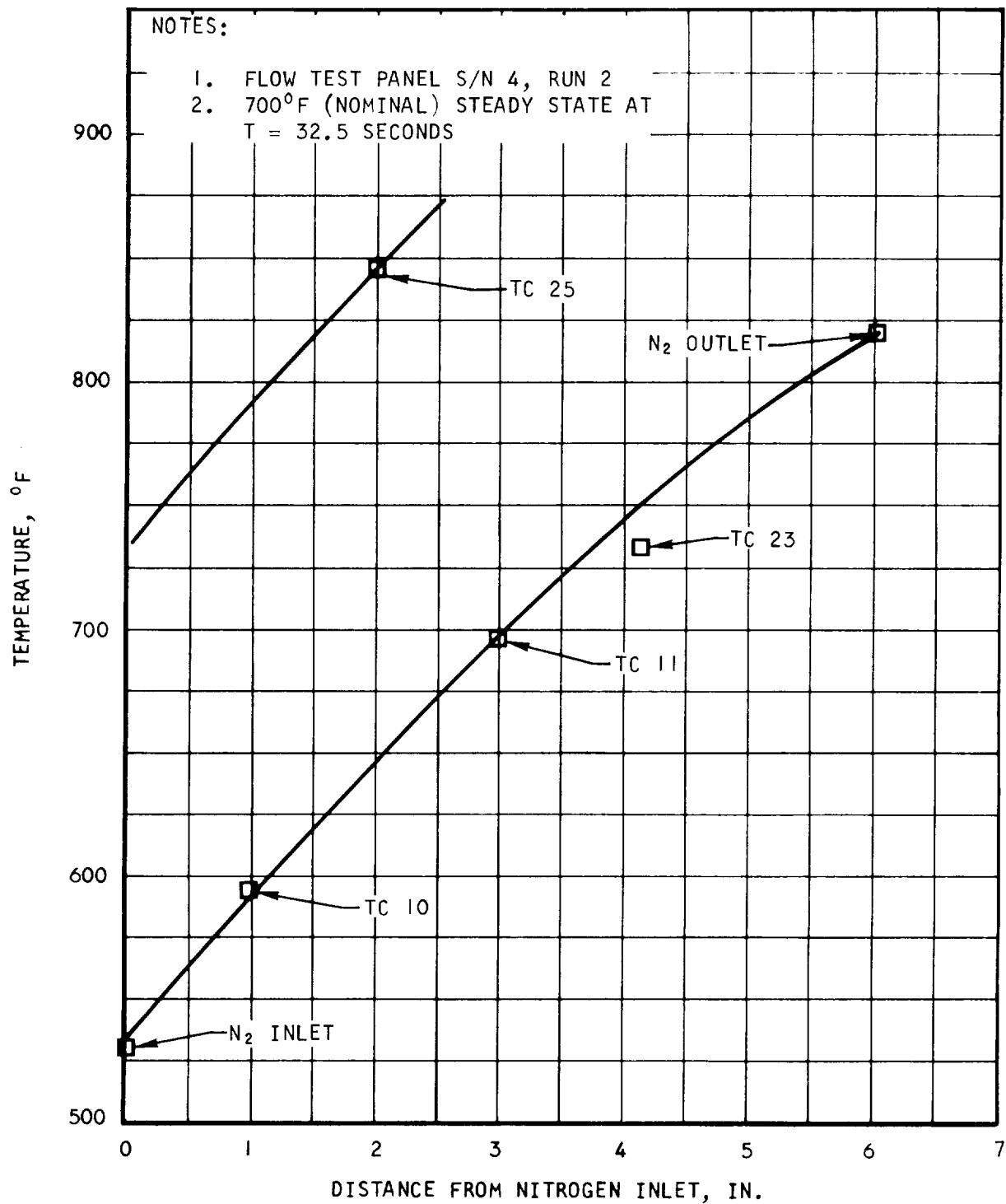
METAL TEMPERATURES FOR THERMAL FATIGUE TESTS

Nominal ΔT	$T_{\text{upper,}}$ °F	$T_{\text{center,}}$ °F	$T_{\text{lower,}}$ °F	ΔT	
				Upper to Center	Upper to Lower
600	1585	905	760	680	825
700	1610	775	580	835	1030
800	1590	665	475	925	1115

An elastic-plastic analysis of the three-layered structure was performed to determine, first, the total strain and, then, the plastic strain per cycle in the upper surface. For the top surface, 1600°F material properties were used, i.e., the hot surface was assumed to yield and develop a stress of 35,000 psi. The center and lower surfaces remain elastic throughout, and an elastic modulus of 25×10^6 psi was used, based upon mean temperatures in these layers of approximately 600°F. The ΔT between the center and lower surfaces



UNCLASSIFIED



A-3214F

Figure 8.2-9. Nitrogen Temperature Distribution



AIRESEARCH MANUFACTURING DIVISION
Los Angeles, California

67-2833
Page 8-18

UNCLASSIFIED

causes a small upward bowing, which tends to alleviate the strain in the upper surfaces. The compressive stress in the upper surface also causes a small bending moment in the structure, which, in turn, produces upward bowing and further alleviation in the upper surface deformation. Finally, the compressive stress in the upper surface causes tensile stresses in the center and lower surfaces, thus further reducing the plastic strain in the upper surface.

Analysis was performed for the three conditions given in Table 8.2-3. Some further generality was introduced into these calculations by solving for total strain in the upper surface for several values of center surface temperature. This was done to verify that the most severe hot surface loading does in fact occur as described above and also to study the relationship between center surface temperature and total strain applied to the upper surface. The computed results are plotted on Figure 8.2-10.

The total strain deformation applied to the upper surface for the three test levels are tabulated below, along with the engine ΔT corresponding to the given amount of total strain:

Nominal Test ΔT , $^{\circ}\text{F}$	Total Strain, (ϵ_{total}) in./in.	Comparable Engine ΔT , $^{\circ}\text{F}$
600	0.00485	530
700	0.00580	630
800	0.00680	730

The total strain is applied biaxially. It is necessary to compute the biaxial stresses in the heated surface and from these stresses the cyclic plastic strain amplitude. During each thermal cycle, the heated surface undergoes plastic deformation at the elevated temperature and then a reversed plastic flow at the cold temperature. If the loading were uniaxial, the plastic strain amplitude would be computed as follows:

$$\epsilon_p = \epsilon_{\text{total}} - \frac{\sigma_c}{E_c} - \frac{\sigma_h}{E_h}$$

For the nominal 800 $^{\circ}\text{F}$ ΔT test, the heated surface alternates between 1590 $^{\circ}\text{F}$ and 475 $^{\circ}\text{F}$. The Ramberg-Osgood expressions for stress versus plastic strain at these temperatures are :

$$\text{at } 475^{\circ}\text{F}, \sigma = 177,000 \epsilon_p^{0.215}$$

$$\text{at } 1590^{\circ}\text{F}, \sigma = 52,500 \epsilon_p^{0.115}$$



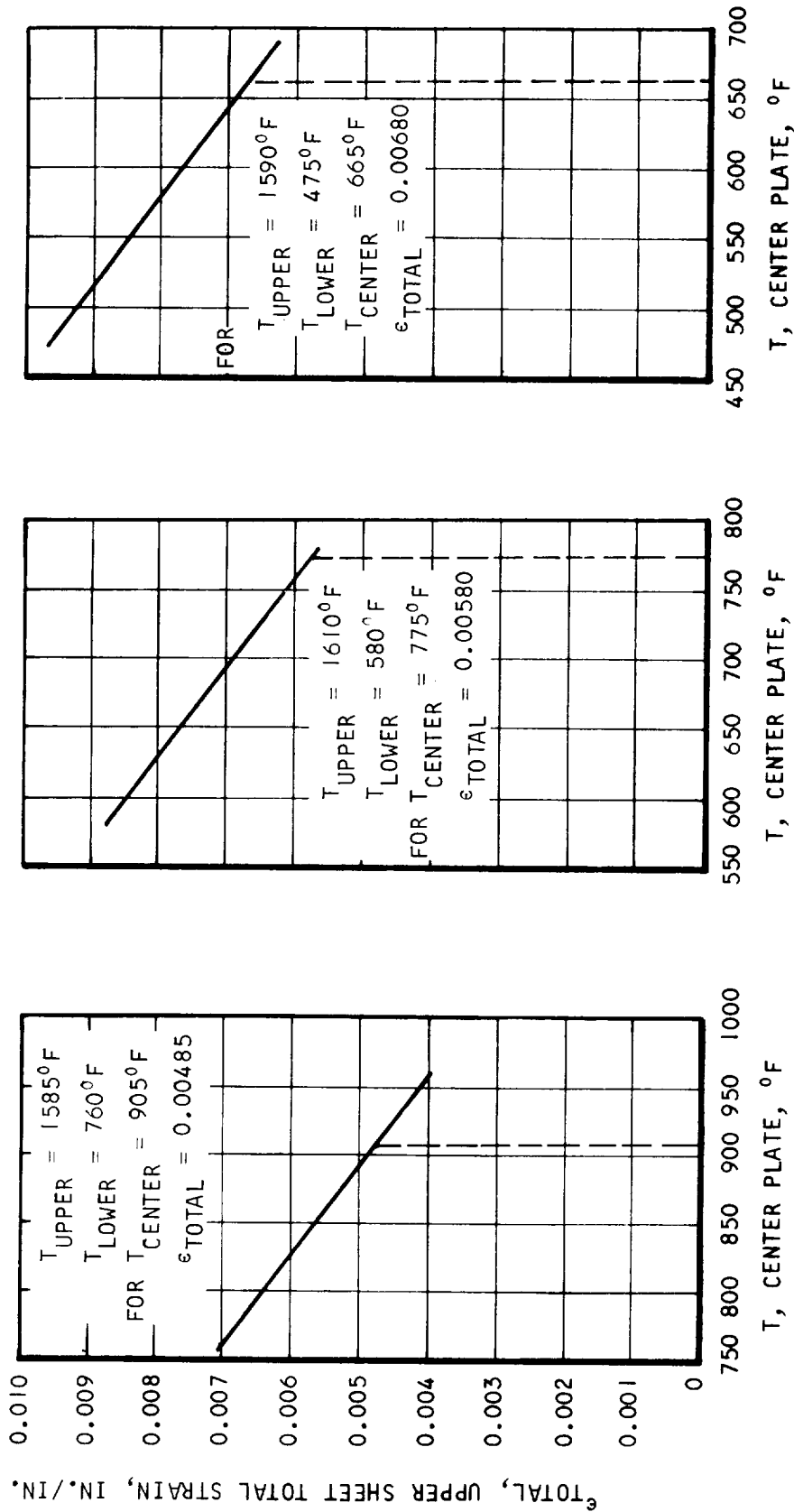


Figure 8.2-10. Upper Surface Total Strain from Panel Fatigue Tests

A-32150

These expressions were used to generate the stress-strain curves. For each specific value of ϵ_p , the elastic strain components at the hot and cold temperatures were computed, and a plot of ϵ_p versus ϵ_{total} was generated. This is shown on Figure 8.2-11.

For equi-biaxial loading, the expressions must be modified to account for the biaxial deformations and constraints. This was accomplished by using the elastic and plastic multiaxial stress-strain relationships and by applying the expressions above for uniaxial stress vs strain. A curve for effective plastic strain vs total strain range was obtained. This curve is also plotted on Figure 8.2-11.

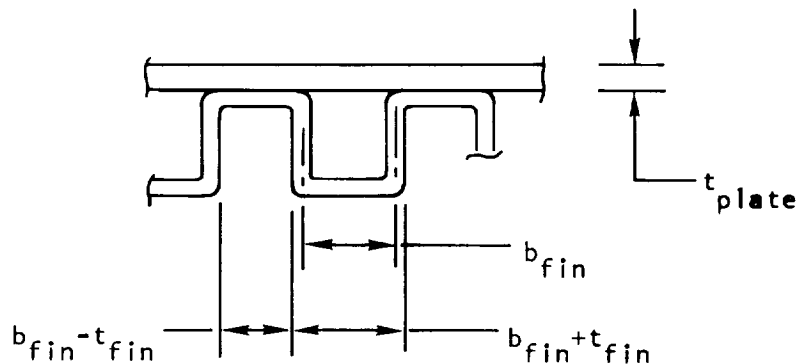
From Figures 8.2-10 and 11, the following plastic strain ranges are obtained for the three nominal ΔT ranges:

$$\Delta T_{nom} = 600^{\circ}, \Delta \epsilon_p = 0.00405 \text{ in./in.}$$

$$\Delta T_{nom} = 700^{\circ}, \Delta \epsilon_p = 0.00565 \text{ in./in.}$$

$$\Delta T_{nom} = 800^{\circ}, \Delta \epsilon_p = 0.00735 \text{ in./in.}$$

The offset plate-fin structure produces a checkerboard-type reinforcement of the heated surface. Once plastic flow starts, the unreinforced areas will be subjected to substantially more strain than the reinforced areas. In the elastic range, the stresses would be approximately inversely proportional to local metal thickness, which means that those regions that yield first will absorb all of the plastic flow. A typical plate-fin cross-section shown below has somewhat less non-reinforced area than reinforced.



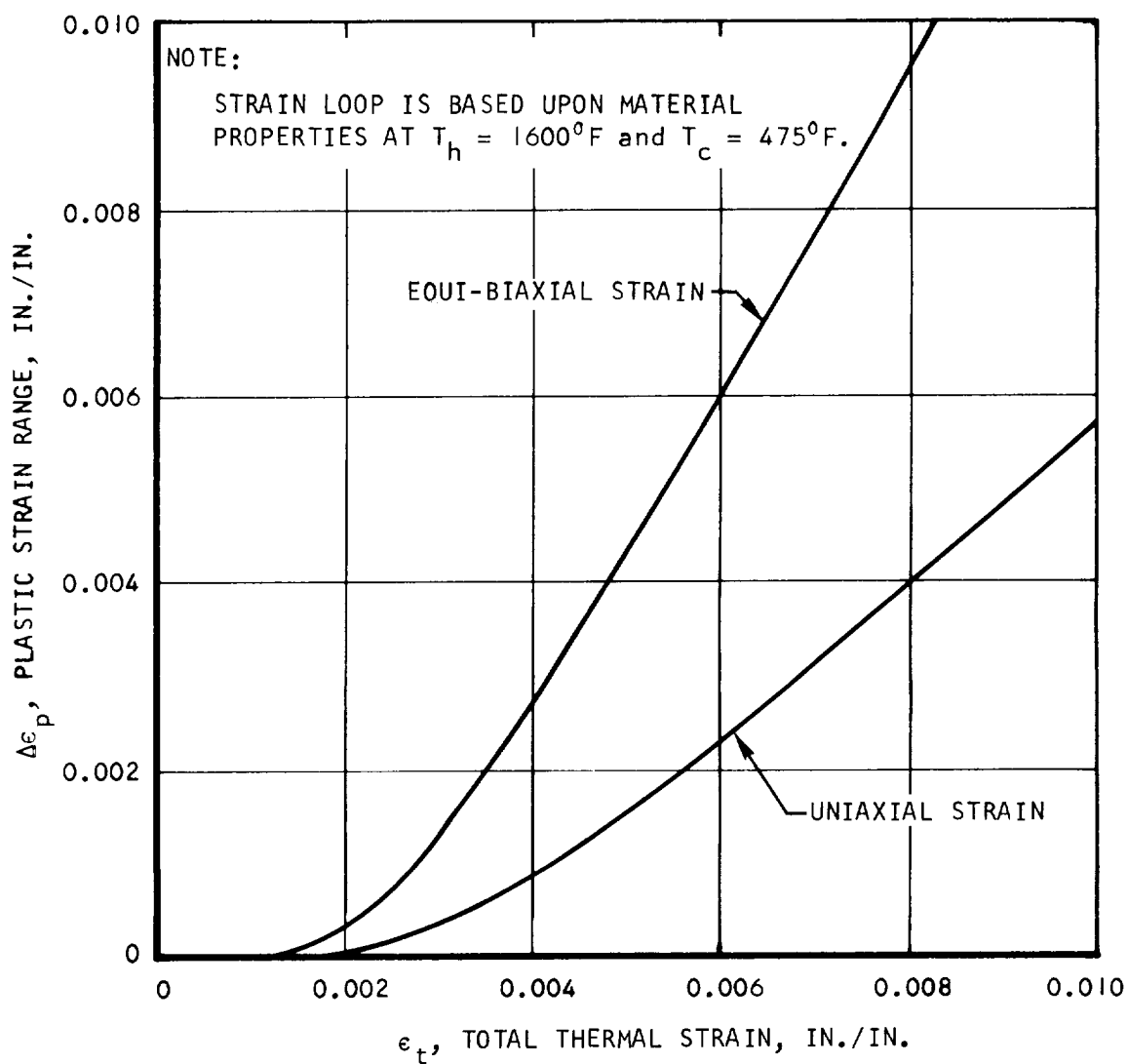
For this structure the ratio of total span to unreinforced span is:

$$K = \frac{2 b_{fin}}{b_{fin} - t_{fin}}$$

With 20 fins/in. and a fin thickness of 0.004 in., the value for K is 2.18. Since braze filletting further reduces the unsupported span, a plasticity concentration factor of 2.5 is used for fatigue analysis.



UNCLASSIFIED



A-32149

Figure 8.2-11. Plastic Strain Range vs Total Thermal Strain



AIRSEARCH MANUFACTURING DIVISION
Los Angeles, California

67-2833
Page 8-22

UNCLASSIFIED

The strain concentration factor for lengthwise deformations cannot be determined analytically. For the present, this factor is assumed to be 2.5.

Cycles to failure are computed from the low cycle fatigue formula:

$$N = \left(\frac{C}{\Delta \epsilon_p} \right)^2$$

The minimum ductility for Hastelloy X over the temperature range is 31.5 percent for 0.109-in. thick sheet. Test data on brazed, thin Hastelloy X sheet indicates that this is reduced to approximately 60 percent of the above figures. The ductility coefficient based upon RA of 20 percent is $C = 0.25$. The following cycle life predictions are obtained for the three nominal ΔT values:

For nominal $\Delta T = 800^\circ\text{F}$

$$\Delta \epsilon_p = (2.5) (0.00735) = 0.0183$$

$$C = 0.25$$

$$N = \left(\frac{0.25}{0.0183} \right)^2 = 183 \text{ cycles}$$

For nominal $\Delta T = 700^\circ\text{F}$

$$\Delta \epsilon_p = (2.5) (0.00565) = 0.0142$$

$$C = 0.25$$

$$N = \left(\frac{0.025}{0.0142} \right)^2 = 310 \text{ cycles}$$

For nominal $\Delta T = 600^\circ$

$$\Delta \epsilon_p = (2.5) (0.00405) = 0.01025$$

$$C = 0.25$$

$$N = \left(\frac{0.25}{0.01025} \right)^2 = 595 \text{ cycles}$$

For nominal $\Delta T = 1000^\circ\text{F}$

$$\Delta \epsilon_p = (2.5) (0.01065) = 0.0266$$

$$C = 0.25$$

$$N = \left(\frac{0.25}{0.0266} \right)^2 = 88 \text{ cycles}$$



8.2.3 Discussion of Test Results and Conclusions

The first specimen, S/N 1, was tested at the 800°F nominal ΔT for 200 cycles and then at 1000°F nominal ΔT until failure, which occurred after another 19 cycles. Based upon the cycle life estimates given in the previous paragraph, this corresponds to a life fraction of

$$L.F. = \frac{200}{188} + \frac{19}{88} = 1.06 + 0.21 = 1.27$$

A careful investigation revealed that the failure occurred at the gap between the two fin sections that were used to fabricate the specimen. The flow length of 4.5 in. is accomplished by the use of a 3.0-in. length fin and a 1.5-in. length fin. It was determined that the gap between these fins was 0.008 in. It was also determined that fin temperature at the joint between the fin and the top surface temperature was nearly 1600°F. In the actual engine, maximum total ΔT and metal temperature occur where there are much higher heat fluxes than in the thermal cycle test. A sizable portion of the ΔT in the engine is taken through the heated surface (200°F to 300°F), which means that the fins are much cooler in the engine than in the test. It was determined, furthermore, that the panel internal pressure of 290 psig was more severe on the basis of time to rupture than the 700 psig operating pressure for the engine fins. A more satisfactory test pressure level was computed to be 200 psig. In spite of the somewhat more severe fin temperature and high fin pressure, the test result was very satisfactory.

Specimen S/N 2 was tested at the 800°F nominal ΔT , and failure occurred after 94 test cycles. This corresponds to a theoretical life fraction of

$$L.F. = \frac{94}{188} = 0.500$$

Performance of this specimen which had an 0.030-in. fin gap and was tested at 290 psig, was not as good as the life fraction obtained with the first specimen. Specimen S/N 2 had developed a pronounced bulge and then cracked through the top surface at the parting line between the fin sections. A close inspection of several micrographs showing material through the crack in the bulged surfaced revealed local fin failures near the bulge. A small amount of local neckdown occurred at the crack. These various effects are indicators of localized concentrated strains, higher than indicated by the calculations. The shortened life can be attributed to the large fin gap and the high test pressure. At this point in the program, it was concluded that the failure was at least partly due to the large fin gap.

The third specimen to be tested was S/N 1. This specimen was similar to the first two, except that it had four small annular plugs added to simulate local joints of the instrumentation pickups and fuel flow injectors. The test was conducted with the 800°F nominal ΔT , and top surface cracking occurred after 73 test cycles. This corresponds to a life fraction of

$$L.F. = \frac{73}{188} = 0.388$$



UNCLASSIFIED

The specimen, which had an 0.010-in. fin gap and was tested at 290 psig, was not prepared for micrographic inspection, but it appears that the failure once again was located at the line between the fin sections. There was no evidence of cracking at the simulated local joints.

A second local joint specimen, S/N 2, was tested next. The test was carried out with an 800°F nominal ΔT and a pressure of 200 psig. A life of 187 cycles was achieved. The computed life fraction is

$$L.F. = \frac{187}{188} = 0.995$$

This failure did not occur at the fin gap. Several cracks were generated in the hot surface, and a large section of the hot surface (approximately 1.0-in. long by 0.75-in. wide) was blown out. The fins underneath the blown out area were intact after the test. It is not possible to determine whether the initiation of the failure was due to hot surface cracking or braze joint separation. The results of this test were substantially better than the preceding two tests. The nature of the failure gives rise to the possibility that the origin of the failure is in the braze joint.

The next specimen tested was a basic flat panel, S/N 3. This specimen had a closely controlled fin gap specified on the fabrication drawing (0.010 in. maximum). The test was carried at a 700°F nominal ΔT and a fin pressure of 200 psig. Failure took place after 131 cycles, giving a life fraction of

$$L.F. = \frac{131}{210} = 0.422$$

The entire middle of the specimen hot surface was bulged outward, and a section 1.5-in. long by 0.75 in. wide had broken away. Several of the fins were broken through, but, in general, it appeared that the hot surface had pulled away from the fins. It appears that the initial failure was in the braze rather than through the hot surface, and that it was at least partly due to the high test temperature at the fin joints.

The last test conducted to date was on a basic flat panel specimen, S/N 4. This test was performed with 50 psig fin pressure to reduce loading on the braze joint. The test was started with a 600°F nominal ΔT with the intention of performing 200 cycles at this level, to be followed by 200 cycles at 700°F nominal ΔT (or until failure, if less), and additional cycles at 800°F nominal ΔT until failure or a maximum of 200 cycles were completed.

Failure occurred after 102 cycles at the 600°F condition, which corresponds to a life fraction of

$$L.F. = \frac{102}{595} = 0.172$$



This was the poorest performance of the six tested specimens. Radiographic and visual inspection of the test piece indicated that the failed zone (a 1.0 in. crack across the specimen width) did not occur at the fin gap. Further metallographic inspection is needed to obtain an explanation for the type of failure and the reason for the early failure.

The actual number of cycles obtained in the six tests were lower than the computed numbers. The lower performance can be due to higher localized strain concentrations than were used in the analysis, lower ductility, or can be due to braze joint failure rather than failure of the heated surface under cyclic loading, or combinations of these.

Except for the last specimen, the scatter in cycles-to-failure is not inconsistent with the nature of the tests. Even for closely-controlled fatigue tests on less complex test specimens, such as rotating beam tests on round bars, a scatter range in cycles-to-fail for the same load intensity generally exceeds ± 50 percent. For low cycle fatigue testing in which the plastic strain amplitude is accurately known, a scatter range of ± 50 percent is typical.

Some further investigation will be carried out to improve the analytical estimate for strain concentration.

8.2.4 Future Action

Testing of additional samples is planned. Additional specimens will be fabricated, with some modification in instrumentation and fabrication techniques based upon the experience gained thus far. Tests with the same nominal ΔT values, but with low hot surface temperature (1450° to 1500°F), must be conducted for a better simulation of braze joint temperature in the engine.

8.3 FLOW TEST PANELS

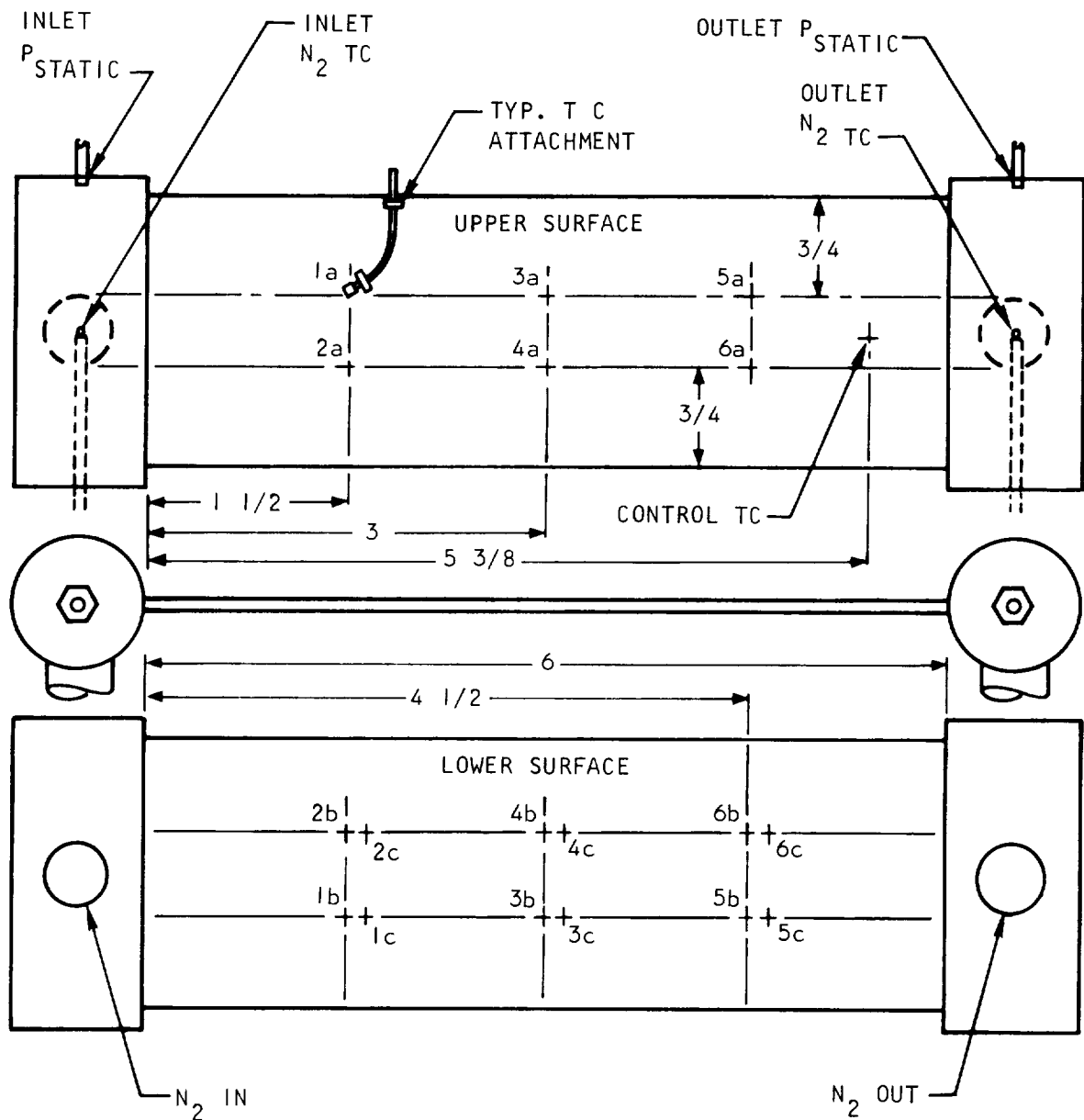
The flow test panel unit was instrumented to record panel metal temperature differences at seven points, and inlet and outlet gas temperature and pressures as shown in Figures 8.3-1 and 8.3-2. In addition, the surface of the test unit was sprayed with a temperature-sensitive paint, capable of indicating surface temperatures to 1600°F . The test setup included a quartz lamp bank as the heat source, heated nitrogen as the coolant, and the necessary controls to modulate the lamps to give a predetermined maximum surface metal temperature. The purpose of this test was to serve as a calibration for thermal cycle panels and flow panels with local inserts. Results of tests on the latter panels have yet to be evaluated.

8.3.1 Test Procedure and Results

During the tests, the unit was subjected to the series of coolant nitrogen flows and heat flux levels listed in Table 8.3-1. It was removed at predetermined intervals and color photographed to record temperature-indicating paint. Based on the temperature-indicating paint, which has a resolution of 50°F or more, a maximum temperature variation of less than 50°F was indicated across the heated surface. This variation is attributed to a combination of flow and



UNCLASSIFIED



NOTES

1. ALL THERMOCOUPLES (TC'S) ARE CHROMEL VERSUS ALUMEL.
2. UPPER SURFACE TC'S ARE 0.040 DIA. INCO SHEATHED.
3. LOWER SURFACE TC'S ARE FIBERGLASS COVERED.
4. ALL TC'S JUNCTIONS ARE SPOTWELDED TO METAL SURFACE.

A-32139

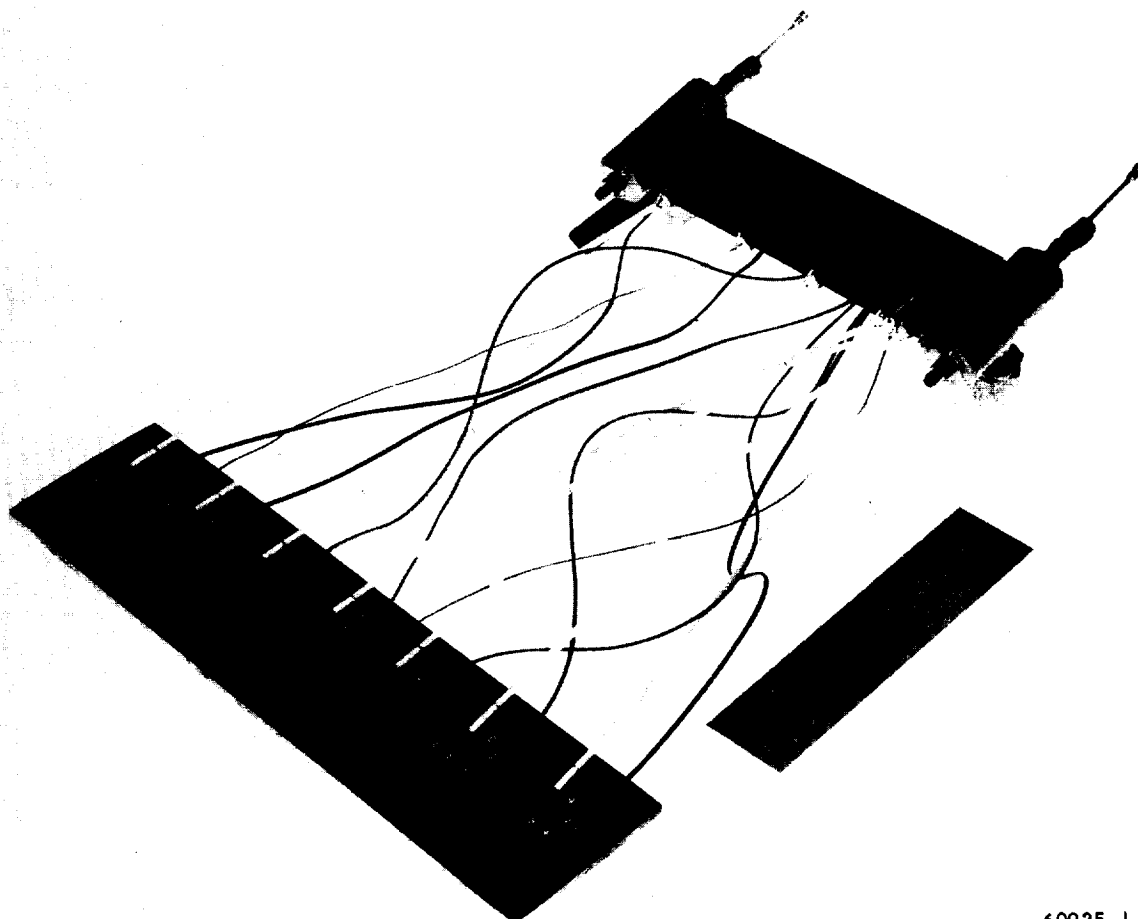
Figure 8.3-1. Thermocouple Installation for Temperature Distribution Flow Test



AIRESEARCH MANUFACTURING DIVISION
Los Angeles, California

UNCLASSIFIED

UNCLASSIFIED



60925-1

Figure 8.3-2. Flat Panel Flow Test Specimen



AIRESEARCH MANUFACTURING DIVISION
Los Angeles, California

67-2833
Page 8-28

UNCLASSIFIED

UNCLASSIFIED

TABLE 8.3-1
COMPARISON OF TEST AND ANALYTICAL RESULTS
FOR FLOW TEST PANEL S/N 1

Run No.	Nitrogen Parameters					Test Panel			
	Flow Rate lb/min	Inlet Temperature, °F	ΔT_N , °F	Inlet Pressure, psig	ΔP , psi	Calculated Heat Flux Btu/sec ft ²	Average Test ΔT , °F	$\frac{\Delta T_{\text{calculation}}}{\Delta T_{\text{test}}}$	$\frac{\rho \Delta P_{\text{calculation}}}{\rho \Delta P_{\text{test}}}$
1B	2.21	78	134	37.0	17.8	18.5	142	1.0	1.72
1D	2.03	79	142	34.0	18.0	17.9	123	1.145	1.575
1E	1.75	79	171	28.2	10.0	17.9	134	1.09	2.42
2A	0.95	79	499	16.3	9.5	29.6	241	1.18	1.32
2B	1.54	79	423	29.3	16.1	39.6	286	1.105	1.39
2C	1.74	94	366	33.6	17.7	39.8	284	1.095	1.44



UNCLASSIFIED

heat flux maldistributions. The pressure drop data indicated a ratio of core to overall pressure drop of 0.994. This indicates a nonuniformity in flow of 0.3 percent.

A total of six test runs were conducted. Comparisons of the test results to the analytical predictions were made for the heat transfer and pressure drop calculation techniques. The calculated overall cross-section ΔT was an average of approximately 10 percent higher than the test ΔT . Thus, the calculated thermal conductance was an average of about 16 percent less than the test thermal conductance. A summary of the test results is presented in Table 8.3-1. Figure 8.3-3 is a plot of calculated data vs test results to augment Table 8.3-1.

8.3.2 Test Data Reduction

Comparisons of the test vs the calculated overall ΔT 's and fin friction $\rho\Delta P$'s, as presented in Table 8.3-1, were generated using the test conditions as the basis of the analytical calculations.

Figure 8.3-4 gives the upper and lower surface temperatures as obtained from Run 2B. The control thermocouple is located at the outlet end of the panel and, therefore, experiences the maximum surface temperature due to the hotter nitrogen. Sample calculations for the heat transfer and the pressure drop data reduction are presented to define the analytical techniques.

8.3.2.1 Typical Heat Transfer Calculation

The overall ΔT , as shown below was determined for the following test conditions:

Run	2B
Fluid	Nitrogen
Flow rate	1.54 lb/min
Inlet Temperature	$T_{in} = 79^{\circ}\text{F}$
Outlet Temperature	$T_{out} = 502^{\circ}\text{F}$
Inlet Pressure	$P_{in} = 29.3 \text{ psig}$
Outlet Pressure	$P_{out} = 13.2 \text{ psig}$

The overall ΔT is defined as:

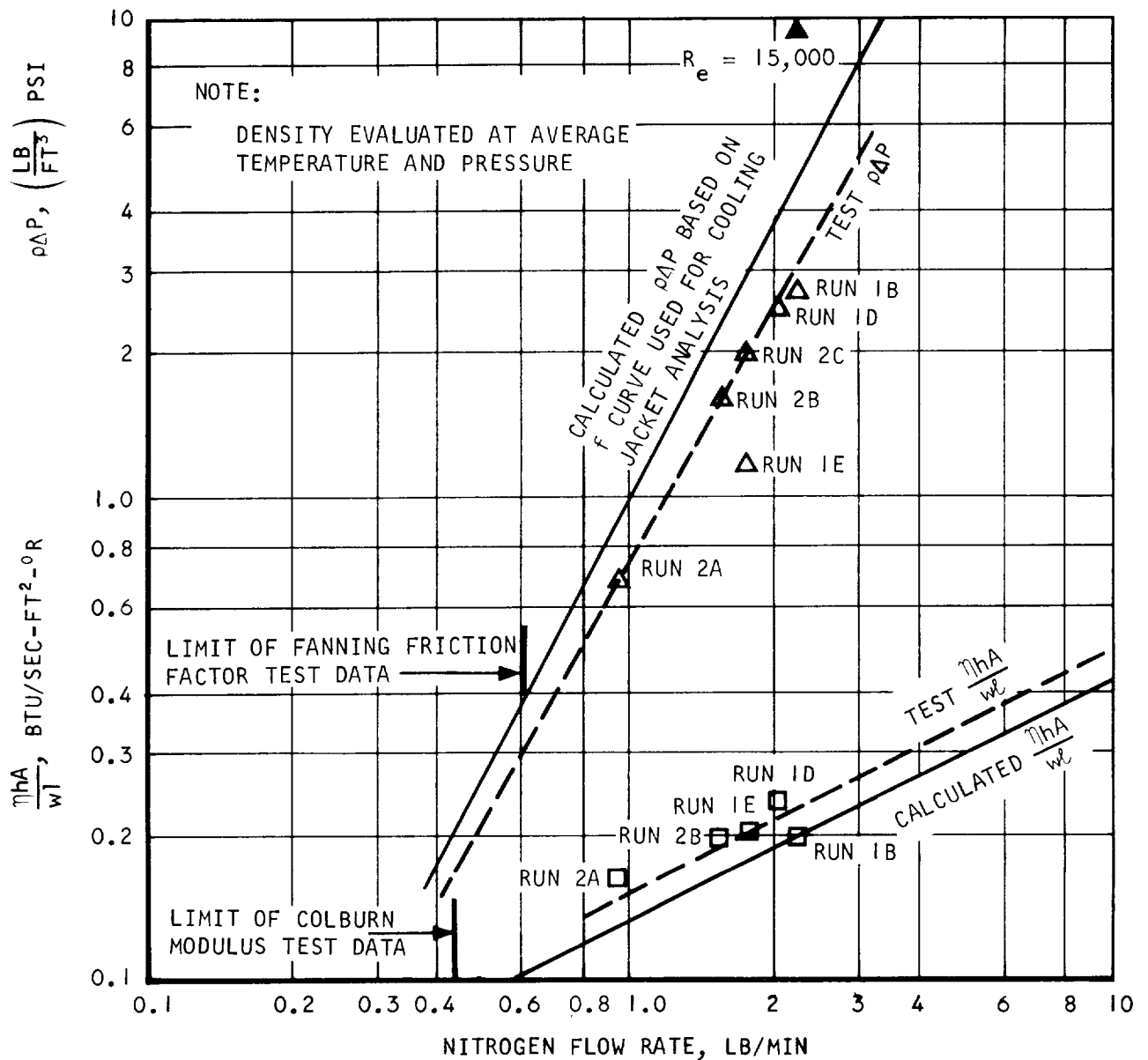
$$\Delta T_{\text{overall}} = \Delta T_{\text{fin}} + \Delta T_w$$

where $\Delta T_w = (Q/A) (K/L)$

$$\Delta T_{\text{fin}} = (A/A)/(\eta hA/WL)$$



UNCLASSIFIED



A-3223R

Figure 8.3-3. Calculated Data versus Test Results
for Flow Test Panel S/N 4

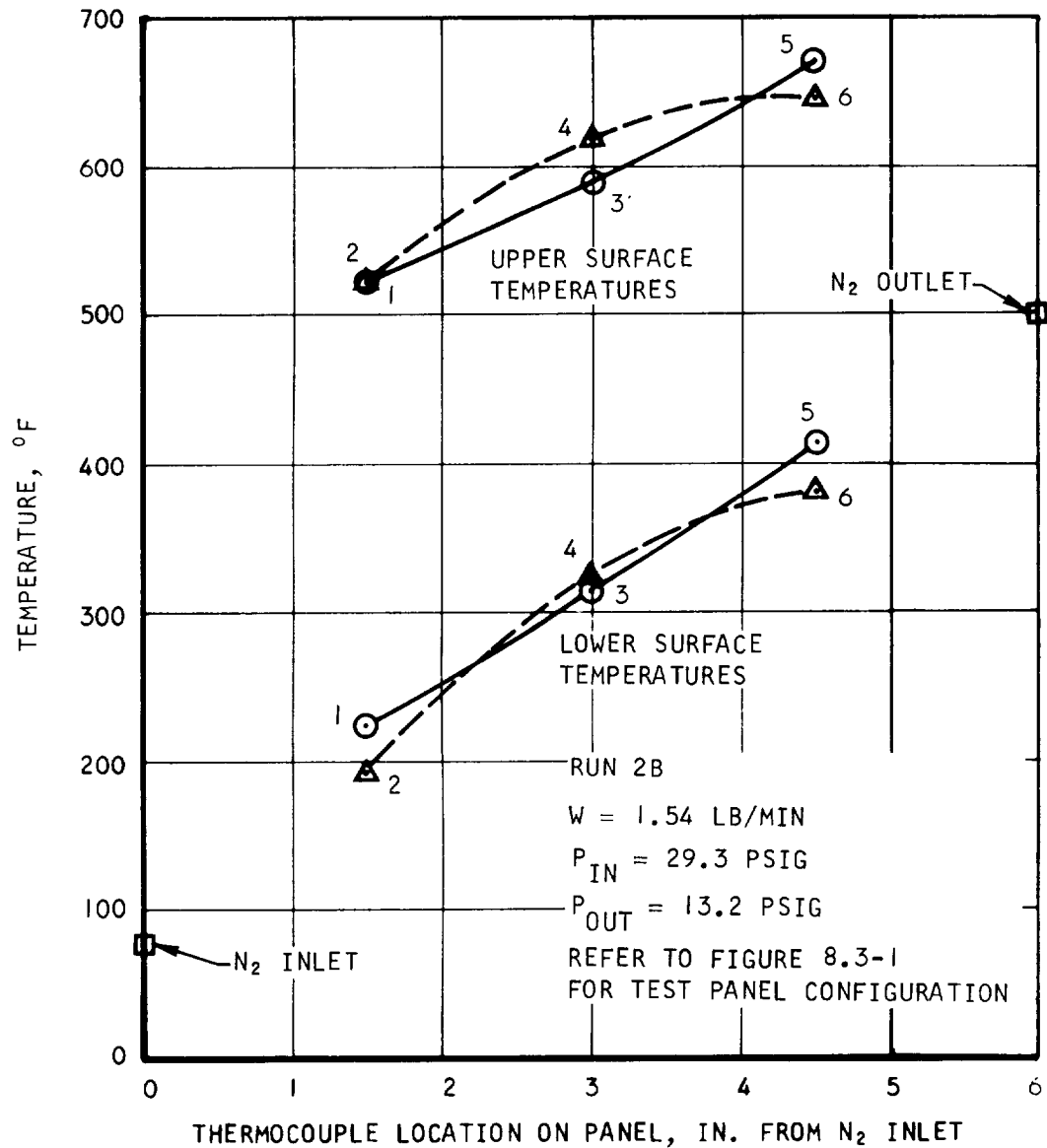


AIRESEARCH MANUFACTURING DIVISION
Los Angeles, California

67-2833
Page 8-31

UNCLASSIFIED

UNCLASSIFIED



A-32086

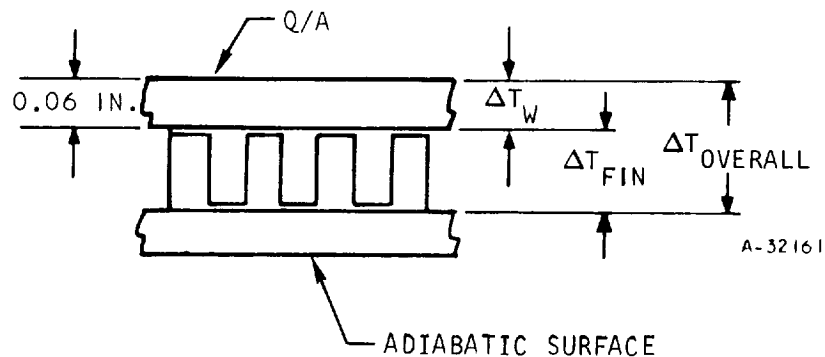
Figure 8.3-4. Temperature Distribution Panel Test Data



AIRESEARCH MANUFACTURING DIVISION
Los Angeles, California

UNCLASSIFIED

UNCLASSIFIED



The heat load, Q , is defined as:

$$Q = M C_p \Delta T_N$$

For this test

$$\Delta T_N = 502 - 79 = 423^\circ\text{F}$$

$$M = 1.54 \text{ lb/min}$$

$$C_{p_N} = 0.243 \text{ Btu/lb } ^\circ\text{F (At } T_{\text{avg}} = 290^\circ\text{F)}$$

Therefore the heat load is

$$Q = (1.54 \times 0.243 \times 423) = 158 \text{ Btu/min}$$

The effective heat transfer area of the upper surface is

$$A = (1.6 \times 6) = 9.6 \text{ sq in.} = 0.0666 \text{ sq ft}$$

Therefore the average heat flux is

$$\left(\frac{Q}{A}\right)_{\text{avg}} = \frac{158}{0.0666} = 2380 \text{ Btu/min sq ft} = 39.6 \text{ Btu/sec sq ft}$$

The wall ΔT is a function of the wall thermal conductivity, which varies with the wall temperature. Using TC3 as an example (for Hastelloy X)

$$T_{\text{TC3}} \approx 580^\circ\text{F}$$

Therefore

$$K = 0.0023 \text{ Btu/sec ft } ^\circ\text{R}$$



UNCLASSIFIED

Therefore the wall ΔT is:

$$\Delta T_w = \frac{39.6}{0.46} = 86^\circ\text{F}$$

The thermal conductance ($\eta hA/wl$) for the 20R - 0.075 - 0.100 - 0.004 Hastelloy X plate fins is shown in Figure 8.3-5 for nitrogen. For a flow per unit width of:

$$\frac{M}{w} = \frac{0.0257}{1.6} = 0.0167 \text{ lb/sec in.},$$

the thermal conductance is:

$$\frac{\eta hA}{wl} = 0.1725 \text{ Btu/sec sq ft } ^\circ\text{F}$$

This yields a fin ΔT of:

$$\Delta T_{\text{fin}} = \frac{39.6}{0.1725} = 230^\circ\text{F}$$

The overall calculated ΔT is therefore,

$$\Delta T_{\text{overall}} = 86 + 230 = 316^\circ\text{F}$$

The measured local overall ΔT 's for Run 2B are tabulated below

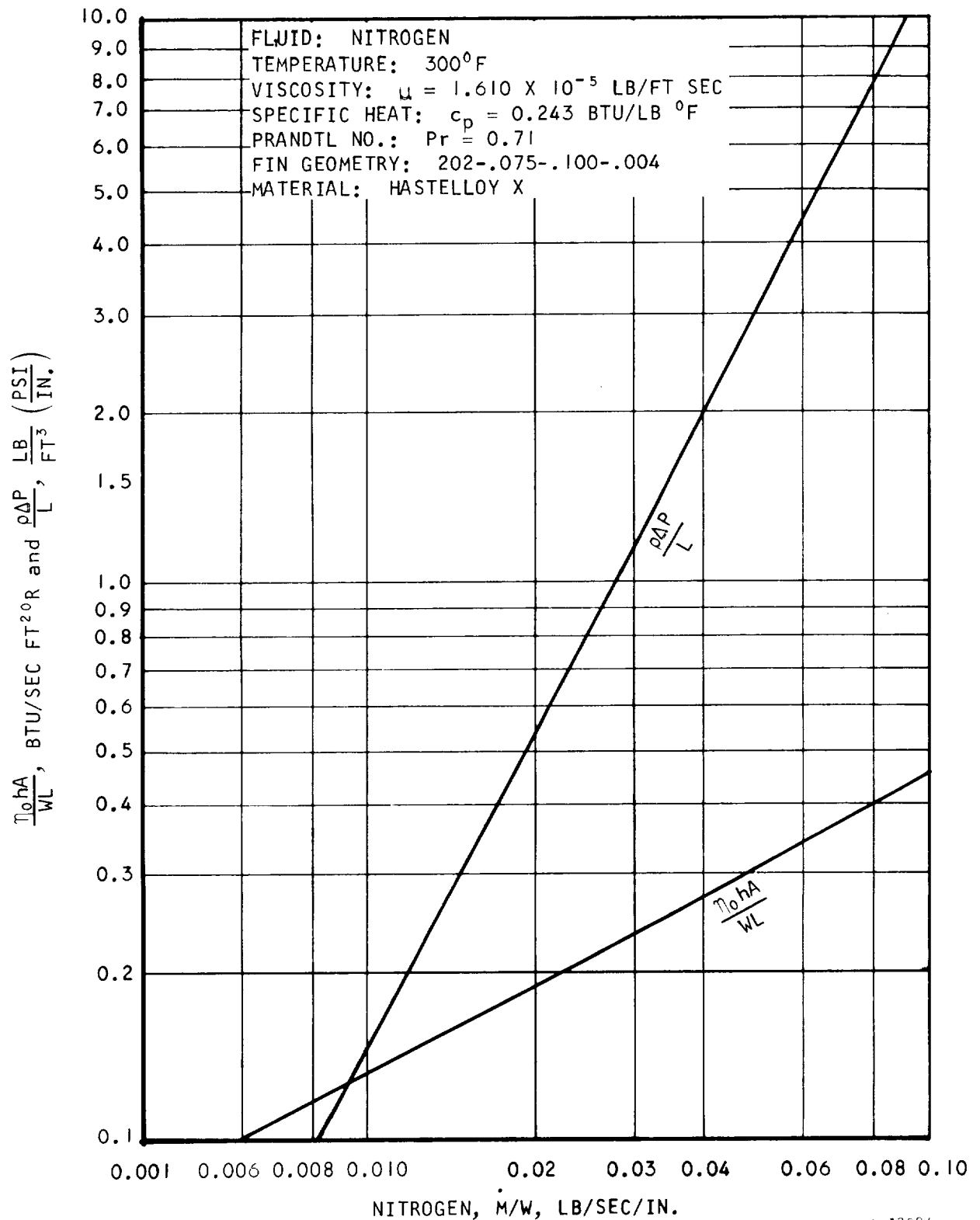
TC No.	Upper Surface Temperature, °F	Lower Surface Temperature, °F	Overall ΔT , °F
1	523	224	299
2	523.5	191	332
3	275	314	275
4	294	325	294
5	256	414	256
6	263	382	263

8.3.2.2 Typical Pressure Drop Calculation

A typical overall pressure drop calculation for a unit of this type would include entrance, exit, momentum, and friction losses. For ease of comparing test data to calculated values, the calculated friction pressure drop is shown in Figure 8.3-3. The entrance, exit, and momentum losses were subtracted from



UNCLASSIFIED



A-52084

Figure 8.3-5. $\eta_0 hA/WL$ and $\rho \Delta P/L$ vs Flow Rate for 20R-.075-.100-.004 Hastelloy X Plate Fin



AIRSEARCH MANUFACTURING DIVISION
 Los Angeles, California

UNCLASSIFIED

the overall test ΔP before calculating of the test $\rho \Delta P$. The calculation technique is presented for Run 2B as an example.

The test overall ΔP is:

$$\Delta P_T = 16.1 \text{ psi}$$

The inlet pressure and temperature are:

$$P_{in} = 44.0 \text{ psia}$$

$$T_{in} = 539^\circ R$$

which yields an inlet density of

$$\rho_{in} = 2.62 \frac{P}{T} = (2.62) \frac{(44)}{(539)} = 0.214 \text{ lb/cu ft}$$

The loss due to entrance is

$$\Delta P_{in} = \frac{2.24 (0.5 W^2)}{0.01042 \rho_{in}} = 103 \frac{W^2}{\rho_{in}}$$

where the nitrogen flow rate is

$$W_N = 1.54 \text{ lb/min} = 0.0257 \text{ lb/sec}$$

Therefore the inlet ΔP is:

$$\Delta P_{in} = \frac{(103)(0.0257)^2}{0.214} = 0.32 \text{ psi}$$

The exit pressure and temperature are:

$$P_{ex} = 27.9 \text{ psia}$$

$$T_{ex} = 962^\circ R$$

which yields an exit density of

$$\rho_{ex} = 2.62 \frac{P}{T} = (2.62) \frac{(27.9)}{(962)} = 0.076 \text{ lb/cu ft}$$

The exit loss is:

$$\Delta P_{ex} = \frac{(2.06)(2.57)^2}{7.6} = 1.79 \text{ psi}$$

The momentum loss is defined as the difference in the inlet and outlet velocity heads, or

$$\Delta P_{mom} = q_2 - q_1 = 2.24 \frac{W^2}{A^2} \left(\frac{1}{P_{ex}} - \frac{1}{P_{in}} \right)$$



$$= (2.24) \frac{(0.0257)^2}{(0.1042)^2} \left(\frac{1}{0.076} - \frac{1}{0.214} \right) = 1.16 \text{ psi}$$

The fin friction loss is therefore

$$\begin{aligned} \Delta P_f &= \Delta P_T - \Delta P_{in} - \Delta P_{ex} - \Delta P_{mom} \\ &= 16.10 - 0.32 - 1.79 - 1.16 \\ &= 12.85 \text{ psi} \end{aligned}$$

The average density is evaluated at the average pressure and temperature and is

$$\rho_{avg} = 2.62 \frac{P_{avg}}{T_{avg}} = (2.62) \frac{(35.95)}{750} = 0.126 \text{ lb/cu ft}$$

which yields an average fin friction of

$$\rho \Delta P = (0.126) (12.875) = 1.62 \left(\frac{\text{lb}}{\text{ft}^3} \right) \text{ psi}$$

From Figure 8.3-3, the analytical $\rho \Delta P$ is:

$$2.28 \left(\frac{\text{lb}}{\text{ft}^3} \right) \text{ psi}$$

Which yields a ratio of calculated-to-test $\rho \Delta P$ of

$$\frac{\rho \Delta P_{cal}}{\rho \Delta P_{test}} = \frac{2.25}{1.62} = 1.39$$

8.3.3 Conclusions

The test on flow panel S/N 1 provided limited verification of the analytical techniques used to generate the coolant heat transfer data (cross section ΔT) and the overall unit pressure drops, both for hydrogen-cooled components and thermal cycle panels (this was not the primary purpose of the test). Flow distribution in the panel was uniform.

The heat transfer data, which is a function of the Colburn modulus (j) varied from analytical predictions by approximately 16 percent. This variation is within the test limitations and tends to verify the j vs Re (Reynolds number) curve being used. The pressure drop, which is a function of the Fanning friction factor (f), and end losses, was lower than the analytical predictions by approximately 28 percent at the limit of previous test data where the Reynolds number was 4000. The calculated curve in Figure 8.3-3 was based on the extrapolated friction factor curve used in cooling jacket design and analyses for the 25R - 0.050 - 0.065 - 0.006 Hastelloy X fins. The extrapolation was to a slope of 1.0 above Reynolds numbers of 10,000. The test data in Figure 8.3-3 indicates a friction factor curve slope of 0.2, since the test data interpretation has a slope of 1.8.



The f and j vs Re curves used are extrapolations from Figure 10-61 of Reference 8-1 for a fin with $L/4 r_h$ of 2.06. The test fin has a value of $L/4 r_h = 1.79$. If this difference were accounted for in the data reduction, the thermal conductance underprediction would be reduced from 16 percent to about 10 percent and the pressure drop overprediction would increase from 28 percent to 45 percent. Further review of the discrepancy in coolant friction pressure drop is planned.

8.4 COMPOUND CURVED MODEL

Four assemblies of the compound curved model discussed in Paragraph 7.1, two of them unserialized because of undersize shell thickness, were tested during the reporting period. The two unserialized assemblies, each brazed under different fixturing conditions, were pressurized at room temperature in an effort to determine the room temperature burst strength. The other two were first subjected to a room temperature proof pressure test at 2200 psig and then to a 1600°F burst pressure test.

8.4.1 Test Results

In order to test the unserialized assemblies, a simple test fixture, consisting of two steel plates with resilient gasket faces clamped to the ends of the specimen by half inch bolts, was used. Neither of these units contained end headers. Pressure was applied by means of water and a high pressure pump. Tests of both assemblies were discontinued because of fixture limitations before rupture could be induced.

Proof pressure testing of the in-tolerance, serialized assemblies was performed by connecting them to a pressurized supply of argon, with the assemblies immersed in a tank of water. The pressure was slowly increased to 2200 psig, held for 1 min and released. Neither of the two assemblies exhibited leakage or deformation as the result of this test.

For the burst test at 1600°F, the assemblies were first instrumented with two chromel-alumel thermocouples, spotwelded to the outer shells. The assemblies then were connected to an argon supply and installed in a rectangular cross section furnace. The temperature of the assemblies was slowly brought to 1600°F, and after sufficient time at temperature had elapsed to ensure stability, the pressure was slowly applied. A hold of 30 sec at each 100 psi



UNCLASSIFIED

increment was incorporated to confirm integrity at the pressure. Results of the four tests are tabulated below:

Specimen	Room Temperature		Burst Test		Remarks
	Proof Pressure, psig	Pressure, psig	Temperature, °F		
Brazement using graphite plug	--	3200	RT		Fixture limited pressure
Brazement using pressurized inner shell	--	3500	RT		Fixture limited pressure
S/N 1 (graphite plug)	2200	185	1600		--
S/N 2 (pressurized inner shell)	2200	1250	1600		--

Following the burst tests, the two assemblies were photographed (Figures 8.4-1 and 8.4-2) and sectioned to ascertain the cause of rupture. The rupture zone in specimen S/N 1 showed a lack of braze between the outer shell and fins over a relatively large area. Metallographic examination of the zone revealed the following:

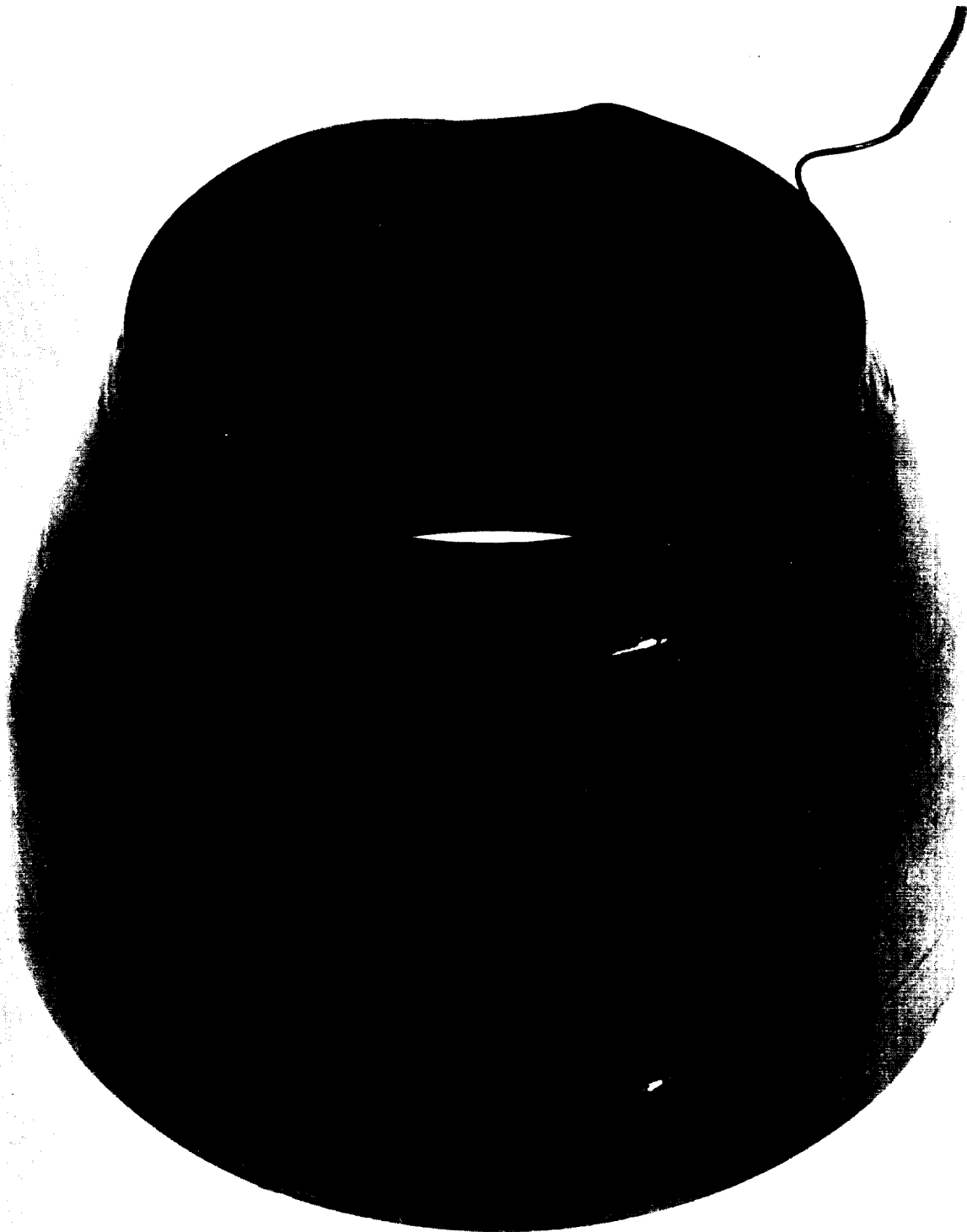
Braze alloy had melted and wetted all areas examined; however, the fins and shell were separated by too large a gap for the braze alloy to fill. Figures 8.4-3 shows the zone adjacent to the actual bulge, which has intermittent braze joints characteristic of excessive clearance. Figure 8.4-4 shows the bulged area, the wetting of the outer shell, and an example of a joint at a point where clearance was approximately 0.007 in.

Where fitup was correct, the braze joints produced were good, indicating satisfactory brazing process. Figure 8.4-5 shows joints between the fin and skin and between the header and skins. Also illustrated by Figure 8.4-5 is a fine, uniform, grain structure of Hastelloy X, which is indicative of satisfactory processing history for the components.

The unbrazed zone in S/N 2 was limited to a small number of fins adjacent to the header in the rupture zone.



UNCLASSIFIED



61457

Figure 8.4-1. Compound-Curved Model S/N 1 After High Temperature Burst Test



AIRESEARCH MANUFACTURING DIVISION
Los Angeles, California

67-2833
Page 8-40

UNCLASSIFIED

UNCLASSIFIED



Figure 8.4-2. Compound-Curved Model S/N 2 After High Temperature Burst Test

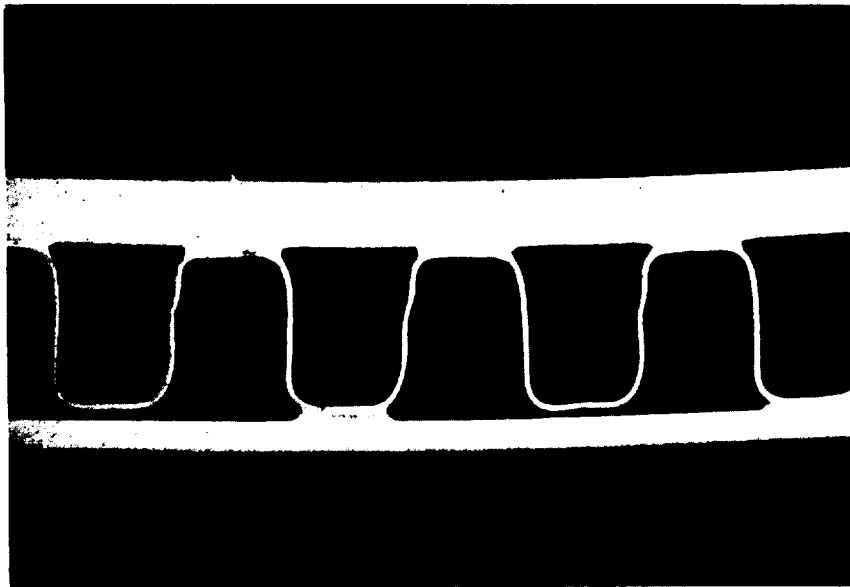


AIRESEARCH MANUFACTURING DIVISION
Los Angeles, California

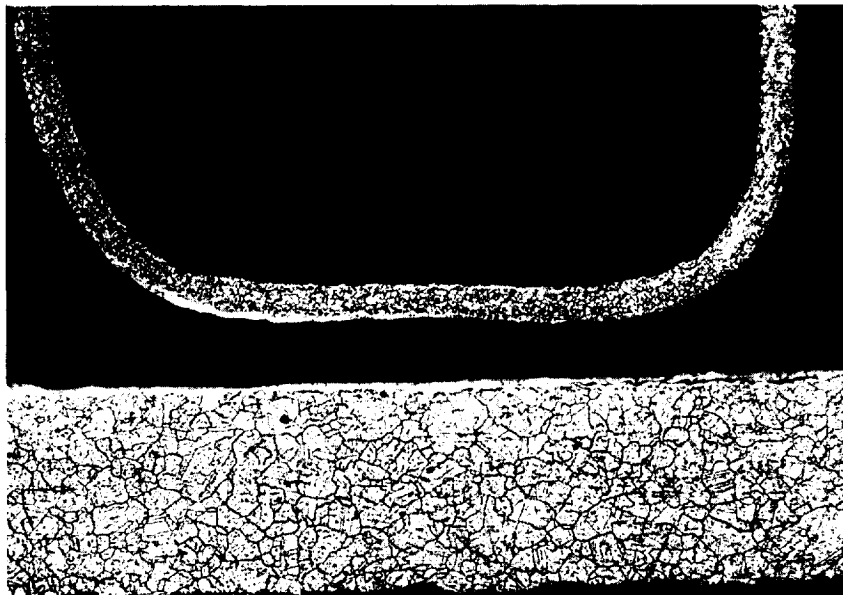
67-2833
Page 8-41

UNCLASSIFIED

UNCLASSIFIED



- a. Cross Section Adjacent to Bulged Area Showing Gap Between Fins and Outer Shell. Etched with 50 ml HCl + 50 ml H₂O + 5 ml HNO₃ + 10 ml H₂O₂. Mag. = 11X



F-8378

- b. Close-up of Unbrazed Joint Showing Brazing Alloy on Both Outer Shell and Fins, Indicating This Particular Fin Contacted Shell During Brazing. In Many Areas Fins Did Not Contact Shell. Same Etchant As Above. Mag. = 75X

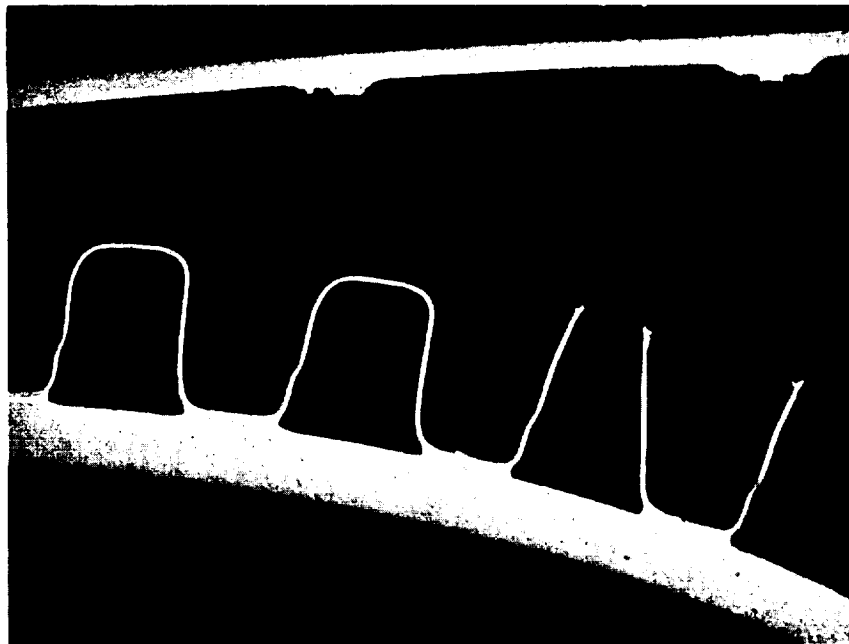
Figure 8.4-3. Photomicrographs of Fin Joints in Compound Curved Model, S/N-1



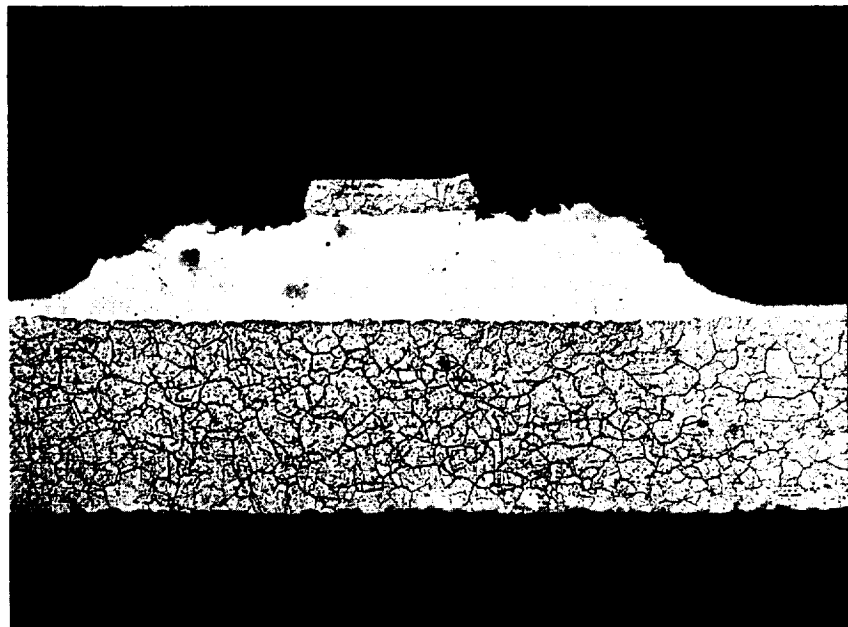
AIRESEARCH MANUFACTURING DIVISION
Los Angeles, California

UNCLASSIFIED

UNCLASSIFIED



- a. Cross Section of Bulged Area Where Improper Fitup Between Fins and Outer Shell Caused Inadequate Brazing. Note Failure in Fins. Outer Shell Shifted in Relation to Fins During Sectioning. Etched with 50 ml HCl + 50 ml H₂O + 5 ml HNO₃ + 10 ml H₂O₂. Mag. = 11X



F-8376

- b. Close-up of Failed Fin-Outer Shell Joint Where Palniro 4 Brazing Alloy Had to Fill a 0.007 in. Gap. Same Etchant as Above. Mag. = 75X

Figure 8.4-4. Photomicrographs of Bulged Area of Compound Curve Model, S/N-1, Illustrating Cause of Failure in Burst Test.



AIRESEARCH MANUFACTURING DIVISION
Los Angeles, California

UNCLASSIFIED

67-2833
Page 8-43

UNCLASSIFIED



- a. Example of Typical Fin-Inner Shell Joint Indicative of Good Brazing Characteristics Obtained for Part. Etched with 50 ml HCl + 50 ml H₂O + 5 ml HNO₃ + 10 ml H₂O₂. Mag. = 75X



F-8377

- b. Cross Section of Header Bar-Shell Joints Showing Brazing to be Satisfactory for This Joint. Same Etchant as Above. Mag. = 75X

Figure 8.4-5. Photomicrographs of Compound Curved Model, S/N 1, Illustrating General Brazing Characteristics of Palniro I Brazing Alloy/Hastelloy X Fin-Shell Joints to be Good.



AIRESEARCH MANUFACTURING DIVISION
Los Angeles, California

UNCLASSIFIED

67-2833
Page 8-44

8.4.2 Conclusions

The results indicate that the emphasis in further evaluation should be in the braze setup, utilizing pneumatic loading of the inner shell. This method provides a relatively simple technique for application of uniform pressure to the inner shell and is more repeatable than loading by graphite plug. The latter technique may still be used for particular areas of the full-scale components.

The low burst pressure for specimen S/N 1 is only in part attributable to differences in fixturing methods. Considerable experimentation was required to achieve satisfactory assembly prior to brazing because of the addition of headers to the assembly. Contamination and slight, but significant, deformation of parts could have occurred during this experimentation and could have affected fitup and, hence, braze joint quality. Specimen S/N 2, which reached a much higher burst pressure, was assembled with a lesser degree of experimentation prior to brazing.

8.5 INLET SPIKE TIP

8.5.1 Test Results and Conclusions

Three additional inlet spike tip models were fabricated from sheet stock, assembled and brazed during this reporting period. Figure 8.5-1 illustrates a typical cone assembly.

A summary of the brazing conditions is shown below:

S/N	Braze Alloy	Furnace	Temperature, °F	Normal Fin Load*, psi
2	Palniro 7 (0.001 in. foil)	Hydrogen	1950	8.7
3	Palniro 1 (0.001 in. foil)	Hydrogen	2070	17.6
4	Palniro 4 (0.001 in. foil)	Hydrogen	2170	13.2

*Normal fin load is the pressure applied perpendicular to the fin.

The above three inlet spike tip models were pressurized through a bellows during the hydrogen brazing cycle to obtain the required fin loading. Figure 8.5-2 shows the fixturing used for the brazing.



UNCLASSIFIED

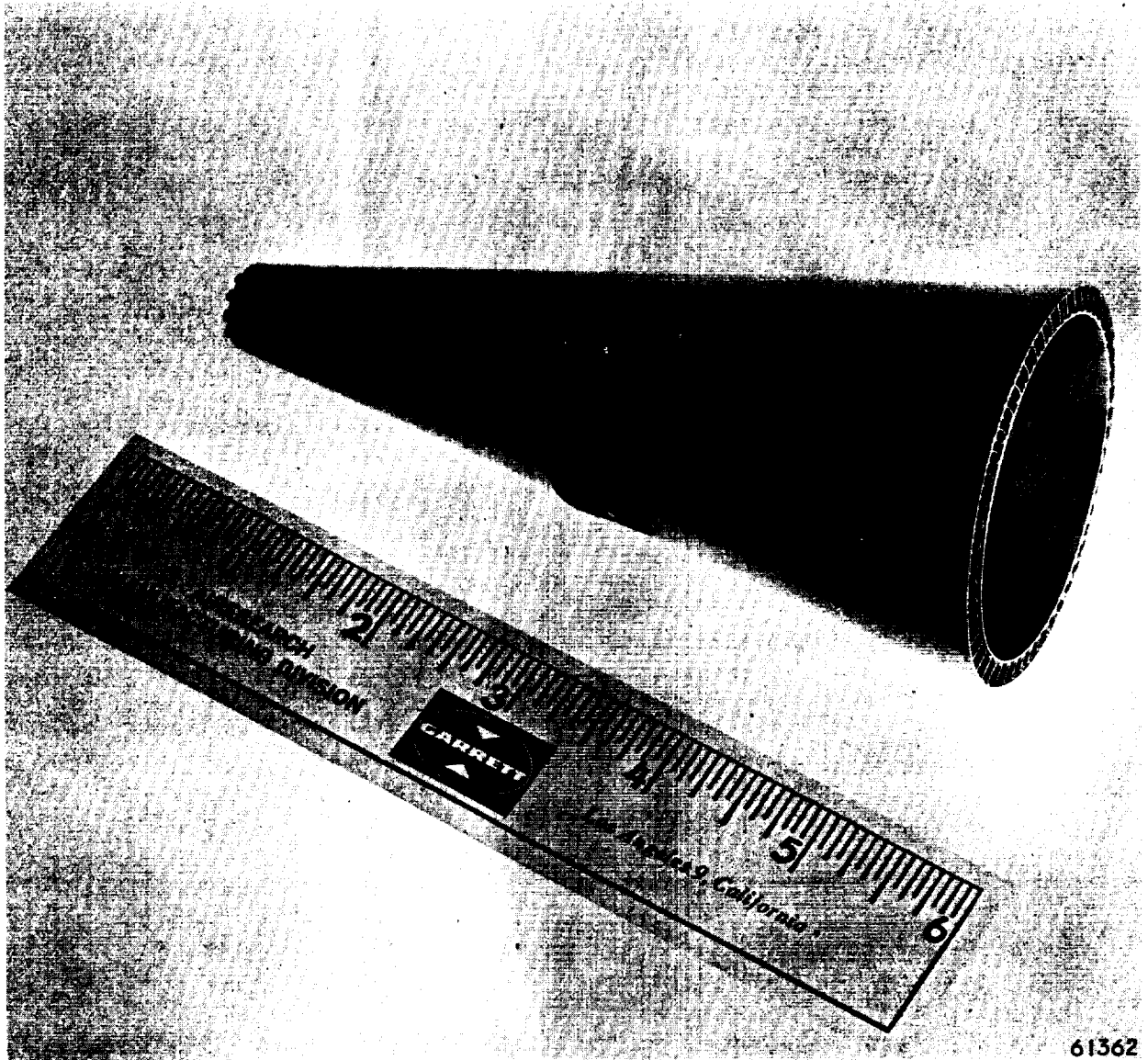


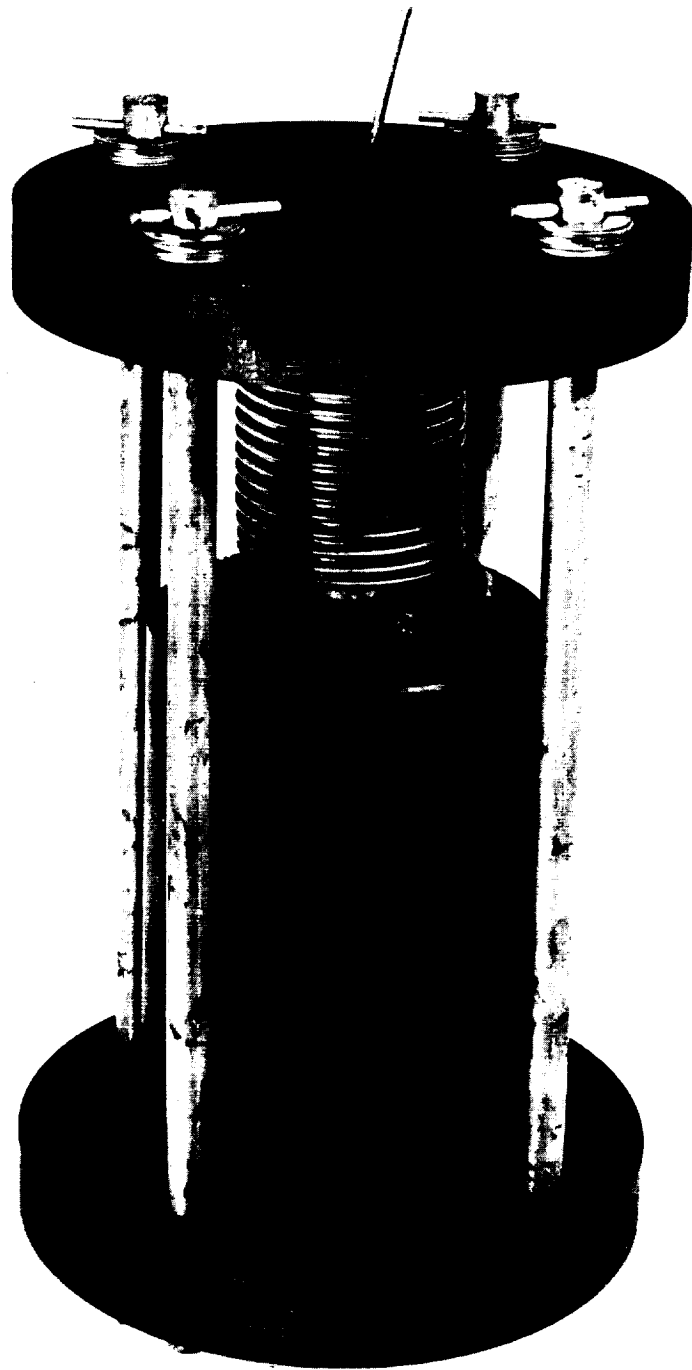
Figure 8.5-1. Inlet Spike Tip Test Section



AIRESEARCH MANUFACTURING DIVISION
Los Angeles, California

UNCLASSIFIED

UNCLASSIFIED



61001-1

Figure 8.5-2. Spike Tip Test Section Braze Fixture



AIRESEARCH MANUFACTURING DIVISION
Los Angeles, California

UNCLASSIFIED

67-2833
Page 8-47

Inlet spike tip S/N 2 was installed in a burst test fixture, as shown in Figure 8.5-3, and hydrostatically pressurized until rupture occurred. At 2500 psig, buckling was observed at three points. Examination of the specimen confirmed that, at these points, the fins had not been joined to the skin.

Inlet spike tip S/N 3 was hydrostatically pressurized to rupture. At a pressure of 3260 psig, buckling was observed at the base and five other locations. Examination of the specimen showed lack of fin-to-skin contact at the points of rupture. Figure 8.5-4 shows the two bulges at the large diameter and a closeup of the larger bulge. These photographs represent a typical rupture resulting from insufficient contact.

Inlet spike tip S/N 4 was hydrostatically pressurized to 1450 psig, at which time rupture occurred in two locations. Examination showed lack of fin-to-skin contact on the outer skin at these locations. The reason for the lower burst pressure was the lack of fixture loading due to bottoming of the inner graphite brazing mandrel on a graphite stop.

A metallurgical check for carbon pickup during the hydrogen brazing of Hastelloy X with graphite fixturings was initiated with inlet spike tip S/N 4. The analysis revealed that carburization occurred to a depth of about 0.008 in. in the 0.015 in. skin (Figure 8.5-5). The source of carbon was the graphite fixture. Hydrogen reacting with the graphite forms methane, which in turn acts as the carburizing medium. S/N 3 showed carburization to a depth of 0.002 in., while S/N 2 showed no evidence of carburization. The undesirable effect of carburization is the forming of a continuous intergranular network, which becomes susceptible to cracking, due to reduced metal ductility.

8.5.2 Future Action

The final configuration of the inlet spike tip assembly will be rolled sheet metal cones and fins of a predetermined length and width in the flat, which are deformed to the required cone shape prior to final assembly.

No further development effort are planned on the fabrication techniques of the inlet spike tip. Further refinements can be included in the fabrication of the full-scale component hardware.

The carburization of the Hastelloy X occurring in a hydrogen furnace with graphite fixturing will limit the use of graphite fixturing to vacuum brazing, argon atmosphere brazing, or low temperature hydrogen brazing.

8.6 CONTINUOUS JOINT PANEL (NOZZLE CROSSOVER MANIFOLD)

A pressure cycle test of the flat plate collector manifold test specimen shown in Figure 8.6-1 was conducted to determine the adequacy of the nozzle-to-innerbody crossover joint. In addition, a limited test of the bending strength of the nozzle shell and ring manifold joint was performed.



UNCLASSIFIED

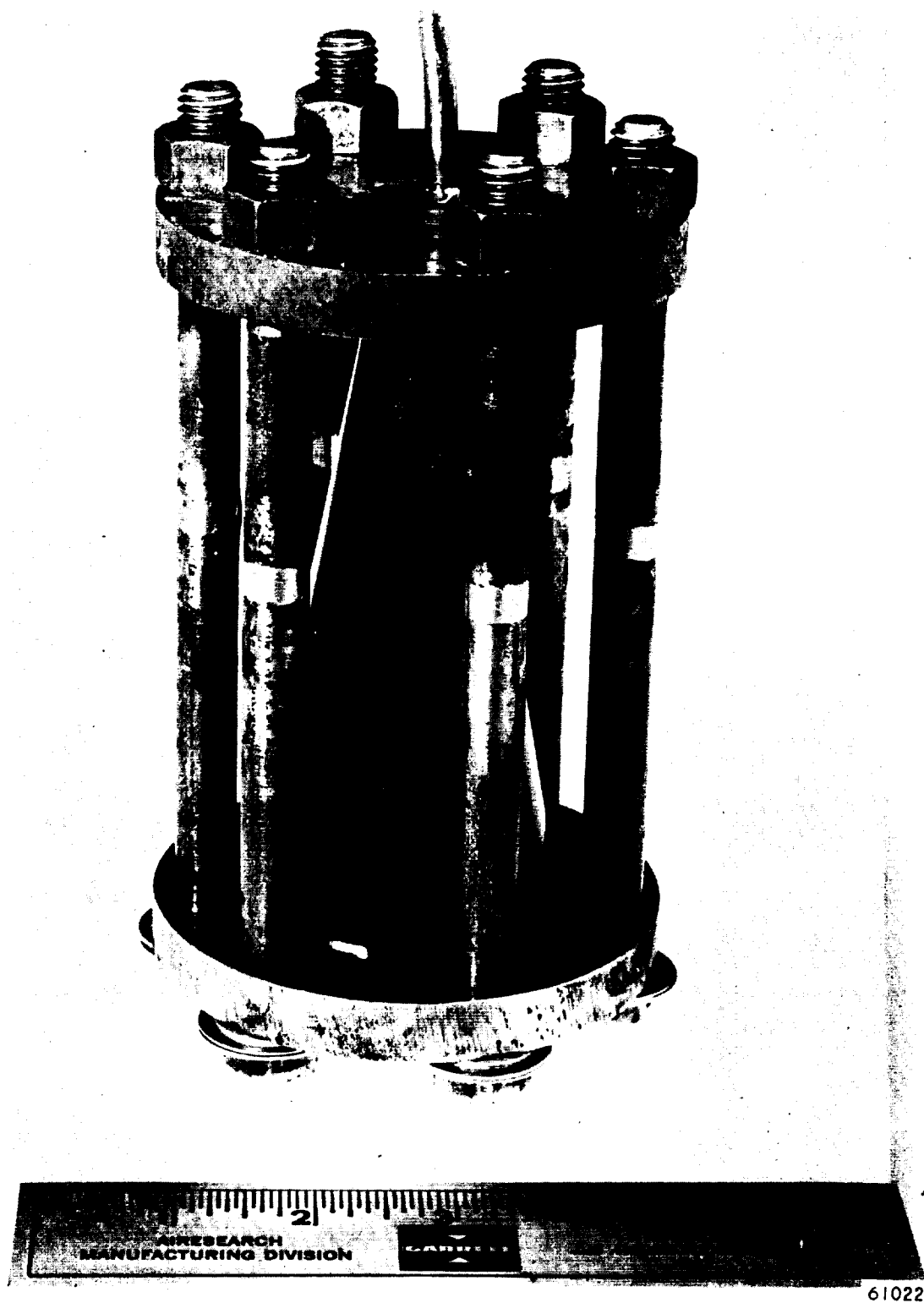


Figure 8.5-3. Spike Tip Test Section Burst Test Fixture

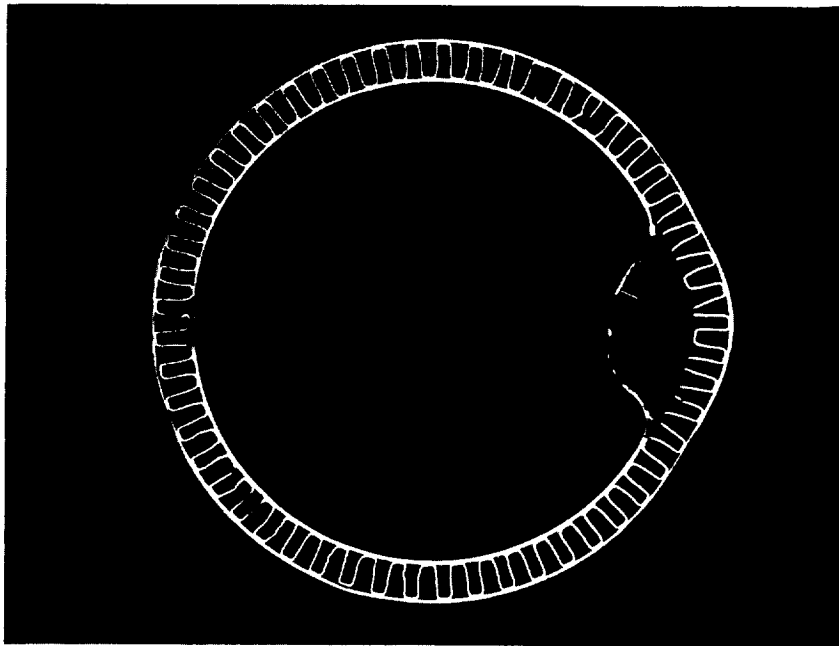


AIRESEARCH MANUFACTURING DIVISION
Los Angeles, California

67-2833
Page 8-49

UNCLASSIFIED

UNCLASSIFIED



a. View of Large Diameter of Spike Tip Showing Two Bulge Areas (180° apart). Mag. = 1.2x



b. Close-up of Large Bulge in a Fin, Illustrating Lack of Brazing Between One Row of Fins and Inner Skin Mag. = 2.5x

F-8366

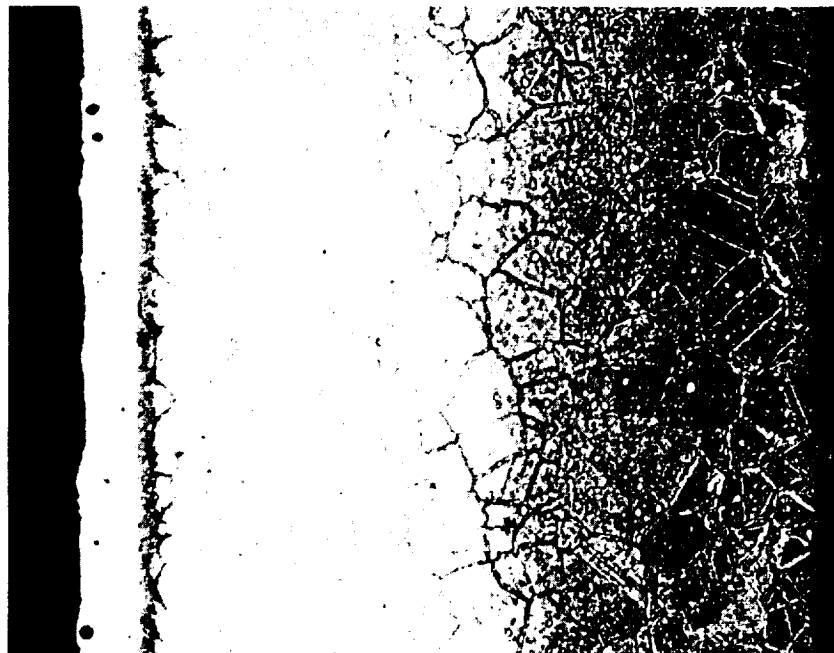
Figure 8.5-4. Photomicrographs of Spike Tip S/N 3 After Pressurizing to 3260 psig



AIRSEARCH MANUFACTURING DIVISION
Los Angeles, California

UNCLASSIFIED

UNCLASSIFIED



F-8365

Kalling's Etchant Mag. = 250X

Figure 8.5-5. Photomicrograph of Hastelloy X Skin From Spike Tip, S/N 4, Illustrating Carburization (Dark Area) After a Palniro 4 Brazing Cycle (2170°F) in Hydrogen Using Graphite Fixturing

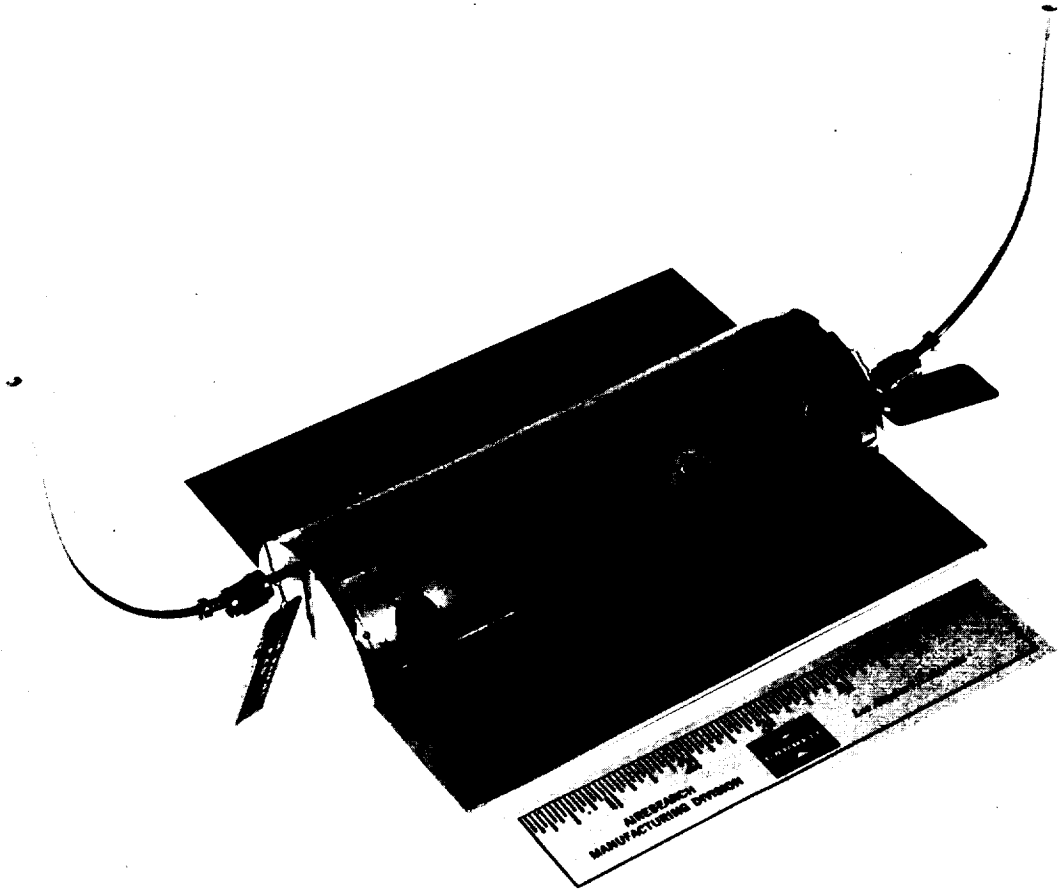


AIRESEARCH MANUFACTURING DIVISION
Los Angeles, California

UNCLASSIFIED

67-2833
Page 8-51

UNCLASSIFIED



61318-2

Figure 8.6-1. Flat Plate Collector Manifold Test Specimen



AIRESEARCH MANUFACTURING DIVISION
Los Angeles, California

UNCLASSIFIED

8.6.1 Test Results

The setup for the pressure cycle test, shown in Figure 8.6-2, consisted of a dual cylinder, pressure cycle rig. The dual cylinder was connected to timers, solenoid valves, and pressure regulators arranged to provide cycling of pressure at controlled rates and values. A cycle of 6 sec total duration, consisting of a 1 sec dwell at maximum and minimum pressure was used for the test. During the course of testing, constant surveillance was maintained for signs of change in the specimen.

The results of the internal pressure test for the two test specimens, summarized in Table 8.6-1, indicate a pressure capability of the nozzle-to-inner body detachable joint of about 3600 psig for 1000 cycles as compared to a desired design value of 1000 cycles at the 1050 psig proof pressure for actual hardware.

The pressure cycle test was conducted on an accelerated fatigue testing basis. Testing was performed by cycling from zero to a maximum internal pressure, p_{max} , and back to zero, with p_{max} increased in 25 percent increments until rupture occurred. The factor of 1.25 was selected based on the desire to increase specimen damage (or reduce life) by a factor of 10 for each incremental pressure level increase.

Testing of the first specimen indicated that its strength was higher than expected. As can be seen in Table 8.6-1, 1000 cycles were conducted at 3180 psig rather than the intended 100 cycles performed on the preceding levels above 1050 psig.

After completing 1000 cycles to 3180 psig, the specimen ruptured after 88 cycles at 4000 psig. Based on the results with the first specimen, the initial test pressure for the second specimen was increased, since no damage would be produced by the relatively low pressures if specimen strength were similar. The second specimen performed as shown in Table 8.6-1, with the testing initiated at 2050 psi. Photographs of the two specimens following the cycle tests are shown in Figures 8.6-3 and 8.6-4. Metallic "K" seals installed in the test assemblies during cycling remained leak tight throughout both tests.

The second test, an axial pull test, was to be conducted to determine the braze strength at the joint of the sandwich structure with the collector ring. The direction of applied load is shown in Figure 8.6-5, and the critical joint is at C. The load path along the sandwich through the rings and bolts and back to the sandwich on the opposite side was intended to cause a bending moment at C that would tend to separate the collector and sandwich. Application of the load as shown in the figure does not produce the desired moment at C because of a counter moment produced by bearing of the rings at B. The specimen, therefore, was tested in the configuration shown in Figure 8.6-6. A single specimen was loaded in the manner shown, and yielding of the sandwich panel occurred. The braze joint between the sandwich and the manifold cracked on one half of the specimen but did not separate. Figure 8.6-7 shows a photo of the specimen after testing. Because geometry changes in the test specimen



UNCLASSIFIED

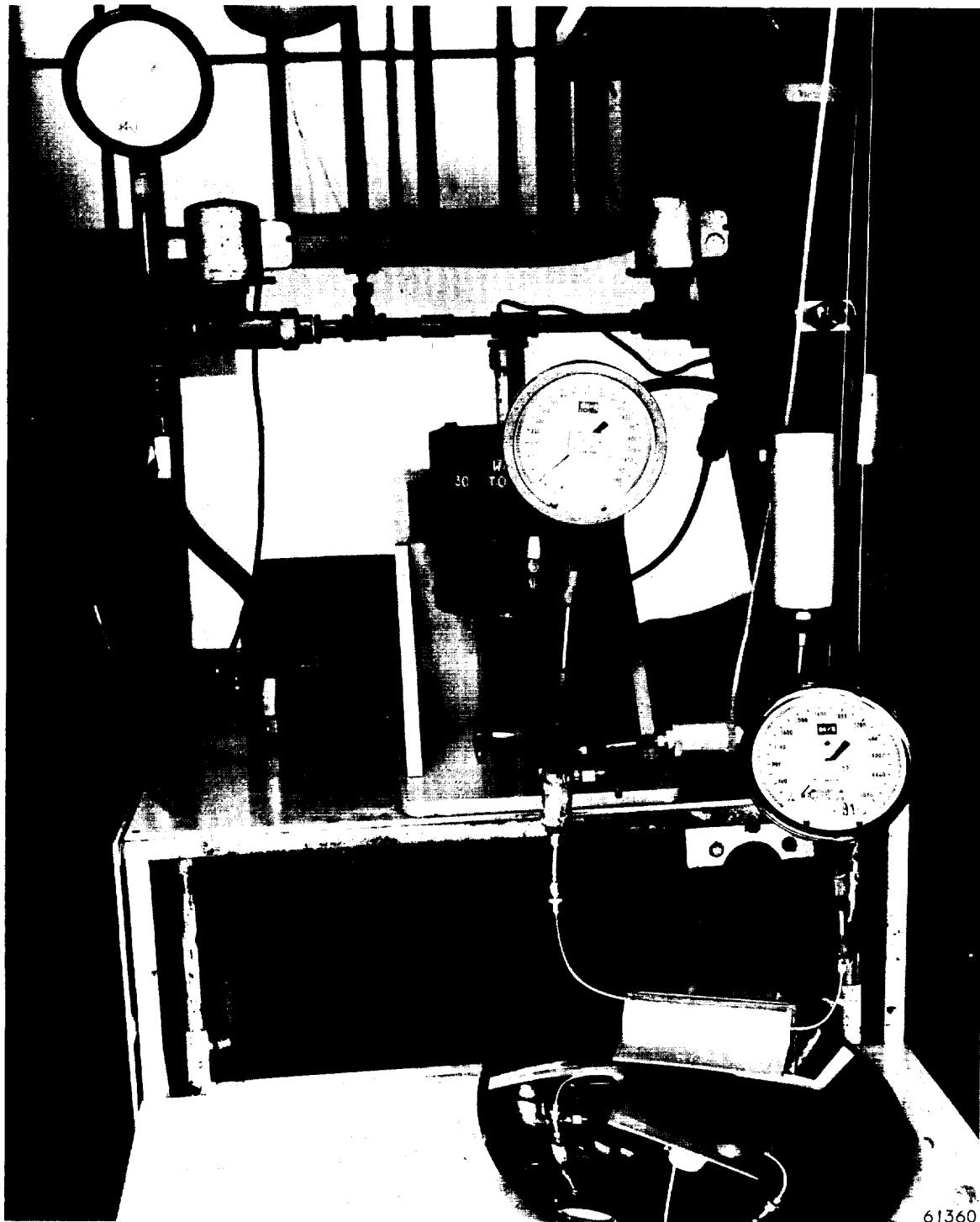


Figure 8.6-2. Setup for Pressure Cycle Test of Flat Plate Collector Manifold



AIRESEARCH MANUFACTURING DIVISION
Los Angeles, California

UNCLASSIFIED

67-2833
Page 8-54

UNCLASSIFIED

TABLE 8.6-1
PRESSURE CYCLE TEST DATA SUMMARY

Continuous Joint Panel Test Unit	Maximum Test Press, psig	No. of Test Cycles at Max Press	No. of Equivalent Cycles At 4000 psig	Total No. of Equivalent Cycles at 4000 psig	Equivalent Stress (3) At 4000 psig, psi
First Specimen	1050	1000	--	--	--
	1310	100	--	--	--
	1640	100	--	--	--
	2050	100	--	--	--
	2480	100	1	--	--
	3180	1000	100	--	--
	4000	88 (2)	88	189	96,000
Second Specimen	2050	100	--	--	--
	2560	100	1	--	--
	3200	100		--	--
	4000	716	716 (2)	716	84,000

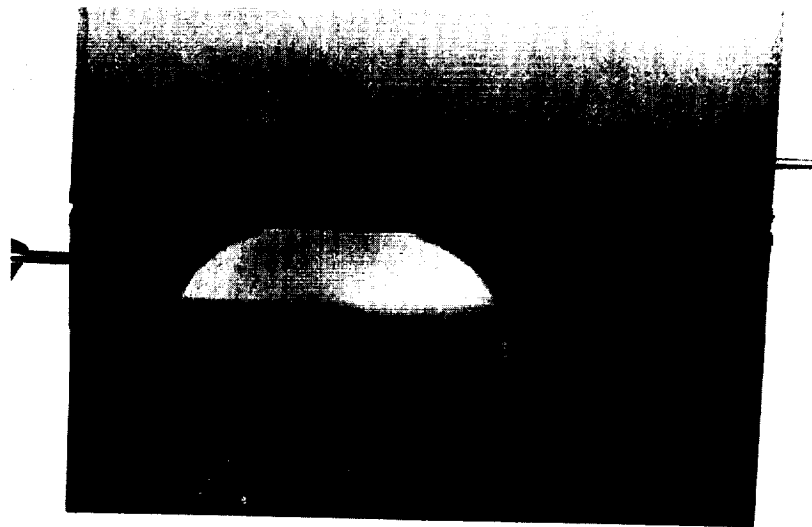
NOTES:

- (1) All tests were conducted at room temperature.
 (2) Rupture occurred at 4000 psig for both specimens after number of cycles shown. Fin
 rupture is believed to have begun in the region of the exit to the collector.
 (3) Obtained from Figure 8.6-8.



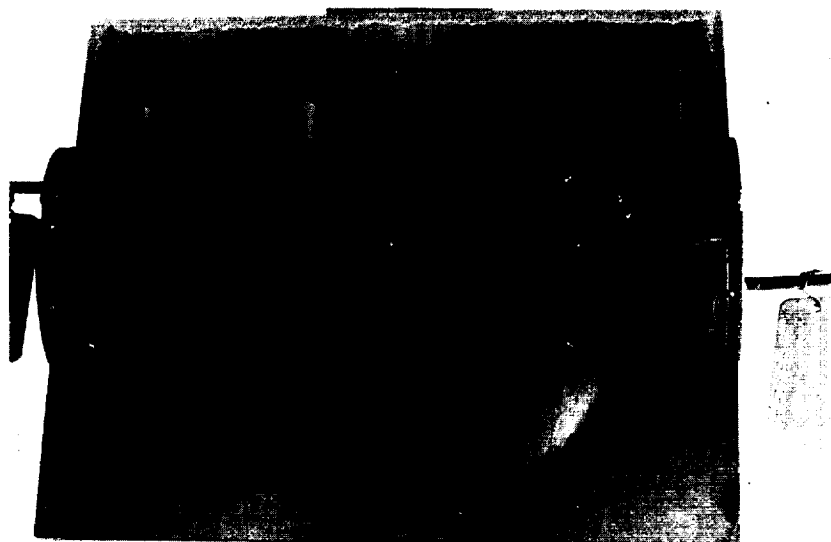
UNCLASSIFIED

UNCLASSIFIED



61482-4

a. Bottom View



61482-3

F-8357

b. Top View

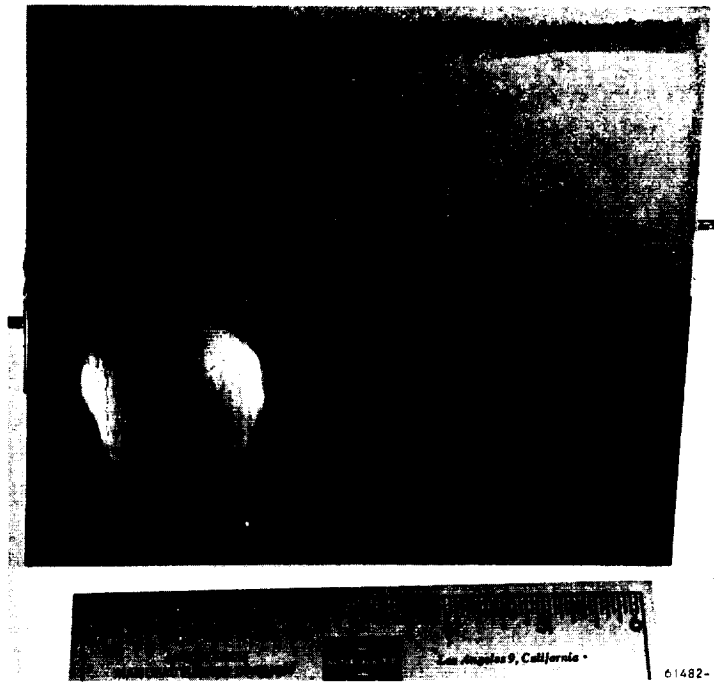
Figure 8.6-3. Flat Plate Collector Manifold (First Specimen) After Pressure Cycle Test



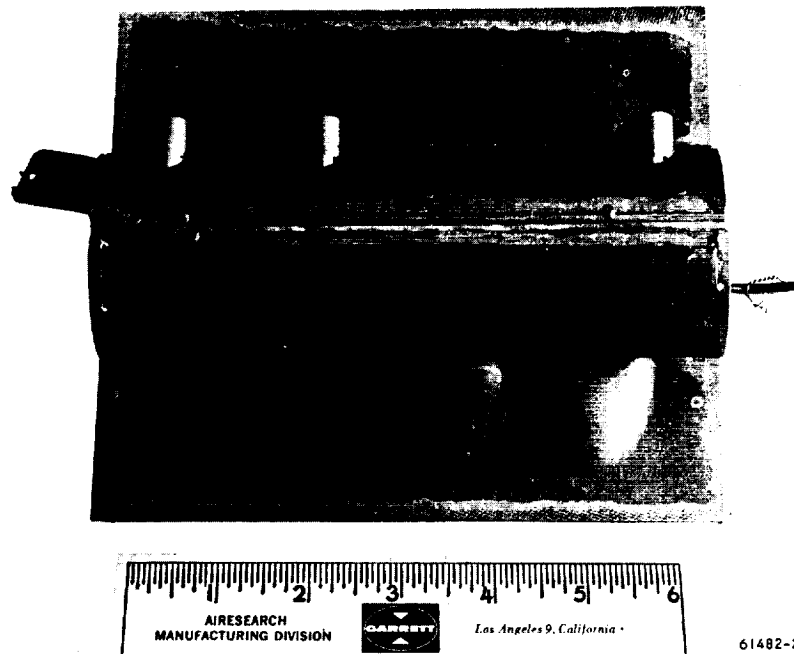
AIRESEARCH MANUFACTURING DIVISION
Los Angeles California

UNCLASSIFIED

UNCLASSIFIED



a. Bottom View



b. Top View

Figure 8.6-4. Flat Plate Collector Manifold (Second Specimen) After Pressure Cycle Test

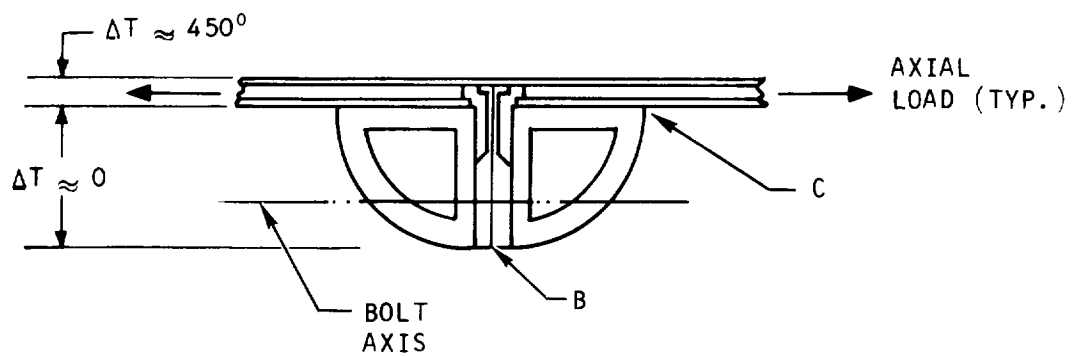


AIRESEARCH MANUFACTURING DIVISION
Los Angeles, California

UNCLASSIFIED

67-2833
Page 8-57

UNCLASSIFIED



A-32158

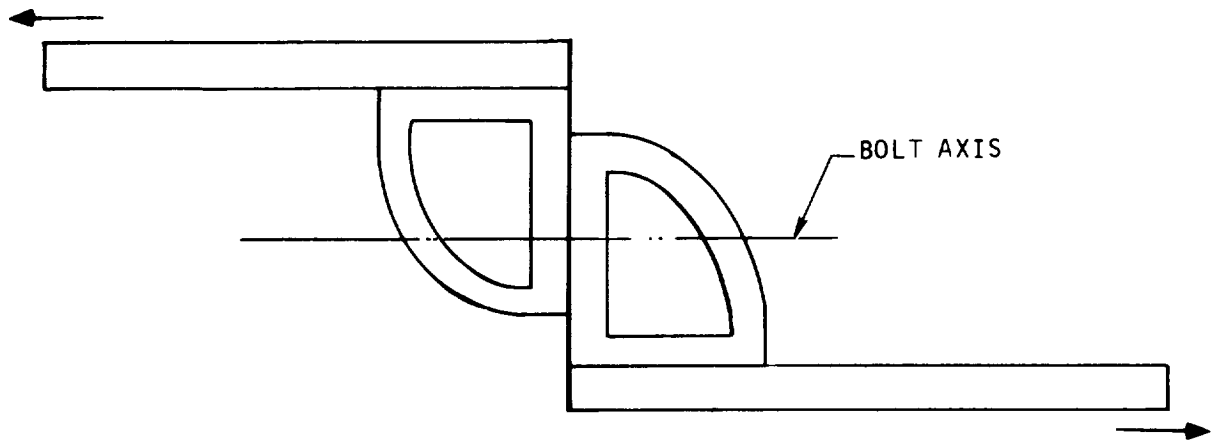
Figure 8.6-5. Flat Plate Collector Manifold Cross-Section



AIRESEARCH MANUFACTURING DIVISION
Los Angeles California

UNCLASSIFIED

67-2833
Page 8-58



A-32159

Figure 8.6-6. Revised Load Scheme



UNCLASSIFIED



F-8367

Figure 8.6-7. Flat Plate Collector Manifold
Section After Pull Test



AIRESEARCH MANUFACTURING DIVISION
Los Angeles California

UNCLASSIFIED

67-2833
Page 8-60

produced changes in the bending moment at C, an accurate estimate of the moment achieved or the moment to cause yielding was not obtained, however, comparative strength of the joint and panel was obtained.

8.6.2 Test Data Reduction

Reduction of test data included (1) determining the equivalent cycles to failure at a given pressure and (2) estimating the bending moment on the sandwich in the pull test. The equivalent number of cycles at 4000 psig listed in Table 8.6-1 above was determined by assuming that:

- (1) The specimen stress levels are proportional to internal pressure
- (2) The number of cycles to failure is related to stress as shown in Figure 8.6-8.
- (3) Minens rule for fatigue damage applies, i.e., failure occurs when:

$$L = \sum_{i=1}^L n_i / N_i$$

where L = number of stress levels tested

n_i = number of cycles at each stress level, i

N_i = number of cycles to failure for each stress level, i

The bending moment at yield for the sandwich panel is estimated to be 300 lb-in. based on a yielding load of approximately 210 lb and a 1.40-in. moment arm. The moment arm is based on the assumption that the initial geometry can be used, i.e., elastic deflections are small. The theoretical section modulus of the sandwich panel is 0.011 in.³, so the bending stress at yield is

$$\sigma_b = \frac{M}{Z} = \frac{300}{0.011} = 27,250 \text{ psi}$$

The maximum combined stress including the tensile stress due to a 210 lb load acting on the sandwich is

$$\sigma_{\max} = 27,000 + \frac{210}{0.038} = 32,500 \text{ psi}$$

Since the quoted yield strength of Hastelloy X at room temperature is about 53,000 psi, this indicates a panel strength efficiency of

$$f = \frac{32,500}{53,000} = 0.61$$



UNCLASSIFIED

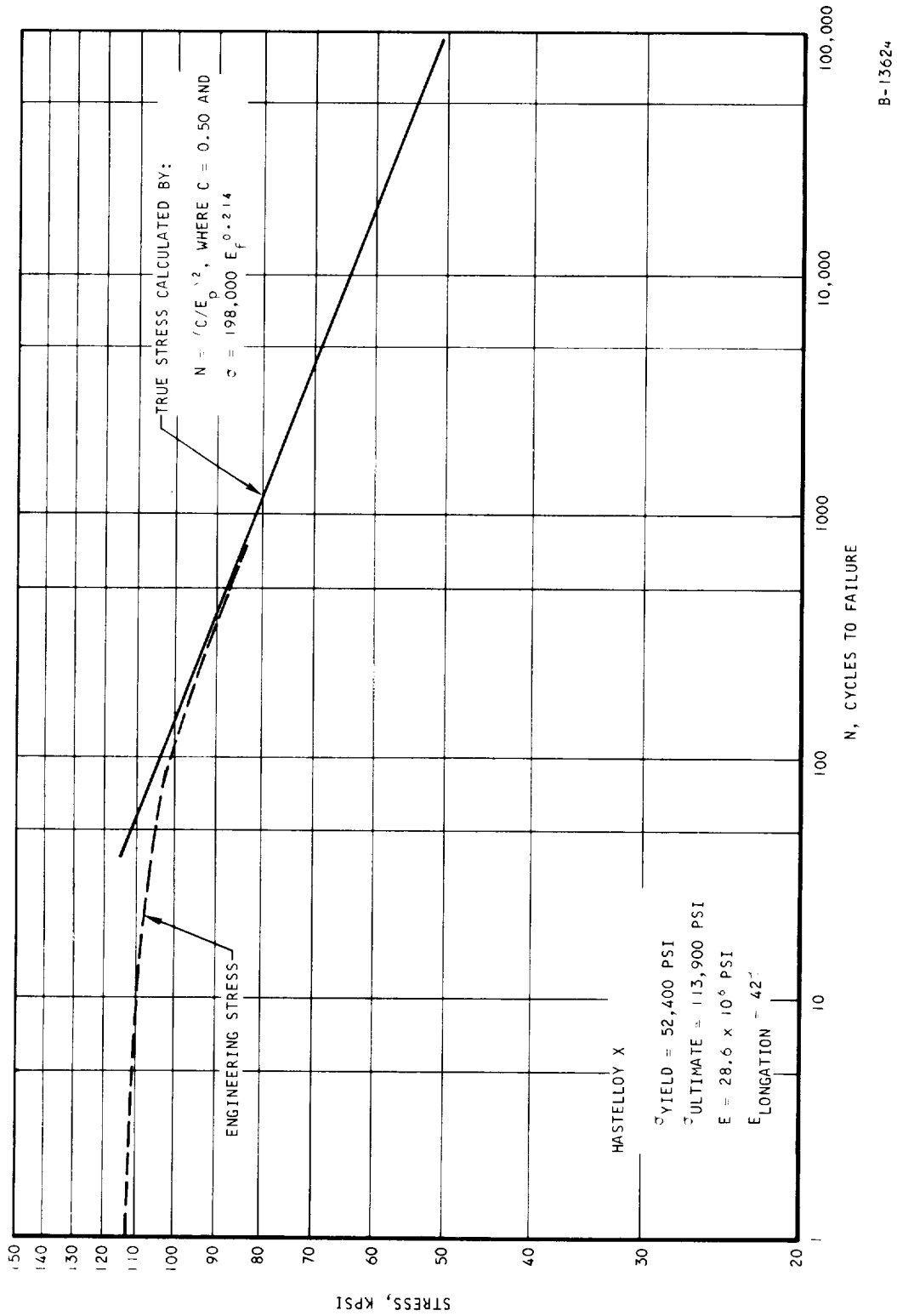


Figure 8.6-8. S-N Curve for Hastelloy X at Room Temperature



UNCLASSIFIED

This efficiency is less than expected for these panels in bending. Tests of Waspaloy panels at AiResearch indicates efficiencies of 0.80 to 0.90 for bending. Figure 8.6-9 depicts the test specimen configuration after yielding and shows the locations of local yielding.

The joints at C and C' were strong enough to load the sandwich into the yield region. Therefore, it is reasonable to conclude that the joint strength between the rings and panel is greater than the panel itself, at least up to the yield stress. One of the joints had cracked during the test. This apparently occurred after sandwich yielding, because the crack is small and loads to 1000 lb were sustained.

8.6.3 Conclusions

The following conclusions were drawn from the test results:

- (1) An infinite cycle life is predicted for the actual hardware at the 1050 psig proof pressure assuming only internal pressure is applied. A 1000-cycle life can be expected for an internal pressure of 3600 psig.
- (2) The ring-to-plate fin sandwich joint strength exceeds the plate fin sandwich strength in bending. The internal pressure tests indicates that the joint area is conservatively designed for this loading. In the actual application, additional loads due to inertia, thermal and nozzle blow-off loads may be superimposed on the internal pressure loading. The additional loads are generally small compared to the internal pressure requirements, and some reduction in ring thickness is considered to be possible.
- (3) Metallic "K" seal performance during the tests was satisfactory.

8.7 LEADING EDGE STRAIGHT SECTION

8.7.1 Test Plan

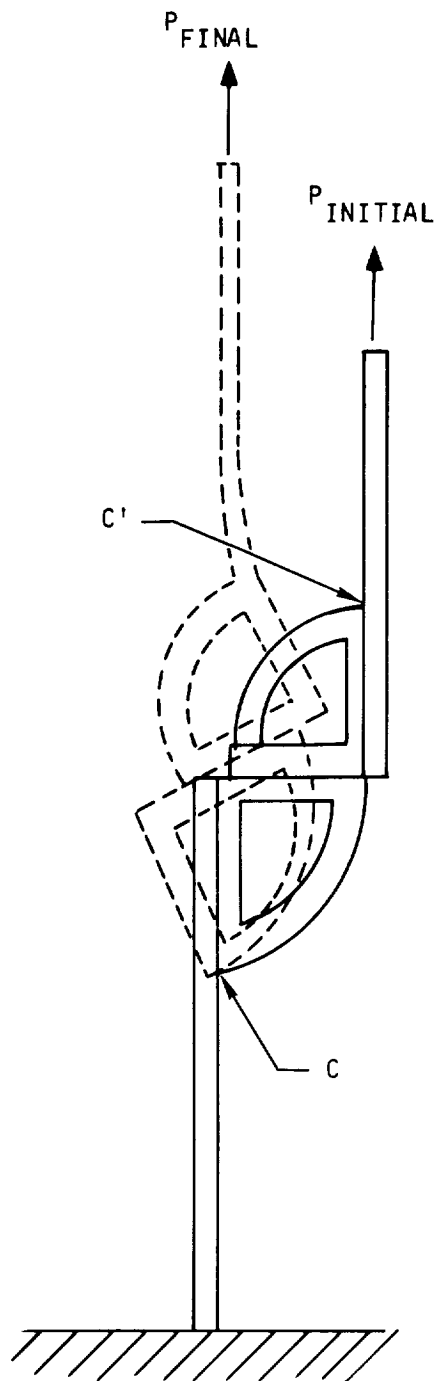
The outer body leading edge straight section test specimen shown in Figure 7.3-1 will be subjected to thermal performance testing, followed by thermal cycling in a simulated flight environment. The simulated flight environment consists of air, heated by a hydrogen-oxygen combustor to temperatures between 2500°R and 4000°R, flowing over the test section at rates between one and 6.5 lb/sec. The test section will be cooled with gaseous hydrogen at an inlet temperature of 200°F and inlet pressure up to 700 psia, at flow rates between 0.05 and 0.25 lb/sec.

8.7.1.1 Test Objective

The test objectives are to evaluate heat transfer performance in the stagnation region, the coolant flow distribution (by temperature measurement), the pressure drop characteristics, and the low-cycle fatigue performance of coolant containment in the stagnation region.



UNCLASSIFIED



NOTE:

SPECIMEN YIELDED LOCALLY
IN THE REGIONS ADJOINING
POINTS C AND C'

A-32160

Figure 8.6-9. Test Specimen Geometry After Yielding



AIRESEARCH MANUFACTURING DIVISION
Los Angeles, California

UNCLASSIFIED

8.7.1.2 Test Setup

The test specimen will be installed in a test setup as shown in Figure 8.7-2. Hydrogen coolant will be supplied to the coolant passages, and high temperature gas from the hydrogen oxygen combustor shown in Figure 8.7-2 will flow in the duct section (Figure 8.7-3) over the exterior of the test specimen.

8.7.1.3 Test Procedures8.7.1.3.1 Thermal Performance Test

(1) Thermal performance will follow the sequence shown below.

TABLE 8.7-1

Condition and Run Sequence	Hot Gas			Coolant (Hydrogen)		
	Flow, lb/sec	Temp, °R	Press, psia	Flow, lb/sec	Temp, °R	Press, ** psia
1	2	2500	*	0.0963	200	700
2	4	2500	*	0.0865	200	700
3	6	2500	*	0.0863	200	700
4	6	2500	*	0.120	200	700
5	6	2500	*	0.050	200	700
6	6	3000	*	0.0865	200	700
7	6	3500	*	0.0865	200	700
8	6	4000	100	0.0863	200	700
9	Repeat Run Number 3			Repeat Run Number 3		
10	Repeat Run Number 8			Repeat Run Number 8		

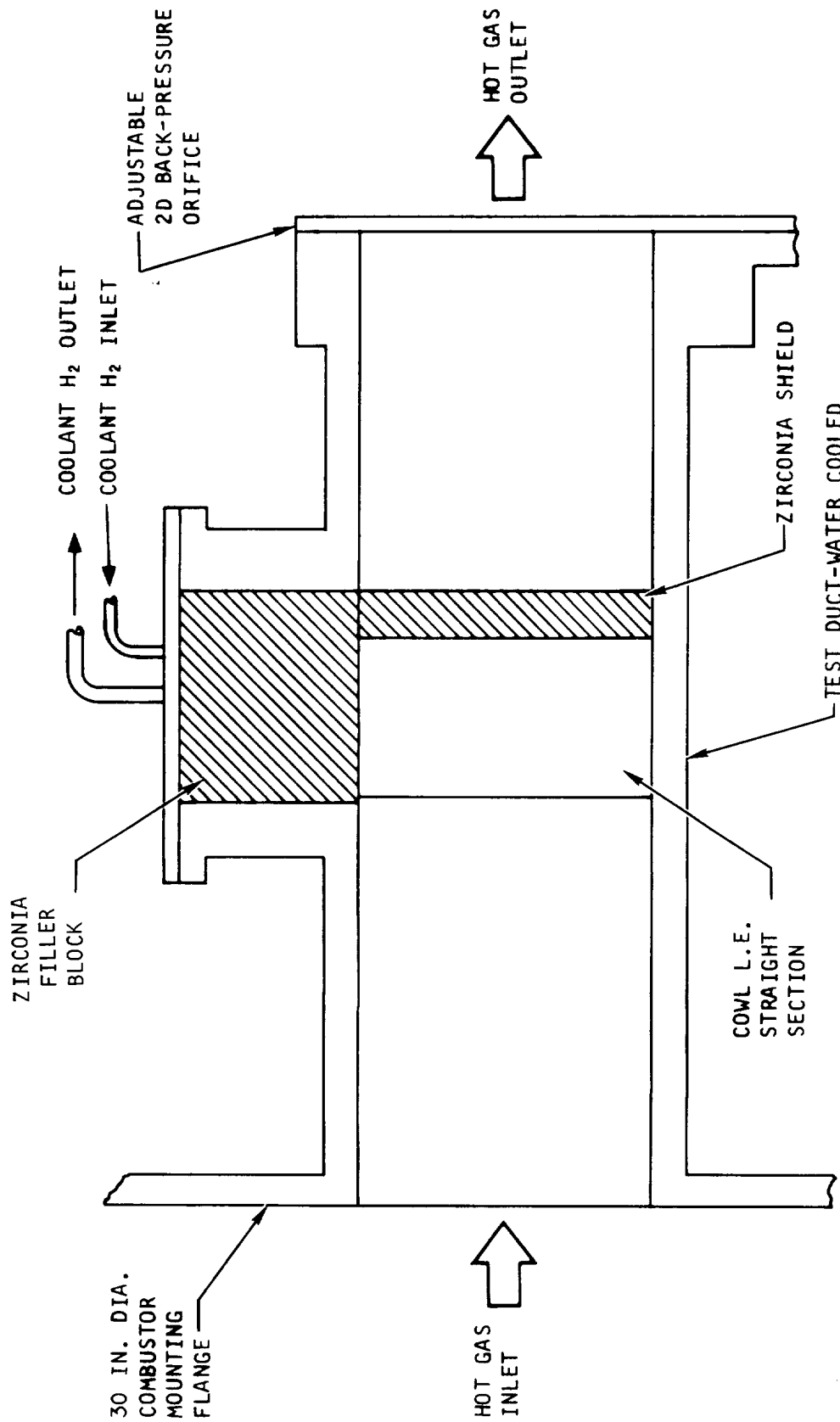
*Pressure as obtained for orifice used to obtain Condition 8.

**Pressure of 400 psia will be used for calibration of initial test section.

- (2) The temperature distribution will be determined from thermocouple temperature monitoring and by the use of temperature-sensitive paint. The paint will be applied over the entire surface of the test specimen prior to testing. It will be inspected, photographed, and replenished, as necessary, following Runs 4, 5, 6, and 7. A Thermindex temperature reference index for Hastelloy X will be provided for use with the test specimen.



UNCLASSIFIED



A-32156

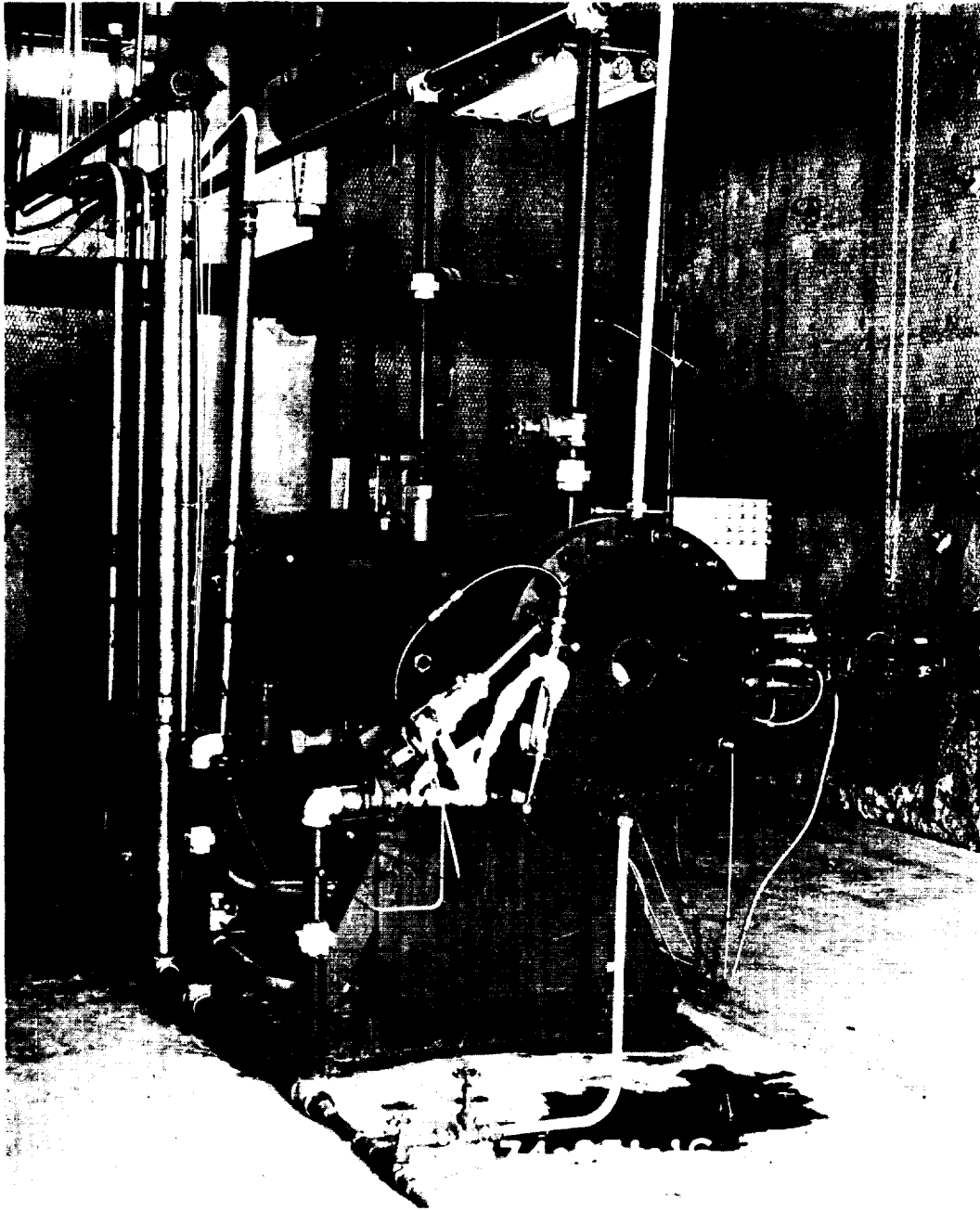
Figure 8.7-1. Straight Section Outer Body Leading Edge Test Setup



AIRESEARCH MANUFACTURING DIVISION
Los Angeles, California

UNCLASSIFIED

UNCLASSIFIED



F-8370

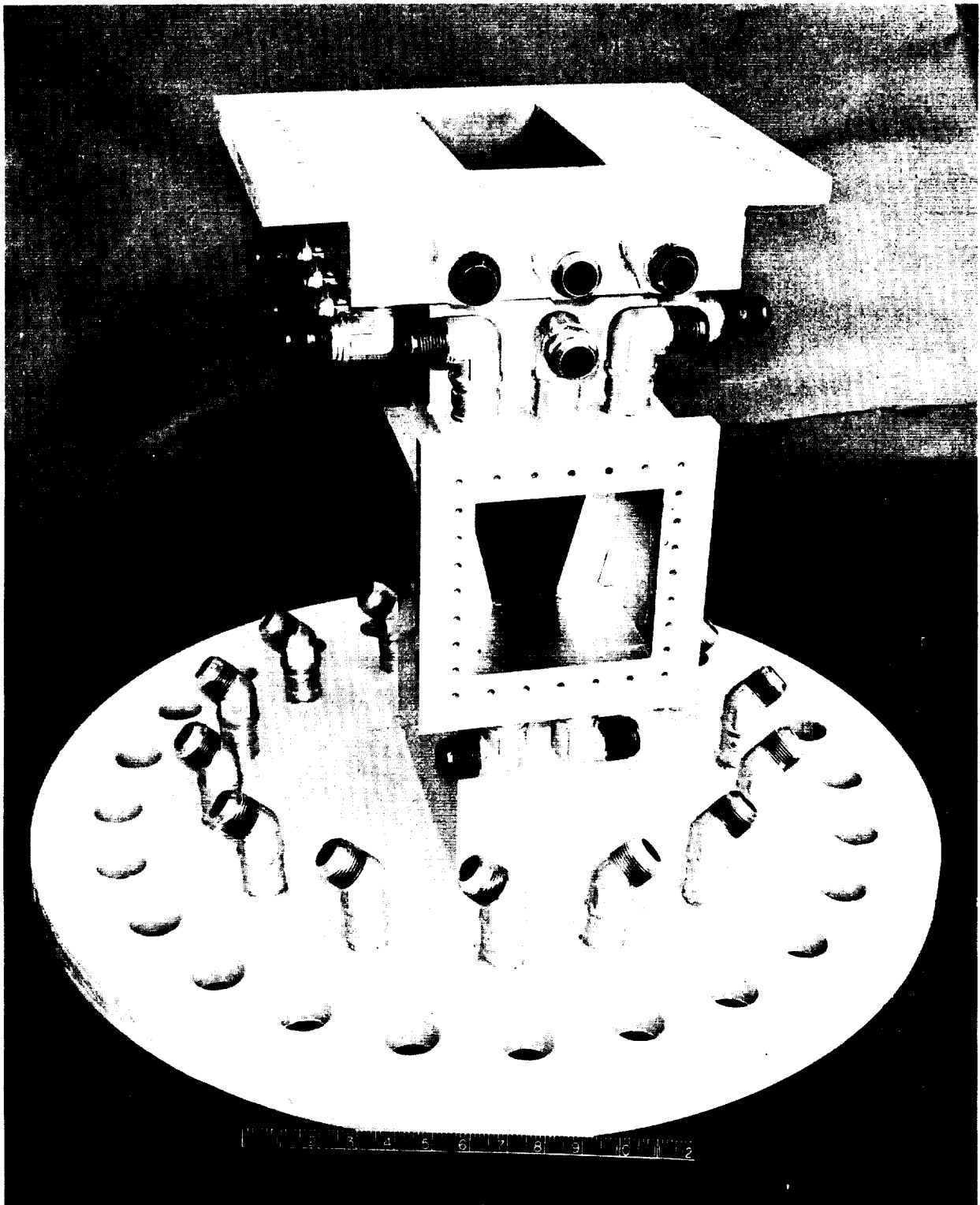
Figure 8.7-2. Hydrogen-Oxygen Combustor Setup and Test Cell



AIRESEARCH MANUFACTURING DIVISION
Los Angeles, California

UNCLASSIFIED

UNCLASSIFIED



F-8-570

Figure 8.7-3. Water-Cooled Test Duct for Straight Section
Outer Body Leading Edge Test



AIRESEARCH MANUFACTURING DIVISION
Los Angeles, California

UNCLASSIFIED

67-2833
Page 8-68

- (3) Color photographs will be taken of the test specimen following Runs 4, 5, 6, 7 and 8 to illustrate the thermal gradients indicated by the temperature indicating paint applied to the surface of the test specimen.
- (4) The following data will be recorded in the steady state condition determined by stabilized coolant outlet temperature.
 - (a) Hot gas flow data once per test condition
 - (b) Coolant flow data once per test condition
 - (c) Metal surface pressure once per test condition
 - (d) Metal surface temperature continuously

The above data will consist of gas temperatures and pressures, metal surface temperatures, orifice gas flow rates, and coolant flow rates.

- (5) The test specimen will be removed from the test fixture for inspection and documentation of the thermal paint with color photographs, as described in 2 and 3 above. At the completion of the specified runs, isotherms will be marked on the test specimen and documented by color photographs.

8.7.1.3.2 Thermal Cycling Test

- (1) Thermal cycling will be run in the same test setup, using the same instrumentation as provided in the thermal performance test.
- (2) The coolant hydrogen flow will be established. The hot gas flow will be established and the rate adjusted as the hot gas inlet temperature is varied. Condition 8, Table 8.7-1, will be used as the maximum cycle condition. The typical cycle will be as follows:
 - (a) Start (520°F) to 4000°F in five minutes
 - (b) Hold at 4000°R for test specimen metal temperature to stabilize (approximately one min)
 - (c) 4000°R to 1500°R in two min
 - (d) Hold at 1500°R for one min
 - (e) 1500°R to 4000°R in two min
 - (f) Repeat steps (b) through (e) for 100 cycles or until failure, whichever occurs first.
- (3) Record all data on the first, ninth and every 10 cycles thereafter.



- (4) For cycles where data is not recorded, hot gas inlet temperature and pressure, metal surface temperatures, and coolant outlet temperatures will be monitored.
- (5) A leak check by the pressure decay method using nitrogen will be made following each 10 cycles or as close to that increment as is practical from a run sequence standpoint.

During this reporting period, an isothermal pressure drop calibration test was completed, using air. Figure 8.7-4 is the resulting $\rho\Delta P$ curve from the isothermal air tests (corrected to include the inlet and exit tube velocity heads).

8.7.3 Future Action

During the next reporting period, the leading edge test sections will be installed in the test setup at the NAR thermal laboratory and subjected to thermal performance and thermal cycling tests.

8.8 SUPPORT STRUT

8.8.1 Test Plan

Support strut testing will be conducted to evaluate the strut design in a supersonic, simulated operational environment, consisting of air, heated by a hydrogen-oxygen combustor to temperatures between 1500°R and 4500°R and then expanded isentropically to flow over the test specimen at supersonic velocities. The testing will consist of a calibration using water cooling, a thermal performance test using gaseous hydrogen cooling, and a thermal cycling test also using gaseous hydrogen cooling.

8.8.1.1 Test Objective

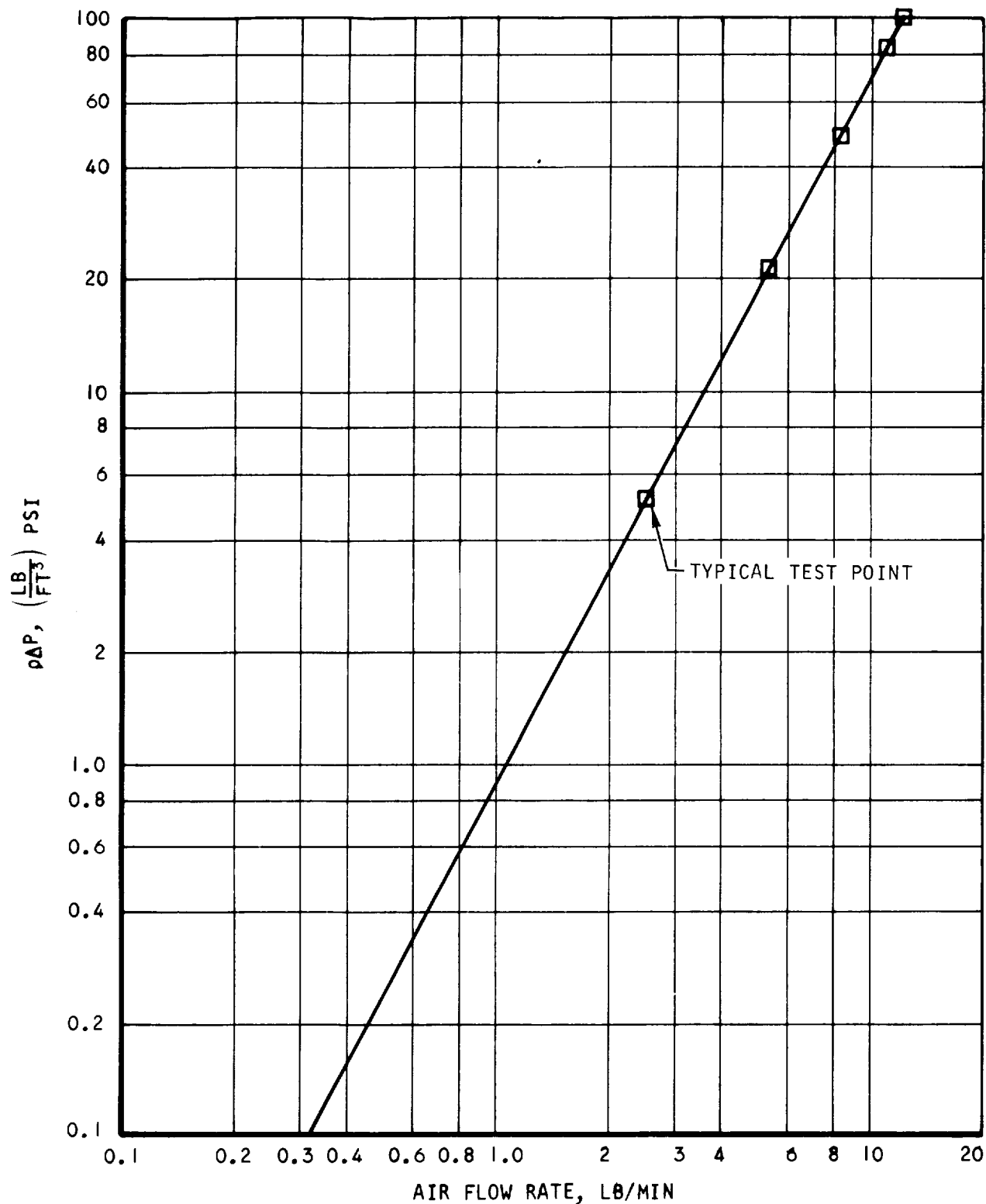
The objectives of the support strut testing are to verify the analytical techniques used for analysis of leading edge heating and to evaluate the effects of shock impingement and of heat transfer in supersonic flow of hydrogen-air combustion products. In addition, panel-to-strut interface cooling, low cycle fatigue of strut and panels, and strut pressure drop characteristics will be evaluated.

8.8.1.2 Test Setup

The strut test specimen assembly will be attached to the outlet end of a gaseous hydrogen-oxygen combustor, which will provide a reservoir of heater air at temperatures up to 4500°R and pressures up to 300 psia for expansion through the two-dimensional supersonic nozzle ($M = 2.3$) at the inlet to the strut test specimen assembly. The support strut will be cooled with 200°R and ambient gaseous hydrogen. The test specimen support ducting will be water cooled.



UNCLASSIFIED



A-32239

Figure 8.7-4. Isothermal Pressure Drop Calibration for Leading Edge Straight Section



AIRESEARCH MANUFACTURING DIVISION
Los Angeles, California

67-2833
Page 8-71

UNCLASSIFIED

8.8.1.3 Test Procedure8.8.1.3.1 Calibration Test

- (1) The test run schedule is shown below. Tests will be performed with water coolant only.

Hot Gas Conditions

Run	Flow Rate, lb/sec	Total Temp, °R	Total Press, psia
1	8.2	1500	200
2	6.1	2500	200
3	5.0	3500	200
4	4.2	4500	200
5	12.3	1500	300
6	9.2	2500	300
7	7.5	3500	300
8	6.2	4500	300
9	4.2	4500	200
10	6.2	4500	300

- (2) The water coolant flow for the various coolant passages are as follows:
- (a) Adapter section: 24 gpm at 100 psig (two routes at 6 gpm and 18 gpm)
 - (b) Side walls: 18 gpm at 100 psig
 - (c) Strut leading edge: 2.25 gpm at 100 psig
 - (d) Strut sides: 1.5 gpm at 100 psig
 - (e) Support panels (Two panels, one route): 18 gpm at 100 psig
- (3) Temperature distribution will be determined from thermocouple temperature monitoring and by the use of temperature sensitive paint. The paint will be applied over the entire surface of the strut prior to testing. It will be inspected, photographed, and replenished as necessary. Isotherms will be marked on the test specimen and documented by color photographs. A Thermindex temperature reference index for Hastelloy X will be provided for use with the test specimen.



- (4) The coolant and hot gas flows for each run will be established and when the steady state condition (indicated by coolant outlet temperature stabilized to 2°F per min drift) is reached. The following data will be recorded:

- (a) Hot gas flow data once per test condition
- (b) Coolant flow data once per test condition
- (c) Metal surface pressure once per test condition
- (d) Metal surface temperature continuously

The above data will consist of gas temperatures and pressures, metal surface temperatures, orifice gas flow rates, and coolant flow rates.

8.8.1.3.2 Thermal Performance Test

The thermal performance test will be run in the same setup as the calibration test, except that gaseous hydrogen will be supplied to the strut coolant passages.

- (1) The test run schedule is show below.

Hot Gas Condition

Run	Flow Rate, lb/sec	Total Temp, °R	Total Press, psia
1	6.2	1500	300
2	6.2	2500	300
3	6.2	3500	300
4	4.2	4500	300
5	6.2	4500	300
6	8.2	4500	300

- (2) Coolant flows will be as follows:

- (a) Water

Adapter section: 24 gpm at 100 psig

Side walls: 18 gpm at 100 psig



(b) Hydrogen

Strut leading edge: 0.020 lb/sec at 700 psia and 200°R max

Strut sides: 0.025 lb/sec at 700 psia and 520°R

Support panels: 0.11 lb/sec at 500 psia and 520°R

- (3) Temperature distribution will be determined the same as for the calibration test
- (4) The steady state flow data will be obtained in the same manner as for the calibration test runs.

8.8.1.3.2 Thermal Cycling Test

The thermal cycling test will be run in the same setup as the thermal performance test. The hot gas temperature will be cycled between 1500°R and 4500°R, with the flow rate maintained at 6.2 lb/sec at 300 psi (reservoir).

- (1) After the coolant and hot gas flows have been established, the hot gas inlet temperature will be varied as follows:
 - (a) Start (520°R) to 4500°R in five minutes.
 - (b) Hold at 4500°R for test specimen metal temperature to stabilize (approximately one min).
 - (c) 4500°R to 1500°R in two minutes
 - (d) Hold at 1500°R for one minute
 - (e) 1500°R to 4500°R in two minutes
 - (f) Repeat steps (b) through (e) for 100 cycles or until failure, whichever occurs first.

Record all data on the first, ninth and every 10 cycles thereafter.

For cycles where data is not recorded, hot gas inlet temperature and pressure, metal surface temperatures, and coolant outlet temperatures will be monitored.

A leak check by the pressure decay method using nitrogen will be made following each 10 cycles, or as close to that increment as is practical from a sequence standpoint.

8.8.2 Future Action

During the next reporting period, fabrication of the NAR facility test equipment will be completed and the support strut test sections will be subjected to the calibration, thermal performance, and thermal cycling tests.



8.9 TUBE-MANIFOLD JOINT SPECIMENS

Tests were performed to verify low cycle fatigue performance of a tube joined to a cold manifold joint for temperature cycling of the tube. The specimens, fabricated from an 0.150 in. diameter, 0.007 in. wall CRES 347 tube and an 0.500 in. Hastelloy X block, are illustrated in Figure 8.9-1. The configuration simulated the fuel injection method used for the first injector station on the outer shell, at the inlet crossover manifold.

An induction coil was used as the heating source for the tube and the base was cooled with water, as illustrated in Figure 8.9-2.

8.9.1 Test Results

Specimens S/N 1 and S/N 2 were cycled at a tube-to-base temperature difference of 800°F for 500 cycles. A single induction coil was used. The cycle conditions were:

Cycle time: 15.3 sec

Tube cycle (200-1200°F): 3.3 sec

Base temperature at tube peak temperature: 400°F

No thermal cracks were observed with dye penetrant checking or by microscopic examination after 500 cycles.

Specimen S/N 1 was cycled at a tube-to-base temperature difference of 1000°F for 1000 cycles. A separated induction coil was used. The cycle conditions were:

Cycle time: 10.5 sec

Tube cycle (200-1270°F): 0.7 sec

Base temperature at tube peak temperature: 240°F

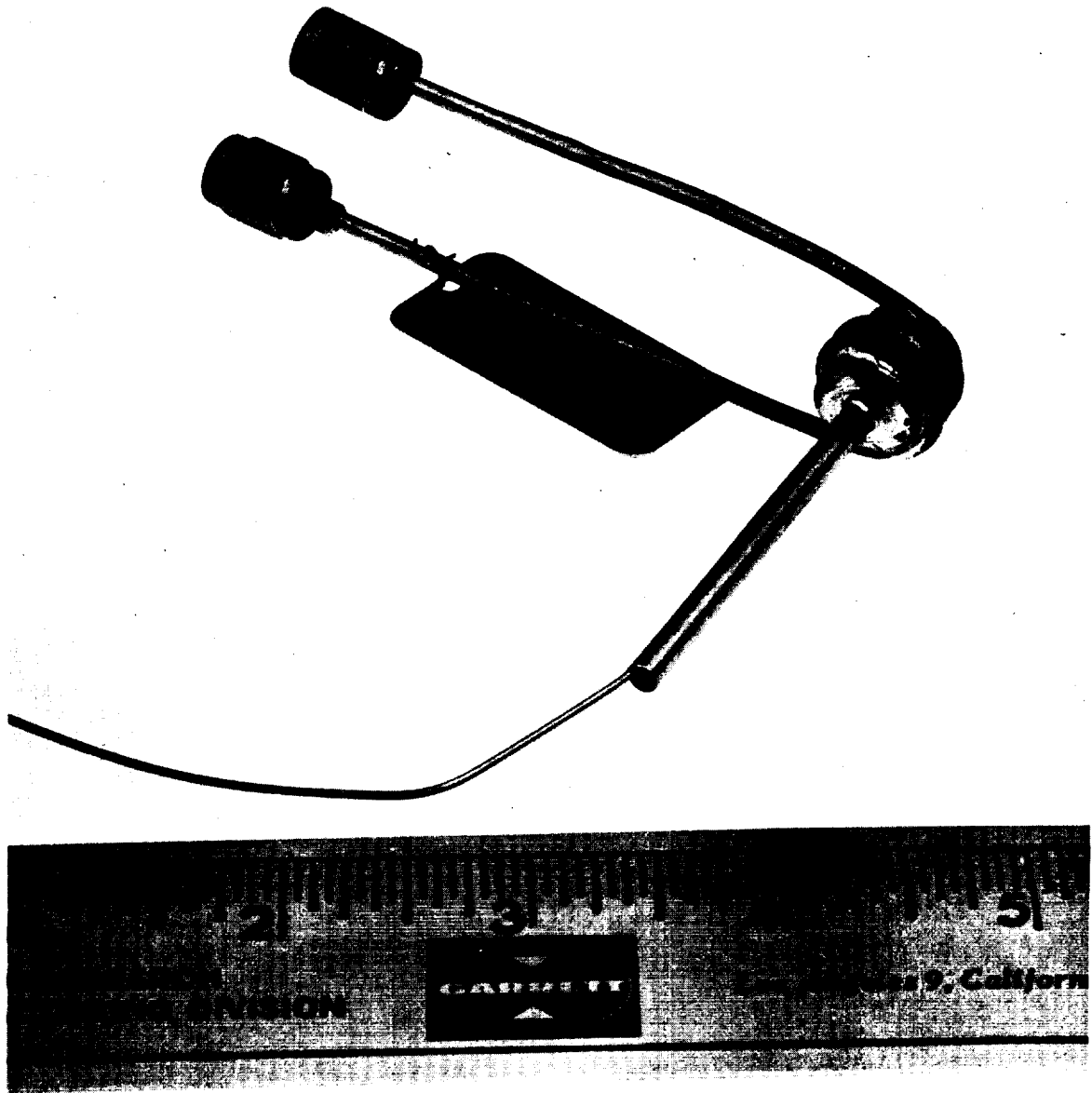
After 1000 cycles, microscopic and dye penetrant checks revealed no thermal cracking in the tube-base joint area.

8.9.2 Conclusions

The above testing demonstrated the integrity of this particular type of joint under severe thermal cycling. The use of stainless steel tubing (Type 347) in this application, in lieu of Hastelloy X tubing, will be satisfactory.



UNCLASSIFIED



61208-2

Figure 8.9-1. Manifold Joint Specimen Tube



AIRESEARCH MANUFACTURING DIVISION
Los Angeles, California

UNCLASSIFIED

67-2833
Page 8-76

UNCLASSIFIED

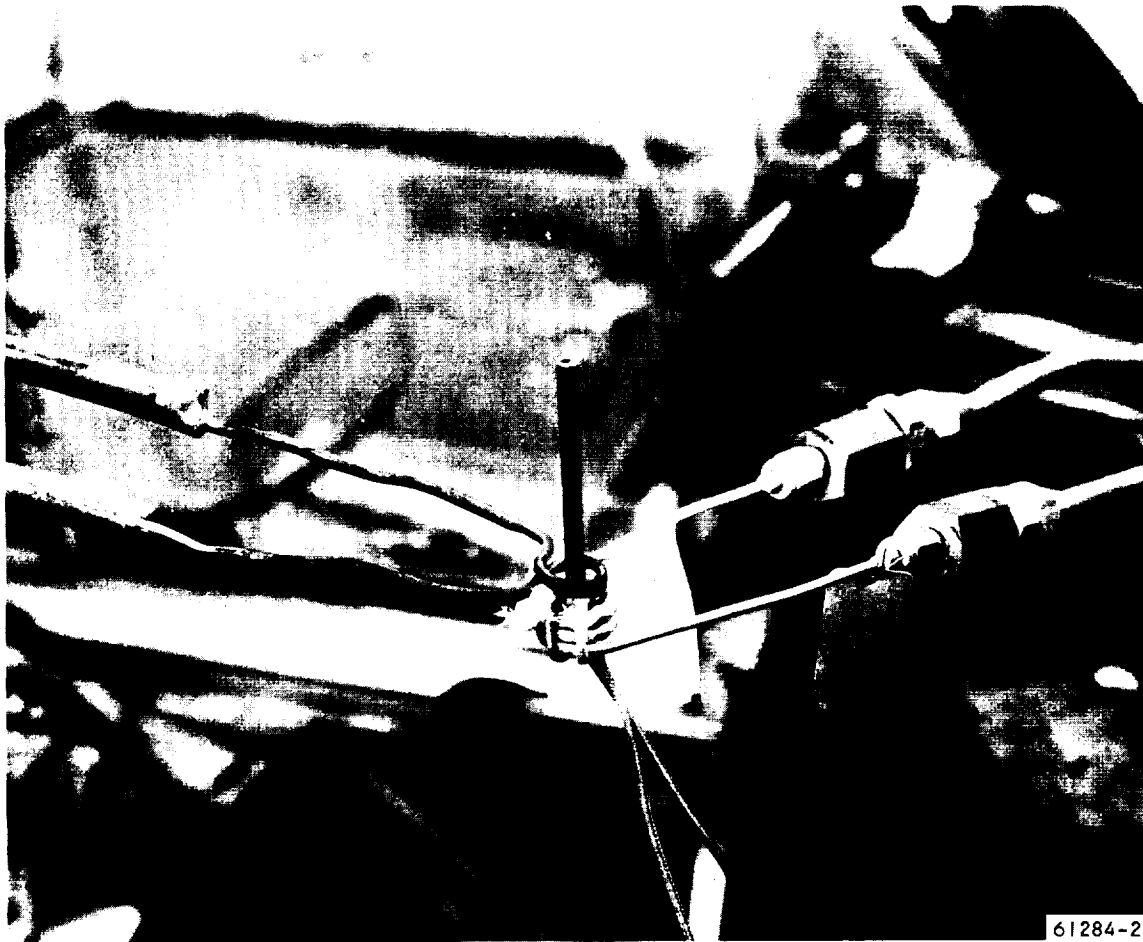


Figure 8.9-2. Manifold Joint Specimen Tube Test Setup



AIRESEARCH MANUFACTURING DIVISION
Los Angeles, California

UNCLASSIFIED

67-2833
Page 8-77

UNCLASSIFIED

9. FUTURE ACTION

Activities planned for the next reporting period will reflect the impact of revised load conditions on engine component design. The current design will be modified in those areas where the basic design concept or configuration is affected. Because the new loads do not affect basic design concepts, manufacturing operations, or envelopes of the inner body (inner shell and nozzle), no inner body design changes will be made at this time.

9.1 FULL-SCALE COMPONENT DESIGN REVISION

The leading edge tip thermal design, the inlet spike structural design, and the outer shell structural design are being revised to reflect the new design load conditions. Layout drawings and detail design drawings will be prepared or revised, as appropriate, and released for fabrication.

9.2 ENGINE DYNAMIC ANALYSES

The engine dynamic analyses will be revised to consider the redefined design configurations, thrust measuring system, and aircraft-to-engine mounting interface. These analyses will be aimed at estimating resonant frequencies in the engine and its components, and will be used to verify the magnitude of inertia and vibration loads used in the component designs.

9.3 INLET SPIKE ACTUATOR DESIGN

The actuator design will be reviewed to evaluate a change from pneumatic to hydraulic operation and changes in bearing surface dimensions by use of a fixed piston and outer sleeve as opposed to a translating piston and outer sleeve. The change to hydraulic operation is desirable to improve dynamic response and for overall simplification of the actuator mechanism. The increased loads currently being used have resulted in considerably increased bearing pressures, which in turn have led to considering methods of increasing the bearing area.

9.4 VIBRATION MODEL DESIGN

Modification of the vibration model designed to the old load conditions and layout and detailing of the revised design will be accomplished during the next reporting period.



UNCLASSIFIED

UNCLASSIFIED

9.5 OUTERBODY LEADING EDGE COOLING SYSTEM

The increased heat fluxes on the leading edge stagnation area due to X-15A-2 shock field conditions, as opposed to free stream conditions, obviate the design previously evolved for the leading edge stagnation area. Layout design and detailing for fabrication, as well as start of fabricating a revised design, is scheduled. The revised design will be incorporated into a leading edge straight section for evaluation.

9.6 COMPONENT TEST ASSEMBLY DESIGN

Detail design of the test assembly and adapter for the inner body full-scale component will be completed and fabrication started. The adapter will be applicable also to the inlet spike with relatively minor changes. Layout and detail design of the leading edge test assembly and adapter will be completed and fabrication started. Layout design of the outer shell test assembly and adapter will be completed.

9.7 ENGINE SURFACE INSULATION

Analytical evaluation of surface insulations for use in the engine will be conducted. Experimental work is not planned at this time, but will be required if the use of insulation shows promise and can be established as acceptably reliable on the basis of available experimental data.

9.8 "ELECTROSHAPE" FORMING EVALUATION

After completing compound-curved model fabrication, evaluation of "Electro-shape" forming is planned. This evaluation will include the use of a specially instrumented die equipped with high response pressure sensors and of stainless steel shells to confirm the results obtained from pressure measurements. The die to be used in the evaluation is of the same configuration as the one used in compound-curved model shell forming. Various techniques to shape the pressure field during forming will be attempted.

9.9 LEADING EDGE TESTING

Flow testing using the initial leading edge test section is in process. Fabrication of test sections using the old design will be completed and fabrication of test sections incorporating the revised leading edge design will be in process. In addition to flow and thermal cycle tests on the test sections, burst tests will be run on both the test sections that complete the flow and thermal cycle test, and on untested test sections.

9.10 STRUT TESTING

Strut Testing with supersonic flow over strut at Mach numbers appropriate to the strut location in the engine will be run. Both steady state and thermal cycle tests will be included, the first to establish the shock and flow patterns around the strut, and the second to evaluate the low cycle fatigue capability of the current strut design.



UNCLASSIFIED

9.11 THERMAL CYCLE TESTING

Following evaluation of data currently available from thermal cycle tests of flat panels, additional panels will be fabricated from parts already available. Modifications will be incorporated into these subsequent panels to the extent permitted by the basic concept.

9.12 FULL-SCALE COMPONENT FABRICATION

Fabrication of all full-scale components (innerbody, leading edge, inlet spike and outer shell) will be carried on. Brazing of the nozzle assembly is expected to be started during the reporting period. Tooling delivery schedules are such that activities for the other components will be primarily aimed at fabrication of detail parts other than the shells. In all cases, however, shell fabrication will be carried through the preforming stage for the experimental components, up to the point of final sizing in the "Electroshape" machine.

9.13 FUEL CONSERVATION

In addition to the evaluation of surface insulations in the engine, other means of limiting fuel consumption during both engine operation and ascent and descent phases of a test mission will be evaluated. These include the use of individual coolant control valves on each of the four coolant flow routes in the engine; water vapor blanket and the use of pure nickel hot shells to reduce cross-section temperature difference and permit operation at higher coolant outlet temperatures. The feasibility of tighter close off of the inlet spike against the leading edge will be considered.

